



TECHNISCHE  
UNIVERSITÄT  
WIEN

DISSERTATION

# Fast and potentially on-line gas chromatographic approaches for the analysis of volatile emissions from lithium-ion batteries

prepared for the purpose of obtaining the academic degree Doctor of Technical Science  
(Doktor der technischen Wissenschaften)

under the supervision of

**Ao.Univ.Prof. Dipl.-Ing. Dr.techn. Egon Erwin Rosenberg**

Institute of Chemical Technologies and Analytics, E-164

submitted at the Vienna University of Technology  
Faculty of Technical Chemistry

by

**Chrysoula Kanakaki, M.Sc.**

Matriculation number: 1128881  
Lustkandlgasse 35/1-2, A-1090, Vienna

Vienna, 2018

.....  
Chrysoula Kanakaki



## ***Kurzfassung***

Ziel dieser Arbeit war die Entwicklung und der Einsatz verschiedener gaschromatographischer Methoden für die Analyse von flüchtigen organischen und anorganischen Substanzen, die von Lithium-Ionenbatterien (LIBs) und ihrer Bestandteile unter Bedingungen des normalen Gebrauchs und des Missbrauchs abgegeben werden

Gaschromatographie mit massenspektrometrischer Detektion (GC-MS), und auch GC mit dem erst vor kurzem eingeführten He-Plasmaentladungsdetektor (*barrier discharge ionization detector*, BID) wurden für *ex situ* Messungen von thermisch abgebauten Elektrolytmischungen eingesetzt.

Die detaillierte Untersuchung von Komponenten unterschiedlicher Flüchtigkeit, wurde mit GC-MS und Headspace-GC-MS Messungen unter Verwendung verschiedener analytischen Säulen, durchgeführt.

Auf Basis der Erhebung des heutigen Wissensstandes über die Abbauprodukte und vorgeschlagenen Reaktionsmechanismen, wurde eine kritische Betrachtung der indentifizierten Komponenten vorgenommen. Eine Vielzahl an Abbauprodukten wurde identifiziert, und zahlreiche neue flüchtige Abbauprodukte und deren Bildungswege vorgeschlagen. Auch Verbindungen mit hoher toxikologischer Bedeutung, wie das Neurotoxin Diisopropylflourophosphat, wurden identifiziert.

Im Vergleich der angewandten Detektionsmethoden konnte gezeigt werden, dass der BID bei der Detektion von Permanentgasen und auch von sehr flüchtigen Verbindungen im Vorteil ist, während massenspektrometrische Detektion eine höhere Empfindlichkeit für ein breiteres Feld an Analyten zeigt und die Möglichkeit ihrer Identifikation bietet.

Zusätzlich wurden *in situ* Messungen mittels GC-MS und der FTIR-GC-MS Konfiguration an kommerziell erhältlichen wie auch am AIT assemblierten LIB-Zellen durchgeführt.

Zahlreiche Abbauprodukte der Elektrolytlösung von Proben, die unterschiedlichen elektrochemischen Bedingungen ausgesetzt worden waren, konnten identifiziert werden. Dabei wurde das theoretische vorhergesagte Verhalten mit den praktischen Beobachtungen verglichen.

Durch die Kombination der verbesserten zeitlichen Auflösung, durch das FTIR und der Selektivität des MS, konnte die Eignung der entwickelten Methode für on-line Messungen von flüchtigen Emmisionen von LIB's gezeigt werden. Um die Zeitauflösung der GC-MS-Messungen zu verbessern, wurde die Möglichkeit der Verwendung der sogenannten Vacuum Outlet (VO)-, oder auch Niederdruck (Low Pressure, LP)-GC-MS für die Anwendung im Bereich der Untersuchung flüchtiger LIB-Emissionen anhand von sehr flüchtigen Standards erforscht.

Eine detaillierte Studie aller relevanten Parametern, dieser Technik wurde durchgeführt. Dadurch konnte gezeigt werden, dass sich die Leistungsfähigkeit dieser Technik durch die Verwendung von Vorsäulen größerer Länge und kleinerer Innendurchmesser, oder auch von längeren analytischen Säulen mit einer

höheren Schichtdicke für die Untersuchung von sehr flüchtigen Substanzen, verbessert. Allerdings verringert sich bei einer derartigen Wahl der Betriebsbedingungen der Vorteile der VO-Technik, da die Laufzeit sich immer mehr der des Betriebs unter normalen Bedingungen annähert.

Um den unter optimalen Bedingungen erzielbaren Geschwindigkeitsgewinn zu testen, wurden Modellsubstanzen mittlerer Flüchtigkeit ausgewählt. Bei diesen beiden Modellsubstanzen handelt es sich um zwei der am häufigsten anzutreffenden UV-Filter-Substanzen, die wahrscheinlich endokrine Wirkung zeigen. Diese wurden nach entsprechender Anreicherung mittels Festphasenmikroextraktion (SPME) mit LP-GC-MS bestimmt.

Obwohl die Anwendung der LP-GC-MS's zur schnellen Bestimmung von sehr flüchtigen Verbindungen, wie der flüchtigen Zersetzungsprodukte der LIB-Elektrolyte nur bedingt von Nutzen ist, kann man für weniger flüchtige Verbindungen eine signifikante Verkürzung der Analysendauer bei gleichzeitiger Steigerung der Empfindlichkeit erwarten.

Im Gegensatz dazu stellt die Verwendung des GC-BID für die sensitive Detektion von Permanentgasen und auch von FTIR-GC-MS für das on-line Monitoring der emittierten Gasphase, eine wertvolle Erweiterung des Spektrums analytischer Techniken im Bereich der LIB-Forschung dar, die die Entwicklung von sichereren und effizienteren LIB's unterstützen kann.

## ***Abstract***

In the frame of this work, different gas chromatographic approaches were evaluated and applied for the analysis of volatile organic and inorganic species emitted from lithium ion batteries (LIBs) and their components used under normal and abuse conditions.

Gas chromatography coupled to a mass spectrometer and the newly released barrier discharge ionization detector (BID) was employed for the *ex situ* measurements of thermally degraded electrolyte mixtures. Selective investigation of compounds belonging to different volatility groups was performed by GC-MS and headspace GC-MS measurements using different analytical columns.

After summarizing the current knowledge on degradation products and proposed reaction mechanisms, critical evaluation of the identified compounds was performed. A wide range of degradation products was identified, with several new volatile compounds and formation pathways being proposed. Compounds with high toxicological relevance were also identified, like the classified neurotoxin diisopropylfluorophosphate.

When the applied detection methods were compared, the significance of the BID in the detection of permanent gases and highly volatile species was demonstrated, while the MS showed increased sensitivity for a wider range of analytes and enabled their identification.

*In situ* measurements of in house-assembled and commercially available cells were additionally performed, using a GC-MS and an FTIR-GC-MS configuration. Degradation products of the electrolyte solution were identified for samples undergoing different electrochemical conditions, while the theoretical characteristics of certain materials were also compared with their actual performance. Utilizing the increased time resolution provided by the FTIR and the selectivity of the MS, the applicability of the developed method in on-line measurements of LIB volatile emissions was demonstrated.

In order to decrease the time requirements of the measurements the Vacuum Outlet (or Low Pressure) GC-MS was investigated for potential application in the field of LIB emissions, using standards of highly volatiles compounds. A detailed study of all chromatographic parameters affecting this fast GC technique was performed, proving the improved performance when longer and wider restrictions as well as longer and thicker film analytical columns are used for the analysis of highly volatile compounds. However, the advantages of VO are compromised when such compounds are targeted. In order to test the performance of the technique under optimum conditions, a set of compounds with intermediate volatilities and potential endocrine disruptive activity was investigated. In particular, two of the most widely used UV filters were analyzed with a fully optimized LP-GC-MS method, employing solid phase micro-extraction (SPME) for the sample extraction and pre-concentration.

While the applicability of the VO in the fast determination of highly volatile compounds, like the emitted gases from LIBs, proved to be compromised, for less volatile compounds significant gains in time-resolution and sensitivity can be expected. Furthermore, the use of GC-BID for the sensitive detection of permanent gases and FTIR-GC-MS for on-line monitoring of the overall gas species, do represent useful additions to the group of analytical techniques employed in the investigated field and will facilitate the development of safer and more efficient LIBs.

## ***Acknowledgement***

First and foremost, I would like to express my heartfelt gratitude to my supervisor Prof. Erwin Rosenberg for giving me the opportunity to do my PhD thesis in his research group. I would like to thank him for his guidance, the invaluable advice and fruitful discussions, the freedom to explore different analytical concepts, but also for his time and patience when revising my thesis.

I am grateful to our project partners from the Austrian Institute of Technology (AIT) and the companies Shimadzu and i-RED for the excellent co-operation. In particular, I would like to deeply thank Dr. Irina Gocheva for the unlimited support, the thought-provoking suggestions and for not only her time but also her friendship. I am also thankful to Alfred Amon for his valuable input in the *in situ* experiments of the Li-ion cells; Prof. Atanaska Trifonova for accepting me at her working group for my final measurements; Mr. Roman Binder and Dr. Peter Walla for the technical support and Dr. Wolfgang Märzinger for the construction of the FTIR system and the evaluation of the infrared data.

I am additionally indebted to the Restek Corporation for kindly providing us with a number of GC columns, and especially to Jaap de Zeeuw for all his support and stimulating discussions.

I also gratefully acknowledge the financial support of this study, provided by the Austrian Research Promotion Agency (FFG, Project “SiLithium”, Project Number 835790). I would like to express my gratitude to the Austrian Research Institute of Chemistry and Technology (OFI) for their trust and for the flexibility in my working schedule, allowing me to finish my studies, and particularly to Dr. Michael Pyerin, Dr. Veronica Osorio and Dr. Nicole Steiner-Reischutz.

For their priceless contribution to the experimental work I am particularly obliged to Özlem Yilmazcan, one of my dearest friends and most favorable working partners, Natalie González Liste, Irantzu Etxebarri, and last but not least Florian Doubek, who provided some much needed humor and entertainment in what could have otherwise been a somewhat stressful laboratory environment.

My time at the Vienna University of Technology was made enjoyable in large part due to the many friends and working partners that became a part of my life. For this reason I would like to thank Winfried Nischkauer, Vanessa Nuernberger, Maria Antoniadou, Klaus Bonazza, Justyna Plotka, Paulina Bigus, Jovana Teofilovic, Vera-Louiza Koulouvatou, Haruka Minemura, Haruna Nagai, Lamprini Ramopoulou, Alina Lanaridi, Korina Manolidi, Vaggelis Trikas, Mary Paulou, Sylwia Socha, Silvie Surmová, Teresa Fernandez-Rosel, Marina Martínez, Jacobo Seijas, Andreas Nagl, Ivita Janovska and the numerous other past and present group members that I have had the pleasure to work with or alongside them.

My deepest appreciation is also extended to Prof. Jacek Namiesnik, Dr. Błażej Kudłak and Dr. Tomasz Dymerski for having me in their group during my short-term internship in Poland, to all my professors and

colleagues at the MSC Euromaster Summer School of 2015, and to Prof. Nikolaos Thomaidis for his trust and immeasurable support during my studies.

I would like to sincerely thank Dr. Svetlana Drozdova-Zaimoglu for the theoretical and practical training on the gas chromatographic and the mass spectrometric systems and for providing me with all the necessary knowledge concerning the use and troubleshooting of GC/MS instruments. She has been a precious and motivational friend, encouraging me to grow not only as a chemist but also as an instructor and independent thinker.

I would also like to thank one of the most caring people I have ever met, Anna Satzinger, for her kindness, her friendship and her very important help with the administrative work.

Since friends are our chosen family, I would be remiss if I didn't acknowledge the love and support of some of my best friends throughout the years. Stratis Papaefstratiou, Eleftheria Stavra, Chrissa Tsiri, Anna-Maria Kosso, Violeta Borova, Maria Masha Babak, Mireille Pelletier and Christos Merentitis, Agapi Tavladaki and Zois Kyristizis, thank you for the unending encouragement and support.

I am eternally obliged to Apostolos Marios Kotrotsos, whose humor has rescued me from peril more times than I can recall, and whose tolerance of my occasional short temper is a testament in itself of his unyielding devotion and love.

Finally, and most importantly, I would like to thank my parents, Theodora Argiana and Nikolaos Kanakakis, whose innumerable sacrifices, quiet patience, unwavering love and faith in me were undeniably the bedrock upon which my entire life has been built.



## ***Abbreviations***

### **A**

AAS - atomic adsorption spectroscopy

AC - alternating current

AES - atomic emission spectrometry or Auger electron spectroscopy

AFM - atomic force microscopy

ARC - accelerating rate calorimetry

ATR - attenuated total reflectance

### **B**

BE - magnetic-electric

BID - barrier discharge ionization detector

### **C**

CCD - charge coupled device

CE - capillary electrophoresis

CGC - capillary gas chromatography

CI - chemical ionization

CV - cyclic voltammetry

### **D**

DBD - dielectric barrier discharge

DC - direct current

DEC - diethyl carbonate

DEDOHC - diethyl 2,5-dioxahexane dicarboxylate

DEI - desorption under electron impact

DEMS - differential electrochemical mass spectrometry

DLLME - dispersive liquid-liquid microextraction

DMC - dimethyl carbonate

DMFTIR - double modulation Fourier-transform infrared reflection spectroscopy

DRIFTS - diffuse reflectance infrared Fourier-transformed spectroscopy

DSC - differential scanning calorimetry

DSPE - dispersive solid-phase extraction

DTA - differential thermal analysis

DTV - differential thermal voltammetry

### **E**

EC - ethylene carbonate

ED - endocrine disrupter

EDS/EDX/EDAX - energy dispersive X-ray spectroscopy/analysis

EI - electron impact ionization

EIS - electrochemical impedance spectroscopy

EMC - ethyl methyl carbonate

EPR - electron paramagnetic resonance (or ESR)

ESI - electrospray ionization

EV - electric vehicle

## **F**

FAB - fast atom bombardment

FAME - fatty acid methyl ester

FID - flame ionization detector

FR - flame retardant

FTIR - Fourier transform infrared reflection spectroscopy

## **G**

GC - gas chromatography

GPC - gel permeation chromatography

## **H**

HEV - hybrid electric vehicle

HPLC - high performance/pressure liquid chromatography

HR - high resolution

## **I**

IC - ion chromatography

ICP - inductively coupled plasma

ID - internal diameter

IGC - isothermal gas chromatography

IL - ionic liquids

IRRAS - infrared reflection absorption spectroscopy

IT - ion trap

## **L**

LC - liquid chromatography

LIB - lithium-ion batteries

LLE - liquid-liquid extraction

LP - low pressure

LTP - low-temperature plasma probe

## **M**

M - molar ( 1 M = 1 mol/L )

MDC - minimum detectable concentration

MEPS - micro extraction by packed sorbent

MFTIR - microscope Fourier transform infrared reflection spectroscopy

MS - mass spectrometry

## **N**

NCI - negative chemical ionization

ND - neutron diffraction

NIST - National Institutes of Standards

NMR - nuclear magnetic resonance

NR - neutron radiography

## **O**

OES - optical emission spectrometry

OCV - open-circuit voltage

## **P**

PAH - polycyclic aromatic hydrocarbon

PBDE - polybrominated diphenyl ether

PC - propylene carbonate

PCB - polychlorinated biphenyl

PE - polyethylene

PEEK - polyetheretherketon

PEG - polyethylene glycol

PEO - polyethylene oxide

PHEV - plug-in hybrid electric vehicle

PES - photoemission spectroscopy

PLOT - porous layer open tubular

PLS - Partial Least Squares

POP – persistent organic pollutant

PM - polarization modulation

PS - 1,2-propylene sulfite / propylsultone / 1,3-propane sultone

PTFE – polytetrafluoroethylene

PVDF - polyvinylidene fluoride

Py - pyrolysis

## **Q**

Q - quadruple

QTRAP - triple quadruple/linear ion trap

QuEChERS - quick, easy, cheap, effective, rugged, and safe

## **R**

RT - retention time or room temperature (depending on the context)

## **S**

SAED - selected area electron diffraction

SBSE - stir bar sorptive extraction

SEC - size or steric exclusion chromatography

SEI - solid electrolyte interphase

SEM - scanning electron microscopy

SERS - surface-enhanced Raman scattering

SFC - supercritical fluid chromatography

SIM – single ion monitoring

SIMS - secondary ion mass spectrometry

SNIFTIR - subtractively normalized interfacial Fourier-transform infrared reflection spectroscopy

SPE - solid polymer electrolyte

SPE – solid phase extraction

SPM - scanning probe microscopy

SPME - solid phase microextraction  
STA - simultaneous thermal analysis  
STEM - scanning transmission electron microscopy  
STM - scanning tunneling microscopy

## **T**

TCC - time compressed chromatography  
TCD - thermal conductivity detector  
TD – thermal desorption  
TEM - transmission electron microscopy  
TGA - thermal gravimetric analysis  
THF - tetrahydrofuran  
TMA - thermomechanical analysis  
TMP - trimethyl phosphate  
TNT - trinitrotoluene  
TOF - time-of-flight  
TPD - temperature programmed desorption/decomposition  
TPGC – temperature-programmed gas chromatography  
TXM - transmission X-ray microscopy

## **U**

UPS - ultraviolet photoelectron spectroscopy  
UV - ultraviolet

## **V**

VC - vinylene carbonate  
VIS - visible  
VO - vacuum outlet  
VOC - volatile organic compound  
VUV - vacuum ultraviolet

## **X**

XPS - X-ray photoelectron spectroscopy  
XRD - X-ray diffraction  
XRF - X-ray fluorescence

## ***Table of content***

<b>Kurzfassung</b> .....	3
<b>Abstract</b> .....	5
<b>Acknowledgement</b> .....	7
<b>Abbreviations</b> .....	9
<b>A. Theoretical part on Lithium-ion batteries</b> .....	17
A.1. Introduction .....	17
A1.1 General description of a battery.....	17
A.1.2 General description of Lithium-ion batteries.....	19
A.2. Degradation mechanisms of LIB components.....	32
A.2.1 Degradation mechanisms under normal conditions.....	33
2.2 Degradation mechanisms under stress conditions .....	54
A.3. Analytical techniques applied for the characterization of LIBs .....	60
A.3.1. Introduction .....	60
A.3.2. Analytical approaches for the analysis of LIB components and degradation products .....	61
<b>B. Ex Situ experiments of selected electrolytes after prolonged storage at different temperatures using GC-MS</b> .....	83
B.1. Introduction .....	83
B.2. Materials and methods.....	83
B.2.1. Chemicals and Reagents .....	83
B.2.2. Instrumentation and operating conditions.....	84
B.2.3. Sample Preparation.....	85
2.4. Toxicological Evaluation .....	87
B.3. Results and discussion .....	91
B.3.1. Headspace measurements .....	91
B.3.2. Liquid phase measurements.....	107
B.4. Conclusions .....	119

<b>C. Ex Situ experiments of selected electrolytes after prolonged storage at different temperatures using GC-BID and GC-MS.....</b>	<b>122</b>
C.1. Introduction .....	122
C.2. Experimental Part .....	122
C.2.1. Instrumentation and operating conditions.....	122
C.2.2. Chemicals and Reagents .....	124
C.2.3. Sample Preparation .....	124
C.3. Results and discussion .....	125
C.3.1. EC .....	125
C.3.2. DMC .....	125
C.3.3. VC.....	126
C.3.4. EC + VC (5% wt) .....	126
C.3.5. EC + LiPF <sub>6</sub> (1M).....	127
C.3.6. EC + LiPF <sub>6</sub> + VC (1M, 5% wt).....	127
C.3.7. DMC + VC (5% wt) .....	127
C.3.8. DMC + LiPF <sub>6</sub> (1M).....	127
C.3.9. DMC + LiPF <sub>6</sub> + VC (1M, 5% wt).....	127
C.3.10. EC/DMC (1:1 vol. %).....	128
C.3.11. EC/DMC+VC (1:1 vol. %, 5% wt).....	128
C.3.12. EC/DMC+LiPF <sub>6</sub> (1:1 vol. %, 1M) .....	128
C.3.13. EC/DMC+VC+LiPF <sub>6</sub> (1:1 vol. %, 1M, 5% wt).....	129
C.3.14. LP30.....	129
C.3.15. LP30+VC (5% wt).....	130
C.3.16. Cycled LIB electrolyte solution .....	131
C.4. Conclusions .....	134

<b>D. In situ GC-MS and FTIR-GC-MS for the identification of gases emitted from in house-assembled and commercially available LIBs under different electrochemical conditions.....</b>	<b>135</b>
D.1 Introduction .....	135
D.2 Materials and methods.....	135
D.2.1 Chemicals and reagents .....	135
D.2.2 Instrumentation and operating conditions .....	136
D.3 Results and discussion.....	143
D.3.1 Correlation between FTIR and GC-MS data.....	143
D.3.2 In situ GC-MS analysis of commercial LIB cells / Gas evolution during charge & overcharge of BPC.....	148
D.3.3 In situ GC-MS analysis of in house-assembled LIB cells .....	155
D.4 Conclusions .....	163
<b>E. Theoretical Part on the vacuum outlet technique.....</b>	<b>164</b>
E.1. Introduction.....	164
E.2. The vacuum outlet technique .....	164
E.2.1. From conventional to fast GC separations.....	164
E.2.2. Fast GC-MS techniques .....	166
E.2.3. Description of the vacuum outlet technique using short wide-bore capillaries .....	169
E.2.4. Comparison of wide-bore and micro-bore columns for vacuum outlet applications .....	174
E.2.5. Vacuum Outlet Applications.....	177
<b>F. Investigations on the optimization parameters of vacuum outlet systems for the determination of highly volatile compounds .....</b>	<b>180</b>
F.1. Introduction.....	180
F.2. Materials and Methods.....	180
F.2.1. Chemicals and reagents.....	180
F.2.2. Instrumentation and operating conditions .....	181
F.3. Results and Discussion.....	183
F.3.1. Method optimization for thick-film wide-bore columns according to pre-column dimensions .....	186

F.3.2. Method optimization for VO column systems according to the analytical column length .....	209
F.3.3. Performance comparison for VO column setups using thicker film and intermediate film thickness analytical columns for the quantification of highly volatile compounds.....	212
F.3.4. Comparison of the performance and compliance with theoretical calculations for a thick film VO column system used under vacuum outlet and atmospheric outlet conditions .....	217
F.4. Conclusions .....	228
<b>G. The vacuum outlet in the determination of selected compounds of intermediate volatility .....</b>	<b>231</b>
G.1. Introduction .....	231
G.2. Materials and Methods .....	232
G.2.1. Chemicals and reagents .....	232
G.2.2. Instrumentation and operating conditions .....	232
G.3. Results and Discussion .....	235
G.3.1. LP-GC-MS detection.....	235
G.3.2. Optimization of SPME conditions.....	237
G.3.3. Analytical figures of merit.....	245
G.3.4. Recovery studies.....	246
G.3.5. Estimation of the uncertainty budget.....	247
G.4. Conclusion.....	250
<b>H. Overall conclusions .....</b>	<b>252</b>
<b>References .....</b>	<b>256</b>



## A. Theoretical part on Lithium-ion batteries

### A.1. Introduction

Batteries play an important part in our everyday life, with many household and industrial applications using them as their power source. The present chapter will describe the general definition of a battery with an emphasis on lithium ion batteries, their operation, composition and development. Starting with a general description of a battery and explaining its main components and how they function, it moves on to the category of lithium ion batteries, which were the main interest of this research work. A short description of their working principle and how their components were developed and selected is then following. The next chapter will then discuss in detail what happens inside these batteries during normal and abuse conditions of work, focusing on the chemical reactions taking place. Then the relevant analytical techniques for investigations in the battery field will be presented, closing with the experimental part of this research work.

#### A1.1 General description of a battery'

With the term “battery” we refer to a device that converts the chemical energy contained in its active materials directly into electric energy by means of an electrochemical oxidation-reduction (redox) reaction. For rechargeable systems, a reversed process takes place when the battery is recharged. In that case, the reaction involves the transfer of electrons from one material to another through an electric circuit.

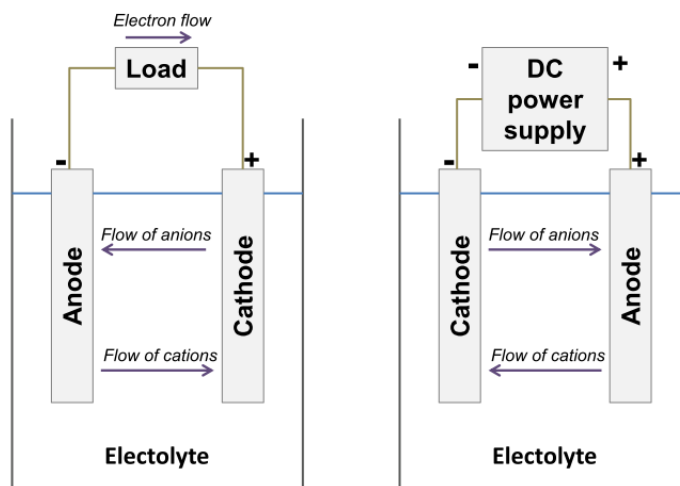


Figure A1.1. Electrochemical operation of a cell (discharge on the left and charge on the right end side).  
Reproduction from Reference 1.

Even though the term “battery” is often used, the basic electrochemical unit being referred to is the “cell”. A battery may consist of one or more cells, connected in series or parallel, or both, depending on the desired output voltage and capacity.

The major components of a cell are the anode, the cathode and the electrolyte. The anode or negative electrode is the reducing or fuel electrode that injects electrons into the external circuit and is oxidized during the electrochemical reaction. The cathode or positive electrode is the corresponding oxidizing electrode that accepts electrons from the external circuit and is reduced during the electrochemical reaction. The electrolyte is the ionic conductor, providing the medium for transfer of charge as ions inside the cell and between the anode and cathode.

Starting with the negative electrode, the properties that the anode should ideally provide are the efficiency as a reducing agent, high specific coulombic output ( $\text{Ah}^i/\text{g}$ ), good conductivity, stability, ease of fabrication and low cost. Mainly metals are used as the anode material, with lithium, the lightest metal with a high value of electrochemical equivalence, being a very attractive option. When the cathode is selected, an efficient oxidizing agent, stable when in contact with the electrolyte and with a useful working voltage is necessary. Commonly selected cathode materials are metallic oxides, while, for example halogens and the oxyhalides or sulfur and its oxides, are also used for special battery systems. Last but not least, the electrolyte must have good ionic conductivity, but it shouldn't be electronically conductive, since that would cause an internal short-circuiting. Other important characteristics are the non-reactivity with the electrode materials, little change in properties with change in temperature, safety in handling and low cost. Typical electrolytes are liquids, such as water or other solvents, with dissolved salts, acids, or alkalis, which impart ionic conductivity. Yet, there are important exceptions, such as in lithium anode batteries, where molten salts and other non-aqueous electrolytes are used to avoid the reaction of the anode with the electrolyte.

An additional component of the batteries is the separator material, which separates mechanically the anode from the cathode, preventing an internal short-circuiting. At the same time, the desired ionic conductivity is maintained, since the separator is permeable to the electrolyte. For certain applications the electrolyte can also be immobilized, creating a non-spill design. Furthermore, a reduction of the internal resistance can be performed by adding to the electrodes electrically conducting grid structures or materials.

In order to prevent leakage and drying out of the batteries, different sealing ways are used, while venting devices or other means may be provided to allow accumulated gases to escape. The fabrication of the battery is then completed, when the cells are positioned in appropriate cases or containers, equipped with the necessary means for terminal connection and labeling. Various battery configurations have been developed, with the cell components being designed to accommodate the particular cell shape. The most

---

<sup>i</sup> The Amp-hour (Ah) capacity of a cell is defined as the amount of current that it can deliver for one hour before its voltage reaches the end-of-life point.

common configurations are presented in Figure A1.2 for lithium ion batteries, the type of batteries investigated in the frame of this research work. A detailed description of these batteries is presented in the following section.

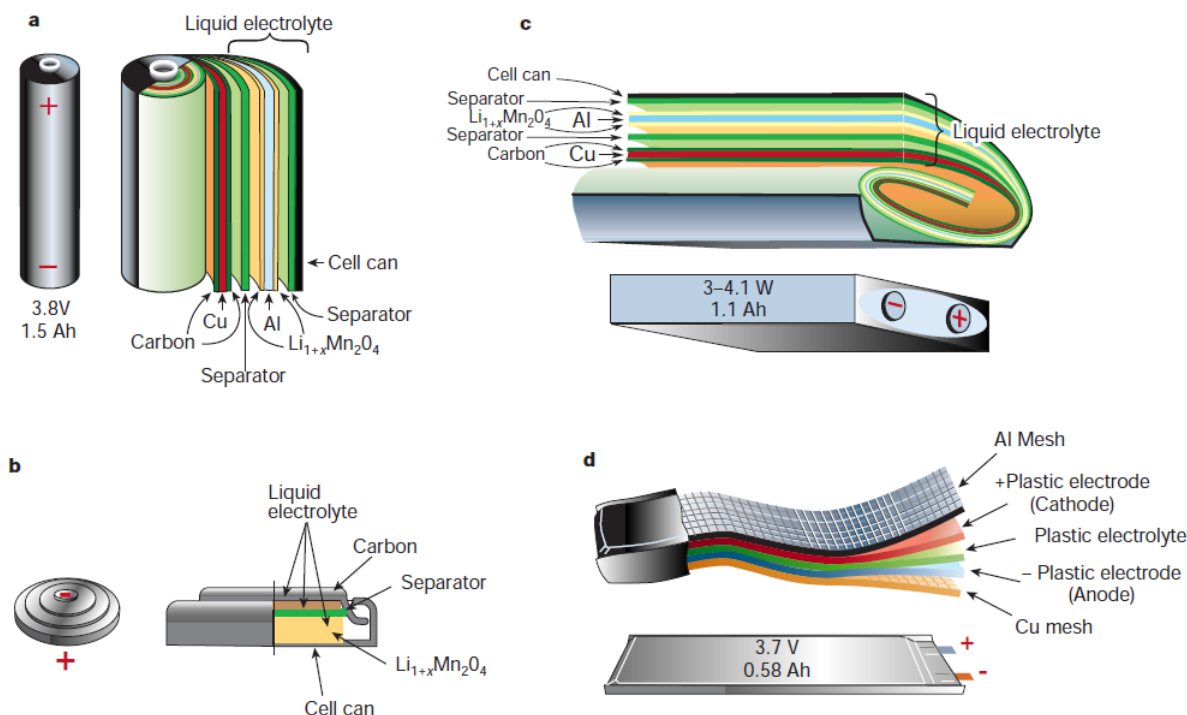


**Figure A1.2. Schematic drawing showing the shape and components of various Li-ion battery configurations (a. Cylindrical; b. coin; c, prismatic; and d, thin and flat).<sup>2</sup>**

### ***A.1.2 General description of Lithium-ion batteries***

The term lithium-ion (Li-ion) refers to an entire family of battery chemistries. While the first lithium-ion batteries (LIBs) were commercialized in Japan in the late eighties-early in the nineties of the previous century<sup>3,4</sup>, it should be noted that lithium-ion battery chemistry is an active area of research and new materials are currently being developed. In the most basic sense, the negative electrode and the positive electrode materials of a Li-ion cell are serving as hosts for the lithium ion ( $\text{Li}^+$ ). In a discharging battery, the electrochemical reduction takes place at the cathode, as lithium ions from the anode intercalate into the voids of its crystallographic structure. As current flows, electrons from the external circuit providing the electrical power and cations from the electrolytic solution of the device move towards the cathode (Figures A1.3 and A1.4). This transfer continues until the potential difference between the two electrodes becomes too low and the cell is considered to be fully discharged. Under charging, the processes are reversed. Since no metallic lithium was present in the entire system during the charging and discharging and only lithium ions are involved in the shuttling from one electrode to another, the term ‘lithium-ion

battery' was introduced.<sup>3</sup> At the same time, such batteries are also referred to as 'rocking chair' cells, since the lithium ion 'rocks' back and forth between the positive and the negative electrodes, the two host materials at the cell, during charge or discharge.<sup>1</sup>

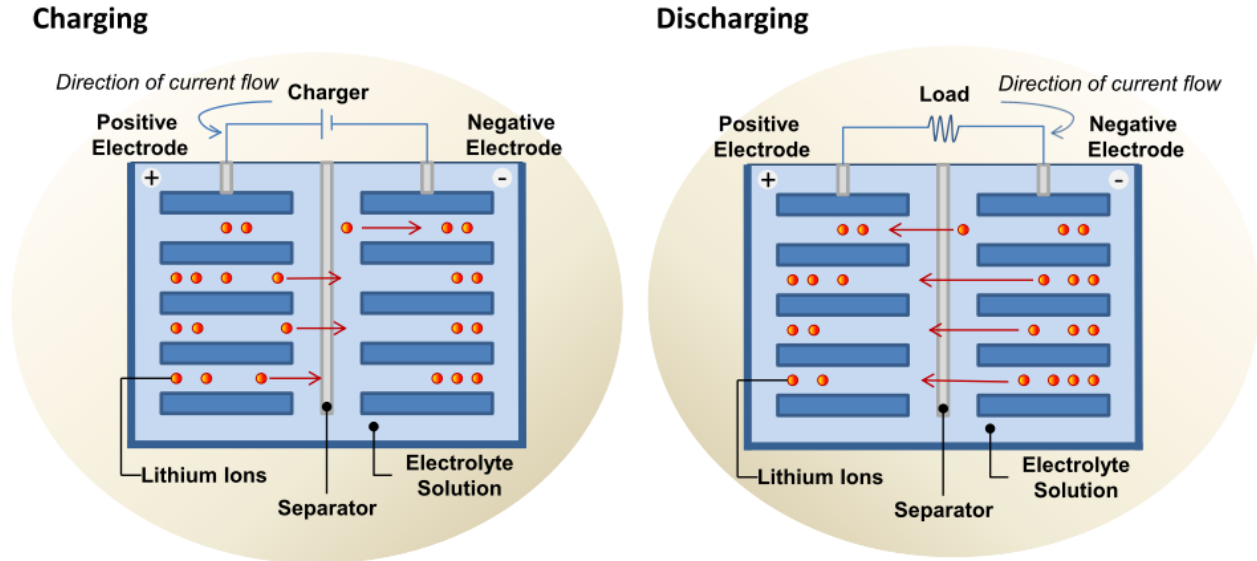


Figure A1.3. Working principle of lithium-ion rechargeable batteries. Reproduction from Reference 5.

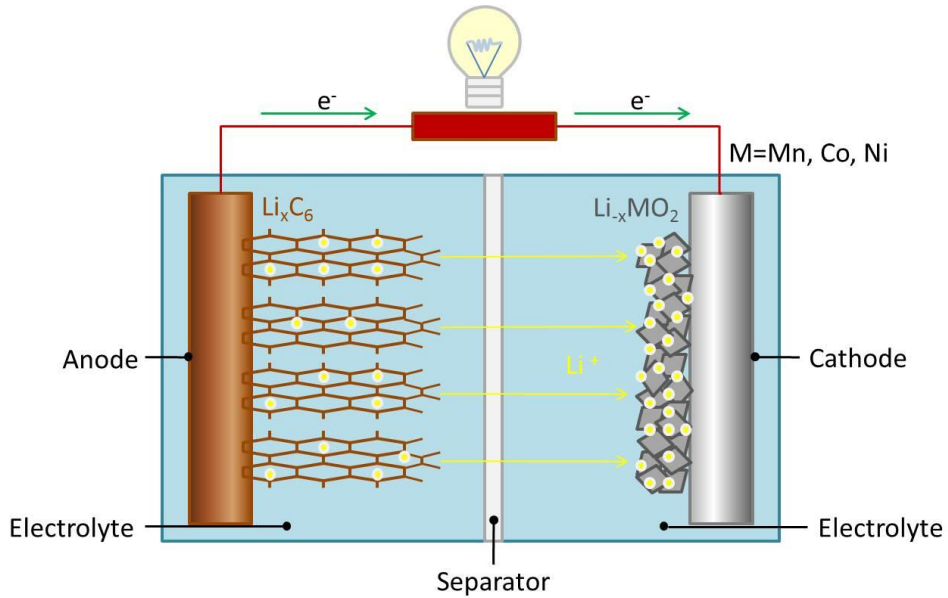
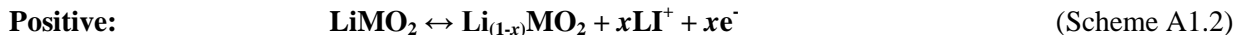


Figure A1.4. Rechargeable lithium-ion battery segment. Reproduction and adaptation from Reference 6.

The vast majority of commercially available LIBs is comprised by carbonaceous negative electrodes, while for the cathodes lithium metal oxides are being used. The process that takes place on such anodes is described in Scheme A1.1, where the direct process corresponds to the charging and the reverse to the

discharge of the cell. The corresponding current producing process for metal oxide positive electrodes is illustrated at Scheme A1.2, and followed by the overall reaction (Scheme A1.3)<sup>1</sup>:



In order to separate the alternating layers of anode and cathode inside a Li-ion cell, a porous film (separator) is used. The medium for Li<sup>+</sup> transport is provided by the electrolyte solution, composed of an organic solvent and a dissolved lithium salt. The batteries are then constructed by inserting these alternating layers of electrodes (forming stacks or rolls) into hard cases sealed with gaskets (most commercial cylindrical cells), laser-welded hard cases, or they are enclosed in foil pouches with heat-sealed seams (commonly referred to as lithium-ion polymer cells).

The mechanical design of the batteries may also include a safety mechanism, such as a charge interrupt device (CID), positive temperature coefficient (PTC) switches, or a burst disk for gas venting.<sup>7</sup> In general, safety is related to the flammability of the electrolyte, the rate of charge and/or discharge, and the engineering of the battery pack. Among the investigated approaches towards the enhancement of LIBs' safety, non-flammable electrolytes and coatings, and polymerizable electrolyte additives are also met.<sup>8,9</sup> Despite the various safety concepts and mechanisms available for the protection of lithium-ion batteries, incidents involving their transport, storage, use and recycling operations continue to take place. However, the severity of such incidents can be significantly higher during transportation, storage or recycling, due to the larger number of batteries present in one given location than in the end-use applications. In general, occurrence of faults and misuse during the production or the operation of the cells at their intended application can lead to internal and external short-circuits, overcharge, deep-discharge or overheating phenomena, which can further result in thermal runaway, venting, fire and/or explosion of batteries, in case of improper handling.<sup>10</sup>

Over the past 20 years, the applications of lithium-ion batteries have grown with a rapid pace. Their diverse applications are resulting from their significant advantages relative to other battery types. Li-ion cells are highly attractive for weight or volume sensitive applications thanks to their high specific energy (cc. 150 Wh/kg) and energy density (cc. 400 Wh/l)<sup>ii</sup>. Furthermore, they exhibit low self-discharge rates (2% to 8% per month), long self and cycle life (greater than 1000 cycles), and a broad temperature range

---

<sup>ii</sup> The gravimetric and volumetric energy densities of a battery, mentioned here as specific energy and energy density, measure how much energy a battery contains in comparison to its weight or volume and are expressed in Watt-hours/kilogram (Wh/kg) and Watt-hours/liter (Wh/l), respectively.

of operation (charge at  $-20^{\circ}\text{C}$  to  $60^{\circ}\text{C}$ , discharge at  $-40^{\circ}\text{C}$  to  $65^{\circ}\text{C}$ ). The operation range of single cells is typically from 2.5 to 4.2 V. Even though this range is approximately three times that of Nickel-Cadmium (NiCd) or Nickel Metal-Hydrate (NiMH) cells, requiring fewer cells for a battery of a given voltage, a lower power density is offered when the cylindrical designs are selected. Li-ion batteries can additionally offer rapid charge capabilities, high rate and power discharge capabilities (with demonstrated discharge at 5C continuous, or 25C pulse) and high coulombic and energy efficiencies. With no memory effects and no maintenance required, Li-ion batteries had from the very beginning the potential to conquer the energy market. Moreover, the very slight adverse effects of LIBs on the environment enable the use of the term 'green batteries' for their description.<sup>11</sup> However, no battery type has only advantages, and for the Li-ion batteries their drawbacks include the moderate initial cost, the need for protective circuitry, the degradation at high temperatures and the capacity loss or consequent thermal runaway when over-charged or crushed.<sup>1</sup>

Although the majority of lithium-ion batteries is intended for power supply of portable electronic devices, like cell phones, MP3 devices, notebooks, digital photo and video cameras, wireless tools, etc, larger scale applications are nowadays considered. Such examples involve the emerging market of hybrid electric vehicles (HEVs), plug-in hybrid electric vehicles (PHEVs) and electric vehicles (EVs)<sup>12</sup>, aiming to revolutionize the way for transportation by reducing gas emissions and fossil fuel dependence. These types of applications could contribute to address global warming and eliminate the danger of social instability and national vulnerabilities arising from the dependence on foreign oil and/or gas supplies. However, the cost and performance of these vehicles need to compete those of conventional ones in order to become the preferred mode of personal transportation. Hence, the need for improvements in the field of lithium-ion batteries is essential, so that their advanced models can meet the demands of the vehicle market. Additionally, such a transition from small-scale applications to larger setups makes the safety issue a priority and points out the necessity of risk assessment for unexpected chemical hazards, due to misuse or extreme operating conditions.<sup>13</sup>

With the consumers being in constant demand for thinner and lighter batteries with larger autonomy and improved safety features, and with the ongoing battery applications, the fields of cell chemistries and configurations are of continuous research activity. The most advantageous combinations of cell components are therefore targeted. Beneficial combinations of anode and cathode materials, for example, should provide a low specific weight, while yielding a high cell voltage and capacity. However, such combinations may not always be practical, due to reactivity with other cell components, polarization, difficulties in handling, high cost and other deficiencies.<sup>1</sup> Therefore, several comprehensive reviews were dedicated on the key requirements and criteria for the successful use of new materials as components of LIBs.<sup>2,11,14-26</sup>

In general, for the optimization of the cell properties and performance criteria, the cell designers have to select wisely not only the electrode materials, but also the particle sizes, particle size distributions, coatings on individual particles, binder materials, cell construction styles, etc. Consequently, no “standard” Li-ion cell exists and even cells that nominally appear to be the same can exhibit significantly different performance and safety behavior.<sup>7</sup> The market, though, is currently dominated by Li-ion cells that have similar designs. In these designs the negative electrode is made from carbon/graphite coated onto a copper current collector, the positive electrode is a metal oxide coated onto an aluminum current collector, while a polymeric separator is used and the electrolyte is composed of a lithium salt in an organic solvent.<sup>5</sup> Still, several alternative cell components have been developed, and the most frequently selected ones and their properties are subsequently presented.

#### ***A.1.2.1 Positive Electrode (Cathode)***

There are several requirements for a Li-ion positive electrode material, including the high lithium ion diffusivity, capability to incorporate large quantities of lithium, high free reaction energy with lithium, reversible incorporation of lithium without structural changes, insolubility in the electrolyte, good electronic conductivity and low cost synthesis. Table A1.1 summarizes some characteristic properties of the most common cathode materials.

Commercially available Li-ion batteries utilize a lithiated metal oxide as the active material of the positive electrode. Apart from the active material, the cathode consists of a binder material, like polyvinylidene fluoride (PVDF), carbon as a conduction enhancer and aluminum foil as a current collector.<sup>5</sup>

The first Li-ion products marketed by Sony used  $\text{LiCoO}_2$ . Despite of the toxicity and high price of cobalt, lithium cobalt dioxide (also referred to as cobalt oxide) remains the most common cathode material.<sup>7</sup> However, less costly materials, such as  $\text{LiMn}_2\text{O}_4$ , or materials with higher coulombic capacity, such as  $\text{LiNi}_{1-x}\text{Co}_x\text{O}_2$ , were later introduced.<sup>1</sup> Safety issues limited the interest in  $\text{LiNiO}_2$ , due to its instability, driven by the energetically favored formation of NiO and oxygen.<sup>1</sup> But mixed metal oxides that include nickel, cobalt, aluminum and manganese oxides, such as the nickel cobalt aluminate (NCA) material ( $\text{LiNi}_{0.8}\text{Co}_{0.15}\text{Al}_{0.05}\text{O}_2$ ) and the nickel manganese cobaltite (NMC,  $\text{LiNi}_{1/3}\text{Mn}_{1/3}\text{Co}_{1/3}\text{O}_2$ ) were then established.<sup>7</sup> Despite its low electronic conductivity,  $\text{LiFePO}_4$  has also been popular (mainly in power tools), thanks to its high rate performance and stability against oxygen release.<sup>27</sup> With the aim to reduce the energy evolved during positive material decomposition, additional new materials have been developed that offer either less evolved energy or higher onset temperatures (as demonstrated by Differential Scanning Colorimetry experiments). Such examples include titan and magnesium doped lithium nickel

cobalt oxides.<sup>1</sup> Moreover, the next generation cathodes are considered to be positive electrodes based on higher voltage (5V) insertion materials.<sup>28</sup>

The working voltage, energy density and rate capability of the cells are mainly determined by the limited theoretical capacity and thermodynamics of the cathode materials, and attribute to their higher cost. Thus, the need for development of advanced cathodes is obvious, and has led to several reviews devoted to the synthesis and developments of the new materials.<sup>29-41</sup>

**Table A1.1. Characteristics of positive electrode materials.<sup>1</sup>**

<b>Material</b>	<b>Specific Capacity (mAh/g)</b>	<b>Midpoint V vs. Li (at 0.05 C)<sup>iii</sup></b>	<b>Advantages and/or Disadvantages</b>
LiCoO <sub>2</sub>	155	3.88	Commercially most common, high price of Co
LiNi <sub>0.7</sub> Co <sub>0.3</sub> O <sub>2</sub>	190	3.70	
LiNi <sub>0.8</sub> Co <sub>0.2</sub> O <sub>2</sub>	205	3.73	Intermediate cost
LiNi <sub>0.9</sub> Co <sub>0.1</sub> O <sub>2</sub>	220	3.76	Intermediate cost
LiNiO <sub>2</sub>	200	3.55	Highest specific capacity <sup>iv</sup>
LiMn <sub>2</sub> O <sub>4</sub>	120	4.00	Most exothermic decomposition
			Low price of Mn, low toxicity, least exothermic decomposition

### **A.1.2.2 Negative Electrode (Anode)**

Lithium metal was initially used as the active material of the anode, due to the high specific capacity of the metal. But the lithium metal was quickly replaced by lithium intercalation into carbon, since changes in the morphology of the metal were leading to safety issues. Petroleum coke was used at the anode of the first Li-ion cells, followed by Mesocarbon Microbead (MCMB) and a variety of carbon types.<sup>1</sup> The nature of the carbon can vary considerably, not only in the source of the graphite (natural or synthetic), but also in purity, particle size, particle size distribution, particle shape and porosity, crystalline phase of carbon, degree of compaction, etc. Some cells utilize natural graphite, available at very low cost, while others use hard carbons, offering capacities higher than possible with graphitic materials.<sup>7</sup> The different types of carbon materials and the structure of the carbon greatly influence the electrochemical properties of the cell, including the lithium intercalation capacity and potential.<sup>1</sup> This influence is illustrated in Table A1.2.

<sup>iii</sup> The midpoint voltage (MPV) refers to the nominal voltage of the cell and is the voltage that is measured when the battery has discharged 50% of its total energy.

<sup>iv</sup> With the term specific capacity ( $Q_{th}$ ) the charge stored per g of battery mass or electrode mass is defined.



**Table A1.2. Properties and performance of various carbons.<sup>1</sup>**

<b>Carbon</b>	<b>Type</b>	<b>Specific Capacity (mAh/g)</b>	<b>Irreversible Capacity (mAh/g)</b>	<b>Particle Size D<sub>50</sub> (μm)</b>	<b>BET<sup>v</sup> Surface Area (m<sup>2</sup>/g)</b>
KS6	Synthetic graphite	316	60	6	22
KS15	Synthetic graphite	350	190	15	14
KS44	Synthetic graphite	345	45	44	10
MCMB 25-28	Graphite sphere	305	19	26	0.86
MCMB 10-28	Graphite sphere	290	30	10	2.64
Sterling 2700	Graphitized carbon black	200	152	0.075	30
XP30	Petroleum coke	220	55	45	N/A
Repsol LQNC	Needle coke	234	104	45	6.7
Grasker	Carbon fiber	363	35	23	11
Sugar Carbon	Hard carbon	575	215	N/A	40

Next generation anodes are negative non-insertion electrodes (e.g., Li-alloying or conversion reactions) making use of nanomaterials, which are usually characterized by impressive capacity gains over classical carbonaceous electrodes. These nanocomposite electrodes, though, were shown to strongly enhance classical electrolyte degradation resulting in the formation of large amounts of inorganic and organic compounds that can turn out to be detrimental to both the battery safety and useful lifetime.<sup>28,42</sup> Anodes composed of silicon, germanium, and titanate materials (Li<sub>4</sub>Ti<sub>5</sub>O<sub>12</sub>) have also been produced or tested, but non-graphitic anodes have only been rarely implemented.<sup>7</sup> Reviews, dedicated to the properties of new anode materials, are also available, however, at a much smaller scale than those summarizing the positive electrode materials.<sup>43-46</sup>

Similar to the case of positive electrodes, negative electrodes consist of not only carbon, which is used as the active material, but also trace additives, such as Li, P, Cu, Na, Co, Ca, K etc., a binder material, like styrene-butadiene rubber (SBR) or carboxymethyl cellulose (CMC), and copper foil as a current collector.<sup>5</sup>

<sup>v</sup> Measured by the BET (Brunauer-Emmett-Teller) method, the BET surface area refers to the total surface area of each particle which contributes to the charge/discharge reactions and can thus affect utilization and high rate discharge capability.

### ***A.1.2.3 Electrolyte Solution***

When a LIB electrolyte is designed, several criteria have to be met, including the high thermal stability and ionic conductivity, wide electrochemical window<sup>vi</sup> and low flammability and toxicity. To fulfill as many of these requirements as possible, different material combinations have been examined, resulting in the development of four types of electrolytes. These are the liquid, gel, polymer and ceramic electrolytes. Starting with the liquid electrolytes, they are solutions of a lithium salt dissolved in one or a mixture of organic solvents (typically carbonates). The polymer electrolytes are solvent-free, liquid materials, where an ionically conducting phase is formed by dissolving a salt in a high molecular weight polymer. For the gel electrolytes, the ionically conductive material contains a salt and a solvent dissolved or mixed with the high molecular weight polymer. Finally, the ceramic electrolytes refer to inorganic, solid-state materials that are ionically conductive.<sup>1</sup>

Typical Li-ion batteries employ liquid electrolytes. Gelling agents are added though to the electrolytes of some pouch cells to mitigate the results of pouch puncture and, in some instances, physically bind the electrodes together.<sup>7</sup> It is generally considered, that the polymer electrolytes can provide improved safety properties, resulting from their low volatility and high viscosity. The fact that the liquid phase is absorbed within the polymer may indeed lead to reduced possibility of electrolyte leakage, which would otherwise pose two potential safety hazards: human contact with the electrolyte and electrolyte residue, and short-circuiting of adjacent electronic systems.<sup>1,7</sup> However, when liquid electrolytes are used, the electrolyte is almost completely absorbed into the electrode and separator materials, and therefore no safety issues resulting from possible solvent leakage are practically encountered.<sup>1</sup>

#### ***A.1.2.3.1 Salts***

The most frequently used electrolyte salt in Li-ion batteries is the lithium hexafluorophosphate (LiPF<sub>6</sub>). The widespread use of LiPF<sub>6</sub>, despite its high price, is due to the facts that its solutions offer high ionic conductivity ( $>10^{-3}$  S/cm), high lithium ion transference number<sup>vii</sup> (approx. 0.35), and acceptable safety properties.<sup>1</sup> This lithium salt is though hygroscopic, and will decompose to form hydrofluoric acid (HF) if mixed with water or exposed to moisture. For this reason cell production and assembly is conducted in “dry rooms” to prevent HF formation, which would otherwise cause degradation of the cells.<sup>7</sup>

Since most cells currently marketed use LiPF<sub>6</sub>, the properties of this salt have been extensively examined. The thermal stability and interaction of LiPF<sub>6</sub> with the organic solvents in the electrolytes have been

---

<sup>vi</sup> A wide electrochemical window ensures that the electrolyte components will be stable, thermodynamically or kinetically, against oxidation or reduction at the electrodes.

<sup>vii</sup> The lithium ion transference number refers to the fraction of the total current carried by the ion.

investigated experimentally by several analytical techniques, like thermogravimetric analysis (TGA), Fourier transform infrared (FTIR) spectroscopy, differential scanning calorimetry (DSC) and accelerating rate calorimetry (ARC), while computational studies have been performed using the density functional theory (DFT) and molecular dynamics (MD) methods. However, different lithium salts have also been used at a lower extent in Li-ion cells, with the most commonly used listed in Table A1.3. For example, the organic salts developed for this application are more stable to water, and thus easier to handle. In particular, lithium bisperfluoroethanesulfonimide (BETI) has received significant attention as its solutions offer high conductivity, it can be easily dried and it does not cause aluminum corrosion, like in the case of other organic salts.<sup>1</sup>

**Table A1.3. Salts Used in Electrolytes for Li-ion Cells.<sup>1</sup>**

Common Name	Formula	MW (g/mol)	Typical Impurities	Comments
Lithium hexafluorophosphate	LiPF <sub>6</sub>	151.9	H <sub>2</sub> O (15 ppm) HF (100 ppm)	Most common
Lithium tetrafluoroborate	LiBF <sub>4</sub>	93.74	H <sub>2</sub> O (15 ppm) HF (75 ppm)	Less hygroscopic than LiPF <sub>6</sub>
Lithium perchlorate	LiClO <sub>4</sub>	106.39	H <sub>2</sub> O (15 ppm) HF (75 ppm)	When dry, less stable than alternatives
Lithium hexafluoroarsenate	LiAsF <sub>6</sub>	195.85	H <sub>2</sub> O (15 ppm) HF (75 ppm)	Contains arsenic
Lithium triflate	LiSO <sub>3</sub> CF <sub>3</sub>	156.01	H <sub>2</sub> O (100 ppm)	Al corrosion below 4.4 V, stable to water
Lithium bisperfluoroethanesulfonimide (BETI)	LiN(SO <sub>2</sub> C <sub>2</sub> F <sub>5</sub> ) <sub>2</sub>	387	N/A	No Al corrosion above 2.8 V, stable to water

#### A.1.2.3.2 Solvents

From the wide variety of non-aqueous solvents used in Li-ion batteries, the carbonates are most frequently used. Even though several ethers and acetates were initially evaluated, carbonates have proven to combine several beneficial features. The advantages of these aprotic, polar solvents include a high (relative) dielectric constant ( $\epsilon_r > 3$ , solvating lithium salts even at high concentration), compatibility with cell electrode materials over a broad range of potentials, excellent stability and good safety properties.<sup>1</sup>

At the beginning the industry focused on propylene carbonate (PC)-based solutions. However, PC proved to cause degradation in graphite electrodes as it co-intercalates with lithium, and results in exfoliation.<sup>1</sup> Therefore current formulations utilize other carbonates, and especially ethylene carbonate (EC), dimethyl carbonate (DMC), ethyl methyl carbonate (EMC) and diethyl carbonate (DEC). Table A1.4 presents the properties of these commonly used solvents.

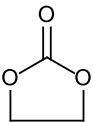
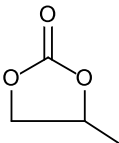
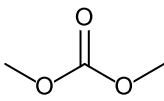
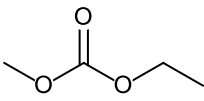
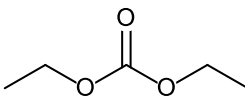
Most Li-ion cells typically contain electrolyte solutions with two to four solvents. The use of multiple solvents provides better cell performance, higher conductivity and a broader temperature range than

possible with a single solvent electrolyte.<sup>1</sup> For example, ethylene carbonate (EC) is associated with low irreversible capacity loss and low capacity fade when used in conjunction with graphitic negative electrodes. It is therefore found in many commercial electrolyte formulations, but is a solid at room temperature. Multiple solvent formulations often include EC, thereby incorporating its desirable properties, while using other solvents to lower the freezing point and viscosity of the mixture. Binary 1:1 mixtures of EC with common Li-ion electrolyte solvents, like EC:DEC, EC:DMC and EC:EMC, are often being used, offering good conductivity and low capacity fade.<sup>1</sup> However, the mixture ratios may vary depending on the desired cell properties (e.g., a cell designed for low-temperature applications will likely contain a lower viscosity electrolyte than one optimized for room temperature applications).<sup>7</sup>

Further improvements in the Li-ion batteries properties are still to be made, particularly when it comes to safety features. With the focus on reducing the electrolyte flammability, several additives have been tested, as well as different non-organic ionic liquids.<sup>47,48</sup>

Nevertheless, the electrolyte degradation is generally inevitable, with its results being discussed in the following section in terms of effects on the battery properties, while the reactions taking place are presented in detail in the next chapter.

**Table A1.4. Characteristics of most common organic solvents.**

Characteristics*	EC	PC	DMC	EMC	DEC
<b>Structure</b>					
<b># CAS</b>	96-49-1	108-32-7	616-38-6	623-53-0	105-58-8
<b>MW (g/mol)</b>	88.1	102.1	90.1	104.1	118.1
<b>Density (g/ml)</b>	1.41	1.21	1.07	1.0	0.97
<b>Melting Point</b>	39°C	-48°C	4°C	-14°C	-43°C
<b>Boiling Point</b>	248°C	242°C	90°C	109°C	126°C
<b>Flash Point</b>	145°C	135°C	18°C	25°C	25°C
<b>Auto-Ignition Temperature</b>	465°C	455°C	458°C	440°C	445°C
<b>Heat of Combustion (kJ/ml)</b>	-17.2	-20.1	-15.9	Not available	-20.9
<b>Dielectric Constant** (40°C)</b>	1.86	2.5	0.59	0.65	0.75
<b>Vapor Pressure** (torr) (36°C)</b>	0.02	0.13	18	27	10
<b>Donor Number** (40°C)</b>	89.6	64.4	3.12	2.9	2.82

\*Values obtained from Ref 1, 7; \*\*T = 20°C unless specified otherwise

#### ***A.1.2.3.3 Solid electrolyte interphase (SEI)***

During the initial cycle of the battery, a thin passivation film, known as the Solid Electrolyte Interphase (SEI), is spontaneously formed on the surface of the electrodes, owing to the decomposition of electrolyte.<sup>49</sup> The degradation of the electrolyte solution occurs on all surfaces, but predominantly on the negative polarized graphite surface, since typical electrolytes are thermodynamically unstable at the operating potential of the anode during charging.<sup>50</sup>

The electrically insulating but ionically conductive SEI layer at first protects the electrode against future corrosion and prevents the electrolyte from followed decomposition at low voltages, as it is almost impenetrable to electrolyte molecules. This phenomenon suppresses the further growth of the SEI layer in conventional graphitic anodes<sup>50</sup>, which is the prerequisite for the effective function of a LIB. Although the formation of SEI occurs first and mainly during the initial few charge discharge cycles, additional growth may take place dependent on both system chemistry and temperature. Furthermore, in next-generation intermetallic anode systems, the SEI morphology changes at different potentials, which indicates a dynamic process.<sup>51</sup>

The SEI features are crucial for the overall battery performance affecting many battery characteristics. For example, the corrosion rate of the Li-metal (when using Li-foil as anode), the quality of the metal deposit, the mechanism of the deposition-dissolution process, the kinetic parameters, and the half-cell potential depend on the character of the SEI.<sup>1</sup> Thus, the development of a robust and thermally stable SEI is a critical issue. Numerous studies on interfacial structure and electrochemical dynamics are therefore focusing on the variations in the composition, behavior and properties of the SEI, observed for different electrode/electrolyte systems and operating conditions. Such investigations have greatly promoted the development of new electrolyte formulations and improved the performance of lithium ion cells.

Cells with electrolyte formulations that contain alkyl carbonates, have demonstrated a low irreversible capacity loss. In EC containing electrolytes, the passivation film formed on the surface of Li-ion electrodes is formed with a minimum amount of lithium. Other solvents, typically esters or different alkyl carbonates such as EMC or MPC (methyl propyl carbonate), also form stable passivation films, but most solvents do not. If an ester or alkyl carbonate is not used, graphite can still be cycled in a solvent that does not form a stable passivation film as long as an additive is introduced to the electrolyte.<sup>1</sup> In general, the use of film-forming additives, like the ones mentioned in the dedicated section on additives, improves the coulombic efficiency of the carbon anode, and thus the cycle performance of a cell.<sup>52</sup>

The SEI formation leads to a complex heterogeneous collection of phases and layers consisting of many secondary interfaces<sup>20</sup>, and its fundamental concepts and principles have been extensively investigated and reviewed.<sup>53,54</sup> Even though the composition of the SEI remains a highly debated subject, it is generally suggested that it compromises a dense layer of inorganic components, which are normally salt degradation

products, close to the carbon material, and a porous organic or polymeric layer close to the electrolyte interface, from the products of partial reduction of the electrolyte composition.<sup>54-59</sup> The proposed reaction mechanisms behind the SEI formation and the overall electrolyte decomposition under normal or extreme operating or storage conditions are later on discussed in detail, since, understanding these mechanisms is of high importance for the improvement of the lithium-ion cells' characteristics and especially those associated with their safety.

#### ***A.1.2.4 Separator***

The Li-ion separators are required to be, among others, easily wetted by the electrolyte, compatible and stable in contact with the electrolyte and the electrode materials, they should not swell or shrink in width and have an effective pore size (less than 1  $\mu\text{m}$ ). Li-ion cells typically use thin (10 to 30  $\mu\text{m}$ ), microporous films to electrically isolate the positive and negative electrodes. Microporous polyolefin materials are nowadays used in the commercially available liquid electrolyte cells as they provide excellent mechanical properties, chemical stability and acceptable cost. Other nonwoven materials have also been developed but have not been widely accepted, in part due to the difficulty in fabricating thin materials with uniform, high strength. Microporous polyolefin materials in current use are made of polyethylene (PE), polypropylene (PPE) or laminates of polyethylene and polypropylene. Tri-layer materials (PPE/PE/PPE) have been developed where a polypropylene layer is designed to maintain the integrity of the film, while the low melting point of polyethylene layers is intended to shut-down the cell if an over-temperature condition is reached (usually around 130°C).<sup>1</sup> That is succeeded by closing the pores of the membrane, interrupting the internal current flow.<sup>60</sup> Also available are surfactant<sup>viii</sup> coated materials, designed to offer improved wetting by the electrolyte.<sup>1</sup>

#### ***A.1.2.5 Additives***

In order to further improve the performance characteristics of the batteries, such as the overcharge resistance, cycle life, calendar life and cell stability, several electrolyte additives have been developed.<sup>7</sup> Characteristic examples are the boron trifluoride ( $\text{BF}_3$ ) and related complexes, designed to passivate the surface of electrode materials and thereby reduce their propensity to degrade.<sup>1</sup> Various sulfur-containing compounds, like propylsulfone (PS,  $(\text{CH}_2)_3\text{SO}_3$ ), ethylene sulfite ( $(\text{CH}_2\text{O})_2\text{SO}$ ) and diethyl sulfite ( $(\text{CH}_3\text{CH}_2\text{O})\text{SO}$ ) have also been investigated as SEI forming additives, while vinylidene carbonate (VC) has demonstrated an improvement in the properties of the anode passivation layer.<sup>61</sup> On the other hand, biphenyl (or phenylbenzene) was found to act as an overcharge preventing additive, polymerising on the

---

<sup>viii</sup> Surfactants are compounds that lower the surface tension between two liquids, or better a liquid and a solid.

cathode surface and thus forming an isolating film.<sup>62</sup> In addition, the hexamethyldisilazane (HMDS,  $(\text{CH}_3)_3\text{SiN}(\text{H})\text{Si}(\text{CH}_3)_3$ ) has been used for the reduction of the interfacial resistance and the overall improvement of the cell performance, reacting with and immobilizing water and HF traces, according to the following reactions.<sup>1</sup>



These reactions belong to a huge group of irreversible and reversible reactions taking place when a LIB is used or just stored under particular environmental conditions. In the next chapter we tried to summarize all the proposed reaction pathways published until now, with a focus more on the volatile species produced. The reason for such a discrimination is based on the hazards accompanying the volatile compounds, as it will later on be discussed in more detail.

## A.2. Degradation mechanisms of LIB components

Major issues of LIB technology are the improvements in the safety, performance and lifetime of the cells. Not only under extreme operating conditions, but also during normal cycling or just storage of the cells, loss of capacity is observed. The last two cases are known as ageing and result into several changes at the different parts of the cells. The large variety of components used in LIBs makes it impossible to give an overview of all ageing mechanisms that are likely to occur in such a cell setup. However, some general hints can be extracted from the relevant literature. Figures A2.1 and A2.2 provide a general description of ageing mechanisms related to the anode and cathode, respectively.

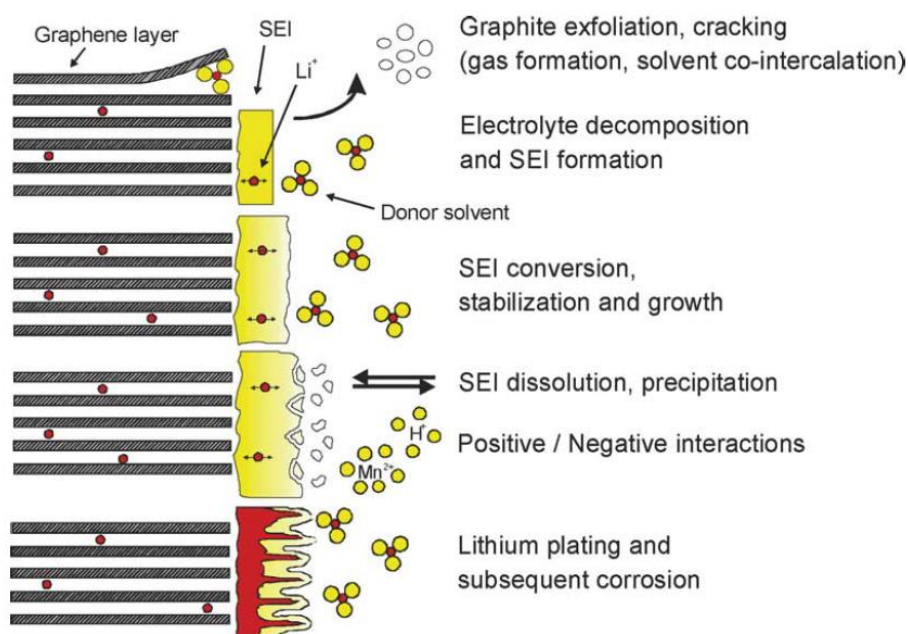
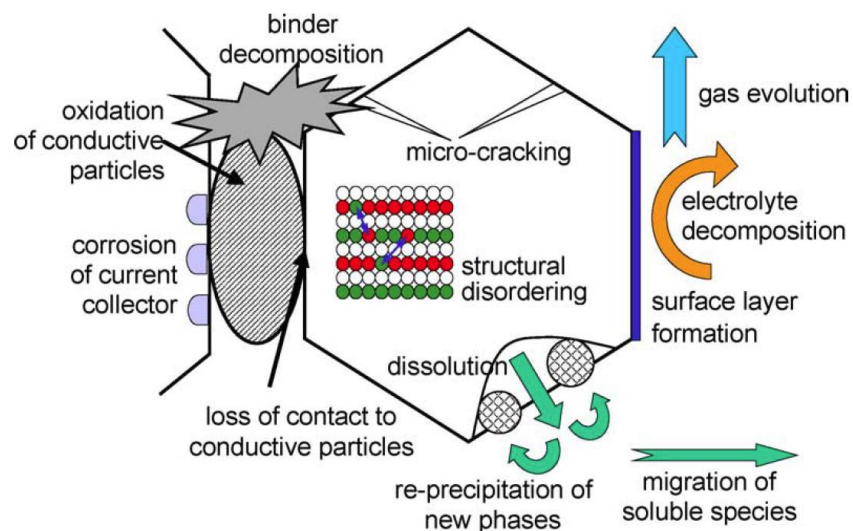


Figure A2.1 Aging processes at the anode / electrolyte interface.<sup>63</sup>

Starting with the negative electrode / electrolyte interface, SEI is initially formed by the electrolyte decomposition. Subsequent SEI conversion and dissolution can occur, while the layered structure of the graphite can be destroyed by exfoliation. At the positive electrode / electrolyte interface, structural changes of the active material and degradation of the electrode can occur. Indications are the loss of contact, micro-cracking and oxidation of conductive particles. These changes, together with the electrolyte degradation, result in increased resistance inside the cell and general deterioration of cell's performance over time.





**Figure A2.2 Aging processes at the cathode / electrolyte interface.<sup>63</sup>**

Focusing, more on the safety features of LIBs, the electrolyte solution is the key factor, not only due to the flammability of the electrolytes, but also due to the variety in species and amounts of degradation products and in particular emitted gases. The decomposition mechanism of standard electrolyte solutions has already been extensively studied. Most common solutions are comprised by alkyl carbonate-based electrolyte mixtures, containing both linear carbonates, like DMC, DEC or EMC, and cyclic carbonates, like EC or PC. These combinations lead to different properties, like viscosity and conductivity, in favor of the physicochemical properties of the cell. In addition,  $\text{LiPF}_6$  is the most commonly used salt in commercial LIBs together with VC or PS as additives.

At such electrolyte solutions several organic and inorganic species have proven to be formed. However, the mechanism of the decomposition products remains controversial and is subject to debate. This chapter summarizes the different opinions expressed and investigated so far, concerning the degradation mechanisms of the electrolyte under both normal and stress conditions.

### ***A.2.1 Degradation mechanisms under normal conditions***

Starting with the definition of normal conditions, with this term we refer to the operating parameters, such as charge/discharge voltages, current densities (referred to specific C-rate) and temperature limits given in data sheets by the battery manufacturers. Even when these conditions are applied, the electrolyte will still undergo some degree of decomposition, as consequence of cell ageing. The decomposition of cyclic and linear electrolyte solutions, such as EC/DMC (1/1 w/w) –  $\text{LiPF}_6$  (1M) or PC/DMC (1/1 w/w) –  $\text{LiPF}_6$  (1M), at low potential, has so far been proposed and mimicked via chemical tests, in both in situ and post-

moreover ways. Electrochemical reduction mechanisms of EC and DMC lead to the formation of inorganic lithium salts, such as lithium carbonate ( $\text{Li}_2\text{CO}_3$ ), lithium methoxide ( $\text{CH}_3\text{OLi}$ ), lithium methyl carbonate ( $\text{CH}_3\text{OCO}_2\text{Li}$ ) and lithium ethylene dicarbonate ( $(\text{CH}_2\text{OCO}_2\text{Li})_2$ ), with some of the basic reactions summarized in Figure A2.3.<sup>28</sup>

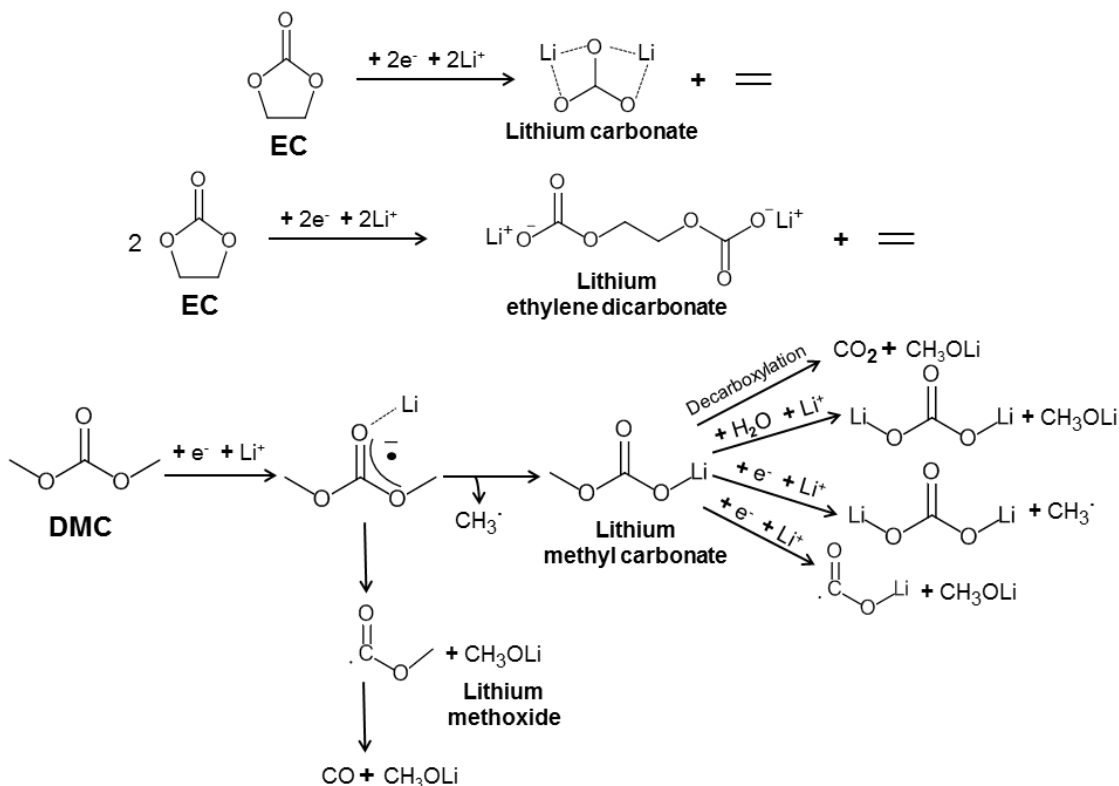


**Figure A2.3. Reaction scheme for the electrochemical reduction mechanisms of EC and DMC. Reproduction from Reference 28.**

Especially the lithium methoxide has proven by Laruelle *et al.*<sup>28</sup> to be the initiator of electrolyte degradation. It has been proposed that such lithium alkoxides originate from the reduction of linear carbonates, as shown in Figure A2.4 and will be later on explained in detail.

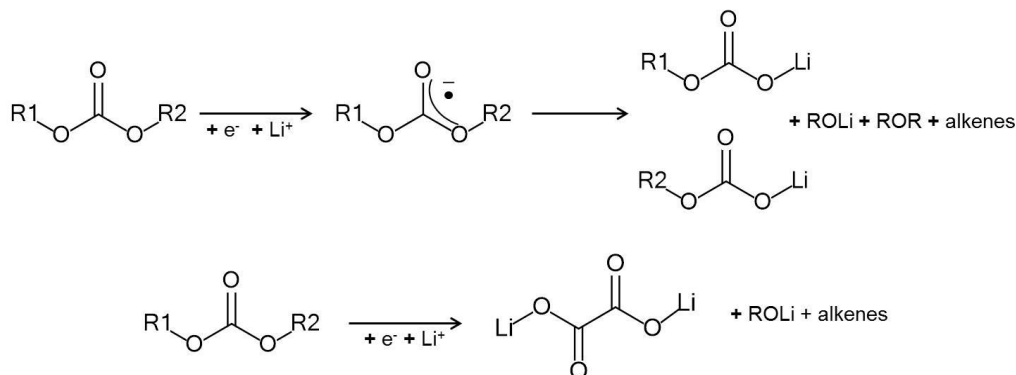


**Figure A2.4. Reaction scheme for the reduction of linear carbonates. Reproduction from Reference 64.**

During the electrolyte degradation ethylene oxide-based oligomers are also produced. These oligomers have identical poly(ethylene oxide) (PEO) units and are solely differentiated by the nature of the termination groups. At the resulting  $1_n$ ,  $2_n$ ,  $3_n$ ,  $4_n$ ,  $5_n$  and  $6_n$  series of products, the ending groups  $R_2/R_1$  are carbonate/carbonate (series  $1_n$ ), carbonate/methoxy (series  $2_n$ ), methoxy/methoxy (series  $3_n$ ), carbonate/hydroxy (series  $4_n$ ), methoxy/hydroxy (series  $5_n$ ), and hydroxy/hydroxy (series  $6_n$ ), respectively.<sup>28</sup>

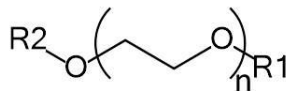


**Figure A2.5. General formula of the ethylene oxide-based oligomers.**

**Table A2.1. Series of ethylene oxide-based oligomers.**

O-R <sub>2</sub>	R <sub>1</sub>		
	-CO <sub>2</sub> Me	-Me	-H
-CO <sub>2</sub> Me	Series 1 <sub>n</sub>	Series 2 <sub>n</sub>	Series 4 <sub>n</sub>
-Me	Series 2 <sub>n</sub>	Series 3 <sub>n</sub>	Series 5 <sub>n</sub>
-H	Series 4 <sub>n</sub>	Series 5 <sub>n</sub>	Series 6 <sub>n</sub>

Among the different mechanisms for the formation of these oligomers that have been proposed so far, Yamachi and co-workers first suggested a trans-esterification mechanism for EC and DMC<sup>65</sup>. Then Ogumi and coworkers proposed an EC attack by an ethoxide anion<sup>66</sup>, where the nucleophile alkoxide anion can attack four possible carbon atoms of EC and DEC (Figure A2.6). However, the  $1_1$  compound, corresponding to the diethyl 2,5-dioxahexane dicarboxylate (DEDOHC), was the only product observed in the performed storage tests of the electrolytes, due to delocalization of any other theoretically possible products.

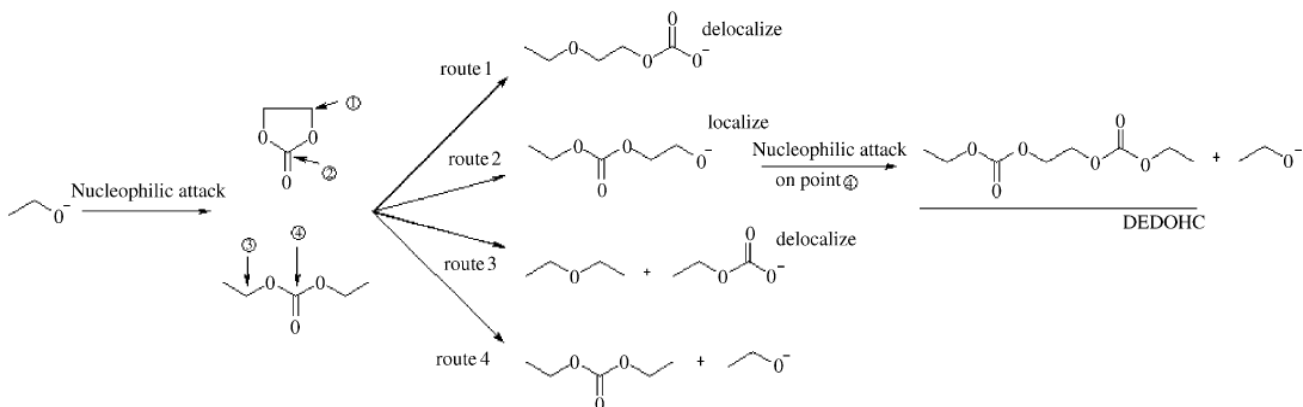


**Figure A2.6. Reaction scheme for DEDOHC formation in 1M  $\text{LiPF}_6/\text{EC} + \text{DEC}$  (1:1, v/v) in the presence of 1 wt.%  $\text{C}_2\text{H}_5\text{OLi}$ .**<sup>66</sup>

In the presence of lithium ethoxide, DEDOHC could also decompose to form EC and DEC, which is the reverse reaction of DEDOHC formation. That would lead to an increase in the concentrations of EC and DEC with storage time at the expense of DEDOHC. In particular, two reaction pathways are possible depending on the direction of bond cleavage upon the first attack of an ethoxide anion on DEDOHC. One is regeneration of DEDOHC, and the other is the formation of DEC and an intermediate A molecule. An intramolecular reaction of intermediate A will lead to the formation of EC and an ethoxide ion. But if the intermediate A attacks another DEDOHC molecule, a tricarbonatone compound will be formed.<sup>66</sup>

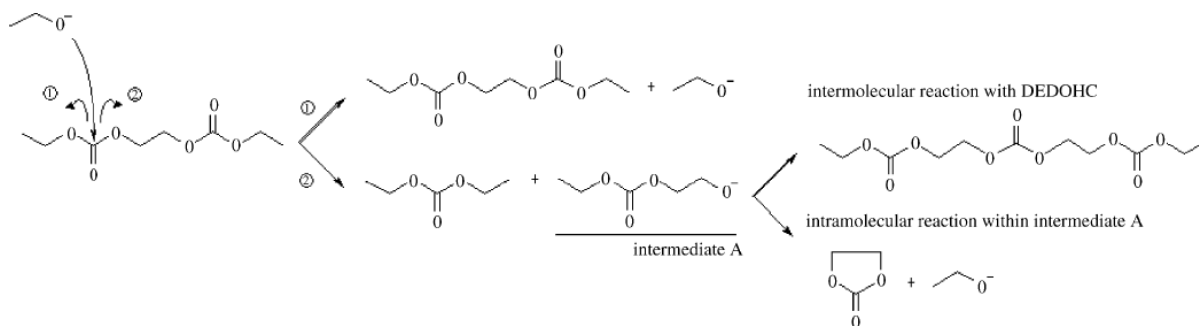


**Figure A2.7. Reaction scheme for the decomposition of DEDOHC in the presence of 1 wt. %  $\text{C}_2\text{H}_5\text{OLi}$ .**<sup>66</sup>

A similar intramolecular reaction was observed in 1 M  $\text{LiPF}_6/\text{EC} + \text{DEC}$  (1:1, v/v) + 1 wt.%  $(\text{CH}_2\text{OLi})_2$  mixtures, leading to EC reformation.<sup>66</sup>

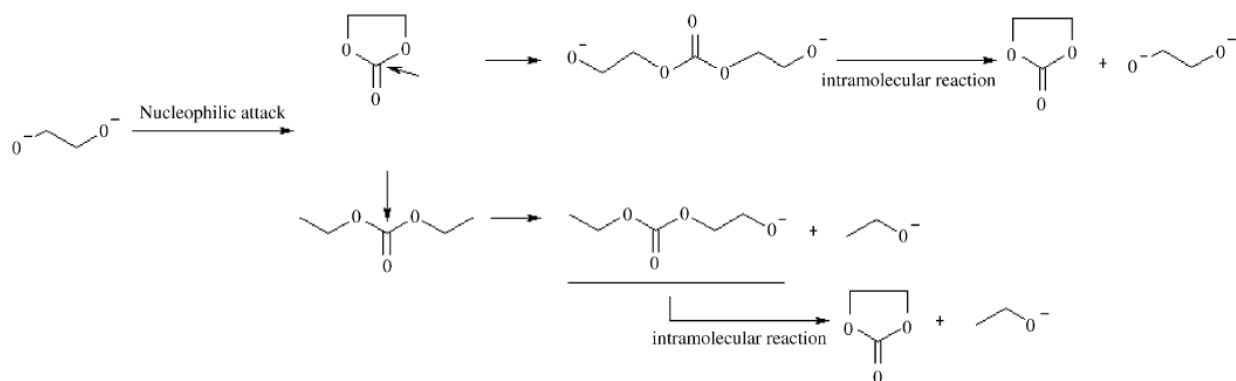


**Figure A2.8.** Reaction scheme for EC and DEC regeneration in 1M LiPF<sub>6</sub>/EC + DEC (1:1, v/v) in the presence of 1 wt. % C<sub>2</sub>H<sub>5</sub>OLi.<sup>66</sup>

Laruelle *et al.*<sup>28</sup> have described in detail a possible reaction sequence towards the formation of ethylene oxide-based oligomers, initiated again by the attack of a lithium alkoxide. Based on performed electrochemical tests, they proposed that all PEO oligomers result from chemical reactions initiated by electrochemical decomposition of the linear carbonate of the electrolyte solution into lithium methoxide. Three possible attacks of lithium alkoxide on a carbonate function were described, consisting of two attacks on C<sub>2</sub> carbon with folding back of either the doublet on the oxygen of the methoxy function to reform MeOLi (“a” attack; solid arrow) or the doublet on the oxygen of the ether function to form new lithium alkoxide (“b” attack, dashed arrow), and a third one on the C<sub>1</sub> carbon with folding back of the doublet on the oxygen of the ether function to form lithium methyl carbonate (“c” attack).<sup>28</sup>

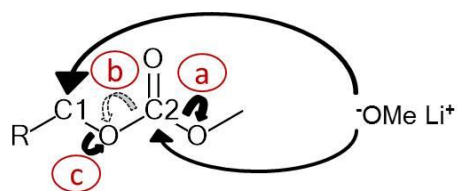


**Figure A2.9.** Possible attacks of lithium methoxide on a carbonate function.<sup>28</sup>

The mechanism paths for the formation of 1<sub>n</sub>, 2<sub>n</sub> and 3<sub>n</sub> series, proven through electrochemical tests, are illustrated in Figures A2.10 and A2.11, revealing the reactivity of the 1<sub>1</sub> compound in the presence of MeOLi.<sup>28,64,65,66</sup>

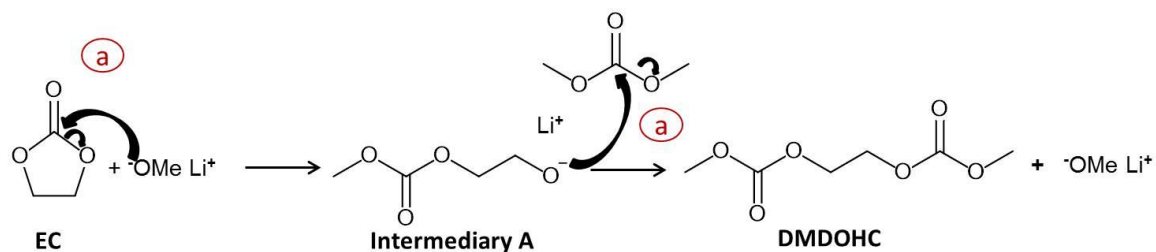


Figure A2.10. Reaction scheme for DMDOHC formation.<sup>28</sup>

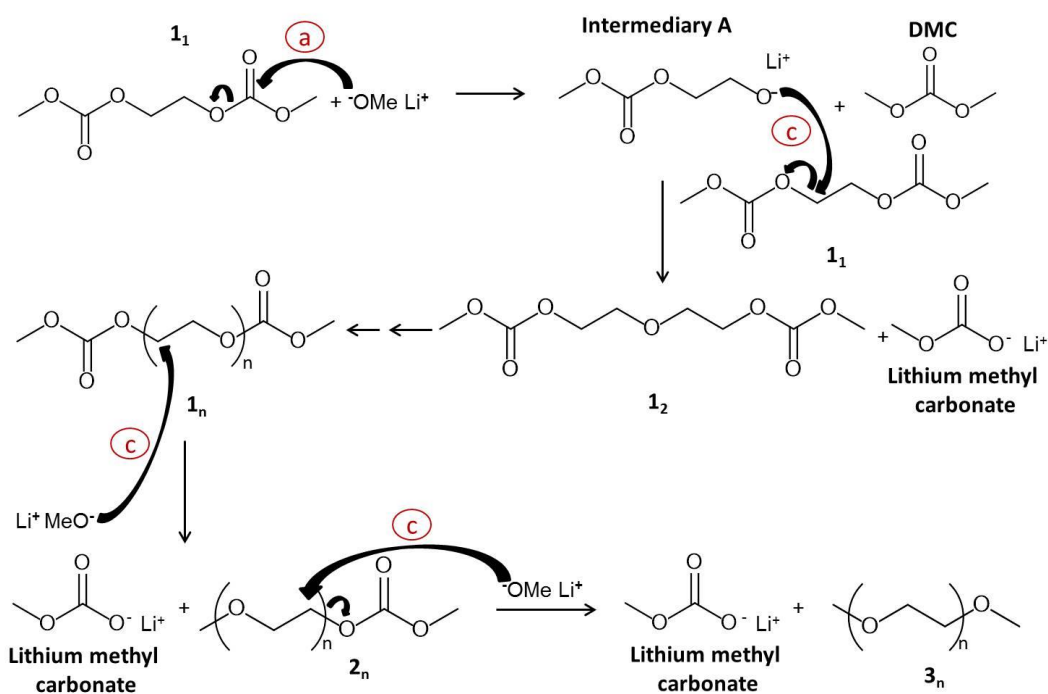


Figure A2.11. Reaction scheme for series  $1_n$ - $3_n$  formation. Reproduction from Reference.<sup>28</sup>

Storage test performed by the same group, proved also the presence of trimethyl phosphate (TMP,  $(\text{CH}_3\text{O})_3\text{PO}$ ), PEO units with phosphate/carbonate ending groups (termed P) and ethylene carbonate chains (denoted as series  $7_n$ ), when phosphorous-containing salts, such as  $\text{LiPF}_6$ , were in the electrolyte solution. The corresponding reaction paths are presented in Figures A2.12, A2.13 and A2.14.<sup>28</sup>

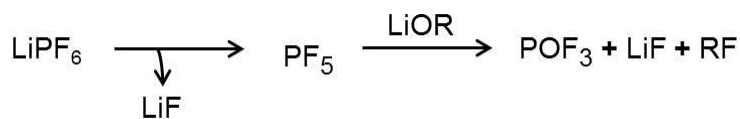


Figure A2.12. Reaction scheme for trifluoro phosphate formation.

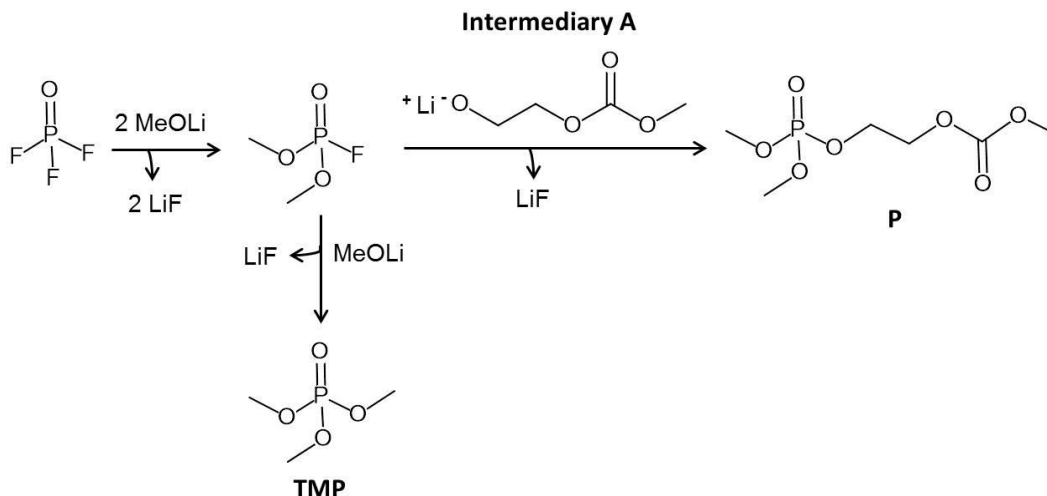


Figure A2.13. Reaction scheme for TMP and P formation. Reproduction from Reference.<sup>28</sup>

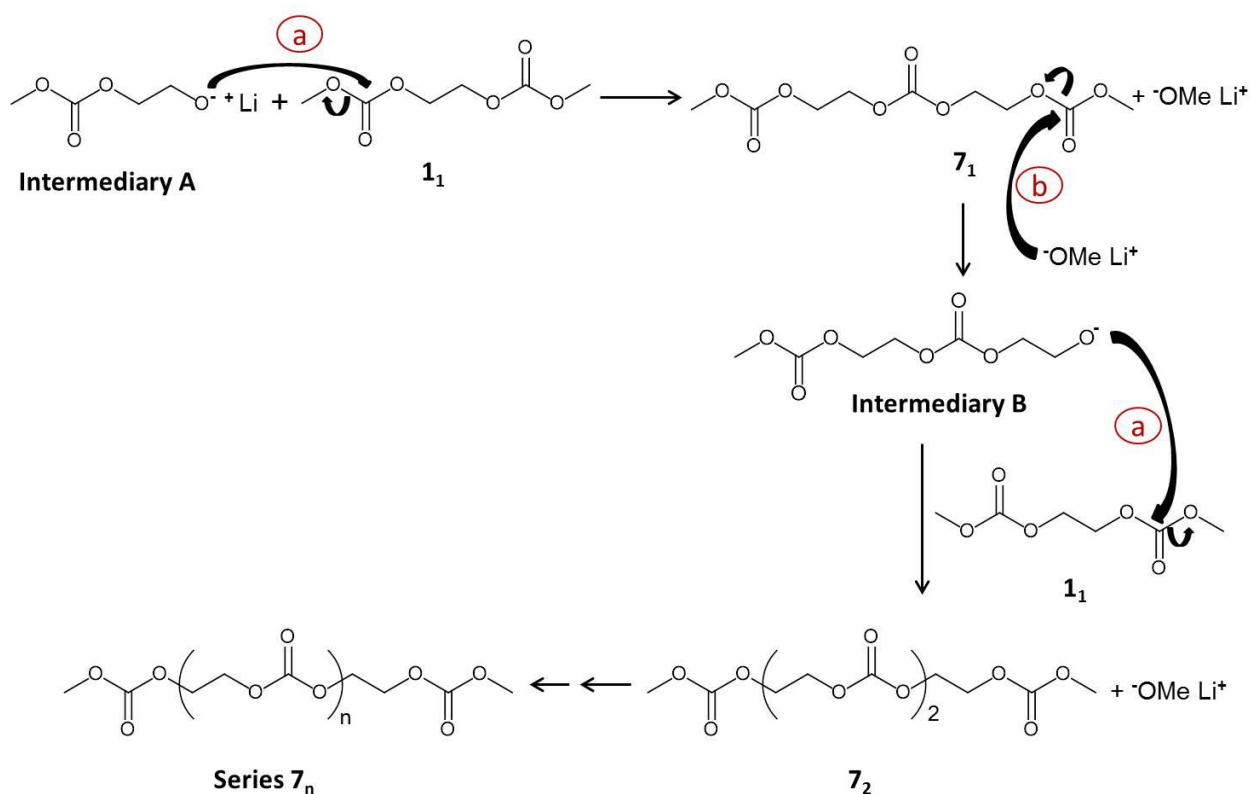


Figure A2.14. Reaction scheme for series 7<sub>n</sub> formation.<sup>28</sup>

Another observation by Laruelle and co-workers involves the different MeOLi concentrations that are required for the formation of different series, since the 2<sub>n</sub> and 3<sub>n</sub> series need a larger MeOLi concentration for their formation (e.g. 1M), although 1<sub>n</sub> series are formed in the presence of low amounts of MeOLi (e.g. 10<sup>-2</sup>M). Under low MeOLi concentrations, the electrolyte degradation stops when the entire amount of

MeOLi is consumed, which was approximately after two weeks of storage at 55°C. Under such conditions the following reaction path was provided:



The entire electrochemical/chemical low-potential degradation processes for an EC/DMC (1/1 w/w)–LiPF<sub>6</sub> salt (1 M) electrolyte is illustrated in Figure A2.15. Experiments performed by Laruelle *et al.*<sup>28</sup>, using PC instead of EC and DEC instead of DMC have confirmed the global character of this electrolyte decomposition mechanism. It has been noticed, though, that when DMC was substituted by another linear carbonate, like DEC, the degradation process was appreciably slowed down upon cycling. For the explanation of this phenomenon, the possibly different reactivity of the EtOLi in comparison to MeOLi was indicated. Moreover, experiments performed by Kawamura *et al.*<sup>67</sup>, proved that EC is more stable in the presence of lithium metal, compared to PC, since EC-based electrolyte solutions showed the best Li-cycling efficiency. That also explains their extended use as the cyclic carbonate of electrolyte solutions in LIBs.

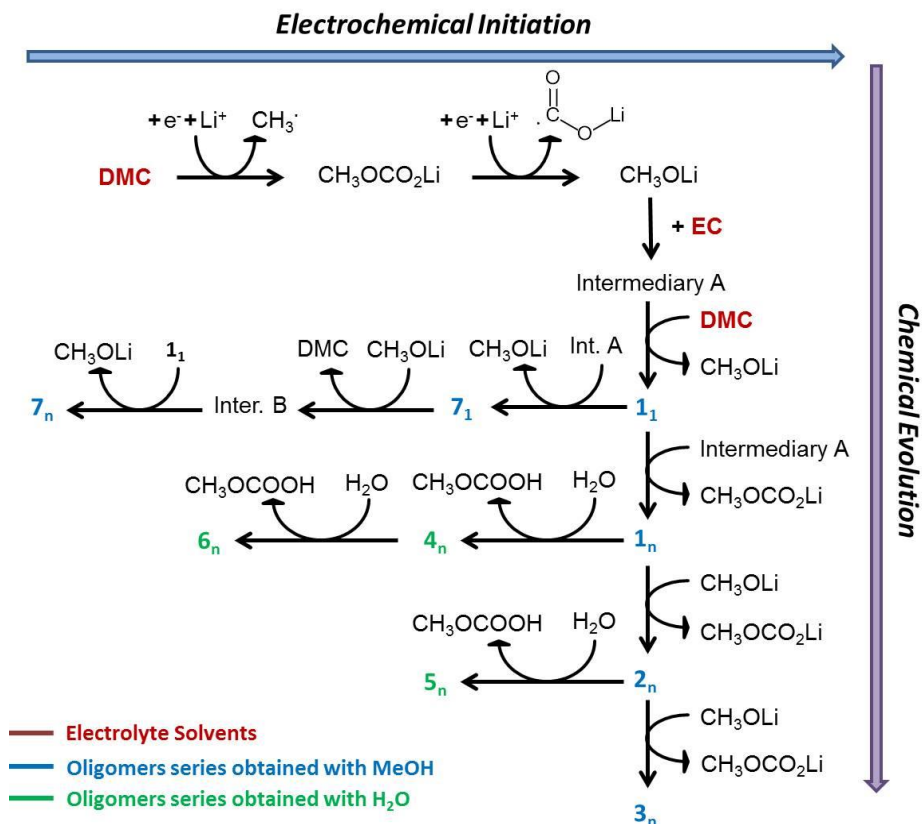
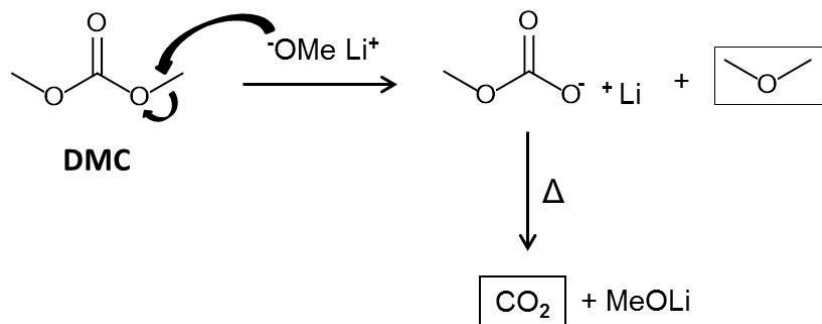


Figure A2.15. Global scheme of electrochemical/chemical low-potential degradation processes described for EC/DMC (1/1 w/w)–LiPF<sub>6</sub> salt (1 M) electrolyte.<sup>28</sup>



It should be noted that, apart from the formation of various series of ethylene oxide-based oligomers, when MeOLi reacts via a nucleophilic attack of the carbonate function with the electrolyte, alkyl-carbonate salts are also produced. The fact that these salts are weakly soluble in the carbonated electrolytes, explains their accumulation within the cell separator causing it to dry-up and leading to the deterioration of the cell-cycling performance.<sup>28</sup>

Another aspect that must be stressed here is that the general scheme for the decomposition of the electrolyte as a result of the electrochemical reduction processes upon cycling also applies for thermal decomposition<sup>68</sup>. For instance, the formation of dimethyl ether ((CH<sub>3</sub>)<sub>2</sub>O) could be explained by a nucleophilic attack of CH<sub>3</sub>OLi on DMC, where CH<sub>3</sub>OLi is acting as the alkylating agent. Dimethyl ether is then formed together with lithium methyl carbonate, which would further decarboxylate while regenerating CH<sub>3</sub>OLi (Figure A2.16).<sup>69,70</sup> However, the observation of dimethyl ether could also be explained by a further DMC decarboxylation catalyzed by the salt at higher temperatures (Figure A2.17).<sup>69</sup>



**Figure A2.16. Reaction scheme for the formation of dimethylether from DMC.<sup>69</sup>**

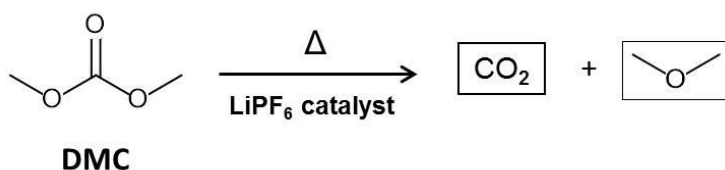


**Figure A2.17. Alternative reaction scheme for the formation of dimethylether from DMC.<sup>69</sup>**

Regarding the species formed in the presence of water traces and when phosphorous-containing salts, like the LiPF<sub>6</sub>, were in the electrolyte solution, a variety of organic and inorganic species can be encountered. The reactions leading to the formation of inorganic phosphates are summarized in Figure A2.18.

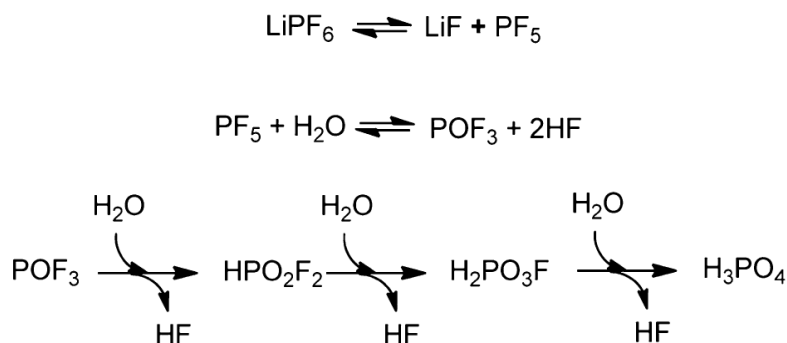


**Figure A2.18. Formation pathway of inorganic phosphates by hydrolysis of LiPF<sub>6</sub>.**<sup>71</sup>

Depending on the solvent mixture used in the Li-ion cell, several reactions take place, leading not only to TMP and P, but also to a big number of organic phosphates and phosphorofluoridates. When it comes to the reaction of oxyfluoride with linear carbonates, the proposed formation mechanism of phosphorofluoridated is presented in Figure A2.18. Apart from the alkyl fluoride (RF), an organic difluoro phosphate is also formed, which after decarboxylation yields further fluorophosphates, contributing to an increase of CO<sub>2</sub> release inside the cell.<sup>69</sup>

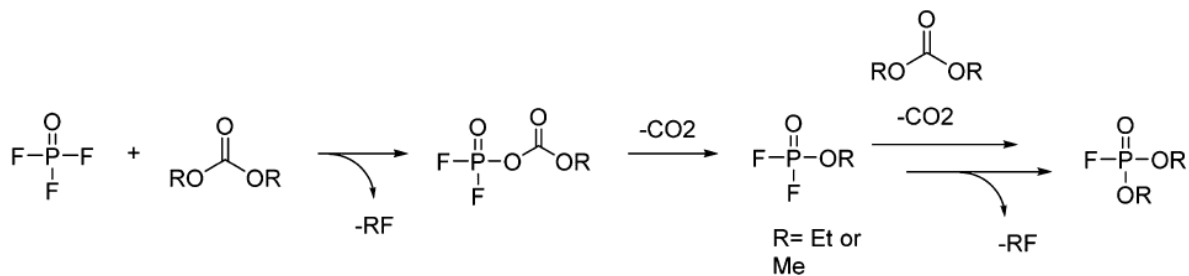


**Figure A2.19. Proposed formation mechanism of phosphorofluoridates.**<sup>72</sup>

When a cyclic carbonate, like EC, is used, a similar degradation process brings additional enhancement of CO<sub>2</sub>, while fluoroalkyl difluorophosphates are also formed. Since these species can further react with the linear and cyclic carbonates present in the electrolyte solution, a possible formation mechanism of these phosphorofluoridates is presented in Figure A2.20.

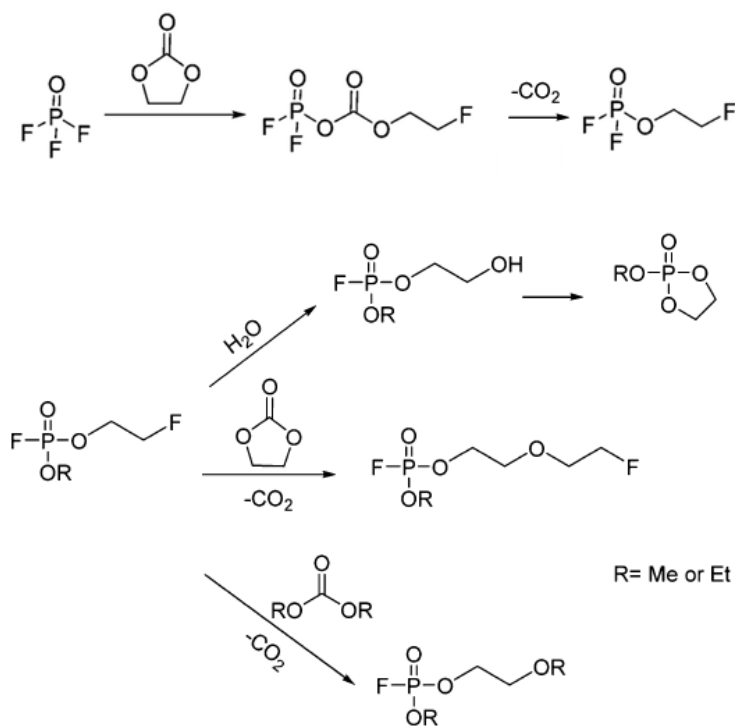


**Figure A2.20. Possible formation mechanisms of further phosphorofluoridates by consecutive reactions with the carbonate solvents.<sup>69,72</sup>**

For extreme temperature conditions met during storage or operation, the decomposition products are becoming even more, not only in number but also in molecular mass, since further organophosphates, phosphorofluoridates and polymerization products are formed. The corresponding reactions and an overall scheme with the proposed decomposition products under stress conditions of use are presented in the dedicated section about the abuse condition of LIBs.

Apart from the several organic and inorganic decomposition products found inside an aged LIB, EMC and DEC were also identified at EC-DMC-based electrolyte cells. Laruelle and co-workers proposed that the appearance of EMC and DEC would imply a two-step EC reduction as starting reaction in order to reach a radical anion formation.<sup>69</sup> In the presence of  $H^\bullet$ , this radical forms lithium ethoxide which could react, as a nucleophile, with DMC yielding EMC and then DEC from further reaction with  $CH_3CH_2OLi$  (Figure A2.21).

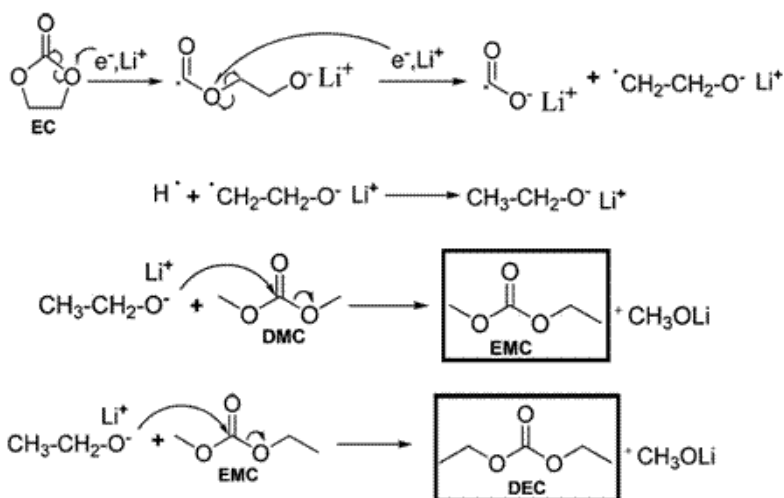


Figure A2.21. Reaction schemes for the formation of EMC and DEC.<sup>69</sup>

After the formation of DEC, K. Xu<sup>64</sup> suggested that an ester exchange reaction mechanism could also occur, leading back to the formation of EMC. According to such a reaction path, alkoxide anions are generated in the first stage and continue to be produced in a chain reaction manner, while the aforementioned ester exchange continues through the various cell cycles and is independent of the SEI formation. However, it was experimentally found that the extent of the ester exchange reaction was dependent on the anode surface passivation, and that the complete formation of the SEI eventually prevented it. Therefore, a termination process has to exist at some stage, and it was proposed that a cathode surface in a charged state would serve as such a terminator by quenching (oxidizing) the alkoxide anions. In view of the acidic nature of the electrolytes based on  $LiPF_6$ , neutralization of alkoxide anions by trace acid is another possible means of termination.

When the cell is initially charged the chain alkyl carbonates are in equilibrium by the following transesterification reaction, activated by lithium alkoxide ( $ROLi$ ), rather than by  $LiCO_3$ ,  $LiOH$  or  $RCOOLi$ .<sup>65,66,70,73,74</sup>



(Scheme A2.2)

The same reaction was also observed during high temperature ( $90^\circ C$ ) storage experiments, leading to the appearance of DEC in the electrolyte solution with main composition (EC:EMC:DMC). J.-H. Lee and co-workers<sup>73</sup> also proposed that rearrangement of carbonates via Lewis acid mediated ester reactions occurs since  $PF_5$  acts as a Lewis acid. The rapid ester exchange reaction suggests again the transient formation of alkoxide anions. The generation of DMC and DEC may occur via alkyl-oxygen cleavage reactions, which frequently accompany transesterification reactions. This reaction is particularly detrimental since upon

ether formation the carbonate anion decarboxylates generating  $\text{CO}_2$  and regenerating an equivalent of methoxide for further decomposition reactions.<sup>73</sup>

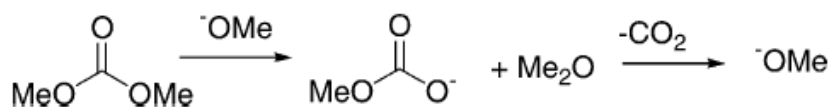
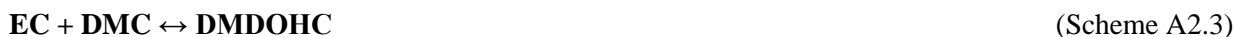


**Figure A2.22.** Decarboxylation reaction of DMC, leading to the regeneration of the methanolate ion.<sup>73</sup>

Additionally, further trans-esterification equilibria are illustrated in Reaction Schemes A2.3-A2.5, where DMDOHC is dimethyl-2,5-dioxahexane carboxylate, EMDOHC is ethylmethyl-2,5-dioxahexane carboxylate and DEDOHC is diethyl-2,5-dioxahexane carboxylate. These reactions occur between electrolyte components at elevated temperatures as well as under storage at room temperature (25°C) conditions.<sup>5,28,64,66</sup>



A competitive process for EC includes the formation of polycarbonates via alkoxides<sup>64</sup>.

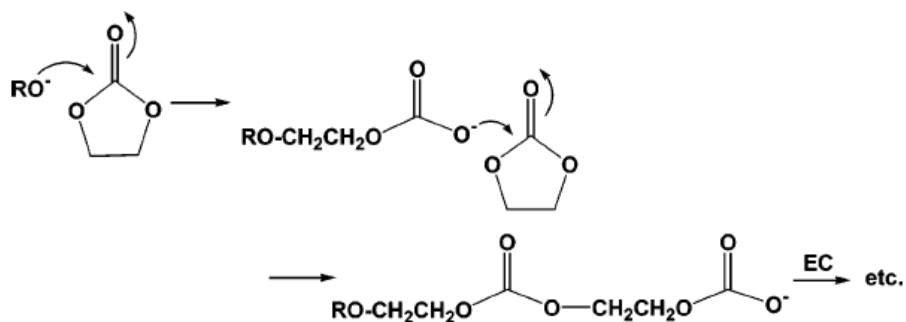


**Figure A2.23.** Reaction scheme for polycarbonates formation.<sup>64</sup>

Further polymeric species that can be formed in the SEI layer, from the ring-opening polymerization of cyclic carbonates initiated by strong Lewis acids as  $\text{PF}_5$ , are the following<sup>64</sup>:

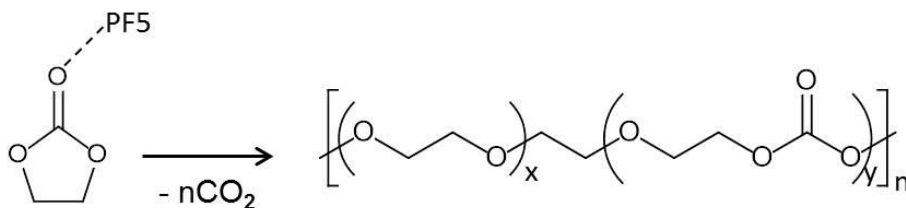


**Figure A2.24.** Reaction scheme for EC polymerization. Reproduction from Reference 64.

The acid-catalyzed ring-opening polymerization of EC also leads to a number of other observations. The PEO-like polymers that are yield alternatively to the oligo-ether carbonates can react further with PF<sub>5</sub> and CO<sub>2</sub> and get reduced to oxalate, carbonate, formate and CO (Figure A2.25).<sup>28,75</sup> It has been postulated by Ogumi and co-workers<sup>75</sup> that within a well-sealed Li-ion cell the evolution of CO<sub>2</sub> will cease once the solution is saturated. Consequently, the polymerization of EC should also cease bringing the system to balance. Removal of the CO<sub>2</sub> should allow the polymerization to proceed and yield polymeric material that may deposit within the electrode structures and result in increased impedance and power fade. But CO<sub>2</sub> is also reducible at the anode under normal operating conditions and has been claimed that it is easier reduced than other components of the electrolyte.

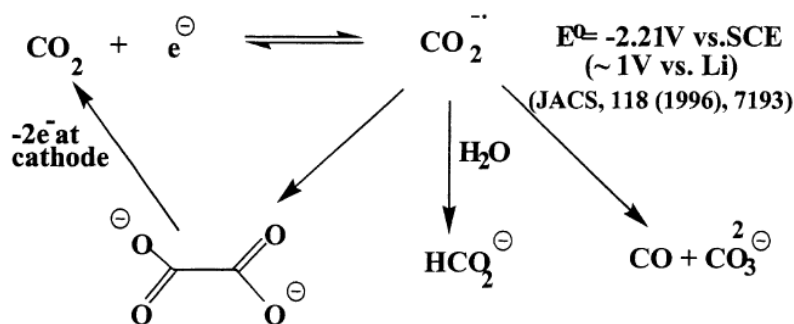


**Figure A2.25 CO<sub>2</sub> shuttle mechanism responsible for reversible self-discharge via oxalate formation.**<sup>75</sup>

In the presence of CO<sub>2</sub> the graphite electrode surface chemistry becomes dominated by Li<sub>2</sub>CO<sub>3</sub> formation.<sup>76</sup> Additional observations of Ogumi and co-workers<sup>75</sup>, prove that from the compounds formed by reduction of CO<sub>2</sub>, oxalate and formate can be re-oxidized at the cathode to CO<sub>2</sub>, providing a reversible self-discharge mechanism. Reduction to CO and carbonate is an irreversible self-discharge mechanism that reduces permanently the capacity and increases the SEI layer thickness on the anode. CO<sub>2</sub> is also known to produce CH<sub>4</sub> and other hydrocarbon gases on exposed copper components in the presence of water. Although the production of such gases is well known during the formation cycle there is also a slow production of hydrocarbon gases during cycle and calendar life which corresponds to a decrease in CO<sub>2</sub> production.

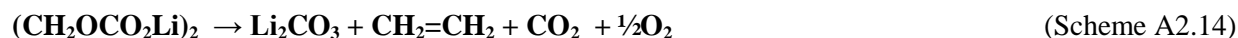
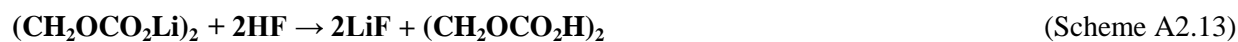
Concerning the behavior of the lithium salt, solid LiPF<sub>6</sub> is in equilibrium with solid LiF and PF<sub>5</sub> gas (Reaction Scheme A2.6). The reaction temperature and the pressure of PF<sub>5</sub> gas determine the position of the equilibrium. Removal of PF<sub>5</sub> consumes LiPF<sub>6</sub> and produces LiF. For a LiPF<sub>6</sub> solution, the analogous equilibrium exists. Because LiF is insoluble, only the concentration of LiPF<sub>6</sub> and PF<sub>5</sub> determine the equilibrium position. In electrolyte solutions, the equilibrium can move toward products, as PF<sub>5</sub> reacts with the solvents.<sup>75</sup>



(Scheme A2.6)

Lithium, or carbon intercalated with lithium, is reactive with all aprotic solvents, salt anions and many of the commonly used conductive polymers.<sup>77</sup> Focusing on the reactions associated with the production of lithium salts, summarized lists are cited below, mainly for the cases where LiPF<sub>6</sub> is used as the initial lithium salt. As it is demonstrated, both cyclic and linear solvents react to form several products, like ROCO<sub>2</sub>Li and ROLi species, as well as species with Li-C bonds. Further reduction of ROCO<sub>2</sub>Li, as well as secondary reactions to these species with trace H<sub>2</sub>O, leads to the formation of surface Li<sub>2</sub>CO<sub>3</sub>. The salt anion (PF<sub>6</sub><sup>-</sup>) and its related contaminants, HF and PF<sub>5</sub>, also react and hence, contribute to the complicated surface chemistry of lithium. In addition to this variety of surface reactions that form a mosaic of insoluble surface species, their sequence further complicates the structure of the surface films formed on lithium. Consequently, the surface films formed on lithium electrodes have a multilayer structure (also confirmed by depth profiling and X-ray photoelectron spectroscopy (XPS)), and are laterally non-uniform, as confirmed by in situ atomic force microscopy (AFM).<sup>78</sup>

Starting with the most commonly used solvents, and in particular with the EC, the reduction paths that this solvent undergoes on both Li and Li carbon surfaces, are the following<sup>28,64,73,77-83</sup>:

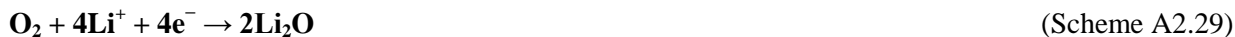


Further decomposition products of the surface film formed on the lithium metal during the decomposition and dissolution cycles are listed below<sup>42,64,73,78-82</sup>:





The next reactions are involved in O<sub>2</sub> reduction to form lithium peroxide (Li<sub>2</sub>O<sub>2</sub>) and lithium oxide (Li<sub>2</sub>O), and its reoxidation, respectively<sup>42,64,79,84</sup>:



Several studies suggest also a direct reduction, occurring though at lower voltages<sup>75</sup>:



It is well known that LiPF<sub>6</sub> in electrolytes reacts with water by the following mechanism<sup>64,67,77,81,83,85,86</sup>:



Li<sub>2</sub>O can also react directly with phosphorus compounds, formed from the decomposition of LiPF<sub>6</sub> and form P<sub>2</sub>O<sub>5</sub> according to the equation<sup>83</sup>:





The evolution of HF and POF<sub>3</sub> prior to PF<sub>5</sub> could only be the result of direct reaction between LiPF<sub>6</sub> and moisture, i.e.<sup>64,77,78</sup>:



The source of water in the cycled batteries is probably HF, which reacted with surface carbonate species. It is generally known that all LiPF<sub>6</sub> solutions may be unavoidably contaminated by hundreds of ppm of HF. HF reacts with both Li<sub>2</sub>CO<sub>3</sub> and ROCO<sub>2</sub>Li, which are formed on carbon anode surfaces by reduction of the alkyl carbonate solvents. The carbonic acids thus formed may then decompose to CO<sub>2</sub>, H<sub>2</sub>O and ROH.<sup>64,77-81,87</sup>



Other possible decomposition patterns of Li<sub>2</sub>CO<sub>3</sub> are the following<sup>79</sup>:



Corresponding to the aforementioned reactions of EC decomposition, the following list describes the reactions on lithium surfaces in the electrolyte solutions that contain DMC as a solvent<sup>28,67,73,77-83,88</sup>:



It has been proposed that instantaneously upon contact, a direct electron transfer occurs between lithium metal electrode and DMC, which, experiencing a symmetrical cleavage of the ester linkage in DMC, generates a rather unstable methyl radical ( $\text{CH}_3\bullet$ ) and a relatively stable anion (with R= methyl, i.e. lithium methyl carbonate). As it is demonstrated in the reactions of DMC mentioned above, the fate of  $\text{CH}_3\bullet$  might have multiple ends, one of which is the recombination and production of ethane, while the anion, serving as a stable intermediate, could rearrange into  $\text{CO}_2$  and  $\text{LiOCH}_3$ .<sup>88</sup> On the other hand, a competitive process may occur, which is characterized by a symmetrical cleavage on the alkyl side of ester linkage like in DMC, generating a rather stable anion ( $\text{CH}_3\text{O}^-$ ) and also a stable alkyl radical. The latter could attack a second DMC molecule, resulting in various oxalate moieties, along with propagation of radical  $\text{CH}_3\text{O}\bullet$ .<sup>88</sup> Accordingly, the formation of a  $\text{CH}_3\text{OCO}\bullet$  radical is also possible. The intermediate radical or ionic compounds created can lead to a number of volatile molecules, like those formed at the following reactions<sup>73,77,88</sup>:



As it is illustrated in the reactions above, some lithium salts are products of the direct reduction of an organic solvent, while others are decomposition products, often further consuming lithium. Some reactions produce water, which can trigger additional salt decomposition steps. Many of the above reactions are interdependent, mostly in equilibrium. This suggests a complex series of cascading reactions at the SEI during storage (Figure A2.26).<sup>79</sup>

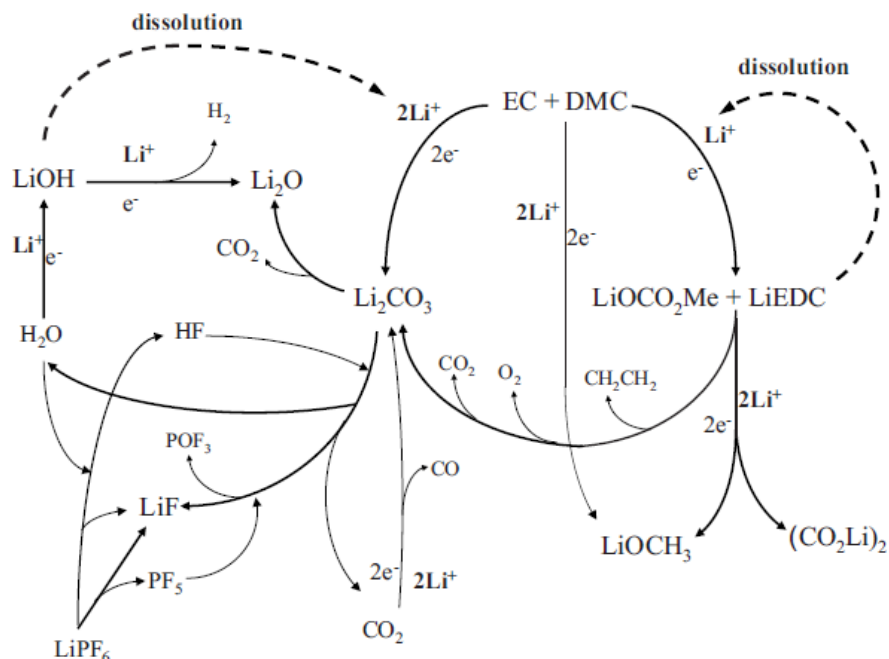


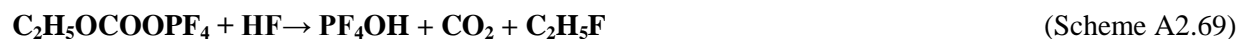
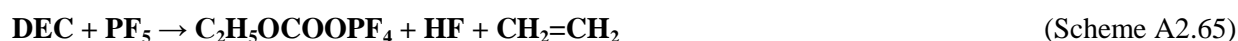
**Figure A2.26. Reactions associated with the formation of SEI films, the decomposition, and the dissolution of the salts, possibly occurring during storage, illustrating progressive lithium consumptions by the reactions when  $\text{LiPF}_6$  was used as the lithium salt and EC and DMC were used as the organicsolvents.<sup>79</sup>**

Reduction pathways that are used in the presence of DMC will also occur when other linear carbonates like DEC or EMC are used as solvents, with respect to their molecular structure similarities, leading to reaction equations like the following<sup>67;83</sup>:



DEC also decomposes in the presence of  $\text{PF}_5$ . This strong Lewis acid attacks the lone electron pair of oxygen of the water molecule and then decomposes. By analogy,  $\text{PF}_5$  may attack the electron lone pair of oxygen of a solvent molecule and then decompose. In more detail, larger electron density causes an immediate attack, with  $\text{PF}_5$  attacking the carbonyl oxygen atom (oxygen atom in C-O) because of its large electron density. Hence, the higher reactivity of DEC than DMC can be explained, since  $\text{C}_2\text{H}_5-$  is – due to

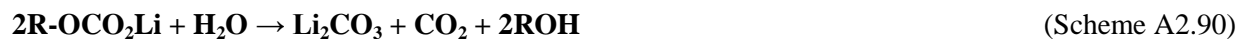
the inductive effect (+I) – a more electron-donating group than CH<sub>3</sub>-. For this reason, DEC may decompose more easily than DMC, following the equations proposed below<sup>67</sup>:



An alkoxide displaces fluoride in PF<sub>5</sub> to produce ROPF<sub>4</sub>. Further addition of alkoxide anions to the same P(V) center can provide (RO)<sub>2</sub>PF<sub>3</sub> and (RO)<sub>3</sub>PF<sub>2</sub>. P(V) compounds containing at least one alkoxide and one halide substituent are susceptible to Arbuzov rearrangements. Rearrangements of ROPF<sub>4</sub>, (RO)<sub>2</sub>PF<sub>3</sub> and (RO)<sub>3</sub>PF<sub>2</sub> produce POF<sub>3</sub>, POF<sub>2</sub>(OR), and POF(OR)<sub>2</sub> respectively, along with one equivalent of alkylfluoride (RF).<sup>70</sup>



Generally, when LiPF<sub>6</sub> is used as the initial lithium salt, and R is either CH<sub>3</sub> or C<sub>2</sub>H<sub>5</sub>; thus R<sub>2</sub> can be either C<sub>2</sub>H<sub>6</sub> or C<sub>4</sub>H<sub>10</sub> respectively, the reactions occurring are described by the following equations<sup>64,77,79,83</sup>:



A decomposition scheme of carbonates by PF<sub>5</sub>/HF is demonstrated in Figure A2.27<sup>64</sup>.

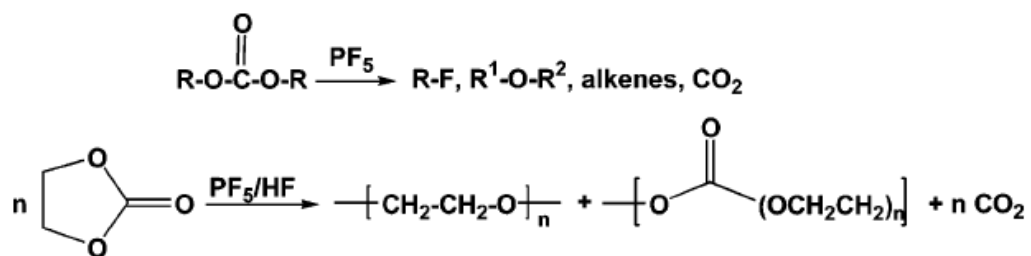
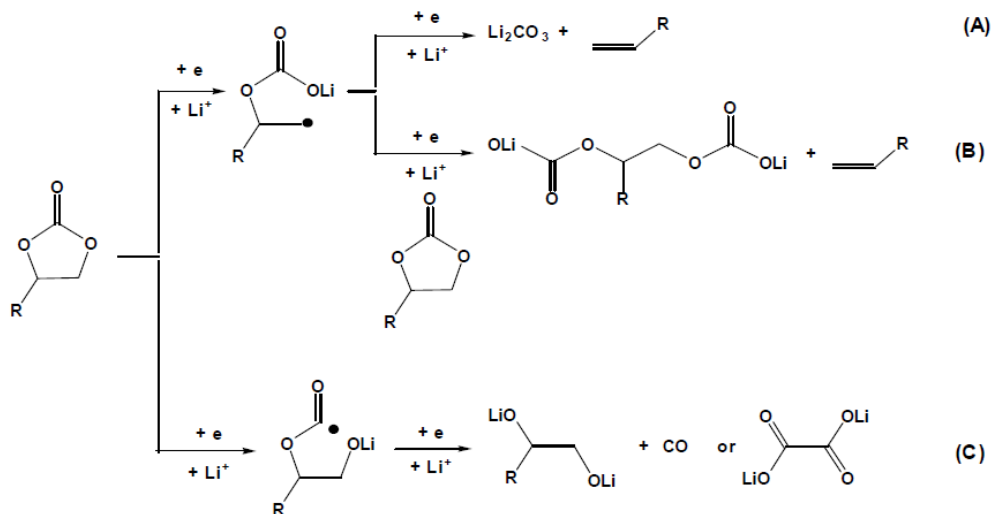


Figure A2.27. Reaction scheme for the decomposition of cyclic or aliphatic carbonates.<sup>64</sup>

An overall formation scheme of ROLi from linear carbonates was presented at Figure A2.2. When a cyclic solvent is used, the following reactions take place under typical conditions of usage/storage<sup>89</sup>:



**Figure A2.28. Three possible pathways for surface reductions of cyclic organic carbonates on graphitic anodes, where R = CH<sub>3</sub> or H: Pathway A represents a two-electron reduction of organic carbonate, which was determined to be an unlikely route; while pathways B and C are mainly responsible for SEI ingredients.<sup>89</sup>**

Comparing the cyclic solvents frequently used in LIBs, PC has proved to be the less stable electrolyte in comparison to EC, as EC-based electrolytes show the best Li-cycling efficiency<sup>77,78,82</sup>. According to another reaction scheme proposed, the reduction of PC can lead to various polymeric species<sup>64</sup>:

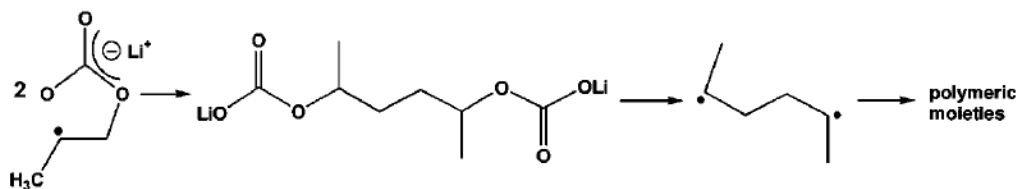


**Figure A2.29. Reaction scheme of PC polymerization.<sup>64</sup>**

## 2.2 Degradation mechanisms under stress conditions

Apart from the experiments performed in order to understand the electrochemical degradation mechanisms of lithium-ion batteries under the conditions of normal use, many different types of abuse tests are also performed to characterize their abuse tolerance. The ones with the widest use are listed below:

- Oven test: This test simply involves exposing the battery to high temperature. For consumer batteries, an oven temperature of 150°C is typically used.
- Short-circuit: A low resistance (<5 mΩ) is connected across the terminals of the battery, while the battery may be preheated. In this test, current flows through the battery generating heat. The battery is heated internally due to current flow, but the external circuit can dissipate heat as well.

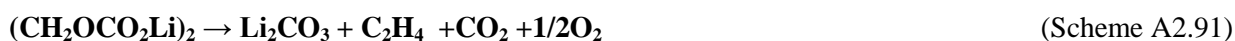
(c) Overcharge test: Current is forced through the cell up to some limiting voltage. Heat is generated by electrochemical reactions and by current flowing through the cell.

(d) Nail: A nail is forced through the battery at a prescribed rate (such as 8 cm/s). Heat is generated by current flowing through the cell, and by current flowing through the nail. Initially the nail is positioned outside of the battery wall and, when the test begins, is forced through the battery wall and into the battery at a constant speed. As the nail moves forward, forming direct shorts between adjacent electrode pairs, the current flowing through the nail itself decreases.

(e) Crush test: A bar is used to press down on the battery until a short-circuit initiates. Heat is generated throughout the battery due to discharge, and locally through the electrode pairs that are physically shorted.<sup>90</sup>

Abuse testing of batteries gives some insight into failure mechanisms, but direct characterization of the materials that constitute the battery can lead to a better understanding of what makes a battery abuse tolerant. The following exothermic reactions have been proposed to take place during abuse testing of lithium-ion batteries:

**SEI layer decomposition:** The breakdown of the passivating SEI layer can occur due to overheating or physical penetration. This SEI layer is assumed to consist of stable (such as LiF and Li<sub>2</sub>CO<sub>3</sub>), and metastable components (such as polymers, ROCO<sub>2</sub>Li and (CH<sub>2</sub>OCO<sub>2</sub>Li)<sub>2</sub>). The metastable components might exothermically react at 90–120°C as follows<sup>80,90,91</sup>:



The initial overheating may be caused by excessive currents, overcharging or high external ambient temperature.<sup>91</sup>

**Reaction of intercalated lithium with electrolyte:** At elevated temperatures (>120°C), the SEI layer does not protect the negative electrode from contact with the electrolyte and an exothermic reaction between intercalated lithium and electrolyte can occur. Solvent might react with lithium (either metallic or intercalated) releasing flammable hydrocarbon gases (ethane, methane and others) but no oxygen<sup>90</sup>:



This typically starts at 100°C but with some electrolytes it can be as low as 68°C. The gas generation due to the breakdown of the electrolyte causes pressure to build up inside the cell. Although the temperature increases beyond the flashpoint of the gases released by the electrolyte, the lack of free oxygen in the cell sustains a fire.<sup>91</sup>

Between 200°C and 240°C, metallic lithium reacts further with EC to produce carbon dioxide and dilithio butylene dialkoxide, which subsequently reacts with PF<sub>5</sub> as follows<sup>91</sup>:



**Reaction of intercalated lithium with fluorinated binder:** For the PVDF–Li<sub>x</sub>C<sub>6</sub> reactions, they are strongly affected by the degree of lithiation of the graphite since they occur only when the carbon electrode is lithiated. These reactions occur when the temperature is higher than 260°C. Possible reactions between the binder and the Li<sub>x</sub>C<sub>6</sub> electrode are the following<sup>90,91</sup>:



**Electrolyte decomposition:** The electrolyte not only reacts with the electrodes, but also decomposes itself at elevated temperatures, around 200–300°C<sup>91</sup>. These reactions will be later on discussed in detail.

**Positive active material decomposition:** At around 130°C the polymer separator melts, allowing the short circuits between the electrodes. Eventually heat from the electrolyte breakdown causes breakdown of the metal oxide cathode material releasing oxygen. The release temperature and the amount of oxygen are highly dependent on the material type (Lithium Manganese Oxide (LMO, LiMn<sub>2</sub>O<sub>4</sub>) < Lithium Nickel Manganese Cobalt Oxide (NMC, LiNiMnCoO<sub>2</sub>) < Lithium Nickel Cobalt Aluminum Oxide (NCA, LiNiCoAlO<sub>2</sub>), no O<sub>2</sub> release for Lithium Iron Phosphate (LFP, LiFePO<sub>4</sub>). This oxygen can react exothermically with electrolyte, or, perhaps the positive material reacts directly with electrolyte, in a highly exothermic way<sup>90,91</sup>:





These reactions do not occur in an exact given order and some of them may happen simultaneously.<sup>91</sup> However, SEI decomposition is the first exothermic phenomenon being observed.<sup>68</sup> In general, the Li-ion thermal runaway phenomenon occurs at elevated usage or storage temperatures. Several stages are involved in the buildup of thermal runaway and each one results in progressively more permanent damage to the cell. Starting from gas release, overpressurization and even rupture of the battery casing may occur. Therefore, this phenomenon has been studied over the last twenty years, giving rise to a valuable comprehensive survey of materials, morphology and role of electrolyte additives that modify the exothermic onset temperature.<sup>68</sup>

When the GC/MS technique was used for the examination of the thermal behavior of Li-ion batteries, several organic compounds were identified after heating  $\text{LiC}_6$  with electrolyte at different temperatures. For both cyclic electrolytes, like EC, and linear electrolytes, such as DMC, the detected species could be sorted in five families, i.e. esters (methyl or ethyl formate, methyl formate or acetate), hydrocarbons ( $\text{C}_2\text{H}_6$  and  $\text{C}_2\text{H}_4$ ), ethers (dimethyl ether, ethyleneoxide, 1,4dioxane, monoglyme, 2-methyl-1,3-dioxolane), carbonates (EMC, DEC), and alcohols (methanol, ethanol).<sup>68</sup> As previously mentioned, the same species as under normal operating conditions were identified, with the same reaction mechanisms being postulated. In particular, the identified compounds were proposed to result from the same two types of reactions: (i) a reduction process of linear or cyclic carbonate and (ii) a reaction involving nucleophilic attack, as schematized below<sup>68</sup>.

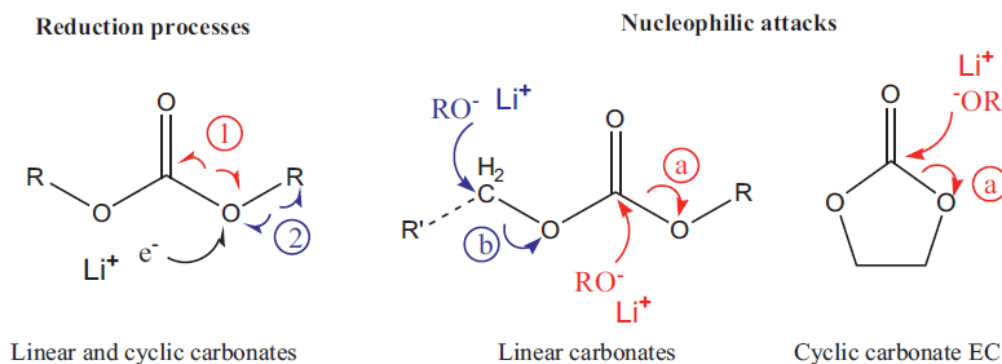


**Figure A2.30. Reduction processes and nucleophilic attacks on both linear and cyclic solvents.**<sup>68</sup>

Resulting from the aforementioned reactions, recombination of the intermediate species and hydrolytic procedures, the various products of electrolyte degradation processes are summarized in Figure A2.31. Apart from these compounds, several polymerization species (e.g PEO compounds) were again identified.<sup>67</sup> Additional lithium salt decomposition resulted in various fluorinated and phosphoric species, with the reaction pathways and more significant products being summarized in Figure A2.32.

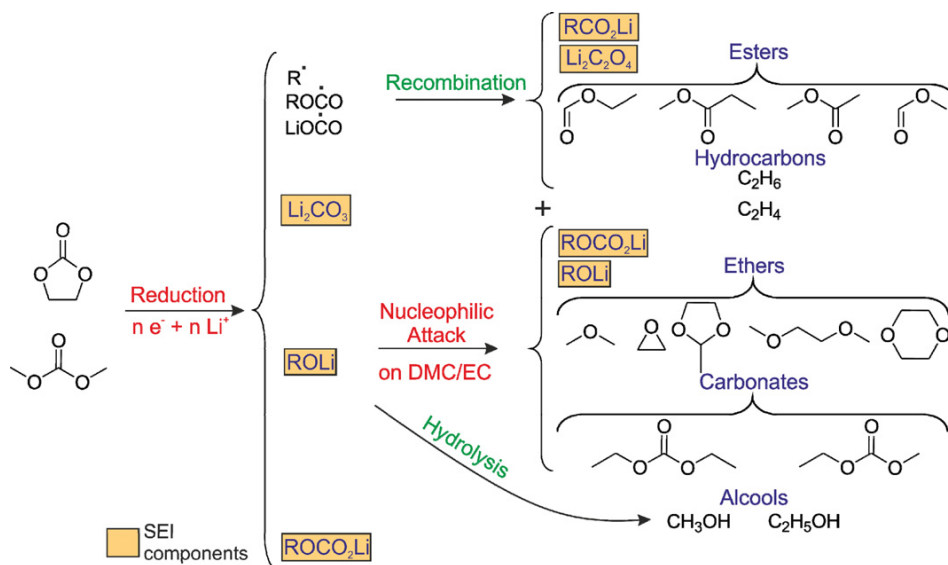


Figure A2.31. Global scheme of solvents degradation processes.<sup>68</sup>

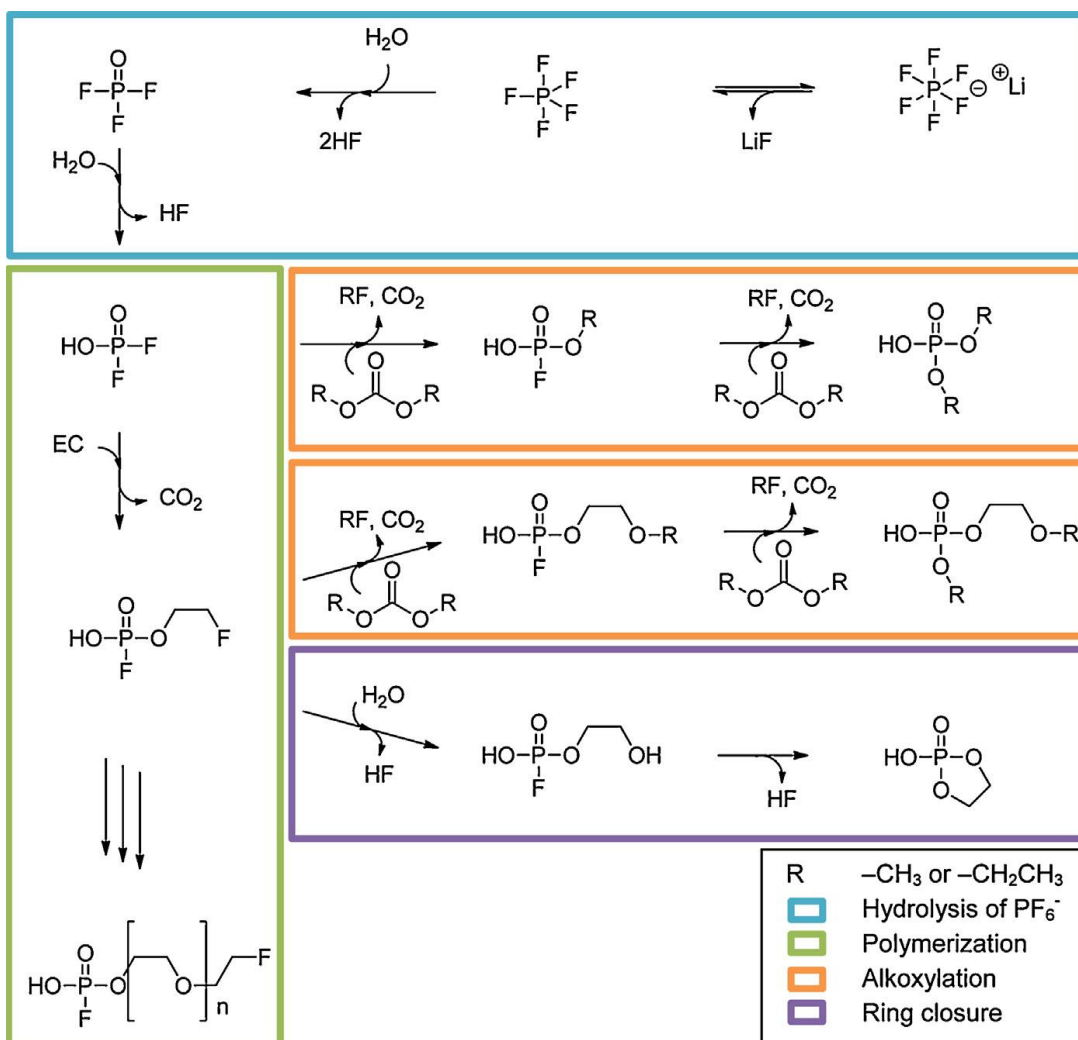


Figure A2.32. Decomposition mechanism of  $LiPF_6$  via difluorophosphate (DFP).<sup>92</sup>

In addition to thermal stability experiments, the behavior of Lithium-ion cells at extreme charging conditions has also been examined. For example, large amounts of CO, CO<sub>2</sub> and hydrocarbons were detected from overdischarged cells, where an overdischarge of -10% of their capacities was performed. Hydrogen was also detected in some electrolyte systems. In the overdischarged state, the copper of the anode current collector dissolved at low potential range, and the cathode was plated with dissolved copper. Thus, no charging reaction occurred at the cathode, and electrolyte decomposition was accelerated. As a result, a large volume of hydrocarbons was produced. From these results, it was assumed that the decomposition of the electrolytes was mainly due to the reduction of the electrolytes. This reaction seemed to be dependent on the change in surface conditions at the cathode.

On the other hand, overcharging a LIB can lead to lithium metal formation which opens the possibilities for further reactions with the solvent and binder. Solvent oxidation reactions occur, generating heat at a much higher rate than the irreversible heating due to the intercalation reactions.<sup>90</sup> By an overcharge of +5% of their capacities, Lithium-ion cells exhibited the production of large amounts of CO<sub>2</sub>. It was assumed that CO<sub>2</sub> was mainly generated by electrolyte decomposition, due to the formation of oxygen from the cathode material during overcharging. Figure A2.33 gives an overview of the gas generation reactions occurring under overcharge and overdischarge conditions.

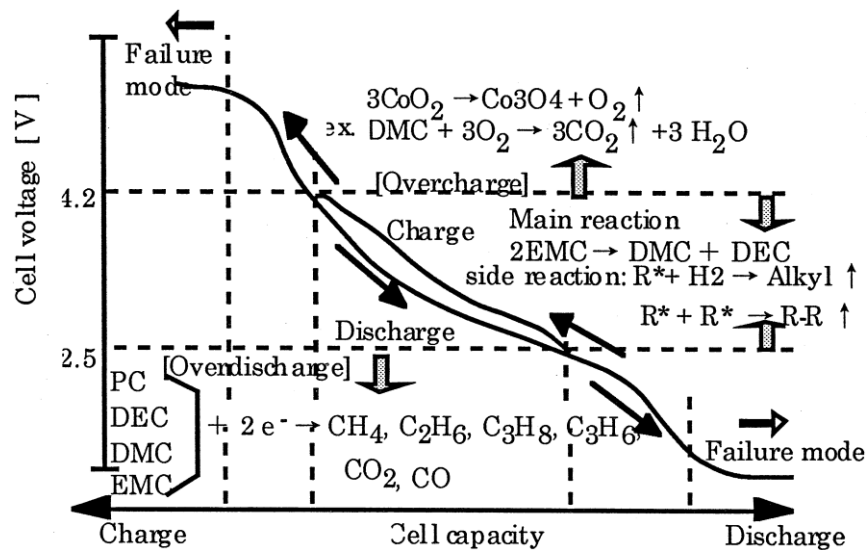


Figure A2.33. Overcharge and overdischarge voltage profiles of Li-ion cell and the corresponding gas generation model.<sup>74</sup>

### ***A.3. Analytical techniques applied for the characterization of LIBs***

#### ***A.3.1. Introduction***

The lithium-ion battery consists of the electrode materials, the SEI formed on the electrode surface, the separator, the electrolyte with its additives and the housing, including all ancillary devices that ensure battery safety. However, the electrolyte solution is the LIB component with the highest relevance for cell safety under normal use and conditions of abuse, with a wide spectrum of compounds being formed inside the cell under both conditions. The need for the identification and quantification of the volatile degradation compounds formed under different conditions of use is of profound importance, since the gaseous emissions lead to internal pressure build-up and cell bulging, de-lamination of the electrodes and de-contacting of the active materials, not only compromising the cell's performance, but also implying serious safety concerns.<sup>93</sup>

Several approaches have been proposed and implemented so far for the analysis of the volatile products as well as for the less and non-volatile ones, and for monitoring the various changes that the cells may undergo during their lifetime. The most important and therefore more frequently used analytical techniques will be discussed in this chapter. With the focus on the volatile compounds formed inside the cells, a review on the applications of Fourier transform infrared spectroscopy (FTIR) and gas chromatography (GC) will be presented. These will be also the techniques applied for the *ex situ* and *in situ* investigations on LIBs, the results of which are presented in the following chapters. Particularly for GC, the introduction of different detectors, depending on the targeted groups of analytes, will be further discussed, focusing on the recently released barrier discharge ionization detector (BID), for which the working principle, construction characteristics, advantages over existing alternatives and general applicability will be presented in more detail.

### ***A.3.2. Analytical approaches for the analysis of LIB components and degradation products***

Depending on the level of battery characterization the various techniques used can be classified into different categories. The basic two categories involve the *in situ* and the *post-mortem* studies, depending on the parameters intended to be controlled each time. By non-destructive, *in situ* studies full cells are investigated, while for *post-mortem* analysis opening of the battery case is required. Further aspects of classification are half-cell testing, solution studies and electrode studies of bulk and surface analysis.<sup>94</sup>

In order to gain insight into the various processes of battery operation, a minimum of sample preparation is necessary. Particular consideration is required in order to maintain the chemical state of the battery unchanged and also prevent mechanical damage, but at the same time to ensure that further handling is safe. Therefore, the design of such operations is important for gaining representative samples that also provide consistency with the *in-use* state of the materials analyzed and avoiding erroneous results. The disassembly methodology of LIBs for *post mortem*-investigations has been reported in detail by Pecht *et al.*<sup>95</sup>, pointing out the various considerations that should be taken into account when different types of investigations are planned and consequently different types of experiments will be conducted. However, the first thing to be always considered is to bring the cells to a safe state, with the procedures to be followed being provided by the cell manufacturers.

For the different types of experiments performed *in situ* or *post-mortem*, a number of electrochemical, thermo-analytical, microscopic, spectroscopic, spectrometric, chromatographic and other techniques, as well as their combinations, have been employed, fulfilling the task of a complete characterization of the cells. Particularly for the *post-mortem* analysis, an overview of the physico-chemical methods applied is illustrated in Figure A3.1.

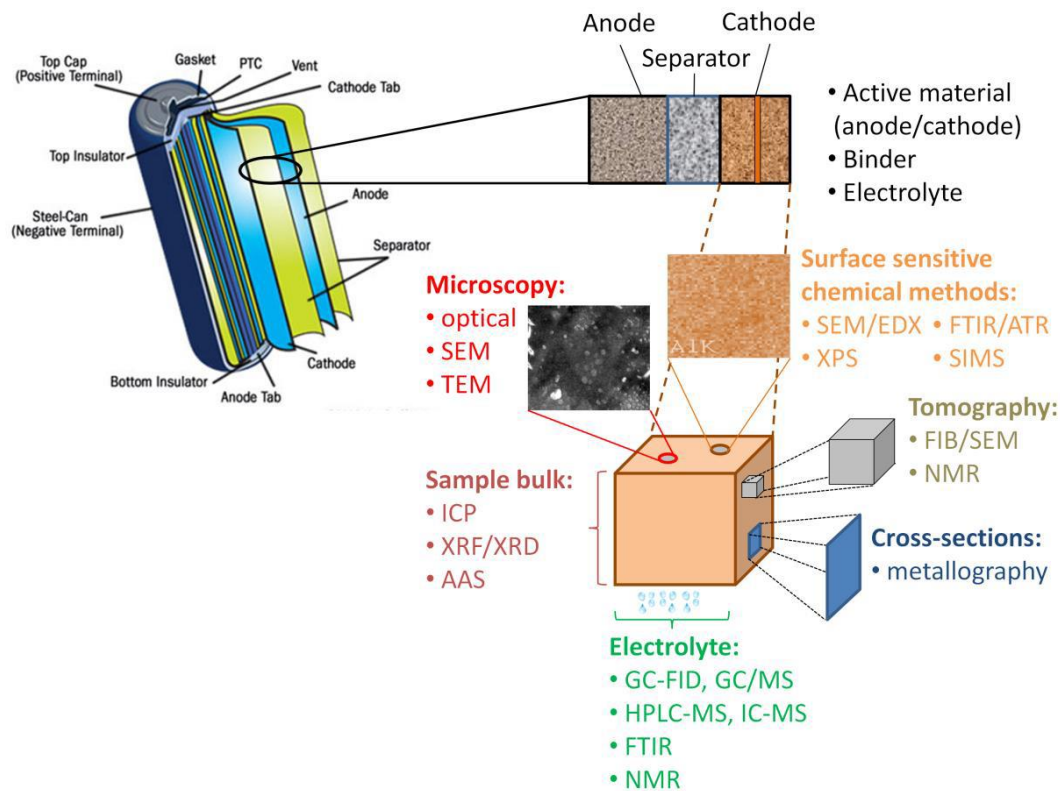


**Figure A3.1 Overview of components inside a Li-ion battery and physico-chemical methods for their characterization after post-mortem analysis<sup>96</sup>**

Starting with the electrochemical techniques, several options are available for the characterization of LIBs and their components. Common approaches, like **chronopotentiometry**<sup>97</sup>, cyclic voltammetry (**CV**)<sup>98</sup> and the recently introduced differential thermal voltammetry (**DTV**)<sup>99</sup>, are used in most of the cases in combination with other analytical tools. Electrochemical impedance spectroscopy (**EIS**)<sup>100</sup>, and scanning tunneling microscopy (**STM**)<sup>101,102</sup> are also employed in electrochemical studies.

The crystal structure of LIB components can be elucidated by the use of diffraction techniques such as X-ray diffraction (**XRD**)<sup>103,104</sup>, selected area electron diffraction (**SAED**)<sup>105</sup> and neutron diffraction (**ND**)<sup>106</sup>. The location of light elements in the lattice provides valuable information about the atomic structure of these components, determining their electrochemical behavior. Specifically, XRD has proven to be the most favorable tool for such *ex situ* investigations, since it does not require any particular preparation of the materials prior to the analysis, like when electron diffraction is used, or any special radiation sources, like in the case of ND<sup>94</sup>.

When it comes to morphological analysis of lithium-ion cells, several microscopic techniques are also implemented<sup>107</sup>. Characteristic examples comprise conventional transmission electron microscopy (**TEM**) or high resolution TEM (**HR-TEM**)<sup>108,109</sup> and analytical TEM (e.g. energy dispersive X-ray spectroscopy/analysis (**EDX**, **EDS** or **EDAX**))<sup>110</sup>, as well as conventional scanning transmission electron

microscopy (**STEM**)<sup>111</sup>. Scanning probe microscopy (**SPM**)<sup>112</sup> is also used, with atomic force microscopy (**AFM**)<sup>113</sup> selected as the main relevant tool, as it enables the *in situ* imaging of almost every type of surface. Recent developments in the field of *in situ* investigations of LIBs using further microscopic approaches, including X-ray fluorescence (**XRF**), **Raman** and transmission X-ray microscopy (**TXM**), have been summarized by Minhua Shao<sup>114</sup>.

However, for surface measurements of LIBs the most useful techniques are considered to be the Fourier transform infrared spectroscopy (**FTIR**) and among the photoemission spectroscopic (**PES**) techniques the X-ray photoelectron spectroscopy (**XPS**)<sup>115-119</sup>. Surface analytical tools are also the previously mentioned **EDS** and **XRD**, as well as the **Raman** spectroscopy<sup>110</sup>, with techniques like the surface-enhanced Raman scattering (**SERS**)<sup>120</sup> being widely applied.

Although XPS is commonly used to characterize electrode surfaces, this technique provides information only on the first few nanometers at the electrode surface, while depth profiling analysis is also necessary for the characterization of the cycled bulk materials, since some of the interesting issues also relate to the bulk composition<sup>121</sup>. For this reason, sputter-depth profiling XPS (**SDP-XPS**)<sup>122</sup> was applied, enabling for example investigations on the thickness, structure and composition of the SEI layer. Alternatively, time-of-flight secondary ion mass spectrometry (**TOF-SIMS**) is a highly sensitive surface analytical technique, with which compositional depth profiles with excellent depth resolution (monolayer) and high sensitivity (ppb) can be readily obtained. TOF-SIMS has been therefore applied to cycled electrode materials providing information about the SEI layer and the depth and lateral distribution of species in the bulk electrode materials<sup>123,124</sup>. From these depth profiles, attempts to estimate roughly the SEI thickness are performed, but, it should be recognized that in TOF-SIMS measurements the molecular species can be decomposed and fragmented when sputtered<sup>125,126</sup>.

The basic approaches towards thermal analysis of LIBs are thermal gravimetric analysis (**TGA**)<sup>127</sup>, differential thermal analysis (**DTA**)<sup>127</sup>, differential scanning calorimetry (**DSC**)<sup>128</sup> and accelerating rate calorimetry (**ARC**)<sup>129</sup>. DTA and DSC provide fundamental thermodynamic data and qualitative and quantitative information on the physical and chemical behavior of processes occurring inside the LIBs (e.g. endothermic or exothermic reaction character and onset temperatures). In contrast to these, TGA measures the mass change as a function of temperature. For this reason, coupling TGA with DTA or DSC can determine the enthalpy values of studied reactions, while coupling with gas analysis techniques can assist the determination of such reaction mechanisms<sup>130</sup>. While simultaneous thermal analysis (**STA**) has also been applied to estimate the safety behavior at the material level, for disassembled cells, and in combination with mass spectrometry (**MS**)<sup>129</sup>, ARC is considered as the most appropriate tool for thermal runaway studies, when implemented alone or in combination with DSC measurements<sup>131</sup>. In a DSC measurement, the thermal stability is often quantified by the total heat flow and the onset temperature for exothermic decomposition<sup>132</sup>, while by ARC the thermal stability of various electrolytes and cells

containing different electrolyte formulations can be characterized by determination of the onset temperature for gas formation. The ARC is equipped to measure total gas pressure from electrolyte vapor pressure and decomposition products (from which volume can be calculated) for electrolyte and cell samples while maintaining a completely adiabatic environment<sup>132</sup>. For large format LIBs extended volume accelerating rate calorimetry (**EV-ARC**) has been used<sup>133,134</sup>. Furthermore, thermomechanical analysis (**TMA**)<sup>135</sup> has been employed e.g. for testing of the thermal and tensile properties of the LIB separators.

*In situ* **colorimetry**<sup>136</sup>, relating the color of an electrode to its state of charge, is another tool to study the kinetics of lithium ion distribution in model graphite electrodes in near-surface regions and to determine the consequent diffusion coefficients of lithium ions according to their overall mobility. This technique can also be used to complement Raman spectroscopy when studying highly intercalated graphite, for which Raman signals are hard to detect due to high electronic conductivity<sup>137</sup>. In addition, the electron-spin resonance method (**ESR**) or electron paramagnetic resonance (**EPR**) was used to examine the existence of compounds with unpaired electrons and shed light to the mechanisms taking place upon cycling. With this technique Endo *et al.* have detected the continuous production of active alkyl radicals in electrolyte during first lithium intercalation<sup>138,139</sup>.

For the determination of elemental composition, the inductively coupled plasma (**ICP**) has proven to be a powerful analytical tool, confirming the stoichiometry of lithium, cobalt, nickel and other metals used as LIB components<sup>129, 140, 141</sup>. Various applications of ICP with optical emission spectrometry (**ICP-OES**)<sup>142-145</sup>, atomic emission spectrometry (**ICP-AES**)<sup>146, 147, 148</sup> and mass spectrometry (**ICP-MS**)<sup>149-156</sup> are presented in the literature. For example, the determination of lithium ratios to transition-metal ions in the pure active material or the disassembled, washed cathodes of lithium-ion cells have been performed by both ICP-OES<sup>157,158</sup> and ICP-AES<sup>159,160</sup>. In addition, not only ICP-OES<sup>142,161</sup> but also ICP-MS<sup>142</sup> coupled to ion chromatography have been used for the characterization of aged cells, however the extent of such applications is still quite limited.

Another technique used extensively to quantify trace amounts of metals and elements is atomic absorption spectroscopy (**AAS**). For this reason, it has been employed to provide bulk information on the SEI components<sup>162</sup> and in the analysis of the surface films formed on lithium metal in various organic analytes<sup>163</sup>. AAS has been used in the recovery process of the metals, for measuring the concentrations of Co, Ni, Mn, Li, Al, Fe and Cu<sup>164,165,166</sup>. The quantitative evaluation of the stability of battery-grade copper foils in electrolytes at open-circuit voltage (**OCV**) was also performed by AAS by detecting the copper dissolution over time<sup>167</sup>.

Nuclear magnetic resonance (**NMR**) spectroscopy is an additional technique applied for investigations on the thermal stability<sup>168</sup> or the anodic stability<sup>169</sup> of electrolytes and the corresponding reaction mechanism of lithium salts in electrolyte solutions on graphite anodes. Like in the case of AAS, NMR is a technique that gives bulk information of SEI components<sup>162</sup>. Apart from the main applications of NMR in LIBs, the



technique has also been used, for purity measurements of synthesized lithium alkyl carbonate salts<sup>126</sup>. NMR measurements were additionally conducted for confirmation of the chemical structure and the purity of LIBs' electrolytes<sup>170</sup>, providing quantitative information<sup>171</sup> for samples under post-mortem conditions but also *in situ* studies<sup>172</sup>.

For the analysis of less and/or non-volatile LIB organic components, high performance liquid chromatography (**HPLC**) has also been employed<sup>173</sup>. Apart from the UV/Vis detector, coupling with MS detection enabled the identification and quantification of organic carbonates and other compounds resulting from thermal aging or other situations of normal and abnormal operation of LIBs. Fresh and treated electrolyte solutions have been analyzed by high mass accuracy MS<sup>n</sup> instruments<sup>174,175,176</sup>, such as an LC instrument with a hybrid triple quadrupole/linear ion trap (**QTRAP**)<sup>177</sup> or an ion trap-time of flight (**IT-TOF**) mass spectrometric detector<sup>178</sup>. An LC-HR-MS instrument equipped with an **ESI-Qq-TOF** detector has also been used in order to confirm the structure of intermediate and final products, when the prospective function of fluorinated imidazolium ionic liquids was investigated<sup>179</sup>.

A suitable analytical tool for compounds of higher molecular masses proved to be the gel permeation chromatography (**GPC**), also known as size or steric exclusion chromatography (**SEC**)<sup>180-185</sup>. According to such studies conducted by Sloop *et al.*<sup>173</sup> on the thermal and electrochemical decomposition reactions of the lithium salt in carbonate solvents and on how these reactions lead to the formation of products that impact the performance of lithium-ion batteries, the polymerization of the electrolyte was observed. In addition, when suitable solid polymer electrolytes (SPEs) were investigated as a replacement for the conventionally used liquid/gel electrolytes, the GPC was used for the determination of the residual monomer content during their synthesis as well as of their actual molecular weight.<sup>173,182,184,186,186,</sup>

Complementary to GPC analysis, the electrolyte solutions and filtrated aqueous solutions of cell components were also investigated by capillary electrophoresis (**CE**)<sup>173,187</sup>. Furthermore, a recent application of CE is combining this chromatographic technique with a direct contactless conductivity detector (C<sup>4</sup>D) for the quantification of fluoride in LIBs, where the results were in good agreement with those obtained with an ion-selective electrode (ISE)<sup>188</sup>.

Ion chromatography (**IC**) has been alternatively used to separate the decomposition products of LiPF<sub>6</sub> and other compounds formed during the thermal aging of commercially available electrolyte systems<sup>161,163,189</sup>. To detect these compounds, several approaches have been investigated, starting with coupling the IC to a conductivity detector for qualitative analysis and moving to more sophisticated options for the unknown compounds, like electrospray ionization mass spectrometry (ESI-MS) and inductively coupled plasma optical emission spectroscopy (ICP-OES)<sup>161</sup>. With the hyphenation of IC with ICP-OES, information about the element composition of each peak was gained. The chemical structures of several identified compounds have been further elucidated with **IC-ESI-MS/MS**<sup>189</sup>. An additional hyphenation option, used in one of the most recent studies conducted by Nowak *et al.*<sup>142</sup>, refers to the use of an **IC-ICP-MS** system,

providing complementary data to those obtained by IC-ESI-MS measurements. Moving towards even more sophisticated instrumentation, for the analysis of thermally decomposed lithium hexafluorophosphate-based LIB electrolytes, two dimensional IC (**IC/IC**) in the heart-cutting mode was used<sup>190</sup>, enabling with higher resolution the separation of the organophosphates, which were later on quantified by phosphorus selective ICP-MS analysis.

While many hyphenated techniques using MS for the detection of the target analytes have proven to be highly suitable for the identification of original LIB components as well as their degradation products, mass spectrometry as a stand-alone technique has been also used for the direct analysis of LIBs samples. Without a preceding separation, high resolution MS (**HRMS**) is essential for differentiating isobaric ions, frequently seen in the various series of proposed polyethylene oxide (PEO)-like isomers resulting from the electrolyte decomposition under different experimental conditions. Conventional electrospray ionization ESI-MS has been used to investigate the solvation of lithium ions in mixed organic solvents, using diluted solutions in methanol<sup>191</sup>. Furthermore, aged electrolyte solutions have been analyzed by both fast atom bombardment (**FAB**), and chemical ionization (**CI**)<sup>192</sup> mass spectrometry.

An alternative rapid method for *in situ* analysis and reaction monitoring in LIB electrolytes, based on HRMS with low-temperature plasma probe (**LTP**) ambient desorption/ionization, was recently presented. In order to identify the time-/condition-dependent formation of electrolyte decomposition compounds, Engelhard *et al.*<sup>193</sup> performed accurate mass measurements in both positive and negative ionization modes, using the LTP probe and an **Orbitrap** detector, enabling qualitative analysis in ambient environment independent of the sample size, geometry and structure. By reducing the need for sample preparation, short analysis times of less than 30 sec were obtained, making this option ideally suited for high-throughput applications and screening of, for example, large compound libraries. Moreover, it eliminated the need of organic solvents or other chemicals that could cause contamination during sampling and could adversely affect the sample composition. Operation under air, though, may probably lead to many electrolyte degradation products otherwise not seen if working under an inert atmosphere.

Differential electrochemical mass spectrometry (**DEMS**) is also one of the basic techniques used to study the processes of electrolyte decomposition, SEI formation and to observe *in situ* the formation of gases on the electrodes. DEMS can be generally used not only to identify products or intermediates of continuous faradaic reactions, but also to characterize submonolayer amounts of adsorbates on polycrystalline and single crystal electrode surfaces by means of their desorption, because of its high sensitivity.<sup>194</sup> One possibility to achieve this is to oxidize a carbonaceous species to CO<sub>2</sub>, which is quantitatively detected in the mass spectrometer. Many adsorbates can also be desorbed at certain potentials as such, or as the hydrogenated product, allowing a more direct characterization of the adsorbate. In some cases, a nonreactive desorption can be induced by displacement with a second adsorbate, yielding additional information. Interfacing an electrochemical cell to a mass spectrometer via a porous Teflon membrane can

be achieved with a variety of cells, depending on the properties of the samples. Several studies employing DEMS in LIB investigations have already been conducted, proving the significance of this particular approach<sup>195 - 208</sup>. The disadvantage of DEMS is that only volatile products can be detected. On the other hand, with techniques like GPC, IC and their hyphenated options, the direct analysis of volatile compounds is not applicable. Therefore, several techniques need to be used complementary for the identification of the entity of compounds formed or existing in LIB electrolytes.

Particularly for the identifications of gaseous emissions formed inside the lithium-ion cells, alternative basic approaches include the use of e.g. CO and CO<sub>2</sub> gas analyzers that measure the generation of carbon monoxide and carbon dioxide respectively, or the O<sub>2</sub> analyzer applied for the investigation of oxygen depletion<sup>209</sup>. However, FTIR spectroscopy and gas chromatography (GC) are two of the most widely used techniques in the characterization of LIB gas emissions and they will be therefore discussed in greater detail in the following sections.

#### **A.3.2.1. FTIR**

FTIR spectroscopy as a stand-alone technique is one of the main analytical tools for both *in situ* and *ex situ* investigations of LIBs, providing information at a molecular level. This versatile technique differentiates between the various functional groups based on the vibrational energies of individual parts of or the entire molecule. The corresponding absorption peaks represent a fingerprint of the sample, while their intensities provide the quantitative information required. The high speed (Felgett or multiplex advantage), high sensitivity (Jacquinot or throughput advantage) and possibility for internal wavelength calibration (Connes or wavelength accuracy advantage) contribute to the extended range of applications. The fact that it does not require ultra-high vacuum conditions makes it a relatively cheap surface analytical technique used in LIBs analysis<sup>210</sup>.

A characteristic example of *ex situ* FTIR measurements involves the identification of the chemical composition of SEI layers on various materials of lithium-ion cells, which have previously been aged or cycled in different electrolyte mixtures<sup>211</sup>. Concerning the *in situ* applications of the technique, oxidation and reduction processes of the electrolyte solutions on the electrodes of the cells<sup>212</sup> or on the non-active materials<sup>213</sup> have been of particular interest. However, the similarity of functional groups present in many of the components of LIBs results in overlapping signals and can make the spectra interpretation tricky when particular compounds are targeted. The components of the SEI layer are such an example, providing mainly carbonyls, alkoxides and alkanes with their characteristic vibrations<sup>214</sup>. On the other hand, this feature of FTIR can be used beneficially, enabling the evaluation of time series of FTIR spectra in which one sees the occurrence or the disappearance of certain absorption features, representing the formation or disappearance of intermediates or final reaction products.

Depending on the different analytical purpose various FTIR modes can be used, like attenuated total reflectance (**ATR**)<sup>215</sup> for analyzing surfaces or as a convenient approach to sample solids or liquids in contact with the ATR crystal surface, infrared reflection absorption spectroscopy (**IRRAS**)<sup>216</sup> as well as polarization modulation IRRAS (**PM-IRRAS**)<sup>217</sup> for analyzing thin films on reflecting surfaces, and diffuse reflectance infrared Fourier-transformed spectroscopy (**DRIFTS**)<sup>218</sup> for the analysis of fine particles and powders as well as rough surfaces. Complimentary use of the various modes provides a higher detail of information and has been recommended for example for the elucidation of alkyl carbonates' reduction pathways by Haregewoin *et al.*<sup>218</sup>. For this study, *ex situ* ATR analysis, performed inside of a glove box, and *in situ* DRIFTS were used to record signals from adsorbates at the electrode surface. Additional FTIR modes that can be met are the subtractively normalized interfacial FTIR (**SNIFTIR**)<sup>219</sup>, used for tracking e.g. certain electrolyte additives, the double modulation FTIR (**DMFTIR**)<sup>220</sup>, emphasizing on surface species on the electrodes, and the transmission FTIR<sup>221</sup>, monitoring the lithium ion insertion into the cathode material, or even the photoacoustic infrared and grazing incidence reflectance infrared absorption<sup>214</sup>, analyzing the solid electrolyte interface. Combinations of the FTIR with other thermal, electrochemical or microscopic techniques have also been documented, as in the case of *in situ* microscope Fourier transform infrared reflection spectroscopy (**MFTIRS**)<sup>222</sup> used for the investigation of interfacial properties of an alloy film anode in electrolyte solution during discharge and charge.

Although most of the applications of FTIR in the field of LIBs are more focused on lower volatility compounds, there have been examples where the technique is used for the determination of volatiles as well as for evolved gases, with one of the most recent examples reported by Lieser *et al.*<sup>223</sup>. In this application, thermogravimetry-FTIR (**TG-FTIR**) was performed for the characterization of a precursor powder for a potential positive electrode. At temperatures below 250°C, only H<sub>2</sub>O and CF<sub>3</sub>COOH were released, while upon temperature increase up to 350°C, CO, CO<sub>2</sub>, COF<sub>2</sub>, (CF<sub>3</sub>CO)<sub>2</sub>O, CF<sub>3</sub>COF and HF were additionally observed. The ability of FTIR to identify such dangerous fluorinated gases, in combination with its high time resolution, justifies the significance of this technique in the determination of volatiles and the LIBs' safety assurance.

As it will be later on discussed, such highly volatile compounds are typically identified by GC-MS. However, the MS database from which the organic species are recognized is, like every database, not exhaustive. In order to provide increased identification capacity, the coupling of GC-MS with FTIR was introduced. A coupled **GC-FTIR-MS** system was recently proposed by Laruelle<sup>224</sup> and Gachot *et al.*<sup>225</sup>. It was used for both the characterization of volatile compounds released upon heating of a lithiated negative electrode active material in contact with an electrolyte and the analysis of gaseous species and volatile or semi-volatile analytes recovered from a swollen commercial cell. In these applications the sample was split for detection with a union tee, with 80% of the flow being directed to the IR and 20% to the MS. The MS

signal was therefore not saturated, while still good sensitivity was obtained in the IR. This system proved its usefulness for the analysis of gaseous species, identifying an extensive range of volatile compounds at an increased level of confidence. The MS detector revealed lots of analytes owing to its higher sensitivity. However, MS alone could have led to a misinterpretation of the results due to spectral overlap, while the use of complementary FTIR data helped revealing that some signals are actually resulting from the chromatographic coelution of two compounds.

The IR detector generally enables the identification of components by providing functional group information and using different databases. The Gram–Schmidt peak intensity is linked to the peak area of the IR spectra and not to their ionization capability. However, the Gram-Schmidt-trace is not compound independent, but its intensity depends instead on whether the analyte is a strong or a weak absorber. Utilizing both IR and MS libraries, highly toxic compounds could be recognized, despite their overlapping fragmentation pattern. Such an example is the ethylene oxide, whose MS spectrum largely coincides with that of acetaldehyde, leading to ambiguous recognition when only the MS data are evaluated. As an ultimate advantage of the complimentary use of the IR technique, detection of volatile compounds, which could be masked under the MS peak of the inert gas (N<sub>2</sub>, Ar) used for moisture-sensitive molecule handling, is thereby enabled. But IR detection also suffers from peak overlap, except when the interference is a monoatomic or homo-diatomic gas, and that the available IR spectral libraries typically have much less entries than the common MS libraries.

While GC-FTIR-MS is an analytical approach introduced only very recently in the field of LIBs, coupling of the FTIR with liquid chromatography has been performed about two decades earlier<sup>226</sup>. In that application, an **HPLC-FTIR-ATR** setup was used for the analysis of electrolyte solutions.

However, since the volatile emissions are more important for battery safety for reasons that have been previously discussed, coupling FTIR with gas chromatography was also the target of our investigations. Considering the high speed at which several of the degradation reactions take place, an increased time resolution was the focus of our investigations. Hence, an **FTIR-GC-MS** system was developed, combining the complimentary features of both instruments.

Even though FTIR does not provide low detection limits and is unable to identify single compounds in complex mixtures, its good temporal resolution is a clear advantage, limited only by the desired spectral resolution. On the other hand, GC-MS has a rather low time resolution, with measurement times typically between 10 and 20 minutes, but it can identify the components of complicated analyte mixtures over a wide range of concentrations. Combining these two techniques into a coupled FTIR-GC-MS configuration overcomes their individual short-comings. As a result, fast, selective and sensitive methods can be developed, where the FTIR is used for monitoring fast concentration changes and the GC-MS for the identification of the analytes. In our application, correlation of the GC-MS and FTIR data was performed by a partial least squares regression model. The system was successfully used for the *in situ* gas analysis

of self-assembled and commercially available Li-ion cells and the results are presented in the corresponding Results and Discussion Section.

#### A.3.2.2. GC

Gas chromatography (GC) is the technique most heavily used for the detection and identification of volatile species. Depending on the sample composition and the target compounds several detectors can be employed. The applications of these detectors in LIB research will be discussed, together with some experimental conditions and sample preparation details.

Gas chromatography-mass spectrometry (**GC-MS**) is the hyphenated technique of choice for gaining information on the composition of organic carbonates and other volatile constituents of the LIBs' electrolyte. For the qualitative analysis of LIB samples several GC-MS and GC-HRMS methods have been employed. Such methods have been used for simulated, post-mortem and even online experiments, like the newly developed online electrochemical mass spectrometric technique<sup>227</sup>, oriented on DEMS systems while operating like a continuously performed classic headspace system.

When the mass spectrometer is operated in the electron ionization mode, various volatile compounds were identified in the analyzed samples of commercially available or in-house assembled Li-ion cells, simply by using the National Institutes of Standards (NIST) library<sup>170,180,228-236</sup>. However, when similar spectra of different organic species were observed (like in the case of organophosphates<sup>237</sup>), complementary analytical approaches were required. Since such spectra can exhibit strong fragmentation of the compounds under EI conditions, chemical ionization (CI) can be used alternatively. Chemical ionization can provide additional information about the identity of the detected species, since this "soft" ionization mode, using a lower energy process, facilitates the unambiguous structural determination of certain compound groups. Consequently, GC-MS experiments with positive chemical ionization (**PCI**) and negative chemical ionization (**NCI**) have been conducted, using CH<sub>4</sub> and NH<sub>3</sub><sup>192,236,238,239,240</sup>.

In order to cover a wider spectrum of electrolyte decomposition<sup>161</sup>, both a non-polar (like the Rxi-5 ms 30 m-0.25 mm-0.25 mm) and a polar column (like the Stabilwax 30 m-0.25 mm-0.5 mm) were used for the analysis of the electrolyte samples. These samples were directly collected from a hole that was made on field-tested LIB cells after crushing the pressure valve of their aluminum housing. The small sample volumes obtained were then diluted in acetonitrile. The corresponding quantitative experiments were performed by the gas chromatography with flame ionization detection (**GC-FID**). However, GC-FID has been used also on its own for the identification of unknown compounds, such as different alcohols obtained upon hydrolysis of the electrolytes and their decomposition products<sup>241,242,243</sup>.

While the use of the GC-FID for the determination of hydrocarbons is straightforward<sup>244,245</sup>, it has to be used with a methanizer for the determination of oxidized compounds such as CO and CO<sub>2</sub><sup>246</sup>. In addition,

a cold on-column inlet has been used for some GC-FID applications, ensuring that no thermal reactions would occur upon injection<sup>247</sup>.

The GC/MS technique was heavily used to perform not only gaseous species analysis<sup>121,248-256</sup>, but also for the analysis of electrolyte and other analyte solutions<sup>236,257-266</sup>, detecting less volatile analytes, like in the case of electrolyte identification<sup>245,267,268,269</sup>. These ‘gas’ and ‘liquid’ analyses are complementary in their scope, and contribute to the identification of the vast array of gaseous and liquid species evolving from the electrolyte thermal, chemical and/or electrochemical reactivity.

#### ***A.3.2.2.1. Sampling and sample preparation in GC analysis of LIB volatiles and semi-volatiles***

For thermal aging investigations performed with standard solutions undergoing thermal treatment, the use of special polymethylpentane (PMP)-GC vials was preferred<sup>266</sup>. The use of glass containers should offer the maximum inertness at temperatures up to 300°C, however, it was speculated that the hydrofluoric acid formed under these conditions would react with the silicon oxide from the glass and lead to the formation of SiF<sub>4</sub> and H<sub>2</sub>O, which itself can induce further electrolyte decomposition. When the evolved gases were analyzed, their transfer to the GC was performed after their extraction into a gas-tight syringe<sup>270,271</sup>, by direct injection<sup>121</sup>, or injection through e.g. a heated six-port valve equipped with an appropriate injection loop<sup>124</sup>. According to some other approaches, the evolved gases were either collected into glass bottles prior to the analysis<sup>272</sup> or into a cold trap using liquid nitrogen<sup>255,273</sup>, and from there they were transferred by heating into the GC system. In the last case, for example, several decomposition products of the electrolyte solution, such as water, carbon dioxide, ethanol, ethylene oxide and their derivatives like dioxane and acetaldehyde were determined<sup>273</sup>.

When thermal aging experiments were performed, like those conducted by Laruelle *et al.*<sup>274,275</sup>, the samples, which would comprise the electrolyte-impregnated separator or the electrolyte solution, were rapidly placed into an aluminum crucible that was sealed and then pierced prior to being introduced into a laboratory-designed stainless-steel furnace cell inside a glove box. For better reproducibility and because of mass spectrometer sensitivity and contamination risk, this furnace cell was carefully washed with acetone then vacuum-dried overnight at 75 °C between each experiment. The samples were then exposed to a certain temperature program inside a furnace and the evolved gases were transferred to a GC/MS system for analysis. Such headspace GC-MS studies, performed on stored, cycled and abused cells, have generally confirmed the formation of permanent gases and highly volatile compounds, like H<sub>2</sub>, N<sub>2</sub>, CO, CO<sub>2</sub>, CH<sub>4</sub>, C<sub>2</sub>H<sub>6</sub>, C<sub>2</sub>H<sub>4</sub>, C<sub>2</sub>H<sub>2</sub>, C<sub>3</sub>H<sub>8</sub>, C<sub>3</sub>H<sub>6</sub><sup>253,270</sup> as well as Et<sub>2</sub>O, EtOH and fluorinated species, such as fluoroethane (C<sub>2</sub>H<sub>5</sub>F), 2-fluoro-2-methylpropane (C<sub>4</sub>H<sub>9</sub>F) and other alkylfluorides, PF<sub>5</sub>, phosphorus oxyfluoride (O=PF<sub>3</sub>), phosphates and fluorophosphates like O=PF<sub>2</sub>(OEt), O=PF(OEt)<sub>2</sub>, O=P(OEt)<sub>3</sub> etc.<sup>268,276</sup>.

In several cases only low amounts of volatile degradation products are formed, making their unambiguous identification difficult. In an attempt to pre-concentrate them, solid phase microextraction (SPME) GC-MS analysis was performed<sup>277</sup>. This analytical approach could provide a clearer picture of the possible degradation pathways that can occur. It could also be of significant importance for smaller scale experiments used to provide evidence of what could take place in larger cells used in different fields, like in hybrid vehicles. In this way, the need for up-scaling would be avoided, together with the corresponding increase of any possible risk, like thermal runaway, explosion, evolution of dangerous gases in big amounts etc.

For the separation of gases and highly volatile constituents of LIBs the use of PLOT columns should be preferred, otherwise large film stationary phase polysiloxane columns (20  $\mu\text{m}$ ) could also be used. When PLOT columns are used, a post-capillary column is necessary, in order to eliminate particulate material bleed that could block or otherwise negatively affect the MS ionization source. Since different sample types (gas or liquid) require different analytical conditions, a wide range of GC columns was used in LIBs' applications. Characteristic examples are the conventional DB-1, DB-5, DB-23, BPX-70 and Stabilwax columns used for liquid samples. The analysis of gas samples was performed with several PLOT columns, but also thicker film DB-5, DB-17 and Stabilwax columns were used.

When liquid samples were analyzed by GC-MS several sample preparation procedures were employed, depending on the type of samples. When electrolyte samples were analyzed, only a small dilution with an appropriate solvent, like methylene chloride or pentane, was considered necessary<sup>278</sup>. This dilution could lessen the effect of salts (e.g.  $\text{LiPF}_6$ ) on the chromatographic column, protecting it against the degradation of its stationary phase. Liquid samples were also obtained from solid cell components after extraction with appropriate solvents, such as methylene chloride, acetonitrile or water. Particularly when purified water was used, the aqueous extracts obtained from the immersion of cell components in water were then solvent extracted with methylene chloride and the resulting solutions were directly analyzed by GC or GC/MS<sup>173</sup>. For the corresponding quantitative treatments, the internal standard used was diethylene glycol dibutylether ( $(\text{CH}_3\text{CH}_2\text{CH}_2\text{CH}_2\text{OCH}_2\text{CH}_2)_2\text{O}$ ). To avoid the reaction of internal standard when present in heated electrolyte solutions, the standard was added to the methylene chloride solution. The electrodes could also be rinsed with DMC (with less than 20 ppm water) to remove the electrolyte, with the rinsing carried out in an argon-atmosphere glove box<sup>272</sup>. Especially for investigations into the chemical composition of the cell ingredients that are highly sensitive to atmospheric constituents (e.g.  $\text{H}_2\text{O}$ ,  $\text{O}_2$  and  $\text{CO}_2$ ) the disassembling is also conducted inside the controlled environment of a glove box. For certain applications, where less rigorous conditions are required, vacuum systems or dry rooms can be used alternatively. However, for the analysis of both the electrolyte solution and the cell components, such as electrodes or separators, performing the sample preparation inside a glove-box is mandatory. In order to collect the remaining electrolyte solution in the dissected batteries, pure isopropanol (dried over molecular



sieves for 24 h at room temperature) has been used<sup>279</sup>. The sample preparation steps followed in that case had the solvent dropping onto the entire length of both electrodes, letting it drip into a collection bottle until a specified final volume. Alternatively, the solvent was used to rinse the battery can and the outside part of the battery core<sup>280</sup>. The isopropanol solutions were also analyzed by Karl Fischer titration for trace water. At another approach, the separator was soaked with the electrolyte. The remaining part of the separator was extracted using extra-dry acetonitrile and centrifuged under argon atmosphere. The supernatant was afterwards diluted in acetonitrile and analyzed by means of GC-HRMS and ESI-HRMS<sup>281</sup>.

An alternative sample preparation approach was recently introduced by Friesen *et al.*<sup>282</sup> based on the application of CO<sub>2</sub> extraction in battery cell electrolytes. Based on the idea patented in 2007 by Sloop *et al.*<sup>283</sup>, the research group at the University of Münster investigated the extraction of the LIB electrolyte with liquid and supercritical carbon dioxide and additional solvents<sup>284</sup>, demonstrating that such an application is possible, while proper adjusting of the extraction conditions (and especially the additional solvents) to the individual cell components (electrode materials, separator, electrolyte and geometry) is necessary. Extraction by supercritical CO<sub>2</sub> demonstrated to be a fast, selective and efficient alternative to solvent extraction, requiring no sample pre-concentration or clean-up<sup>285,286</sup>. The extracted samples were then analyzed by gas and ion chromatography hyphenated to mass spectrometry.

Temperature programmed desorption or decomposition coupled with gas chromatography-mass spectrometry (**TPD-GC-MS**) was also employed, for example, to define the surface functionalities of anode materials and to detect generated gases, such as CO<sub>2</sub> and SO<sub>2</sub> from the SEI<sup>287,288,289</sup>. A liquid-nitrogen cooled trap was used for the collection of generated gases, and these were transferred by heating to the GC system. The main advantage of this approach was that it enabled the determination of decomposition products together with the onset temperature of decomposition. Simple **TPD-MS** has also been used e.g. for the direct observation of gas species resulting from several electrolyte degradation pathways<sup>228,273,290,291</sup>.

An alternative approach towards the identification of permanent gases was the coupling of GC to a thermal conductivity detector (**TCD**)<sup>244,245,246,272</sup>. GC-TCD has been used, for example, for the determination of oxygen, nitrogen, acetone and water<sup>292</sup>. In a recent application of the technique, the TCD assisted in the composition analysis of the gases generated inside the Li-ion cells, investigating the thermal runaway phenomenon<sup>293</sup>. For these experiments two different columns were used, a molecular sieve packed column and a porous layer open tubular column<sup>294</sup>. The GC system was calibrated for H<sub>2</sub>, O<sub>2</sub>, N<sub>2</sub>, CO, CO<sub>2</sub>, CH<sub>4</sub>, C<sub>2</sub>H<sub>2</sub>, C<sub>2</sub>H<sub>4</sub> and C<sub>2</sub>H<sub>6</sub>, with Ar and He being used as carrier gases.

When the FID and the TCD are used complementary, the FID for the analysis of hydrocarbons and the TCD for inorganic gases, different amounts of sample are introduced into the systems. Such an example involves the injection of 0.5 ml of gas for the TCD detector, while only 5 $\mu$ l were considered adequate for the FID, pointing out their difference in sensitivity<sup>244</sup>. Since the volume of the generated gas inside the cell is another very important parameter, in order to enable such a determination Kumai *et al.*<sup>245</sup> constructed an apparatus that they used with commercial LIBs after long cycling. This apparatus was a closed and sealed system inside which the cycled cells, having a hole of 4 mm in diameter drilled at the center of their positive terminal cap, were placed. The system was then vacuumed until approximately 0.1 Torr, with the generated gases inside the cells being released into a vessel puncturing by a needle. Using this device, the volume of generated gas in the cell was measured directly, and the total volume of gas was calculated from the pressure and the space volume in each part of the apparatus, enabling the determination of up to 0.01 ml in volume. After the analysis, the cells were removed from the gas release vessel and an organic solvent, like dichloromethane, was added and left for 30 min to leach the electrolytes and eliminate the risk of cross-contamination.

Although MS, TPD-MS and DEMS have been extensively applied for the detection and identification of gaseous and volatile decomposition products of the electrolyte solvents, when it comes to the presence of polymer-like substances pyrolysis/gas chromatography/mass spectrometry (**Py-GC-MS**) was one of the selected techniques. The analysis of such high-molecular weight compounds has been performed by Py-GC-MS, proving the presence of decomposition products of the electrolyte solution like oligomers with oxyethylene units (such as ethylene glycol, di(ethylene glycol) and tri(ethylene glycol) methyl ester), acetaldehyde, 1,4-dioxane and various alcohols, giving additional evidence of the chemical constituents of the SEI layer<sup>295,296</sup>. Furthermore, when the thermal stability of positive-electrode materials was questioned, evolved gas analysis was performed by pyrolysis of the sample and subsequent mass spectrometric analysis of the generated gases<sup>297</sup>. Whenever though Py-GC-MS analyses are performed, it has to be demonstrated that the identified degradation products are already formed during cycling or operation of the LIB, and not during the pyrolysis step.

Despite the wide use of the GC-MS technique, there are still some limitations when using it not only in the field of LIBs, but also in other types of applications. As already observed, according to the analyte's volatility, different chromatographic columns are required for the analysis of all degradation products. In addition, the peak intensity on the chromatogram not only depends on the compounds' concentration but also on their ionization efficiency which can be quite different. Furthermore, the single database from which the compounds are recognized is not exhaustive. For these reasons, complimentary approaches have to be considered and investigated, trying to overcome these limitations and provide an increased identification and detection capacity. Such approaches may respectively involve coupling of GC with

other analytical techniques, like the aforementioned FTIR, or the use of alternative detectors, such as the BID detector discussed in the next section.

### **A.3.2.3. BID**

As already discussed, most conventional gas phase detectors do not completely fulfill contemporary analytical needs, with the ultratrace analysis of permanent gases being a characteristic example. The Barrier Discharge Ionization Detector (BID), though, is claimed to be the detector of choice when permanent gases and other highly volatile species need to be analyzed. Since such species are common among LIB emission products, this recently released GC detector was chosen from our group for further investigations.

The BID was developed by using an atmospheric non-equilibrium plasma as a photo ionization source<sup>298</sup>. In particular, the BID creates analyte ions from a Helium-based, dielectric barrier discharge (DBD) plasma of extremely high photon energy (17.7 electron volt)<sup>299</sup>. Although dielectric barrier discharges using He as discharge gas were already utilized since 1988<sup>300</sup>, the DBD detectors are one of the latest additions in the GC detectors family, with the BID being introduced in the market in 2013 by the Shimadzu Corporation. In this chapter we will discuss the technique on which BID is based, the ionization principle of the detector, its structure, characteristics and basic applications.

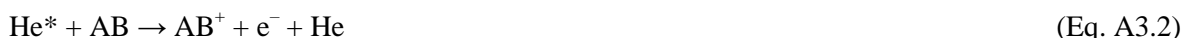
#### **A.3.2.3.1. Dielectric Barrier Discharges**

The dielectric barrier discharge is a typical non-equilibrium gas discharge generated from the collision between high-energy electrons and ambient gas molecules. A dielectric barrier discharge is also called "silent discharge"<sup>301</sup>, a name that is still frequently used in English, German (stille Entladung) and French (décharge silencieuse) scientific literature. To produce the discharge, a frequency of few Hz to MHz and an alternating (AC) voltage with an amplitude of 1 to 100 kV is required, with the preferred pressure ranging between 10 kPa and 500 kPa<sup>302</sup>. First experimental investigations on DBD were reported by Siemens<sup>303</sup> in 1857.

Concerning the configuration of a DBD, at least one dielectric barrier should be present, with the gap distance between the electrodes being in the order of 0.1 to 10 mm<sup>304</sup>. The working gas filling the discharge space of a DBD is usually air, argon, nitrogen, or helium<sup>305</sup>. To initiate the discharge between two electrodes, the applied AC voltage should exceed the breakdown voltage of the working gas, creating electrons with high average kinetic energy (1–10 eV), high energy photons and metastable species<sup>306</sup>.

These highly reactive species are subsequently used to fragment and excite or even atomize the analytes of interest.

The applications of DBD as a GC detector have been discussed by Luong *et al.*<sup>307</sup>. When the He ionization mode was applied, and since for the design of the investigated GC-DBD detector the analytes did not pass at any point directly through the plasma, the proposed ionization mechanism was described by the following equations:



At this application, the primary mechanism of excitation was considered to be the Penning effect, responsible for the generation of long lived metastables (Eq. A3.1)<sup>308</sup>. These metastables were resulting in the ionization of the analytes within the reaction chamber (Eq. A3.2).

DBD is generally characterized by its high dissociation ability at low working temperatures and low power consumption, the simple and adjustable configuration, the ambient working conditions and long lifetime<sup>305</sup>. While the industrial applications of the DBD have been summarized by Kogelschatz<sup>302</sup>, the analytical applications of the DBD, involving the areas of atomic spectrometry, chemiluminescence, gas chromatographic detectors, mass spectrometry, and ion mobility spectrometry, were addressed by Xiandeng Hou *et al.*<sup>305</sup>. Further optimizations in the design of DBD detectors have led to the construction of the BID, a highly sensitive, long-term stable and nearly universal GC detector that enables the detection of all compounds, except helium (the plasma gas) and neon (due to its very high ionization energy, equivalent to 21.6 eV<sup>309</sup>).

#### ***A.3.2.3.2. BID Ionization Principle***

For the BID detector, dielectric barrier discharge occurs using He as the discharge gas and alternating currents at relatively low frequencies, achieving stable, pulsed discharges at atmospheric pressure. The created vacuum ultraviolet (VUV) radiation is emitted when the excited He molecules in the discharge of the He gas return to their ground state (Figure A3.2)<sup>298</sup>. Contrary to the ionization mechanism proposed at previous GC-DBD applications<sup>307,308</sup>, sample ionization due to the reaction with metastable helium (generated in the plasma through the Penning effect) is not considered as the dominant process for VUV generation in the BID<sup>298</sup>. That was verified when the effect of the discharge gas in the ion generation was investigated, showing that even without metastable He being mixed with the sample gas, adequate ionization current was achieved<sup>308</sup>.

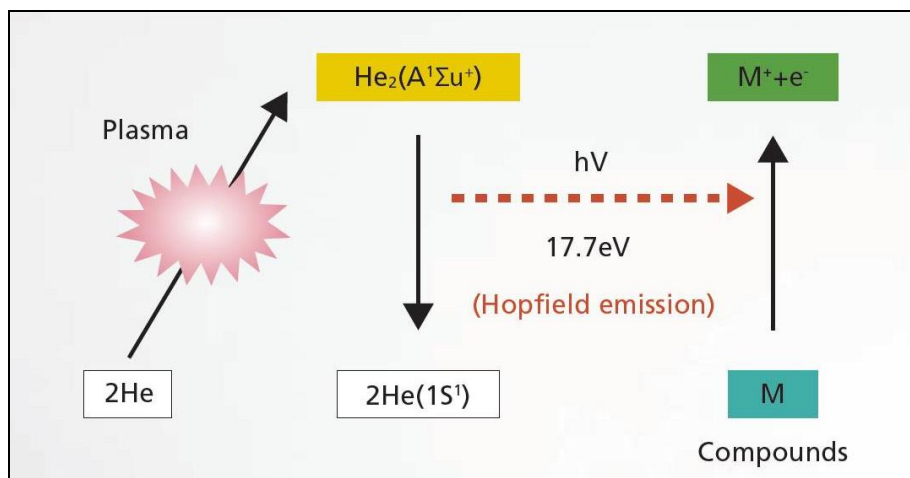
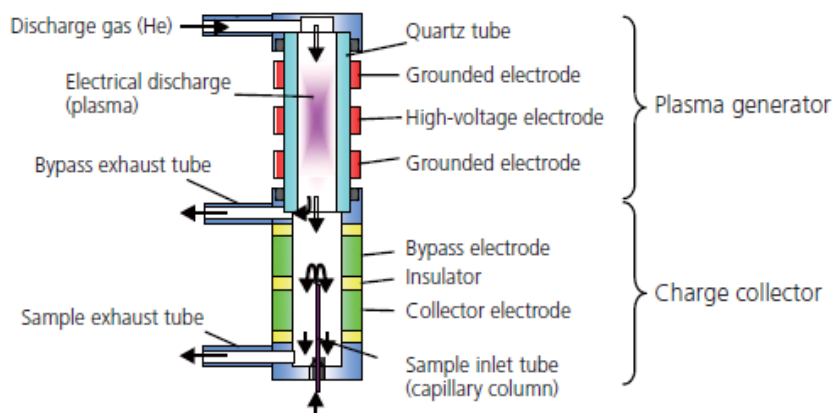


Figure A3.2 Principle of ionization reaction<sup>310</sup>.

### A.3.2.3.3. BID Layout and Characteristics

As described by Nishimoto *et. al.*<sup>298</sup> in a review, the detector is comprised of two basic parts: a plasma generator and a charge collector (Figure A3.3). A quartz tube, passing through three cylindrical electrodes, is the major component of the plasma generator (Figure A3.4). Only high-purity helium gas (99.9999 vol. % or better) is supplied through the discharge gas inlet tube, as illustrated by the arrows on top of Figure A3.3, showing the direction of the gas flow (for both the discharge and the sample gas). An alternating high voltage (5 to 30 kHz, 5 to 10 kV) is applied to the central electrode, while the two outer electrodes are grounded and the walls of the quartz tube play the role of the dielectric barrier. A dielectric barrier discharge occurs inside the quartz tube and between the two grounded electrodes. The surface of the paired discharge electrodes is coated with a dielectric material, restricting the current flow and suppressing their overheating. In that way, sputtering of the electrode material due to the plasma is inhibited, preventing changes or deterioration of the discharge characteristics and therefore resulting in a stable discharge.



**Figure A3.3 BID Cross-sectional diagram showing the gas flow.**<sup>298</sup>

Between the plasma generator and the charge collector, a bypass exhaust is connected. As indicated by its name, this bypass is used to exhaust part of the discharge gas. In that way, a high enough flow rate can be maintained in the plasma generator section, while the flow rate in the charge collector is restricted to desirable values<sup>298</sup>.

The high flow rate in the plasma generator ensures a stable detector performance, since it prevents any contaminations from diffusing against the gas flow. Such contaminations may originate from decreased gas purity, outgassing from the tube inner walls and/or high concentrations of solvent or sample molecules. Since most substances can be ionized by the BID, this will also happen with the impurities in the discharge gas, resulting in higher baseline for the detector output signals and consequently lower S/N ratios and decreased sensitivity. That implies the absolute need of a gas supply via a He purifier, stainless steel tubing, plasma generator materials with low levels of outgassing and appropriate sample volumes and chromatographic conditions that will prevent overloading of the detector. On the other side, the design of the detector also enhances its sensitivity and robustness, since the non-equilibrium plasma generated inside the BID has a very low gas temperature. This low heat generation reduces the detector noise by restricting the causes of fluctuations in the plasma, such as the aforementioned outgassing from the plasma generator walls<sup>298</sup>.

Although the high flow rate at the plasma generator will reduce the noise and therefore improve the S/N ratio, the opposite effect will be caused at the charge collector. If high discharge gas flow rates reach the downstream section of the BID, the sample gas will be diluted, resulting in reduced signal intensities for the identified species. These inverse functions of the discharge gas flow rate dictate the necessity of the bypass exhaust for accomplishing an overall increased sensitivity<sup>298</sup>.

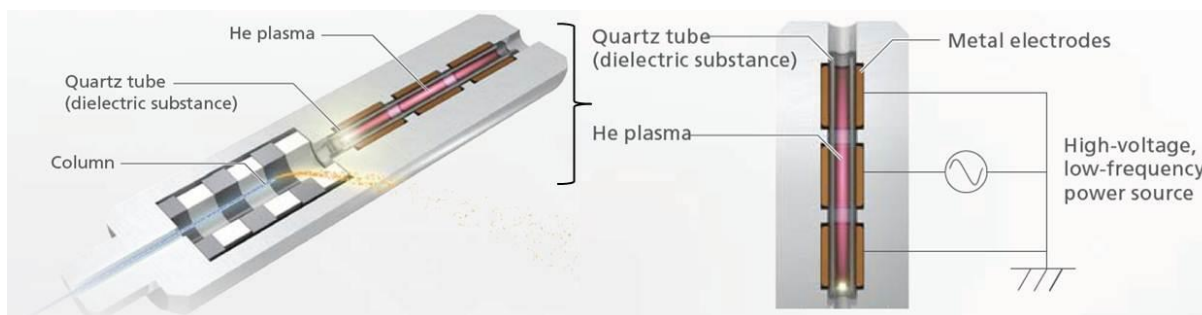


**Figure A3.4 BID-2010 Plus Cross section drawings, with a magnification of the plasma generator section.**<sup>310</sup>

The charge collector of the BID consists of two cylindrical electrodes separated by an insulator. While a direct (DC) voltage is applied to the upper (bias) electrode, the lower (collector) electrode is connected to a current amplifier. The electrical field between the two electrodes leads the generated ions to accumulate on the collector electrode, resulting in their detection as a voltage signal<sup>298</sup>.

To avoid baseline fluctuations, the purity of the insulator material also plays an important role. The electrical resistance of the insulator drops at higher temperatures, with the increasing leak current having a significant effect on the detector's performance. As the electrical resistance is strongly depending on the purity of the insulator, only high purity insulators should be selected, resulting in increased volume resistivity at high temperatures<sup>298</sup>.

#### **A.3.2.3.4. Advantages of BID**

As already mentioned, the BID is a universal detector, with only neon and helium being excluded from its comprehensive detectability range. The architecture of the BID is designed in such a way that the plasma generation zone is maintained at ambient temperature, while the electrodes are positioned where they do not have direct contact with the plasma. This configuration improves the electrical insulation of the electrometer even when high operating temperatures are used. As a consequence, the system is extremely robust, so that no routine maintenance is required, eliminating the need for consumables<sup>298</sup>.

In addition, the discharge stability attributed to both-side barrier discharge and the reduced baseline output achieved by suppressing possible impurities (e.g. from the inner walls of the plasma generator), further enhance the sensitivity and durability of the detector<sup>298</sup>.

Together with a linearity of typically  $10^5$  (1 pg to 100 ng for dodecane) and detection limits of e.g. less than 1.0 pg C/sec for dodecane (estimated from the noise amplitude, according to the ASTM method)<sup>298</sup>, the prominent features of simple operation, long lifetime, and the good adaptability, make the BID a significant alternative to conventional GC detectors and a favourable option for various gas chromatographic applications.

#### *A.3.2.3.5. Comparison of the BID with FID and TCD detectors*

With the FID and TCD being two of the most commonly used detectors in gas chromatography, a comparison of their performance with that of BID is inevitable. Even though not many BID applications have been published yet, the research groups using this instrument have also focused on the comparison of the results obtained with GC-BID with those resulting from GC-FID and GC-TCD analyses<sup>310-313</sup>.

While the FID is the selection of choice when it comes to determination of hydrocarbons, its poor response towards compounds with other functional groups (e.g. halogens, alcohols and aldehydes) is a serious limitation of this detector. In addition, the use of a methanizer is required when, for example, permanent gases like CO and CO<sub>2</sub> or formic acid have to be detected.

Although TCD is an appropriate detector for all samples other than the carrier gas, and can be used complementary to FID for the identification of inorganic gases, its lower sensitivity may impede the accurate quantitation of species present at trace levels. For this reason, when complex samples of organic compounds with permanent gases have to be examined, it is common to use a combination of the aforementioned detectors to solve the analytical problem.

The BID, on the other hand, is a detector that has proven to be capable of analyzing both categories of compounds, with sensitivities that are claimed to be over 100 times higher than those obtained with TCD and twice that of the FID<sup>298,299</sup>. At the same time it is claimed to show less variations in the relative response of species with different functional groups, with the relative sensitivities for alcohols and chlorine-containing compounds being more than 10 times higher than those of FID<sup>298</sup>. Its maximum operating temperature of 350°C supports the analysis of even high-boiling-point liquid samples, detecting compounds up to n-C44<sup>299</sup>. The reduced baseline fluctuations and long term stability of BID, resulting from its optimized design discussed previously, ensure its high repeatability and reproducibility<sup>303</sup>. However, the dynamic range of FID of 7 orders of magnitude cannot be met by BID, with the latter having a linearity range that covers approximately 5 orders of magnitude<sup>298</sup>.

The complementary use of both detectors was demonstrated in the application of a customized GC system for the ultrafast analysis of natural and refinery gas, where the permanent gases were analyzed with a BID and the hydrocarbons with an FID, having columns of different selectivity connected to each detector<sup>310</sup>.



#### ***A.3.2.3.6. Applications of GC-BID***

Since the BID has only recently been commercialized, its applications are still limited. The basic proposed applications of BID though are focusing on permanent gases<sup>299,310</sup> and low molecular weight compounds<sup>311,312,313</sup>. That is because the BID is concentration specific (= mol/volume) while the response of the FID is mass specific (= mass/volume), which represents an increasing advantage for the FID as the analyte molecules become bigger. Thus, the highest relative sensitivity of the BID vs. the FID is for low-MW compounds while for higher MW compounds, the BID is at disadvantage compared with the FID.

In this regard, the application of BID in the determination of ethanol and water in several commercial products<sup>311,312,313</sup> is a convincing example that allows the BID to demonstrate its superiority to the FID in terms of sensitivity, repeatability and reproducibility. In these applications, not only the use of the BID represents the novel aspect, but also the use of an ionic liquid (IL) stationary phase for the analytical column used.

Despite the above discussed limitations, BID is a universal detector, capable of analysing liquid samples of both lower and higher volatility compounds. This property was extensively investigated in our research group by Maria Antoniadou<sup>314</sup> who examined the GC-BID's efficiency in the analysis of several organic compounds belonging to different compound classes. The results were then compared to those obtained with GC-FID under identical conditions. The investigated test compound set was comprised of alcohols, anilines, aldehydes, phenols, alkanes, esters, cyclic and aromatic compounds, and halogenated species. As expected, the majority of the detection limits for the BID were in the same order of magnitude or lower than those resulting from GC-FID analysis. The results also indicated the possible dependence of the BID's performance on the molecular weight of the analyte. A very interesting observation was though based on the significance of the analyte's nature on the instruments sensitivity. The effect of the analyte's characteristics on the instrument's response is clearly illustrated in Figure A3.5, where higher sensitivities for the BID were observed for alkanes and esters. Similar sensitivity variations were apparently present for FID, where the lowest sensitivities were attributed to alcohols, phenols, aldehydes and halogenated compounds.

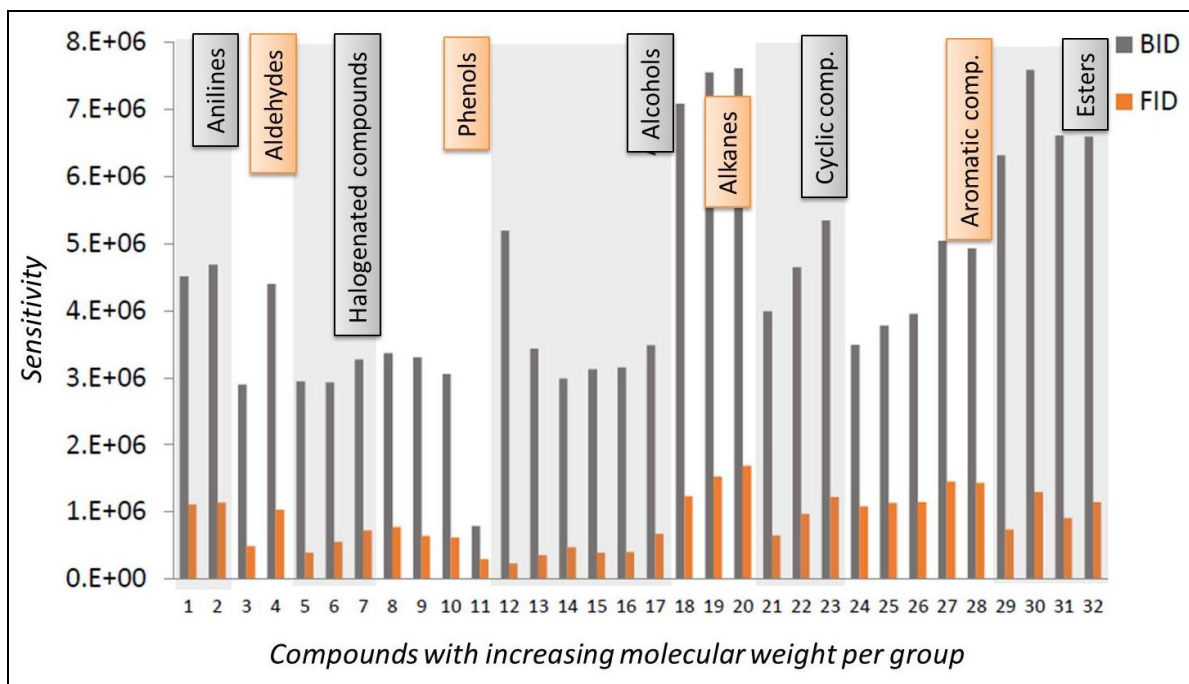


**Figure A3.5 Comparison of BID and FID sensitivities. 1: n,n-dimethylaniline, 2: n,n- diethylaniline, 3: isovaleraldehyde, 4: benzaldehyde, 5: 1-bromo-3-chloropropane, 6: 1-bromohexane, 7: 1-bromodecane, 8: phenol, 9: 2,4-dichlorophenol, 10: 4-chlorophenol, 11: pentachlorophenol, 12: ethanol, 13: 2-propanol, 14: 1-butanol, 15: isoamyl alcohol, 16: 1,4-butanediol, 17: 1-octanol, 18:heptane, 19: decane, 20: dodecane, 21: cyclohexane, 22: cyclododecane, 23: cyclododecane, 24: benzene, 25: toluene 26: ethylbenzene, 27: butylbenzene, 28: pentyl benzene, 29: ethyl acetate, 30: butyl acetate, 31: ethyl-2-methoxy-1-propyl, 32: 2-acetic butoxyethyl<sup>314</sup>**

The combination of GC-BID with a sample pre-concentration technique, and in particular with SPME, was subsequently realized by Kloskowski *et al.*<sup>315</sup>. The ionogel HS-SPME-GC-BID, utilizing hybrid silica-based materials with immobilized ionic liquids as SPME fiber coatings, was applied for the determination of aromatic volatile compounds. Utilizing the advantages provided by both the sample preparation and detection technique, not only very high enrichment factors and recoveries were observed, but also a very good overall sensitivity and precision.

Last but not least, the application of BID in the field of LIBs was already mentioned by the producer company, with such an example being included in the brochure of the Tracera GC-BID instrument<sup>299</sup>. Being triggered by such a statement, we decided to investigate the extent of the BID's applicability in the determination of LIB's volatile emissions. Therefore the next chapters are dedicated to the results obtained by GC-MS and GC-BID measurements for electrolyte samples stored under thermal degradation conditions. Following these *ex situ* investigations, the results from *in situ* experiments using the FTIR-GC-MS system will be presented.

## ***B. Ex Situ experiments of selected electrolytes after prolonged storage at different temperatures using GC-MS***

### ***B.1. Introduction***

In this chapter the results from *ex situ* thermal ageing experiments of LIB electrolytes will be presented. Starting from single component samples and moving stepwise to samples of increasing complexity representing real electrolyte solutions, the volatile compounds formed under different temperatures over a time window of two week were identified using GC-MS. Comparison of these results with the ones obtained for a cycled electrolyte solution, aged under the same thermal conditions, was performed in order to examine additionally the effect of normal cycling conditions to the solution. Both the headspace and the liquid phase of the electrolyte, after appropriate sample preparation, were investigated. The species detected are presented below, together with information on the formation pathways for the most frequently met compounds. The toxicity of the identified species will also be briefly discussed, based on data provided by the Toxtree software.

### ***B.2. Materials and methods***

#### ***B.2.1. Chemicals and Reagents***

All the electrolyte solution components investigated were obtained from the Mobility Departments of the AIT (Austrian Institute of Technology GmbH, Giefinggasse 2, 1210 Vienna, Austria). In particular, ethyl methyl and dimethyl carbonate ( $\geq 99\%$ ,  $\text{H}_2\text{O} \leq 20$  ppm, methanol  $\leq 30$  ppm), ethylene carbonate ( $\geq 99\%$ ,  $\text{H}_2\text{O} \leq 20$  ppm, ethylene glycol  $\leq 30$  ppm) and LP30 (DMC/EC 1:1 by weight, 1M  $\text{LiPF}_6$ ,  $\text{H}_2\text{O} \leq 20$  ppm, HF  $\leq 50$  ppm) were originally purchased from the SelectiLyte product line of Merck (Darmstadt, Germany). The vinylidene carbonate (99.5%,  $\text{H}_2\text{O} < 100$  ppm, acid  $< 200$  ppm) was also purchased from Merck, while the  $\text{LiPF}_6$  salt (battery grade,  $\geq 99.99\%$  trace metal basis) was purchased from Alfa Aesar (Karlsruhe, Germany). Additionally, electrolyte solution collected at AIT from cycled lithium-ion cells was received and further investigated. Dichloromethane used as the solvent at the liquid phase measurements was purchased from Sigma-Aldrich (Vienna, Austria).

Handling of the air and moisture sensitive battery materials was conducted inside an Ar-filled glove box (where:  $\text{O}_2 \leq 0.1$  ppm,  $\text{H}_2\text{O} \leq 0.1$  ppm), available at the Institute of Applied Synthetic Chemistry of the Technical University of Vienna.

### ***B.2.2. Instrumentation and operating conditions***

Analysis of both the headspace and the liquid phase of the samples used for the initial *ex situ* experiments was carried out on a Thermo Fisher Scientific TraceGC Ultra gas chromatograph (Thermo Fisher Scientific Inc., Waltham, MA) equipped with a programmed temperature vaporization (PTV) injector and a Thermo Fisher Scientific AS2000 Autosampler. Helium (purity >99.999%, Messer, Gumpoldskirchen, Austria) was used as the carrier gas. Chromatographic separation was achieved on a RTX-5MS 30 m × 0.25 mm ID, 0.25 µm film thickness capillary column, coated with 95% dimethyl-/5% diphenylpolysiloxane polymer (Restek, Bellefonte, PA). The silcosteel PTV liner used was equipped with deactivated glass wool and the injector was operated in split mode using constant temperature. Instrument control and data processing was done with the Xcalibur 2.1 software. The NIST Mass Spectral Library, version 11, was used for the compound identification.

Starting from the gas phase measurements, 200 µL of the sample headspace were manually injected into the GC, using a 1.0 ml gas tight syringe. The parameters of the GC/MS method used are summarized in Table B1. A split ratio of 10:1 was selected in order to prevent the overload of the detector, while no solvent vent time was applied. Since several compounds were observed at the preliminary measurements to elute close to the overloading peak of argon, the same detector voltage was prevailed throughout the entire run, with the detector gain set to the autotune values. Positive ion detection mode was always used, while Full Scan-mode was selected, measuring a mass range of  $m/z$  10-500.

**Table B1. GC/MS parameters for the headspace measurements.**

GC	
Injection Temperature	250°C
Column Flow (constant)	1.6 mL/min
Purge Flow	3 mL/min
Split Ratio	10:1
Oven Program	40°C (3 min) → 15°C/min → 260°C (5 min)
MS	
Interface Temperature	260°C
Ion Source Temperature	200°C
Scanning Range	10-500 $m/z$

For the liquid phase measurements, the parameters of the GC/MS method used are summarized in Table B2. A lower split ratio was selected, since scanning was starting after the solvent peak had eluted. The sample volume of 1 µL was injected automatically into the GC by the autosampler. In order to avoid any sample carryover, several pre- and post-injection washes with the sample solvent were applied. In particular 3 and 6 rinses with 5 µL dichloromethane were performed before and after the injection, respectively.

**Table B2. GC/MS parameters for the liquid phase measurements.**

GC	
Injection Temperature	250°C
Column Flow (constant)	1.6 mL/min
Purge Flow	3 mL/min
Split Ratio	7:1
Oven Program	40°C (3 min) → 15°C/min → 260°C (10 min)
MS	
Interface Temperature	260°C
Ion Source Temperature	200°C
Solvent Vent Time	1.60 min
Scanning Range	10-500 m/z

### B.2.3. Sample Preparation

For the *ex situ* experiments on thermal degradation of LIB electrolyte solutions the temperatures selected for investigation were the ambient temperature (25°C), the elevated temperature of 60°C (upper temperature limit for safe working conditions of LIBs) and the high temperature of 150°C (at which thermal decomposition is expected). All sample mixtures investigated were prepared inside a glove box and stored for two weeks under the particular thermal conditions. The different sample types investigated are listed in the Table B3. All sample types were prepared in 6 replicates, from which duplicates were used for the storage under different temperatures.

**Table B3. The different sample types investigated during the preliminary *ex situ* experiments.**

Sample Type	Composition
1	EC
2	DMC
3	EMC
4	VC
5	LiPF <sub>6</sub>
6	LP30
7	EC/DMC (1:1 vol. %)
8	EC + VC (5% wt)
9	DMC + VC (5% wt)
10	LP30 + VC (5% wt)
11	EC/DMC + VC (1:1 vol. %, 5% wt)
12	EC + LiPF <sub>6</sub> (1M)
13	DMC + LiPF <sub>6</sub> (1M)
14	LiPF <sub>6</sub> + VC
15	EC/DMC + LiPF <sub>6</sub> (1:1 vol. %, 1M)
16	EC + LiPF <sub>6</sub> + VC (1M, 5% wt)
17	DMC + LiPF <sub>6</sub> + VC (1M, 5% wt)
18	EC/DMC + LiPF <sub>6</sub> + VC (1:1 vol. %, 1M, 5% wt)
19	Cycled LIB electrolyte solution

For all the liquid samples the final volume was 0.1 ml. This volume was carefully selected, so that the overpressure created by the reactions taking place inside the headspace vials will not result in any damage of the vial itself or the septa used. To estimate the acceptable sample volumes for the particular headspace vials used, a single component DMC sample was taken as a representative example. DMC has a molecular weight close to 90 g/mol and density close to 1 g/ml (so that 90 g/mol = 90 ml/mol). Under the assumption that it reacts and gives three products we will have in the 0.1 ml sample volume 0.001 mol DMC and 0.003 mol of the corresponding reaction products. By rearranging the ideal gas equation we can calculate the gas volume produced at atmospheric pressure conditions in the extreme case of 150°C as follows:

$$V_{m, 150^{\circ}\text{C}} = (R * T) / P = [(8.314 \text{ L kPa mol}^{-1} \text{ K}^{-1}) * (423.15 \text{ K})] / (101.325 \text{ kPa}) = \mathbf{34.72 \text{ L/mol}},$$

$$V = n * V_{m, 150^{\circ}\text{C}} = (0.003 \text{ mol}) * (34.72 \text{ L/mol}) = 0.104 \text{ L} = \mathbf{104.2 \text{ ml}},$$

Where  $V_m$ : molar volume of an ideal gas in L/mol, R: gas constant in L kPa mol<sup>-1</sup> K<sup>-1</sup>,

T: temperature in K, P: pressure in kPa and V: volume in L.

For these experiments 27 ml headspace vials were used. Rearranging the equation resulting from the Boyle's law for the gases, we can calculate the pressure inside the vials:

$$P_f = (P_{atm} * V_{atm}) / V_f$$

$$P_f = [(104.2 \text{ ml}) * (1 \text{ bar})] / (27 \text{ ml}) = \mathbf{3.6 \text{ bar for } 150^{\circ}\text{C}},$$

Where  $V_{atm}$ : volume at atmospheric pressure ( $P_{atm}$ ) and  $P_f$ ,  $V_f$ : final pressure and volume inside the vials used.

Under these simulated sample conditions and even for the highest temperature applied, the sample vials can withstand such a pressure increase.

When the VC additive was included, the portion present in the sample was equivalent to 5% by weight, corresponding to approximately 9 µl. Since 1M (1 mol/l) of the conductive salt is expected to be present in the LIBs, for a 0.1 ml sample the 0.0001 mol corresponding would result into 15.2 mg of LiPF<sub>6</sub>, according to the following calculations:

$$m = n * MW = (0.0001 \text{ mol}) * (151.91 \text{ g/mol}) = 15.191 \text{ mg} \sim \mathbf{15.2 \text{ mg}},$$

Where m: mass in grams, n: amount of substance in mol and MW: molecular weight in g/mol.

Since the EC at room temperature (RT) is solid, in order to perform a precise sampling, the standard was heated to its melting point (34°C) inside the glove box using a thermal plate. The mild heating was performed with great care and under inert atmosphere, so that any significant degradation of the electrolyte would be prevented.

When both the linear and the cyclic carbonate were present in the sample, the same volume was used for each of them. In that way, the commonly used EC/DMC ratio (1:1 vol. %) was achieved, resulting in a more realistic simulation of the LIBs electrolyte solution.

For the liquid phase measurements, a dilution step was also required, so that the sample volume could easily be handled and the concentration range would be more appropriate for the subsequent GC-MS analyses. To perform this dilution the headspace vials containing the samples were opened inside the glove-box. The dilution solvent was dichloromethane, with 1 to 2 ml of  $\text{CH}_2\text{Cl}_2$  being added to the headspace vials and later on transferred to GC vials. The same samples used for the headspace analysis were used for the analysis of the liquid phase as well, meaning that the septa of the headspace vials were penetrated before the samples were transferred into the glove-box and approximately 0.3 ml of their headspace were used for the headspace measurements. The produced overpressure inside the vials together with the very small aliquots of the headspace used for the initial analyses was considered to prevent any back diffusion of air.

The higher amount of solvent (namely 2 ml) was used for the sixth sample category (the LP30 sample) at 60 and 150°C, and for fifth and nineteenth samples (the  $\text{LiPF}_6$  and the cycled electrolyte sample) at all temperatures. These particular samples had to stay for about 15 min without being shaken and then only the supernatant was collected to avoid the presence of solid materials inside the GC vial. For these samples, different conditions were also used for the autosampler, avoiding the pull-ups that would cause mixing of the sample and injection of any remaining particles into the GC system.

## ***2.4. Toxicological Evaluation***

Apart from the identification of gaseous emissions of LIBs, an additional investigation regarded the toxicity of the overall detected species. For this reason, the Cramer decision tree, commonly referred to as Cramer scheme, was used. Proposed by Cramer, Ford and Hall in 1978<sup>316</sup>, it is considered the most widely used approach for classifying and ranking chemicals according to their expected level of oral systemic toxicity. That decision tree categorises chemicals, mainly on the basis of chemical structure and reactivity, into three broad classes indicating a high (Class III), medium (Class II) or low (Class I) level of concern. In particular, Class I contains substances of simple chemical structure with known metabolic pathways and innocuous end products which suggest a low order of oral toxicity. Class II contains substances of intermediate complexity. They are less innocuous than those in Class I but they do not contain structural features that are suggestive of toxicity like those in Class III. Class III contains substances with complex chemical structures that permit no strong initial impression of safety and may even suggest a significant toxicity.

The original Cramer decision tree consists of 33 questions, each answered 'yes' or 'no' and leading to another question or to the final classification into one of the three classes. The logic of the sequential questions (Figure B1) was based on the available knowledge on toxicity and on how chemical structures were metabolised in mammalian metabolic pathways. The tree is generally intended for use with all ingested, structurally defined organic and metallo-organic substances.

The Cramer decision tree was subsequently used by Munro and co-workers<sup>317</sup> with the purpose of deriving human exposure levels (Threshold for Toxicological Concern, TTC values) for toxicity endpoints other than carcinogenicity. In concept, TTC is relevant to any human exposure. In practice, it is limited by the underlying databases, supporting analyses, and also by regulatory/legal barriers. Each Cramer class is associated with a specified human exposure level, below which chemicals are considered to present a negligible risk to human health. In the absence of experimental hazard data, these exposure threshold values have formed the basis of priority setting in the risk assessment process. To facilitate the application of the TTC approach, an extended version (Table B4) of the original Cramer scheme has been implemented in Toxtree<sup>318</sup>, a freely available software tool for predicting toxicological effects and mechanisms of action. That tool was used also for our data evaluation, with the results on the dedicated Cramer Class mentioned in the tables summarizing the overall identified species during the headspace and the liquid phase measurements. Noteworthy, there was no underestimation of toxicity when compared with the available chronic oral toxicity data<sup>319</sup>. Hence, from a regulatory perspective, the Cramer classification scheme can be applied for basic toxicological characterization of the detected compounds.

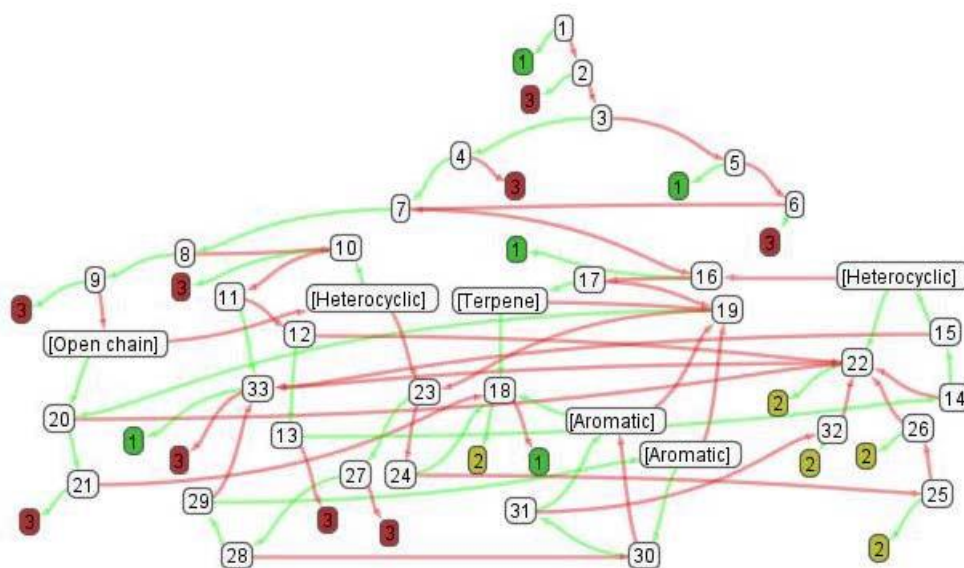


**Figure B1. Decision tree of the Toxtree - Cramer scheme (original). Yes branch in green. No branch in red. Terminal nodes (labelled 1, 2 & 3) refer to Cramer classifications I, II and III.<sup>320</sup>**



**Table B4. Questions of the Cramer decision tree: the original scheme (Q1-33) and the extended scheme (Q40-44) as implemented in the Toxtree software.<sup>320</sup>**

Question No.	Question title	If YES, assign label	If YES, go to rule	If NO, assign label	If NO, go to rule
1	Normal constituent of the body	Low (Class I)			2
2	Contains functional groups associated with enhanced toxicity	High (Class III)			3
3	Contains elements other than C, H, O, N, divalent S		4		43
4	Elements not listed in Q3 occur only as a Na, K, Ca, Mg, N salt, sulphamate, sulphonate, sulphate, hydrochloride ...		40	High (Class III)	
40	Possibly harmful organophosphate or organophosphothionate...	High (Class III)			41
41	Removes phosphates	Low (Class I)			77
7	Heterocyclic		8		16
8	Lactone or cyclic diester		9		10
9	Lactone, fused to another ring, or 5- or 6-membered $\alpha,\beta$ -unsaturated lactone	High (Class III)			[Open chain]
[Open chain]	Open chain		20		[Heterocyclic]
20	Aliphatic with some functional groups		21		22
21	3 or more different functional groups	High (Class III)			44
44	Free $\alpha,\beta$ -unsaturated heteroatom...	High (Class III)			18
18	One of the list	Intermediate (Class II)		Low (Class I)	
22	Common component of food	Interm. (Class II)			33
33	Has sufficient number of sulphonate or sulphamate groups	Low (Class I)		High (Class II)	
[Heterocyclic]	Heterocyclic		10		23
10	3-membered heterocycle	High (Class III)			11
11	Has a heterocyclic ring with complex substituents.		33		12
12	Heteroaromatic		13		22
13	Does the ring bear any substituents?		14	High (Class II)	

Table B4(continued). Questions of the Cramer decision tree: the original scheme (Q1-33) and the extended scheme (Q40-44) as implemented in the Toxtree software.<sup>320</sup>

Question No.	Question title	If YES, assign label	If YES, go to rule	If NO, assign label	If NO, go to rule
14	More than one aromatic ring		15		22
15	Readily hydrolysed		[Heterocyclic]		33
[Heterocyclic]	Heterocyclic		22		16
16	Common terpene	Low (Class I)			17
17	Readily hydrolysed to a common terpene		[Terpene]		19
[Terpene]	Common terpene		18		19
19	Open chain		20		23
23	Aromatic		27		24
27	Rings with substituents		28	High (Class III)	
28	More than one aromatic ring		29		30
29	Readily hydrolysed		[Arom.]		33
[Aromatic]	Aromatic		30		19
30	Aromatic Ring with complex substituents		31		[Arom.]
31	Is the substance an acyclic acetal or ester of substances defined in Q30?		[Arom.]		32
[Aromatic]	Aromatic		18		19
32	Contains only the functional groups listed in Q30 or Q31 and those listed below.	Intermediate (Class II)			22
24	Monocarbocyclic with simple substituents		18		25
25	Cyclopropane, ...	Intermediate (Class II)			26
26	Monocycloalkanone or a Bicyclocompound	Intermediate (Class II)			22
43	Possibly harmful divalent sulphur (not detected via Q3)...	High (Class III)			5
5	Simply branched aliphatic hydrocarbon or a common carbohydrate	Low (Class I)			6
6	Benzene derivative with certain Substituents	High (Class III)			42
42	Possibly harmful analogue of benzene...	High (Class III)			7

## ***B.3. Results and discussion***

### ***B.3.1. Headspace measurements***

Starting the measurements with single component standards, the degradation of the electrolytes with increasing temperature was investigated. In order to assign the correct retention times to the examined solvent electrolytes, samples stored at room temperature were measured. With these analyses the formation of any species at ambient conditions, directly from the interaction of the individual electrolyte constituents, could also be checked. All samples were injected after reaching room temperature, so whenever a higher temperature is mentioned it will refer to the storage conditions of the sample. For identification purposes, the NIST library was the only tool used, while background subtraction was always performed prior to the library search for all detected species. However, the chemical properties of the proposed species were also evaluated, even for compounds for which high probabilities were provided by the library. Such a control was necessary for the correct estimation of the detected degradation products.

#### ***B.3.1.1. DMC***

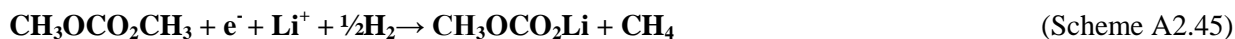
Beginning with DMC stored for two weeks at 25°C, the basic identified peaks were those of the electrolyte, eluting at 1.89 minutes, and the Ar peak at 1.19 min. Since all samples were prepared inside a glove box filled with argon, the largest peak expected in all chromatograms is that of the noble gas. Apart from the siloxanes found in all chromatograms and for every sample (due to column bleed), the DMC samples contained dichloromethane (at 1.47 min) under all sample treatment conditions. Since it cannot be connected to any of the sample components, we attribute its presence to contaminations of the standard solution. The atmosphere inside the glove box cannot have been responsible for this contamination, since other samples that did not contain DMC, such as the EC samples mentioned in the subsequent section, had no dichloromethane peak at their chromatograms. Traces of an organic acid ester (the propanoic acid 2-methyl-(1,1-dimethylethyl)-2-methyl-1,3-propane diylester,  $C_{16}H_{30}O_4$  at 12.83 min) were also observed, but the exact structure of the compound cannot be confirmed with a high probability. However, such a compound could indeed have been caused due to excessive storage of the electrolyte. Unfortunately there was no date of first use or expiration date reported for the portions of the standards obtained from AIT, since they were not delivered in their original container, with their labels including only the information about the sample composition.

When the 60°C sample was analysed, the only additional observation was the presence of a compound eluting at 11.60 min. The small signal obtained resulted in a very low probability for its identification. According to the library search, the peak was assigned to a long chain, branched, unsaturated alcohol.

However the proposed 3-methyl-hepta-1,6-dien-3-ol (C<sub>8</sub>H<sub>14</sub>O) should have an earlier elution time and is therefore not considered as a valid match.

In the chromatogram of the 150°C DMC sample, we additionally identified at 1.23 min a peak assigned to methanol. At 1.58 min d-(+)-Glyceric acid (C<sub>3</sub>H<sub>6</sub>O<sub>4</sub>, 90% spectral similarity according to the NIST library) was identified, although the particular acid has not been documented as a degradation product of DMC. Together with the argon peak, carbon monoxide was detected to co-elute at around 1.20 min. As expected, the peak area of DMC has increased significantly when the highest temperature was used, since this temperature is above the boiling point of the solvent, increasing the portion of DMC transferred to the sample's headspace further than the increase in the vapour pressure of the sample.

From the aforementioned compounds identified in the DMC samples, methanol and carbon monoxide, have been already mentioned in the literature as degradation products of the electrolyte solvent. The reactions dedicated to the formation of methanol were the following:



or



Both reaction schemes propose the formation of methanol from DMC in the presence of lithium ions and water. According to the first mechanism (Scheme A2.45 and A2.50), DMC also consumes protons (H<sup>+</sup>) and at the same time picks up two electrons: one to reduce H<sup>+</sup> to elemental ½ H<sub>2</sub>, and the second to reduce one oxygen of the organic carbonate to an (an-) ionic carbonate. The release of methane and subsequently of carbon dioxide gases takes place subsequently, while the second path (Scheme B1 and B2) results in the emission of hydrogen gas. Even though traces of water can be found also inside the glove box, the lithium salt was not added to the sample to justify the aforementioned reactions. Therefore, methanol must have been formed through a different pathway, induced by the applied thermal energy.

The fact, that carbon monoxide was also identified in the samples, further supports the first reaction scheme as the most probable, since this gas is formed from the produced carbon dioxide (Scheme A2.15). Another possibility is that the CO originates directly from DMC (Scheme A2.43). Both reactions, however, require the presence of Li ions in the electrolyte solution.



or



Corresponding to the last reaction mentioned, when no lithium ion is present in the sample, both detected products could result from the reaction of DMC with hydrogen gas (reduced to H<sup>+</sup> ions) as follows:

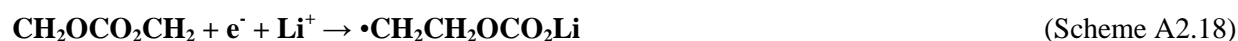


This reaction could be induced by the thermal energy provided to the sample, so that the contribution of Li could be avoided.

### B.3.1.2. EC

When the EC samples were analysed, no additional peaks except those for EC at 6.30 min, and argon at 1.20 min were observed. However, for the higher storage temperature of 60°C, traces of DMC (at 1.85 min) and 1,4-dioxane (at 2.72 min) were also identified. The number of peaks detected (further) increased for the samples stored at 150°C, with acetaldehyde (at 1.27 min), 1,3-dioxolane (at 1.79 min) and 2-methyl-1,3-dioxolane (at 2.05 min) being detected, with mass spectral match factors equivalent to or higher than 65%. Further species proposed by the library with lower probabilities were 2,3-Dihydro-1,4-dioxin at 2,32 min and a long carbon chain diester at 10.87 min. While the most dominant peaks for the 150°C chromatogram were those of acetaldehyde and DMC, the EC peak was missing, indicating the high reactivity of the solvent under these particular conditions. This remark will be later on justified by the findings from the liquid phase measurements of the EC samples at 150°C.

From the identified species in the EC samples, only acetaldehyde and 1,4-dioxane have been previously documented. The mechanism proposed for the formation of both species was involving the presence of lithium ions, according to the following reactions:



However, no lithium salt was present in the particular samples, indicating that the formation of both species may also occur under thermal conditions according to alternative pathways.

Assuming that for EC the reaction mechanism is the same as the one proposed for PC by Arakawa *et al.*<sup>321</sup>, the formation of acetaldehyde and 2-methyl-1,3-dioxolane may occur according to the reactions of Figure B2. Then by demethylation of 2-methyl-1,3-dioxolane, 1,3-dioxolane could be formed. In that case, however, the initiation factor would have been the increased temperature and not related to the salt intercalation into the graphite, as proposed for the experiments performed by the other research group<sup>321</sup>.

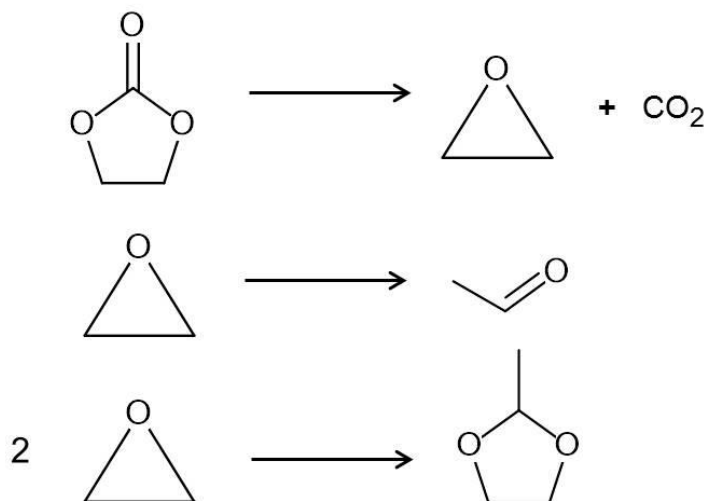


**Figure B2. Formation pathway proposed for 2-methyl-1,3-dioxolane from EC.**

If these thermal conditions could also initiate a reaction between the intermediate ethylene oxide and the identified acetaldehyde, the formation of 1,3-dioxolane could also be explained by the following reaction:



### ***B.3.1.3. LiPF<sub>6</sub>***

In the cases where only the lithium salt was added to the headspace vials, the picture was quite different, with several fluorinated compounds being identified, even for the experiments performed at room temperature. From the reaction of the volatile fluorinated compounds present in the sample with the stationary phase of the analytical column, species like tetrafluorosilane (SiF<sub>4</sub>) at 1.21 min and methylfluorosilane (CH<sub>3</sub>F<sub>3</sub>Si) at 2.45 min were detected with similarities close to 70%. For higher temperatures, difluorophosphoric acid (PO<sub>2</sub>HF<sub>2</sub>) was additionally identified at 1.42 min, together with another fluorinated derivative at 6.38 min, the exact structure of which was not clearly indicated, due to its very low intensity and poor similarity data.

From the identified species at the LiPF<sub>6</sub> samples, difluorophosphoric acid was the only compound that did not result from any reactions with the stationary phase of the analytical column and was unambiguously identified. Its formation in the presence of water was discussed already in the theoretical part of this work, and was proposed to occur according to the following reactions:



#### **B.3.1.4. VC**

When only VC containing samples were analysed, no peaks related to decomposition were identified. The only peaks present in the chromatograms of the different storage temperatures were those of Ar, water, DMC and the VC peak at 3.38 min. The peak of water was explained by the higher water content of the standard in comparison to the battery grade standards used for the electrolytes. DMC was most likely a contamination of the standard. The possibility of any cross-contamination was excluded, since the obtained areas for DMC were comparable for all the measurements, while the peak was not present at the blank sample measured among the different samples investigated. In contrast to the remark made for the DMC samples, the area of VC had a stable value throughout the different investigated temperatures, since the boiling point of VC (b.p. 162°C) is above the maximum temperature used.

#### **B.3.1.5. EMC**

A sample of EMC was also measured to verify the retention time of the solvent, since it belongs to the compounds normally formed at the electrolyte solvent mixtures. Apart from the peak of EMC at 2.56 min, at higher temperature traces of a possible dioxane derivative were also present in the chromatogram. The exact structure of the compound could again not be confirmed with a high probability.

#### **B.3.1.6. EC/DMC (1:1 vol. %)**

For EC/DMC mixtures at room temperature (RT), the interesting changes to the single component chromatograms were the presence of EMC and 1,4-dioxane, as well as the identification of acetone (at 1.36 min) and 2,2-dimethyl-1,3-dioxolane (at 2.48 min) traces. Although the presence of the first two species has been already covered in the existing literature on LIBs, the latter ones are for the first time mentioned as possible electrolyte solvent degradation products. Interesting is also the absence of the EC peak, resulting from the possible reactions that took place decreasing its concentration at the headspace to non-identified levels. Such reactions were previously proposed to occur in the presence of lithium salt leading to a two-step EC reduction (Scheme A2.18 and B6), forming a radical which would further react with H• (Scheme A2.19) and subsequently with DMC, producing the identified EMC (Scheme B7).



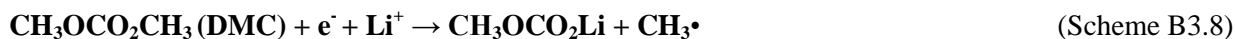
An alternative mechanism would refer to the formation of DEDOHC (diethyl 2,5-dioxahexane dicarboxylate) from the EC molecules first, with the DEDOHC then decomposing to form EC and DEC. That DEC could then react with DMC and produce the EMC, according to the following reaction:



Equivalent reactions could also lead to the formation of 2,2-dimethyl-1,3-dioxolane via methylation of 2-methyl-1,3-dioxolane. The formation path of the latter has already been documented and discussed for the EC samples.

Storage at 60°C didn't prove to change much the headspace composition of our samples, with EMC and 1,4-dioxane belonging to the dominant degradation products identified. At 150°C though, significant additions were observed. The species appearing for the first time at the chromatograms were the following: methyl acetate (C<sub>3</sub>H<sub>6</sub>O<sub>2</sub> at 1.45 min), 1,1-dimethoxy ethane (C<sub>4</sub>H<sub>10</sub>O<sub>2</sub> at 1.69 min), bis-(2-methoxyethyl) carbonate (C<sub>7</sub>H<sub>14</sub>O<sub>5</sub> at 2.00 min), and, as for the EC samples under the same conditions, acetaldehyde, 2-methyl-1,3-dioxolane and 2,3-dihydro-1,4-dioxin. Although methyl acetate has been previously discussed, the other two newly mentioned substances are also firstly assigned as possible electrolyte degradation species.

As for the previously mentioned compounds formed in that mixture (EMC and 1,4-dioxane), the presence of methyl acetate has already been confirmed, but its formation was again proposed to occur in the presence of lithium, according to the following reactions:



Again, the applied thermal energy was proposed to have led to the same final products.

### ***B.3.1.7. EC/DMC + VC (1:1 vol. %, 5% wt)***

When VC was added to the EC/DMC mixture, apart from the original sample constituents only EMC was additionally identified at 25 and 60°C. Acetone was only observed at 150°C, together with acetaldehyde, 2-methyl-1,3-dioxolane and 2,3-dihydro-1,4-dioxane. Methanol, which was present at the DMC sample at 150°C and was not identified for the EC/DMC sample at the same temperature, was again detected. However, methyl acetate, 1,1-dimethoxy ethane and bis-(2-methoxyethyl) carbonate, identified at 150°C when the additive was absent, were now missing. From these observations we could conclude that methanol can further react to produce other compounds, therefore it is not always present at the thermally abused samples at detectable amounts. In addition, the overall number of identified compounds in the



presence of the additive was smaller, indicating that it may contribute to the thermal stability of the electrolyte solution, suppressing its degradation.

#### ***B.3.1.8. DMC + VC (5% wt)***

When DMC + VC samples were analysed, at RT and 60°C only EMC was additionally identified, with its area increasing with the increase of temperature. Despite what we would have expected (but following the observation made for the EC/DMC sample), methanol was again not detected at the 150°C. Concerning the presence of EMC at the particular sample, an alternative reaction path must have led to its formation.

#### ***B.3.1.9. DMC + LiPF<sub>6</sub> (1M)***

When LiPF<sub>6</sub> was added to DMC, apart from the single sample components (comprising DMC and the some fluorinated species) only EMC was identified at RT. At higher temperatures, biphenyl was also detected at 9.61 min for the 60°C sample, as well as a phthalate (C<sub>23</sub>H<sub>26</sub>O<sub>9</sub>) at 150°C. Biphenyl is an electrolyte additive, acting as an overcharge protection polymerising on the cathode surface and forming an isolating film<sup>322</sup>. The presence of phthalates at the samples undergoing storage at higher temperatures was also expected, since phthalates are typical plasticizers used to improve the physical properties of plastic materials, like the septa sealing the caps of the headspace vials. However, it does not belong to the degradation products of the electrolyte solution.

#### ***B.3.1.10. EC + VC (5% wt)***

For the corresponding mixtures with the EC solvent, when VC was added to the electrolyte, DMC and EMC were identified at RT. Traces of acetone and 1,4-dioxane, were also detected at all investigated temperatures. The presence of DMC in the VC samples has already been discussed, so the similarities to the results obtained for the EC/DMC samples were anticipated. The most interesting observation though is the steady increase in the number of detected siloxanes, indicating the existence of additional unidentified active species in the sample headspace, reacting with the stationary phase of the analytical column. Those species may have been formed at the expense of EC, with its peak areas decreasing with the increased storage temperatures, leading to the absolute absence of the EC peak at 150°C.

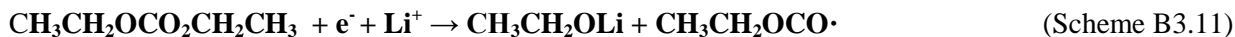
#### ***B.3.1.11. EC + LiPF<sub>6</sub> (1M)***

When EC + LiPF<sub>6</sub> mixtures were analysed, the new compound identified at RT was the diethyl ether (C<sub>4</sub>H<sub>10</sub>O) at 1.39 min, while 2-methyl-1,3-dioxolane appeared again at 60°C. Like for the case of dimethyl

ether formed from DMC via decarboxylation, diethyl ether can originate from DEC, according to the next reaction paths:



or



Even though DEC was not detected in the present sample, it can be formed from EMC and DMC, with both those species being detected.

The main peaks observed at 150°C were those of 2-methyl-1,3-dioxolane and 1,4-dioxane, showing a direct relation between their areas and the applied temperature. However, even more peaks appeared at the highest temperature, including those for acetaldehyde and methylacetate and traces of 1,4-pentadiene (C<sub>5</sub>H<sub>8</sub> at 1.44 min), benzene (at 2.12 min), 3,5-dimethyl cyclohexene (C<sub>8</sub>H<sub>14</sub> at 4.39 min) and 2-propyl-1,3-dioxolane (C<sub>6</sub>H<sub>12</sub>O<sub>2</sub> at 4.83 min). From all those new species detected though, not only spectral similarity was very low, but also their structures did not lead to plausible degradation products, with the only possible exception the 2-propyl-1,3-dioxolane. Benzene could have been formed by the decomposition of the biphenyl additive. However, such a reaction seems rather unlikely. The presence of several species at trace concentrations prevents their unambiguous characterization, while pointing out the need for up-scaled experiments. However, when up-scaling is considered, the corresponding experiments should also be performed under appropriate safety precautions.

### ***B.3.1.12. LiPF<sub>6</sub> + VC***

A sample mixture of just the lithium salt with the additive, using the same amounts as at the corresponding electrolyte solutions, was also investigated. While DMC was present at all temperatures, the presence of 1,4-dioxane and 2-methyl-1,3-dioxolane traces was confirmed only at higher temperatures.

### ***B.3.1.13. EC + LiPF<sub>6</sub> + VC (1M, 5% wt)***

When EC was mixed with the lithium salt and the additive, diethyl ether appeared again at RT, together with DMC, 2-methyl-1,3-dioxolane and 1,4-dioxane. EMC and acetone, both present at RT samples of EC + VC mixtures, were not identified, since either they were not present at all in the samples or their formation occurred at too low concentrations to be identified. Contrary to the species whose presence was not reproducible in the new samples, peaks assigned to fluorinated compounds (such as a possible polyfluorinated organic compound at 3.53 min) appeared again in the chromatograms. No further species

were observed at 60°C, but for the 150°C samples acetaldehyde, ethanol (C<sub>2</sub>H<sub>6</sub>O at 1.31 min), 1,4-pentadiene, methyl acetate, benzene, 2-ethyl-1,3-dioxolane (C<sub>5</sub>H<sub>10</sub>O<sub>2</sub> at 3.34 min) and 3-(1-ethoxyethoxy)-2-methyl-1-butanol (C<sub>9</sub>H<sub>20</sub>O<sub>3</sub> at 6.82 min) were detected. As already discussed, 1,4-pentadiene and benzene are not very plausible electrolyte degradation products. However, peaks at the same retention times have appeared also at the EC + LiPF<sub>6</sub> sample stored at 150°C, showing that the spectrum of degradation compounds may be even wider than estimated and leading to the tentative identification of even more decomposition products whenever such experiments are performed.

For the identified ethanol and based on the reactions mentioned previously as the first steps towards the formation of diethyl ether from DEC, the following reaction paths have been proposed:



or



Although DEC was again not detected, its formation from EC is plausible and has already been discussed.

#### ***B.3.1.14. DMC + LiPF<sub>6</sub> + VC (IM, 5% wt)***

When DMC was mixed with the additive and the lithium salt, instead of the expected EMC, we identified at RT conditions traces of diethylether, 2-methyl-1,3-dioxolane and 1,4-dioxane, together with several fluorinated species. The picture remained the same at 60°C, while at 150°C dimethoxy methane (C<sub>3</sub>H<sub>8</sub>O<sub>2</sub> at 1.42 min) was additionally detected. Also these experiments verified the lower degree of reactivity attributed to the linear electrolyte in contrast to the cyclic one investigated under thermal degradation conditions.

Even though the presence of several ethylene oxide-based oligomers, such as the 1,2-dimethoxy ethane (3<sub>1</sub>), has been excessively discussed, with several PEO oligomers being detected in the LIBs solvent solutions, the dimethoxy methane is mentioned for the first time. Despite the chemical similarity of the aforementioned compounds, the dimethoxy methane cannot result from the same reactions, requiring a different formation pathway to be proposed.

#### ***B.3.1.15. LP30***

Commercial LP30 mixture was also analysed, consisting of the EC and DMC solvents together with the LiPF<sub>6</sub> salt. As expected, at RT the main peaks appearing in the chromatograms were those of both solvents, together with some traces of compounds associated to the lithium salt. An additional peak at 1.32

min was also observed, with the proposed compound from the library being the 2,4,6-trimethyl-1,3-dioxane (C<sub>7</sub>H<sub>14</sub>O<sub>2</sub>). Such a structure is not very likely to result from these particular sample constituents, with its retention time making more profound the mismatch. Although 60°C did not result in any detectable change in the sample composition, at 150°C we additionally identified acetaldehyde, methyl formate (C<sub>2</sub>H<sub>4</sub>O<sub>2</sub> at 1.27 min), ethyl formate (C<sub>3</sub>H<sub>6</sub>O<sub>2</sub> at 1.42 min, instead of the previously identified dimethoxy-methane), acetone, methylacetate, 1,3-dioxolane, 2-methyl-1,3-dioxolane, 1,4-dioxane, 1,3-dihydro-1,4-dioxin (C<sub>4</sub>H<sub>6</sub>O<sub>2</sub> at 2.32 min), and ethylene glycol monoformate (C<sub>3</sub>H<sub>6</sub>O<sub>3</sub> at 3.94 min).

The presence of methyl and ethyl formate as solvent decomposition products has been discussed already in the theoretical part. As mentioned before, when acid-catalyzed ring-opening polymerization of EC (Figure A2.24) takes place, the PEO-like oligomers may further react with PF<sub>5</sub> and CO<sub>2</sub> leading to the formation of formate and oxalate derivatives and the release of CO. For the rest of the identified compounds formation pathways have not been yet proposed.

#### ***B.3.1.16. LP30 + VC (5% wt)***

When VC was added to the LP30 mixture, the peak of EC was not detected, while EMC was identified. At 60°C also phosphorodifluoric acid (at 1.21 min) was identified by the library, and at 150°C the corresponding peaks for acetaldehyde, methylacetate, 2-methyl-1,3-dioxolane and 1,4-dioxane were again detected. The new species appearing were the methylpropionate (C<sub>4</sub>H<sub>8</sub>O<sub>2</sub> at 1.89 min), 2-methoxy-ethanol (C<sub>3</sub>H<sub>8</sub>O<sub>2</sub> at 1.92 min), methoxyethane (C<sub>3</sub>H<sub>8</sub>O at 1.28 min), 1,2-dimethoxyethane (C<sub>4</sub>H<sub>10</sub>O<sub>2</sub> at 2.10 min), 1-methoxy-2-propanone (C<sub>4</sub>H<sub>8</sub>O<sub>2</sub> at 4.71 min), methoxyethylacetate (C<sub>5</sub>H<sub>10</sub>O<sub>3</sub> at 4.80) and another fluorinated organic silane (at 3.30 min). From the detected species, the presence of 1,2-dimethoxy ethane is easily explained by the reaction sequences mentioned for the PEO units, since it belongs to the first member of the methoxy/methoxy series (3<sub>n</sub>).

The remaining species identified in the chromatogram of the highest storage temperature investigated are detected for the first time, and despite the difficulty in proposing a mechanism for their formation, they are all plausible degradation products of the examined analytes.

#### ***B.3.1.17. EC/DMC + LiPF<sub>6</sub> (1:1 vol. %, 1M)***

Apart from using only the LP30 mixture for investigations on the EC/DMC + LiPF<sub>6</sub> mixture, the same sample constituents were added separately and the analysis of corresponding thermal degradation products was repeated with the newly prepared sample. For RT the identified species were methanol, ethylene glycol diformate and ethylether, as well as the typical fluorinated organic species. When the storage temperature increased to 60°C, the peak for EMC appeared, while the methanol peak was not identified anymore. In the last case, where 150°C were used, acetaldehyde, methyl formate, methyl acetate, 2-

methoxy ethanol, 2-methyl-1,3-dioxolane, 1,2-dimethoxy ethane, 1,4-dioxane and 2-ethyl-1,3-dioxolane were identified. Apart from these species, t-butyl-2-ethylhexanoate ( $C_{12}H_{24}O_2$  at 1.91 min), (2Z)-1-ethoxy-2-heptene ( $C_9H_{18}O$  at 3.08 min) and 2-tert-butyl-1,3-dioxolane ( $C_7H_{14}O_2$  at 4.82 min) were detected. From these new species, the presence of t-butyl-2-ethylhexanoate at such an early retention time is highly doubted, and the formation of (2Z)-1-ethoxy-2-heptene cannot be easily resulting from a reaction among the sample components. In addition, the peak of 2-methoxy ethanol was only met when VC was added to the sample, while far more degradation products were expected from the comparison with the LP30 equivalent mixture, or with the results from the single solvents with the additive. Repetition of the measurement proved that the sampling was not responsible for the lower number of compounds being identified. Sealing malfunction at the vials could have though resulted in this observation.

#### ***B.3.1.18. EC/DMC + LiPF<sub>6</sub> + VC (1:1 vol. %, 1M, 5% wt)***

Our last sample combination involved the mixture where both electrolyte solvents, the lithium salt and the additive were present, as at the equivalent LP30 + VC mixture. For these samples and at 25 and 60°C peaks corresponding to acetaldehyde, 1,2-dimethoxy propane, ethylether, dimethoxy methane, methyl acetate, 2-methyl-1,3-dioxolane, 1,2-dimethoxy ethane, 1,4-dioxane and the various fluorinated organic species were observed. Apart from 1,2-dimethoxy propane and ethylether, which were not anymore detected at 150°C, the peaks for methyl formate, acetone, 1,1-dimethoxy-ethane ( $C_4H_{10}O_2$  at 1.68 min), methyl propionate ( $C_4H_8O_2$  at 1.90 min), 2-methoxyethanol ( $C_3H_8O_2$  at 1.95 min) and 2-ethyl-1,3-dioxolane ( $C_4H_8O_2$  at 2.01 min) were also identified. These results are in a very good agreement with those obtained for the LP30 + VC mixture, verifying to a big extend our findings.

The presence of 2-methoxyethanol is easily justified, since it is the first member of the methoxy/hydroxy poly(ethylene oxide) (PEO) units (series 5<sub>n</sub>) resulting from solvent degradation. Despite not having been until now identified, the presence of 1,1-dimethoxy ethane could also be easily explained by a methylation reaction occurring at the 1,1-dimethoxy methane identified before (at the DMC + VC + LiPF<sub>6</sub> sample).

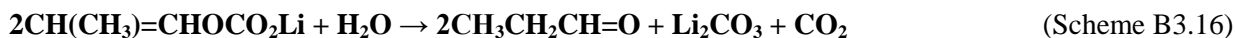
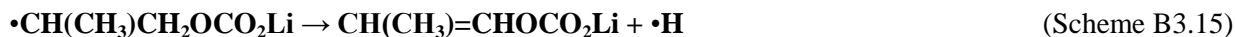
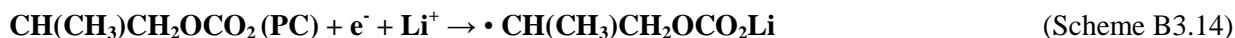
#### ***B.3.1.19. Cycled LIB electrolyte sample***

In addition to the sample mixtures prepared in our laboratory, the electrolyte solution extracted from a cycled lithium-ion cell was also thermally degraded and analyzed. With these measurements we wanted to investigate which volatile compounds are formed due to the cycling of LIBs under normal conditions of use and which result from the exposure to higher temperatures applied under *ex situ* conditions. It is important to point out the loss of any highly volatile species formed exclusively during the cycling of the LIB, since for the extraction of the remaining electrolyte solution the cells were opened inside the glove box, with any gaseous emissions escaping to the glove box and being transferred to the exhaust. However,

some of the volatile emissions produced managed to remain in the solution and were identified at the samples stored at RT.

The detected degradation products at 25°C according to their retention times were: phosphoric difluoride (PHOF<sub>2</sub> at 1.33 min), acetone, difluorophosphoric acid, formic acid ethylester 1,3-dioxolane, 2-methyl-1,3-dioxolane, EMC, 1,4-dioxane and DEC (at 3.87 min). Despite the spectral similarity (above 90%), the presence of 1,1-diethoxy-pentane (C<sub>9</sub>H<sub>20</sub>O<sub>2</sub>) at 1.50 min was considered rather a misassignment. The electrolyte solvents were also identified together with the VC additive and some typical fluorosilanes present at all samples where the lithium salt was added. It is worth to point out the identification of DEC, the formation of which proved to be facilitated by the electrochemical procedures far more than by the heat transfer. The rest of the detected species on the other hand, proved to result from both thermal and electrochemical reaction mechanisms. Further formations of volatiles were observed at 60°C, since PC (propylene carbonate, C<sub>4</sub>H<sub>6</sub>O<sub>3</sub> at 6.57 min), tetraethylenglycol dimethylether (C<sub>10</sub>H<sub>22</sub>O<sub>5</sub> at 8.08 min) and dimethyl diglycol carbonate (C<sub>8</sub>H<sub>14</sub>O<sub>7</sub> at 8.63 min) were also identified together with biphenyl and octyl cyclohexane carboxylate (C<sub>15</sub>H<sub>28</sub>O<sub>2</sub> at 7.40 min). The origin of biphenyl has been already discussed. Even though polymerization products of biphenyl were not identified in our samples, traces of 2,2'-dimethylbiphenyl and 2-ethyl-biphenyl (C<sub>14</sub>H<sub>14</sub> at around 11.83 min) were detected. For octyl cyclohexane carboxylate now, not only the structure cannot be explained but also the retention time, proving ones again how critical we have to be with the matches proposed by the library. Finally, at 150°C, methanol, ethanol and propanal (C<sub>3</sub>H<sub>6</sub>O at 1.37 min) were also detected, as well as a non-identified compound at 2.40 min, with a dioxolane derivative being proposed by the library.

Even though the presence of PC was verified from the experiments performed at 60°C, it should have been an additional electrolyte of the LIB cell and not formed under the applied electrochemical or thermal conditions. Its reaction at higher temperatures may follow the sequence observed for EC, resulting in the formation of acetaldehyde (Scheme A2.18, A2.20 and A2.22), leading this time to the formation of propanal:



### ***B.3.1.20. Overall compounds identified in the sample HS***

The following table summarizes the compounds identified at the headspace of the various samples analysed after prolonged storage at different temperatures. Targeting a fast toxicological screening of the detected species the Toxtree software was used for the categorization of the compounds into different

groups/classes according to the potential hazard they could impose on human health. Even though this information was missing for several of the identified species, with no matches provided by the software, members of the Cramer Class III were indeed present at our results. For these compounds, among which are the frequently met 1,3-dioxolane and 1,4-dioxane, high toxicity risk is suggested, underlining the need for safety precautions when these experiments are performed. It is also worth mentioning the high toxicity risk assigned to the cyclic electrolytes (accompanying the flammability of such compounds) and additives like the biphenyl. Therefore, handling of the original components of the electrolyte solution should be done under enhanced safety conditions.

**Table B5. Overall identified species from the *ex situ* thermal degradation experiments of the LIBs' electrolyte solution constituents**

No	RT	Compound Name	Molecular Formula	CAS#	Cramer Class
1	1.17	Carbon monoxide	CO	630-08-0	1
2	1.20	Carbon dioxide	CO <sub>2</sub>	124-38-9	1
3	1.21	Tetrafluorosilane	SiF <sub>4</sub>	7783-61-1	-
4	1.23	Methanol	CH <sub>3</sub> OH	67-56-1	1
5	1.23	Difluorodimethylsilane	C <sub>2</sub> H <sub>6</sub> F <sub>2</sub> Si	353-66-2	-
6	1.27	Acetaldehyde	C <sub>3</sub> H <sub>4</sub> O	75-07-0	1
7	1.28	Methoxyethane	C <sub>3</sub> H <sub>8</sub> O	540-67-0	1
8	1.31	Ethanol	C <sub>2</sub> H <sub>6</sub> O	64-17-5	1
9	1.33	Phosphoric difluoride	PHOF <sub>2</sub>	14939-34-5	-
10	1.36	Acetone	C <sub>3</sub> H <sub>6</sub> O	67-64-1	1
11	1.37	Propanal	C <sub>3</sub> H <sub>6</sub> O	123-38-6	1
12	1.39	Ethylether	C <sub>4</sub> H <sub>10</sub> O	60-29-7	1
13	1.41	Difluorophosphoric acid	POF <sub>2</sub> OH	13779-41-4	-
14	1.42	Dimethoxy methane	C <sub>3</sub> H <sub>8</sub> O <sub>2</sub>	109-87-5	1
15	1.42	Ethyl formate	C <sub>3</sub> H <sub>6</sub> O <sub>2</sub>	109-94-4	1
16	1.44	1,4-Pentadiene	C <sub>5</sub> H <sub>8</sub>	591-93-5	1
17	1.45	Methyl acetate	C <sub>3</sub> H <sub>6</sub> O <sub>2</sub>	79-20-9	1
18	1.46	Dichloromethane	CH <sub>2</sub> Cl <sub>2</sub>	75-09-2	3
19	1.50	1,1-Diethoxy-pentane*	C <sub>9</sub> H <sub>20</sub> O <sub>2</sub>	3658-79-5	-
20	1.58	d-(+)-Glyceric acid	C <sub>3</sub> H <sub>6</sub> O <sub>4</sub>	473-81-4	-
21	1.69	1,1-Dimethoxy ethane	C <sub>4</sub> H <sub>10</sub> O <sub>2</sub>	534-15-6	1
22	1.79	1,3-Dioxolane	C <sub>3</sub> H <sub>6</sub> O <sub>2</sub>	646-06-0	3
23	1.84	Dimethyl carbonate (DMC)	C <sub>3</sub> H <sub>6</sub> O <sub>3</sub>	616-38-6	1
24	1.89	Methylpropionate	C <sub>4</sub> H <sub>8</sub> O <sub>2</sub>	554-12-1	1
25	1.91	t-Butyl-2-ethylhexanoate*	C <sub>12</sub> H <sub>24</sub> O <sub>2</sub>	71648-27-6	-
26	1.92	2-Methoxy-ethanol	C <sub>3</sub> H <sub>8</sub> O <sub>2</sub>	109-86-4	1
27	2.00	Bis-(2-methoxyethyl) carbonate*	C <sub>7</sub> H <sub>14</sub> O <sub>5</sub>	626-84-6	-
28	2.05	2-Methyl-1,3-dioxolane	C <sub>4</sub> H <sub>8</sub> O <sub>2</sub>	497-26-7	-
29	2.10	1,2-Dimethoxyethane	C <sub>4</sub> H <sub>10</sub> O <sub>2</sub>	110-71-4	3
30	2.12	Benzene	C <sub>6</sub> H <sub>6</sub>	71-43-2	3
31	2.32	2,3-Dihydro-1,4-dioxin	C <sub>4</sub> H <sub>6</sub> O <sub>2</sub>	543-75-9	-

**Table B5 (continued). Overall identified species from the *ex situ* thermal degradation experiments of the LIBs' electrolyte solution constituents**

No	RT	Compound Name	Molecular Formula	CAS#	Cramer Class
32	2.48	2,2-Dimethyl-1,3-dioxolane	C <sub>5</sub> H <sub>10</sub> O <sub>2</sub>	2916-31-6	-
33	2.56	Ethylmethyl carbonate (EMC)	C <sub>4</sub> H <sub>8</sub> O <sub>3</sub>	623-53-0	1
34	2.64	1,2-Dimethoxy ethane	C <sub>4</sub> H <sub>10</sub> O <sub>2</sub>	110-71-4	3
35	2.67	1,4-Dioxane	C <sub>4</sub> H <sub>8</sub> O <sub>2</sub>	123-91-1	3
36	3.06	Ethylene glycol diformate	C <sub>4</sub> H <sub>6</sub> O <sub>4</sub>	629-15-2	-
37	3.08	(2Z)-1-Ethoxy-2-heptene*	C <sub>9</sub> H <sub>18</sub> O	51149-74-7	-
38	3.34	2-Ethyl-1,3-dioxolane	C <sub>5</sub> H <sub>10</sub> O <sub>2</sub>	2568-96-9	-
39	3.38	Vinylene carbonate (VC)	C <sub>3</sub> H <sub>2</sub> O <sub>3</sub>	872-36-6	-
40	3.94	Ethylene glycol monoformate	C <sub>3</sub> H <sub>6</sub> O <sub>3</sub>	628-35-3	-
41	4.39	3,5-Dimethyl cyclohexene	C <sub>8</sub> H <sub>14</sub>	823-17-6	-
42	4.71	1-Methoxy-2-propanone	C <sub>4</sub> H <sub>8</sub> O <sub>2</sub>	5878-19-3	-
43	4.80	Methoxyethylacetate	C <sub>5</sub> H <sub>10</sub> O <sub>3</sub>	110-49-6	1
44	4.82	3-(1-Ethoxyethoxy)-2-methyl-1-butanol*	C <sub>9</sub> H <sub>20</sub> O <sub>3</sub>	59410-44-5	-
45	4.82	2-Tert-butyl-1,3-dioxolane	C <sub>7</sub> H <sub>14</sub> O <sub>2</sub>	2568-29-8	-
46	4.83	2-Propyl-1,3-dioxolane	C <sub>6</sub> H <sub>12</sub> O <sub>2</sub>	3390-13-4	-
47	6.30	Ethylene carbonate (EC)	C <sub>3</sub> H <sub>4</sub> O <sub>3</sub>	96-49-1	3
48	6.57	Propylene carbonate (PC)	C <sub>4</sub> H <sub>6</sub> O <sub>3</sub>	108-32-7	3
49	8.08	Tetraethylglycol dimethylether*	C <sub>10</sub> H <sub>22</sub> O <sub>5</sub>	143-24-8	1
50	8.63	Dimethyl diglycol carbonate	C <sub>8</sub> H <sub>14</sub> O <sub>7</sub>	8729-23-7	-
51	9.18	Diethoxydiformate	C <sub>6</sub> H <sub>10</sub> O <sub>5</sub>	1609-47-8	1
52	9.61	Biphenyl	C <sub>12</sub> H <sub>10</sub>	92-52-4	3
53	12.83	Propanoic acid 2-methyl-(1,1-dimethylethyl)-2-methyl-1,3-propane diylester	C <sub>16</sub> H <sub>30</sub> O <sub>4</sub>	74381-40-1	-

\*These compounds had a library match above 90%, however their retention times are not supporting their identification.

The following figures illustrate the variety of species formed under thermal degradation conditions. Categorization of the identified compounds was performed according to their chemical structure, showing the different groups that can be encountered. Among these compounds, several linear and cyclic oxygenated and polyoxygenated compounds were met. Fluorinated species were also identified, with the silyl compounds mentioned belonging to reaction products with the stationary phase of the column and not to actual LIBs degradation products. Various permanent gases, hydrocarbons, alcohols, ethers, esters, aldehydes and carbonates were also detected, being in good agreement with the theoretical expected electrolyte decomposition species. Organic acids were also encountered, however, their trace level prohibited an unambiguous identification. In addition, several species were for the first time documented to be present at thermally abused electrolyte solutions. For some of these species formation mechanisms were proposed, but additional experiments utilizing larger volumes of the solution are required for the determination of the exact conditions under which these compounds are occurring and their corresponding formation pathways.



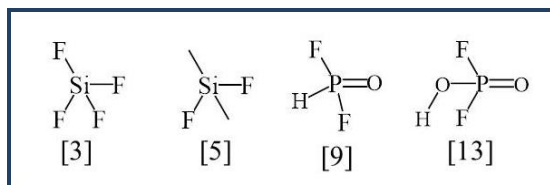


**Figure B3.** Structural formulas of the fluorinated compounds identified from the *ex situ* thermal degradation experiments of the LIBs' electrolyte solution constituents. The numbers correspond to the compound names mentioned in Table B5.

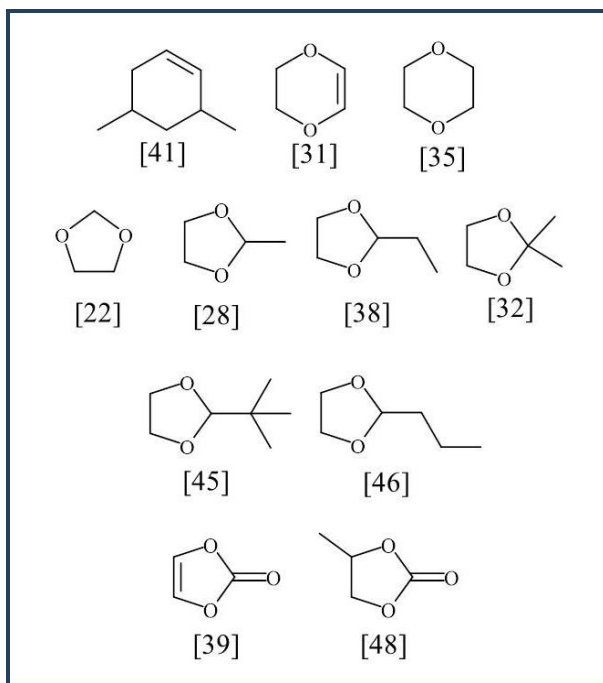


**Figure B4.** Structural formulas of the cyclic compounds identified from the *ex situ* thermal degradation experiments of the LIBs' electrolyte solution constituents. The numbers correspond to the compound names mentioned in Table B5.

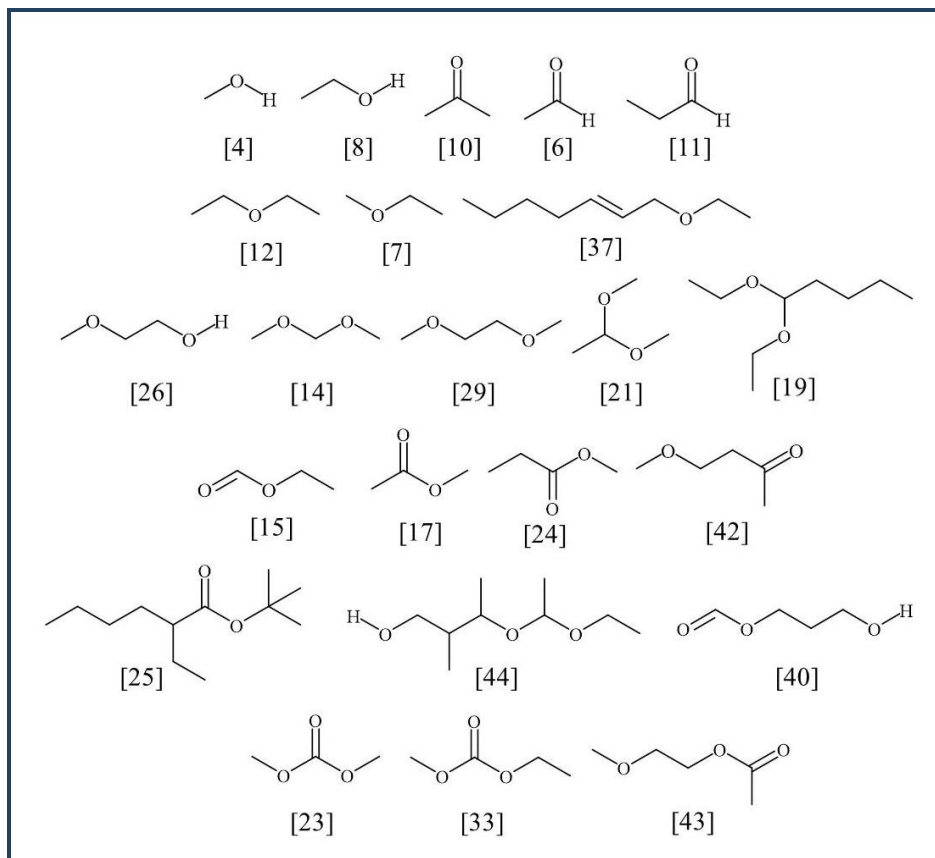


**Figure B5. Structural formulas of the linear oxygenated compounds identified from the *ex situ* thermal degradation experiments of the LIBs' electrolyte solution constituents. The numbers correspond to the compound names mentioned in Table B5.**

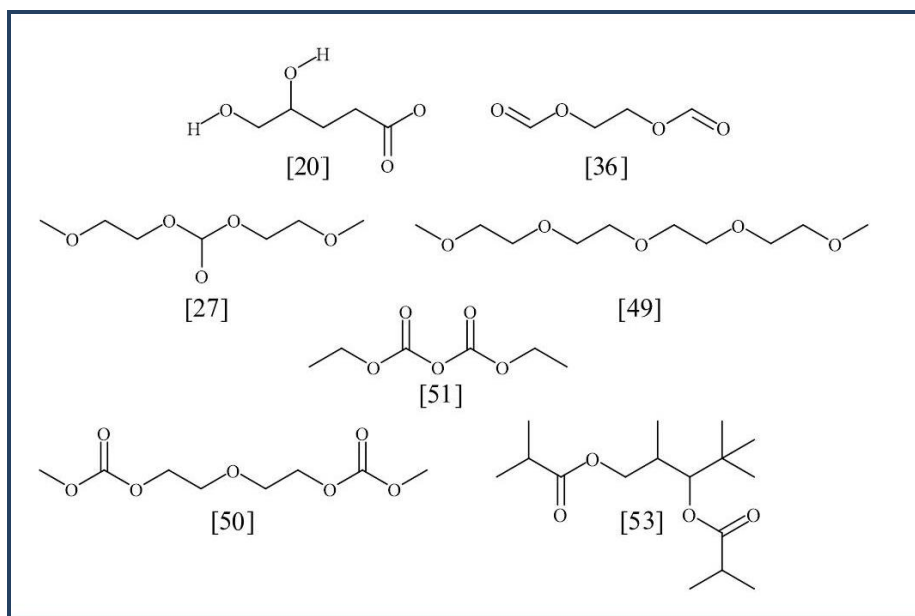


**Figure B6. Structural formulas of the linear polyoxygenated compounds ( $O \geq 4$ ) identified from the *ex situ* thermal degradation experiments of the LIBs' electrolyte solution constituents. The numbers correspond to the compound names mentioned in Table B5.**

### ***B.3.2. Liquid phase measurements***

Complementing the aforementioned headspace measurements, liquid phase analyses were also performed. This time the less volatile sample constituents were targeted. The identified species are presented below, together with the results of a fast toxicological screening using the Toxtree software.

#### ***B.3.2.1. Single component samples***

Starting again with the single component samples, when DMC was analysed, only dichloromethane traces were detected, together with the DMC peak at 1.99 min. The differences in the retention times of the solvents are resulting from the much higher peaks obtained with the liquid injection of the samples, since bigger amounts of the solvents were transferred to GC for analysis.

For VC samples, the additive was detected at 4.64 min, together with BHT (butylated hydroxytoluene,  $C_{15}H_{24}O$  at 12.19 min). BHT is a derivative of phenol, widely used to prevent oxidation in fluids and other materials where free radicals must be controlled. Therefore, BHT could have been used as an anti-oxidant to the VC standard. In addition, both peaks were identified only at the 25 and 60°C samples and not for the 150°C. Even though exhaustive volatilization of the compounds during sample storage at the high temperature is quite unlikely, losses during the additional sample preparation (dilution step) required for the liquid phase experiments could explain these results.

On the other hand, when samples containing only the lithium salt were analysed, no plausible compound was detected. The only existing peak at the chromatograms of 25 and 60°C was assigned to 1,2,3,4,5-pentamethylcyclopentane ( $C_{10}H_{20}$  at 5.95 min) traces, with a similarity match of around 30%, leading us to consider the detected compound as unknown.

When a room temperature sample of EMC was analysed, apart from the solvent peak at 3.01 min, two additional peaks were identified. Those peaks belonged to DEC (at 4.26 min) and BHT. For the same reasons mentioned before, BHT must have been added to the EMC standard. Concerning the DEC, it could have indeed been formed from EMC ( $2EMC \leftrightarrow DMC + DEC$ ), as we have already discussed in the theoretical part. Even though EC was not identified in the liquid phase of the EMC sample, the presence of 1,4-dioxane verifies its (maybe short-term) existence. This decomposition product of EC has proven to occur in the presence of lithium ions. Traces of  $LiPF_6$  present at the sample could also explain the observed fluorinated species identified in the EMC sample.

The results of the EC samples are this time presented at the end of the single component samples, due to the very high complexity of the chromatograms obtained for the 150°C sample. Although at RT the corresponding chromatogram included only the EC peak at 8.78 min, for 60°C one additional peak assigned to 1,2-ethanediol ( $C_2H_6O_2$  at 2.63 min) also appeared. The chromatogram for the sample stored at 150°C though, had a significant number of peaks present (Figure B7). More than seventy peaks were

detected (without considering those of the additional siloxane derivatives present exclusively at the 150°C sample), belonging to several different functional groups. From the identified peaks, the ones mentioned also at the headspace measurements are the following: 1,3-dioxolane, DMC, 2-methyl-1,3-dioxolane, 2,3-dihydro-1,4-dioxin, 1,4-dioxane and finally 2-methoxy-ethanol, which was though only present at LP30 mixtures. Additional species detected were the 2-ethoxy-ethanol (at 2.79 min), 2-(vinylloxy)-ethanol ( $C_4H_8O_2$  at 2.95 min), ethylene glycol monoacetate ( $C_4H_8O_3$  at 5.15 min), 1,3-dioxolane-2-methanol ( $C_4H_8O_3$  at 8.06 min), dipropoxydiacetate ( $C_4H_{18}O_5$  at 8.33 min), triethylene glycol monoethylether acetate ( $C_9H_{18}O_5$  at 8.67 min), 1,4-dioxan-2-yl hydroperoxide ( $C_4H_8O_4$  at 9.11 min) and triethylene glycol diacetate ( $C_{10}H_{18}O_6$  at 11.21 min). Furthermore, several polyethylene glycols, dioxolane and diol derivatives, as well as different trioxanes (like 1,3,6-trioxocane,  $C_5H_{10}O_3$ , at 5.72 min and 2-methyl-1,3,6-trioxocane,  $C_6H_{12}O_3$ , at 6.41 min) and other polyoxygenated cyclic compounds (e.g. ethylene oxide cyclic hexamer,  $C_{12}H_{24}O_6$ , at 9.44 min) were detected. Apart from these species, for which the exact structure was not unambiguously determined, all other identified compounds are listed in Table B6.

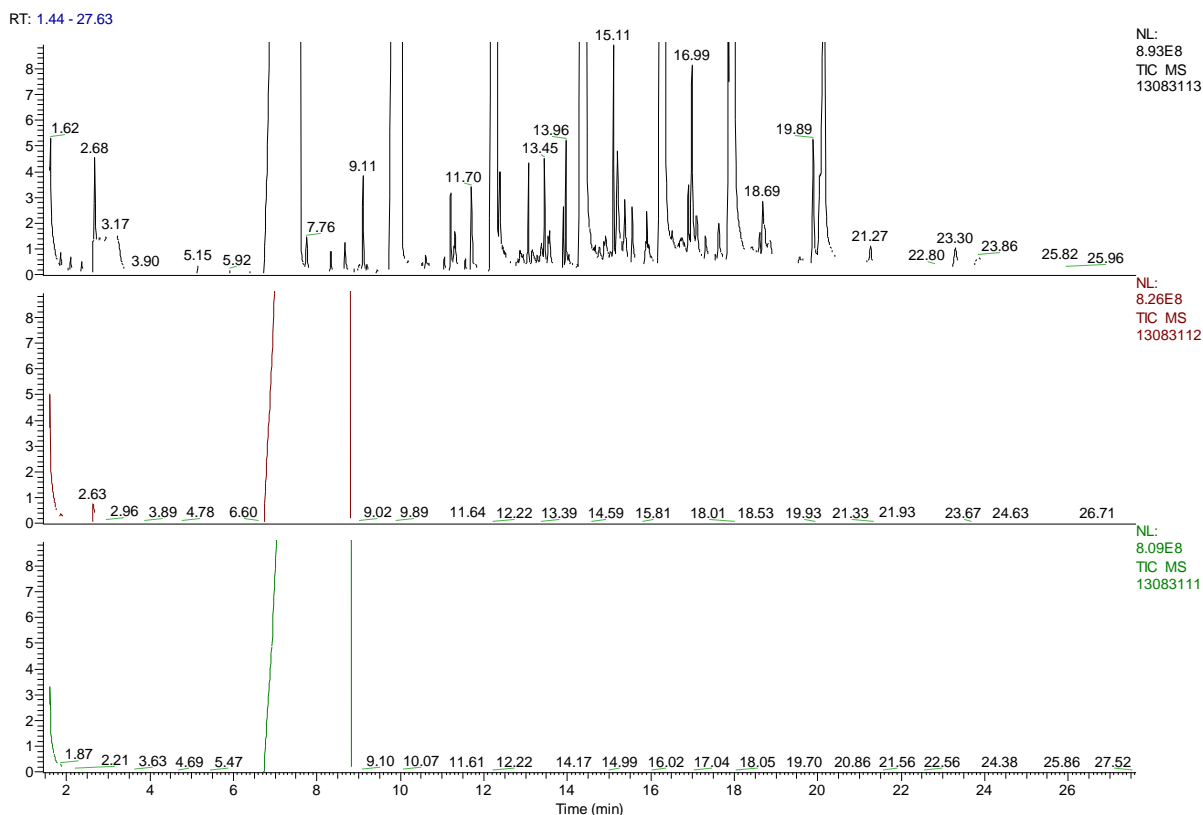


**Figure B7. Comparison of the magnified chromatograms obtained from liquid phase measurements of EC at 25°C (green), 60°C (red) and 150°C (black).**

**Table B6. Identified species from the *ex situ* thermal degradation experiments of the EC solvent at 150°C by liquid injection measurements.**

No	RT	Compound Name	Formula	CAS
1	1.86	1,3-Dioxolane	C <sub>3</sub> H <sub>6</sub> O <sub>2</sub>	646-06-0
2	1.90	Dimethyl carbonate	C <sub>3</sub> H <sub>6</sub> O <sub>3</sub>	616-38-6
3	2.05	2-Methoxy-ethanol	C <sub>3</sub> H <sub>8</sub> O <sub>2</sub>	109-86-4
5	2.10	2-Methyl-1,3-Dioxolane	C <sub>4</sub> H <sub>8</sub> O <sub>2</sub>	497-26-7
6	2.37	2,3-Dihydro-1,4-dioxin	C <sub>4</sub> H <sub>6</sub> O <sub>2</sub>	543-75-9
7	2.68	1,4-Dioxane	C <sub>4</sub> H <sub>8</sub> O <sub>2</sub>	123-91-1
8	2.79	2-Ethoxy-ethanol	C <sub>4</sub> H <sub>10</sub> O <sub>2</sub>	110-80-5
9	2.95	2-(vinylxy)-Ethanol	C <sub>4</sub> H <sub>8</sub> O <sub>2</sub>	764-48-7
11	5.15	Ethylene glycol, monoacetate	C <sub>4</sub> H <sub>8</sub> O <sub>3</sub>	542-59-6
12	5.72	1,3,6-Trioxocane	C <sub>5</sub> H <sub>10</sub> O <sub>3</sub>	1779-19-7
13	6.41	2-Methyl-1,3,6-trioxocane	C <sub>6</sub> H <sub>12</sub> O <sub>3</sub>	2781-01-3
14	7.53	Ethylene carbonate	C <sub>3</sub> H <sub>4</sub> O <sub>3</sub>	96-49-1
17	7.61	Diethylene glycol	C <sub>4</sub> H <sub>10</sub> O <sub>3</sub>	111-46-6
18	8.06	1,3-Dioxolane-2-methanol	C <sub>4</sub> H <sub>8</sub> O <sub>3</sub>	5694-68-8
19	8.33	Dipropyloxydiacetate	C <sub>4</sub> H <sub>18</sub> O <sub>5</sub>	85688-79-7
20	8.33	n-Nonaldehyde	C <sub>9</sub> H <sub>18</sub> O	124-19-6
21	8.67	Triethylene glycol monoethylether acetate	C <sub>9</sub> H <sub>18</sub> O <sub>5</sub>	3610-27-3
22	8.92	2,2-Dimethoxy-ethanol	C <sub>4</sub> H <sub>10</sub> O <sub>3</sub>	30934-97-5
23	9.01	2-Methyl-1,3,6-Trioxocane	C <sub>6</sub> H <sub>12</sub> O <sub>3</sub>	2781-01-3
24	9.11	1,4-Dioxan-2-yl, Hydroperoxide	C <sub>4</sub> H <sub>8</sub> O <sub>4</sub>	4722-59-2
25	9.20	2-Heptyl-1,3-Dioxolane	C <sub>10</sub> H <sub>20</sub> O <sub>2</sub>	4359-57-3
26	9.44	Ethylene oxide cyclic hexamer	C <sub>12</sub> H <sub>24</sub> O <sub>6</sub>	17455-13-9
27	10.04	Triethylene glycol	C <sub>6</sub> H <sub>14</sub> O <sub>4</sub>	112-27-6
29	10.61	2-(2-(2-ethoxyethoxy)ethoxy)-Ethanol	C <sub>8</sub> H <sub>18</sub> O <sub>4</sub>	112-50-5
35	10.67	1,4,7,10,12-Pentaoxacyclo-pentadecane	C <sub>10</sub> H <sub>20</sub> O <sub>5</sub>	33100-27-5
36	10.80	1,3,2,4-di-o-methylene-d-Arabitol	C <sub>7</sub> H <sub>12</sub> O <sub>5</sub>	55780-55-7
37	11.21	Triethylene glycol diacetate	C <sub>10</sub> H <sub>18</sub> O <sub>6</sub>	111-21-7
38	11.56	1,4,7,10-Tetraoxacyclododecan-2-one	C <sub>8</sub> H <sub>14</sub> O <sub>5</sub>	77055-61-9
29	11.70	1-(2-(2-(1-methoxyethoxy)ethoxy)ethoxy)-Ethanol	C <sub>9</sub> H <sub>20</sub> O <sub>4</sub>	29681-21-8
40	11.98	Butoxytriethylene glycol	C <sub>10</sub> H <sub>22</sub> O <sub>4</sub>	143-22-6

The variety of degradation compounds detected at the EC samples at 150°C is significantly bigger than that of the LP30 mixtures or the cycled electrolyte sample, discussed later on. If all those species resulted from the very high reactivity of the EC solvent, they must have been prevailed or even enhanced by the

presence of additional compounds on the sample, which was, however, not experimentally proved. This could be explained by the fact that for all the other samples mentioned a higher portion of solvent (2 ml instead of one) was used for the extraction of the formed species, due to the nature of the samples. Specifically, the dark coloured film covering the inner walls of the samples was partially dissolved, so after shaking the samples with the solvent they were let stand still for about 15 min, covered with the vial caps, so that only the supernatant could be collected for the liquid phase measurements. In this way we avoided the use of any filtration step, which would have otherwise been necessary. This further dilution of the sample reduces to half the sensitivity for those measurements, explaining to an extent the differences in the obtained chromatograms. Additionally, several species may have remained trapped at the solid precipitant of the sample. Therefore, their detection may have been prevented by inadequate extraction by the selected solvent and conditions. These conditions were however chosen according to the extraction procedures described in the literature for similar applications. Any more rough extraction media or temperature conditions were also excluded, since they could have contributed to further decomposition of the samples constituents bringing artefacts into our investigations.

#### ***B.3.2.2. LP30***

For the LP30 samples, several compounds were detected already from the 25°C storage temperature. Even though less species were identified for the sample stored at 60°C, several different compounds were present at the chromatogram corresponding to the 150°C sample. Wrong assignment of the samples was excluded, since different species were present at each sample, and not just additional peaks at the higher temperatures, as may have been expected. Therefore, this remark also implies that the solvent extraction performed was probably not always equally efficient. A different justification would have involved the extent of changes at different storage conditions, with the species detected in the liquid phase of the sample at RT having disappeared at the 60°C, leading to the formation of more volatile compounds. However, that would have resulted in a much more enhanced headspace for the 60°C, which was not the case for the investigated samples. That makes the former consideration about the extraction efficiency a more evident cause for the observed variations. Since the focus of these investigations was in the volatile species, and the liquid phase measurements were only performed complementary, the extraction procedure was not further optimized.

The obtained results were evaluated and only the most plausible identified species will be discussed. Under RT conditions, when only the LP30 mixture was present in the headspace vial, the detected compounds were the DMC, EMC, EC, BHT, 2-methyl-1,3-dioxolane, 1,4-dioxane, methyl allyl diglycolcarbonate ( $C_{10}H_{16}O_7$  at 9.16 min), 2-methoxyethoxy-ethene ( $C_5H_{10}O_2$  at 9.41 min), as well as several polyethylene glycol and other polyoxygenated branched or heterocyclic hydrocarbons. Since the

lithium salt is also present at the LP30 mixture, the presence of phosphorus oxyfluoride ( $\text{POF}_3$  at 2.46 min) and other fluorinated derivatives was expected and verified by the library search for at least three additional peaks. At  $60^\circ\text{C}$ , apart from the solvent peaks, three more species were detected. These were the bis-(2-methoxyethyl) ether ( $\text{C}_6\text{H}_{14}\text{O}_3$  at 9.36 min) and two further cyclic polyoxygenated species. Then, at  $150^\circ\text{C}$ , the species assigned to the new peaks were again 1,3-dioxolane, ethylene glycol diformate, ethylene glycol monoacetate, 1,3-dioxolane-2-methanol, with the additional peaks of dihydroxyacetone ( $\text{C}_3\text{H}_6\text{O}_3$  at 2.86 min), 2-propanone 1-hydroxy acetate ( $\text{C}_5\text{H}_8\text{O}_3$  at 6.05 min), 2-propanol 1-isobutoxy ( $\text{C}_7\text{H}_{16}\text{O}_2$  at 6.48 min), 1,4-dioxan-2-ol ( $\text{C}_4\text{H}_8\text{O}_3$  at 7.83 min), 2,2'-bis-1,3-dioxolane ( $\text{C}_6\text{H}_{10}\text{O}_4$  at 8.41 min), triethylene glycol monomethylether acetate ( $\text{C}_9\text{H}_{18}\text{O}_5$  at 8.56 min), (2-(2-(carboxymethoxy)ethoxy)ethoxy) acetic acid ( $\text{C}_8\text{H}_{14}\text{O}_7$  at 9.20 min) and diethylene glycol dipropionate ( $\text{C}_{10}\text{H}_{18}\text{O}_5$  at 9.34 min).

### **B.3.2.3. LP30 + VC (5% wt)**

As also observed for the headspace measurements, the addition of VC to LP30 resulted in several differences in the chromatograms, in respect to the identified species. In general, the evolving peaks at  $25^\circ\text{C}$  were significantly less than those present at the mixture without the additive. Additionally to DMC, EMC, VC, EC, BHT, 1,4-dioxane and phosphorus oxyfluoride, the possible species detected were the methylethylphosphono fluoridate ( $\text{C}_3\text{H}_8\text{FO}_2\text{P}$  at 7.87 min), 2-hydroxy- $\gamma$ -butyrolactone ( $\text{C}_4\text{H}_6\text{O}_3$  at 8.27 min), bis-(2-methoxyethyl) ether and dimethyl pentyl phosphate ( $\text{C}_7\text{H}_{17}\text{O}_4\text{P}$  at 11.41 min). Further long chain aldehydes and organic acid esters were also detected, without the exact structures being unambiguously proposed.

The most significant difference about the  $60^\circ\text{C}$  sample involves the identification of the peak at 11.42 min. The lower background signal enabled the identification of this peak with a higher similarity value, assigning it to diisopropylfluorophosphate ( $\text{C}_6\text{H}_{14}\text{FO}_3\text{P}$ ). The identification of this particular compound is of high importance due to its classification as a neurotoxin.<sup>323</sup> Its high toxicity is a consequence of the reaction with the enzyme acetylcholinesterase (AChE). The function of AChE is to hydrolyse acetylcholine, which is an essential neurotransmitter for the peripheral nervous system (PNS). By reaction between the organophosphate and AChE a covalent bond is formed and the enzyme is stopped from functioning (Figure B8). The resulting accumulation of unhydrolysed acetylcholine leads to paralysis, suffocation and decease. The tentative identification of diisopropylfluorophosphate has already been discussed by Nowak *et al.*<sup>324</sup>. However, when such critical compounds are discussed their identification has to be unambiguous. That cannot be accomplished based only on the library search results, providing indications about the nature of the compounds present in a sample, but not clear evidence. Critical evaluation of the library results and background knowledge in the field of application are essential and can

help us provide some estimations for the identified species with a lower uncertainty. Retention indices may also help sort out some misassignments. But the use of corresponding standards of the detected compounds, measured under the same chromatographic conditions as the samples, is irreplaceable.

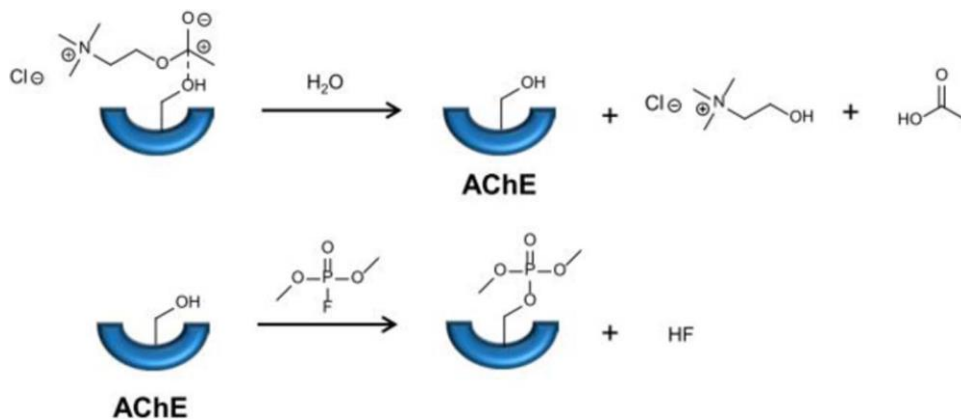


**Figure B8. Catalytic decomposition of acetylcholine (AChE) by hydrolysis (top). Blocking of AChE by reaction with an organophosphate (bottom). The P-F bond of the organophosphate is responsible for this reaction.<sup>324</sup>**

Last, for the 150°C, the species detected included further the 2-methoxyethanol, methoxymethylacetate (C<sub>5</sub>H<sub>10</sub>O<sub>3</sub> at 4.93 min) and bis-(2-methoxyethyl) carbonate (C<sub>7</sub>H<sub>14</sub>O<sub>5</sub> at 6.32 min). Interestingly, the peak appearing at 17.88 min also at the 150°C chromatogram of the LP30 mixture, was now identified as methylphosphonic acid fluoroanhydride 2-ethoxyethylester (C<sub>5</sub>H<sub>12</sub>FO<sub>3</sub>P), the presence of which is possible in a reactive mixture of alkoxides with fluorophosphoric species. However, its retention time implies a misassignment. Since this compound is apparently a homologue of the diisopropylfluorophosphate, the importance of additional identification procedures is again underlined.

#### ***B.3.2.4. Cycled LIB electrolyte sample***

Together with the LP30 mixture with the additive, the cycled electrolyte sample was the most interesting sample to be investigated, comprising all the investigated analytes. For the sample stored at RT, the most abundant peak detected was that of EMC, followed by DMC, DEC, 1,4-dioxane co-eluting with EC and that of biphenyl. Smaller concentrations of phosphorus oxyfluoride and methylphosphono fluoridic acid, as well as bis-(2-methoxyethyl) ether, 2,5,8,11-tetraoxadodecane (C<sub>8</sub>H<sub>18</sub>O<sub>4</sub> at 9.22 min) and carbonic acid ethylpropylester (C<sub>6</sub>H<sub>12</sub>O<sub>3</sub> at 5.53 min) were detected. Additional traces of polyoxygenated species, like 2,2'-oxybis-1-propanol (C<sub>6</sub>H<sub>14</sub>O<sub>3</sub> at 3.53 min), 1,1'-(propylenedioxy)di-2-propanol (C<sub>9</sub>H<sub>20</sub>O<sub>4</sub> at 9.47 min), diethyloxy diformate (C<sub>6</sub>H<sub>10</sub>O<sub>5</sub> at 10.58 min) and dimethyldiglycol carbonate (C<sub>8</sub>H<sub>14</sub>O<sub>7</sub> at 9.86 min) were tentatively identified. Again the picture didn't change much when the storage temperature of 60°C was applied. With the dominant sample constituents being the same as at 25°C, the identification of PC (with 95% probability) and the decrease in the number of oxygenated species present, were the only remarkable



observations. At 150°C, even less peaks were identified, with the basic components of the sample being observed at lower concentration levels. This indicated that either the sample had escaped from the sample vessel at these temperatures as the cap was not sealing well anymore, or that the electrolyte has choked under these conditions, or at least polymerized, and thus there was again less soluble material available. At this temperature, instead of the EC - 1,4-dioxane peak, the PC peak was more intensive, and the only traces detected were those attributed to bis-(2-methoxyethyl) ether, dimethyldiglycol carbonate and diethyloxy diformate.

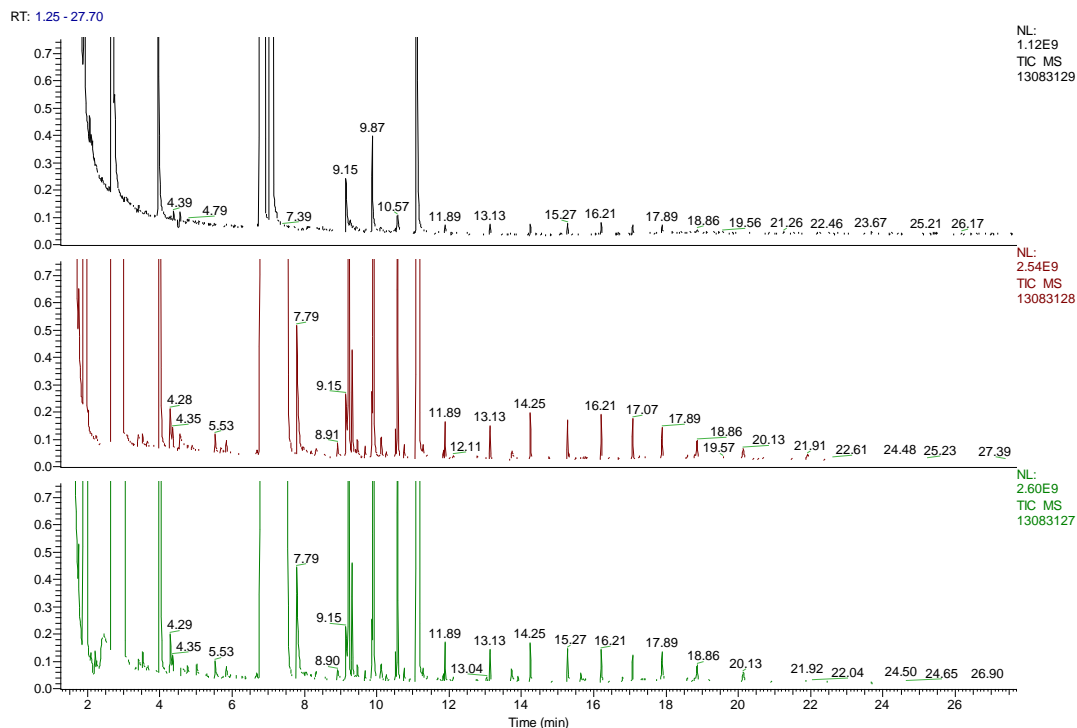


**Figure B9. Comparison of the magnified chromatograms obtained from liquid injection measurement of the cycled electrolyte sample at 25°C (green), 60°C (red) and 150°C (black).**

### ***B.3.2.5. Overall compounds identified in the sample solution***

As mentioned before, the extraction efficiency of the sample components for the different mixtures cannot be precisely estimated, while further optimization of the procedure is necessary for future investigations. However, it is clearly demonstrated that many different species are present in the sample solution compared to its headspace. In particular, these analyses are targeting the less volatile species formed under elevated temperatures. To point out these differences, Table B7 contains the compounds identified only in the diluted liquid phase of the samples. From this list, not only the species present in the samples' headspace are excluded, but also the derivatives of various diols, dioxolanes, polyethylene glycols and cyclic polyoxygenated compounds, whose exact formula could not be estimated with a sufficient degree of confidence.

**Table B7. Overall identified species from the *ex situ* thermal degradation experiments of the LIBs' electrolyte solutions after liquid phase measurement.**

No	RT	Compound Name	Mol. Formula	CAS*	Cramer Class
1	1.85	3,3,4,4,-Tetrafluorohexane	C <sub>6</sub> H <sub>10</sub> F <sub>4</sub>	648-36-2	-
2	2.05	2-Methoxy-ethanol	C <sub>3</sub> H <sub>8</sub> O <sub>2</sub>	109-86-4	1
3	2.45	Phosphorus oxyfluoride	POF <sub>3</sub>	13478-20-1	-
4	2.63	1,2-Ethanediol	C <sub>2</sub> H <sub>6</sub> O <sub>2</sub>	107-21-1	1
5	2.79	2-Ethoxy-ethanol	C <sub>4</sub> H <sub>10</sub> O <sub>2</sub>	110-80-5	1
6	2.86	Dihydroxyacetone	C <sub>3</sub> H <sub>6</sub> O <sub>3</sub>	96-26-4	1
7	2.95	2-(vinylxy)-Ethanol	C <sub>4</sub> H <sub>8</sub> O <sub>2</sub>	764-48-7	-
8	3.42	Methylphosphono-fluoridic acid	CH <sub>4</sub> FO <sub>2</sub> P	1511-67-7	-
9	4.26	Diethylene carbonate (DEC)	C <sub>5</sub> H <sub>10</sub> O <sub>3</sub>	105-58-8	1
10	4.55	2-Hexanoic acid, butylester	C <sub>10</sub> H <sub>20</sub> O <sub>2</sub>	5441-16-4	
11	4.76	(S)-Isopropyl lactate	C <sub>6</sub> H <sub>12</sub> O <sub>3</sub>	63697-00-7	-
12	4.93	Methoxymethyl acetate	C <sub>5</sub> H <sub>10</sub> O <sub>3</sub>	110-49-6	1
13	5.03	2-tert-butoxyethanol	C <sub>6</sub> H <sub>14</sub> O <sub>2</sub>	7580-85-0	-
14	5.08	Ethylene glycol monoacetate	C <sub>4</sub> H <sub>8</sub> O <sub>3</sub>	542-59-6	1
15	5.53	Carbonic acid, ethyl propyl ester	C <sub>6</sub> H <sub>12</sub> O <sub>3</sub>	35363-40-7	-
16	5.86	Carbonic acid, hexyl methyl ester	C <sub>8</sub> H <sub>16</sub> O <sub>3</sub>	39511-75-6	-
17	5.95	1,2,3,4,5-Pentamethylcyclopentane	C <sub>10</sub> H <sub>20</sub>	33067-32-2	-
18	5.96	2,4-Dimethyl furan	C <sub>5</sub> H <sub>8</sub> O <sub>3</sub>	3710-43-8	-
19	6.05	2-Propanone, 1-hydroxy, acetate	C <sub>5</sub> H <sub>8</sub> O <sub>3</sub>	592-20-1	-
20	6.12	Carbonic acid, ethyl isobutyl ester	C <sub>7</sub> H <sub>14</sub> O <sub>3</sub>	35363-42-9	-
21	6.32	Bis-(2-methoxyethyl) carbonate	C <sub>7</sub> H <sub>14</sub> O <sub>5</sub>	626-84-6	-
22	6.48	2-Propanol, 1-isobutoxy	C <sub>7</sub> H <sub>16</sub> O <sub>2</sub>	23436-19-3	3
23	6.68	2,5-Dimethyl-tetrahydrofuran	C <sub>6</sub> H <sub>12</sub> O	1003-38-9	-
24	6.68	Butyric acid, 2-methyl, 2-methylbutylester	C <sub>10</sub> H <sub>20</sub> O <sub>2</sub>	2445-78-5	-
25	7.61	Diethylene glycol	C <sub>4</sub> H <sub>10</sub> O <sub>3</sub>	111-46-6	1
26	7.83	1,4-Dioxan-2-ol	C <sub>4</sub> H <sub>8</sub> O <sub>3</sub>	22347-47-3	-
27	7.87	Methylethylphosphono fluoridate	C <sub>3</sub> H <sub>8</sub> FO <sub>2</sub> P	665-03-2	-
28	8.06	1,3-Dioxolane-2-methanol	C <sub>4</sub> H <sub>8</sub> O <sub>3</sub>	5694-68-8	-
29	8.27	2-Hydroxy-gamma-butyrolactone	C <sub>4</sub> H <sub>6</sub> O <sub>3</sub>	19444-84-9	-
30	8.29	Carbonic acid, allyl heptyl ester	C <sub>11</sub> H <sub>20</sub> O <sub>3</sub>	NA	
31	8.33	Dipropyloxydiacetate	C <sub>4</sub> H <sub>18</sub> O <sub>5</sub>	85688-79-7	
32	8.41	2,2'-Bi-1,3-dioxalane	C <sub>6</sub> H <sub>10</sub> O <sub>4</sub>	6705-89-1	-
33	8.44	2,2'-oxybis-1-propanol	C <sub>6</sub> H <sub>14</sub> O <sub>3</sub>	108-61-2	-
34	8.56	Triethylene glycol monomethylether acetate	C <sub>9</sub> H <sub>18</sub> O <sub>5</sub>	3610-27-3	-
35	8.72	Hexahydro-(1,4)-dioxino (2,3-b)-(1,4)-dioxin	C <sub>6</sub> H <sub>10</sub> O <sub>4</sub>	4362-05-4	-

**Table B7 (continued). Overall identified species from the *ex situ* thermal degradation experiments of the LIBs' electrolyte solutions after liquid phase measurement.**

No	RT	Compound Name	Mol. Formula	CAS*	Cramer Class
36	8.92	2,2-Dimethoxy-ethanol	C <sub>4</sub> H <sub>10</sub> O <sub>3</sub>	30934-97-5	-
37	9.11	1,4-Dioxan-2-yl, Hydroperoxide	C <sub>4</sub> H <sub>8</sub> O <sub>4</sub>	4722-59-2	-
38	9.16	Methyl allyl diglycolcarbonate	C <sub>10</sub> H <sub>16</sub> O <sub>7</sub>	87292-24-8	-
39	9.20	2-Heptyl-1,3-Dioxolane	C <sub>10</sub> H <sub>20</sub> O <sub>2</sub>	4359-57-3	-
40	9.20	(2-(2-(carboxymethoxy)-ethoxy)ethoxy) acetic acid	C <sub>8</sub> H <sub>14</sub> O <sub>7</sub>	13887-98-4	-
41	9.22	2,5,8,11-Tetraoxadodecane	C <sub>8</sub> H <sub>18</sub> O <sub>4</sub>	112-49-2	3
42	9.34	Diethylene glycol, dipropionate	C <sub>10</sub> H <sub>18</sub> O <sub>5</sub>	6942-59-2	-
43	9.37	Bis-(2-methoxyethyl) ether	C <sub>6</sub> H <sub>14</sub> O <sub>3</sub>	111-96-6	3
44	9.41	2-Heptyl-1,3-dioxalane	C <sub>10</sub> H <sub>20</sub> O <sub>2</sub>	4359-57-3	-
45	9.47	1,1'-(propylenedioxy)di-2-propanol	C <sub>9</sub> H <sub>20</sub> O <sub>4</sub>	1638-16-0	-
46	9.86	Dimethyl diglycol carbonate	C <sub>8</sub> H <sub>14</sub> O <sub>7</sub>	87292-23-7	-
47	10.04	Triethylene glycol	C <sub>6</sub> H <sub>14</sub> O <sub>4</sub>	112-27-6	1
48	10.58	Diethyloxy diformate	C <sub>6</sub> H <sub>10</sub> O <sub>5</sub>	1609-47-8	1
49	10.61	2-(2-(2-ethoxyethoxy)ethoxy)-Ethanol	C <sub>8</sub> H <sub>18</sub> O <sub>4</sub>	112-50-5	1
50	10.67	1,4,7,10,12-pentaoxacyclo-pentadecane	C <sub>10</sub> H <sub>20</sub> O <sub>5</sub>	33100-27-5	3
51	10.80	1,3,2,4-Di-O-methylene-d-arabitol	C <sub>7</sub> H <sub>12</sub> O <sub>5</sub>	55780-55-7	-
52	11.21	Triethylene glycol diacetate	C <sub>10</sub> H <sub>18</sub> O <sub>6</sub>	111-21-7	1
53	11.28	Diphenylmethane	C <sub>13</sub> H <sub>12</sub>	101-81-5	3
54	11.41	Dimethyl pentyl phosphate	C <sub>7</sub> H <sub>17</sub> O <sub>4</sub> P	55955-88-9	-
55	11.42	Diisopropylfluorophosphate	C <sub>6</sub> H <sub>14</sub> FO <sub>3</sub> P	55-91-4	3
56	11.56	1,4,7,10-Tetraoxacyclododecan-2-one	C <sub>8</sub> H <sub>14</sub> O <sub>5</sub>	77055-61-9	-
57	11.70	1-(2-(2-(1-methoxyethoxy)ethoxy)ethoxy)-Ethanol	C <sub>9</sub> H <sub>20</sub> O <sub>4</sub>	29681-21-8	-
58	11.83	2-Ethyl-biphenyl	C <sub>14</sub> H <sub>14</sub>	1812-51-7	3
59	11.84	2,2'-Dimethylbiphenyl	C <sub>14</sub> H <sub>14</sub>	605-39-0	3
60	11.98	Butoxytriethylene glycol	C <sub>10</sub> H <sub>22</sub> O <sub>4</sub>	143-22-6	1
61	12.16	2,4-di-tert-butyl-phenol	C <sub>14</sub> H <sub>22</sub> O	96-76-4	1
62	12.19	Butylated hydroxytoluene	C <sub>15</sub> H <sub>24</sub> O	128-37-0	2
63	13.07	Pentaethylene glycol	C <sub>10</sub> H <sub>22</sub> O <sub>6</sub>	4792-15-8	1
64	13.73	Ethylene oxide cyclic hexamer	C <sub>12</sub> H <sub>24</sub> O <sub>6</sub>	17455-13-9	3
65	16.88	Heptaethylene glycol	C <sub>14</sub> H <sub>30</sub> O <sub>8</sub>	5617-32-3	-
66	17.40	Hexanoic acid, 2-ethyl-, diester with tetraethylene glycol	C <sub>24</sub> H <sub>46</sub> O <sub>7</sub>	18268-70-7	1
67	17.88	Methylphosphonic acid, fluoroanhydride, 2-ethoxyethylester**	C <sub>5</sub> H <sub>12</sub> FO <sub>3</sub> P	NA	-
68	18.65	Octaethylene glycol monododecylether	C <sub>28</sub> H <sub>58</sub> O <sub>9</sub>	3055-98-9	-

\*NA: not available, \*\* Despite a library match above 90%, the retention time is not supporting the identification.

The data extracted from Toxtree are presented for the identified compounds. Even though many of these compounds were not included in the database used by the software, more than 15% of the identified species belong to Cramer Class III. This observation points out the paramount significance of safety measures when handling the samples. With one of the identified compounds, namely the diisopropylfluorophosphate, having demonstrated neurotoxicity, the necessary up-scaling experiments required for better characterization of the electrolyte degradation products must include precise planning and be executed under enhanced safety conditions, since a significantly higher total amount of compounds of high toxicological concern are expected to be formed.

The chemical formulas of additional fluorinated and phosphoric species identified from the liquid injection measurements are summarized in Figure B10. The rest of the presented figures maintain some categorization, initiated at the section dedicated to headspace measurements, presenting the identified glycols and ethanolic species, as well as esters, ketones, carboxylic species, polymeric products, and several cyclic, oxygenated and aromatic compounds. An even wider spectrum of compounds is therefore illustrated at the results of the diluted electrolyte samples, making their identification and their formation pathways a difficult task. Consequently, the use of additional analytical approaches is required for the elucidation of the chemistry of degraded LIB electrolyte solutions.

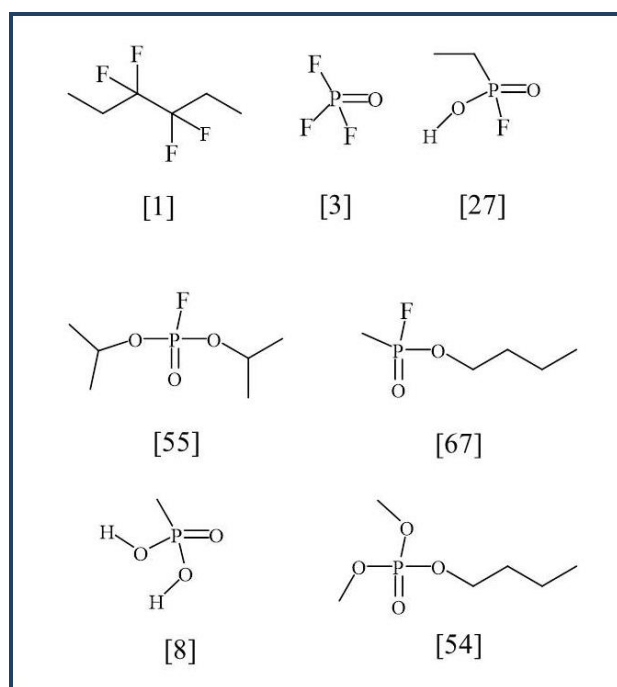


**Figure B10. Structural formulas of the fluorinated and phosphoric compounds identified from the *ex situ* thermal degradation experiments of the LIBs' electrolyte solutions after liquid phase injection. The numbers correspond to the compound names mentioned in Table B7.**

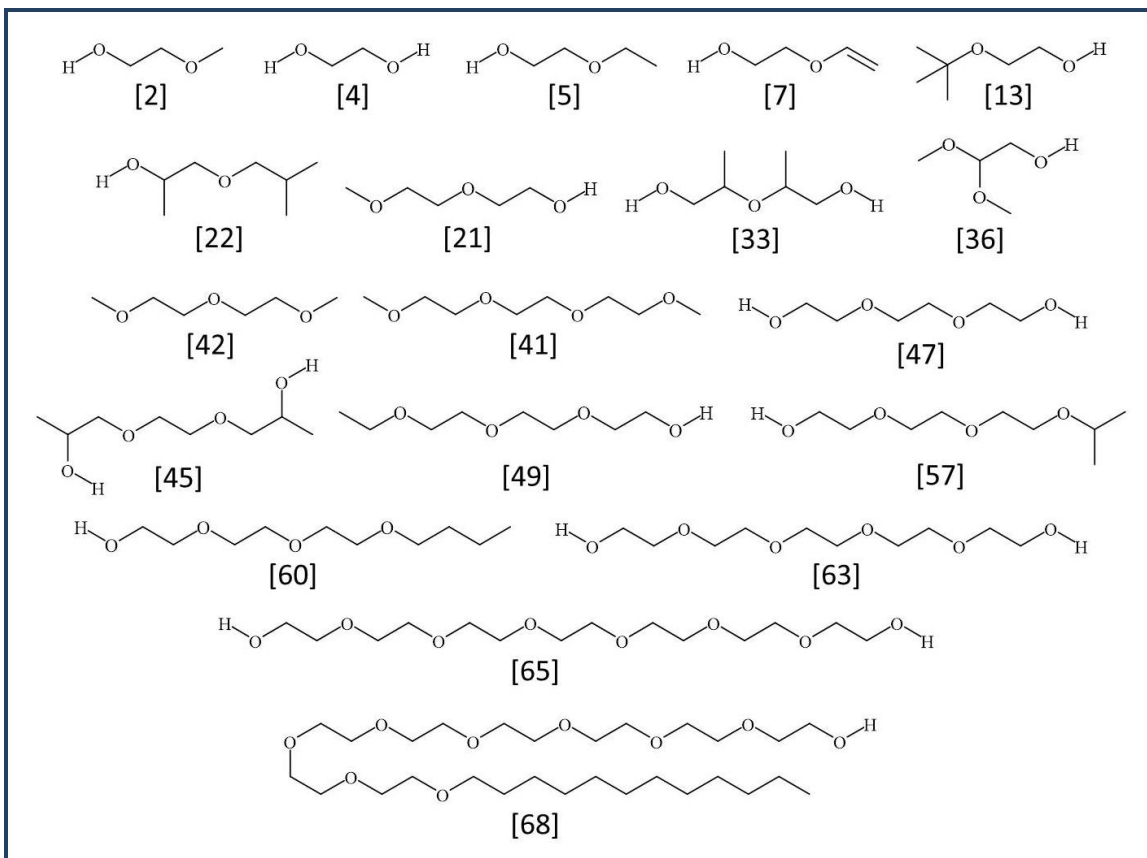


**Figure B11. Structural formulas of several glycols and further ethanolic species identified from the *ex situ* thermal degradation experiments of the LIBs' electrolyte solutions after liquid phase injection. The numbers correspond to the compound names mentioned in Table B7.**

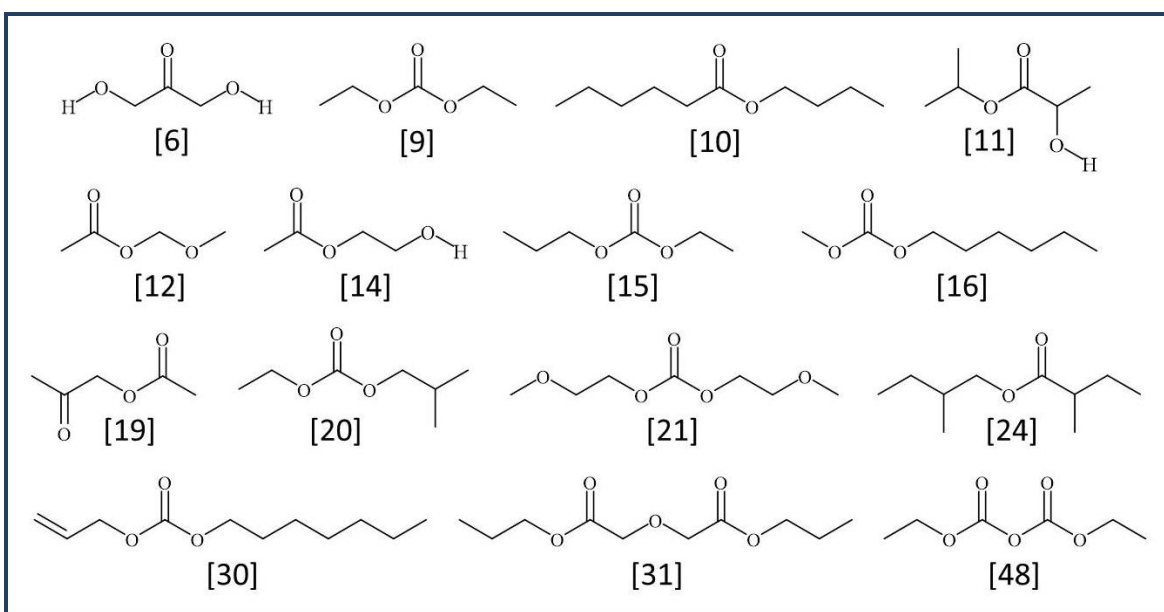


**Figure B12. Structural formulas of the ketonic and esteric species identified from the *ex situ* thermal degradation experiments of the LIBs' electrolyte solutions after liquid phase injection. The numbers correspond to the compound names mentioned in Table B7.**

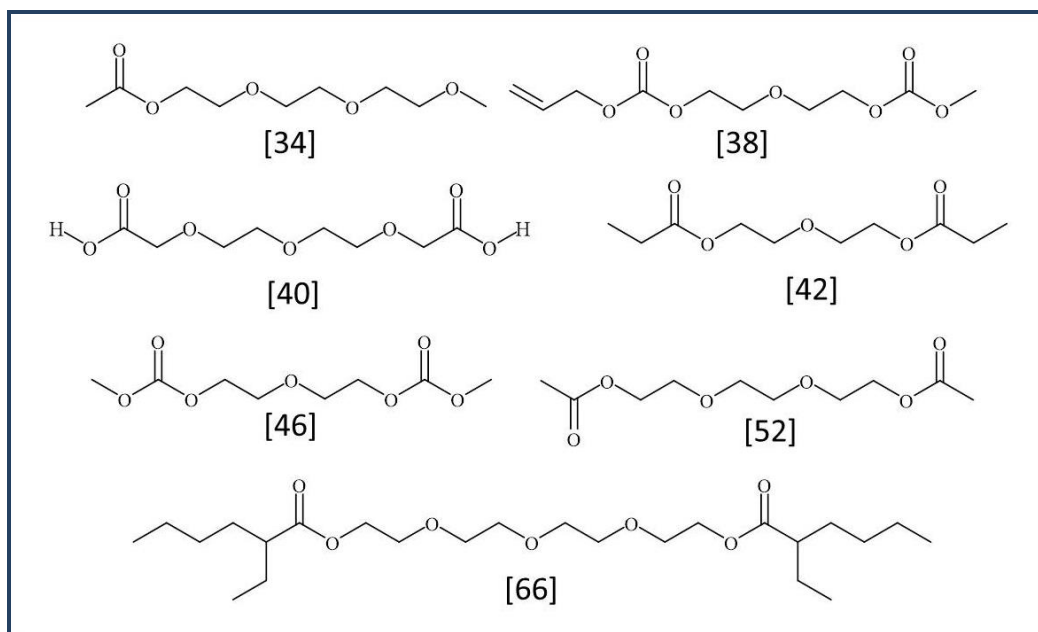


**Figure B13.** Structural formulas of the polymerized etheric, ester and carboxylic species identified from the *ex situ* thermal degradation experiments of the LIBs' electrolyte solutions after liquid phase injection. The numbers correspond to the compound names mentioned in Table B7.

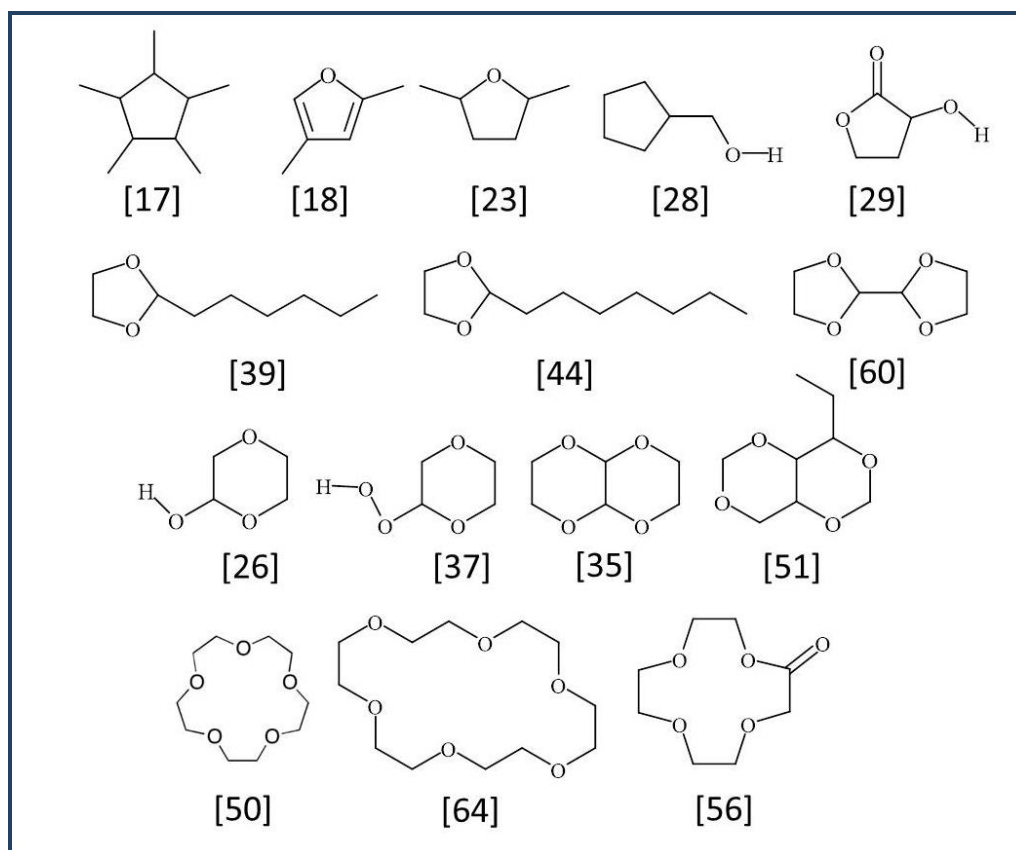


**Figure B14.** Structural formulas of the cyclic compounds identified from the *ex situ* thermal degradation experiments of the LIBs' electrolyte solutions after liquid phase injection. The numbers correspond to the compound names mentioned in Table B7.

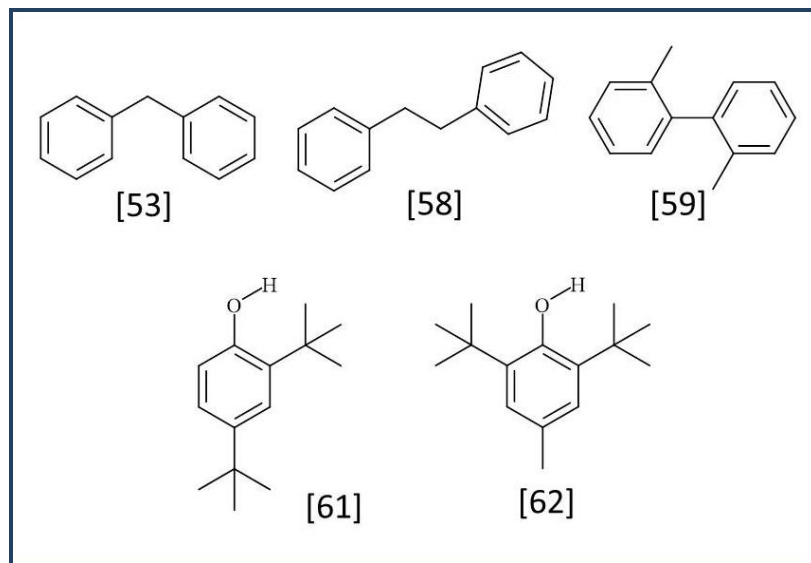


**Figure B15. Structural formulas of the aromatic compounds identified from the *ex situ* thermal degradation experiments of the LIBs' electrolyte solutions after liquid phase injection. The numbers correspond to the compound names mentioned in Table B7.**

#### ***B.4. Conclusions***

Investigating not only the headspace but also the liquid phase of the thermally aged electrolyte solutions by GC-MS analysis revealed a big number of degradation compounds being formed. These compounds belonged to various groups, with permanent gases, alcohols, aldehydes, ethers, esters, ketones and fluorinated species dominating the headspace of the thermally abused samples. Additional carbonates, glycols and different oxygenated species were also part of the volatile compounds formed inside the vials containing samples of increasing complexity. Cycled electrolyte from commercial cells was also analysed before and after the application of higher temperatures. The assumption mentioned at the theoretical chapter on the degradation mechanisms, according to which most compounds formed under cycling and thermal ageing follow the same reaction paths, or at least result in equivalent decomposition products, was now experimentally proven.

The spectrum of these products proved to be even wider when the liquid phase of the samples was analysed, identifying several glycols, alcohols, ethers, carbonates, higher esters and ketones, polymeric products, as well as cyclic, oxygenated and aromatic compounds. The measurements performed with the diluted samples in dichloromethane revealed the need for further optimization of the solvent extraction procedure, leading to a more uniform yield in less volatile decomposition products, without altering the species formed exclusively by the experimental conditions.

For safety reasons, only small sample volumes were selected after detailed planning that would exclude the possibility of extreme pressure build-up inside the sample vials. Such an incident could lead to damage

of the septum sealing the sample and consequently loss of some volatile emissions and erroneous final results. More rapid pressure build-up could even destroy the glass vials leading to damages on the equipment used or potential danger for the analysts. However, up-scaling of the experiments is considered essential for future investigations, due to the low levels of many decomposition products determined. Being close to the detection limit of the method, several compounds were not unambiguously identified, while others were not detected at samples where, according to previous experiments, their presence was expected. This observation though, could result from the high reactivity of many intermediate decomposition products as well as from the reversible nature of many of the reactions taking place.

In general, the identified compounds were in good agreement with the electrolyte decomposition products proposed in the literature, when similar experimental conditions were applied. A number of new species was also presented, belonging to both high and intermediate volatility ranges and appearing in the headspace and the liquid phase of the samples, respectively. The same groups of compounds (e.g. alcohols, ethers, carbonates and fluorinated species) were though always suggested, enabling the proposal of formation paths in some occasions.

Although most of the identified compounds were already documented at the research work of other groups, the reaction schemes proposed were almost exclusively involving the presence of lithium ions. Since our experiments were not restricted to the entire electrolyte solution but simple mixtures without the  $\text{LiPF}_6$  were also investigated, alternative formation mechanisms for the same species have to be introduced, based on thermally induced reactions.

Clarification of the exact conditions under which the detected volatile compounds are formed is important. For this reason, any contaminations in the samples should be eliminated, since they could result in different reaction products. That is particularly true for most of the reactions taking place among the electrolyte components, which are based on equilibria. Such contaminations may originate from the standards, like the water traces present at the VC solution used. Therefore, only battery grade standards should be used and the entire sample preparation procedure has to be executed carefully inside a glove-box. The glass wool present at the PTV liner during both headspace and liquid phase measurements was also considered a potential source of carry-over effects. Therefore, no glass wool was inserted into the liners used later on for the GC-MS and GC-BID experiments performed, using a different column that would enable an enhanced separation of the volatile compounds.

The demonstrated complexity of the aged samples is remarkable, even though many peaks appearing at the chromatograms of the electrolyte solutions remained unassigned. Structural elucidation of all the detected compounds is necessary for understanding the interdependent processes taking place inside the electrolyte solution and consequently inside the LIB. That would be the key step for the development of safer cells, comprised of non-hazardous components. A general screening was performed using the Toxtree software, revealing the high toxicological concern assigned to some solvents (e.g. EC and PC),



additives (e.g. biphenyl) and frequently detected decomposition products (e.g. 1,4-dioxane and 1,3-dioxolane). The suspected occurrence of fluorinated organic compounds has also led to concern about the safety of LIBs used under stress conditions, with the aforementioned investigations providing evidence for the existence of compounds with demonstrated toxicity, such as diisopropylfluorophosphate, a neurotoxin identified at the diluted LP30 sample stored at 60°C. With more than 15% of the identified compounds belonging to the Cramer Class III, containing substances that permit no strong initial impression of safety and may even suggest a significant toxicity, safety precautions are essential when the electrolyte solution is investigated, while even more questions are arising concerning the overall safety associated with the use of LIBs.

## ***C. Ex Situ experiments of selected electrolytes after prolonged storage at different temperatures using GC-BID and GC-MS***

### ***C.1. Introduction***

The performance of the BID in the detection of volatile decomposition products of LIB electrolyte solutions was tested. For the identification of the detected peaks, GC-MS analysis of selected samples was performed. For both methods the same GC column was used, enabling the identification of the detected species based on their retention times. The selection of the samples measured also by GC-MS was made according to the GC-BID results. Knowing which samples produced more complex chromatograms, these were mainly used for reproduction of the experiment and consequently analysis with both methods. Some additional GC-MS measurements were performed to control the purity of the standards. The obtained results were also used for a comparison of both detectors in terms of sensitivity, based on the absolute number of peaks observed and the corresponding peak areas of the detected compounds.

### ***C.2. Experimental Part***

#### ***C.2.1. Instrumentation and operating conditions***

The GC-BID measurements were performed using the Shimadzu Tracera GC-2010 Plus coupled to the BID-2010 Plus. All samples were analyzed using a 25 m x 0.25 mm x 8  $\mu$ m PoraPLOT U porous layer open tubular (PLOT) column by Agilent. Helium 5.0 was used as the carrier and discharge gas, which was additionally purified by a He purifier (VICI). All experiments were performed without glass wool inside the splitless deactivated fused silica liner used. The GC-BID analytical conditions are summarized in Table C1.

**Table C1. GC-BID parameters.**

GC	
InjectionTemperature	200°C
Column Flow (constant)	2.45 mL/min
Purge Flow	3 mL/min
Split Ratio	10:1
Oven Program	40°C (3 min) → 10°C/min → 190°C (20 min)
BID	
Sampling Rate	40 msec
Temperature	300°C
Discharge Gas Flow	50 ml/min
Ventil Temperature	50°C

For the GC/MS measurements, the analysis was carried out using a Shimadzu GCMS-QP2010 Plus system. The same analytical column and gas chromatographic conditions were used, so that the variations in the results will be based on differences in the detectors' performance. The mass spectrometer was equipped with an electron impact ion source and a quadrupol mass analyser. The GCMS Solution software was used for the data evaluation, with the NIST Mass Spectral Library (version 11). Table C2 summarizes the parameters of the GC/MS method.

**Table C2. GC-MS parameters.**

GC	
InjectionTemperature	200°C
Column Flow (constant)	2.45 mL/min
Purge Flow	3 mL/min
Split Ratio	10:1
Oven Program	40°C (3 min) → 10°C/min → 190°C (20 min)
MS	
Interface Temperature	200°C
Ion Source Temperature	200°C
Scanning Range	10-300 m/z

In order to avoid losses due to leakage at the injector, the septum was changed every 20 injections. The thicker needle of the gas-tight syringe used for the manual injections proved to deteriorate the septum much faster than the thinner needles of the autosampler syringes.

### C.2.2. Chemicals and Reagents

The same standards used at the initial ex-situ experiments were also used in the present section. For the thermal degradation studies we used: DMC ( $\geq 99\%$ ,  $\text{H}_2\text{O} \leq 20$  ppm, methanol  $\leq 30$  ppm), EC ( $\geq 99\%$ ,  $\text{H}_2\text{O} \leq 20$  ppm, ethylene glycol  $\leq 30$  ppm) and LP30 (DMC/EC 1:1 by weight, 1M  $\text{LiPF}_6$ ,  $\text{H}_2\text{O} \leq 20$  ppm, HF  $\leq 50$  ppm) purchased from the SelectiLyte product line of Merck (Darmstadt, Germany); VC (99.5%,  $\text{H}_2\text{O} < 100$  ppm, acid  $< 200$  ppm) also purchased from Merck and  $\text{LiPF}_6$  salt (battery grade,  $\geq 99.99\%$  trace metal basis) from Sigma-Aldrich (St.Louis, MO, USA). Handling of materials was conducted inside the glove box.

### C.2.3. Sample Preparation

Samples comprised of individual solvents (EC or DMC) and their mixtures (EC and DMC), with or without the addition of  $\text{LiPF}_6$  salt and/or VC additive and the LP30 solution were investigated. The samples were prepared inside the glove box and analyzed after storage at room temperature (RT),  $80^\circ\text{C}$  and  $150^\circ\text{C}$  for 3 hours (Table C3). The total volume of each sample was 100  $\mu\text{L}$ , as for the previously performed *ex situ* thermal degradation studies. Whenever present in the solution, the additive had a volume of 5  $\mu\text{L}$  (5% v/v), while 15.2 mg (1M) of the  $\text{LiPF}_6$  salt were added. Also for these experiments 27 ml headspace vials were used. An extended discussion on the selection of the analyte portions has been already presented in Section B.2.3. The headspace volume manually injected in the GC was always 500  $\mu\text{L}$ , with all the samples being cooled down to room temperature prior to their analysis. Every sample composition was prepared and analyzed twice.

**Table C3. The different sample types investigated during the preliminary *ex situ* experiments.**

Sample Type	Composition
1	EC
2	DMC
3	VC
4	LP30
5	EC/DMC (1:1 vol. %)
6	EC + VC (5% wt)
7	DMC + VC (5% wt)
8	LP30 + VC (5% wt)
9	EC/DMC + VC (1:1 vol. %, 5% wt)
10	DMC + $\text{LiPF}_6$ (1M)
11	$\text{LiPF}_6$ + VC
12	EC/DMC + $\text{LiPF}_6$ (1:1 vol. %, 1M)
13	EC + $\text{LiPF}_6$ + VC (1M, 5% wt)
14	DMC + $\text{LiPF}_6$ + VC (1M, 5% wt)
15	EC/DMC + $\text{LiPF}_6$ + VC (1:1 vol. %, 1M, 5% wt)
16	Cycled LIB electrolyte solution

### ***C.3. Results and discussion***

#### ***C.3.1. EC***

When only EC was measured at room temperature and after heating for 3 h at 80 and 150°C, several volatile compounds were identified. These compounds were the same for all temperatures, with the only notable differences being the additional occurrence of methanol at 150°C and the significant increase in the amount of CO<sub>2</sub> produced at the same temperature. The rest of the identified compounds were: pentane, ethyl ether, acetone, tetrahydrofuran, DMC and EMC, mentioned according to their elution order. Measurement of the sample at 150°C with GC-MS showed the same compounds present in the sample.

Although all samples were prepared inside the glove box, the presence of water and air traces cannot be excluded, leading to reactions and consequently to the formation of species that are not exclusively formed due to thermal aging. For water, a well-defined peak at 9.85 min confirms its presence. It should also be mentioned that the standards used were not freshly opened, unless stated so. Therefore any reactions taking place due to these contaminations but at extremely slow rate had sufficient time to result in products with amounts that can be well determined with our detection method. Thus, more attention will be paid in significant concentration changes and further species identified at higher temperatures, considering partially the results from the experiments performed at room temperature as blanks for the samples used.

#### ***C.3.2. DMC***

When these experiments were performed, two DMC samples were available for investigation, from which one was from a bottle opened on the day of the experiment. The analysis of both samples disclosed some information on the degradation of the solvent with the time in comparison to temperature assisted decomposition. When the older DMC sample was analysed, the same compounds were present at all investigated temperatures. Only the amounts of CO<sub>2</sub> and DMC were increasing for the higher temperatures applied. The higher amounts of CO<sub>2</sub> clearly indicated decomposition of the electrolyte. For DMC, the increased vapour pressure at increased temperatures simply shifted the gas/liquid phase equilibrium to the gas phase. However, when the new sample was analysed, the peak for methanol was present only at higher temperatures. We could therefore conclude that the same reactions taking place under prolonged storage of the electrolyte at room temperature, resulting in methanol formation, are occurring when elevated temperatures are applied, however at a higher rate. The formation of methanol at 150°C was also demonstrated at the previously discussed thermal degradation experiments, where the samples were stored for two weeks at elevated temperatures.

The rest of the peaks present in the chromatograms were assigned to pentane, ethyl ether, acetone and tetrahydrofuran. GC-MS analysis of a DMC sample confirmed the presence of all the aforementioned compounds, proving that they were not contaminations coming from the system but rather from the sample itself. Traces of methyl formate were also identified when GC-MS analysis of the sample at 150°C was performed.

### ***C.3.3. VC***

When the VC standard at room temperature was measured, additionally to the VC peak, CO<sub>2</sub>, pentane, ethyl ether, acetone, tetrahydrofuran and DMC were detected. Traces of 2-methyl-butane, hexane, and EMC were also identified. Temperature increase from room temperature to 80°C resulted in the formation of propene, fluoroethane, 1,4-dioxane and DEC. At 150°C no further species were identified, however the concentration of CO<sub>2</sub>, DMC, VC and EMC increased. Apart from CO<sub>2</sub> and possibly EMC, the increase in the amount of DMC and VC is better explained by the increased vapour pressure inside the sample vial. Interestingly, the peak of water at 80°C was notably smaller than for the other two temperatures, indicating that it may also result from the sealing efficiency of the vials and not only from the humidity present at the standards or inside the glovebox. When GC-MS measurement of the sample at 150°C was performed, the same peaks were detected; with the only additional occurrence of acetaldehyde, however at trace amounts.

### ***C.3.4. EC + VC (5% wt)***

For the EC mixture with the additive, no further compounds were identified, apart from the species present at the EC chromatograms (pentane, ethyl ether, acetone, hexane, tetrahydrofuran, DMC and EMC) and the additional peaks of VC and DMC. The same electrolyte-additive ratio as expected inside the cells was used for these experiments. Therefore, any further species identified before at the VC sample, with the reduction in the investigated portion of VC, are now below the limit of detection of the applied method.

A peak assigned to acetaldehyde was present for the highest temperature measurement, which was also present at the corresponding GC-MS results for VC at 150°C. In contrast to the MeOH peak present at the EC chromatogram at 150°C, such a peak was not present for the sample mixture at the same temperature. This could indicate increased thermal stability of the electrolyte in the presence of the additive.

### ***C.3.5. EC + LiPF<sub>6</sub> (1M)***

When EC was mixed with the lithium salt and exposed to higher temperatures, the obtained results were essentially identical to those presented for the single EC sample. The only difference was in the presence of ethanol traces at the sample kept at room temperature. Not being detected at higher temperatures, though, indicates that ethanol might be an intermediate product, rather than an artefact.

### ***C.3.6. EC + LiPF<sub>6</sub> + VC (1M, 5% wt)***

Analysis of the mixture of EC with the lithium salt and the additive revealed the presence of dimethyl phosphonic fluoride (C<sub>2</sub>H<sub>6</sub>FOP), when the sample was heated at 150°C. All other sample components were the same as described for the previous sample types, with acetaldehyde being detected only at the highest investigated storage temperature.

### ***C.3.7. DMC + VC (5% wt)***

The same observations made for the EC+VC mixture were repeated for the DMC+VC one. Again, acetaldehyde was identified at 150°C storage temperature, like for the VC sample stored under the same conditions.

### ***C.3.8. DMC + LiPF<sub>6</sub> (1M)***

When the mixture of the electrolyte with the salt was analysed, the peak for dimethyl phosphonic fluoride appeared already at 80°C. When the storage temperature of the sample increased further, methyl formate was also identified. The rest of the detected compounds were already discussed for the single electrolyte mixture, with their relative peak areas following the same trends.

### ***C.3.9. DMC + LiPF<sub>6</sub> + VC (1M, 5% wt)***

For the mixture of DMC with both the lithium salt and the additive, dimethyl phosphonic fluoride was only identified in the sample stored at 150°C, similar to the corresponding mixture with EC. The requirement for higher temperature for the formation of this decomposition product could again indicate thermal stability of the electrolyte in the presence of the additive. Methoxy ethane was also identified at the highest temperature, together with methyl formate. Apart from these additional peaks, no further change in the detected species was observed.

### ***C.3.10. EC/DMC (1:1 vol. %)***

When both electrolytes were used for the thermal degradation experiments, already at room temperature traces of ethylene and acetaldehyde were identified. By increasing the temperature, the amount of CO<sub>2</sub> experienced a continuous increase, reaching its highest value for the sample stored at 150°C. At this temperature, methanol, methyl formate and ethanol were additionally identified.

### ***C.3.11. EC/DMC+VC (1:1 vol. %, 5% wt)***

The addition of VC in the previous mixture reduced the number of identified compounds at the lower temperatures, proving improved thermal stability in the presence of the additive. Acetaldehyde was only identified in the sample after storage at 150°C, while no peak for ethylene was detected. Fluoroethane, identified at the VC sample for the experiment performed at 80°C, was again detected, but only when 150°C storage temperature was used.

### ***C.3.12. EC/DMC+LiPF<sub>6</sub> (1:1 vol. %, 1M)***

Contrary to our expectations, the analysis of the both electrolytes in the presence of the lithium salt did not result in the identification of the compounds detected before for less complex samples. The same peaks were identified at all temperatures, with only a small increase in the peak area of CO<sub>2</sub> being observed. To control the validity of these results, we performed a comparison among the CO<sub>2</sub> area for this sample composition and that of the other two EC/DMC-containing samples at 150°C. The significantly lower value of CO<sub>2</sub> clearly indicated an error during the sample preparation or injection procedure. Therefore, only the results obtained from the equivalent LP30 mixture should be taken into consideration for evolved electrolyte degradation compounds from this experimental set. Detailed evaluation, based on the identity of the peaks, took place after all GC-BID measurements were executed, using the GC-MS data obtained from these subsequent measurements. Therefore, repetition of a particular sample was not a straight forward procedure, since the system configuration was already changed, with the analytical column being transferred to another instrument. Such a repetition was, though, not necessary, since the only samples for which the results were ambiguous were the ones that were already repeated with a different standard solution containing the same electrolyte components, namely the LP30 standard.



### ***C.3.13. EC/DMC+VC+LiPF<sub>6</sub> (1:1 vol. %, 1M, 5% wt)***

This mixture was also expected to contain the electrolyte decomposition products identified previously. However, only propene was detected additionally to the volatile components of the solution. The same observation concerning the CO<sub>2</sub> peak was repeated here, leading to the conclusion that problems with either the caps of the GC vials or the syringe used for manual injection on that day have been responsible for these results. Errors during the sample preparation can be excluded, since all the volatile sample components were identified.

### ***C.3.14. LP30***

When LP30 was analysed, the results were in good correlation with the observations made for the single component samples and their mixtures, with several additional compounds being detected. Table C4 summarizes these results, showing the species that evolved at different temperatures.

As illustrated at the table, the increase in the sample temperature triggered additional reactions, leading to the formation of methyl formate, methyl acetate and possibly EMC and DEC at concentrations above the limit of detection for our GC-BID method. The temperature increase also increased the vapour pressure of EC and thus its concentration in the gas phase. One more peak was observed in the GC-BID data, which could not be identified due to its absence in the GC-MS data. These GC-MS data were obtained for only for 150°C, showing the existence of one additional peak at 14.01 min, which was assigned to 2-methyl butane. However, the peaks of methanol and ethanol were absent in both GC-MS and GC-BID results, indicating again that the identified alcohols might not always be the final products of the reaction paths followed. This assumption was also supported by the corresponding *ex situ* results, involving the two-week storage of the electrolyte mixture at elevated temperatures.

**Table C4. GC-BID results for LP30 stored for 3h at different temperatures.**

Peak #	RT (min)	Compound Name	LP30		
			25°C	80°C	150°C
1	2.23	Carbon dioxide	X	X	X
2	2.93	Silicon tetrafluoride	X	X	X
3	8.85	Methyl chloride	X	X	X
4	9.58	Dimethylether	X	X	X
5	9.96	Water	X	X	X
6	11.58	Acetaldehyde	X	X	X
7	11.81	Dimethylphosphinic fluoride		X	X
8	12.69	Methyl formate			X
9	14.59	Pentane	X	X	X
10	15.02	Ethyl Ether	X	X	X
11	15.18	Methylene chloride	X	X	X
12	15.36	Aceton	X	X	X
13	15.54	Methyl acetate			X
14	17.22	Hexane		X	X
15	17.45	Tetrahydrofuran	X	X	X
16	17.89	DMC	X	X	X
17	20.68	EMC		X	X
18	24.65	DEC		X	X
19	34.78	EC		X	X

***C.3.15. LP30+VC (5% wt)***

When the additive was present at the LP30 sample, all previously identified compounds were again detected. Methyl formate, EMC and DEC were now present at all temperatures, while methyl acetate was present already at 80°C. Further species identified were propene (at 7.37 min) and 3-ethoxy-1-propene (at 17.58 min). Thus, no sign of thermal stability resulting from the addition of VC was this time observed. On the contrary, more species were identified at this sample mixture.

GC-MS results for an equivalent sample stored at 150°C demonstrated the additional presence of ethanol, 2-methyl-1-butane, 1,4-dioxane and possibly 2,2,3-trimethylbutane (at 17.17 min) traces. Since only the sample stored at 150°C was analysed by GC-MS, tracking of the relevant temperatures for the appearance of the additional species is not possible for that sample. Therefore, also the 80°C sample was analysed for the next and final sample mixture investigated.

### ***C.3.16. Cycled LIB electrolyte solution***

For the particular sample composition the experiments at all three investigated temperatures were repeated and the samples were measured with both methods. The obtained results are presented in Table C5, where the retention times according to the GC-BID results are used. The corresponding values are relatively smaller for the MS, since the vacuum applied at the end of the analytical column facilitates a faster elution of the analytes. Only in the case where a compound was exclusively detected by MS, the retention time from the GC-MS results was used (e.g. for EC). Since the identification of the compounds was only possible based on the MS data, peaks that are present only at the GC-BID chromatograms could not be assigned unambiguously to any compound.

As expected, at room temperature the total number of detected compounds was smaller. This observation could imply which ones have already been caused by discharge and handling of the cell and which are thermally induced. However, some of the highly volatile electrolyte emissions must have been lost during opening of the cells. Therefore, the origin of each compound can only be speculated.

When the results from the GC-BID and GC-MS measurements were compared, differences in the total number of identified compounds were observed only for the higher temperatures. At 80°C, four peaks were exclusively present in the GC-BID chromatogram, while two more peaks were only detected at the corresponding GC-MS data. From the peaks present only in the BID results, the carbon monoxide peak was the single peak identified, with the other three remaining undetermined. On the other hand, the two peaks present at the GC-MS results were easily assigned to 2-methyl-2-pentanal and EC, after library search.

When the sample was heated at a higher temperature, 8 more peaks were present in the GC-BID chromatogram. From these peaks, the one with the highest retention time, was assigned to 2-methyl-2-pentanal, since this compound was already identified at the experiment performed at 80°C. By increasing the storage temperature, the concentration of this compound was also increased to a value beyond the limit of detection for the BID, which proved to be less sensitive for the particular electrolyte degradation product.

Evaluating in total the obtained results with both methods, it is clear that BID provided higher sensitivity in the analysis of the same sample using the same column configuration. However, looking into the MS Peak Area / BID Peak Area ratio of the detected compounds, the advantageous properties of BID for more volatile compounds and its limitations for compounds with higher retention times, was clearly illustrated. Table C6 presents some characteristic examples of these sensitivity differences.

**Table C5. Identified compounds with the MS and the BID detector for the cycled LIB electrolyte solution stored for 3 hours at 25, 80 and 150°C.**

Peak #	RT (min)	Compound Name	Mix @ 25°C		Mix @ 80°C		Mix @ 150°C	
			MS	BID	MS	BID	MS	BID
1	2.02	Carbon monoxide				X		X
2	2.22	Carbon dioxide	X	X	X	X	X	X
3	2.61	Ethylene	X	X	X	X	X	X
4	7.31	Unknown						X
5	7.37	Propene			X	X	X	X
6	7.51	Fluoroethane	X	X	X	X	X	X
7	8.91	Unknown				X		X
8	9.61	Dimethylether	X	X	X	X	X	X
9	10.05	Water	X	X	X	X	X	X
10	11.66	Acetaldehyde	X	X	X	X	X	X
11	11.91	Dimethylphosphinic fluoride			X	X	X	X
12	12.76	Methoxy ethane	X	X	X	X	X	X
13	12.89	Methyl formate	X	X	X	X	X	X
14	13.80	Trimethylsilylfluoride					X	X
15	14.32	Ethanol			X	X	X	X
16	14.70	Pentane	X	X	X	X	X	X
17	15.03	Propanal	X	X	X	X	X	X
18	15.13	Ethyl Ether	X	X	X	X	X	X
19	15.29	DMC	X	X	X	X	X	X
20	15.47	Aceton					X	X
20	15.71	3-Methoxy-1-propene	X	X	X	X	X	X
21	15.80	Formic acid ethyl ester	X	X	X	X	X	X
22	15.83	Unknown						X
23	17.38	Unknown						X
24	17.60	Tetrahydrofuran	X	X	X	X	X	X
25	17.75	3-Ethoxy-1-propene			X	X	X	X
26	17.84	Unknown						X
27	18.02	Ethyl acetate	X	X	X	X	X	X
28	18.20	Unknown				X		X
29	20.09	Unknown						X
30	20.62	1,4-Dioxane			X	X	X	X
31	20.78	EMC	X	X	X	X	X	X
32	17.84	Unknown						X
33	22.57	2-Methyl-2-Butanal-E			X	X	X	X
34	24.87	DEC	X	X	X	X	X	X
35	28.17	2-Methyl-2-pentanal			X		X	X
36	34.78	EC			X		X	

**Table C6. Areas of characteristic compounds identified at the same sample, for the same GC column configuration, using the MS and BID detectors.**

RT (min)	Compound Name	Mix @ 150°C		
		Area <sub>MS</sub>	Area <sub>BID</sub>	Area <sub>MS</sub> /Area <sub>BID</sub>
2.02	Carbon monoxide	-	111897	0
7.37	Propene	28931	54081	0.5
11.66	Acetaldehyde	424536	463840	0.9
14.32	Ethanol	684205	710628	1.0
18.02	Ethyl acetate	547865	576687	1.0
20.78	EMC	11397791	5698897	2.0
24.87	DEC	3965917	1354408	2.9
34.78	EC	176608	-	-

As also mentioned in the introductory section, the dependence of the BID's performance on the molecular weight of the analyte was demonstrated. Enhanced sensitivity, corresponding to relatively bigger peak areas, was observed only for the first 18 min of the run. After this time, the identified compounds were producing higher peak areas when the MS was used. However, the fact that a bigger total number of peaks was detected in the GC-BID chromatogram can indicate higher sensitivity of the detector towards specific compounds/compound groups or volatility ranges. The fact, though, that the MS data were required for a more accurate identification than by using e.g. retention indices, demonstrated the complimentary nature of both detectors.

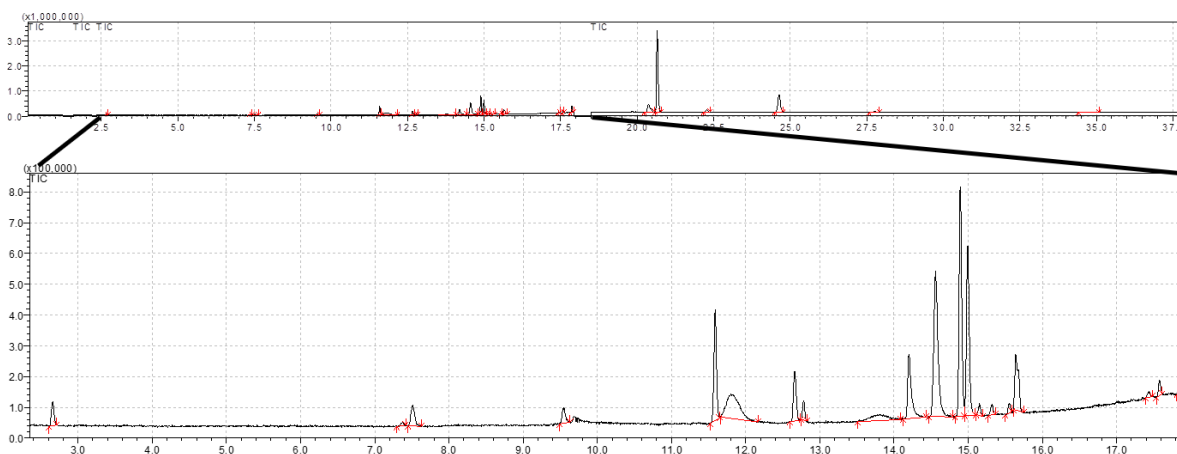


**Figure C1. The entire GC-MS chromatogram for the electrolyte solvent mixture at 150°C and a magnification of the most abundant part in peaks (2.5 min to 18 min).**

## ***C.4. Conclusions***

Targeting the analysis of volatile degradation products from LIB electrolytes, the applicability of GC-BID was investigated through a comparison of its performance with that of GC-MS. For this comparison the same chromatographic conditions were selected and the same GC column was used.

Starting from single component samples and moving towards representative electrolyte solutions the increase in the number of decomposition compounds at elevated temperatures was demonstrated. Although for the electrolyte solutions undergoing only thermal ageing, the results of both GC-MS and GC-BID were comparable, with only a small number of peaks being present at both chromatograms, when the cycled electrolyte sample was analysed, further decomposition products were detected exclusively by the BID. Unfortunately, the corresponding compounds were not identified, since only the retention indices could have been calculated, leading in any case to ambiguous results. The decreased duration of thermal ageing was also indicating that the focus of these experiments was not the identification of further degradation species in comparison to the previous experiments, where a time window of two weeks was used, but the relative performance of the two detectors.

Although the bigger number of peaks detected with the BID was a clear indication of higher sensitivity compared with the MS, this advantage of BID does not prevail throughout the entire run. In particular, when the peak areas of the detected compounds were used for the sensitivity comparison, the differences observed for both detectors were only for the first 10 minutes clearly in favour of the BID, while compounds with elution times higher than 18 minutes had significantly bigger peaks at the corresponding GC-MS chromatograms.

This observation demonstrates the complementary use of both detectors. When the concentration of permanent gases and other highly volatile species is of interest, especially when the identity of these compounds does not need to be defined by the particular measurement, the BID is the most appropriate detector to be used. It should be noticed, though, that the advantageous sensitivity of the BID for highly volatile compounds could be counteracted if the MS is also used as an only quantitative detector, moving from full scanning mode to the more sensitive single ion monitoring. However, when unknown screening of compounds belonging to a wider range of volatilities is intended, the MS can hardly be replaced by any other GC detector.

## ***D. In situ GC-MS and FTIR-GC-MS for the identification of gases emitted from in house-assembled and commercially available LIBs under different electrochemical conditions***

### ***D.1 Introduction***

The FTIR-GC-MS system developed in the frame of the SiLithium project was used for the characterization of gaseous emissions from LIBs with high time resolution. A measuring station, constructed at AIT, allowed the continuous monitoring of evolved gases via simultaneous analysis by FTIR and GC/MS. A partial least squares regression model was used to correlate the GC/MS data with the FTIR signal. While FTIR monitors fast concentration changes with high time resolution, the GC/MS allows the identification of the evolved analytes. This method was successfully applied to characterize the gas evolution from in house-assembled and commercially available cells.

### ***D.2 Materials and methods***

#### ***D.2.1 Chemicals and reagents***

As already mentioned in the *ex situ* experiments section, dimethyl carbonate ( $\geq 99\%$ ,  $\text{H}_2\text{O} \leq 20$  ppm, methanol  $\leq 30$  ppm), ethylene carbonate ( $\geq 99\%$ ,  $\text{H}_2\text{O} \leq 20$  ppm, ethylene glycol  $\leq 30$  ppm) and LP30 (DMC/EC 1:1 by weight, 1M LiPF<sub>6</sub>,  $\text{H}_2\text{O} \leq 20$  ppm, HF  $\leq 50$  ppm) were purchased from the SelectiLyte product line of Merck (Darmstadt, Germany). LiPF<sub>6</sub> and LiClO<sub>4</sub> salts (battery grade,  $\geq 99.99\%$  trace metal basis) as well as the Lithium ribbons (99.9% trace metal basis, 0.38 mm thickness) were purchased from Sigma-Aldrich (St.Louis, MO, USA). Watman glass fiber separators (diameter: 18 mm, thickness: 1mm) from stock at the AIT were used. The LVP (Li<sub>3</sub>V<sub>2</sub>(PO<sub>3</sub>)<sub>4</sub>) high voltage cathode material was synthesized at AIT in the frame of the FFG-AIMS project (Advanced and Innovative Materials for Electrochemical Energy Storage).

For in house-assembled coin cells, the test cell ECC-DEMS, purchased from the EL-CELL (Hamburg, Germany) company, was used for gas sampling. Handling of air and/or moisture sensitive materials and cell assembling was conducted in an Ar-filled glove box provided by MBRAUN (Garching, Germany) (where:  $\text{O}_2 \leq 0.1$  ppm,  $\text{H}_2\text{O} \leq 0.1$  ppm).

The tests with commercial cells were performed using Swing 4400 batteries from Boston Power (Westborough, MA, USA). The Boston Power Cell (BPC), has a nominal capacity of 4400mAh at a

nominal voltage of 3.7 V. The specified operating temperature range is -10 to 60°C for charging and -40 to 70°C for discharging. The recommended charging current is 0.7 C for up to 4.2 V. It consists of a graphitic carbon anode and the cathode active material is a mixture of LiCoO<sub>2</sub> (LCO) and LiMn<sub>2</sub>O<sub>4</sub>, with an approximate fraction of 78 wt % and 22 wt %, respectively. This composition information was determined by powder X-ray diffraction and X-ray fluorescence analysis, conducted by MSc. Raad Hamid at the Austrian Institute of Technology. LP30 was the electrolyte used, as determination by GC-MS analysis performed by MSc. Alfred Amon.

For the in house-assembled cells, electrodes were also isolated from BPC. To obtain them, the batteries were discharged to voltages below 1.5 V and then the metal casing was carefully cut and opened. The electrodes were removed from the cells and the coating was also removed from one side of the current collector. Circular electrodes of 15 mm diameter were cut, weighted and vacuum dried overnight at 120°C. Circular counter electrodes with the same diameter were also cut from the lithium ribbons inside the glove box.

## ***D.2.2 Instrumentation and operating conditions***

The entire experimental work under *in situ* conditions has been performed at the Mobility Department - EDT of the Austrian Institute of Technology, located at Giefinggasse 2, 1210 Vienna, Austria.

### ***D.2.2.1 Electrochemical equipment***

All electrochemical measurements, i.e. cyclic voltammetry and battery charging programs, were performed using a BioLogic VSP-potentiostat. The device was initially equipped with a VMP3B-20 booster channel, working as an amplifier and allowing fast charging of the cells. Although the booster was used at the initial measurements done at AIT by Alfred Amon, by the time of the experiments described here, the booster was out of order. Therefore, only slow charging of the cells was possible and the experimental conditions were appropriately adjusted.

The charging was started from open circuit voltage (OCV)<sup>ix</sup> and the cells were charged to certain upper voltages. The cut off voltage<sup>x</sup> was selected based on the materials under test. Upper voltages, equal to 4.0, 4.2, 4.6, 4.7 or even 5.2 V, were selected. These values were higher than the voltages recommended by the

---

<sup>ix</sup> Open circuit voltage (OCV): the difference of electrical potential between two terminals of a device when disconnected from any circuit.

<sup>x</sup> Cut off voltage: the discharge voltage limit which is recommended for safe use of the battery.



producer (in the case of BPC) or the normal operating voltages for LCO or LVP, in order to induce electrolyte decomposition.

The given potentials were defined versus the Li/Li<sup>+</sup> redox couple. Following the IUPAC convention, cathodic currents are defined with a negative sign and anodic currents with a positive sign.

#### ***D.2.2.2 GC/MS***

For the GC/MS measurements, the analysis was carried out using a Shimadzu GCMS-QP2010 Plus system (Duisburg, Germany). The GC was equipped with a heatable automatic 10-port switching valve, operated as a 6-port valve (Figure 1). A sample loop of 500  $\mu$ L was used. A split/splitless injector, with a splitless deactivated fused silica liner, was also used. As in all GC/MS measurements, Helium 5.0 was the carrier gas. Targeting the identification of highly volatile compounds and permanent gases, a 30 m x 0.32 mm x 10  $\mu$ m Rt-Q-BOND porous layer open tubular-column (PLOT) was selected. The entire column setup (Table 1) consisted of a guard column connected directly to the injector side, the analytical column, and a particle trap installed at the MS side, protecting the mass spectrometer from dislodged particles. The mass spectrometer was equipped with an electron impact ion source and a quadrupole mass analyzer.

The parameters of the GC/MS method used are summarized in Table 2. Some of these parameters differ from the method used previously at AIT. A comparison of the results obtained for a BPC with the latter method will be presented at the Results and Discussion section. The changes targeted a more robust method, using higher temperatures at some compartments of the system. In particular, the temperatures for the injector port, the interface and the ion source were set from 100, 130 and 150°C, respectively, to 200°C. Since the investigated analytes are thermally stable, the higher temperatures would ensure that less volatile compounds would not be accumulated at any part of the system, and that all analytes would ionize well enough, preventing any ion source-related peak broadening. The new parameters are particularly necessary when liquid samples are used for analysis. Even though such measurements were not performed during the experiments described in the following sections, this generic method was developed for subsequent use at AIT for further investigations and realistic comparisons. A deviation from this method was only applied for the second part of the measurements, for which a lower detector gain (from 1.62 to 0.95 kV) was selected for the first 1.75 min. Since a saturated air peak was observed at the beginning of the chromatogram, the detector gain value was adjusted, so that the peak area would stay within the linear range. Thus, the multiplier would also be protected, prolonging its lifetime.

The GCMS Solution software was again used for the data evaluation, while apart from the NIST Mass Spectral Library, version 11, the Wiley Registry of Mass Spectral Data, 9th edition, was also used.

**Table D1. Specifications of the gas chromatographic columns used.**

Column	Stationary Phase	Length (m)	Inner Diameter (mm)	Film thickness ( $\mu\text{m}$ )
Guard Column	medium polarity, deactivated	5	0.32	-
Rt-Q-BOND	Divinylbenzene	30	0.32	10
Particle Trap	None	2	0.32	-

**Table D2. GC/MS parameters.**

GC	
Injection Temperature	200°C
Inlet Pressure	75.3 kPa
Column Flow (constant)	2.38 mL/min
Purge Flow	1 mL/min
Linear Velocity	50 cm/s
Split Ratio	8:1
Oven Program	35°C (2.25 min) → 20°C/min → 190°C (5 min)
MS	
Interface Temperature	200°C
Ion Source Temperature	200°C
Scanning Range	10-300 m/z

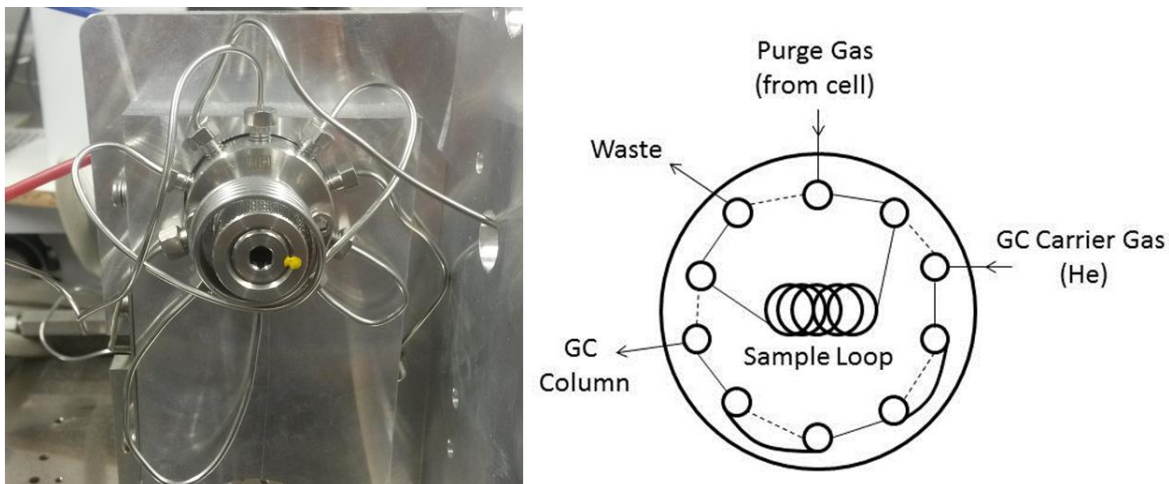


**Figure D1.** Left hand side: Picture of the 10-port sampling valve. Right hand side: Graphical scheme of the port connections. The internal switching connections between the ports are representing the sample loading position (solid lines) and the injection position (dotted lines).

### ***D.2.2.3 FTIR***

Both the spectrometer and the wave-guide system were constructed by Dr. Wolfgang Märzinger from the company i-RED (Linz, Austria). This equipment consists of an electronic control device and an integrated interferometer unit with a silicon carbide rod, commonly known as Globar, as the thermal light source. The available spectral range goes from approximately 1500 to 3600  $\text{cm}^{-1}$ . The optical system of the interferometer is constantly purged with nitrogen gas and connected to a hollow wave-guide made of a 1 m x 0.5 mm ID silver halide coated fused silica capillary. The light enters the waveguide through a  $\text{MgF}_2$ -window at the one end and reaches the Peltier cooled CCD detector after passing through the inner gas volume and the outlet window. The hollow waveguide has gas entry ports at both ends, allowing the sample or purge gas to flow through the inner volume of the waveguide. With this configuration the optical path length of the infrared beam and the sensitivity are maximized even for small gas volumes. The hollow waveguide was embedded in a thermally insulating sleeve together with a heating wire, in order to avoid the condensation of products inside the waveguide and was kept at a temperature of 55°C. For monitoring the analyte concentrations via FTIR, Dr. Märzinger has developed a multivariate model based on the GC/MS data. With a temporal resolution below 30 s, the FTIR system provided 70 averaged interferograms for each recorded spectrum, resulting in a full spectrum every 24 s. The entire FTIR-GC-MS system is presented in Figure 2.

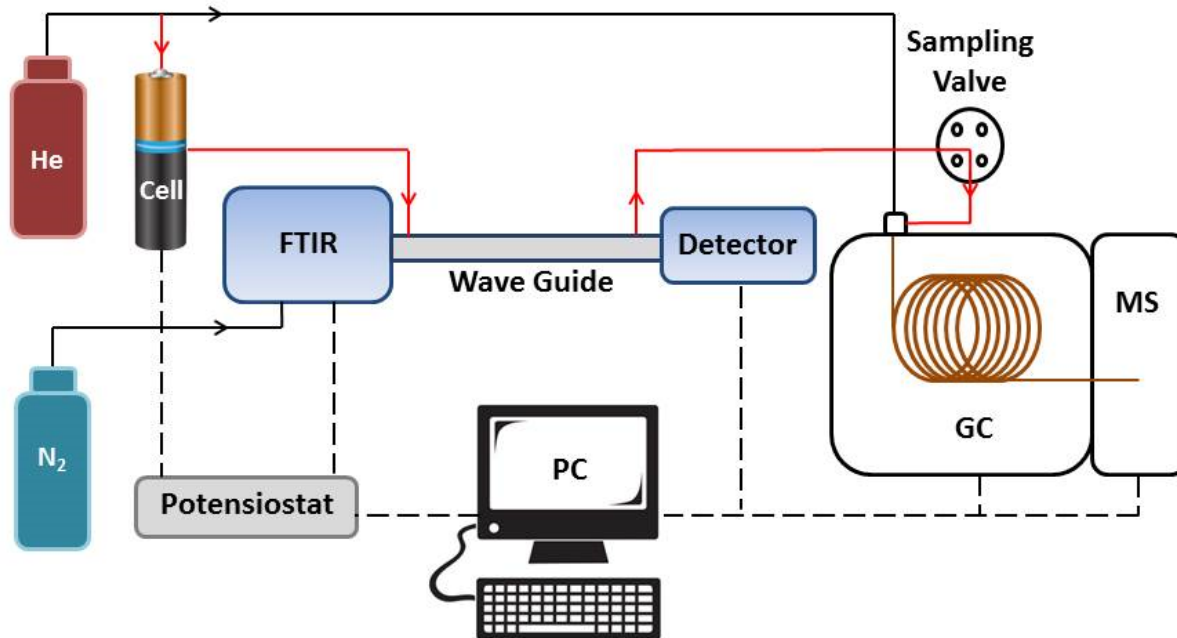
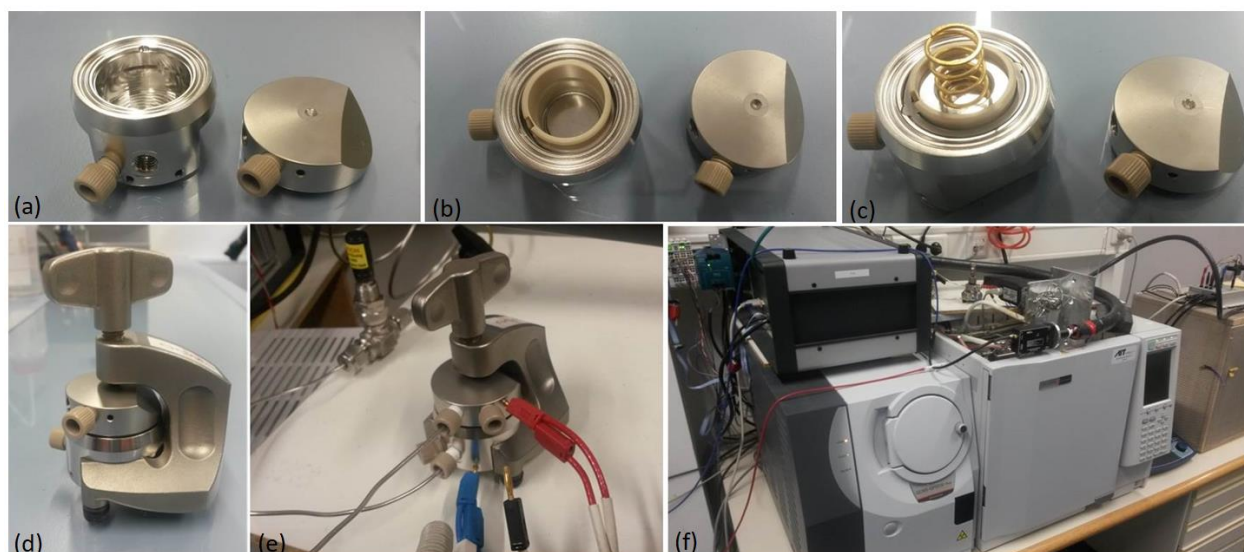


Figure D2. *In situ* FTIR-GC-MS setup. Solid lines represent the gas connections, where the red one is the path of the analytical gas. Dashed lines represent the electrical/control connections.

#### D.2.2.4 Gas sampling cells

Both in house-assembled and commercial cells were investigated. For each sample type a dedicated gas sampling setup was designed. Starting from the in house-assembled batteries, an ECC-DEMS cell was used. All cell-assembling steps described later on are performed inside an argon-filled glove box. The stainless steel body of the ECC-DEMS cell was comprised of a bottom and a top lid. Both lids were provided with gas connections used, in our case, for purging with inert gas (Figure 3.a). The gas comes in through the cell lid, while the circular channels at the base enable better gas purging (Figure 3.b). All other ports of the ECC-DEMS cell were closed to seal it against the atmosphere (Figure 3.d). The inner volume of the ECC-DEMS cell was approximately 9 ml. Figure 4 depicts the cross section of the ECC-DEMS cell, showing all the purchased parts accompanying it. Concerning the assembling procedure established for our *in situ* experiments, after the PEEK (polyetheretherketon) sleeve was inserted into the cell base and the locking ring was mounted, a spacer was positioned onto the cell's base, followed by the working electrode and the separator. A varying amount of the electrolyte solution (approx. 0.5 mL) was then dispensed onto the separator, on top of which a lithium metal disc (15 mm diameter) was placed. The plunger was then put on top of the lithium metal counter electrode and the cell was closed with the upper lid, above which a gold coated spring ensures electrical contact (Figure 3.c). A PE (polyethylene) sealing gasket was used to separate the upper from the lower part, preventing short circuiting of the cell. Finally,

the cell was inserted into the bracket and the wing nut was tightened (Figure 3.d). The size of the cell, including the bracket, was 90 mm x 54 mm x 70 mm (height x width x depth) and it weighed 650 g. The temperature operation range of this manifold was from -20°C to 70°C. This configuration enabled additionally the use of a lithium metal reference electrode (Figure 3.e), which was not considered necessary for our investigations. During charge/discharge, a controlled stream of He was purged through the spiral-type flow field below the working electrode and transferred first to the FTIR and then to the GC/MS instrument (Figure 3.f) for the analysis of the volatile species.



**Figure D3. (a-d): Assembling steps of the ECC-DEMS cell gas sampling setup. (e): The ECC-DEMS cell alone and provided with all gas and electrical connections (red cable: working electrode, blue cable: counter electrode, white cable: reference electrode, black cable: ground line). (f): The entire *in situ* FTIR-GC-MS setup.**

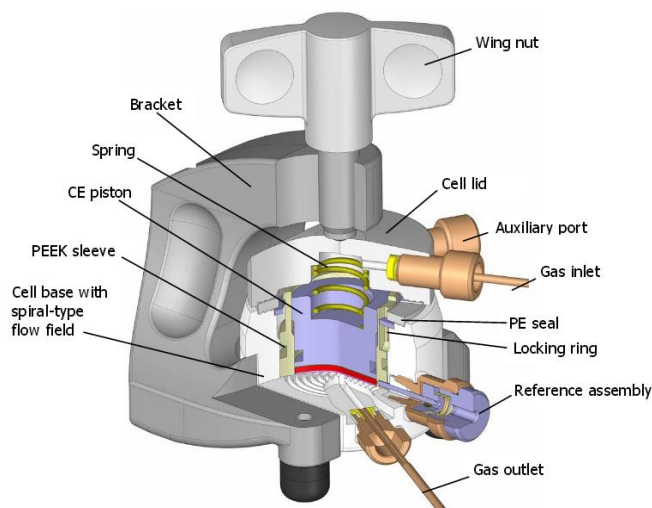


**Figure D4. Schematic cross section of the ECC-DEMS cell<sup>325</sup>.**

For the investigation of commercial cells, the gas sampling chamber consisted of a PTFE (polytetrafluoroethylene) container (height: 10.4 cm, ID: 6.2 cm) with a screw-on lid (Figure 5). The body of the chamber had two valves for gas introduction and gas outlet, enabling the purging of the evolved gases from the cell into the instrument. A cell holder was attached to the inner side of the lid and leads for the electrical connection were passed through the lid. A type K thermocouple was additionally installed for optional monitoring of the battery temperature during the experiment. The inner gas volume of the container, without the battery, was approximately 270 ml. For the gas measurements the safety vent of the battery was pierced carefully with a hammer and a sharp screwdriver in order to provide an opening for the evolving gases.



**Figure D5. Picture of the PTFE gas sampling cell. Left: Cell body. Right: Lid with attached cell and thermocouple.**

## ***D.3 Results and discussion***

### ***D.3.1 Correlation between FTIR and GC-MS data***

Already from the *ex situ* experiments we verified that there is a big number of substances formed when the electrolyte undergoes thermal aging. The *in situ* experiments also proved that the evolved gas species may change from experiment to experiment, depending on the cell chemistry and the electrochemical conditions applied to the cells. However, for the evaluation of the FTIR data, only a very small database was available. Problems were therefore declared at the building procedure of evaluation models with multivariate data analysis. Since doubts about the consistency of the FTIR database were expressed, the FTIR data were used only for the evaluation of the released CO<sub>2</sub>.

Carbon dioxide is one of the basic decomposition products of the electrolytes during cycling of the cell, as well as when the cell undergoes any type of abuse. As demonstrated in the theoretical part, a large number of reactions taking place inside the cell can lead to the production of CO<sub>2</sub>. Following different reaction paths and catalysed by the transition metal (cathode material) or the presence of humidity, the electrolytes decompose and form various polymeric species, of which the SEI is comprised. Oxidation of the electrolyte solvents or their reaction products is also expected in the presence of oxygen. The volume of gases, and in particular of CO<sub>2</sub>, released in the nominal voltage range of LIBs is very small, however, stress conditions of heating or charging result in the generation of much bigger gas volumes. The extent of gas generation is being intensively investigated due to its consequences for the cells and for the safety of their users (e.g. degradation of cell's performance, formation of toxic gases, possible cell explosion). The selection of CO<sub>2</sub> in this comparative study allowed us to use that part of the FTIR data that was more complete and more reliable, and also focused on the most abundant reaction product.

The area under the CO<sub>2</sub> absorption peak from 2300 to 2380 cm<sup>-1</sup> is proportional to its concentration in the gas cell (in our case the hollow waveguide). Therefore, this signal was evaluated and compared to the one provided from subsequent GC-MS measurements. We could thus check the extent at which the FTIR and GC-MS data correlate. A reliable measurement system should prove that gas concentration trends shown by the GC-MS system are repeated by the FTIR system. Experiments performed under different charging conditions and cell chemistries were used in these comparisons. All relevant information about these experiments are summarized in Table D3.

**Table D3. Cells used for the correlation experiments between FTIR and GC-MS.**

Experiment #	Cell Type [/ Composition]	Charging Range (V)
1	<b>EL-CELL</b> [LVP* vs Li in LiPF <sub>6</sub> (EC : DMC) 1M]	2.9 – 4.4
2	<b>EL-CELL</b> [LVP vs Li in LiPF <sub>6</sub> (EC : DMC) 1M]	3.1 – 4.8
3	<b>EL-CELLL</b> [LVP vs Li in LiClO <sub>4</sub> (EC : DMC) 1M]	3.7 – 5.5
4	<b>BPC</b>	4.3 – 4.5
5	<b>BPC</b>	4.5 – 4.6
6	<b>BPC</b>	4.6 – 4.7

\*LVP: Li<sub>3</sub>V<sub>2</sub>(PO<sub>4</sub>)<sub>3</sub>

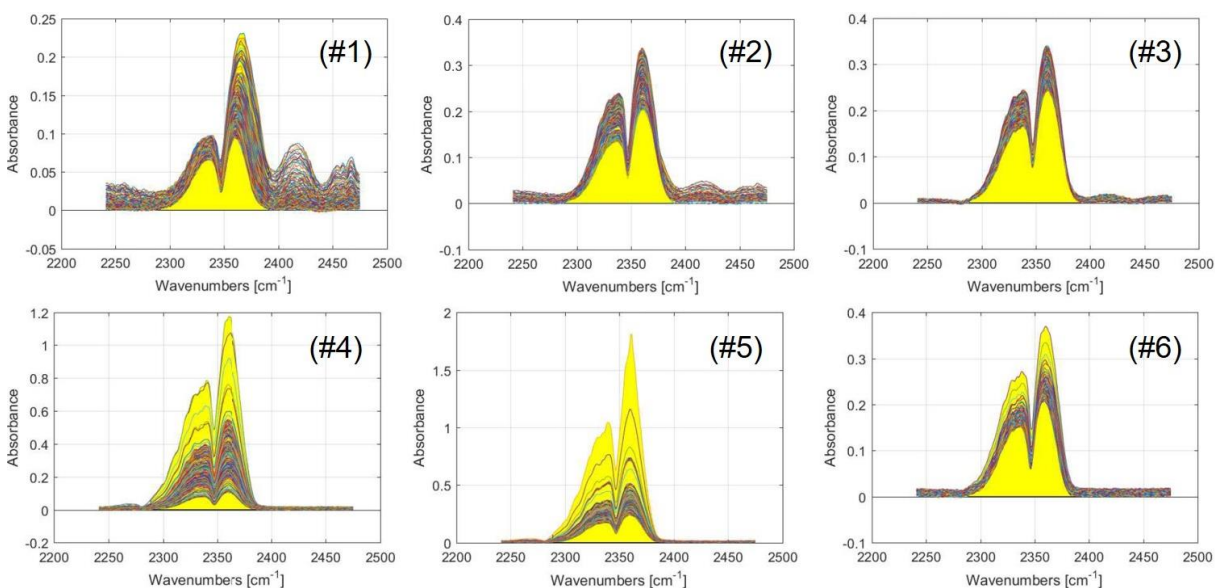


**Figure D6. CO<sub>2</sub> absorption peak sections of FTIR spectra. The spectra are grouped by experiment number, with those performed with EL-CELLS presented on the top and with BPC cells on the bottom.**



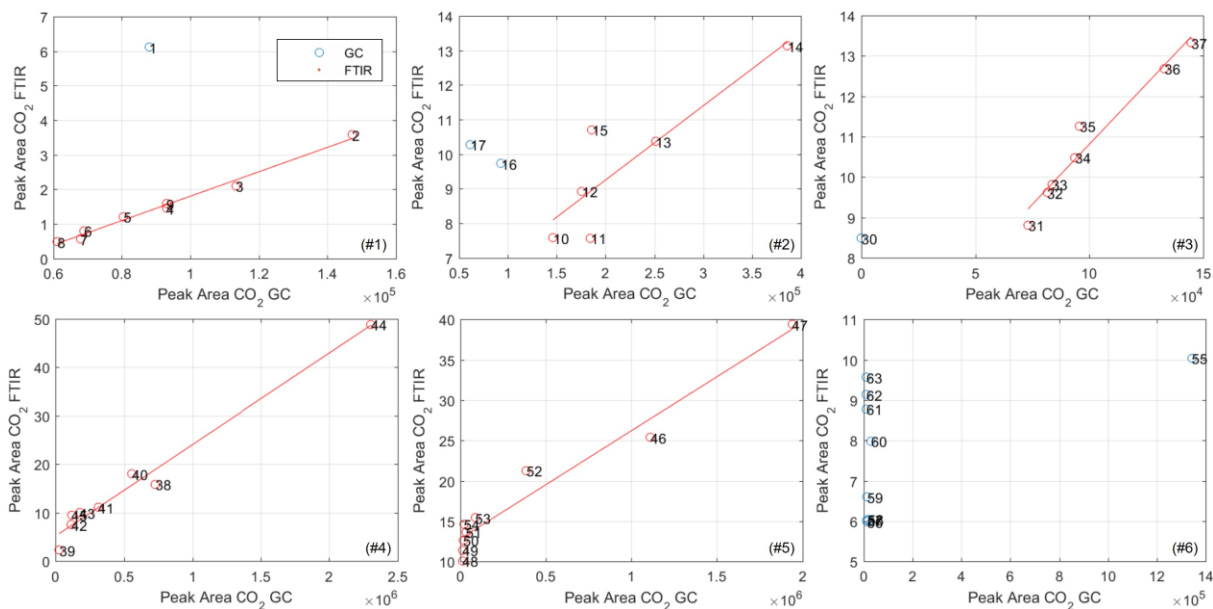


**Figure D7. Peak area of CO<sub>2</sub> measured by GC-MS (x-axis) versus peak measured by FTIR (y-axis). The order of the graphs follows that of the FTIR spectra.**

In order to decide on the charging rate for the in house-assembled cells, the capacity of the active material (in mAh/g) and the weight (in g) of the electrode were taken into consideration. For the LVP (Li<sub>3</sub>V<sub>2</sub>(PO<sub>4</sub>)<sub>3</sub>) electrodes the theoretical capacity was 197 mAh/g<sup>326</sup>. Taking one of the electrodes used as an example, which weighted cc. 3.54 mg, the charging rate of the battery was 0.697 mAh (1 C = 197 mAhg<sup>-1</sup> \* 0.00354 g = 0.697 mAh). Since a rate equal to C/3 was selected for the experiments involving testing of the material before, this parameter was used also for our experiments. Charging of the EI-Cell was then performed at approx. 0.2 mA. The weight of all LVP electrodes tested was comparable and the charging current was in a similar range.

For the BPC, with a documented by the manufacturer capacity of 4400 mAh and recommended charging rate of 1C, the current used should have been 4.4 A. However, without a booster such charging rate was not applicable. Therefore a C/10 rate was selected. That rate would correspond to 440 mA, but due to restrictions in the accepted values of the program the applied current was eventually 400 mA.

The corresponding CO<sub>2</sub> absorption peak sections of the FTIR spectra are presented in Figure D6. The spectra are grouped by experiment and the yellow marked areas below the absorption peak were the ones evaluated. These data were then compared to the ones obtained by GC-MS. The results are presented in Figure D7, where the peak area for CO<sub>2</sub> measured by GC-MS versus the one measured by FTIR are plotted.

When the absolute areas were compared, a very good correlation could be observed for almost all the experiments. The only experiment for which no correlation was found was #6. For this experiment, the first GC chromatogram obtained showed an excessive air peak, more than an order of magnitude higher

than expected. After this run, the peaks of all compounds were in a very small dynamic range. A leak test performed after the experiment was over, proved that the column connections had to be fixed, since both sides of the glass connector used were significantly leaking. The peak areas were nevertheless calculated and the results were sent for correlation with the FTIR data, which were evaluated externally by Dr. Wolfgang Märzinger, without any comment or justification, to check the accuracy of FTIR data processing. An additional consideration was to use these values, in order to check if any similar leak was occurring at the former part of our system. Since the FTIR compartment was placed before the GC and no such leak was present at that part, the results presented for the particular experiment were, as expected, not correlating with the GC-MS data. On the contrary, they were at a plausible range of values, verifying that the FTIR system was working properly.

There were also some single measurements at which the correlation of the FTIR and GC-MS data was poor, like for the first run at experiments #1 and #3 or the last two runs at experiment #2. Lower values than expected at the first injection could be explained by possible errors when starting the measurements. Such an error may involve starting the first GC injection before the sample loop was completely filled with a proportional gas volume from the cell. When the last injections showed poor correlation, though, no explanation could easily be provided. In addition, such a trend was not present when the experiment was repeated with a similar cell chemistry, where even further overcharging was performed. At that experiment (#3) the potential reached successfully 5.5 V without any significant mismatch between the FTIR and the GC-MS data. Hence, the poor correlation between the last two GC-MS runs and the corresponding FTIR results remains unexplained. A bigger number of experiments and respective runs is therefore required for more comprehensive evaluation of the correlation of the two techniques, and the accuracy of the evaluation procedures applied to the FTIR raw data.

An alternative approach to the FTIR data processing involved the generation of experiment specific peak area models, using all spectra recorded during each experiment. Only for the last experiment (#6) no specific model could be generated, due to the lack of any useful correlation between the GC-MS and FTIR results. For this experiment the model generated from experiment #1 was applied. Even though the use of the models generated for the experiments #4 or #5 would lead to better approximations, since the same cell type was used, this information was not available to the person developing the models to be taken into consideration. Therefore, simply the model from the experiment with the best correlation between the GC and FTIR data was used. The plots illustrated in Figure D8 demonstrate the application of these experiment specific models to the obtained data.

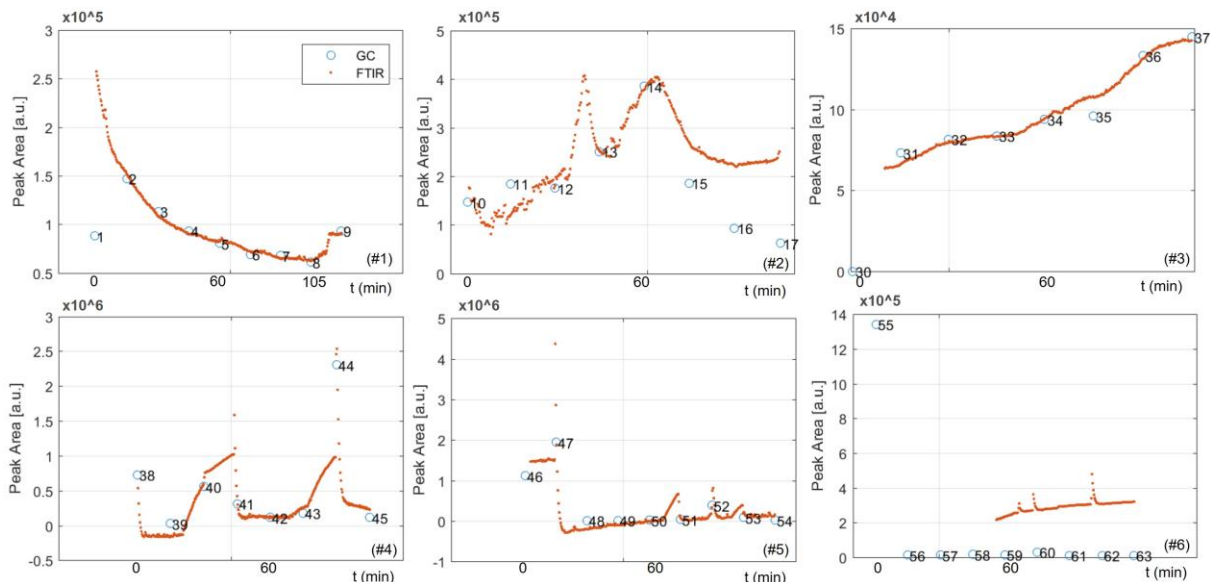


**Figure D8. Application of experiment specific FTIR peak area models on all spectra recorded during the experiments. The order of the graphs follows that of the FTIR spectra.**

As shown in the respective plots, very good agreement of GC-MS and FTIR data was seen for all experiments, except for #6 for reasons discussed before. However, the outliers present at the plots depicting the absolute GC-MS data versus the FTIR ones are still present at the results provided by the use of models.

The most significant observation is though made for the experiment #2, where between the number 12 and 13 GC-MS data points, an increase in the peak area of CO<sub>2</sub> was demonstrated only at the FTIR results, since the time resolution of GC cannot allow this change to be recorded. Similar examples are present at the experiment #4 between the runs 40 and 41, and at the experiment #5 between the runs 46 and 47. These rapid changes expected in the concentration of various gaseous products demonstrate the need for selective and sensitive techniques and for analytical systems that are also fast enough to track them. The very good correlation between the FTIR and the GC-MS values proved that our approach can contribute towards fast and sensitive analysis of LIB emissions. Although problems with multivariate data analysis still remain to be addressed, the use of a bigger database could significantly improve the situation.

### ***D.3.2 In situ GC-MS analysis of commercial LIB cells / Gas evolution during charge & overcharge of BPC***

The first charge and overcharge experiments with commercial cells, using the FTIR-GC-MS configuration, were performed by Alfred Amon<sup>327</sup> after the installation of the system at the laboratory of AIT. Although the system already then showed a small leak which could not be located, this did not affect the system's feasibility. When the experiments described in this section were performed, our investigations started by searching for the leaking part.

By comparing blank measurements performed with the FTIR-GC-MS setup with simple column blank GC-MS measurements (where the valve was bypassed), we concluded that a permanent leak exists in our coupled system. Several attempts were made to locate the position of the leak and close this leak. However, this task proved not to be realizable for the current configuration. The 10-port valve alone was checked with lighter gas, showing no indication of a leak. It was then assumed that the leak was located at the optical window of the hollow wave guide. Relatively broad peaks of co-eluting O<sub>2</sub> and N<sub>2</sub> at the retention time of approximately 1.40 min and of water around 4.4 to 4.5 min were observed. The significant increase in their magnitude compared with the initial measurements showed a deterioration of the system, however, no maintenance of the FTIR lightguide was performed after its installation. Since the air and water peaks were constantly present at the *in situ* FTIR-GC-MS measurements, they were considered as part of the background signal and were not labeled in the subsequent chromatograms. In order to stay within the linear range and protect the electron multiplier from saturation by the air signals, a lower detector gain was applied for the first 1.75 min of every GC-MS measurement. As it will be demonstrated later on, the peak for methane was partially co-eluting with the overloaded air peak, therefore the detector was not switched off during that time.

Additionally, the malfunction of the booster did not allow us to perform fast charging of the cells. Faster charge would have resulted in higher reaction rates and corresponding concentrations of the formed species. However, such experimental conditions may have prevented the identification of intermediate compounds existing in the analyzed gas mixture. Such intermediates could also co-elute with the final products present at significantly higher concentrations, since our GC method was a general screening one and resolution of all predicted degradation species was not possible in a single run. Besides, when we overcharged the cells we wanted to screen the changes (if any) in gas composition in a reliable time window for the experiment and the detection method. Therefore, the slower rate of charge actually turned out to be advantageous and slow charging rate experiments were performed. An additional consideration was that slower charging rates would keep the temperature inside the cell at a safe range.

Since multivariate data analysis was considered still questionable for FTIR, while that compartment of our system contributed to significant air contaminations, the FTIR was bypassed for the experiments

performed with the Swing 4400 cells. Therefore, the sample degradation occurring due to exposure of the electrolyte to air contaminations could be minimized. That was particularly important for the experiments we were targeting, for which the samples were kept overnight, after charging at certain voltages, and measuring was performed the next day. Preliminary experiments verified that continuous measurements of the gases produced from a BPC charged at 0.09 C did not lead to any significant input on the produced gas species or the reaction mechanisms. Due to the low amounts of gaseous products formed, no particular compound could be identified. The cells were therefore chosen to undergo overcharging stepwise. When a particular cutoff voltage was reached, charging was interrupted and the cell was left without any He flow overnight. The next morning another overcharging experiment was performed, with the first run showing the species formed from the reactions initiated by the last voltage applied. The storage time significantly contributed to the increased concentration of degradation products, since, under the slow charge rate used, the reaction rates were also slowed down. In that way, we could compare the effect of charging at certain voltages for slow electrolyte degradation reactions to that of faster charging. We could thus check what cutoff value was the minimum requirement for vast gas generation. Aim was to check if or to what extent we could reproduce the results presented in Alfred Amon's master thesis<sup>327</sup> for the overcharging experiment performed. To this aim, the BPC was charged stepwise, starting from OCV, with the charging steps being summarized in Table 4. The storage time of the cells was kept constant but was not optimized. Such an optimization would have been an excessively time-consuming task, while security regulations at AIT brought severe time restrictions to the work. However, shorter storage times would not bring any additional information to our targeted investigations. The concentrations of the reaction products detected were not high enough for any intermediates to be identified.

**Table D4. Charging conditions for the BPC experiments.**

<b>Experiment #</b>	<b>Charging range (V)</b>
1_BPC	3.7 – 4.2
2_BPC	4.15 – 4.6
3_BPC	4.52 – 4.7

Below are presented the chromatograms obtained from the first run of each experiment (Figure D9). The gas evolution is clearly illustrated, with more and higher peaks arising at the chromatograms belonging to respectively higher voltages. Only the first run is presented for each experiment, since the reactions occurring at such a slow charging rate had a speed that did not result in sufficient amounts of gases generated. The result was a decrease in the concentration and the number of peaks appearing to the subsequent chromatograms in each experiment, even though the applied voltages were gradually

increasing with the time. This effect is clearly illustrated in Figure D10, where the first, second, third and last (ninth) measurement of the Experiment #3\_BCP are presented.

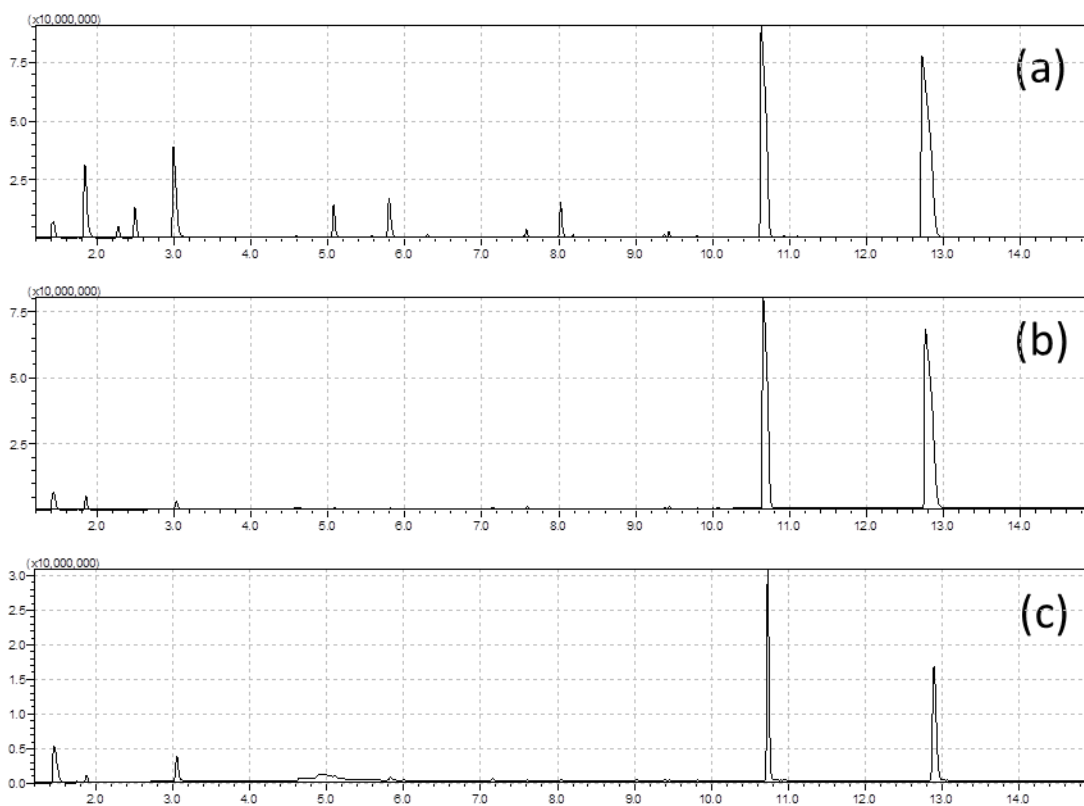


**Figure D9. Chromatograms obtained from the first run of experiment #1\_BPC (c), #2\_BPC (b) and #3\_BPC (a).**

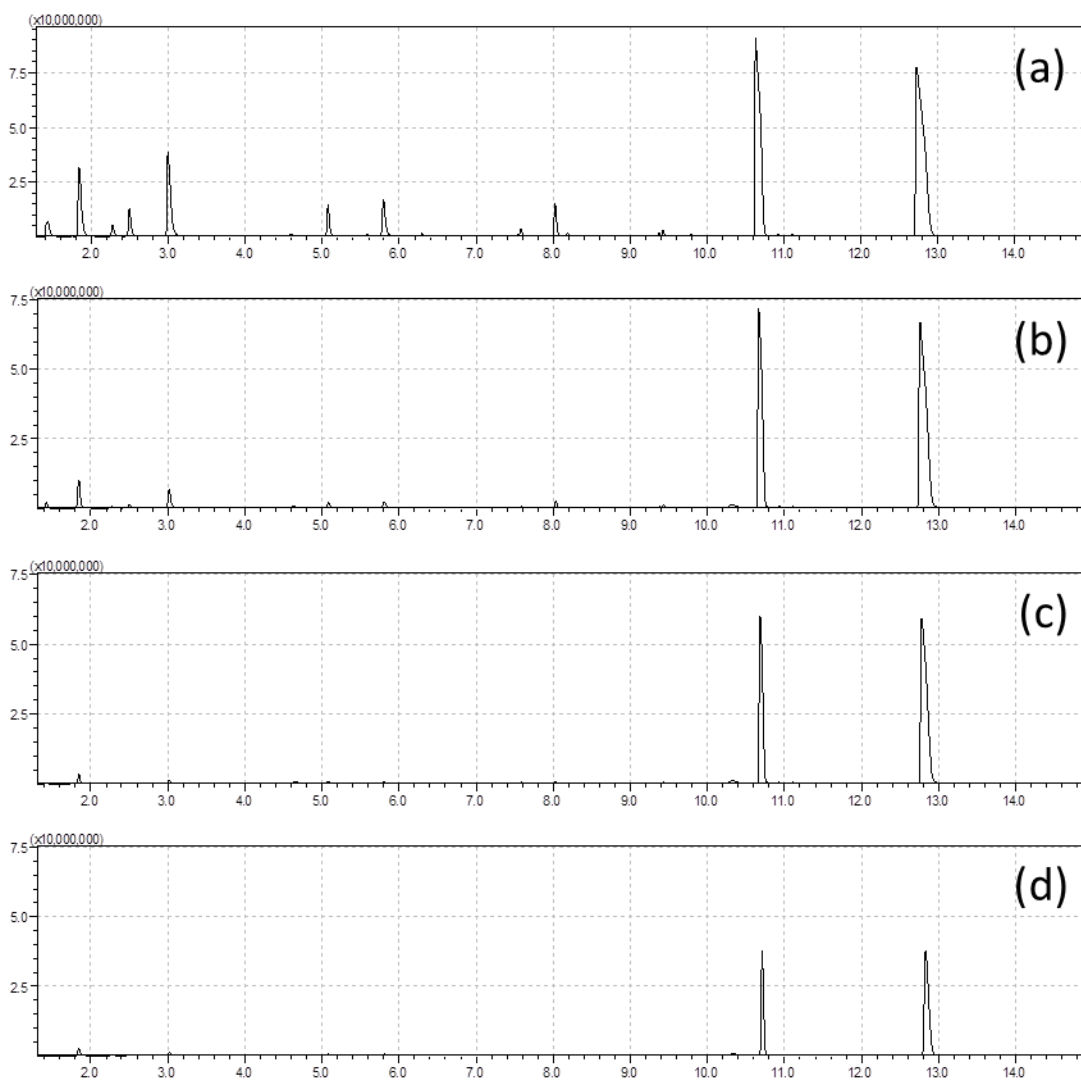


**Figure D10. Chromatograms of the first (a), second (b), third (c) and last (d) run of the overcharging experiment #3\_BPC. The same magnification window is used for all presented chromatograms.**

The flow of the purge gas was measured with a flowmeter before the EI-cell was connected, in order to ensure that the same stable flow was always used. The optimum flow range was selected during the preliminary method development and was not questioned later on. However, after the Experiment #6 (at the FTIR & GC-MS data correlation measurements) was performed, showing an excessive  $N_2$  peak at the beginning of the first chromatogram, we decided to check before every experiment that the flow indication on the needle valve was providing the correct value and a stable flow.

Even though the purge gas flow was not further optimized, it is interesting to consider the influence it has on the experiment. A very low flow would result in insufficient purge of the cell. If high gas concentrations are present inside the cell, a very low flow could also result in concentrations above the dynamic range of the FTIR, leading to overloaded peaks. Such results cannot be used for neither

quantitative nor qualitative data. On the contrary, too high flows may dilute the gas sample beyond the limits of detection for its constituents. An excessive flow can also contribute significantly to the temperature of the cell. Cooling of the cell would subsequently result in slowing down the electrolyte degradation reaction, providing unrealistic conditions and conclusions on the performance of the cells.

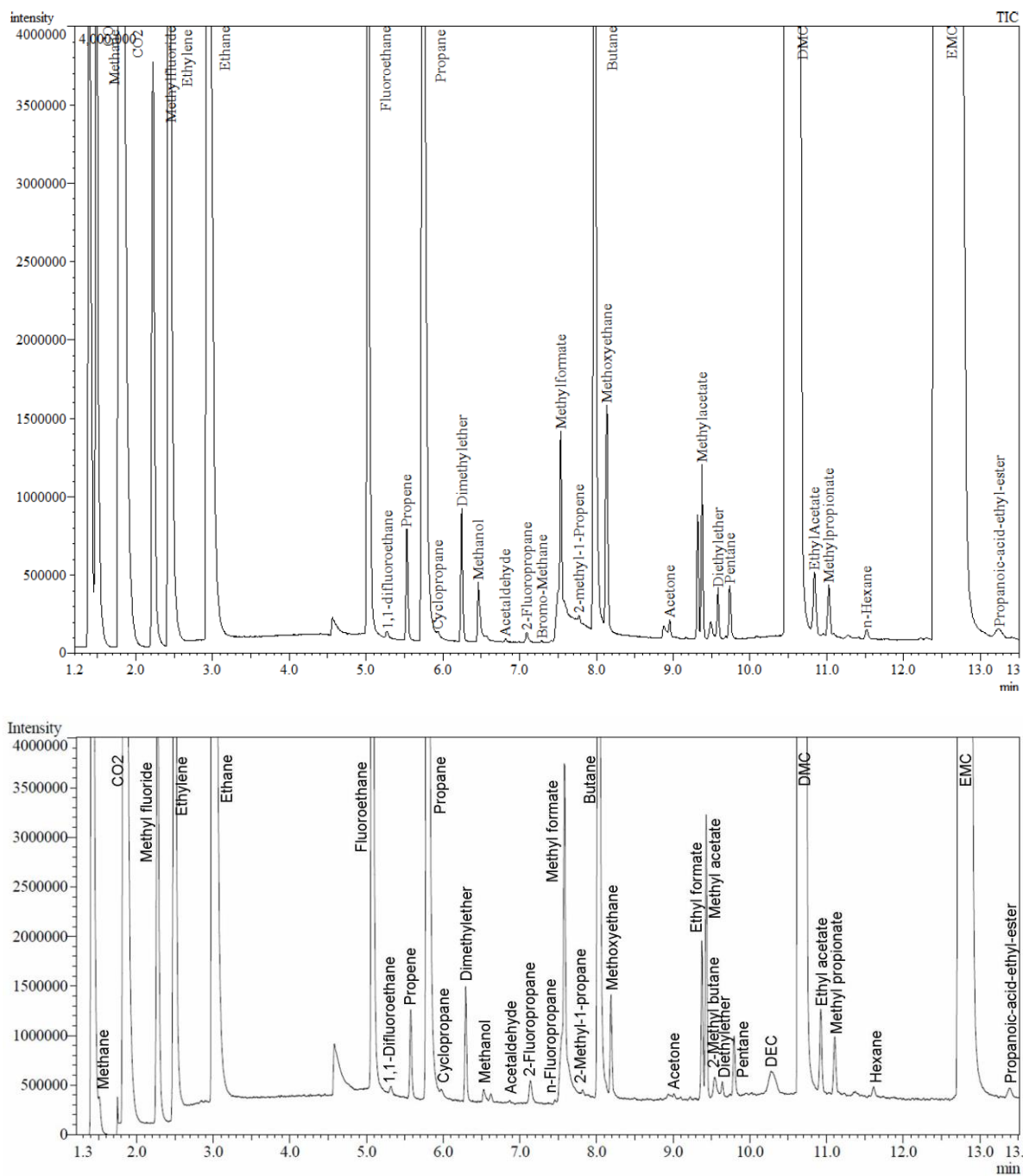


**Figure D11. Top: Chromatogram obtained for BPC at 4.75 V, after continuous overcharging.<sup>327</sup> Bottom: Chromatogram obtained for BPC at 4.6 V, after slower stepwise overcharging and storage of the cell without a gas flow overnight.**



As clearly demonstrated in Figure D11, the two chromatograms obtained for different BPC and under overcharging conditions present significant similarities. Even though the charging rate and sampling times were different, the voltage at which the gas formation was performed in our measurements is the same with the preliminary experiment performed by Alfred Amon, where only the overall gas generation potential was investigated. At that experiment charging at 1C and stepwise sampling of the formed gases was performed. Satisfactory resolution of the emitted species was not possible, since a RTX-5 MS column was used, leading to the co-elution of most compounds present in the gas sample. However the 4.6 V was the clear point at which the massive gas evolution started. The experiment he performed, at which the 4.75 V were declared as the starting point for gas generation, used a slower charging rate, which subsequently slowed down the reaction rates. However, the vast majority of the identified species were the same at both presented chromatograms, having highly comparable amounts (in terms of peak height and area, although the raw data of the experiment were not available for a direct comparison). This observation proves that the same reaction paths were followed or at least that the same final products were formed. Table D5 summarizes the identified species, their retention times and their MS spectra similarities according to the NIST library.

Taking a closer look into the identified compounds in both chromatograms, we can observe that at the experiment performed under stepwise overcharging, the peaks of the solvents (DMC and EC) were reduced in size. That is easily explained by the fact that during the slow charging steps carrier gas was passing through the battery removing gradually the electrolyte solvents that were in the gas phase, cooling down the cell simultaneously, so that also a smaller amount of the electrolytes would be transferred to the gas phase. This amount would be additionally available for the reactions occurring during the storage time of the cell, reducing even more the portion of the electrolytes remaining for subsequent identification. A small decrease in the amount of methanol was also observed, leading to the assumption that it indeed belongs to the intermediate products in some reaction pathways of electrolyte degradation. For example, the following reaction of methanol with lithium methyl carbonate could produce acetic acid and lithium methoxide:



Even though acetic acid was not detected in these measurements, it was clearly identified when the cathode material of a BPC was used for testing of in house-assembled cells. These results are presented in the following section (D.3.3).

A peak assigned to DEC was additionally present under stepwise charging. DEC was indeed one of the expected reaction products, since, as already mentioned in the theoretical part, both EMC and DEC electrolytes were detected in aged EC-DMC-based electrolyte cells. Their appearance implied a two-step

EC reduction as the starting reaction in order to reach a radical anion formation, resulting in lithium ethoxide ( $\text{CH}_3\text{CH}_2\text{OLi}$ ). The lithium ethoxide could then react, as a nucleophile, first with DMC yielding EMC and then with the EMC, producing DEC.

**Table D5. Identified compounds from BPC after overcharge at 4.6 V and overnight storage.**

Retention Time (min)	Compound	Formula	Hit
1.51	Methane	$\text{CH}_4$	99
1.85	Carbon dioxide	$\text{CO}_2$	90
2.28	Methyl fluoride	$\text{CH}_3\text{F}$	86
2.50	Ethylene	$\text{C}_2\text{H}_4$	97
2.99	Ethane	$\text{C}_2\text{H}_6$	90
4.58	Water	$\text{H}_2\text{O}$	97
5.08	Ethyl fluoride	$\text{C}_2\text{H}_5\text{F}$	92
5.32	Ethane, 1,1-difluoro	$\text{C}_2\text{H}_4\text{F}_2$	93
5.58	Propene	$\text{C}_3\text{H}_6$	97
5.80	Propane	$\text{C}_3\text{H}_8$	91
5.97	Cyclopropane	$\text{C}_3\text{H}_6$	90
6.30	Dimethyl ether	$\text{C}_2\text{H}_6\text{O}$	96
6.53	Methanol	$\text{CH}_4\text{O}$	91
6.62	Difluoromethylsilane	$\text{CH}_3\text{F}_2\text{Si}$	70
6,87	Acetaldehyde	$\text{C}_2\text{H}_4\text{O}$	87
7,14	Isopropyl fluoride	$\text{C}_3\text{H}_7\text{F}$	90
7,46	n-Propyl fluoride	$\text{C}_3\text{H}_7\text{F}$	80
7,54	Dimethylfluorosilane	$\text{C}_2\text{H}_6\text{FSi}$	85
7,58	Methyl formate	$\text{C}_2\text{H}_4\text{O}_2$	87
7,64	Isobutane	$\text{C}_4\text{H}_{10}$	90
7,82	2-Butene	$\text{C}_4\text{H}_8$	83
8,03	Butane	$\text{C}_4\text{H}_{10}$	92
8,19	Ethanol	$\text{C}_2\text{H}_5\text{O}$	92
8,94	Trimethylfluorosilane	$\text{C}_3\text{H}_9\text{FSi}$	83
9,01	Acetone	$\text{C}_3\text{H}_6\text{O}$	80
9,38	Ethyl formate	$\text{C}_3\text{H}_6\text{O}_2$	86
9,43	Methyl acetate	$\text{C}_3\text{H}_6\text{O}_2$	87
9,54	2-Methyl butane	$\text{C}_5\text{H}_{12}$	89
9,64	Diethylether	$\text{C}_4\text{H}_{10}\text{O}$	90
9,80	Pentane	$\text{C}_5\text{H}_{12}$	96
10,28	Diethyl carbonate	$\text{C}_5\text{H}_{10}\text{O}_3$	93
10,63	Dimethyl carbonte	$\text{C}_3\text{H}_6\text{O}_3$	88
10,93	Ethyl acetate	$\text{C}_4\text{H}_8\text{O}_2$	96
11,11	Methyl propionate	$\text{C}_4\text{H}_8\text{O}_2$	93
11,62	Hexane	$\text{C}_6\text{H}_{14}$	86
11,73	Ethylmethyl carbonate	$\text{C}_4\text{H}_8\text{O}_3$	87
13,39	Propanoic acid ethyl ester	$\text{C}_5\text{H}_{10}\text{O}_2$	81

Traces of 2-butene were also identified at 7.82 min. Furthermore, the peaks at 9.38 min and 9.54 min, present at both chromatograms, were positively identified as ethyl formate and 2-methyl butane, respectively. The compound assigned to the peak at 7.46 min, previously ambiguously identified as bromo-methane, was now, after background subtraction, determined to be n-propyl fluoride; an indeed more plausible degradation product. Lastly, the peaks at 6.62, 7.54 and 8.94 min, present also at both chromatograms, were identified as trace amounts of difluoro methyl silane, dimethyl fluoro silane and trimethyl fluoro silane, showing the interaction between the gas emissions of the cell and the stationary phase of the analytical column.

### D.3.3 *In situ* GC-MS analysis of in house-assembled LIB cells

In house-assembled cells with two different cathode materials were used for *in situ* investigation of the gases emitted under different electrochemical conditions. The active materials selected were the LVP, synthesized at AIT, and the LCO (LiCoO<sub>2</sub>), extracted from Boston Power Cells. For each material two experiments were performed, using the same electrolyte solution. One further experiment was performed with the LVP cathode where a different lithium salt was used. The cell compositions are summarized in Table D6. The LVP cells were already presented at the comparison of FTIR and GC-MS data, for which charging up to different voltages was performed. Contrary to these measurements, when the LCO cathode was used, cycling voltammetry was applied. The applied electrochemical conditions to each cell are summarized in Table D6.

**Table D6. In house-assembled cells used for *in situ* GC-MS analysis.**

Experiment #	Cell Composition	Charging Range (V)
1	LVP* vs Li in LiPF <sub>6</sub> (EC : DMC 1:1 vol. %) 1M	2.9 – 4.4
2	LVP vs Li in LiPF <sub>6</sub> (EC : DMC 1:1 vol. %) 1M	3.1 – 4.8
3	LVP vs Li in LiClO <sub>4</sub> (EC : DMC 1:1 vol. %) 1M	3.7 – 5.5
4	LCO** vs Li in LiPF <sub>6</sub> (EC : DMC 1:1 vol. %) 1M	3.1 – 4.7 – 2.7 – 3.1
5	LCO vs Li in LiPF <sub>6</sub> (EC : DMC 1:1 vol. %) 1M	3.8 – 4.7 – 2.7 – 3.8

\*LVP: Li<sub>3</sub>V<sub>2</sub>(PO<sub>4</sub>)<sub>3</sub>, \*\*LCO: LiCoO<sub>2</sub>, lithium cobalt oxide

Starting with the cells where LVP was used, the concentration changes of CO<sub>2</sub> have already been investigated and now will be discussed the rest of the gases produced during charging and overcharging of the cells, as determined only by the GC-MS data. Table D7 summarizes the identified compounds for the first three experiments. Since the aim of our investigations was to track concentration changes of the identified species, compounds that were at trace levels and/or only ambiguously identified are not mentioned.

**Table D7. Summary of compounds identified for the in house-assembled cell configurations where LVP was the active material.**

Ret. Time (min)	Compound Name	Formula	Exp. #1	Exp. #2	Exp. #3
1.56	Carbon monoxide	CO	+	+	+
1.85	Carbon dioxide	CO <sub>2</sub>	+	+	+
6.54	Methanol	CH <sub>4</sub> O	+	+	+
8.18	Ethanol	C <sub>2</sub> H <sub>6</sub> O	+	+	-
7.61	Dimethylphosphinic fluoride	C <sub>2</sub> H <sub>6</sub> FOP	-	+	-
9.02	Acetone	C <sub>3</sub> H <sub>6</sub> O	+	+	+
10.19	EC	C <sub>3</sub> H <sub>4</sub> O <sub>3</sub>	+	+	+
10.56	DMC	C <sub>3</sub> H <sub>6</sub> O <sub>3</sub>	+	+	+
12.88	EMC	C <sub>4</sub> H <sub>8</sub> O <sub>3</sub>	+	+	-

Before investigating the concentration changes of the various species, as indicated by the changes in their peak areas, it was checked if all identified compounds are present in the measurements of same (or similar) cell chemistries. Although the most extreme conditions were applied at the experiment #3, it was the one where fewer volatile were detected. That could be an indication of higher stability of the electrolyte solution when LiClO<sub>4</sub> is the lithium salt used. This observation does not comply with the properties of the salt declared in the literature<sup>328</sup>. In particular, lithium perchlorate has a satisfactory solubility, high conductivity and anodic stability (up to 5.1 V on a spinel cathode surface of EC/DMC, and therefore the upper voltage for overcharging was chosen to be at 5.5 V). It is less hygroscopic than other lithium salts and therefore stable to ambient moisture. However, the high oxidation state of chlorine (VII) in perchlorate makes it a strong oxidant, which readily reacts with most organic species in violent ways under certain conditions, such as high temperature and high current charge. Hence, LiClO<sub>4</sub> was declared as an impractical electrolyte solute for industry purposes already since the 1970s. Nevertheless, it is still frequently used as a salt of convenience in various laboratory tests because it is easy to handle and economical.

As expected from the properties of LiClO<sub>4</sub>, more oxidation products should have been identified from the cell containing that lithium salt and at higher voltages. The limited time-resolution of GC-MS could be responsible for not recording them, dictating the need for faster methods. Their presence in concentrations below the detection limit of our method was also possible. The flow of the purging gas, which by that time was not controlled by the flow meter, is another significant factor. A higher flow could not only cool down the cell, but also dilute the gas phase, resulting in lower concentrations of the emitted species. Tracking the area of N<sub>2</sub> in those measurements proved, however, that the purging gas flow was not to be blamed, since it remained stable in all experiments.

Moving on to the rest of the identified species, dimethylphosphoric fluoride was only detected at the experiment #2. Its absence in the chromatograms of the experiment #1 is nevertheless reasonable, since it

was formed only when voltages above 4.55 V were applied. However, no further degradation products were detected at higher voltages.

During the experiment #1, all species, apart from EC, experienced a decline in their concentrations with the time, even though the charging voltage was increasing. However, CO<sub>2</sub> exhibited an additional increase in its concentration at the last GC run, when the cell was under the highest applied voltage (Table D8). Similarly, concentration increases at 3.3 and 3.9 V were observed for CO, also at 3.9 V for methanol, and at 4.0 V for ethanol and acetone. The initial high peak areas of almost all peaks could be due to humidity and air contaminations of the cells during their transfer from the glove box and their connection to the measuring system. However, the higher areas close to 4.0 V can indicate the first step of gas generation due to the charging process. The stepwise increase in the concentration of EC can be a result of a temperature build up, leading to the evaporation of the solvent. Furthermore, a small minimum around 3.5 V also indicated that after this voltage decomposition of the electrolyte was taking place, reducing slightly its concentration while contributing to the formation of other species. Table D8 summarises the peak areas of the identified species throughout the GC runs of experiment #1, starting from the second run recorded. The first run was, as mentioned at the FTIR and GC-MS data comparison section, excluded due to unrealistic small signals (possibly caused by partial filling of the sample loop). The same trends and relative amounts of the detected compounds were observed for the experiment #2, verifying the reproducibility in the production of these in house-assembled cells and the absence of artifacts in our measurements. The only difference observed was, as already mentioned, the formation of dimethylphosphoric fluoride at voltages higher than 4.5 V, but without any further decomposition species being identified.

**Table D8. Peak areas of the identified species throughout the GC runs of experiment #1 (Cell Configuration: LVP vs Li in LiPF<sub>6</sub> (EC : DMC 1:1 vol. %) 1M.**

Compound Name	Run # / Voltage (V)							
	2 / 3.09	3 / 3.28	4 / 3.47	5 / 3.66	6 / 3.85	7 / 4.04	8 / 4.23	9 / 4.42
CO	105326	107739	95745	94594	97758	85874	80898	79056
CO <sub>2</sub>	164664	121789	103896	88505	74572	69550	66886	100770
Methanol	57601	41259	37964	21568	24337	18632	15352	18693
Ethanol	174022	109269	69803	47589	30453	43509	28830	23850
Acetone	29419	13793	0	0	0	15544	0	0
EC	744683	990321	900656	970082	1016211	1090850	1135739	1144091
DMC	132278347	71940388	49738666	37719080	30382935	25102462	20704769	20573830
EMC	92424	39947	36353	27338	0	0	0	0

When the experiment #3 was performed, some similar trends were observed for the identified compounds, even though they were fewer in number. In particular, the peaks for ethanol and EMC were not present, as well as the peak of dimethylphosphoric fluoride at overcharging conditions. Table D9 summarizes the information obtained from all chromatographic runs performed during the experiment.

**Table D9. Peak areas of the identified species throughout the GC runs of experiment #3 (LVP vs Li in LiClO<sub>4</sub> (EC : DMC) 1M)**

Compound Name	Run # / Voltage (V)						
	1 / 3.70	2 / 4.00	3 / 4.30	4 / 4.60	5 / 4.90	6 / 5.20	7 / 5.50
CO	55606	56140	49637	46727	50979	46825	47844
CO <sub>2</sub>	78117	94326	95781	93650	112728	149866	169822
Methanol	63220	50487	39894	39135	37032	31427	27665
Acetone	30158	21449	18239	12600	10043	14709	20428
EC	27828	9645	786812	979439	1006985	1066774	1137969
DMC	36821445	26430065	20181214	16393715	13990712	12290585	10905020

From these measurements we could see that the identified compounds were again experiencing different concentration patterns. The peak areas for methanol and DMC were steadily decreasing, as also demonstrated at the previous experiments. The opposite behaviour was now observed for CO<sub>2</sub> and EC, for which their peak size increased continuously, demonstrating an ongoing decomposition of the electrolyte and an increase in the cell's temperature, respectively. The concentration changes for acetone and CO had a more complex pattern. The decreasing peak area of acetone switched to higher values after the application of 4.6 V, while at the same voltage an increase at the peak area of CO was also observed. This voltage is close to the value at which the additional decomposition product, namely the dimethylphosphoric fluoride, was previously observed and coincides with the value at which the exhaustive gas generation was observed for the BPC. It is higher though than the point of gas generation observed in the other two experiments using the same cathode material. That could again indicate that using a different salt may have indeed contributed positively to the electrochemical behaviour of the cell and the enhancement of its stability towards overcharging. However, if the sole criterion for cell stability was the CO<sub>2</sub> gas generation, the properties of LiClO<sub>4</sub> would comply more with our findings. Then the smaller amount of the gas at the initial measurements could be explained by the less hygroscopic nature of the salt, since water and air contaminations are considered responsible for the high values of decomposition species during the first runs. The increasing amount of CO<sub>2</sub> with the voltage could then be used as an indicator of electrolyte decomposition due to the charging and overcharging conditions applied, proving also the stronger oxidative character of the salt.

When the cells containing LCO as the cathode material were tested, a total number of 35 and 48 chromatograms was recorded for the experiments #4 and #5, respectively. When the experiment #4 was executed, the sequence table used at the GC software was not long enough to record the entire electrochemical experiment. Interruption of the GC-MS measurements took place at around 63.000 s, when the cell had already reached 4.7 V and returned to its OCV (Figure D12). Therefore, all reaction products formed due to charging, overcharging of the cell and further discharging were successfully recorded. When the second experiment with the same cell composition was performed, the entire process was chromatographically tracked. The corresponding cyclic voltammograms for experiment #4 and #5 are presented in Figures D13 and D14, respectively.

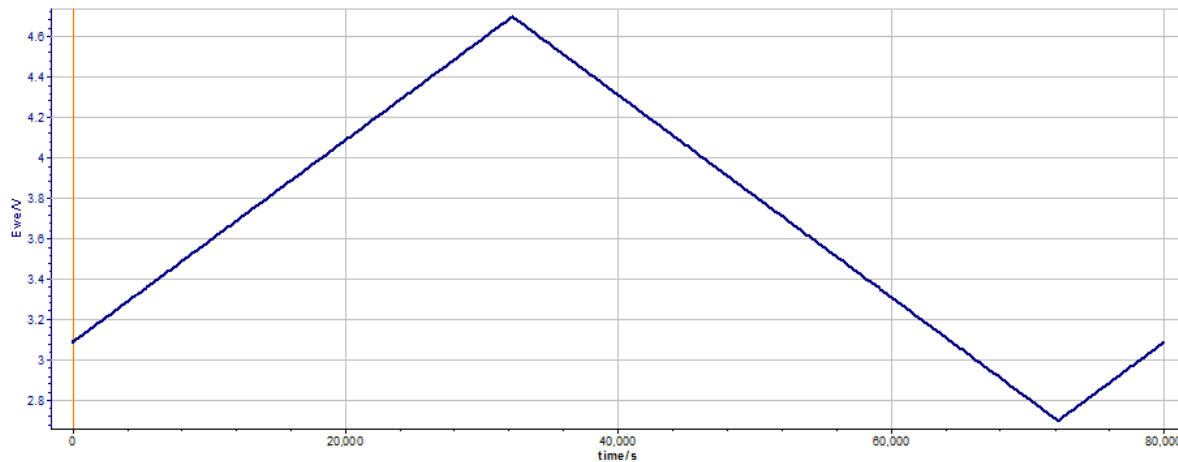


**Figure D12.** Graph illustrating the changes in voltage (V) with the time (s) for the cyclic voltammetry experiment #4.

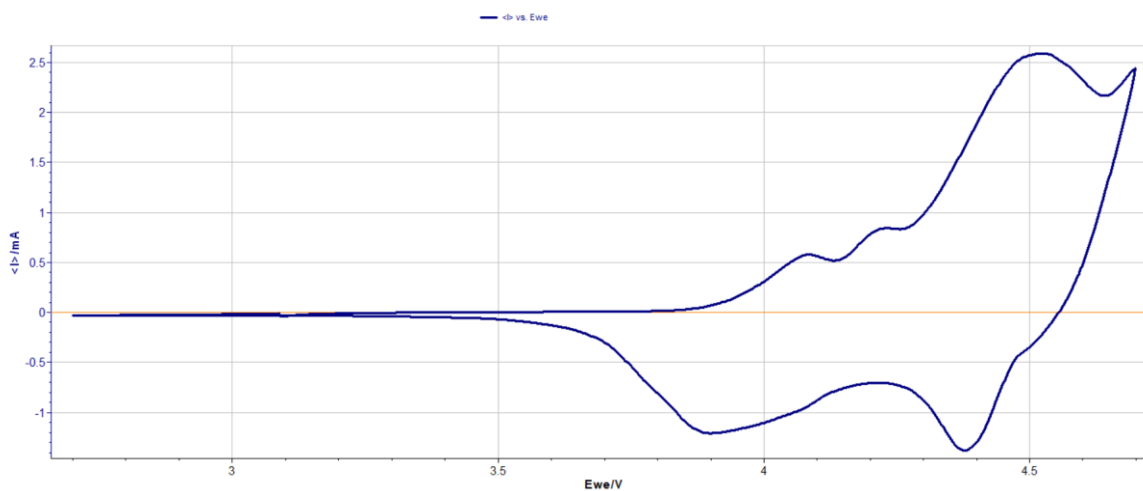


**Figure D13.** Cyclic voltammogram of experiment #4. The potential (V) is presented in the x-axis while y-axis presents the current (mA).

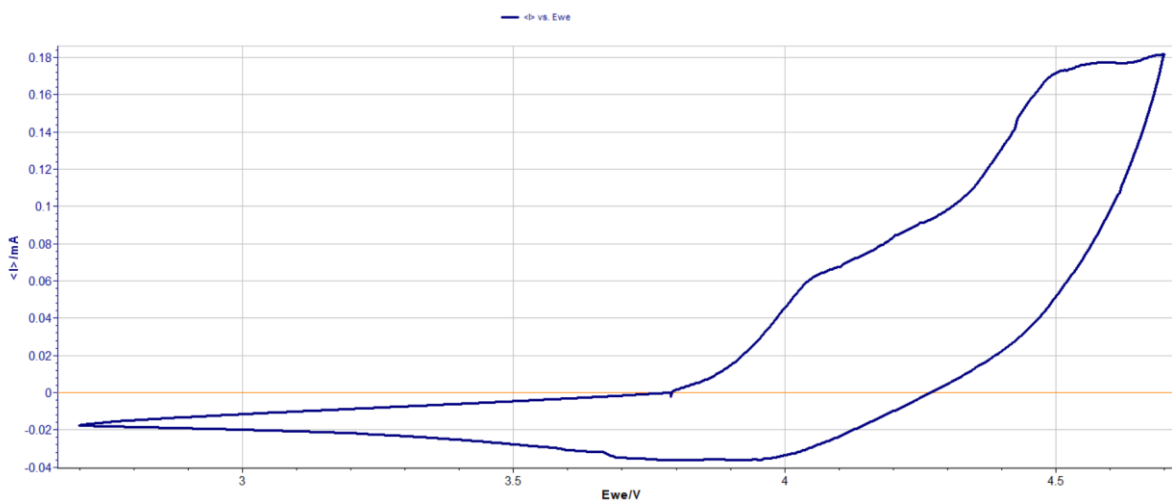


**Figure D14.** Cyclic voltammogram of experiment #5. The potential (V) is presented in the x-axis while y-axis presents the current (mA).



Even though the same cell composition was used for both cells, the electron transfer was quasi reversible during the experiment #4 (with current of reversed polarity and similar oxidation and reduction peak shapes being observed) and irreversible for the experiment #5. Looking into the GC-MS results of both experiments, the different performance of the cells was also reflected here. For the first experimental set (#4), several compounds were identified throughout the entire experiment. When the next cell (#5) was tested, a relatively big number of gases was present only at the first chromatogram, while the species present during the rest of the measurements were fewer than those observed for the experiment #4. The reason for such a behavior could be a contamination with water and/or air, due to e.g. problematic sealing of the EI-cell. This observation could interpret the change in the performance of the cell, since degradation of the electrolyte solution must have occurred before the charging was actually initiated. The identified compounds for both experiments are summarised in Table D10, with the exception of the additional species present exclusively at the first run of experiment #5.

**Table D10. Summary of compounds identified for the in house-assembled cells where LCO was the active material and cyclic voltammetry was performed. Additional species present exclusively at the first run of experiment #5 were excluded.**

Ret. Time (min)	Compound Name	Formula	Exp. #4	Exp. #5
1.85	Carbon Dioxide	CO <sub>2</sub>	+	+
2.54	Ethylene	C <sub>2</sub> H <sub>4</sub>	+	-
6.52	Methanol	CH <sub>4</sub> O	+	+
7.59	Methyl formate	C <sub>2</sub> H <sub>4</sub> O <sub>2</sub>	+	-
8.18	Ethanol	C <sub>2</sub> H <sub>6</sub> O	+	+
9.01	Acetone	C <sub>3</sub> H <sub>6</sub> O	+	+
9.12	Methylene chloride	CH <sub>2</sub> Cl <sub>2</sub>	+	-
9.22	Dimethylsulfide	C <sub>2</sub> H <sub>6</sub> S	+	+
9.44	Methyl acetate	C <sub>3</sub> H <sub>6</sub> O <sub>2</sub>	+	-
10.16	EC / 1,3-Dioxolane *	C <sub>3</sub> H <sub>4</sub> O <sub>3</sub> / C <sub>3</sub> H <sub>6</sub> O <sub>2</sub>	+	+
10.54	DMC	C <sub>3</sub> H <sub>6</sub> O <sub>3</sub>	+	+
11.37	2-Methoxy-1,3-dioxolane	C <sub>4</sub> H <sub>8</sub> O <sub>3</sub>	+	-
11.79	1-Hydroxy-2-propanone	C <sub>3</sub> H <sub>6</sub> O <sub>2</sub>	+	-
12.45	1,1'-oxybis[2-methoxy-ethane]	C <sub>6</sub> H <sub>14</sub> O <sub>3</sub>	+	-
12.91	EMC	C <sub>4</sub> H <sub>8</sub> O <sub>3</sub>	+	+

\* At different runs different compounds at the same retention time were observed in Exp. #5.

The additional species identified at the first chromatogram of the second cell (Exp. #5) investigated were: acetaldehyde (6.88 min), dimethylphosphinic fluoride (7.61 min), propanal (C<sub>3</sub>H<sub>6</sub>O, 8.94 min), acetic acid (C<sub>2</sub>H<sub>4</sub>O<sub>2</sub>, 11.13 min), 1,4-dioxane (C<sub>4</sub>H<sub>8</sub>O<sub>2</sub>, 12.48 min) and 2-methyl-2-butenal (C<sub>5</sub>H<sub>8</sub>O, 14.09 min). Furthermore, methanol, ethanol and acetone were also identified exclusively at the first run of the experiment. From the five main compounds present in the chromatograms of the experiment #5, DMC concentration experienced a linear decrease. A similar decrease was observed for EMC, however less

linear, as expected from a compound that was not initially present in the sample mixture, but belongs to the reaction products. At 10.16 min and during the first part of the measurements (for charging until approx. 3.8 V), only the decomposition product of the solvent, namely 1,3-dioxolane, was present at a concentration above the detection limit of the method. At the second half (at approx. 4 V and during the discharge step), the peak was readily assigned to EC. The area of the peak was this time increasing, indicating a temperature increase inside the cell, which enhanced the transfer of electrolyte to the gas phase and supported its identification. Since the respective mass spectra for that peak were gradually changing, indicating the presence of different species, an asterisk was used at the table with the identified compounds. The peak of dimethylphosphinic fluoride presented the same trends as those observed for CO<sub>2</sub>. An increase was observed for both compounds during the charging step, showing a maximum at around 3.5 V. However, that compound was previously identified at much higher voltages, proving that factors besides the applied voltage have now contributed more to the decomposition of the electrolyte.

Concerning the experiment #4, fourteen compounds were generally identified. From them, DMC, EMC and acetone had a steady decreasing concentration. EC was identified at a small range of peak areas, demonstrating relatively stable temperature conditions at the cell. While only traces of ethanol were identified at the first chromatogram recorded, the peak of methanol had a continuous increase, with only a small decrease in the peak area of methanol being observed at around 4.5 V. Interestingly, around this voltage two other species were identified. These were the 2-methoxy-1,3-dioxolane (between 4.2 and 4.6 V) and 1-hydroxy-2-propanone (among 4.2, the maximum 4.7 and again back to 4.6 V). Ethylene was also identified only between 4.1 and 4.4 V, showing a maximum peak area around 4.3 V. Around the same voltage an increase in the carbon dioxide peak area was also observed (between 3.9 and 4.4 V), showing a maximum at the same voltage (4.3 V). After charging at 4.0 V, methyl formate was also detected in the gas sample, while after 4.1 V its concentration started to decrease. Even though none of these compounds could have been a direct reaction product of methanol, alternative reaction paths occurring at the same voltage seemed to slow down the formation of the alcohol. Two further species identified only until 3.6 V and 3.7 V were the dimethylsulfide and methylene chloride, respectively. Despite the high similarity scores provided by the library for these two peaks, leading to their relatively unambiguous identification, the sources of both compounds are questionable for the particular cell composition.

## ***D.4 Conclusions***

The high degree of correlation between the FTIR and the GC-MS data, provided by our experiments with both in house-assembled and commercially available cells, proved that *in situ* FTIR-GC-MS measurements are a very promising approach for application with LIBs. In particular, the concentration changes recorded only by FTIR, due to its faster scanning capacity, denote its contribution to not only sensitive but also fast detection methods for the elucidation of the occurring reaction mechanisms.

The deconvolution of the FTIR data was solely based on the provided GC-MS data. With this data evaluation approach several errors may occur. For some compounds the corresponding GC-MS signals were too small, therefore unambiguous identification could not be achieved. That could be one source of errors that is however not significant, since the sensitivity of FTIR is lower than that of GC-MS. Overloaded GC-MS signals though for other species hinder their quantification, providing data which should not be used for tuning of the FTIR. Hence, alternative procedures for the FTIR tuning should be considered. The use of a larger FTIR database is also essential for the development of trustworthy evaluation models with multivariate data analysis. When commercial batteries were tested under charge and overcharge conditions, a variety of species was detected. These experiments were performed under different charging rates. The initial measurements utilized the booster that was in the past available in the laboratory. When only slower charging rates were applicable, a storage step of the cells was introduced. During this step the charging was interrupted, so that further formation of degradation products could be avoided, unless the degradation was autocatalytic. The slowed down reactions were thus assisted, and the necessary time was given for their products to reach amounts above the detection limits of the GC-MS method. Under these conditions, the same species, as with faster charging, were formed at the same potential and at comparable concentrations, as illustrated by the respective peak areas. Knowing the target compounds, further investigations of their concentration profiles would contribute in the elucidation of their reaction mechanisms. Such investigations could be performed by a further optimized FTIR-GC-MS setup.

Last but not least, in house-assembled cells were produced and tested. Different cathode materials and lithium salts were selected for a wider range of observations concerning the reaction products. Different electrochemical conditions were additionally applied, with one cell type being charged and overcharged, while a second type had to undergo cyclic voltammetry experiments. By comparing the number, nature and concentration profiles of the reaction products, conclusions on the performance of the different cell chemistries were made. In addition, by comparing the theoretical characteristics of certain materials with their actual performance, the necessity of fast, selective and sensitive techniques was demonstrated. *In situ* FTIR-GC-MS measurements could therefore significantly contribute to the evaluation of new materials and the production of safer batteries.

## **E. Theoretical Part on the vacuum outlet technique**

### ***E.1. Introduction***

Since phenomena like thermal runaway and subsequent emission of gases occur extremely fast when a LIB is abused, fast analytical techniques are required. Starting with the FTIR-GC-MS approach, the gaseous emissions from LIBs during cycling were able to be measured quasi-on-line. Among the various options available for fast GC separation, we chose to investigate the so-called vacuum outlet (VO) or low pressure (LP) GC-MS technique, whose characteristics are going to be discussed and evaluated in the subsequent sections.

Starting with a short review on the developments in gas chromatography and how the requirements for fast separations evolved, we will move on to the parameters responsible for achieving fast GC analyses. The Vacuum Outlet and, in more detail, the theory behind the VO technique, how such a system is constructed, its advantages over other fast GC techniques and its applications, will be discussed. The investigations based on optimization and comparison of VO systems intended for the analysis of highly volatile species will then be presented. Using a standard mixture of highly volatile compounds, the VO technique was evaluated on its applicability for future use in the field of LIBs. This research work on VO was then concluded with the successful combination of the technique with solid phase micro-extraction (SPME), targeting the simultaneous enhancement of sensitivity and speed. This combined system was used for the identification and quantification of compounds with intermediate volatilities. Focusing again on species that may have a negative impact on human health, we selected to use the SPME-LP-GC-MS for the determination of two of the most commonly used UV filters, which are suspected to be endocrine disrupters, in swimming pool waters.

### ***E.2. The vacuum outlet technique***

#### ***E.2.1. From conventional to fast GC separations***

Gas chromatography, or more precisely gas-liquid partition chromatography, was conceptualized by Martin and Synge in 1941 and introduced in practice by James and Martin in 1952.<sup>329</sup> The introduction of open tubular columns by Golay in 1957/58 initiated a revolution in analytical chemistry. With the simultaneous development of highly sensitive detectors, much progress in capillary gas chromatography (CGC) was made during the following years. Columns of various materials and dimensions were used from the onset, while capillaries with inner diameters between 35  $\mu\text{m}$  and 2 mm were already used around

1960.<sup>330</sup> Advances in glass capillary column technology in the 1960s and 1970s were followed by the introduction of fused silica capillaries in 1979.<sup>330</sup> As a result of these advances, chromatographers now have a wide-ranging choice of open tubular columns. Commercially available columns have diameters between “narrow-bore” and “wide-bore” (typically 50 and 750  $\mu\text{m}$  respectively) and the stationary phase film thickness can be anywhere between 0 and 5  $\mu\text{m}$ . These columns can be operated over a wide temperature range at outlet pressures from vacuum up to tens of bars.<sup>330</sup>

Since the invention of GC, there has been an increasing interest within the chromatographic community for faster GC methods. This is not only related to the fact that the number of samples subjected to GC analysis has risen greatly, but more importantly to the need of getting results in the shortest possible time, enabling even a quasi-on-line analysis mode, impossible for separations that last long (e.g. 30 to 90 minutes). Nowadays, in routine analytical applications, sample throughput is often the most important aspect considered when choosing an analytical method. Gas chromatographic instrumentation has been subjected to continuous and considerable improvement, with high-speed injection systems, electronic gas pressure controls, rapid oven heating/cooling and fast detection being currently available in a variety of commercial gas chromatographs.<sup>331</sup> As a consequence, high-speed GC, providing faster analysis times while maintaining resolution, is being increasingly employed for routine analysis in different fields. Furthermore, the employment of dedicated software makes the passage from a conventional to a fast GC method rather simple.<sup>331</sup>

Gas chromatographic analytical procedures consist essentially of six separate steps: sample preparation; sample injection; separation; detection; GC oven cooling time; and data evaluation.<sup>331</sup> Each of these processes contributes to the overall analysis time, with analysis speed depending mainly on the weakest link in this chain of events. The first step has the greatest impact on analytical time-costs, selectivity, sensitivity, precision and accuracy.<sup>331</sup> However, emphasizing on GC separation time, we should not overlook the fact that both sample preparation and separation have the highest importance and have undergone a great deal of development.

The major objective of any GC method is the total separation of the most critical sample components in the minimum time. It is evidently preferable to deliver entirely resolved analytes to the detector system, even if a mass spectrometer is employed. The use of a 25–30 m x 0.25–0.32 mm id capillary column, while ensuring satisfactory separation (often over-resolved) on simple-to-medium complex samples, is also characterized by a substantial disadvantage: the cost in analytical time (e.g. for most food applications this is typically 0.5–1.5 h)<sup>331</sup>. This becomes a disadvantage especially for laboratories with a high sample throughput and/or where there is a need for quick and reliable results. Assuming that the most selective conventional GC column for a specific application is being used, the most evident routes towards reducing retention times will be discussed in the following sections.

### E.2.2. Fast GC-MS techniques

Faster GC method development and validation can be simplified if key concepts are kept in mind (number of components to be analyzed and their physico-chemical properties, selection of column and carrier gas, separation at optimized flow-rate, optimal temperature program, sample capacity)<sup>332</sup>. In order to increase the speed of GC analysis, it is possible to increase the carrier gas flow rate (F) and/or increase the temperature program heating rates, until the lowest degree of acceptable analyte separation is attained; to use a carrier gas that provides efficient separation even at high linear flow rates such as hydrogen; to reduce the column length (L), the column diameter ( $d_c$ ), or the thickness of the stationary phase; and to use a detector that operates at a lower outlet pressure ( $p_o$ ).<sup>333,331</sup> Table E1 summarizes the various options of accelerating gas chromatographic separation together with the gain in time and the practical aspects that are implied. An inappropriate combination of these changes complicates the method development process. It is also important to keep in mind that when the separation speed is optimized, other parameters are compromised. In that case, separation power, sample capacity, or both must – at least in part – be sacrificed (as illustrated in Figure E1)<sup>333</sup>. If any single attribute was to be maximized (e.g. speed), the other two would then be compromised. Therefore, any fully optimized chromatographic method is a tuned compromise between speed, capacity and resolution ( $R_s$ ). Whatever attribute gets priority or focus depends on the specific goals or requirements of the analysis.

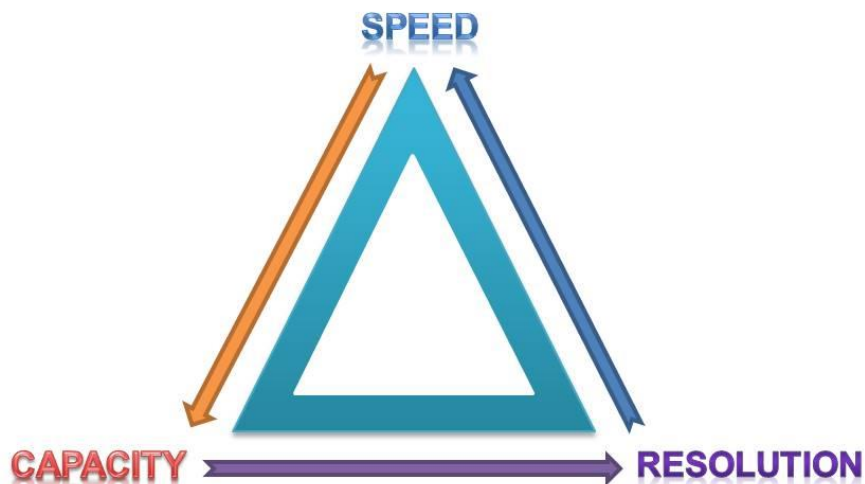


**Figure E1. Optimization triangle of compromise. The apices represent maxima for each of three dependent variables and minima for the other two. Any given separation requires a combination of the three variables, with analytical goals or requirements dictating which attributes are favored over the other.<sup>333</sup>**

**Table E1. Routes towards faster GC.**<sup>334</sup>

No.	SPEEDING UP OPTIONS	GAIN IN TIME AND PRACTICAL ASPECTS
(I) Minimize resolution to value just sufficient		
1	Shorter column length	Time gain is proportional to length reduction in isothermal GC (IGC). In temperature-programmed GC (TPGC), gain is smaller if larger temperature range is covered, because run time is now determined by time taken for oven to reach temperature needed to elute last component. Shortening a column is irreversible. Recommend starting with option 2.
2	Above optimum carrier gas velocity	Time gain is proportional to velocity increase in IGC. Gain in TPGC is small, especially if larger temperatures are covered. Maximum velocity restricted by pressure regulators.
3A	Higher isothermal temperature (isothermal GC only)	Gain approx. two-fold for each 15 °C temperature increase (IGC). Bear in mind maximum operating temperature.
3B	Higher initial temperature	Gain in TPGC strongly depends on original and final program.
3C	Higher final temperature	Typical gains only several minutes.
4A	Faster temperature programming	Gain proportional to increase in rate (TPGC). Programming rates above approx. 20–40°C/min require special instrumentation.
4B	Convert isothermal GC to temperature-programmed GC	Substantial gains possible upon going from IGC to TPGC.
5	Pressure/flow programming	Gain generally modest; requires electronic pressure/flow control.
6	Lower film thickness	Gain proportional to reduction of film thickness (thin-film columns); larger gains for thick-film columns.
(II) Maximize selectivity of chromatographic system		
7	Use more selective stationary phase or apply coupled columns	Significant gain in elution time is possible, but phase selection can be tedious.
8	Use (conventional) 2D GC*	Unresolved peaks can be transferred to second column for further separation on different stationary phase. Very large gain possible, but more complex instrumentation is required.
9	Use selective detection	Significant gain possible because compounds of interest have to be separated only from each other. Separation from matrix compounds no longer necessary. Can also be used in combination with other options.
10	Apply MS detection	Significant gain possible, especially in combination with spectral deconvolution techniques. Can also be used combined with other options.
11	Apply backflush	Typical gain, 2–5-fold. Requires special instrumentation.
(III) Implement method that reduces analysis time at constant resolution		
12	Reduce column inner diameter	Gain proportional to reduction of column i.d. (high-pressure drops) or square of reduction (low-pressure drops). Ruggedness and capacity can be problematic.
13	Use hydrogen as carrier gas	Gain 60% vs. He or 100% vs. N <sub>2</sub> ; requires special safety precautions.
14	Apply vacuum-outlet conditions	Up to 6-fold gain for short, wide-bore columns. Gain for standard columns negligible. Only possible with MS detection.
15	Apply turbulent-flow conditions	Not a viable option for daily practice.

\*Comprehensive GC x GC is not included

Selective detection represents another valid possibility for faster GC techniques. Early attempts to couple packed GC columns with mass spectrometry (MS) date back to the late 1950s.<sup>329</sup> The first commercial GC-MS systems, for packed column use, were the Swedish LKB (magnetic sector field) instruments in the mid 1960s followed by the American Finnigan and then the Hewlett-Packard (quadrupole) systems in the late 1960s and early 1970s.<sup>329</sup> GC-MS is a versatile technique which has significantly improved over the decades and offers several advantages over GC with other selective detectors (universal detection with high selectivity, ability to identify or confirm unknown analytes, sensitivity, use for quantitative analysis,

ability to distinguish co-eluting peaks, use of spectral libraries), and its applicability for low-pressure gas chromatography (LP-GC) is yet another benefit.<sup>335</sup> However, the scope of conventional GC-MS is limited owing to two main reasons:

1. Relatively nonvolatile molecules (such as large polycyclic aromatic hydrocarbons) are incompatible with gas chromatography and especially incompatible with the mass spectrometer ion source. The temperature limit of the ion source results in a relatively early onset of chromatographic peak tailing.
2. Many classes of compounds are thermally labile and decompose in the gas chromatograph or in the mass spectrometer ion source.<sup>336</sup>

These two limitations are often interrelated. If a mixture contains both relatively nonvolatile compounds and thermally labile compounds, then at the temperatures required to handle the relatively nonvolatile compounds in the GC and ion source, the thermally labile molecules dissociate.

An obvious and known approach to further enhance the scope of GC-MS with thermally labile compounds is – apart from derivatization – the use of short columns, as already mentioned. This fast GC technique is reducing the residence time of the analyte in the separation column and thereby minimizes its dissociation.<sup>337</sup> Because the analyte peak concentration reaching the mass spectrometer is greater with shorter columns than with longer columns, lower detection limits are also possible.<sup>338</sup> However, some more demanding separation problems may require a bigger length of the separation column, making this technique inapplicable when conventional columns need to be used.

Over the past decades several approaches to fast gas chromatography have been proposed and developed with various outcomes.<sup>339-347</sup> Several reviews have been reported describing the most important existing high-speed GC<sup>332,334,348,349,350</sup> and GC-MS methods.<sup>329,350</sup> The main approaches to fast GC coupled to mass spectrometry (MS), include:

- (i) the use of short micro-bore (0.1 mm internal diameter (i.d.)) capillary GC columns coupled with time-of-flight MS or other high duty cycle detectors for analysis;
- (ii) fast temperature programming using resistive heating or conventional GC ovens;
- (iii) low-pressure GC-MS using a mega-bore (0.53 mm i.d.) column;
- (iv) supersonic molecular beam for MS at high carrier-gas flow; and,
- (v) pressure-tunable (also called stop-flow) GC x GC.

The low-pressure GC-MS technique using mega-bore columns was selected to be the fast GC technique used at the projects presented in this research work, considering among others the extended dynamic range, no compromise in sensitivity, high sample capacity and lack of changes needed in the instrumentation when employing this approach. The description of this technique and a following comparison with the use of narrow-bore capillaries will prove the superiority of short mega-bore columns for fast GC-MS analyses.



### ***E.2.3. Description of the vacuum outlet technique using short wide-bore capillaries***

The so-called vacuum outlet capillary GC or low-pressure GC is realized when columns are operated at reduced pressure. Performing the separation under reduced pressure leads to several advantages, as it was first demonstrated by Giddings in 1962<sup>339</sup> and will be discussed later on. The first application of the technique was in 1969, using a packed stainless-steel column and a thermal conductivity detector.<sup>351</sup> The coupling of LP-GC with a photoionization detector was published in 1991 by Puig and Sacks<sup>352</sup>, while Whiting *et al.* used in 2001 a portable vacuum outlet GC vapor analyzer employing air as carrier gas and surface acoustic wave detection<sup>353</sup>. However, the need for a vacuum source, tight seals, as well as injection and detection systems that could withstand vacuum conditions led the advantages of LP-GC to remain widely unrealized for a couple of decades.<sup>354</sup> Coupling though with mass spectrometers made vacuum outlet gas chromatography very easy to implement and promoted its applicability.

Under vacuum-outlet conditions, short, mega-bore columns are the most suitable to use, since the vacuum would extend across the whole column length, providing a higher analysis speed than the same column operated at atmospheric outlet pressures.<sup>355</sup> By contrast, when narrow-bore columns are operated at vacuum-outlet conditions, only a fraction of the column length is operated at sub-ambient pressures. This means that the gain in speed for narrow-bore columns with high theoretical plate numbers, operated under vacuum conditions, becomes less important.

As discussed by van Deursen *et al.*<sup>356</sup>, to enable vacuum operation through coupling a wide-bore column to a mass spectrometer, the use of a restriction at the head of the column is necessary (Figure E2), otherwise operational problems will occur. Particularly, the carrier-gas inlet and the injection system have to be operated at above-atmospheric pressures. In addition, the high column outlet flow might increase the pressure in the ion source of the mass spectrometer to a level exceeding the tolerable limit. Typical flow-rates of a wide-bore column with an inner diameter of 530  $\mu\text{m}$  and a length of 10 m are approximately 7-10 mL/min for normal operation with ambient outlet pressure. In general, the maximum pumping capacity of an MS is already reached at a column flow-rate of 5 mL/min. If, on the other hand, the pumping system of the MS does not have sufficient capacity to maintain pressure at an acceptable level, a complication will be that the inlet pressure in the injector will decrease to sub-ambient values. Although advantageous in terms of speed, this might cause additional practical problems. But, if a restriction coupled to the column inlet is used, the flow is restricted to an acceptable level, the injection system can operate at above-atmospheric pressures and still low-pressure conditions prevail throughout the entire column.

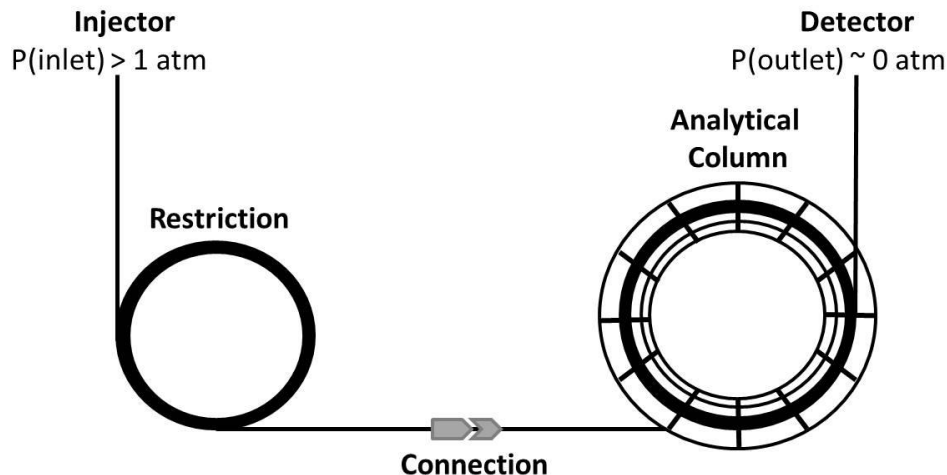


**Figure E2.** Typical vacuum outlet column setup using a longer, small inner diameter uncoated pre-column as a restrictor.

Van Deursen *et al.*<sup>356</sup> have also investigated three types of column flow restrictions. As it is illustrated in Figure E3, the first method uses a narrow bore pre-column (60 cm length x 100  $\mu$ m i.d.), the second method relies on the use of a tapered on column supercritical fluid chromatography restrictor (SFC-restriction), whereas the third method makes use of a micro-injection valve, acting as a flow restrictor. It was concluded that the best performance was obtained using the narrow-bore column restriction and the SFC-type restriction, since the micro-injection valve showed a contribution to band broadening by additional dead-volume effects.<sup>356,357</sup>

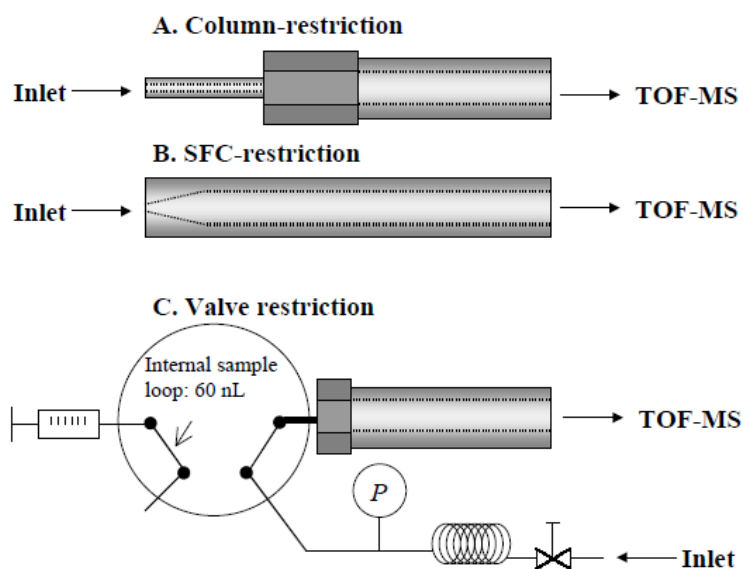


**Figure E3.** Schematic drawing of the three restriction types: (A) narrow-bore pre-column (Varian/Chrompack), (B) SFC-restriction (produced in house) and (C) valve restriction. Restriction column at inlet: 15 m x 250  $\mu$ m (uncoated).<sup>356</sup>

Under these circumstances, vacuum can be created successfully inside the analytical column by coupling a capillary with a large diameter (0.53 mm) to a deactivated restriction capillary, which is positioned at the inlet section. The function of the restriction, as already mentioned, is to deliver an optimal carrier gas flow for the MS system, ensuring as well that the column head pressure can be precisely maintained by electronic pressure control without the need of additional instrumentation. In this way, no modifications of the injector system are needed and almost any GC-MS instrument may be used in LP-GC-MS.<sup>358</sup> Such a restriction can vary, depending upon whether a very short capillary of 20  $\mu\text{m}$  i.d. (“Rapid-MS<sup>TM</sup>”)<sup>354</sup> or a longer capillary of 0.1–0.15 mm i.d. is used, but since it serves also as a guard column, a practical advantage is given to the use of the longer and wider restrictor dimensions, like the 3 m  $\times$  0.15 mm i.d. over a 0.6 m  $\times$  0.1 mm i.d. option.<sup>358</sup>

A new way of making restrictions was introduced by de Zeeuw *et al.* in 2009<sup>359</sup> and concerns the incorporation of the restriction into the injection port, providing easier and more robust vacuum outlet GC systems. In this way, the need of a special connector is avoided, together with the special skills that its production requires and the possible leaks, dead volume, activity and thermal mass issues that may occur. For example, if part of the restriction becomes active by the sample matrix, peaks will start to broaden and tail even before they reach the analytical column, demanding the replacement of the entire restriction. In such cases it is not practical to cut off a piece of it, since the pressure characteristics of the restriction, as well as the column flow, will be changed. By the new way proposed by de Zeeuw *et al.*, one can make a restriction using a Press-Tight type connector and well-defined short pieces of fused silica with internal diameter of 0.025 mm, and position this inside the injection port, as illustrated in Figure E4.<sup>359</sup>

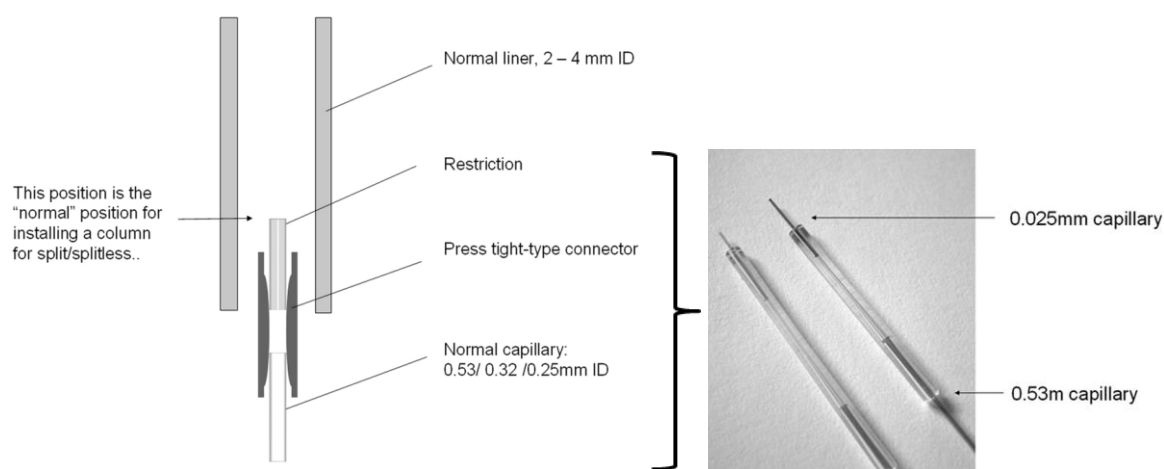


**Figure E4. Position of the restriction inside the injection port (left end side) and of the restriction tubing in the Press-Tight connector (right end side).<sup>359</sup>**

The actual pressure in a 0.53 mm capillary will obviously be much lower than with a 0.25 mm column. Since the optimum velocity increases with lower pressure, the gain in optimum linear gas velocity for 0.53 mm columns will be higher than that found with 0.25 mm columns.<sup>354</sup> The optimum average carrier gas

velocity is proportional to the average binary gas-phase diffusion coefficient and both of these vary inversely with pressure, so the low-pressure GC arrangement opens the opportunity for fast separations.<sup>357</sup> As it is demonstrated in Figure E5, lowering the pressure inside the capillary shifts the van Deemter curve to the right due to the fast diffusion in the gas phase.<sup>359</sup> This effect will be stronger when applying a higher vacuum through the whole capillary. That is why the effect is the biggest on 0.53 mm i.d. columns. This will also work for smaller diameter columns, but then the column itself will act as a restriction. Therefore, narrow i.d. columns must be very short to experience the effect.<sup>359</sup> Nearly all GC-MS methods entail vacuum outlet conditions in which the low-pressure region extends up the analytical column to a certain distance, but only in LP-GC-MS, that distance could essentially cover the whole length of a 10 m x 0.53 mm i.d. analytical column.<sup>360</sup>

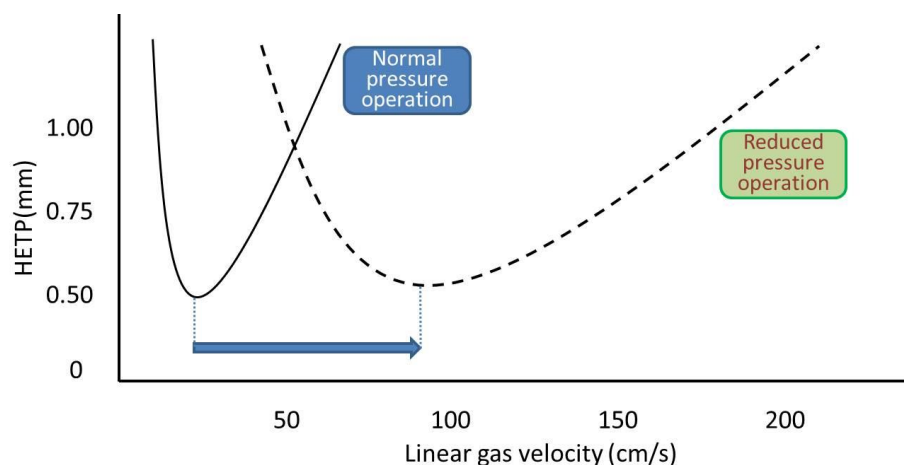


**Figure E5. Van Deemter plots of 0.53 mm columns under pressurized and vacuum conditions for He as carrier gas.**<sup>359</sup>

In practice, this optimal velocity, using a 0.53 mm column operated at reduced pressure lies a factor of four higher than when using GC columns under normal pressures (i.e. using 0.25 or 0.32 mm columns, having optimal velocities around 25 cm/s), resulting in flow-rates of 90–100 cm/s for helium used as carrier gas. With these velocities and while using a shorter column (10 m instead of 30 m) the reduction of the analysis time by a factor of 10 is theoretically possible. Practically, however, this factor could only be reached for isothermal analyses. For thermally programmed GC analyses, lower reduction factors (i.e. factors around 3–7) were obtained.<sup>361</sup>

As it is well known, when the column dimensions and the pressure difference between inlet and outlet are constant, the volumetric flow of a carrier gas is dictated by the column oven temperature, and during a gradient temperature program, if pressure programming is not employed, the carrier flow rate can slow down appreciably. Hydrogen maintains high efficiency over a wide range of flow rates and temperatures, since it has the flattest van Deemter profile (lowest plate height, highest efficiency) over the widest range of linear gas velocities. That makes it the most appropriate carrier gas for capillary chromatography,

followed by helium and nitrogen respectively. In addition, the use of hydrogen carrier gas results in higher optimum velocities as well as even lower optimum inlet pressures than those obtained with helium.<sup>362</sup> However, when helium is used as carrier gas and while the MS creates a vacuum inside the wide-bore column, the viscosity of He is reduced (shifting the optimal flow rate to greater velocities), providing H<sub>2</sub>-like properties.<sup>360,363</sup>

The optimal velocity of around 90–100 cm s<sup>-1</sup> for helium was found by de Zeeuw *et al.*<sup>354</sup>, using a 10 m x 0.53 mm CP-Sil 5 CB column with a restriction at the inlet and a quadrupole MS as detection device. It is obvious that such high velocities will result in very short analysis times. Normally under these high-speed conditions the eluting peaks are very narrow and there is a problem in peak determination due to the limited speed of data rate collection. However, the peaks that elute from a 0.53 mm i.d. column are relatively broad, leading to a sufficient data collection rate when they are used under vacuum-outlet conditions, and thus MS scan rate does not have to be faster than that commonly used in conventional GC-MS systems.

Because of the high linear velocity, peaks are not only eluting quicker, but are also relatively high. Higher peaks results in better signal to noise ratios (S/N), with improvements by a factor of around three having practically been achieved.<sup>354,359</sup> Correspondingly the detection limits of the method are also reduced. For this reason, implementation of this technology can make screening analysis at low analyte levels much faster.

When the vacuum outlet technique is used, the sample components are measured, identified and quantified at much lower temperatures, achieving a rapid separation with reduced oven cool-down times. De Zeeuw *et al.*<sup>354</sup> have reported elution temperatures which can be 50–70 K lower as compared with normal pressure operation. Thus, this technology enables the analysis of thermally labile compounds (e.g. drugs in the pharmaceutical industry), which used to be analyzed via liquid chromatography, but now, in combination with the higher flow rates and the reduced time of residence both in the injector and in the column, exhibit reduced degradation. The lower elution temperatures will also allow heavy components to elute in shorter time, improving analysis time and sensitivity. In addition, a lower elution temperature will generate less stationary phase bleed, providing better mass spectra (with higher S/N) and reduced risk of pollution of the ion source.

The 0.53 mm column will additionally provide larger sample capacity as compared to a narrow-bore column, owing to the fact that thicker stationary phases are used. Moreover, the low pressure in the LP-GC-MS analytical column slightly affects the vaporization temperature of the solvent and reduces its condensation.<sup>335</sup> Thus, larger volume injections in solvent could be made, as long as the liner is not flooded, which is of particular interest if traces have to be analyzed. However, an inherent factor with large volume injection is that the cleanliness of the injected sample limits injection volume more than the technical ability to inject larger volumes. Gains in detectability are made as more of the sample is injected

only to the extent that matrix interferences are not the limiting source of noise.<sup>335</sup> Generally, the efficiency of capillary columns operated at low pressure is lower than predicted from theory. Under vacuum-outlet conditions, the number of theoretical plates will be about 30-40% lower, compared with the theoretical plate number of an atmospheric outlet.<sup>354</sup> However, the separation conditions are not optimized in terms of separation power (we have the selectivity of the MS for that), but to make the technique workable.

Summarizing, LP-GC-MS in comparison to conventional GC-MS offers improvements in terms of shorter run times, increased sample loading (due to thicker film) and greater sensitivity, earlier elution of less volatile compounds and reduced thermal degradation (due to higher flows), reduced peak tailing, and increased ruggedness (due to wider columns and thicker films). In addition, it does not require special adaptation on the injection or detection side of the instrument, which represents a significant advantage in comparison to the other fast chromatographic procedures. The only compromise is in separation efficiency, but the greater selectivity of MS can overcome that sole disadvantage.<sup>360</sup>

Furthermore, considering the validation results produced by Walorczyk and Gnusowski<sup>364</sup>, important advantages of LP-GC versus conventional GC can be identified. The LP-GC technique was found to be superior over the conventional GC with respect to linearity, accuracy and precision parameters. The lower limits of detection, achievable by the LP-GC with the MS detector in all data acquisition modes (scan, single ion monitoring (SIM) and MS/MS), allows the presumption that LP-GC based methods (especially those utilizing highly sensitive and specific MS/MS detection mode) might be of practical value in application areas requiring reliable determination at very low concentration levels, e.g. the analysis of pesticides in baby foods.

#### ***E.2.4. Comparison of wide-bore and micro-bore columns for vacuum outlet applications***

As it was already mentioned, one of the parameters that can be optimized in order to provide faster GC methods is the internal diameter of the capillary. Table E2 summarizes the dependence of various chromatographic parameters on the diameter of the column.<sup>349</sup> In order to explain the choice of wide-bore columns for the development of a fast GC-MS method for our research work, the major advantages and restrictions of both wide-bore and micro-bore columns are demonstrated and discussed below.

**Table E2. Summary of the dependence of various chromatographic parameters on the characteristic diameter of the capillary in high speed GC applications.<sup>349</sup>**

Parameter	Dependence on capillary diameter $d_c$
Analysis time	$d_c$
Pressure drop	$1/d_c$
Sample capacity	$d_c^3$
Volumetric flow-rate	$d_c$
Temperature programming rate (r)	$1/d_c$

One seemingly promising approach, commonly referred to as “Time Compressed Chromatography” (TCC), couples micro-bore-based fast GC with time-of-flight fast mass spectrometry, thereby enabling fast GC-MS.<sup>365</sup> The option of using a TCC-GC-TOF-MS method for achieving fast chromatography is based on the increased number of theoretical separation plates (per unit length) associated with the reduction of the capillary column internal diameter, and leads to increased GC resolution. But, as Amirav *et al.*<sup>365</sup> have discussed when comparing mega-bore with micro-bore GC columns, when a 0.53 mm i.d. column is compared with a 0.1 mm i.d. one of similar length, the gain in resolution is only a factor of 2.3 (i.e. the square root of the column diameter ratio) and is also counteracted by the limited capacity of the micro-bore column. Since the sample capacity relates to the column diameter to the power of 3 (approximately), the micro-bore column is easily overloaded, showing peak fronting that reduces its practical resolution in some cases. It also shows limited measurement dynamic range, is more susceptible to injection broadening, ion source related peak tailing and even the appearance of ghost peaks due to column performance deterioration. In addition, it is commonly asserted that, since very narrow GC peak widths are associated with time compressed fast GC-MS, time-of-flight mass spectrometry must be used for fast GC-MS when micro-bore capillaries are used.<sup>366</sup>

When a mega-bore column, having an internal diameter of 0.53 mm, is replaced by a micro-bore column with an internal diameter of 0.10 mm, a reduction of the column length by a factor of 5.3 without losing chromatographic resolution is possible.<sup>365</sup> Furthermore, if the temperature programming rate is increased by the same factor and the column flow rate is reduced by a factor of 28 (keeping the same carrier gas velocity), then the chromatography time will be reduced (“compressed”) by a factor of 5.3, while identical resolution is maintained.<sup>365</sup> Moreover, vacuum outlet GC-MS with wide-bore columns produces, as it was already mentioned, broader peaks with typical peak widths at the base of 1.6 s (for a component with  $k=3$ ), compared with 0.28 s for a 3 m x 0.10 mm i.d. column.<sup>361</sup> And that makes it possible to use a conventional, lower cost ion trap or quadrupole analyzer as the mass spectral detector.

According to some further considerations about the micro-bore columns, the column head pressure which they require is higher by a factor equal to the square root of the column diameter reduction (after the

length reduction).<sup>365</sup> This increase in head pressure results in higher average gas density and lower optimal carrier gas velocity in the micro-bore column, and this effect is more pronounced with GC-MS as a result of its vacuum outlet. The chromatography time is therefore reduced by a factor which is less than the reduction of the column length.<sup>365</sup>

In order to obtain maximum separation, most gas chromatographic analyses are performed with temperature programming of the GC oven. While this programming rate can be increased, the GC oven cooling rate is at its maximum value and cannot be time compressed. As a result, the time required to initiate the next analysis, which can be a few minutes, cannot be reduced, adding another limiting factor to the use of narrow-bore columns.<sup>365</sup> On the other hand, with larger column diameters and their aforementioned ability of higher flow rates, a higher initial GC oven temperature, a smaller temperature programming range and thus a shorter time between the end of one analysis and the beginning of the next one are possible. Higher flow rates, available with mega-bore columns during injection and analysis also facilitate splitless on-column injections, providing effective handling capabilities for thermally labile compounds, as well. Amirav *et al.*<sup>365</sup> demonstrated that when a micro-bore column is used, the injection rate is reduced by a factor of 28 along with the column flow rate, and compared with a similar length mega-bore column, the peak width is narrower by a factor of 2.3, requiring a further increase in the split flow by this factor in order to prevent injection-related peak broadening and to retain the achievable chromatographic resolution. As a result, the amount injected with a micro-bore column must be reduced by a factor of 65 ( $2.3 \times 28$ ) in comparison to the amount injected on a mega-bore column, leading to a severe sacrifice of the minimum detectable concentration (MDC), the most important parameter when not only the speed but also the sensitivity of an applied method is an issue.

Evaluating again the speed of both techniques, mega-bore columns allow flow programming on a wide range of flows, which, unlike temperature programming, can be reset in a fraction of a second and thus allow faster analyses. This is not an option for micro-bore columns, due to the very high impedance (proportional to the diameter to the fourth power) that they impose, and thus result in a very limited benefit from the flow programming.<sup>365</sup>

For all the above-mentioned reasons, large column working ranges and detectability of low minimum analyte concentrations require the use of wide-bore columns. However, narrow-bore thin-film columns are preferable when low absolute detection limits are to be achieved and suitable instrumentation is available.

367



### E.2.5. Vacuum Outlet Applications

As it was already mentioned at the beginning of this section, one of the basic goals in routine monitoring of sample categories like pesticide residues and drugs by regulatory and private contract laboratories is to attain quick sample turnaround time and high sample throughput. In addition to being fast, useful methods must also achieve high quality results for a wide scope of analytes and matrices, have excellent robustness for routine use, meet low detection limits and be affordable, simple to perform, environmentally friendly and safe.<sup>368</sup>

Despite the many advantages and demonstrated feasibility of LP-GC-MS in the literature by several researchers, it was not widely implemented for routine monitoring analysis for many years. Commercial patent issues<sup>369</sup> have been one reason for this, but since the patent was not renewed, other vendors were free to market the approach. Additionally, the introduction of UHPLC-MS/MS may have also led to aroused interest for faster separations also in gas chromatography. As a matter of fact, after the UHPLC-MS/MS started being commonly employed, instrument manufacturers took a renewed look at LP-GC-MS.<sup>368</sup>

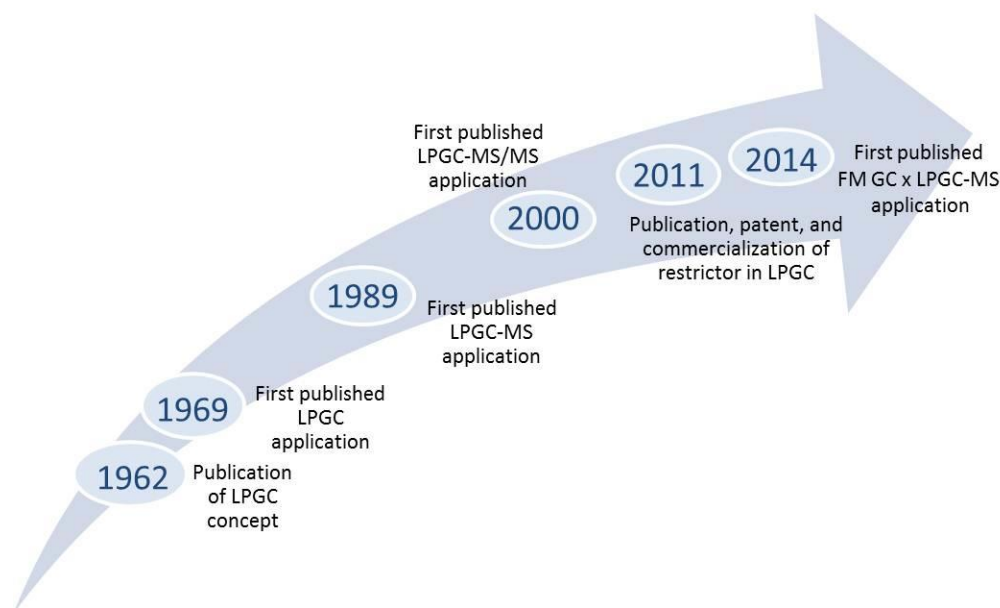


**Figure E6. Graphical summary of the milestones in LP-GC. (Graph reproduced and extended from Reference<sup>370</sup>)**

In the past few years, the application of vacuum GC has been developed and optimized successfully for the rapid analysis of pesticides and metabolites<sup>(332,335,337,364,371-395)</sup>, polycyclic aromatic hydrocarbons (PAHs)<sup>387,395,396,397</sup> and other hydrocarbons<sup>354</sup>, fragrances (from plant and flower essential oils)<sup>398,399</sup>, organotin compounds<sup>400</sup>, pharmaceutical products<sup>401</sup>, steroid estrogens<sup>402</sup>, phytosterols, polyphenolic

compounds and natural antioxidants<sup>403</sup>, flame retardants (FR), like polybrominated diphenyl ethers (PBDEs)<sup>387,394,395,404,405</sup>, persistent organic pollutants (POPs), like polychlorinated biphenyls (PCBs), and other semi-volatile organic compounds (VOCs)<sup>406,395</sup>, as well as in the impurities profiling of explosives<sup>362</sup>, like trinitrotoluene (TNT)<sup>407</sup>. As illustrated in Figure E7, LP-GC-MS has proven to provide the greatest speed of analysis when compared with other practical GC methods applied for the determination of pesticides.<sup>370</sup> However, it should be mentioned that if we consider the number of theoretical plates that can be achieved in a given time, then GCxGC is certainly the most successful technique.

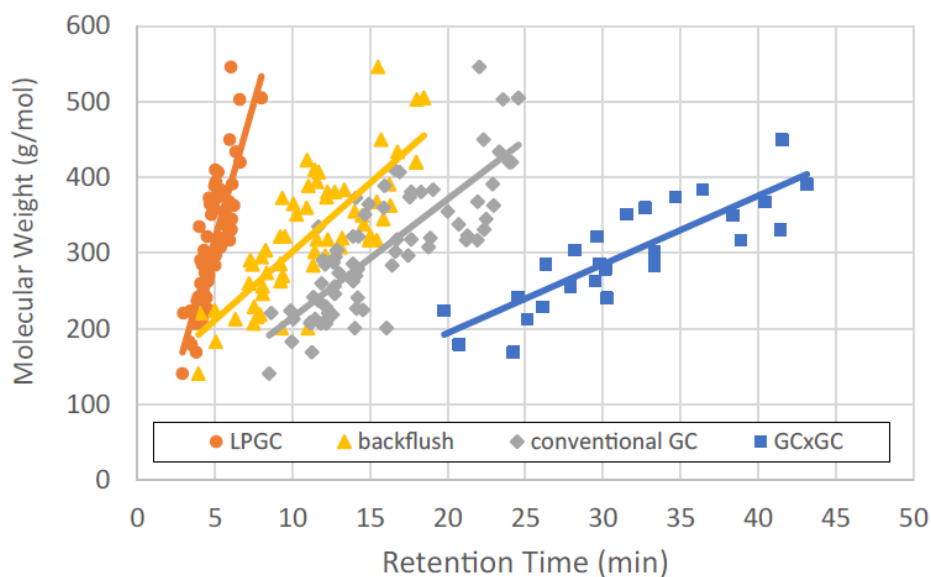


**Figure E7. Comparison of retention times vs. molecular weights of pesticides in 4 different published GC(xGC)-MS(/MS) methods.<sup>370</sup>**

All these applications demonstrate that a fast GC-MS method without the need of additional instrumentation can be performed, enabling sensitive measurements that will be the future to even more fields of applications. Therefore, the vacuum outlet GC-MS technique as a potential analytical approach in the determination of gaseous emissions was selected for investigation.

The renewed interest of the analytical society in the vacuum outlet has been demonstrated, with our work on conventional LP-GC systems<sup>408,409</sup> and the application of VO at comprehensive two-dimensional gas chromatographic systems by Tranchida *et al.*<sup>410</sup>, belonging to the most recent publications on LP-GC. Concerning the latter publication, combination of GC x GC with the VO, not only utilized the advantages of LP-GC, but also compensated the drawback of flow modulation (FM) GC x GC, referring to the high gas flows required. That was partially accomplished by the use of a long accumulation loop, while a wide-bore column (10 m × 0.53 mm ID) was used for the second dimension. The restrictor (1.5 m × 0.25 mm ID) was used between the flow modulator and the second dimension, and the low-pressure conditions

were generated by connecting the outlet of the secondary column to a rapid-scanning quadrupole mass spectrometer (qMS). A key feature of the cryogenic modulation is the generation of very narrow analyte plugs that are suitable for very fast analysis on a short micro-bore column in the second dimension. However, using a flow modulator equipped with a loop the concentration profiles are maintained during the accumulation period. Such a factor can have a negative effect on peak shape, the improvement of which when LP-GC-MS is applied has already been discussed. The successful merge or vacuum outlet and GC x GC was proven by the application of FM GC x LP-GC-qMS in pure standard compounds, as well as in milk and fish oil fatty acid methyl esters (FAME).

Additional considerations about the optimization of both most time-consuming steps, the sample preparation and the analysis, led to the combination of LP-GC-MS with different sample preparation procedures. With the pesticide residues analysis governing the LP-GC applications (Figure E8), several sample preparation procedures have been followed, with the beneficial pre-concentration method called QuEChERS (which stands for “quick, easy, cheap, effective, rugged, and safe”) providing even quicker overall analysis times.<sup>358,368,377,380, 384,385,388,389,395</sup> Alternatively, the combination of SPME and LP-GC-MS gives an environmentally friendly and time efficient method with high sensitivity and selectivity, avoiding clean-up steps and reducing sample manipulation.<sup>374</sup> The advantages of a SPME-LP-GC-MS system drove our investigations to combining these techniques for the determination of UV filters in swimming pool water samples.

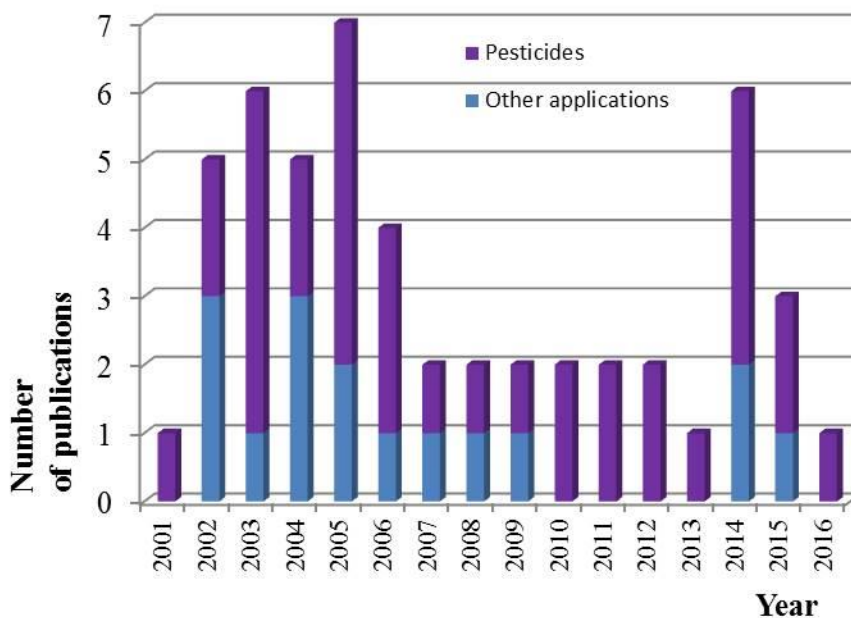


Figure E8. LP-GC-MS applications.

## ***F. Investigations on the optimization parameters of vacuum outlet systems for the determination of highly volatile compounds***

### ***F.1. Introduction***

Emphasizing on highly volatile compounds, and therefore investigating the applicability of VO for the analysis of gases and other volatile species emitted from LIBs, a standard mixture containing six volatile compounds was selected for the optimization of the parameters affecting the separations under VO conditions. The contribution of not only the pre-column, but also the analytical column dimensions was investigated. Starting with the pre-column, four different inner diameters were selected, while the length of the restriction was also examined. Concerning the analytical column parameters, the optimisation was focused on the length of the column and the film thickness, with two different GC columns being tested. For each column setup the optimum inlet pressure and isothermal temperature were experimentally defined, based on the calculated number of theoretical plates corresponding to the compounds under investigation. Comparison of the performance of a VO column setup used under vacuum outlet (GC-MS) and atmospheric outlet (GC-FID) conditions was then performed, together with a correlation study of the experimental results with those obtained by dedicated software, for both outlet conditions.

### ***F.2. Materials and Methods***

#### ***F.2.1. Chemicals and reagents***

The compounds selected for VO method optimization are typical solvents used for liquid phase GC measurements, with their characteristic parameters listed in Table F1. Mentioned according to their elution order, a mixture of iso-propanol, hexane, chloroform, cyclohexane, iso-butanol and heptane at a concentration of 1 mg/ml was prepared, using methanol as solvent. The HPLC-grade methanol used was purchased from Sigma Aldrich.

**Table F1. List of standards used for LP-GC-MS method optimization.**

Compound Name	Chemical Formula	Cas No	Supplier	MW (g/mol)	b.p (°C)	Density (g/cm <sup>3</sup> )
Chloroform	CHCl <sub>3</sub>	67-66-3	Sigma-Aldrich	119.37	61.2	1.489
Iso-propanol	C <sub>3</sub> H <sub>8</sub> O	67-63-0	Fluka	60.10	82.6	0.786
Iso-butanol	C <sub>4</sub> H <sub>10</sub> O	78-83-1	Riedel-de-Haën	74.12	107.9	0.802
Cyclohexane	C <sub>6</sub> H <sub>12</sub>	110-82-7	Sigma-Aldrich	84.16	80.7	0.778
Hexane	C <sub>6</sub> H <sub>14</sub>	110-54-3	Fluka	86.18	68.5	0.655
Heptane	C <sub>7</sub> H <sub>16</sub>	142-82-5	Fluka	100.21	98.4	0.680

Since the biggest part of the measurements was performed by manual injections, the selected group of analytes was chosen aiming the highest possible stability of the sample concentration and the minimum possible losses during the sample handling. Those facts restricted our group of compounds to species with relatively lower volatilities than the intended ones for our application, ensuring though more reliable results and subsequent conclusions.

### ***F.2.2. Instrumentation and operating conditions***

The first sets of LP-GC-MS experiments were performed after manual injection of the samples at a Shimadzu GC-2010 (Shimadzu Corp., Kyoto, Japan) equipped with a split/splitless injector. Another Shimadzu GC system, equipped with an Optic 3 high performance injector (GL Sciences Inc., Torrance, CA, USA) and a Shimadzu AOC-5000 Plus Autosampler, was later used for both the LP-GC-MS and the GC-FID measurements. The autosampler, as expected, contributed to the reproducibility of the measurements, while saving time and workforce.

Two wide-bore analytical columns of different film thickness were tested. Considering that the application of the technique would target highly volatile compounds, a thicker film DB-624 column was initially used. With this GC column, the investigations on the restriction parameters were performed. This mid polarity fused silica capillary column, with a 6% Cyanopropyl-phenyl / 94% dimethyl polysiloxane stationary phase (Cat. No. 125-1314, Ser. No. USC644923B, J&W Scientific Inc., Folsom, CA, USA), had a length of 15 m, which was later reduced to 10 m, an inner diameter of 0.53 mm and a film thickness of 3 µm. The second analytical column used had the same phase composition as the DB-624 and was a 15 m x 0.53 mm x 1 µm d<sub>f</sub> RTX-1301 column (Cat. No. 16052-QA; Ser: No. 1251664, Restek, Bellefonte, PA, USA).

For the optimization of the pre-column dimensions, several length and width combinations of deactivated fused silica capillary columns were tested, as illustrated in Table F2. As mentioned before, these investigations were performed exclusively with the thicker film DB-624 column. The thinner film RTX-1301 was only tested with a 4 m x 0.10 mm restriction. For the GC-FID measurements, the 5 m x 0.15 mm restriction was used.

**Table F2. Restriction dimensions investigated.**

Restriction No	Length (m)	Inner Diameter (mm)
1	5	0.10
2	4	0.10
3	3	0.10
4	2	0.10
5	1	0.10
6	1	0.075
7	1	0.05
8	0.5	0.05
9	5	0.15

For all the investigated column setups, the restriction was connected to the analytical column through a Supelco capillary butt connector with a graphite-vespel ferrule, like the one illustrated in Figure F1.

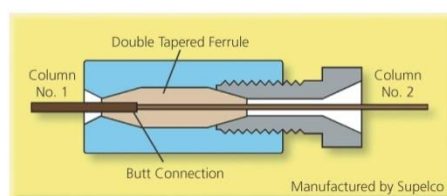


**Figure F1. Cross-section of a Supelco capillary butt connector using a graphite-vespel ferrule.<sup>411</sup>**

Helium (purity > 99.999%, Messer, Gumpoldskirchen, Austria) was always used as carrier gas. The GC injector was operated using a 1:100 split at 250°C. The injection volume was 1 µL and isothermal elution at 30°C, 40°C, 50°C and 60°C was applied. Only when the RTX-1301 column was used, the applied temperatures started again from 30°C and went up to 90°C. The constant pressure mode was selected, while the inlet pressure was set to a value ranging from 25 kPa to 700 kPa. For the GC-FID measurements the same four temperatures were applied for isothermal elution of the analytes, while the inlet pressure range used was 25 kPa – 400 kPa. As makeup gas, a N<sub>2</sub>/air mixture was used at 30.0 ml/min. The air flow was set to 400.0 ml/min and the hydrogen flow to 40.0 ml/min, while the detectors temperature was 200°C and the sampling rate was 4 ms.

Mass spectrometric detection was performed using a Shimadzu GCMS-QP2010 Plus for the initial LP-GC-MS experimental setups and a GCMS-QP2010 Ultra for all other measurements performed. The temperatures used for the transfer line and the ion source were set to 250°C and 200°C, respectively. Positive ion detection mode was used. Mass spectra were acquired in the electron impact ionization mode at 70 eV. The measurements were performed in full scan mode using the m/z range of 15-450. Only for the measurements performed at 90°C the scan range was restricted to 30-450 m/z, in an attempt to lower the background signal. Peak parameters for the target analytes were calculated by the GCMSsolution (Shimadzu Corporation, version 2.70) software. The theoretical values for the vacuum outlet (MS) and atmospheric outlet (FID) comparisons were calculated with the GC×GC Calculator - MS (Version 1.21: 19-08-2005) and GC×GC Calculator – FID (Version 2.2: 08-08-2005), respectively.<sup>412</sup>

### ***F.3. Results and Discussion***

In order to identify the optimum conditions for the separation of the investigated compounds using a vacuum outlet GC/MS system, different column setups were tested. For each setup, isothermal elution was performed at different temperatures (mainly 30, 40, 50 and 60°C, but also 70, 80 and 90°C for one particular setup), while for each temperature a range of inlet pressures was tested. This range included pressures from 25 kPa up to 700 kPa, although the upper value tested depended on the pre-column parameters and the temperature conditions applied, as demonstrated later on, in the detailed presentation of the results.

For the analysis of highly volatile compounds, the use of a thicker film capillary column is necessary. It is generally accepted that increasing the film thickness enhances the retention and improves the resolution of volatile analytes. This effect is particularly important when wide-bore columns are used, because the inner diameter of a wide-bore column reduces the trapping efficiency for volatile compounds.

A column targeting the analysis of volatiles should have a phase ratio of less than 100. Since this value is calculated dividing the inner diameter of the column (in microns) by the film thickness multiplied by four [ $\beta = (\text{i.d.}) / (4 \times d_f)$ ], efficient trapping of volatiles using wide-bore columns can only be performed when the film thickness is higher than 1  $\mu\text{m}$ . The more typical film thickness of 1  $\mu\text{m}$ , used in many vacuum outlet applications, would result in a phase ratio closer to what is expected for normal operating conditions and would not provide the optimum trapping and separation conditions required for our intended application. However, the vacuum outlet was generally selected for applications concerning less volatile compounds, for which wide-bore columns without excessively thick films were required. Nevertheless, a 1  $\mu\text{m}$   $d_f$  capillary column was also used for comparative reasons in this study.

Although a thicker film wide-bore column may be advantageous for the analysis of volatiles, that higher film thickness is expected to result in a significant contribution of the mass transfer coefficient in the stationary phase ( $C_{sp}$ ). Such an increase in the value of the mass transfer coefficient would change the slope of the Golay equation towards higher values and compromise the benefits provided by the vacuum outlet conditions, as illustrated in Figure F2. However, the extent of these antagonistic contributions has not been yet investigated. The Golay equation is used below, since only capillary columns were tested. The formulae of the longitudinal diffusion and mass transfer terms are also presented in Figure F2.

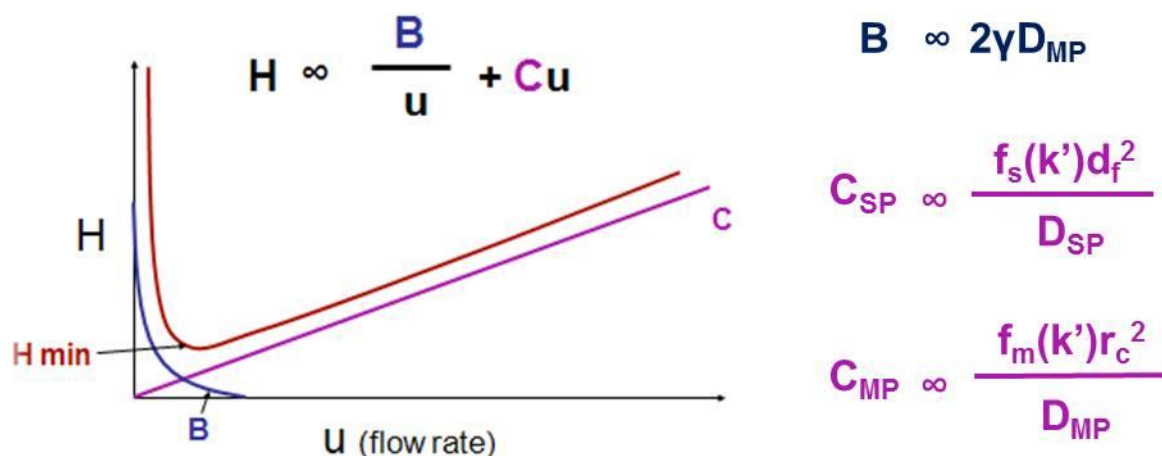


**Figure F2.** The Golay equation and curve for gas chromatographic systems using capillary columns and the formulae of the longitudinal diffusion and mass transfer terms, where **B**: longitudinal-diffusion; **C<sub>SP</sub>**: mass transfer coefficient in the stationary phase; **C<sub>MP</sub>**: mass transfer coefficient in the mobile phase; **D<sub>MP</sub>**, **D<sub>SP</sub>**: diffusion coefficients in the m.p./s.p.; **k'**: capacity factor ( $t_R/t_M$ ); **d<sub>f</sub>**: thickness of the liquid film of the s.p.; **f<sub>(x)</sub>**: function of the x; **γ**: labyrinth factor of the pores in the s.p.; **r<sub>c</sub>**: capillary radius.

The selected experimental setups provided us with the necessary analytical data for the construction of the equivalent of the Golay curves, for which the inlet pressures were used in the x-axis instead of the flow rate or the average linear velocities. The linear velocities or flow rates were not used, since it is impossible to practically measure the outlet flow when no open end is available. These values could only be calculated using dedicated software (like the Agilent Flow Calculator used in our case). However, we tried to check the validity of these estimations using the experimental hold up time observed for particular analytical conditions and for one of the investigated column setups, with the results being controversial. Table F3 summarizes the calculated results, proving that for 30°C, 100 kPa and keeping the holdup time stable, when the length or the inner diameter of the columns used in that particular column setup were selected, huge differences in the flows and corresponding average velocities appeared. In particular, for the vacuum outlet system where the inner diameter of the retention gap (0.150 mm) was selected (case #1), the corresponding length of the equivalent column providing a holdup time of 0.54 min was equal to about 13 m, while an average velocity of 40 cm/s was theoretically achieved. However, when the inner diameter of the analytical column was used (0.53 mm, case #2), a 47 m equivalent column was proposed, which would result in an average velocity of more than 140 cm/s. In the last case, where the overall length of both the retention gap and the analytical column was used, the theoretically equivalent inner diameter was 0.217 mm, providing an average velocity of about 60 cm/s. The diversity of the calculated values proves that such approximations lead to controversial setups in terms of equivalent column dimensions. Each setup results in significantly different flows and average velocities, with no possible proof available



for the set that provides the more realistic values. The only observation made for these approximations is that the restriction offers the more prominent contribution in the resulting flow and average velocity values, with the results in cases 1 and 3 having a closer correlation.

**Table F3. Theoretical values (highlighted with bold) provided by the Agilent Flow Calculator for the experimental setup of a 5 m x 0.15 mm pre-column & a roughly 15 m x 0.53 mm x 3  $\mu\text{m}$   $d_f$  analytical column, used at 30°C and for 100 kPa inlet pressure.**

Case #	Holdup Time (min)	Length (m)	Inner Diameter (mm)	Flow (ml/min)	Average Velocity (cm/s)
1	0.54	<b>13.27</b>	0.150	<b>0.56</b>	<b>40.6</b>
2	0.54	<b>46.92</b>	0.530	<b>24.75</b>	<b>143.5</b>
3	0.54	19.20	<b>0.217</b>	<b>1.70</b>	<b>58.8</b>

In Table F4 are also summarized the results from the calculations for the restriction and the analytical column separately. However, adjustment of the values was performed so that the calculated inlet pressure for the analytical column was used as the outlet pressure for the restriction. In that case, the negative value for the inlet pressure of the analytical column (-74 kPa) corresponds to the difference from the atmospheric conditions expected. Since one atmosphere is equal to 101.3 kPa, or roughly 100 kPa, the difference between 1 atm and vacuum would be equal to approximately 26 kPa, set as the outlet pressure of the restriction. However, the holdup times provided for each column, with a sum that also differs from the experimental value, demonstrate again the bias that could occur if any linear velocities were used in the Golay plot instead of the actual experimental values provided for the inlet pressures.

**Table F4. Theoretical values provided by the Agilent Flow Calculator for the restriction and the analytical column at 30°C.**

<i>Restriction</i>		<i>Analytical Column</i>	
Length (m)	5.00	Length (m)	14.20
Inner Diameter (mm)	0.15	Inner Diameter (mm)	0.53
Film Thickness ( $\mu\text{m}$ )	0	Film Thickness ( $\mu\text{m}$ )	3
Temperature ( $^{\circ}\text{C}$ )	30	Temperature ( $^{\circ}\text{C}$ )	30
Inlet Pressure (kPa)	100	Inlet Pressure (kPa)	-73.76
Outlet Flow (ml/min)	1.465	Outlet Flow (ml/min)	1.465
Average Velocity (cm/s)	104.517	Average Velocity (cm/s)	63.466
Outlet Pressure	26.00 kPa	Outlet Pressure	Vacuum
Holdup Time (min)	0.08	Holdup Time (min)	0.37

Summarizing the results obtained for each column configuration, the corresponding surface plots were constructed, illustrating the overall best temperature-inlet pressure combinations in terms of number of theoretical plates. The parameters optimized were the dimensions of the restriction and the analytical column. Mentioned in chronological order, the inner diameter and the length of the retention gap were the first to be optimized using the same analytical column. Then, the length of the analytical column was also reduced, checking how much the pressure drop at the beginning of the analytical column would affect the efficiency of the separations. The efficiency of the vacuum outlet separations in terms of height equivalent to a theoretical plate (HETP) and run time was then compared to that of atmospheric outlet system, provided by an FID detector. The experimental and theoretically expected values provided from each approach were put side by side, checking the extent at which the film thickness affects the simulations used for vacuum outlet and atmospheric outlet systems. The comparisons on the analytical column were concluded by testing a column of intermediate film thickness used under vacuum outlet conditions. These results were compared to the ones obtained with the thicker film column used initially, for the analysis of the same group of volatiles. The purpose of this final comparison was mainly to determine the optimum conditions for the separation of volatiles as well as to check the applicability and any possible limitations of the vacuum outlet technique when highly volatile compounds are targeted.

### ***F.3.1. Method optimization for thick-film wide-bore columns according to pre-column dimensions***

As mentioned before, the method parameters optimized were the temperature at which isothermal elution was executed and the inlet pressure. Having one parameter stable, the other one was changed, leading to sets of experiments, and consequently sets of methods, like the ones listed in Table F5. Similar sets of methods were used for the optimization experiments performed for all column setups, with the pre-column dimensions varying in terms of inner diameter and length. The same temperatures were used for every column setup, while the selected pressure ranges were subject to instrument tuning. Specifically, the entire range of pressures (namely from 25 to 700 kPa) was not applicable for all sets of pre-column dimensions and elution temperatures, but it was slightly varying, adapting to the performance of each system.

**Table F5. GC methods applied for the optimization of the first investigated VO column setup. The variations in the GC methods involved only the oven temperature and inlet pressure.**

Method No.	Oven Temp. (°C)	Inlet Pressure (kPa)	Method No.	Oven Temp. (°C)	Inlet Pressure (kPa)
1	<b>30</b>	<b>600</b>	13	<b>50</b>	<b>600</b>
2	<b>30</b>	<b>500</b>	14	<b>50</b>	<b>500</b>
3	<b>30</b>	<b>400</b>	15	<b>50</b>	<b>400</b>
4	<b>30</b>	<b>300</b>	16	<b>50</b>	<b>300</b>
5	<b>30</b>	<b>200</b>	17	<b>50</b>	<b>200</b>
6	<b>30</b>	<b>100</b>	18	<b>50</b>	<b>100</b>
7	40	600	19	60	600
8	40	500	20	60	500
9	40	400	21	60	400
10	40	300	22	60	300
11	40	200	23	60	200
12	40	100	24	60	100

The last change in each method concerned the total run time. Since an excessive number of experiments was required, with every method applied in triplicates and most of the measurements being executed after manual injection of the sample, the total run time was reduced close to the minimum time possible, in an attempt to decrease the overall time requirement. Consequently, care should be taken when judging the method performance by the obtained chromatograms shown in the dedicated figures, since no absolute overlay is possible. The main scope of these figures is to illustrate the separation efficiencies, while reduced retention times are always occurring when the temperature or the inlet pressure is increased.

In order to estimate the efficiency of each column setup and to find the optimum temperature and pressure conditions from the Golay equations, the number of theoretical plates (N) was calculated first. For compounds that are adequately resolved, N can be directly extracted from the software. However, when separation of the peak from the background or from neighbouring peaks is not possible, the extracted ion chromatograms were used, with the characteristic ions for every compound listed in Table F6. These ions were selected so that they are practically not present in adjacent peaks. This general criterion leads many times to the selection of ions that are not the most abundant. In such cases, when relatively small extracted ion peaks are selected, the use of a magnification factor is necessary, providing better observation properties to the peak.

**Table F6. Extracted ions used for each of the standard compound analyzed by LP-GC-MS.**

<b>Compound Name</b>	<b>Extracted Ion (m/z)</b>
Iso-propanol	45
Hexane	57
Chloroform	83
Cyclohexane	69
Iso-butanol	74
Heptane	71

But, also when the extracted ion peaks were evaluated, the same equation for the number of theoretical plates was used, as the one applied by the GCMSolution software<sup>413</sup>. That is the Equation F1, presented below, using the half peak height method. Since the peak width at half the peak height can be easily calculated by hand, it is the most widely used method. This is also the method used by the DAB (German Pharmacopeia), BP (British Pharmacopeia) and EP (European Pharmacopeia).

$$N = 5.54 \left( \frac{t_R}{w_{1/2}} \right)^2$$

**Equation F1. Formula for calculating the number of theoretical plates (N) according to the half peak height method, where  $t_R$  is the retention time of the peak and  $w_{1/2}$  is the peak width at half the peak height.**

As already mentioned, knowing the number of theoretical plates allows us to calculate the height equivalent to a theoretical plate (HETP or H), used for the construction of the Golay plots. The HETP is easily calculated by the Equation F2.

$$\text{HETP} = \frac{L}{N}$$

**Equation F2. Formula for calculating the height equivalent to a theoretical plate (HETP), where L is the length of the analytical column (mm) and N is the number of theoretical plates.**

Utilizing the HETP calculated for each compound and for every investigated inlet pressure, the corresponding Golay plots were constructed for the different investigated temperatures. Finally, the summarized data from all the experiments performed with every column setup were illustrated at surface plots, showing the optimum inlet pressure – isothermal elution temperature combinations for every analyte.

### F.3.1.1. Method optimization for a 0.10 mm i.d. pre-column

While for this set of experiments, the analytical column was always a 15 m DB-624 with 0.53 mm i.d. and 3  $\mu\text{m}$  film thickness, the first restriction used was a 5 m x 0.1 mm i.d. uncoated capillary. Then the length of the restriction was reduced stepwise to 4, 3, 2 and 1 m.

Starting with the pre-column having the entire 5-m length, the VO column setup was tested under different oven temperature and inlet pressure conditions. The obtained chromatograms are presented in Figure F3.

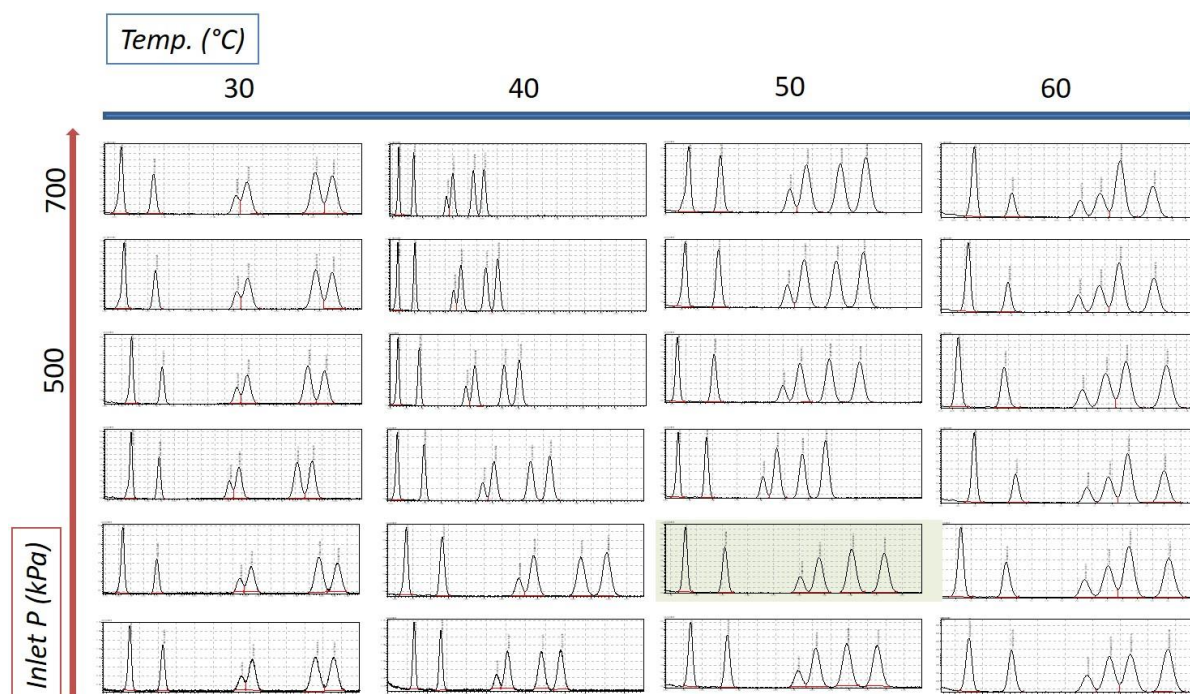


**Figure F3. LP-GC-MS Chromatograms produced with the 5 m x 0.10 mm pre-column and the 15 m x 0.53 mm x 3 $\mu\text{m}$  d<sub>r</sub> DB-624 analytical column after isothermal elution at 30, 40, 50 and 60 $^{\circ}\text{C}$  using inlet pressures between 200 and 700 kPa. The chromatogram corresponding to optimum conditions in terms of separation efficiency is marked with light green. The total runtimes had been in many cases optimized and are different for the chromatograms obtained with different methods. The scale for the intensities also differs among the chromatograms.**

As demonstrated by the corresponding chromatograms, in almost all the sets of different temperature- inlet pressure (T-P) combinations, the compounds are adequately resolved. For this reason, the number of theoretical plates could be directly extracted from the software. However, particularly the chloroform peak is in several chromatograms partially co-eluting with the peak for cyclohexane. In all the cases where baseline separation was not succeeded, the extracted ion peaks were used for manual calculation of the number of theoretical plates and the subsequent HETP values. The compounds that did not exhibit baseline resolution more frequently were chloroform, cyclohexane and iso-butanol. For reasons of consistency, when the extracted ion peaks were necessarily used for one or more of the compounds under

certain T-P combinations, then same conditions (the extracted ion peaks) were used for all measurements performed with the particular column setup for those compounds. It was clearly, though, demonstrated that when a peak was sufficiently resolved from its neighbouring ones, the calculated value for N was practically the same as the one obtained from the software (less than 2% difference). For this reason, our manual calculations were restricted to those certain compound peaks (without baseline resolution) and were not generally applied to the entire group of investigated compounds.

Summarizing the results extracted directly from the software and the ones requiring manual calculations, the Golay or the equivalent Van Deemter curves were plotted for every compound and for every investigated temperature. As previously discussed, for these plots the inlet pressure was used instead of the average linear velocity, avoiding the addition of any bias. Trend lines, marked with red colour, were also used to demonstrate the agreement of the experimental data with those produced by a second order (and in some rare cases a higher order) polynomial. The following figures present the Van Deemter plots obtained for the different compounds at 30, 40, 50 and 60°C (Figures F4 - F7).

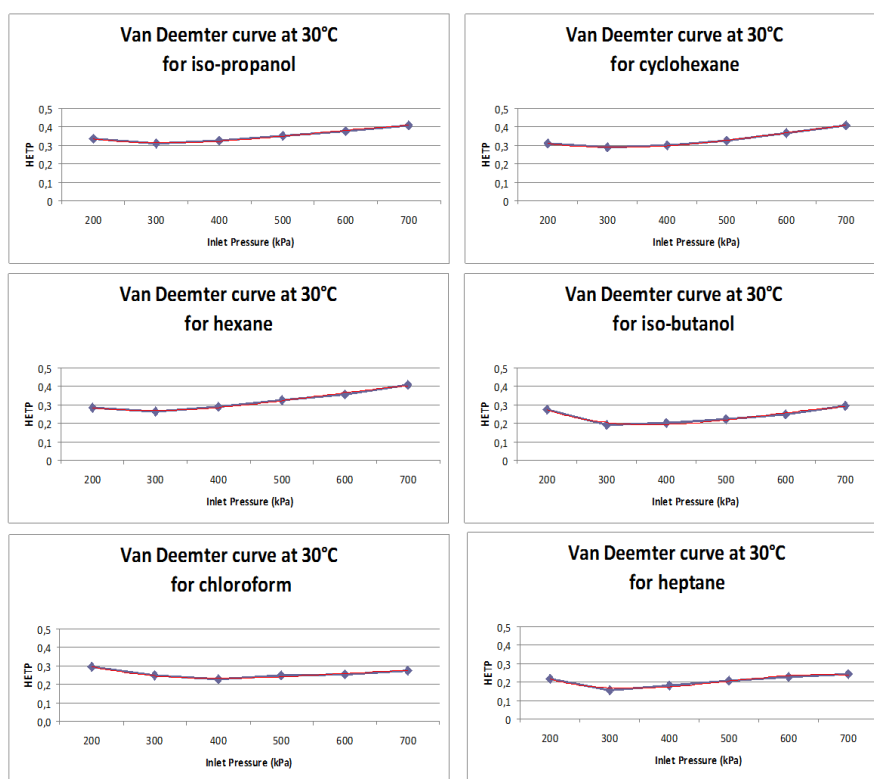


**Figure F4.** Van Deemter plots produced for the investigated compounds at 30°C, for measurements performed with the 5 m x 0.10 mm pre-column and the 15 m x 0.53 mm x 3µm d<sub>f</sub> DB-624 analytical column.

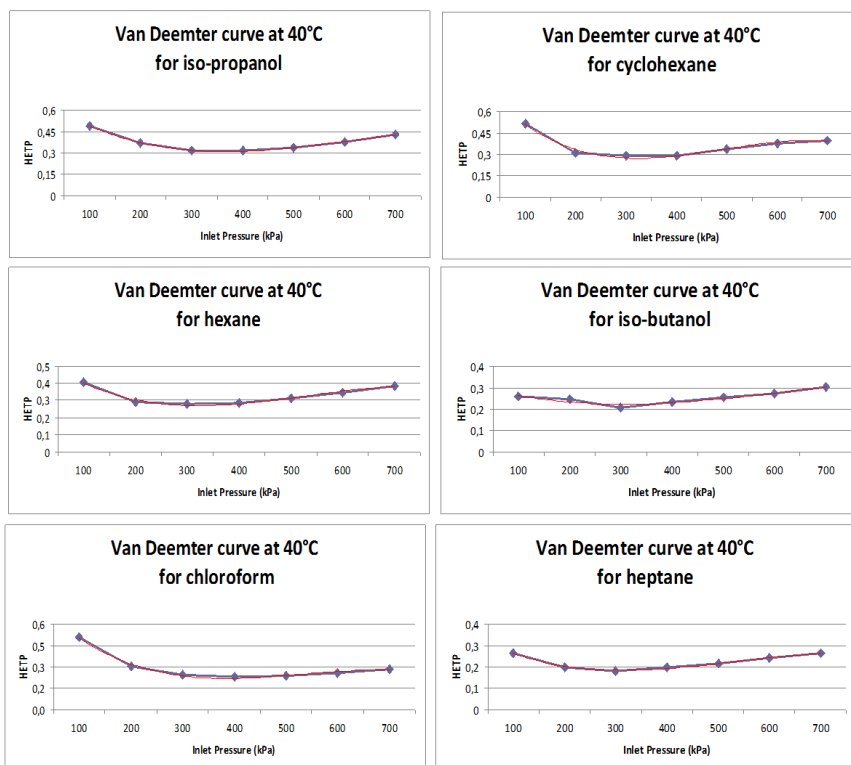


Figure F5. Van Deemter plots produced for the investigated compounds at 40°C, for measurements performed with the 5 m x 0.10 mm pre-column and the 15 m x 0.53 mm x 3 $\mu$ m  $d_f$  DB-624 analytical column.

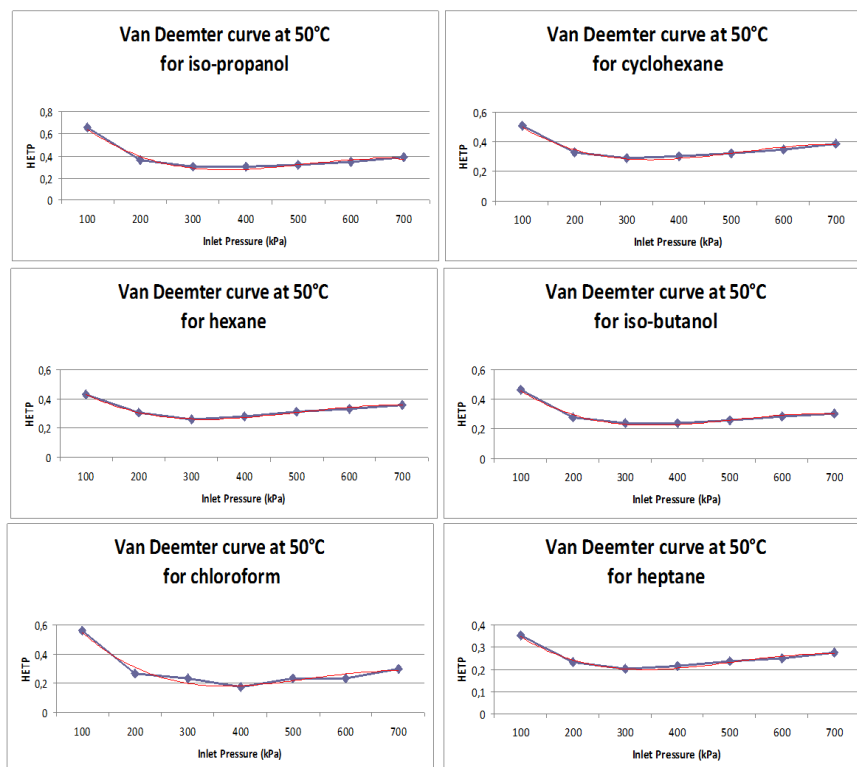
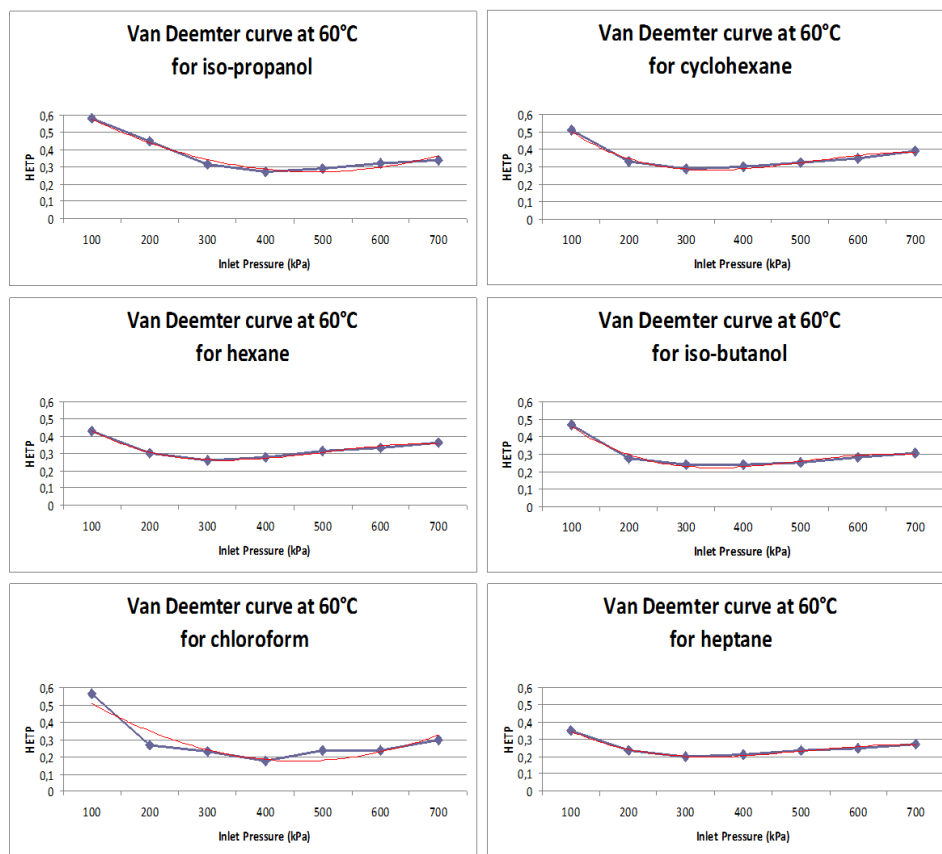


Figure F6. Van Deemter plots produced for the investigated compounds at 50°C, for measurements performed with the 5 m x 0.10 mm pre-column and the 15 m x 0.53 mm x 3 $\mu$ m  $d_f$  DB-624 analytical column.



**Figure F7. Van Deemter plots produced for the investigated compounds at 60°C, for measurements performed with the 5 m x 0.10 mm pre-column and the 15 m x 0.53 mm x 3 $\mu$ m d<sub>f</sub> DB-624 analytical column.**

The information about not only the optimum pressures, but also the optimum temperatures for the elution of each compound can be summarized in surface plots. In these plots, the x-axis represents the examined pressures, the y-axis the calculated number of theoretical plates and the z-axis refers to the temperature at which each experimental set was performed. Since the surface plots include the information provided by the corresponding Van Deemter plots, for the rest of the VO column sets only the surface plots will be presented. The corresponding surface plots for the first column setup investigated (using the 5 m x 0.10 mm restriction) are summarized in Figure F8.



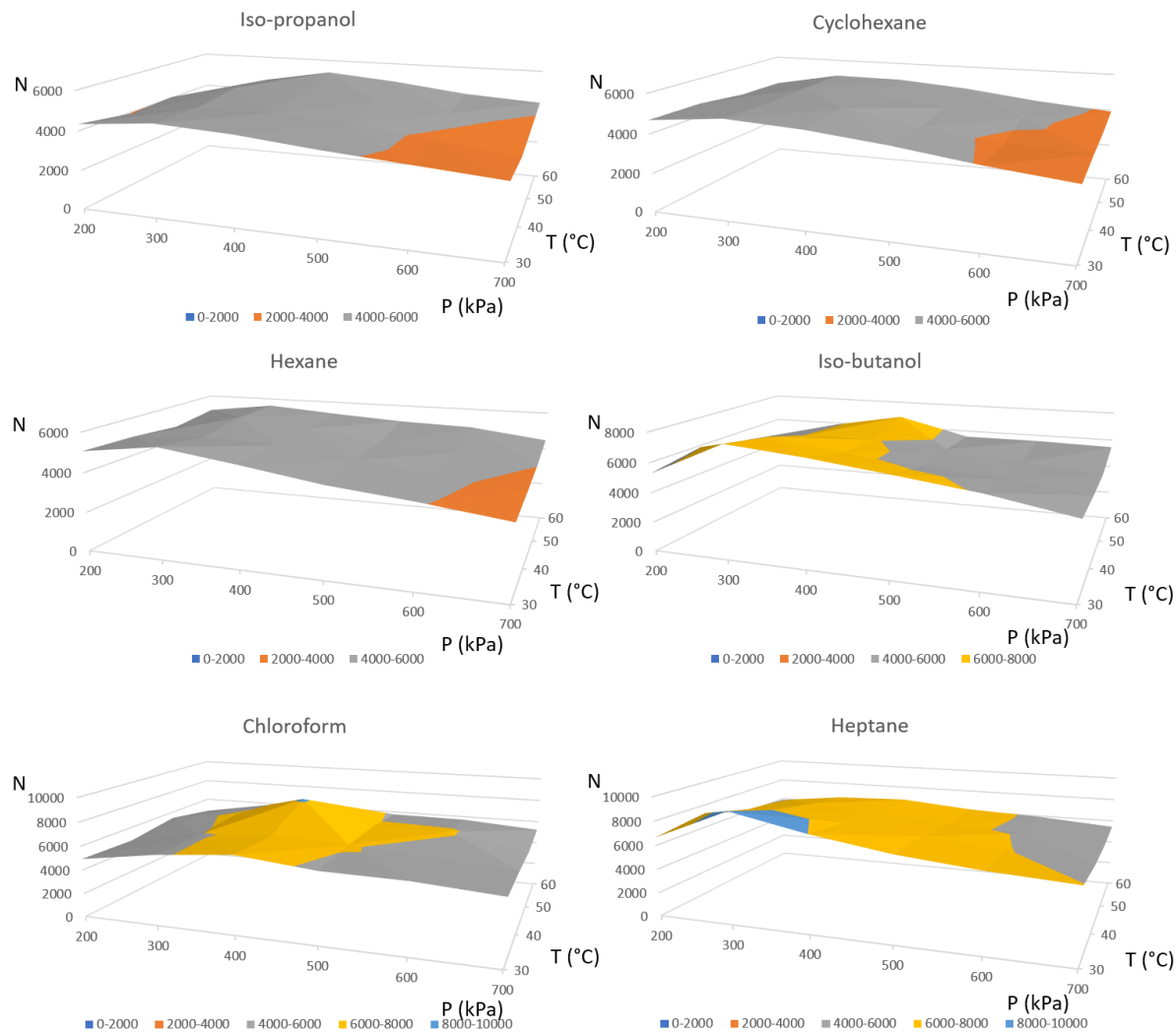


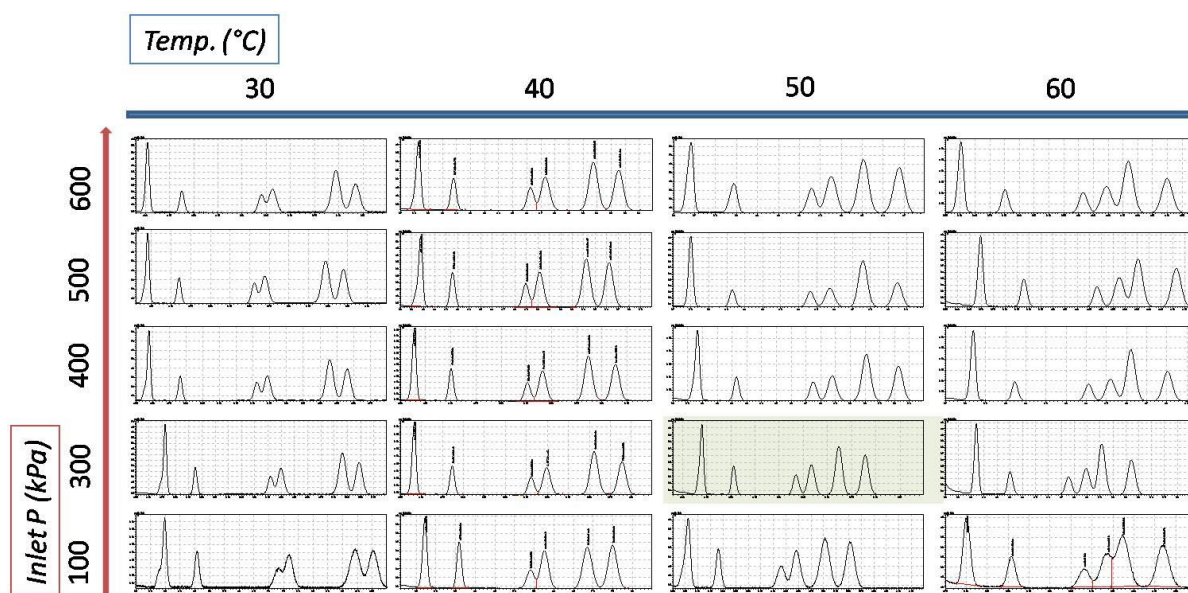
**Figure F8.** Surface plots produced for the investigated compounds, for measurements performed with the 5 m x 0.10 mm pre-column and the 15 m x 0.53 mm x 3 $\mu$ m d<sub>f</sub> DB-624 analytical column.

**Table F7.** Number of theoretical plates corresponding to the optimum inlet pressure conditions (mentioned in brackets) for the investigated compounds under the isothermal temperatures tested, for measurements performed with the 5 m x 0.10 mm pre-column and the 15 m x 0.53 mm x 3 $\mu$ m d<sub>f</sub> DB-624 analytical column.

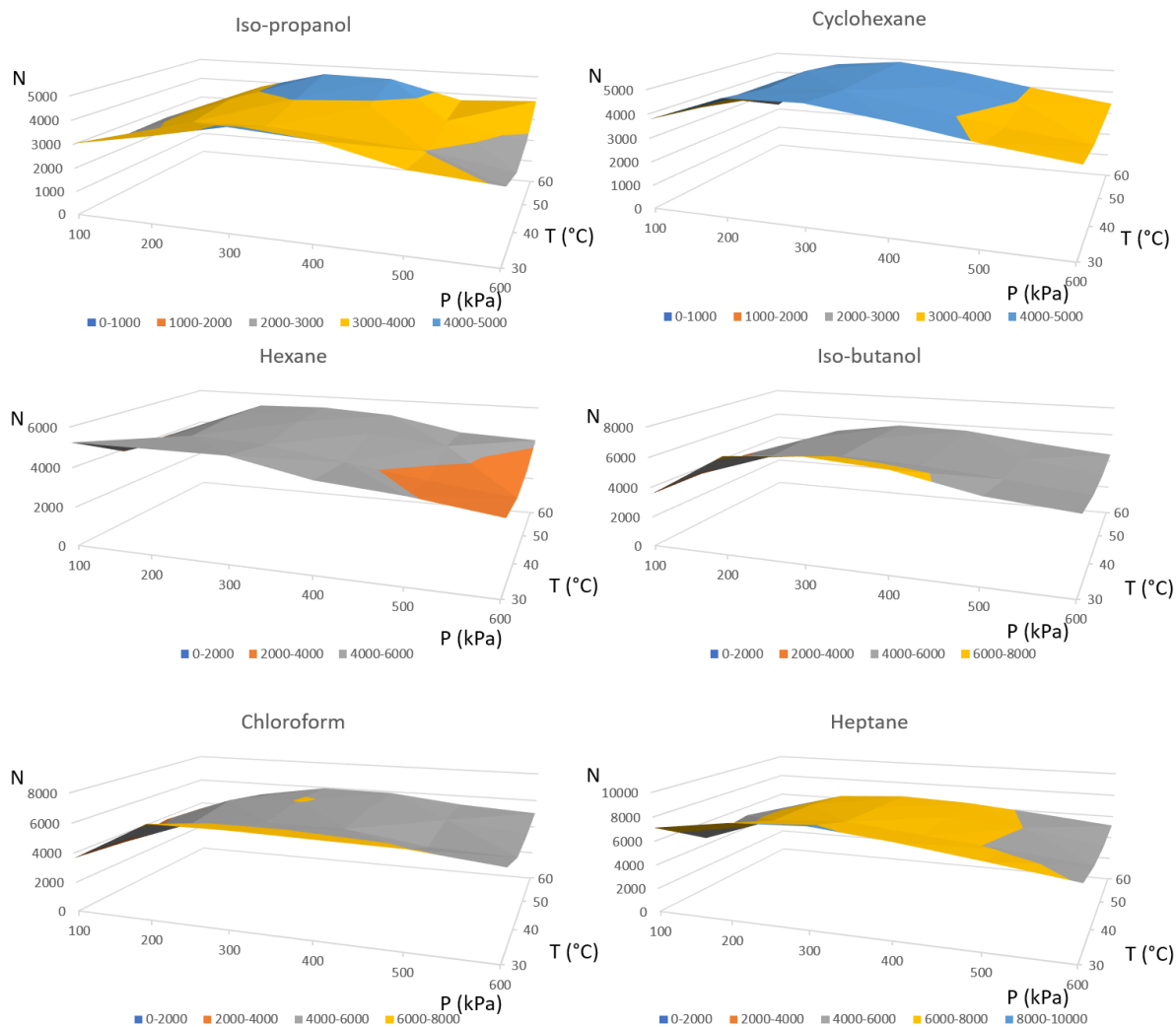
Compound Name	Number of Theoretical Plates at:			
	30°C	40°C	50°C	60°C
Iso-propanol	4689 (@300 kPa)	4571 (@300 kPa)	4833 (@300 kPa)	<b>5278</b> (@400 kPa)
Hexane	5552 (@300 kPa)	5214 (@300 kPa)	5570 (@300 kPa)	<b>5590</b> (@300 kPa)
Chloroform	5870 (@300 kPa)	<b>7906</b> (@300 kPa)	6218 (@300 kPa)	5802 (@300 kPa)
Cyclohexane	<b>5712</b> (@300 kPa)	5312 (@300 kPa)	5042 (@300 kPa)	5051 (@300 kPa)
Iso-butanol	<b>7605</b> (@300 kPa)	6983 (@300 kPa)	6038 (@300 kPa)	6001 (@400 kPa)
Heptane	<b>9281</b> (@300 kPa)	7991 (@300 kPa)	7210 (@300 kPa)	6735 (@300 kPa)

Table F7 summarizes the number of theoretical plates obtained for the optimum inlet pressures applied at different oven temperatures for the investigated compounds and for the 5 m restriction. As demonstrated from these values, the optimum temperature varies for the different compounds, with the early eluting peaks (for iso-propanol and hexane) having the lowest HETP/ highest N at the highest investigated temperature of 60°C. The best temperature conditions are then gradually moving towards the lower temperature tested, with the three last eluting compounds performing best at 30°C, in terms of HETP / N. The optimum pressure for most of the T-P combinations is that of 300 kPa, while only at the experiments performed at 60°C the first eluting compound, namely iso-propanol, and the last two eluting solvents perform best under 400 kPa. There is a clear tendency towards better performance with the increase in elution time, with the sole exception of chloroform which performs better than expected, judging exclusively from its elution order.

The second restriction tested was the 4 m x 0.10 mm one, produced from reduction of the pre-column length by one meter, while the connection between the restriction and the analytical column was kept intact. The corresponding chromatograms are illustrated in Figure F9 and the surface plots in Figure F10. Table F8 summarizes the information about the theoretical plates provided at the optimum inlet pressure for every compound at every temperature tested.



**Figure F9. LP-GC-MS Chromatograms produced with the 4 m x 0.10 mm pre-column and the 15 m x 0.53 mm x 3 $\mu$ m  $d_f$  DB-624 analytical column after isothermal elution at 30, 40, 50 and 60°C using inlet pressures from 100 k Pa and between 300 and 600 kPa. The chromatogram corresponding to optimum conditions in terms of separation efficiency is marked with light green. The total runtimes had been in many cases optimized and are different for the chromatograms obtained with different methods. The scale for the intensities also differs among the chromatograms.**



**Figure F10.** Surface plots produced for the investigated compounds, for measurements performed with the 4 m x 0.10 mm pre-column and the 15 m x 0.53 mm x 3 $\mu$ m  $d_f$  DB-624 analytical column.

**Table F8.** Number of theoretical plates corresponding to the optimum inlet pressure conditions (mentioned in brackets) for the investigated compounds under the isothermal temperatures tested, for measurements performed with the 4 m x 0.10 mm pre-column and the 15 m x 0.53 mm x 3 $\mu$ m  $d_f$  DB-624 analytical column.

Compound Name	Number of Theoretical Plates at:			
	30°C	40°C	50°C	60°C
Iso-propanol	4240 (@300 kPa)	3482 (@300 kPa)	4054 (@300 kPa)	<b>4588</b> (@300 kPa)
Hexane	5243 (@100 kPa)	5021 (@200 kPa)	5267 (@200 kPa)	<b>5367</b> (@300 kPa)
Chloroform	<b>7055</b> (@300 kPa)	5681 (@300 kPa)	6024 (@300 kPa)	5944 (@300 kPa)
Cyclohexane	<b>5340</b> (@300 kPa)	4691 (@200 kPa)	4846 (@300 kPa)	4888 (@300 kPa)
Iso-butanol	<b>6872</b> (@300 kPa)	5675 (@300 kPa)	5754 (@300 kPa)	5694 (@300 kPa)
Heptane	<b>8269</b> (@300 kPa)	7091 (@300 kPa)	6885 (@300 kPa)	6623 (@300 kPa)

From these data we can conclude that, for the 4-m restriction, the optimum inlet pressure is again in most of the cases that of 300 kPa, independently of the elution temperature. Only hexane showed an increase in the optimum pressure with the temperature increase, starting with that of 100 kPa at 30°C and 200 kPa at 40°C, until it reached the optimum 300 kPa for the rest of the investigated temperatures. The optimum temperatures stay almost identical to those observed also for the 5-m restriction, with only chloroform shifting its optimum temperature to the lowest one investigated. This brings two optimum temperatures, the highest investigated for the first eluting peaks, decreasing to the lowest investigated for those compounds spending more time inside the analytical column. The trend towards better performances with elution time remains unchanged. However, a small reduction was observed in the number of theoretical plates calculated from the corresponding chromatograms for all the examined compounds, showing a slight deterioration in the performance of the VO system with the reduction in the restriction length, when the inner diameter is kept constant.

To confirm the last observation, further stepwise reductions in the restriction length were performed and the produced column systems were again checked in terms of optimum temperature and inlet pressure conditions and corresponding separation efficiencies. The chromatograms and surface plots produced with the 3-m restriction are illustrated in Figures F11 and F12, while the respective numbers of theoretical plates calculated under optimum P-T conditions are shown in Table F9.

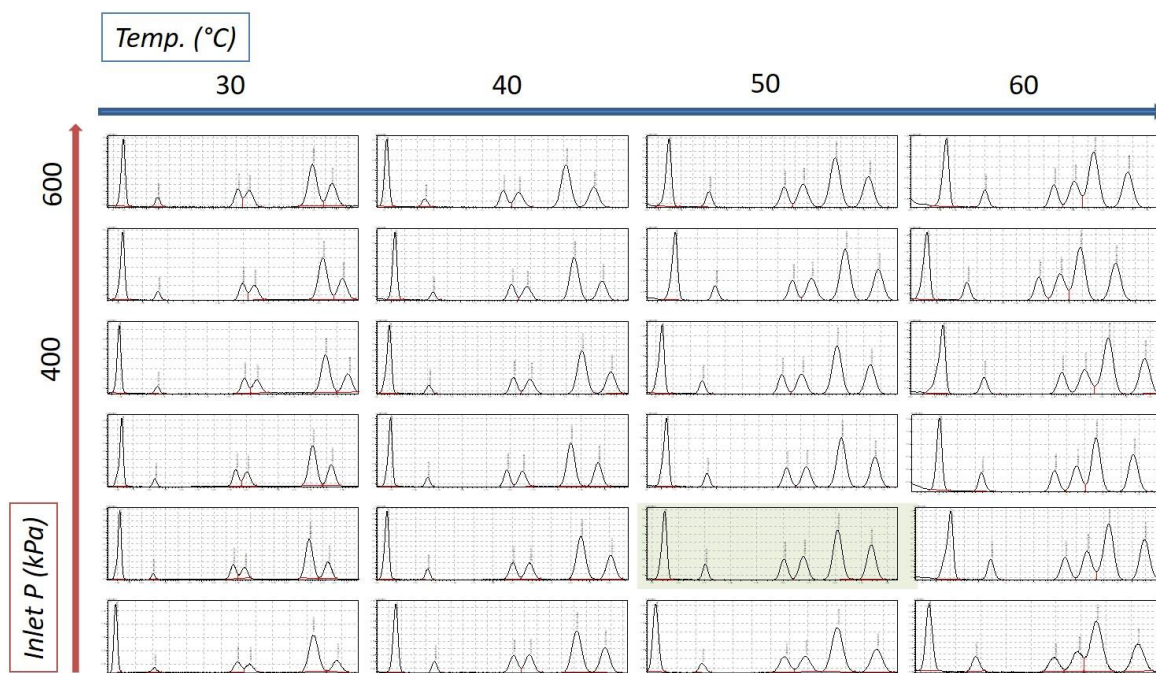


**Figure F11.** LP-GC-MS Chromatograms produced with the 3 m x 0.10 mm pre-column and the 15 m x 0.53 mm x 3 $\mu$ m d<sub>f</sub> DB-624 analytical column after isothermal elution at 30, 40, 50 and 60°C using inlet pressures between 100 and 600 kPa. The chromatogram corresponding to optimum conditions in terms of separation efficiency is marked with light green. The total runtimes had been in many cases optimized and are different for the chromatograms obtained with different methods. The scale for the intensities also differs among the chromatograms.

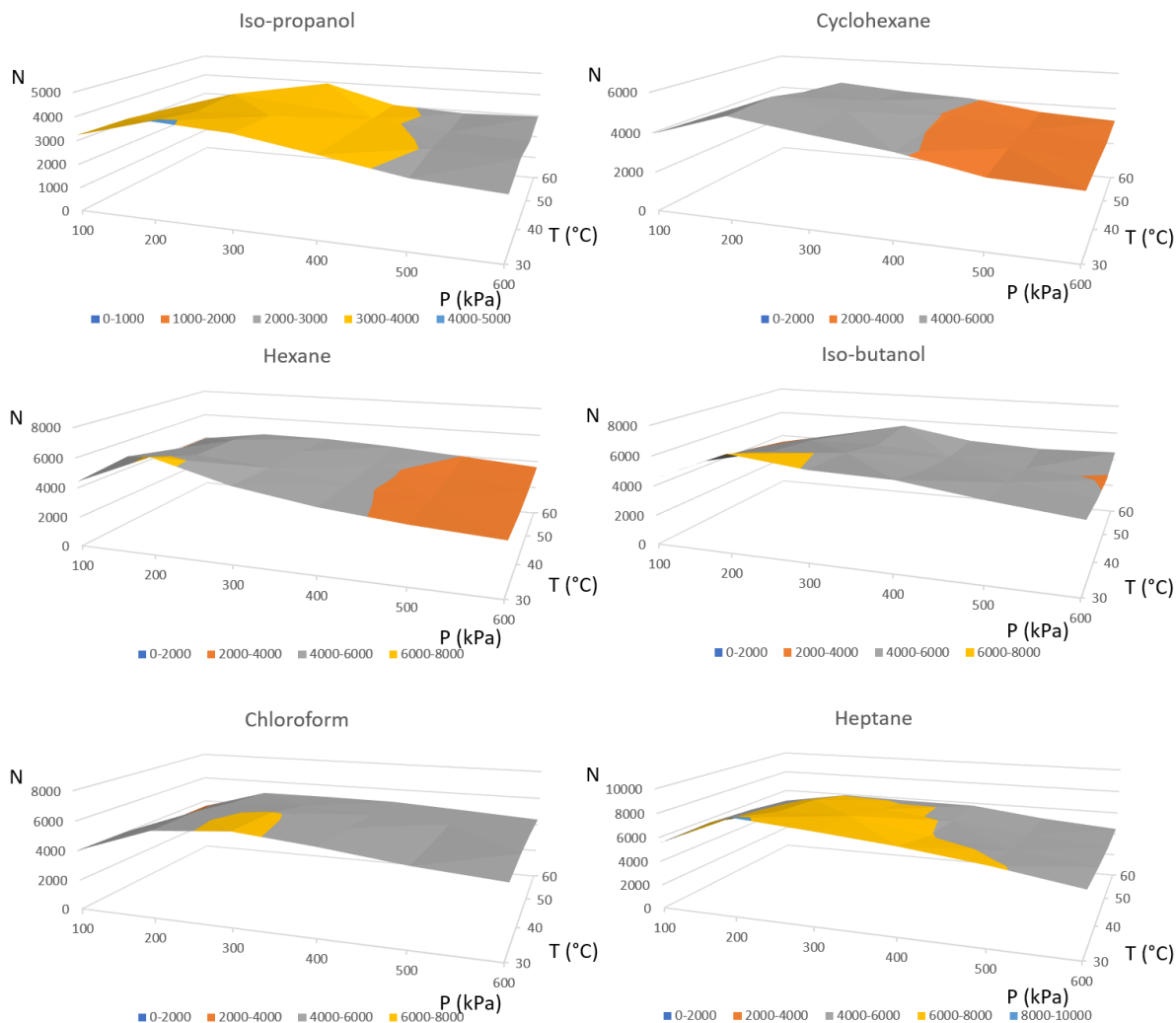


**Figure F12.** Surface plots produced for the investigated compounds, for measurements performed with the 3 m x 0.10 mm pre-column and the 15 m x 0.53 mm x 3 $\mu$ m  $d_f$  DB-624 analytical column.

**Table F9.** Number of theoretical plates corresponding to the optimum inlet pressure conditions (mentioned in brackets) for the investigated compounds under the isothermal temperatures tested, for measurements performed with the 3 m x 0.10 mm pre-column and the 15 m x 0.53 mm x 3 $\mu$ m  $d_f$  DB-624 analytical column.

Compound Name	Number of Theoretical Plates at:			
	30°C	40°C	50°C	60°C
Iso-propanol	<b>4065</b> (@200 kPa)	3771 (@300 kPa)	3837 (@200 kPa)	3933 (@300 kPa)
Hexane	<b>6461</b> (@200 kPa)	5379 (@200 kPa)	5312 (@200 kPa)	4658 (@200 kPa)
Chloroform	6004 (@200 kPa)	<b>6121</b> (@300 kPa)	5453 (@300 kPa)	5045 (@300 kPa)
Cyclohexane	<b>5611</b> (@200 kPa)	5214 (@200 kPa)	4771 (@200 kPa)	4101 (@200 kPa)
Iso-butanol	<b>6539</b> (@200 kPa)	5790 (@300 kPa)	5156 (@300 kPa)	4905 (@300 kPa)
Heptane	<b>8744</b> (@200 kPa)	7266 (@300 kPa)	6779 (@200 kPa)	5919 (@200 kPa)

From the summarized results produced by the 3 m restriction we observed that the optimum inlet pressure was ranging between 200 and 300 kPa, showing a gradual decrease with the respective reduction in the restriction's length. The optimum temperature for almost all the compounds was 30°C, apart from chloroform, for which a slightly improved number of theoretical plates was calculated for the 40°C. So, for the particular pre-column dimensions, the elution order of the compounds seemed not to affect the optimum temperatures, providing a more uniform character to the investigated analytes, as long as this optimization parameter is concerned. The best performance in terms of HETP / N was again demonstrated for heptane, with the number of theoretical plates generally increasing with the increase in the retention time. However, the reduction in the performance with the reduction in the restriction's length was not generally observed for all compounds, but only half of the investigated species were negatively affected, following the trend observed in the previous two column setups. In particular the values were slightly improved for the investigated alkanes while for the rest of the species tested the opposite effect was observed. The respective data produced with the 2-m restriction are presented in Figures F13 and F14 and in Table F10.

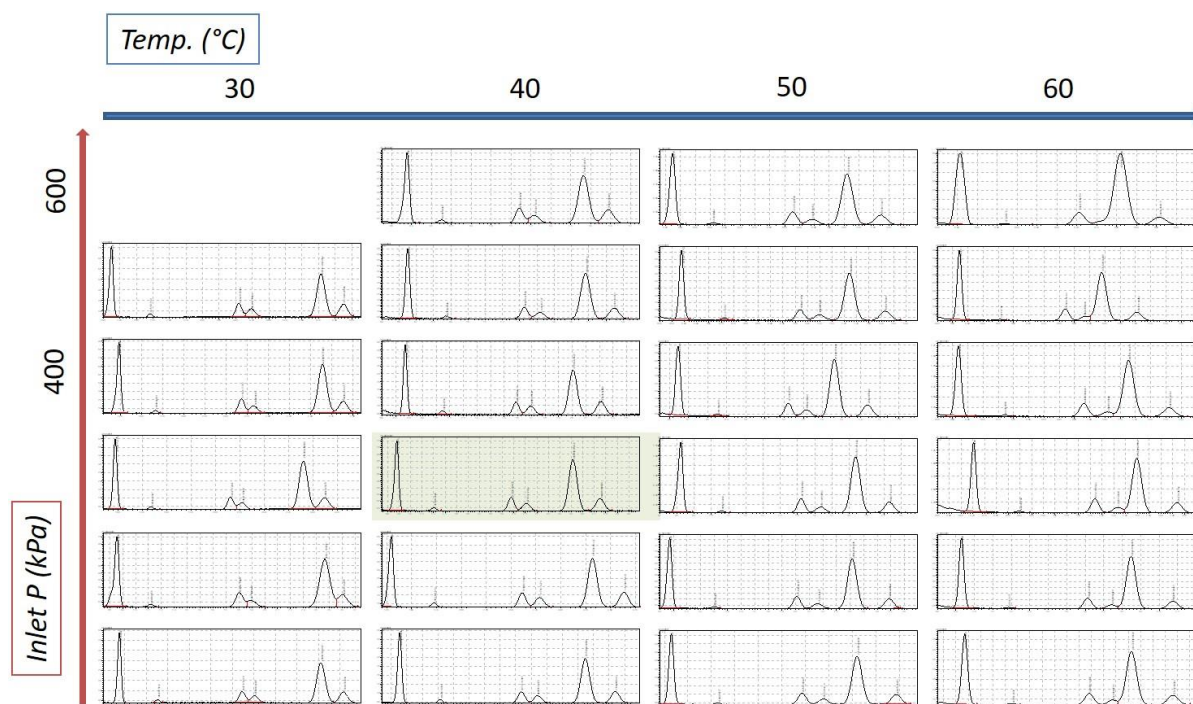


**Figure F13. LP-GC-MS Chromatograms produced with the 2 m x 0.10 mm pre-column and the 15 m x 0.53 mm x 3µm d<sub>f</sub> DB-624 analytical column after isothermal elution at 30, 40, 50 and 60°C using inlet pressures between 100 and 600 kPa. The chromatogram corresponding to optimum conditions in terms of separation efficiency is marked with light green. The total runtimes had been in many cases optimized and are different for the chromatograms obtained with different methods. The scale for the intensities also differs among the chromatograms.**

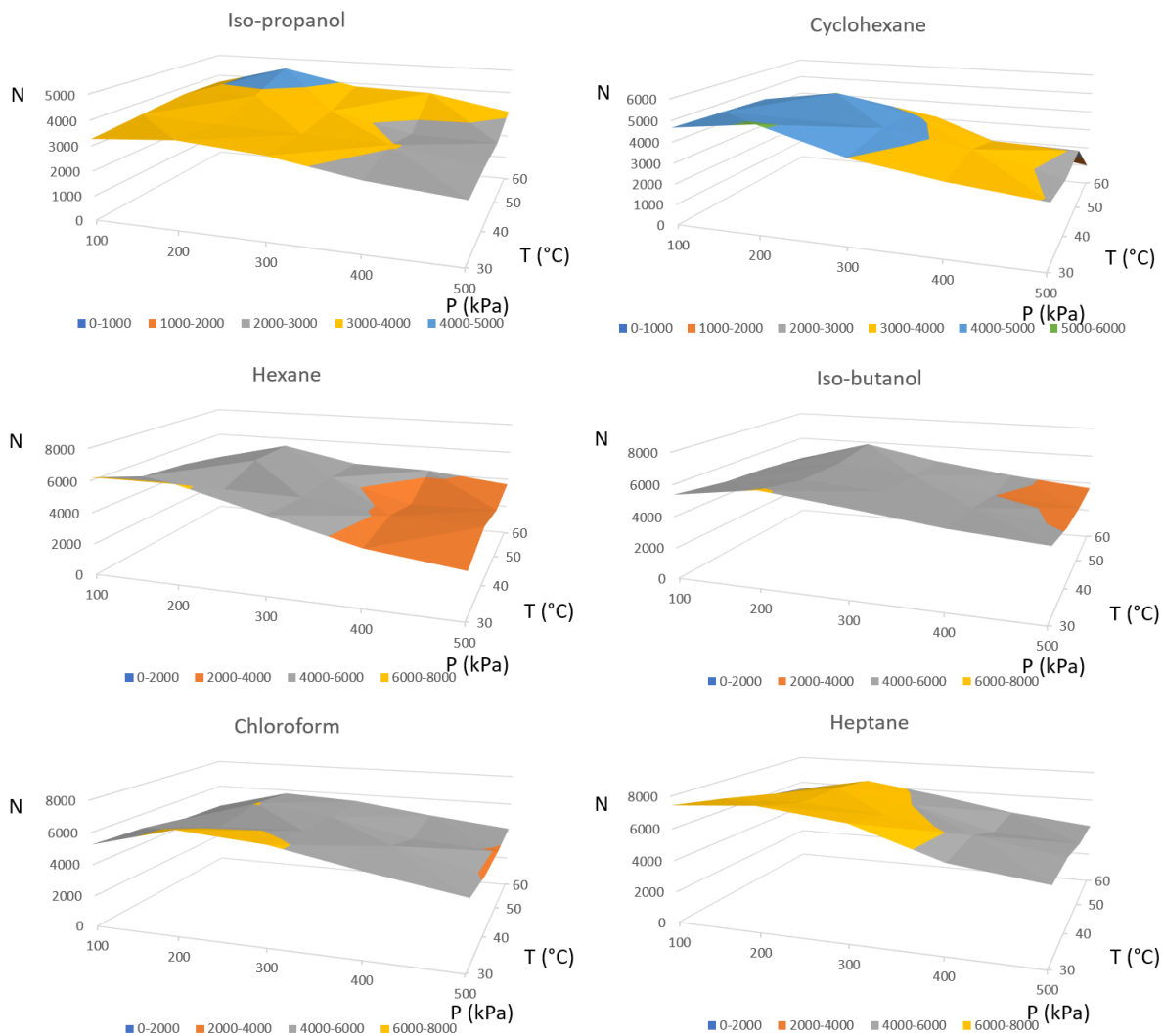


**Figure F14.** Surface plots produced for the investigated compounds, for measurements performed with the 2 m x 0.10 mm pre-column and the 15 m x 0.53 mm x 3 $\mu$ m  $d_f$  DB-624 analytical column.

**Table F10.** Number of theoretical plates corresponding to the optimum inlet pressure conditions (mentioned in brackets) for the investigated compounds under the isothermal temperatures tested, for measurements performed with the 2 m x 0.10 mm pre-column and the 15 m x 0.53 mm x 3 $\mu$ m  $d_f$  DB-624 analytical column.

Compound Name	Number of Theoretical Plates at:			
	30°C	40°C	50°C	60°C
Iso-propanol	3514 (@200 kPa)	3470 (@100 kPa)	3849 (@200 kPa)	<b>4536</b> (@200 kPa)
Hexane	<b>6240</b> (@200 kPa)	4715 (@100 kPa)	5396 (@200 kPa)	5956 (@400 kPa)
Chloroform	<b>6933</b> (@200 kPa)	5708 (@300 kPa)	6029 (@200 kPa)	5750 (@200 kPa)
Cyclohexane	<b>5692</b> (@200 kPa)	4552 (@100 kPa)	4755 (@200 kPa)	3604 (@200 kPa)
Iso-butanol	<b>6107</b> (@200 kPa)	5472 (@200 kPa)	5409 (@200 kPa)	5388 (@200 kPa)
Heptane	<b>7791</b> (@200 kPa)	6877 (@200 kPa)	6871 (@200 kPa)	6443 (@200 kPa)

Even when the restriction length was further reduced to 2 m, heptane remained the compound performing best in terms of HETP / N values. Concerning the general trend towards reduced efficiencies for the reduced restriction lengths, all compounds provided lower numbers of theoretical plates when compared to the initial ones calculated from the experiments produced with the original 5-m restriction. However, when the data from the stepwise reduction of the pre-column's length are considered, the corresponding values varied even greater for the different compounds, with no clear trend accompanying the changes noticed when moving from the 3-m to 2-m restriction. With this restriction, all compounds maintained the same optimum temperatures as for the 4-m restriction, with the 30°C being almost exclusively the optimum temperature condition. In most of the cases the optimum pressure was the 200 kPa, however, the range of optimum values for the different T-P examined combinations moved further towards lower values, with 100 kPa being the optimum pressure for iso-propanol, hexane and cyclohexane when analyzed at 40°C.

The last length investigated for the 0.10 mm restriction was that of 1 m. The produced chromatograms, surface plots and the corresponding number of theoretical plates calculated for the investigated temperature-inlet pressure combinations are summarized in Figures F15, F16 and Table F11.

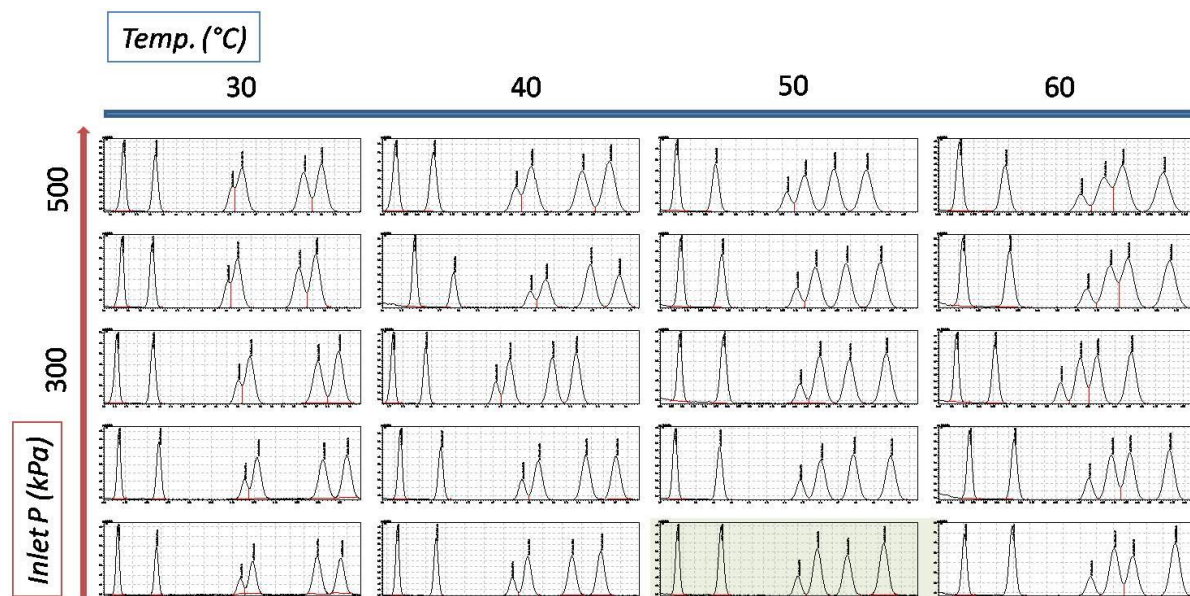


**Figure F15.** LP-GC-MS Chromatograms produced with the 1 m x 0.10 mm pre-column and the 15 m x 0.53 mm x 3 $\mu$ m d<sub>f</sub> DB-624 analytical column after isothermal elution at 30, 40, 50 and 60°C using inlet pressures between 100 and 600 kPa. The chromatogram corresponding to optimum conditions in terms of separation efficiency is marked with light green. The total runtimes had been in many cases optimized and are different for the chromatograms obtained with different methods. The scale for the intensities also differs among the chromatograms.



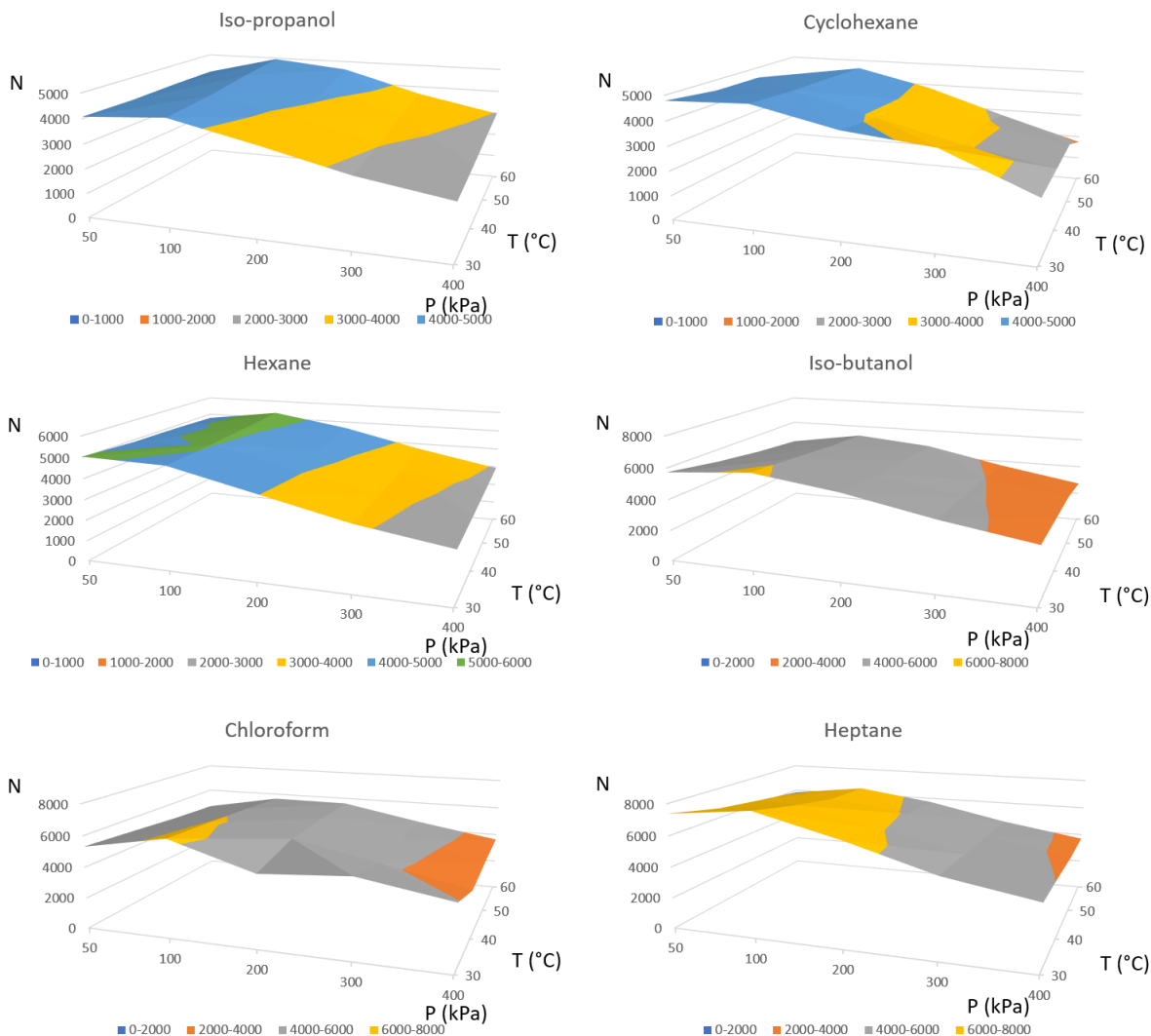


**Figure F16.** Surface plots produced for the investigated compounds, for measurements performed with the 1 m x 0.10 mm pre-column and the 15 m x 0.53 mm x 3 $\mu$ m  $d_f$  DB-624 analytical column.

**Table F11.** Number of theoretical plates corresponding to the optimum inlet pressure conditions (mentioned in brackets) for the investigated compounds under the isothermal temperatures tested, for measurements performed with the 1 m x 0.10 mm pre-column and the 15 m x 0.53 mm x 3 $\mu$ m  $d_f$  DB-624 analytical column.

Compound Name	Number of Theoretical Plates at:			
	30°C	40°C	50°C	60°C
Iso-propanol	3842 (@100 kPa)	4065 (@100 kPa)	4404 (@100 kPa)	<b>4474</b> (@100 kPa)
Hexane	<b>5179</b> (@100 kPa)	4938 (@100 kPa)	4988 (@100 kPa)	4978 (@100 kPa)
Chloroform	<b>7066</b> (@100 kPa)	6312 (@100 kPa)	6299 (@100 kPa)	5663 (@100 kPa)
Cyclohexane	<b>5492</b> (@100 kPa)	5121 (@100 kPa)	4798 (@100 kPa)	4412 (@100 kPa)
Iso-butanol	<b>7081</b> (@100 kPa)	6068 (@100 kPa)	5743 (@100 kPa)	4972 (@100 kPa)
Heptane	<b>8721</b> (@100 kPa)	7557 (@100 kPa)	6786 (@100 kPa)	6287 (@100 kPa)

From the aforementioned data it can be clearly seen that, when the restriction length was reduced to 1 m, the optimum temperature for each compound followed the same trends observed for the 5 m-long restriction with most of the investigated compounds having the 30°C as their optimum temperature. The optimum pressure was universally the 100 kPa, dictating the use of even lower pressures, so that the constructed Van Deemter plots could indeed illustrate the minimum value for the theoretical plate height. It was a general observation that the shorter the restriction, the lower the optimum pressures and the lower the maximum inlet pressures that could be applied and maintained from the system. That effect was self-explained by the role of the restriction. The influence of the temperature in those pressure limits was also profound. Consequently, when the 1-m restriction was used, the inlet pressure limits were 430, 460, 490 and 520 kPa for 30, 40, 50 and 60°C.

Comparing the rest of the observations made for each column setup, heptane remained once again the compound providing the highest number of theoretical plates. Additionally, like with the 2-m restriction, no clear trend was demonstrated for the improvement or deterioration of the system's performance when comparing the absolute results produced for the last two investigated reduction lengths. However, when summarizing the best HETP values obtained from the overall combinations of T-P conditions applied for the different column setups (with only the restriction length varying), the 5-m restriction showed superior performance for almost all the compounds. Since the peaks of the investigated compounds did not experience background separation in all the cases, and the extracted ions had to be applied, a minor effect in the calculated values is to be expected, blurring the lines between the optimum conditions identified for the various setups.

Summarizing the method optimization results for the 0.10 mm column, the highest number of theoretical plates was generally observed when the longer restriction was used. The 30°C was the optimum temperature for almost all the compounds and for all restriction lengths. However, the optimum inlet pressure was varying, with reduced pressures being more favourable for shorter restrictions, and with the 300 kPa producing better results for the 5 and 4-m restrictions, the 200 kPa for the 3 and 2-m restrictions and the 100 kPa being optimum for the 1-m restriction. The number of theoretical plates was also the highest for the latest eluting compound, and namely for heptane. The increased elution time was for most compounds accompanied by an increase in the number of theoretical plates. This effect was demonstrated for all the investigated compounds in most of the column setups, with the sole exception the performance of chloroform which was better than expected from the elution order of the compound, demonstrating however the influence that the compound's nature may also have in its performance under vacuum outlet and in general chromatographic conditions. But, as a rule of thumb, we can conclude from the obtained data that the lower the volatility of a compound, the better its performance under VO conditions.

### F.3.1.2. Method optimization for a 0.075 mm i.d. pre-column

Moving gradually not only towards shorter, but also thinner pre-columns, a 0.075 mm x 1 m restriction was selected for investigation. Since the obtained chromatograms little differ from the ones presented for the previous column setups, they will not be further mentioned, unless significant differences in the peak resolution or the runtime were observed. Therefore, only the surface plots and number of theoretical plates will be presented for this column setup (Figure F17 and Table F12, respectively).

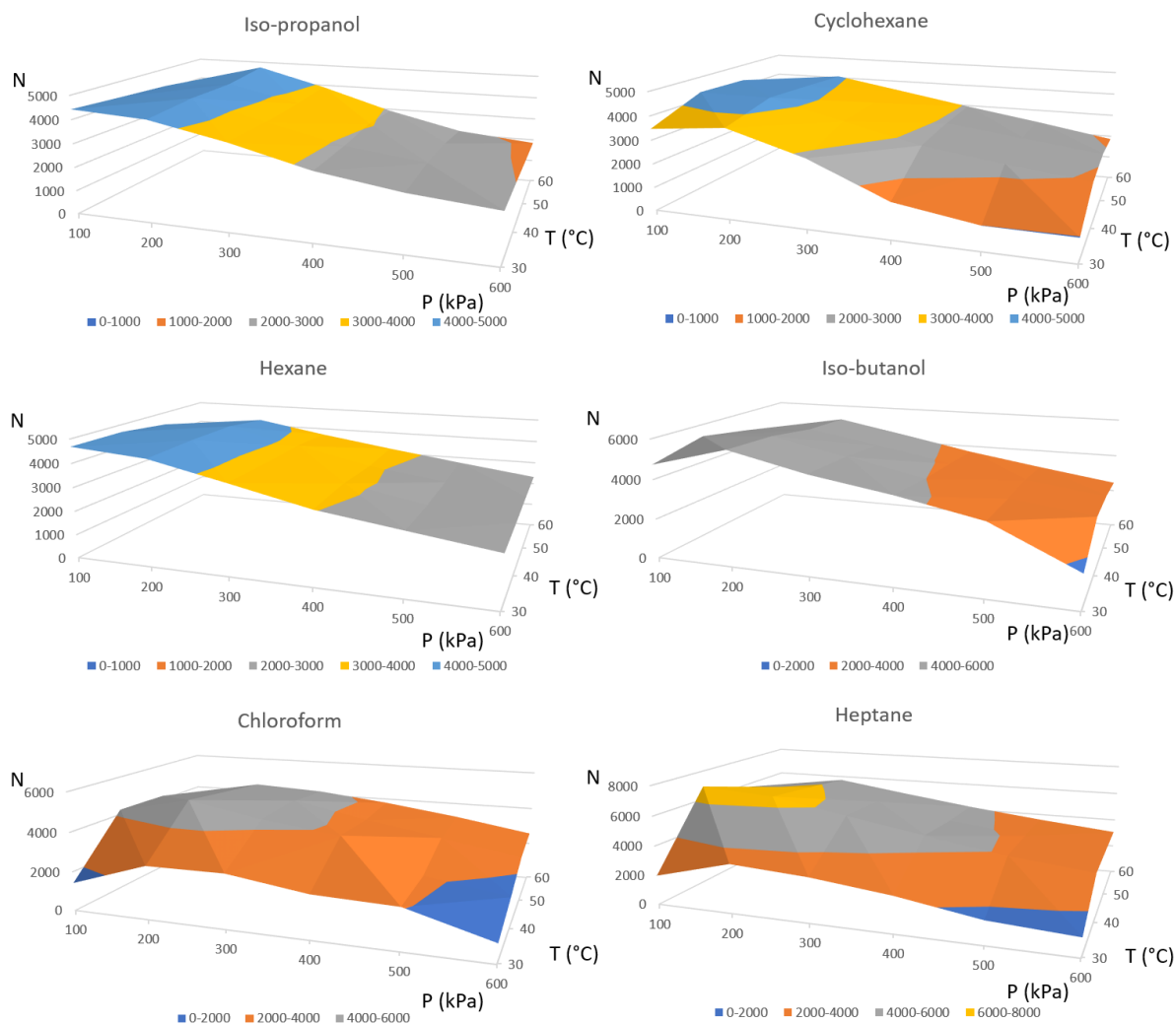


Figure F17. Surface plots produced for the investigated compounds, for measurements performed with the 1 m x 0.075 mm pre-column and the 15 m x 0.53 mm x 3 $\mu$ m d<sub>f</sub> DB-624 analytical column.

**Table F12. Number of theoretical plates corresponding to the optimum inlet pressure conditions (mentioned in brackets) for the investigated compounds under the isothermal temperatures tested, for measurements performed with the 1 m x 0.075 mm pre-column and the 15 m x 0.53 mm x 3 $\mu$ m d<sub>f</sub> DB-624 analytical column.**

Compound Name	Number of Theoretical Plates at:			
	30°C	40°C	50°C	60°C
Iso-propanol	4427 (@100 kPa)	4441 (@200 kPa)	4461 (@200 kPa)	<b>4731</b> (@200 kPa)
Hexane	<b>4685</b> (@100 kPa)	4674 (@100 kPa)	4530 (@200 kPa)	4265 (@200 kPa)
Chloroform	2722 (@300 kPa)	<b>5051</b> (@200 kPa)	4721 (@200 kPa)	4392 (@200 kPa)
Cyclohexane	3776 (@200 kPa)	<b>5331</b> (@100 kPa)	4272 (@100 kPa)	4069 (@200 kPa)
Iso-butanol	<b>6745</b> (@200 kPa)	5636 (@200 kPa)	5265 (@200 kPa)	5162 (@200 kPa)
Heptane	3307 (@200 kPa)	<b>7903</b> (@100 kPa)	6158 (@200 kPa)	5714 (@200 kPa)

For the 0.075 mm i.d. pre-column, even though iso-propanol had an optimum temperature of 60°C, the lower investigated temperatures provided the maximum number of theoretical plates for the rest of the examined compounds. The optimum inlet pressures were almost exclusively ranging between 100 and 200 kPa, and the general tendency towards higher number of theoretical plates under the optimum conditions for the later eluting compounds was clearly demonstrated.

Comparing the results obtained for the 1-m restrictions of 0.10 and 0.075 mm i.d., the wider restriction provided higher numbers of theoretical plates for all the compounds. To verify this assumption, an even thinner restriction was examined.

### *F.3.1.3. Method optimization for a 0.05 mm i.d. pre-column*

The next set of experiments investigated the performance of an even thinner pre-column. In that case, a 0.05 mm i.d. pre-column was used, with a length of initially 1 m, which was later on reduced to 0.5 m. Starting with the presentation of the results obtained with the longer restriction, Figure F18 summarizes the respective surface plots and Table F13 the number of theoretical plates calculated for the different experimental conditions tested.

**Table F13. Number of theoretical plates corresponding to the optimum inlet pressure conditions (mentioned in brackets) for the investigated compounds under the isothermal temperatures tested, for measurements performed with the 1 m x 0.05 mm pre-column and the 15 m x 0.53 mm x 3 $\mu$ m d<sub>f</sub> DB-624 analytical column.**

Compound Name	Number of Theoretical Plates at:			
	30°C	40°C	50°C	60°C
Iso-propanol	<b>6414</b> (@500 kPa)	5814 (@600 kPa)	4534 (@600 kPa)	4236 (@500 kPa)
Hexane	<b>4586</b> (@600 kPa)	4401 (@400 kPa)	4083 (@500 kPa)	3663 (@500 kPa)
Chloroform	<b>4301</b> (@500 kPa)	4266 (@400 kPa)	4071 (@600 kPa)	3809 (@600 kPa)
Cyclohexane	4938 (@500 kPa)	<b>5386</b> (@500 kPa)	4219 (@600 kPa)	3931 (@500 kPa)
Iso-butanol	<b>6491</b> (@500 kPa)	5793 (@600 kPa)	5405 (@600 kPa)	4953 (@600 kPa)
Heptane	<b>7589</b> (@600 kPa)	5850 (@500 kPa)	5997 (@600 kPa)	5515 (@600 kPa)

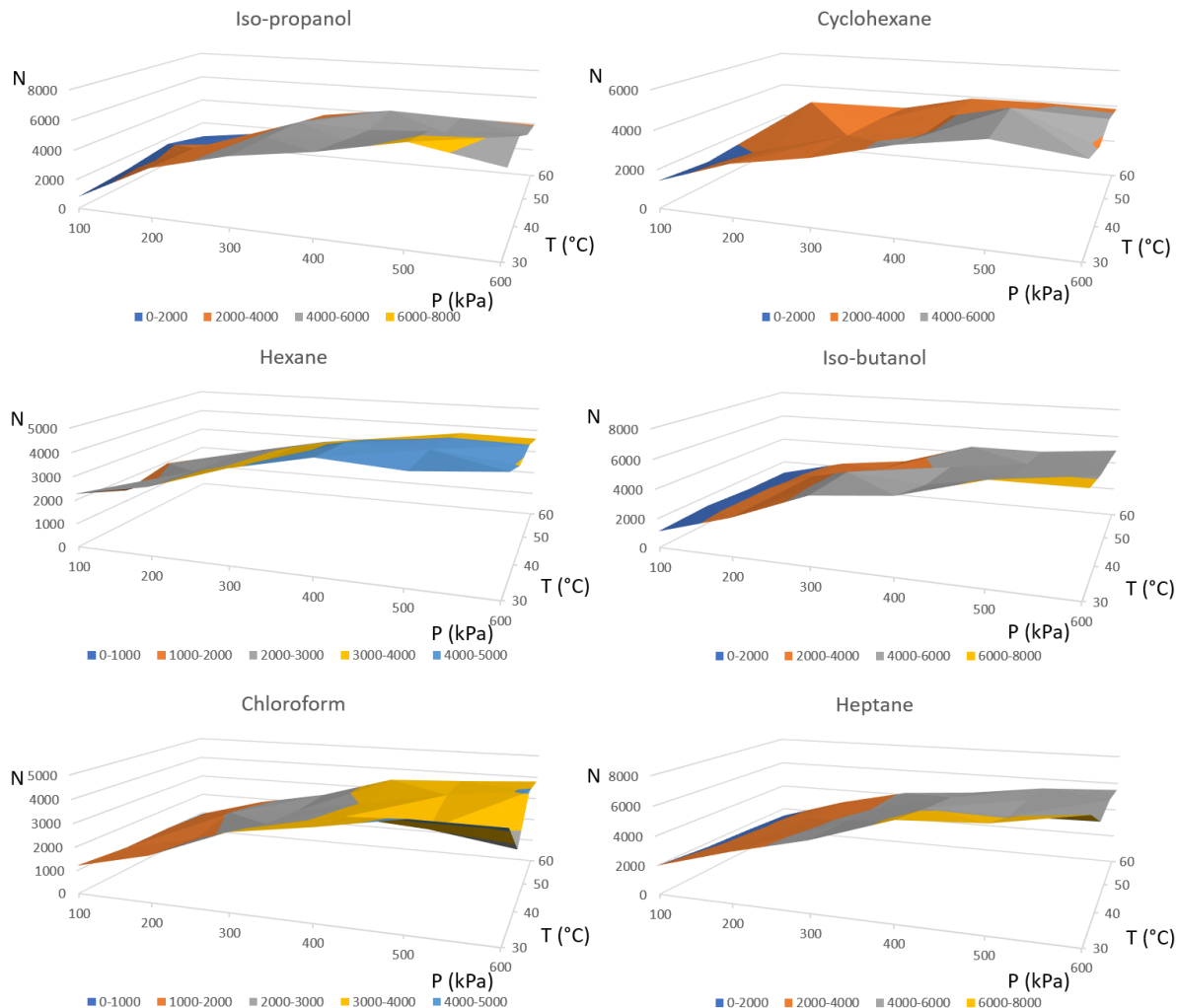


**Figure F18. Surface plots produced for the investigated compounds, for measurements performed with the 1 m x 0.05 mm pre-column and the 15 m x 0.53 mm x 3 $\mu$ m  $d_f$  DB-624 analytical column.**

When the thinner pre-column was used, the optimum temperature was for almost all the compounds the 30°C, with the number of theoretical plates being gradually reduced as the isothermal temperature was increased. The optimum inlet pressure was fluctuating between 400 and 600 kPa and the best results for every compound were produced for just the 500 or 600 kPa. A general tendency towards higher performance for the later eluting compounds was again observed, with the exceptions of iso-propanol, showing a much better performance than expected solely by its elution order, and hexane.

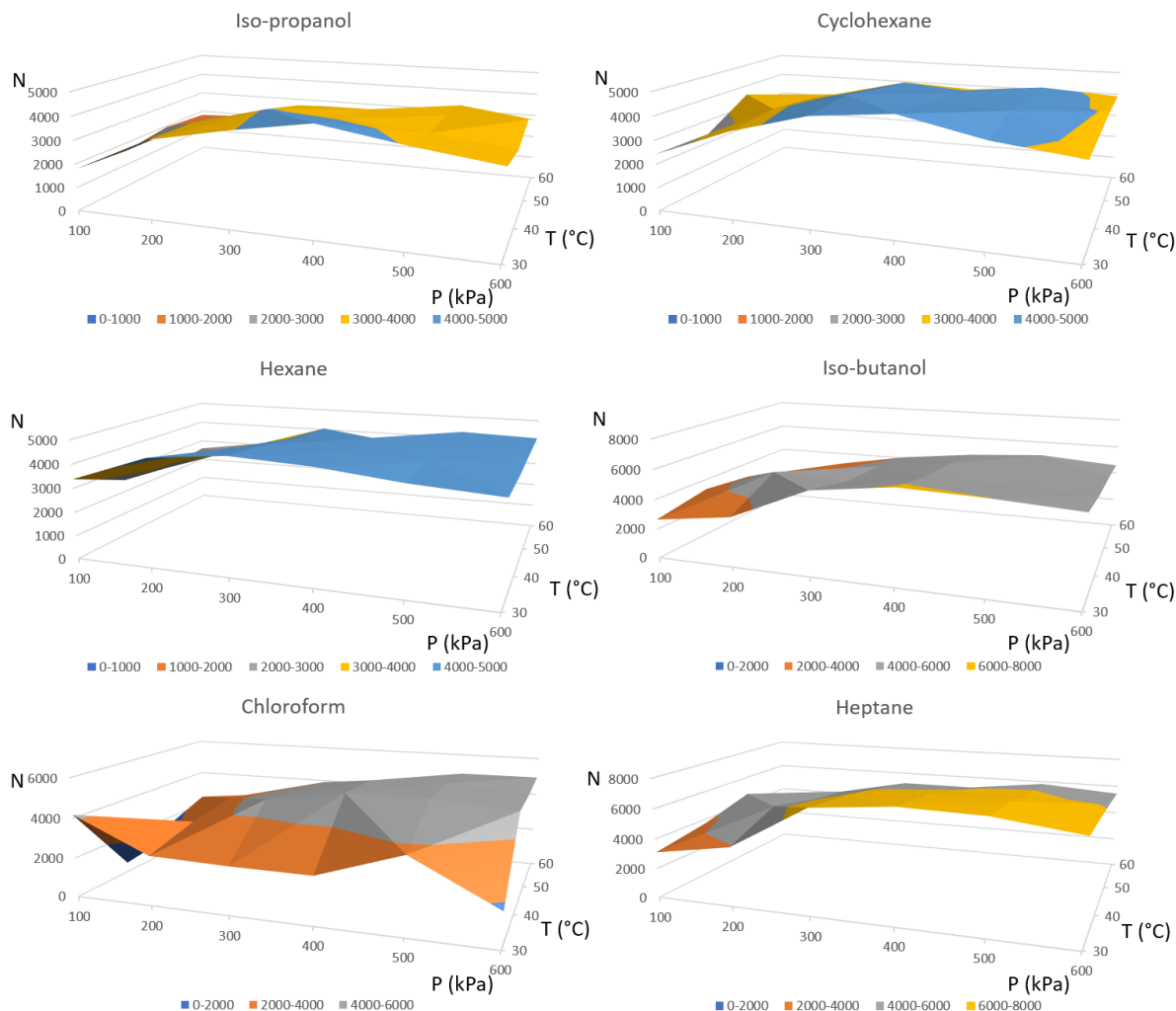


**Figure F19.** Surface plots produced for the investigated compounds, for measurements performed with the 0.5 m x 0.05 mm pre-column and the 15 m x 0.53 mm x 3 $\mu$ m  $d_f$  DB-624 analytical column.

**Table F14.** Number of theoretical plates corresponding to the optimum inlet pressure conditions (mentioned in brackets) for the investigated compounds under the isothermal temperatures tested, for measurements performed with the 0.5 m x 0.05 mm pre-column and the 15 m x 0.53 mm x 3 $\mu$ m  $d_f$  DB-624 analytical column.

Compound Name	Number of Theoretical Plates at:			
	30°C	40°C	50°C	60°C
Iso-propanol	4483 (@400 kPa)	4041 (@300 kPa)	3585 (@600 kPa)	3252 (@500 kPa)
Hexane	4816 (@300 kPa)	4580 (@300 kPa)	4426 (@400 kPa)	4283 (@500 kPa)
Chloroform	3733 (@500 kPa)	4627 (@300 kPa)	<b>5184</b> (@500 kPa)	4950 (@600 kPa)
Cyclohexane	<b>5832</b> (@400 kPa)	4647 (@300 kPa)	4304 (@400 kPa)	4109 (@500 kPa)
Iso-butanol	<b>6191</b> (@400 kPa)	5535 (@400 kPa)	5194 (@400 kPa)	4992 (@500 kPa)
Heptane	<b>7377</b> (@400 kPa)	6895 (@400 kPa)	6126 (@500 kPa)	5823 (@500 kPa)

Figure F19 and Table F14 present the respective data for the 0.5 m x 0.05 mm pre-column. For this column setup, the tendency towards better performance for the later eluting peaks is unambiguously observed, while the 30°C remain the optimum temperature for almost all the investigated compounds. The optimum inlet pressure, however, was slightly lower than that for the longer restriction, fluctuating now between 300 and 600 kPa, while being the 400 kPa for the majority of the compounds.

Comparing firstly the results produced by the last two examined column setups, the optimum temperature for almost every investigated standard was the 30°C. Only the cyclohexane for the 1 m restriction and the chloroform for the 0.5 mm restriction performed better at 40°C and 50°C, respectively. The optimum pressure was for both setups ranging between 400 and 600 kPa, showing a clear shift towards higher optimum pressures, as generally expected for VO applications. Heptane was again the compound with the highest N value, proving once again that later eluting peaks perform better under VO conditions.

Even though the superiority of the longer restriction was for the 0.05 mm i.d. pre-column not that evident as in the case of the 0.10 mm one, with 4 out of the 6 compounds performing better with the 1-m instead of the 0.5-m long column, the trend for longer restrictions remained. Moreover, when the length of the restriction was kept the same, with the 1 m x 0.10 mm, the 1 m x 0.075 mm and the 1 m x 0.05 mm i.d. pre-columns being compared, the wider restriction led to better performance which was step-wise deteriorating for all compounds, except the first-eluting standard (possibly due to poorer resolution from the solvent peak).

#### ***F.3.1.4. Method optimization for a 0.15 mm i.d. pre-column***

The last restriction investigated was, contrary to the previous two, a wider one, and in particular a 5 m x 0.15 mm i.d. pre-column. In that case, and judging by the results produced by the 0.10 mm i.d. pre-column (according to which the longer restriction had the best performance), no length reduction was performed. The results for that column setup are summarized in Figure F20 and Table F15.

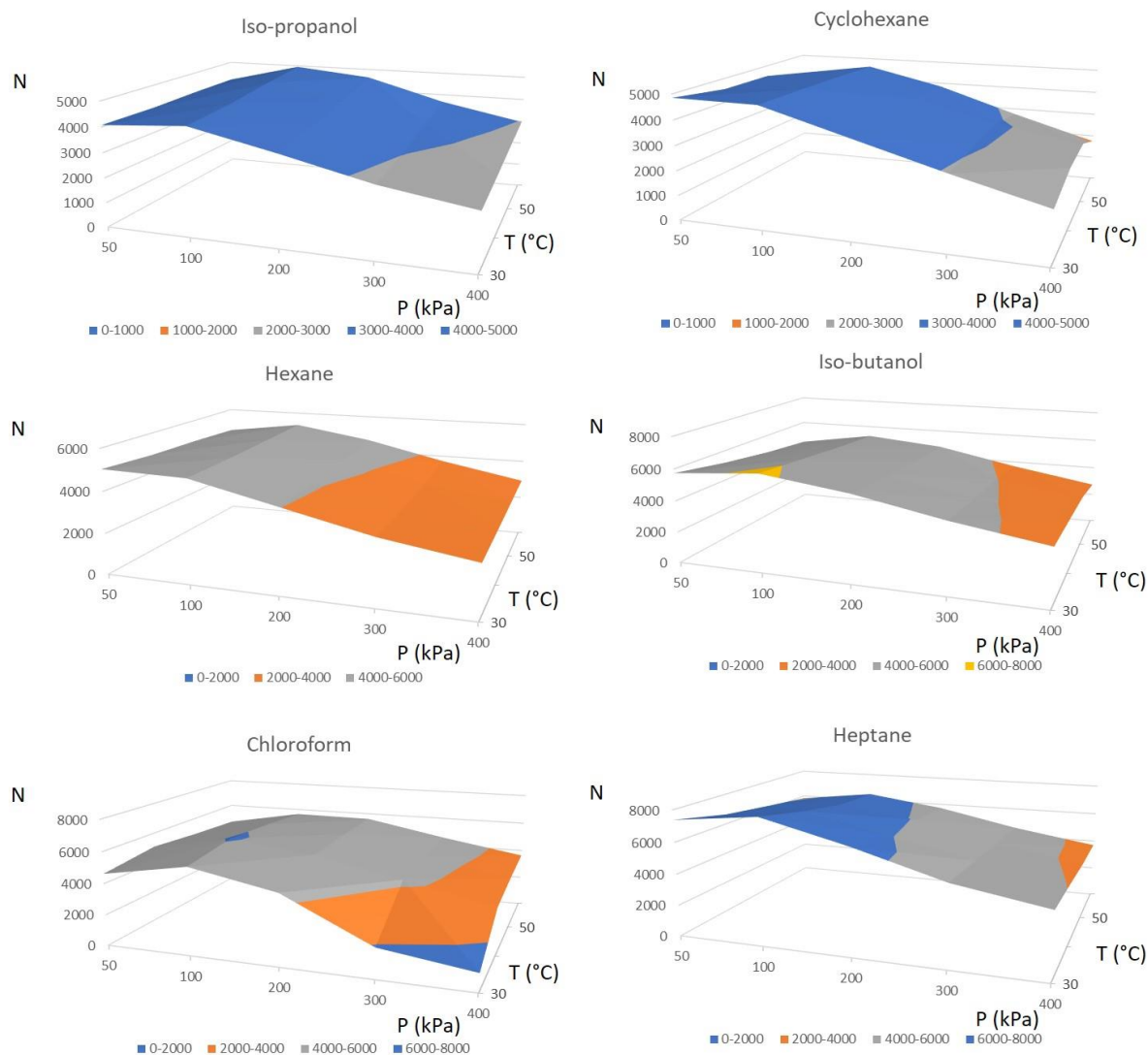


**Figure F20.** Surface plots produced for the investigated compounds, for measurements performed with the 5 m x 0.15 mm pre-column and the 15 m x 0.53 mm x 3 $\mu$ m  $d_f$  DB-624 analytical column.

**Table F15.** Number of theoretical plates corresponding to the optimum inlet pressure conditions (mentioned in brackets) for the investigated compounds under the isothermal temperatures tested, for measurements performed with the 5 m x 0.15 mm pre-column and the 15 m x 0.53 mm x 3 $\mu$ m  $d_f$  DB-624 analytical column.

Compound Name	Number of Theoretical Plates at:			
	30°C	40°C	50°C	60°C
Iso-propanol	4301 (@ 100 kPa)	4462 (@ 100 kPa)	4729 (@ 100 kPa)	<b>4950</b> (@ 100 kPa)
Hexane	5041 (@ 50 kPa)	5028 (@ 100 kPa)	5163 (@ 100 kPa)	<b>5303</b> (@ 100 kPa)
Chloroform	5535 (@ 100 kPa)	<b>6076</b> (@ 100 kPa)	5901 (@ 100 kPa)	5634 (@ 100 kPa)
Cyclohexane	<b>4854</b> (@ 50 kPa)	4768 (@ 100 kPa)	4710 (@ 100 kPa)	4613 (@ 100 kPa)
Iso-butanol	<b>6162</b> (@ 100 kPa)	5840 (@ 100 kPa)	5502 (@ 100 kPa)	5255 (@ 100 kPa)
Heptane	<b>7945</b> (@ 100 kPa)	7219 (@ 100 kPa)	6631 (@ 100 kPa)	6465 (@ 100 kPa)



When the 0.15 mm i.d. 5 m restriction was installed to the analytical column, the tested range of inlet pressures had to be adjusted, since such a wide pre-column could hardly allow at lower temperatures the pressure to exceed 400 kPa. Similar to the 1 m x 0.10 mm restriction, this effect was resulting from a higher flow reaching the end of the column setup and compromising the vacuum at the MS detector, leading also to instability and potential loss in performance. In particular, for 30°C the maximum inlet pressure was 430 kPa, which gradually increased to 480 kPa at 40°C, and then 490 kPa at 50°C, reaching slowly the pressure range applied for the previously examined column setups. Therefore, it comes as no surprise that for almost every compound and temperature, the optimum inlet pressure was observed for the lower values, and almost exclusively at 100 kPa, or even 50 kPa for hexane and cyclohexane when the isothermal elution was performed at 30°C. Such low optimum pressures were apparently observed when the 1 m x 0.10 mm pre-column was investigated. On the other hand, the optimum temperatures followed exactly the same trends as in the case of the 5 m x 0.10 mm restriction, showing a gradual reduction for the later eluting compounds.

When the 5-m restrictions of 0.10 and 0.15 mm i.d. were compared, the 0.10 mm i.d. pre-column demonstrated superior performance for all the investigated standards, showing that wider columns of this length are either below the optimum and may require even longer columns to be used. When these experiments were performed, a longer pre-column of this inner diameter was not readily available for a comparison, and the connection of an additional restriction of the same inner diameter was not tested, since the addition of one more column to the setup was considered to have a high leak potential.

### ***F.3.2. Method optimization for VO column systems according to the analytical column length***

Apart from our investigations concerning the pre-column dimensions, those of the analytical column were also involved in our method optimization procedure. The effect of the analytical column's length was the first parameter to be checked. Inspiration for this investigation was a discussion with Prof. J. G. M. (Hans-Gerd) Janssen, from the University of Amsterdam, on LP-GC-MS and our preliminary method optimization results, presented at the 38th International Symposium on Capillary Chromatography, in Riva del Garda, Italy. The 15-m analytical column used in our VO setups was considered by Prof. Janssen longer than the column length used in conventional VO applications, potentially compromising the extent of the vacuum inside the analytical column. Therefore, we decided to examine the effect in the system's efficiency by reduction of the analytical column's length from 15 to 10 m. For this set of experiments, the previously investigated VO system (comprised from a 5 m x 0.15 mm i.d. restriction and a 15 m wide-bore column) was used, with the length of the wide-bore column being simply reduced to 10 m from the

detector's side, leaving the rest of the connections intact. The results obtained with the new VO column setup are presented in Figure F21 and Table F16, while a comparison between the results obtained with the 15-m and 10-m analytical columns are summarized in Table F17.

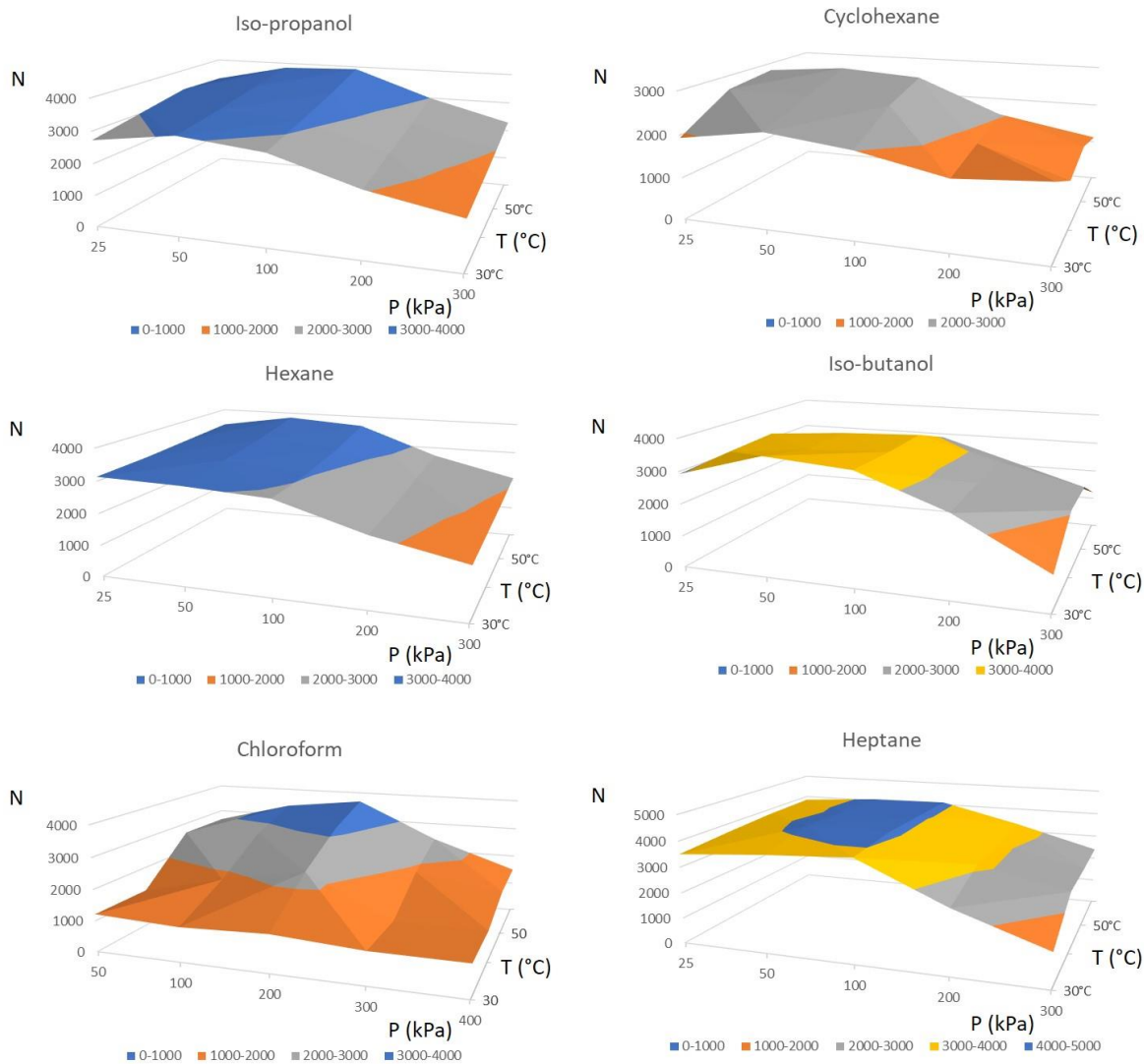


**Figure F21.** Surface plots produced for the investigated compounds, for measurements performed with the 5 m x 0.15 mm pre-column and the 10 m x 0.53 mm x 3µm d<sub>f</sub> DB-624 analytical column.

**Table F16. Number of theoretical plates corresponding to the optimum inlet pressure conditions (mentioned in brackets) for the investigated compounds under the isothermal temperatures tested, for measurements performed with the 5 m x 0.15 mm pre-column and the 10 m x 0.53 mm x 3 $\mu$ m d<sub>f</sub> DB-624 analytical column.**

Compound Name	Number of Theoretical Plates at:			
	30°C	40°C	50°C	60°C
Iso-propanol	3082 (@50 kPa)	3296 (@50 kPa)	3583 (@50 kPa)	<b>3914</b> (@100 kPa)
Hexane	3133 (@25 kPa)	3280 (@50 kPa)	3515 (@50 kPa)	<b>3828</b> (@50 kPa)
Chloroform	1211 (@25 kPa)	2334 (@100 kPa)	3164 (@100 kPa)	<b>3676</b> (@100 kPa)
Cyclohexane	2231 (@50 kPa)	2663 (@25 kPa)	<b>2976</b> (@50 kPa)	2327 (@50 kPa)
Iso-butanol	<b>3664</b> (@50 kPa)	3426 (@100 kPa)	3454 (@100 kPa)	2874 (@100 kPa)
Heptane	3929 (@100 kPa)	<b>4126</b> (@100 kPa)	4107 (@100 kPa)	4103 (@100 kPa)

**Table F17. Number of theoretical plates corresponding to the optimum inlet pressure and temperature conditions for the investigated compounds, for measurements performed with the 15 m and the 10 m x 0.53 mm x 3 $\mu$ m d<sub>f</sub> DB-624 analytical columns using always a 5 m x 0.15 mm pre-column.**

Compound Name	Analytical Column Dimensions		Number of Theoretical Plates Difference (%)*
	10m-5m x 0.15	15m-5m x 0.15	
Iso-propanol	3914	4950	20.9
Hexane	3828	5303	27.8
Chloroform	3676	6076	39.5
Cyclohexane	2976	4854	38.7
Iso-butanol	3664	6162	40.5
Heptane	4126	7945	48.1

\*The Number of Theoretical Plates Difference ( $\Delta N$ ) was calculated by the following equation:

$\Delta N = 100 - [(100 * N_{15m} / N_{10m})]$ , where  $N_{15m}$  and  $N_{10m}$  are the numbers of theoretical plates for the 15 m and the 10 m analytical column, respectively.

As for the wider pre-column, the inlet pressure range was again optimized, including lower values, since the optimum conditions proved to be even around 25 kPa. The optimum temperatures seemed to differ from those observed when the longer analytical column was used, however, the shift from higher temperatures for the first eluting peaks to lower ones was again evident (apart from heptane, for which the result of using different isothermal temperatures was almost statistically insignificant).

The aforementioned typical column length (of 10 m) refers to applications where compounds of intermediate volatility were analysed. Shifting our application range to more volatile species while requiring a system that would provide sufficient sensitivity, selectivity and reduce significantly the analysis time would demand a longer analytical column. The fact that our analytical column has a large inner diameter is counterproductive for our application purposes, therefore, as already discussed, we turned to thicker film columns. The proposed deviations from what is described as the optimum range of parameters for the VO in literature were not random, but in accordance to our intended application and the theory of chromatographic separation, and were experimentally compared to the VO standard conditions.

Focusing first on the analytical column length, a reduction from 15 m to 10 m proved to cause also an increase in the HETP values and a subsequent decrease in the number of theoretical plates for all tested compounds, as illustrated in Table F17 for the optimum temperature – inlet pressure combinations. This deterioration on the performance of the column setup is clearly justified by the reduced stationary phase present in the shorter analytical column.

Knowing from the previous measurements that the optimum pressure was expected at lower values, our experiments were restricted to inlet pressures up to 300 kPa, for which the Van Deemter curves included a clear minimum. And those optimum inlet pressure conditions were indeed mostly between 50 and 100 kPa. At the same time the optimum isothermal temperature was generally shifting from the highest to the lowest applied values as we go from early to late eluting compounds. From these experiments and for the best HETP values obtained from the different T-P data sets, an approximately 30% reduction in the length of the analytical column resulted in a N reduction of around 20% for the first eluting peak to values close to 50% lower for the compound eluting last. These results prove that, at least for highly volatile compounds (like the ones we investigated), the use of a longer analytical column under VO conditions is not only justified but also advisable for future applications. Under these conditions not only higher efficiencies are achieved, but also a wider range of restrictions can be tested without risking the performance and life-time of the detector, due to higher than tolerable carrier gas flows reaching the MS system.

### ***F.3.3. Performance comparison for VO column setups using thicker film and intermediate film thickness analytical columns for the quantification of highly volatile compounds***

Further investigations on the effect of the analytical column's film thickness in the performance of the VO setup, were conducted using a 15 m x 0.53 mm x 1 µm df Rtx-1301 analytical column and a 4 m x 0.10 mm pre-column. Since the stationary phase of the thinner film analytical column was the same as for the thicker film DB-624 column (6% Cyanopropyl-phenyl / 94% dimethyl polysiloxane), the results obtained with the new column system were compared to those obtained with the previously used analytical column connected to a restriction of the same dimensions.

During the method optimization procedure for the new column system, we observed that the HETP values were improving for the higher temperatures and inlet pressures applied. For those calculations the extracted ions were used, since interferences were encountered when the TIC signals were evaluated. Therefore, our investigations were not restricted to the temperature range applied before, but we tested stepwise higher temperatures, until further method optimizations were required (e.g. changes in the

scanning mass range). For this reason, we used oven temperatures up to 80°C or even 90°C. However, the elevated background signal observed for temperatures above 80°C dictated the need for a smaller scanning mass range for the MS, so that the early eluting peaks could be easier separated from the background using still the TIC. Therefore the 90°C were also tested; however, this change in the method does not let us use the results for any objective comparison, and the respective results are not presented. Characteristic chromatograms obtained with this column setup are presented in Figure F22. Table F18 summarizes the results from our first set of experiments, where the same temperature range as before was used, while Table F19 presents the results obtained from measurements at higher temperatures and Figures F23 and F24 illustrate the corresponding surface plots. Moreover, Table F20 comprises the best results provided with each VO column setup at the investigated temperatures and for the optimum inlet pressures.

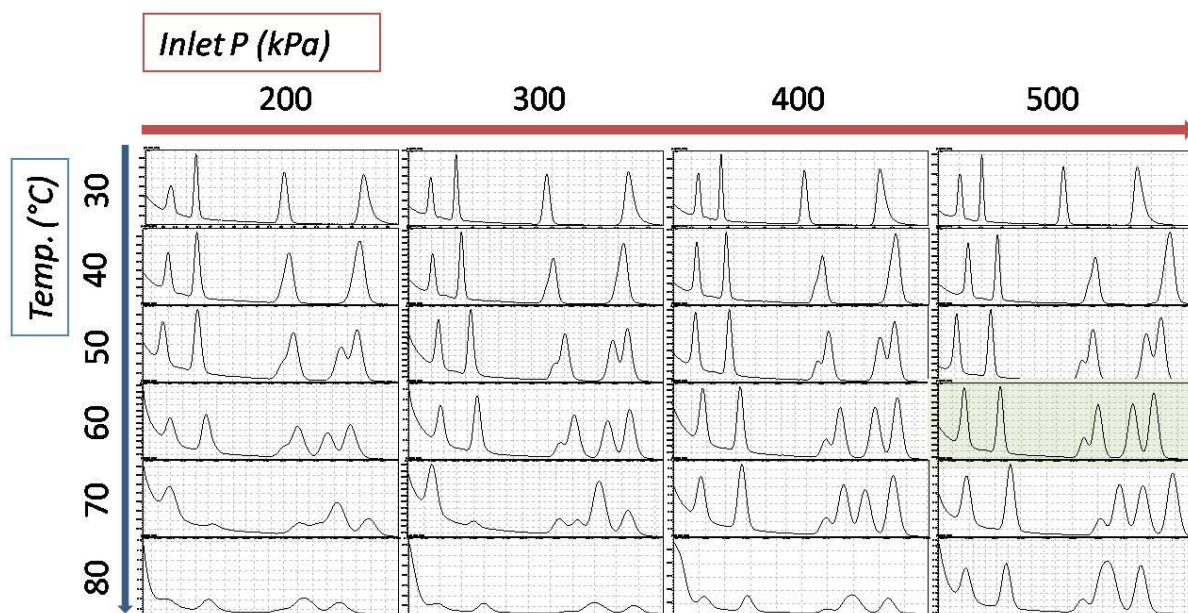


**Figure F22. LP-GC-MS Chromatograms produced with the 4 m x 0.10 mm pre-column and the 15 m x 0.53 mm x 1 $\mu$ m d<sub>f</sub> Rtx-1301 analytical column after isothermal elution at 30, 40, 50, 60, 70 and 80°C using inlet pressures between 200 and 500 kPa. The chromatogram corresponding to optimum conditions in terms of separation efficiency is marked with light green. The total runtimes had been in many cases optimized and are different for the chromatograms obtained with different methods. The scale for the intensities also differs among the chromatograms.**

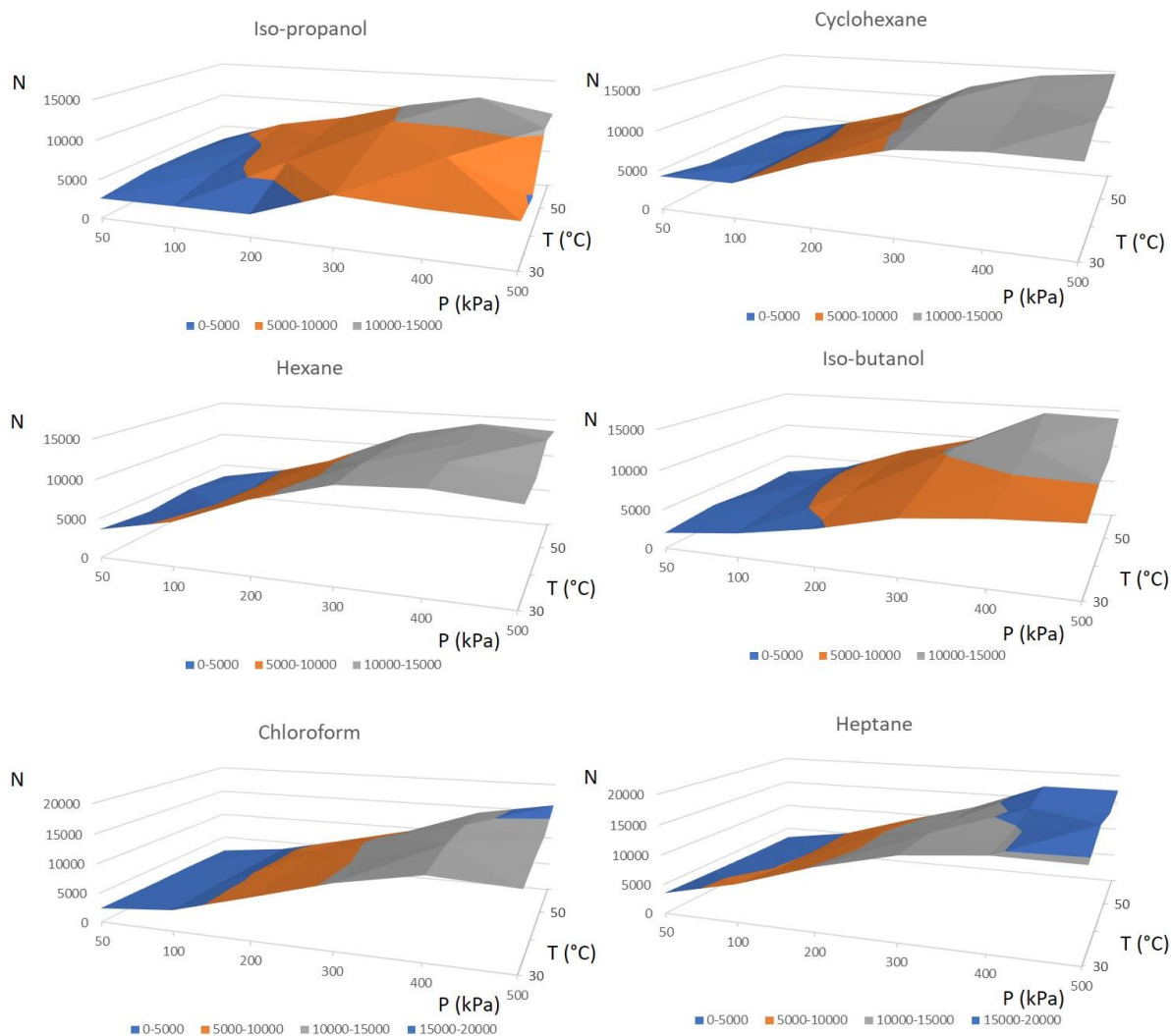


**Figure F23.** Surface plots produced for the investigated compounds, for measurements performed with the 4 m x 0.10 mm pre-column and the 15 m x 0.53 mm x 1 $\mu$ m  $d_f$  Rtx-1301 analytical column (temperature range 30 - 60°C).

**Table F18.** Number of theoretical plates corresponding to the optimum inlet pressure conditions (mentioned in brackets) for the investigated compounds under the isothermal temperatures tested, for measurements performed with the 4 m x 0.10 mm pre-column and the 15 m x 0.53 mm x 1 $\mu$ m  $d_f$  Rtx-1301 analytical column.

Compound Name	Number of Theoretical Plates at:			
	30°C	40°C	50°C	60°C
Iso-propanol	6177 (@300 kPa)	8732 (@400 kPa)	10628 (@500 kPa)	<b>12092</b> (@400 kPa)
Hexane	12233 (@400 kPa)	12868 (@400 kPa)	<b>14132</b> (@500 kPa)	13927 (@400 kPa)
Chloroform	13134 (@400 kPa)	14435 (@400 kPa)	14425 (@400 kPa)	<b>16192</b> (@500 kPa)
Cyclohexane	10955 (@400 kPa)	12791 (@500 kPa)	13005 (@500 kPa)	<b>14706</b> (@500 kPa)
Iso-butanol	8470 (@500 kPa)	10068 (@500 kPa)	11385 (@400 kPa)	<b>14159</b> (@400 kPa)
Heptane	14693 (@400 kPa)	17079 (@500 kPa)	15815 (@500 kPa)	<b>17234</b> (@500 kPa)

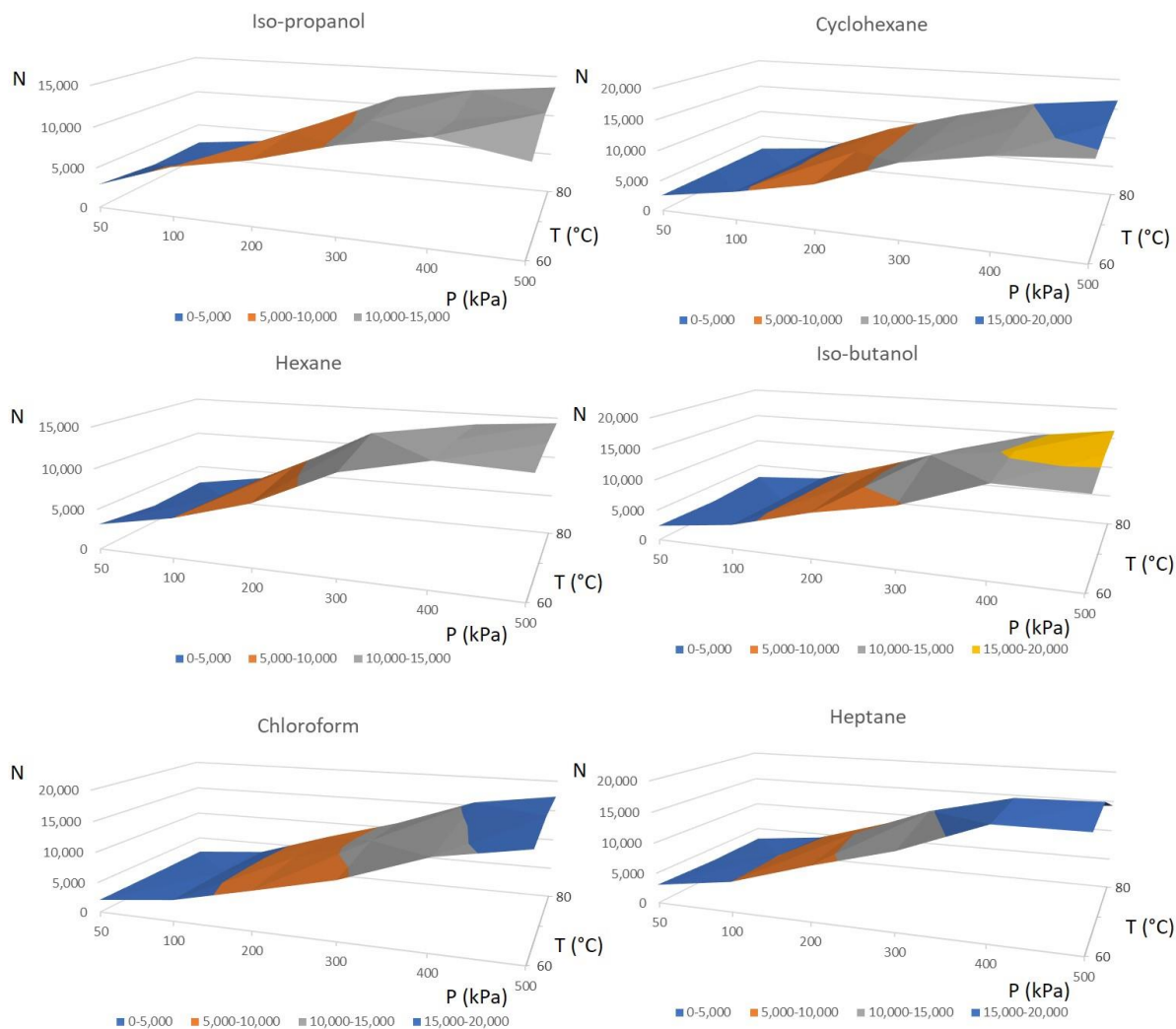


**Figure F24.** Surface plots produced for the investigated compounds, for measurements performed with the 4 m x 0.10 mm pre-column and the 15 m x 0.53 mm x 1 $\mu$ m  $d_f$  Rtx-1301 analytical column (temperature range 60 - 80°C).

**Table F19.** Number of theoretical plates corresponding to the optimum inlet pressure conditions (mentioned in brackets) for the investigated compounds under the isothermal temperatures tested, for measurements performed with the 4 m x 0.10 mm pre-column and the 15 m x 0.53 mm x 1 $\mu$ m  $d_f$  Rtx-1301 analytical column.

Compound Name	Number of Theoretical Plates at:		
	60°C	70°C	80°C
Iso-propanol	12092 (@400 kPa)	12849 (@500 kPa)	<b>13646</b> (@500 kPa)
Hexane	13927 (@400 kPa)	15353 (@600 kPa)	<b>15949</b> (@600 kPa)
Chloroform	16192 (@500 kPa)	17362 (@500 kPa)	<b>19103</b> (@600 kPa)
Cyclohexane	14706 (@500 kPa)	16005 (@500 kPa)	<b>16483</b> (@500 kPa)
Iso-butanol	14159 (@400 kPa)	16415 (@600 kPa)	<b>17281</b> (@600 kPa)
Heptane	17234 (@500 kPa)	<b>18082</b> (@500 kPa)	14272 (@500 kPa)

**Table F20. Number of theoretical plates corresponding to the optimum inlet pressure and temperature conditions (from the temperature range mentioned in brackets) for the investigated compounds, for measurements performed with the 15 m x 0.53 mm x 3 $\mu$ m d<sub>f</sub> DB-624 and the 15 m x 0.53 mm x 1 $\mu$ m d<sub>f</sub> Rtx-1301 analytical columns, using always a 4 m x 0.1 mm pre-column.**

Compound Name	Analytical Column (film thickness)		
	DB-624 (3 $\mu$ m) (30 – 60°C)	Rtx-1301 (1 $\mu$ m) (30 – 60°C)	Rtx-1301 (1 $\mu$ m) (30 – 80°C)
Iso-propanol	4588	12092	13646
Hexane	5367	14132	15949
Chloroform	7055	16192	19103
Cyclohexane	5340	14706	16483
Iso-butanol	6872	14159	17281
Heptane	8269	17234	18082

For the thinner film column setup, the inlet pressures at which the maximum number of theoretical plates was met for every compound and every temperature were ranging between 400 and 600 kPa, with a general tendency towards higher optimum inlet pressures when the isothermal temperature was increased. The optimum temperature from the range investigated was almost exclusively the highest tested. Particularly, separation at 80°C produced the best results for all compounds, apart from heptane, which had a clear optimum at 70°C. In addition, we do not observe here the trend present at the measurements performed with the same pre-column (4m x 0.10 mm) but the wider film thickness analytical column setup, according to which the retention of the compounds seemed to correlate with the optimum temperature. As it was previously observed for the thicker film column setup, the earlier eluting peaks had higher optimum isothermal temperature than the peaks eluting later on. Such a categorization is not possible for the thinner film columns, where all the compounds eluted more efficiently at higher temperatures (70 - 80°C).

Comparing now the number of theoretical plates calculated for each compound and for the optimum conditions of each column, the thinner film analytical column showed a 2 to 3-fold increase. In particular, for the first eluting peak the number of theoretical plates was 2.6 times higher for the thinner film column, when compared to the thicker film DB-624 column, while this improvement was gradually getting smaller for the later eluting peaks, reaching the factor of 2.1 for heptane. But, only at much higher pressures were the compound peaks sufficiently high and most of them adequately resolved not to require the exclusive use of extracted ions. Therefore, the corresponding extracted ions for each compound were always used for the necessary calculations. That was not the case when the thicker film column was used, where complete resolution of all peaks was possible after method optimization (Figure F9). Consequently, the thinner film column can provide higher efficiency in terms of number of theoretical plates, but, still, sufficient resolution of all investigated peaks was not possible. Increased resolution can be provided, though, but only for a limited number of T-P systems, showing that such a column system would require a



fine tuning of the analytical parameters when the sample components are known, and would result in insufficient separations when unknown screening would be performed using VO methods. For such unknown sample components, a reduced amount of information could be provided, when the technique is used for identification purposes. Under these circumstances, thicker film columns would be preferable, providing enhanced separation of the sample components for a wider range of temperature and inlet pressure conditions. This is a result of the combined effect of the separation provided by the thicker film and the reduced background resulting from the lower temperatures required.

The lower optimum temperatures are also beneficial in terms of prolonging the columns lifetime. However, they do not expand the applicability range of compounds, since no thermally sensitive compounds are expected in the group of highly volatile species intended for investigation. But when targeted compounds are of interest, the thinner film column setup would provide more sensitive methods. The higher optimum pressures provided by such column setups, where the film thickness does not exceed 1  $\mu\text{m}$ , is also closer to the theoretical expected values, which would make the used He carrier gas approach  $\text{H}_2$ -like properties and contribute to the increased efficiency of the VO system.

#### ***F.3.4. Comparison of the performance and compliance with theoretical calculations for a thick film VO column system used under vacuum outlet and atmospheric outlet conditions***

In order to investigate the effect of the vacuum outlet conditions in comparison to the atmospheric outlet, we performed both GC-MS and GC-FID measurements using the same column setup. The selected setup was comprised by the 5 m x 0.15 mm pre-column and the 15 m x 0.53 mm x 3  $\mu\text{m}$   $d_f$  DB-624 analytical column. The selection of the particular system was made, considering that the obtained results could be further used to check the compliance of the experimental values to the calculated ones from dedicated approximations used for multi-dimensional column systems, when the film thickness exceeds the standard column dimensions proposed for vacuum outlet applications.

The dedicated software used for the theoretical calculations (GC×GC Calculator - MS (Version 1.21) and GC×GC Calculator – FID (Version 2.2)) are taking into account the film thickness of the columns used, without any limit value being mentioned. The corresponding equations being used for the calculation of the plate height for the first-dimension column are presented in Figure F25. Analogous equations are also used for the second-dimension column.

$${}^1H = \frac{1}{{}^1CE} \left( \left( \frac{{}^2D_{m,o}}{{}^1u_o} + \frac{f({}^1k){}^1d_c^2}{{}^1D_{m,o}} \right) {}^1f_1 + \frac{g({}^1k){}^1d_f^2}{{}^1D_s} {}^1f_2 \right)$$

$$f({}^1k) = \frac{(1 + 6{}^1k + 11{}^1k^2)}{96(1 + {}^1k)^2} \quad g({}^1k) = \frac{{}^2k}{3(1 + {}^1k)^2}$$

$${}^1f_1 = \frac{9({}^1p_o^4 - 1)({}^1p_o^2 - 1)}{8({}^1p_o^3 - 1)^2} \quad {}^1f_2 = \frac{3({}^1p_o^2 - 1)}{2({}^1p_o^3 - 1)}$$

$${}^1p_o = \frac{{}^1p_{in}}{{}^1p_{out}} \quad {}^1u_o = \frac{{}^1F}{(\pi/4){}^1d_c^2}$$

$$D_s = \frac{D_m}{50\,000} \quad {}^1D_{m,o} = \frac{{}^2D_{m,o}{}^2p_{out}}{{}^1p_{out}}$$

**Figure F25. Equations used from the GC×GC Calculator - MS (Version 1.21) for the calculation of the plate height for the first-dimension column, where H: plate height; CE: coating efficiency; D<sub>s</sub>: analyte diffusion coefficient in the stationary phase; D<sub>m</sub>: analyte diffusion coefficient in the mobile phase; D<sub>m,o</sub>: analyte diffusion coefficient in the mobile phase at outlet pressure; d<sub>c</sub>: column diameter; d<sub>f</sub>: stationary phase film thickness; u<sub>o</sub>: outlet linear velocity; k: retention factor; f(k) and g(k): functions of the retention factor; f<sub>1</sub> and f<sub>2</sub>: pressure correction factors; F: volumetric flow through the column; p<sub>in</sub>: inlet pressure; p<sub>out</sub>: outlet pressure**

412

Additionally, the trueness of the experimental results provided by the particular column setup, used under vacuum outlet conditions, was tested by disassembling the system and connecting the columns again, followed by repetition of the method optimization measurements. In that way, any potential experimental artefacts could be identified, ensuring that the subsequent comparison between the experimental and theoretical data would be realistic and free from bias. The following Figures (F26-F29) and Tables F21-F30 summarize the results obtained from the new measurements with the particular column system, tested first under vacuum outlet and then under atmospheric outlet conditions. The results in every case are illustrated separately for each system, but also in a more comprehensive way that will allow comparisons among the obtained analytical data.

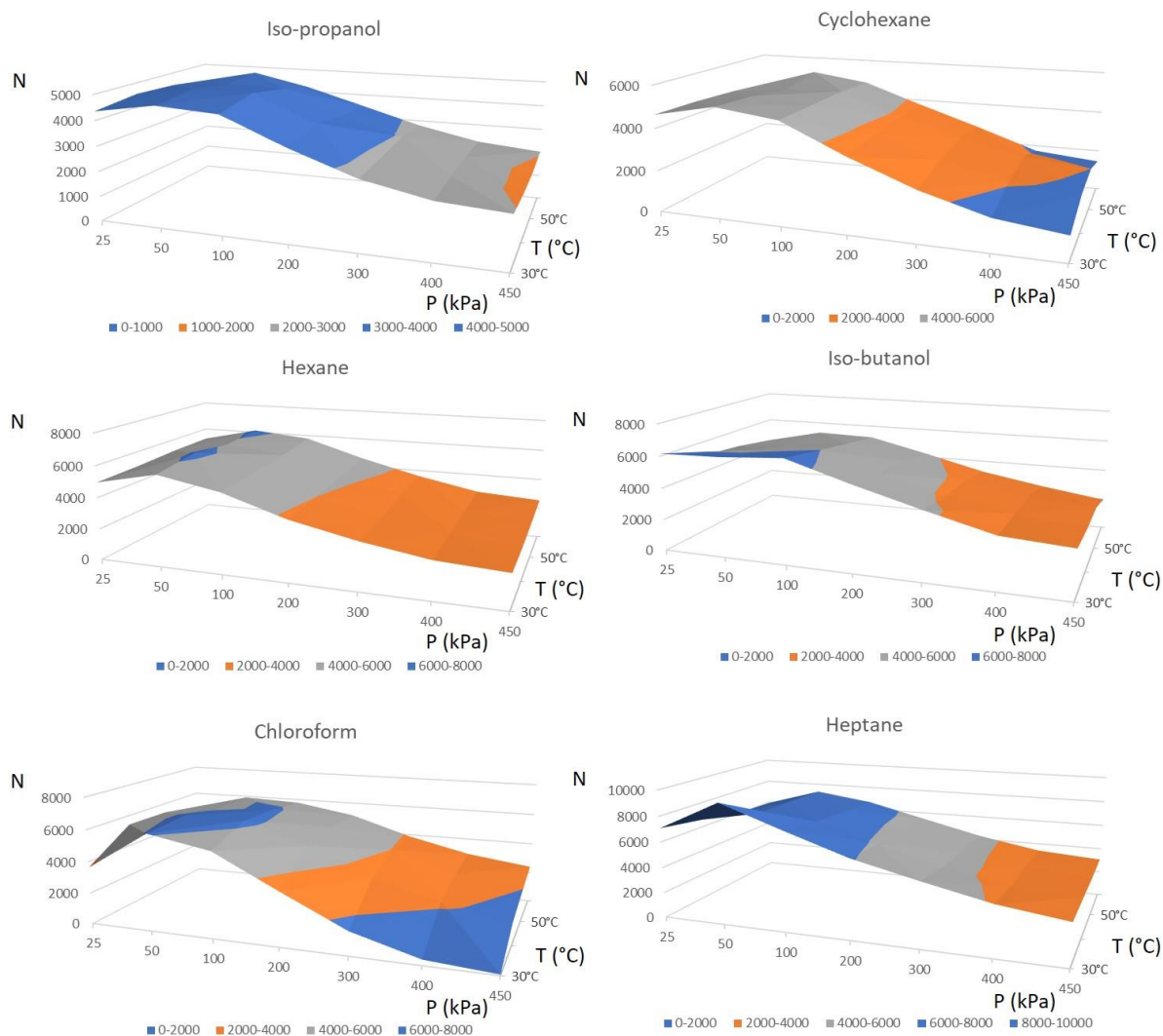


**Figure F26.** Surface plots produced from the experimental data calculated for the investigated compounds, for measurements performed with the 5 m x 0.15 mm pre-column and the 15 m x 0.53 mm x 3 $\mu$ m df DB-624 analytical column, under vacuum outlet conditions (GC-MS).

**Table F21.** Experimentally obtained number of theoretical plates corresponding to the optimum inlet pressure conditions (mentioned in brackets) for the investigated compounds under the isothermal temperatures tested, for measurements performed with the 5 m x 0.15 mm pre-column and the 15 m x 0.53 mm x 3 $\mu$ m d<sub>f</sub> DB-624 analytical column under vacuum outlet conditions (GC-MS).

Compound Name	Number of Theoretical Plates at:			
	30°C	40°C	50°C	60°C
Iso-propanol	4742 (@50 kPa)	<b>4895</b> (@100 kPa)	4651 (@50 kPa)	4733 (@50 kPa)
Hexane	5759 (@50 kPa)	<b>6175</b> (@50 kPa)	5917 (@50 kPa)	6132 (@50 kPa)
Chloroform	6071 (@50 kPa)	<b>6298</b> (@50 kPa)	6120 (@100 kPa)	5920 (@50 kPa)
Cyclohexane	<b>5216</b> (@50 kPa)	5079 (@50 kPa)	4902 (@100 kPa)	5191 (@50 kPa)
Iso-butanol	<b>6508</b> (@100 kPa)	6033 (@100 kPa)	5575 (@100 kPa)	5262 (@50 kPa)
Heptane	<b>8375</b> (@50 kPa)	7452 (@50 kPa)	7416 (@50 kPa)	7306 (@50 kPa)

**Table F22. Comparison between the previous and new number of theoretical plates corresponding to the optimum inlet pressure and temperature conditions for the investigated compounds, for measurements performed with the 15 m x 0.53 mm x 3 $\mu$ m d<sub>f</sub> DB-624 analytical columns using a 5 m x 0.15 mm pre-column, under vacuum outlet conditions (GC-MS).**

Compound Name	Analytical Column Dimentions		$(N_{old} / N_{new}) \times 100\%$
	N <sub>old</sub>	N <sub>new</sub>	
Iso-propanol	4950	4895	101.1
Hexane	5303	6175	85.9
Chloroform	6076	6298	96.5
Cyclohexane	4854	5216	93.1
Iso-butanol	6162	6508	94.7
Heptane	7945	8375	94.9

As demonstrated by the differences at the number of theoretical plates provided under the optimum conditions when measurements with the same column setup (with the 5 m x 0.15 mm restriction) were performed, the results were highly reproducible. Any differences in the calculated values could be justified by the condition of the detector when each set of measurements was performed, using a new tuning file for the repetition of the measurements. In addition, no internal standard was used to correct any effect of e.g. the injection step. Furthermore, the facts that the optimum inlet pressures were again in the range of 50 to 100 kPa and the same trend for the optimum temperature (decrease for later eluting peaks) were prevailed, proved that the experimental results contain no artefacts and any variance in the calculated values has a random nature. Last but not least, repeatability measurements were also performed, using an n-alkane mixture. Isothermal elution at 60°C was performed, using an inlet pressure of 400 kPa, and the results obtained for 12 repetitions of the measurements are summarized in Table F23. The RSD% values calculated for the absolute and relative areas of the standards, using C9 as internal standard, proved the very high repeatability of methods performed under vacuum outlet conditions, even when the inlet pressures are not the optimum. The particular selection of inlet pressure was also made, so that any potential backwards contamination due to air drawn from other parts of the system and affecting negatively the stability of the VO system and the response of the detector, would have been identified. However, such an effect was not observed for our system.

**Table F23. Results of repeatability measurements performed for a n-alkane mixture (C6-C12) and for 12 repetitions, using the 15 m x 0.53 mm x 3 $\mu$ m d<sub>f</sub> DB-624 analytical column and a 5 m x 0.15 mm pre-column, under vacuum outlet conditions (GC-MS). The calculations of STD<sub>1</sub>% and STD<sub>2</sub>% are based on the absolute and relative areas, respectively.**

n-Alkanes	Retention Time (min)	RSD <sub>1</sub> %	RSD <sub>2</sub> %*
C6	1.787	3.3	1.49
C7	3.678	2.8	0.44
C8	6.67	2.8	0.29
C9	8.302	2.8	-
C10	9.511	2.7	0.21
C11	10.523	2.6	0.33
C12	11.419	2.6	0.35
<b>Average Values:</b>		<b>2.8</b>	<b>0.52</b>

\*RSD<sub>2</sub>% calculated from the relative areas, using C9 as internal standard.

As already mentioned in the dedicated paragraph on instrumentation and operating conditions (F.2.2.), the GC x GC Calculators for MS and FID were used to calculate the theoretical values for the plate numbers when vacuum outlet and atmospheric pressure conditions were used. Starting with the results on the MS measurements and the respective theoretical values, Figures F26 and F27 show inconsistency between the values calculated from the produced chromatograms and those provided by the aforementioned software. Specifically, neither the optimum temperatures nor the inlet pressures were the same, with the number of theoretical plates being significantly smaller than predicted (Tables F21 and F24). While the predicted optimum conditions were the 60°C for all investigated compounds and 200 kPa for most of them (ranging from 100 to 300 kPa), the respective experimental values were between 50 and 100 kPa and 30 to 40°C, respectively. As already mentioned, the plate number for the optimum conditions of the experimental data were significantly lower than those predicted under the theoretically optimum conditions (Table F25). However, those differences become even greater when the theoretically optimum conditions were chosen and the corresponding experimentally obtained numbers of plates were compared to the calculated ones (Table F26). That observation dictated the need for these experiments, since the theoretical models would not provide realistic analytical conditions, when unconventional column dimensions are used. As a result, applications requiring the use of thicker film columns could not use method parameters based on predicted values, but should rather be based on experimental method optimization data. Last but not least, the inadequate modelling of those systems may result from the higher than considered contribution of the mass transfer coefficient in the stationary phase ( $C_{SP}$ , Figure E10) to the approximations used by the software.

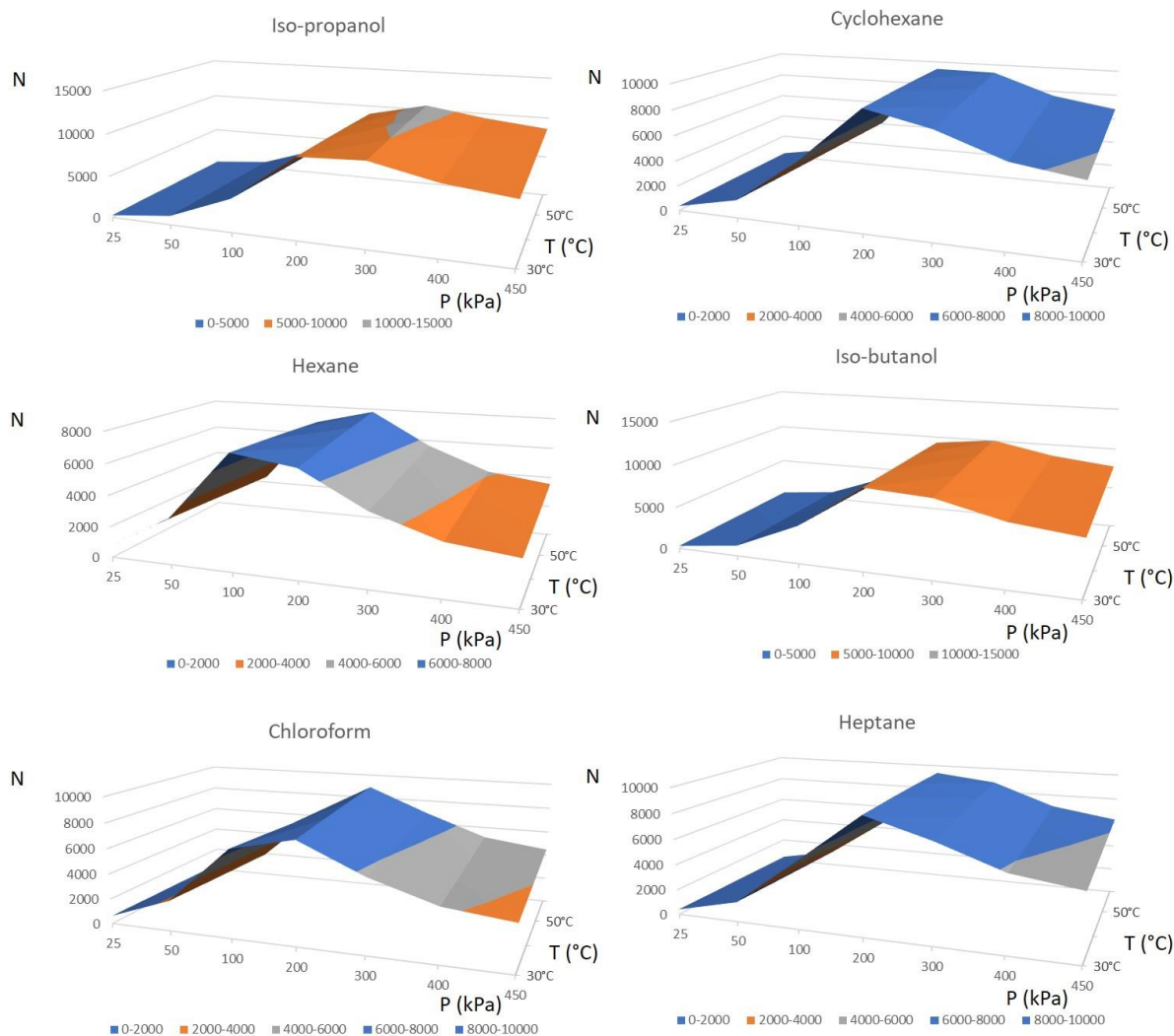


**Figure F27.** Surface plots produced from the theoretical data calculated for the investigated compounds, for measurements performed with the 5 m x 0.15 mm pre-column and the 15 m x 0.53 mm x 3 $\mu$ m df DB-624 analytical column, under vacuum outlet conditions (GC-MS).

**Table F24.** Theoretically obtained number of theoretical plates corresponding to the optimum inlet pressure conditions (mentioned in brackets) for the investigated compounds under the isothermal temperatures tested, for measurements performed with the 5 m x 0.15 mm pre-column and the 15 m x 0.53 mm x 3 $\mu$ m d<sub>f</sub> DB-624 analytical column under vacuum outlet conditions (GC-MS).

Compound Name	Number of Theoretical Plates at:			
	30°C	40°C	50°C	60°C
Iso-propanol	9640 (@ 300 kPa)	9996 (@ 300 kPa)	10307 (@ 300 kPa)	<b>10572</b> (@ 300 kPa)
Hexane	7253 (@ 100 kPa)	7159 (@ 100 kPa)	7449 (@ 200 kPa)	<b>7814</b> (@ 200 kPa)
Chloroform	7895 (@ 200 kPa)	8268 (@ 200 kPa)	8611 (@ 200 kPa)	<b>8918</b> (@ 200 kPa)
Cyclohexane	9203 (@ 200 kPa)	9317 (@ 200 kPa)	9377 (@ 200 kPa)	<b>9386</b> (@ 200 kPa)
Iso-butanol	9379 (@ 200 kPa)	9384 (@ 200 kPa)	9727 (@ 300 kPa)	<b>10056</b> (@ 300 kPa)
Heptane	8984 (@ 200 kPa)	9161 (@ 200 kPa)	9287 (@ 200 kPa)	<b>9362</b> (@ 200 kPa)

**Table F25. Comparison between the theoretically and experimentally obtained number of theoretical plates corresponding to the optimum inlet pressure and temperature conditions for the investigated compounds, for measurements performed with the 15 m x 0.53 mm x 3 $\mu$ m d<sub>f</sub> DB-624 analytical columns using always a 5 m x 0.15 mm pre-column, under vacuum outlet conditions (GC-MS).**

Compound Name	Number of Theoretical Plates		$(N_{\text{theor}} / N_{\text{exp}}) \times 100\%$
	$N_{\text{experimental}}$	$N_{\text{theoretical}}$	
Iso-propanol	4895	10572	46.3
Hexane	6175	7814	79.0
Chloroform	6298	8918	70.6
Cyclohexane	5216	9386	55.6
Iso-butanol	6508	10056	64.7
Heptane	8375	9362	89.5

**Table F26. Comparison between the theoretically obtained number of theoretical plates, corresponding to the optimum inlet pressure and temperature conditions for the investigated compounds, and the experimentally values, corresponding to the same conditions, for measurements performed with the 15 m x 0.53 mm x 3 $\mu$ m d<sub>f</sub> DB-624 analytical columns using always a 5 m x 0.15 mm pre-column, under vacuum outlet conditions (GC-MS).**

Compound Name	Number of Theoretical Plates		$(N_{\text{theor}} / N_{\text{exp}}) \times 100\%$
	$N_{\text{experimental}}^*$	$N_{\text{theoretical}}$	
Iso-propanol	2795	10572	26.4
Hexane	4589	7814	58.7
Chloroform	5104	8918	57.2
Cyclohexane	3741	9386	39.9
Iso-butanol	3245	10056	32.3
Heptane	5455	9362	58.3

\*at optimum temperature and inlet pressure conditions expected from the theoretical calculations

When the respective method optimization experiments were performed for atmospheric outlet conditions, using a GC-FID system and the same column setup, the correlation between the theoretical and the experimental data was evident (Figures F28 and F29). In particular, for most experiments the optimum inlet pressure was proven to be that of 150 kPa, while the 150 and 200 kPa were also predicted to be the optimum values (Tables F27, F28 and F29). Although the optimum temperature followed the trend demonstrated also in the vacuum outlet measurements (decreasing for the later eluting compounds), for the predicted data the contribution of the temperature was insignificant, as long as the optimum inlet pressure was selected. Therefore, the predicted number of theoretical plates was always around 17000, showing that the elution order or the nature of the compounds affected these results at a much lesser extent. Moreover, the consistency between the experimental and predicted results becomes notably high when the predicted optimum values are used for the comparison of the corresponding calculated and experimental data (Table F30). Consequently, the model used for the atmospheric pressure applications

does not suffer from the effect of higher film thicknesses, proving that this analytical parameter is of paramount importance only when vacuum conditions are applied at the column, limiting significantly the advantages of low-pressure systems.

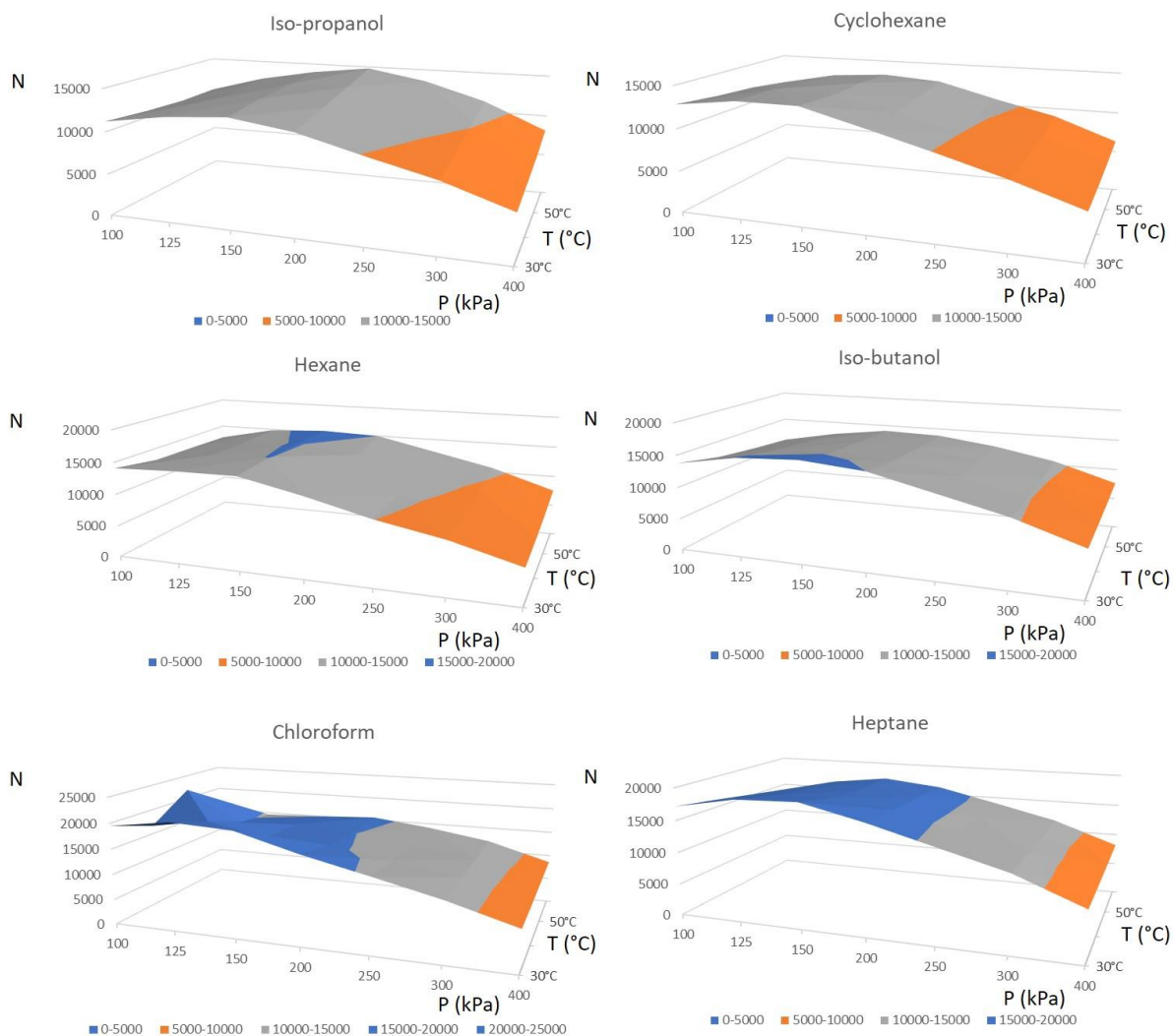


**Figure F28. Surface plots produced from the experimental data obtained for the investigated compounds, for measurements performed with the 5 m x 0.15 mm pre-column and the 15 m x 0.53 mm x 3 $\mu$ m df DB-624 analytical column, under atmospheric outlet conditions (GC-FID).**



**Table F27. Experimentally obtained number of theoretical plates corresponding to the optimum inlet pressure conditions (mentioned in brackets) for the investigated compounds under the isothermal temperatures tested, for measurements performed with the 5 m x 0.15 mm pre-column and the 15 m x 0.53 mm x 3 $\mu$ m d<sub>f</sub> DB-624 analytical column under atmospheric outlet conditions (GC-FID).**

Compound Name	Number of Theoretical Plates at:			
	30°C	40°C	50°C	60°C
Iso-propanol	12811 (@150 kPa)	13309 (@150 kPa)	13729 (@200 kPa)	<b>14797</b> (@200 kPa)
Hexane	14480 (@150 kPa)	15033 (@150 kPa)	15100 (@150 kPa)	<b>15312</b> (@150 kPa)
Chloroform	21108 (@125 kPa)	18514 (@125 kPa)	<b>21896</b> (@100 kPa)	15589 (@100 kPa)
Cyclohexane	<b>13717</b> (@125 kPa)	13583 (@125 kPa)	13425 (@150 kPa)	13128 (@150 kPa)
Iso-butanol	<b>15843</b> (@150 kPa)	14689 (@150 kPa)	14289 (@150 kPa)	14035 (@150 kPa)
Heptane	<b>19178</b> (@150 kPa)	17789 (@150 kPa)	17186 (@150 kPa)	17249 (@150 kPa)

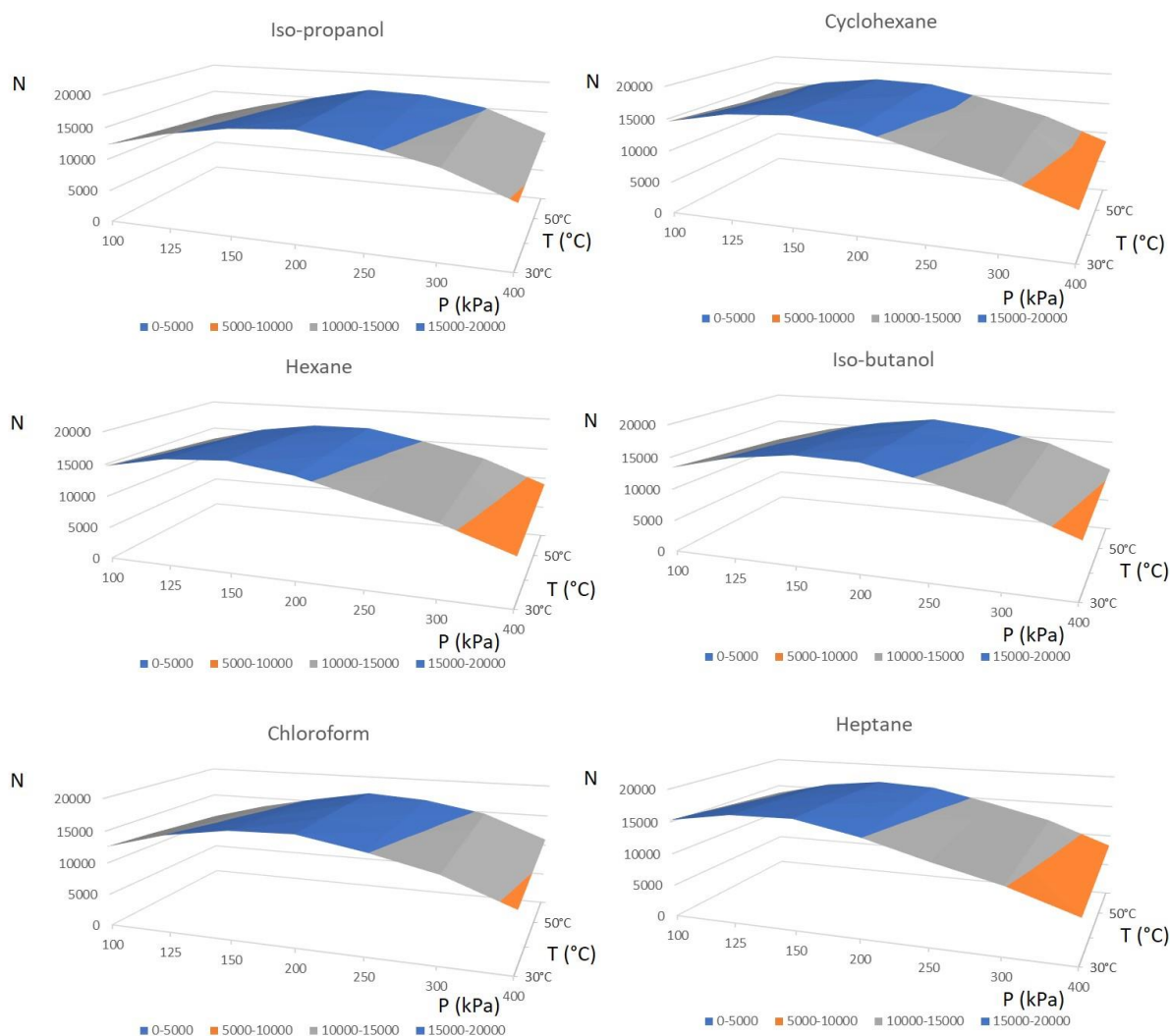


**Figure F29. Surface plots produced from the theoretical data calculated for the investigated compounds, for measurements performed with the 5 m x 0.15 mm pre-column and the 15 m x 0.53 mm x 3 $\mu$ m d<sub>f</sub> DB-624 analytical column, under atmospheric outlet conditions (GC-FID).**

**Table F28.** Theoretically obtained number of theoretical plates corresponding to the optimum inlet pressure conditions (mentioned in brackets) for the investigated compounds under the isothermal temperatures tested, for measurements performed with the 5 m x 0.15 mm pre-column and the 15 m x 0.53 mm x 3 $\mu$ m d<sub>f</sub> DB-624 analytical column under atmospheric outlet conditions (GC-FID).

Compound Name	Number of Theoretical Plates at:			
	30°C	40°C	50°C	60°C
Iso-propanol	16954 (@200 kPa)	17066 (@200 kPa)	<b>17079</b> (@200 kPa)	17002 (@200 kPa)
Hexane	<b>17021</b> (@150 kPa)	16987 (@150 kPa)	16860 (@150 kPa)	16730 (@200 kPa)
Chloroform	16807 (@200 kPa)	16992 (@200 kPa)	<b>17078</b> (@200 kPa)	17071 (@200 kPa)
Cyclohexane	<b>17022</b> (@150 kPa)	16966 (@150 kPa)	16818 (@150 kPa)	16818 (@150 kPa)
Iso-butanol	16808 (@150 kPa)	16810 (@200 kPa)	16989 (@200 kPa)	<b>17076</b> (@200 kPa)
Heptane	16948 (@150 kPa)	17020 (@150 kPa)	16994 (@150 kPa)	<b>16879</b> (@150 kPa)

**Table F29.** Comparison between the theoretically and experimentally obtained number of theoretical plates corresponding to the optimum inlet pressure and temperature conditions for the investigated compounds, for measurements performed with the 15 m x 0.53 mm x 3 $\mu$ m d<sub>f</sub> DB-624 analytical columns using always a 5 m x 0.15 mm pre-column, under atmospheric outlet conditions (GC-FID).

Compound Name	Number of Theoretical Plates		$(N_{\text{theor}} / N_{\text{exp}}) \times 100\%$
	$N_{\text{experimental}}$	$N_{\text{theoretical}}$	
Iso-propanol	14797	17079	86.6
Hexane	15312	17021	90.0
Chloroform	21896	17078	128.2
Cyclohexane	13717	17022	80.6
Iso-butanol	15843	17076	92.8
Heptane	19178	17020	112.7

**Table F30.** Comparison between the theoretically obtained number of theoretical plates, corresponding to the optimum inlet pressure and temperature conditions for the investigated compounds, and the experimental values, corresponding to the same conditions, for measurements performed with the 15 m x 0.53 mm x 3 $\mu$ m d<sub>f</sub> DB-624 analytical columns using always a 5 m x 0.15 mm pre-column, under atmospheric outlet conditions (GC-FID).

Compound Name	Number of Theoretical Plates		$(N_{\text{theor}} / N_{\text{exp}}) \times 100\%$
	$N_{\text{experimental}}^*$	$N_{\text{theoretical}}$	
Iso-propanol	13729	17079	80.4
Hexane	14480	17021	85.1
Chloroform	15123	17078	88.5
Cyclohexane	13699	17022	80.5
Iso-butanol	13780	17076	80.7
Heptane	17789	17020	104.5

\*at optimum temperature and inlet pressure conditions expected from the theoretical calculations

The last comparison discussed, involves the performance of the vacuum and atmospheric outlet systems. While Table F31 illustrated the higher number of theoretical plates obtained by the GC-FID measurements at optimum temperature and inlet pressure conditions, Figure F30 demonstrates the profound advantage in runtime, provided by the vacuum outlet. However, both effects are complying with our initial assumptions based on the theoretical aspects of the vacuum outlet. Therefore, both the 3-fold increase in the number of theoretical plates for the GC-FID system and the 2.5-fold gain in analysis speed for the LP-GC-MS system, are justified by the fundamental considerations on the technique discussed at the introductory part. However, the advantage of selectivity provided by the MS detector can counteract for the decreased performance, particularly when unknown screening is aimed at, demonstrating the overall superiority of the vacuum outlet approach.

**Table F31. Comparison between the number of theoretical plates provided for the vacuum outlet (GC-MS) and atmospheric outlet (GC-FID) conditions, for values corresponding to the optimum inlet pressure and temperature conditions and for measurements performed with the 15 m x 0.53 mm x 3 $\mu$ m d<sub>f</sub> DB-624 analytical column and a 5 m x 0.15 mm pre-column.**

Compound Name	Number of Theoretical Plates		$(N_{MS} / N_{FID}) \times 100\%$
	$N_{MS}$	$N_{FID}$	
Iso-propanol	4895	14797	33.1
Hexane	6175	15312	40.3
Chloroform	6298	21896	28.8
Cyclohexane	5216	13717	38.0
Iso-butanol	6508	15843	41.1
Heptane	8375	19178	43.7

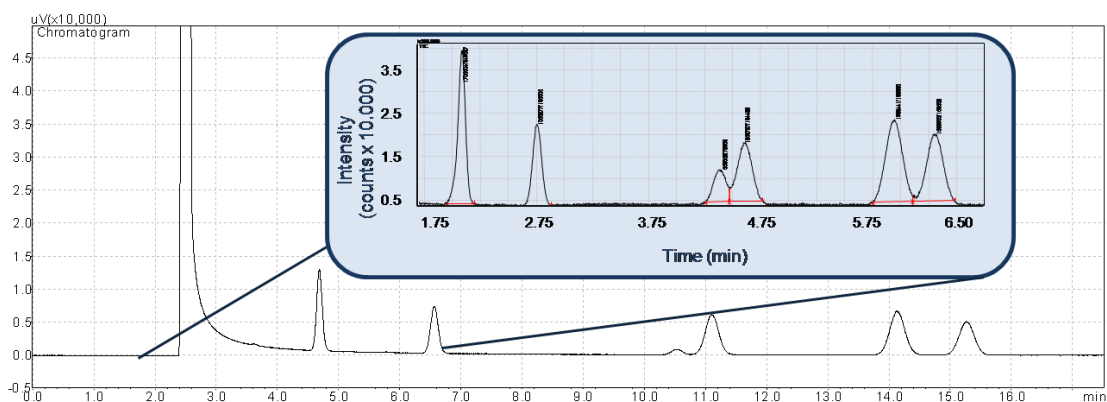


**Figure F30. Comparison of a LP-GC-MS and a GC-FID chromatogram, both produced with the 5 m x 0.15 mm pre-column and the 15 m x 0.53 mm x 3 $\mu$ m d<sub>f</sub> DB-624 analytical column after isothermal elution at 30°C and inlet pressure of 200 kPa.**

#### ***F.4. Conclusions***

A comprehensive investigation on the optimization parameters of vacuum-outlet column systems was performed. The parameters evaluated involved not only the restriction, but also the analytical column. When the restriction dimensions were optimized, different lengths and inner diameters were tested. The corresponding optimization performed for the analytical column parameters was focused on the length of the column and the film thickness. For each column setup method optimization was performed for a group of volatile compounds and concerning the inlet pressure and the isothermal temperature applied. The HETP was in every case calculated, defining the relevant range of inlet pressures tested (so that a minimum HETP value was included) and showing which value was optimum for each compound at every temperature. The corresponding surface plots were produced, demonstrating the optimum temperature-inlet pressure conditions that provide the highest number of theoretical plates for every standard.

Due to system limitations the measurements were always performed near the optimum, leading to minor changes in column efficiency. Being limited to the low-flow-end of the curve by the pressure drop between inlet and vacuum, going to even smaller flow rates was not possible. And at the high end side of the flows, the physical limits of the instruments were again approached, concerning both pumping capacity of the MS and pressure applied to the inlet. Therefore the data space that we have looked at had too narrow borders to really see a significant difference. If these limitations would not exist, it would be interesting to cover a larger range of parameter values in order to see more pronounced trends and differences. However, a significant number of observations was still possible.

Summarizing the obtained results we can firstly conclude that wider and longer restrictions provide better results in terms of number of theoretical plates. This conclusion results from investigations involving nine different column systems, where the same analytical column was used and only the restriction parameters were changing. In addition, low temperatures were preferable for the isothermal elution of most compounds, with 30°C being the optimum temperature for the majority of the standards and column systems tested. However, in many experimental sets a general preference for higher temperatures for early eluting compounds was observed, with the optimum values decreasing until they reached the lowest applied for the last eluting peak. Concerning the inlet pressure, it was demonstrated that longer restrictions of the same inner diameter resulted in higher optimum inlet pressures. Furthermore, the wider the inner diameter of the restriction, the lower the experimental optimum value for the inlet pressure, when restrictions of the same length were compared. These observations are in compliance with the role of the pre-column in the VO setup, since shorter and wider pre-columns will provide less efficient restrictions, challenging the performance of the detector and the stability of the system. Consequently, when such restrictions are tested, lower inlet pressures are expected to provide better performances, since they would not increase further the flow to the detector.

When the dimensions of the analytical column were in the focus, the effect of the column's length in the performance of the VO system was initially tested. What we observed was that the 15-m column selected by our group provided significantly better results than those produced with the equivalent 10-m column, corresponding to standard VO applications. It was therefore proven that the extended column length selected for our application, provided the necessary separation efficiency required for volatile compounds, regardless of any compromise in the extension of the vacuum inside the analytical column.

Our last optimization parameter involved the film thickness of the analytical column. The stationary phase film thickness selected for the determination of highly volatile compounds was equal to 3  $\mu\text{m}$ . This unconventional value for vacuum outlet applications was chosen in order to provide enhanced retention and improved resolution for the targeted group of compounds. Efficient trapping of the analytes is generally compromised when wide-bore columns are used. Therefore, the increased film thickness was selected to counteract this effect. However, the thicker films result in slower diffusion of analyte molecules. The significant contribution of the mass transfer coefficient in the stationary phase, changes the slope of the Golay equation towards higher values and limits the benefits provided by the application of vacuum inside the analytical column. To compare these antagonistic effects we compared the results provided for the thicker film column to those provided by columns of conventional film thickness. What we observed was that the thinner film column provided higher efficiencies in terms of number of theoretical plates, but not sufficient resolution of all investigated peaks. Therefore the selected ions had to be used exclusively, resulting in tedious and time consuming data evaluation procedures. Efficient resolution was possible only for a limited number of temperature – inlet pressure combinations, showing that such a column system would require a fine tuning of the analytical parameters when the sample components are known. It would also result in insufficient separations when unknown screening would be performed, reducing the amount of information provided, when the technique is used for identification purposes. Hence, thicker film columns would be preferable, when the sample constituents are unknown, providing enhanced separation for a wider range of temperature and inlet pressure conditions. Moreover, with the thicker film column lower temperatures were required, reducing the background signal and prolonging the column's lifetime, while expanding further the applicability range of such VO methods to thermally sensitive compounds. Consequently, it should be considered whether the sensitivity or the separation efficiency should be compromised, leading to the application of thicker film analytical columns or thinner film ones, respectively. This observation also leads to the conclusion that highly volatile compounds do not belong to the optimum range of analytes for vacuum outlet applications, since and longer and thicker analytical columns generally required compromise the advantages of VO.

The slower diffusion of analyte molecules in the thicker film column resulted also in discrepancies between the practical and the theoretical values, obtained from dedicated software, for vacuum outlet measurements. Even though the thickness of the film layer was taken into account for the modelling of

two-column systems, the predicted optimum conditions and HETP values were significantly different from the ones obtained from the experimental data, underlining the significance of the aforementioned investigations. This effect was not present when atmospheric outlet conditions were applied, using the same column setup. Therefore, the GC-FID approximations provided by system modelling coincide with the experimental results, proving that the contribution of the film thickness is under these conditions less significant and that for further investigations, the actual performance of respective experiments is not necessary.

The comparisons of vacuum outlet and atmospheric outlet conditions were finally performed, using the actual results produced experimentally by the application of one wide-bore, thicker film column setup. These investigations demonstrated that the application of vacuum inside the column system reduced the analysis time by a factor of 2.5, however, the number of theoretical plates experienced also a 3-fold reduction. Having already discussed the theory of low pressure separations, these opposite effects come as no surprise. It should be though pointed out that the enabling feature of VO is the selectivity provided by the MS, which counteracts for the decreased performance, particularly when unknown screening is targeted.

Last but not least, one of the investigated column setups was additionally disassembled and put together again, and the same experiments were repeated, to ensure that no bias was involved in our calculations and that our results were sufficiently reproducible. Therefore, any differences in the obtained values from measurements performed with the same column system have a random nature. Repeatability measurements were also successfully performed, using an n-alkane mixture. For these measurements, the analytical conditions were carefully selected, checking the stability of the VO system. The average RSD% value of 0.5% calculated when one of the standards was used as internal standard, proved that our system is stable, even at the highest limit of inlet pressures applied for the particular column setup. Furthermore, it proved that no potential backwards contamination of air drawn from other parts of the system, affecting negatively and the performance of the detector, was present. Hence, the conclusions based on experimental results and their comparison with theoretical values obtained from dedicated software, can be considered realistic. This also dictates the need for method optimization based on experimental data, or changes in the available software, so that the performance of unconventional VO column configurations can be also successfully modelled.

## ***G. The vacuum outlet in the determination of selected compounds of intermediate volatility***

### ***G.1. Introduction***

Considering the limitations in the applicability of vacuum outlet for highly volatile compounds, species of intermediate volatility were selected for further investigations. With this requirement being fulfilled for octinoxate and oxybenzone, two of the most widely used UV filters in cosmetic products and suspected endocrine disrupters<sup>414</sup>, these two compounds were selected for fast and sensitive determination using the vacuum outlet technique.

Endocrine disrupters (EDs) have become a serious public health concern over the past decades, since these chemicals alter the steroid metabolism or function and so they might have long-term effects on the human population<sup>415</sup>. The presence of organic UV filters in surface water<sup>416</sup> added to the controversy about the potential endocrine disrupting activity of some of these compounds<sup>417</sup> and triggered our interest in the particular application of VO for selected and representative chemicals.

Particularly for the analysis of endocrine disrupting chemicals in water matrices by GC-MS, many sample preparation techniques have been applied, among which we can find conventional extraction methods, such as liquid–liquid extraction (LLE)<sup>418</sup> and solid phase extraction (SPE)<sup>419-423</sup>, as well as approaches like dispersive solid-phase extraction (DSPE)<sup>420</sup>, dispersive liquid–liquid micro extraction (DLLME)<sup>424,425,426</sup>, micro extraction by packed sorbent (MEPS)<sup>427</sup> and micelle mediated extraction-solvent back extraction<sup>428</sup>. In several cases, both LLE<sup>429</sup> and DLLME<sup>426</sup>, as well as SPE<sup>430</sup> and DSPE<sup>420</sup> have been combined with derivatization procedures, making them even more time-consuming and expensive, while also requiring the use of hazardous reagents. In addition, SPE has been applied in GC-MS/MS studies<sup>418,431,432</sup>, leading to detection limits below 1 ng/L. Comparably high sensitivities have also been reported when stir bar sorptive extraction (SBSE) was used, although these applications required additionally the derivatization of the analytes and the use of a thermal desorption (TD) unit connected to the GC-MS system<sup>433,434,435</sup> or involved the use of TOF-MS<sup>436</sup>.

Aiming at a convenient and environmentally friendly extraction of the selected analytes from matrices like swimming pool waters, solid-phase micro-extraction (SPME) was chosen for application. SPME can be easily automated and allows, in a single step, pre-concentration and a rapid direct extraction, without the use of organic solvents. Consequently, SPME is becoming more widely used, owing to its ability for quick screening of targeted analytes and its simplicity<sup>437</sup>, with existing applications in the field of UV filters. However, the more sensitive applications require the use of additional reagents for the derivatization of the analytes<sup>438</sup> or the measurements were performed by tandem mass spectrometry<sup>439</sup>. Some recent

reviews have been published on new trends in solid phase micro-extraction which emphasize new aspects of the use of this most versatile technique, including new fiber coatings<sup>440</sup>, and its potential application for *in situ* analysis, field sampling and *in vivo*-analysis<sup>441,442,443</sup>.

An alternative approach towards sensitive but also fast separations could involve the combination of SPME with LP-GC-MS. The application of this approach will be discussed in the present chapter. All the experimental parameters affecting the extraction procedure were intensively investigated and the analytical characteristics of the LP-GC-MS method were compared to a conventional GC-MS method and critically evaluated. Real swimming pool water samples were then analyzed to demonstrate the applicability of the proposed fast GC-MS method in routine analysis.

## ***G.2. Materials and Methods***

### ***G.2.1. Chemicals and reagents***

UV filter chemicals (oxybenzone (2-hydroxy-4-methoxybenzophenone) and octinoxate (ethylhexyl methoxycinnamate)), hydrochloric acid (37%) and HPLC-grade methanol and water were purchased from Sigma Aldrich (Vienna, Austria). Sodium chloride was acquired from Merck (Darmstadt, Germany). Each of the UV filter stock solutions (1.0 mg/L) was prepared in methanol, and stored at 4°C. Ultra-pure water was used for the dilution of the stock solutions prior to the performance of the SPME-GC-MS and SPME-LP-GC-MS measurements.

### ***G.2.2. Instrumentation and operating conditions***

#### ***G.2.2.1. Conventional and fast Gas Chromatography-Mass Spectrometry (GC-MS and LP-GC-MS)***

For the conventional GC-MS method, the analysis was carried out using a Thermo Fisher Scientific Trace GC Ultra gas chromatograph (Thermo Fisher Scientific Inc., Waltham, MA, USA) equipped with a programmed-temperature vaporization (PTV) injector and a Thermo Fisher Scientific AS2000 Autosampler. A non-polar RTX-5MS fused silica capillary column with 5% phenyl / 95% dimethyl polysiloxane (Restek, Bellefonte, PA, USA) and dimensions of 29.5 m x 0.25 mm x 0.25 µm was used. The LP-GC-MS experiments have been performed using a Shimadzu GC (Shimadzu Corp., Kyoto, Japan) equipped with an Optic3 high performance injector (GL Sciences Inc., Torrance, CA, USA) and a Shimadzu AOC-5000Plus Autosampler. A 5 m x 0.10 mm deactivated fused silica capillary column was



used as a restriction, and was connected through a Supelco capillary butt connector with a graphite-vespel ferrule to a 10 m x 0.53 mm x 1.5  $\mu\text{m}$  non-polar DB-1 fused silica capillary column with a 100% dimethyl polysiloxane (J&W Scientific Inc., Folsom, CA, USA) stationary phase.

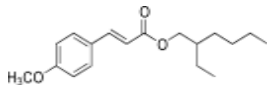
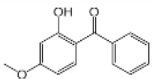
For both methods, helium (purity > 99.999%, Messer, Gumpoldskirchen, Austria) was used as carrier gas. For the conventional GC-MS method a flow rate of 1 mL/min at constant flow mode and considering vacuum conditions at the end of the column was used. The GC injector was operated in the splitless mode at 260°C. The injection volume was 1  $\mu\text{L}$ , and the oven temperature was programmed as follows: 60°C for 1 minute, then increased to 110°C at a rate of 25°C/min and further increased to 300°C at a rate of 60°C/min which was held for 5 minutes. This program resulted in a total analysis time of 16 minutes per sample.

The LP-GC-MS experiments were performed using for the two-column setup an inlet pressure of 500 kPa, in constant flow mode. The Optic injector was operated at the constant temperature of 250°C. The injection volume was 1  $\mu\text{L}$ , and for the optimization of the method, liquid injections were performed at a split ratio of 50:1, using a fritted liner (GL Sciences Inc.) with a frit at 15 mm from the bottom. For the SPME measurements, a splitless liner (GL Sciences Inc.) of 1 mm inner diameter was used at a split ratio of 2:1, and isothermal elution was performed at 250°C for 2 minutes.

Mass spectrometric detection was performed using a Thermo Fisher DSQ II single quadrupole detector for the conventional GC-MS method and a Shimadzu GCMS-QP2010 Ultra for the LP-GC-MS measurements. The following conditions were applied to both detectors: Transfer line temperature set to 250°C and ion source set to 200°C. Positive ion detection mode was used. Mass spectra were acquired in the electron impact mode at 70 eV. Measurements were performed in SIM (selected ion monitoring) mode and in Full Scan Mode using the  $m/z$  range of 50-650. Peak area ratios of target analytes were calculated by Xcalibur (Thermo Fisher Scientific Inc., version 1.4 SR1) and GCMSsolution (Shimadzu Corporation, version 2.70) software, respectively.

The samples were analyzed in triplicates and blank runs were done before and after each analysis. Retention times and the identification and quantification of ions selected for the target compounds are shown in Table G1. The change in the elution order of the examined analytes results from the different stationary phases used with the different techniques (a RTX-5MS was used for the GC-MS and a DB-1 for the LP-GC-MS measurements).

**Table G1. Retention times and selected ions for the analysis of the target compounds by DI-SPME-GC-MS and DI-SPME-LP-GC-MS.**

Compound	Chemical Structure	Retention Time $t_R$ (min)		Molecular weight (g/mol)	Monitored $m/z$
		GC-MS	LP-GC-MS		
Octinoxate		9.22	1.75	290.40	290, 178, 161
Oxybenzone		10.16	1.43	228.24	228, 151, 105

### G.2.2.2 Solid Phase Micro-Extraction (SPME)

A manual SPME holder and fibers with different coatings: PDMS (polydimethyl siloxane, 100  $\mu\text{m}$  film thickness) and PA (polyacrylate, 85  $\mu\text{m}$  film thickness) were obtained from Supelco (Bellefonte, PA, USA). Before their first use, each fiber was conditioned as described in the supplier specifications followed by blank analysis to determine the quality of conditioning. Depending on the extraction mode investigated, glass vessels of different type but of the same nominal capacity were used. For the direct immersion measurements, 10 mL crimp top headspace vials were used and sealed with PTFE lined rubber septa. When headspace analysis was performed, 10 mL glass vials were used and sealed with the corresponding Mininert valve caps (Supelco). A magnetic stir bar, sized to fit the different vials (e.g. 10mm  $\times$  4mm), was always used for stirring the samples during extraction.

### G.2.2.3 Sample preparation

During the SPME process, equilibrium between the coated fiber and sample matrix is eventually attained<sup>444,445</sup>. At equilibrium, the distribution of the organic compound between the solid phase and the aqueous phase is described by equation (1) according to the phase equilibrium theory by Nernst:

$$K = C_s/C_a \quad (1)$$

where  $C_s$  is the concentration of the organic compound in the solid phase,  $C_a$  is the concentration of organic compound in the aqueous phase, and  $K$  is the partition coefficient for the solid phase/aqueous phase system. The  $K$  values have been calculated for many environmental compounds and determine the efficiency of pre-concentration of organic compounds from a water sample. During the SPME extraction process it is of paramount importance for reproducible results that the relevant variables are controlled.

These include sample volume, stirring speed, the sampling method (headspace or immersion), extraction time and temperature etc.

In this study, 5 ml volume of spiked pool water samples are placed in 10 ml vials. The samples are stirred before and during extraction, at a rate of 800 rpm. The fiber is exposed to the aqueous phase for a period of 45 min, at room temperature ( $25 \pm 2^\circ\text{C}$ ). The SPME holder with the fiber is then transferred from the sample to the desorption chamber, in this case the hot GC injection port, where the extracted analytes are desorbed and injected to the analytical column for separation and detection. Because of the small volume of the SPME extraction phase, desorption is typically achieved very quickly and the analyte can be introduced in a very narrow band, thereby significantly improving S/N ratios simply by compressing the sample into a smaller volume. Fast desorption of the analyte is promoted by the use of narrow injector liners specifically designed for SPME fibers, enhancing the sensitivity by minimizing the dispersion.

#### ***G.2.2.4 Quality Assurance / Quality Control Considerations***

The success of quantitative analysis by SPME is known to critically depend on the precise control of various operational parameters. These include: extraction time, extraction temperature, stirring speed, sample and headspace volume and the condition of the fiber<sup>444</sup>. Except for the latter, these parameters were part of the optimization study reported in this work, and we will, for the purpose of estimating the expanded uncertainty, make assumptions for the variability of these parameters in the absence of experimental data that would allow deriving Type A contributions to the uncertainty budget<sup>446</sup>.

### ***G.3. Results and Discussion***

The optimum experimental conditions for the extraction and quantitation of both selected analytes, were investigated using the aforementioned conventional GC-MS method. Below are presented the results from the optimization experiments of the SPME method, as well as those performed for the LP-GC-MS method that was finally used. Both the conventional GC-MS and the corresponding fast LP-GC-MS approach have been validated and compared in terms of sensitivity and total analysis time.

#### ***G.3.1. LP-GC-MS detection***

A very fast and quantitative determination of the analytes of interest was achieved by isothermal elution at  $250^\circ\text{C}$ . However, when conventional GC-MS methods were employed, the use of isothermal conditions

was not a considerable option, since it led to an excessive increase in analysis time, while the resolution of the obtained chromatograms was also suffering.

Selection of the optimum inlet pressure was based on the van Deemter curve obtained for each compound. For the two-column system examined, inlet pressures are presented in the x-axis of the van Deemter plots. The corresponding linear velocities were not presented since their values may vary depending on the procedure selected for the calculation, providing an estimate that does not easily translate to a different system for further applications of the proposed technique.

Lowering the pressure inside the capillary shifts the van Deemter curve to the right (i.e. to higher linear flow velocities) due to fast diffusion in the gas phase. Since this effect is stronger when higher vacuum is applied through the whole capillary, this effect is maximized when using 0.53 mm I.D. columns. The same effect is also observed for smaller diameter columns, but then the column itself will act as a restriction. Consequently, although almost all GC-MS methods entail vacuum outlet conditions, in which the low-pressure region extends up to a certain distance inside the analytical column, only in LP-GC-MS that distance could essentially cover the entire column length. Under such low pressure or vacuum outlet conditions, the viscosity of Helium is reduced, providing higher diffusion coefficients in the mobile phase and consequently a more efficient mass transfer, resulting in flatter van Deemter plots. The optimal flow rate is shifted to greater velocities and provides H<sub>2</sub>-like properties to the carrier gas. Because of these higher linear velocities, peaks are not only eluting quicker but also relatively higher, resulting in a better signal-to-noise ratio (S/N) and leading to correspondingly lower detection limits (LODs). The lower LOD values obtained for the proposed LP-GC-MS method in comparison to the conventional GC-MS approach are presented in Table G2, fulfilling the expectations for the vacuum outlet technique.

**Table G2. Analytical performance characteristics of DI-SPME-GC-MS and DI-SPME-LP-GC-MS for octinoxate and oxybenzone determinations in swimming pool water samples.**

Compound	GC-MS					LP-GC-MS				
	Correlation Coefficient <sup>a</sup> (R <sup>2</sup> )	LOD <sup>b</sup> (µg/L)	% RSD <sup>c</sup>		Rec. <sup>d</sup>	Correlation Coefficient <sup>e</sup> (R <sup>2</sup> )	LOD <sup>b</sup> (µg/L)	% RSD <sup>c</sup>		Rec. <sup>d</sup>
			Interday	Intraday				Interday	Intraday	
Octinoxate	0.999	1.16	1.9	4.8	87	0.999	0.17	1.9	4.3	80
Oxybenzone	0.990	1.93	1.2	4.2	95	0.997	0.29	0.7	3.7	83

a: Concentration range 5-50 µg/L

b: LOD = limit of detection, defined as the concentration which produces a signal (peak area) 3 times higher than the baseline noise

c: RSD = relative standard deviation (mean of three replicate experiment C: 5 µg/L)

d: Recoveries of swimming pool water samples spiked at 5µg/L

e: Concentration range 0.5-25 µg/L

As illustrated in Figure G1, the selected inlet pressure of 500 kPa leads to the optimum value with the lowest Height Equivalent to a Theoretical Plate. Our observations for different restriction lengths, presented at the previous chapter, support our selection of a longer restriction.

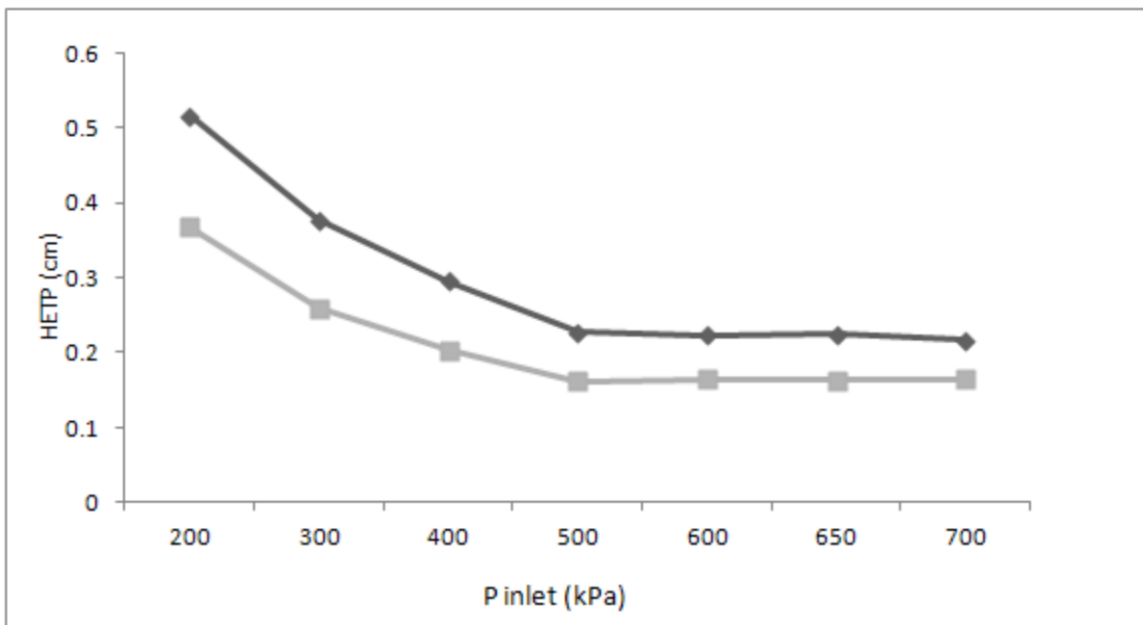


**Figure G1. Van Deemter plots for oxybenzone (a) and octinoxate (b), obtained for isothermal analysis at 250°C performed with the LP-GC-MS method.**

Moreover, the film thickness of the analytical column was selected in a range that will not decrease the separation efficiency, since films up to 1.5  $\mu\text{m}$  prevail full advantage of the gain in speed when operating wide-bore columns at vacuum outlet conditions<sup>356</sup>. The volatility range of the analytes supports further our selection.

### ***G.3.2. Optimization of SPME conditions***

#### ***G.3.2.1. Fiber Coating***

The chemical nature of the analyte determines the type of polymer used for the extraction. Selection of the coating is based primarily on the polarity and volatility of the target compound. As a first consideration, the simple rule ‘like dissolves like’ applies well for liquid polymeric coatings<sup>419</sup>. For this purpose, the two commercially available SPME fibers (PDMS, 100  $\mu\text{m}$  film thickness and PA, 85  $\mu\text{m}$  film thickness) are compared (Figure G2). Extraction with the PA fiber yielded the highest chromatographic area for both target analytes, and it was therefore chosen for the continuation of the SPME optimization experiments.

PA fibers generally have high affinity for aromatic compounds (such as octinoxate), probably due to  $\pi$ - $\pi$  interactions, justifying the higher extraction yield obtained with this fiber<sup>447</sup>.

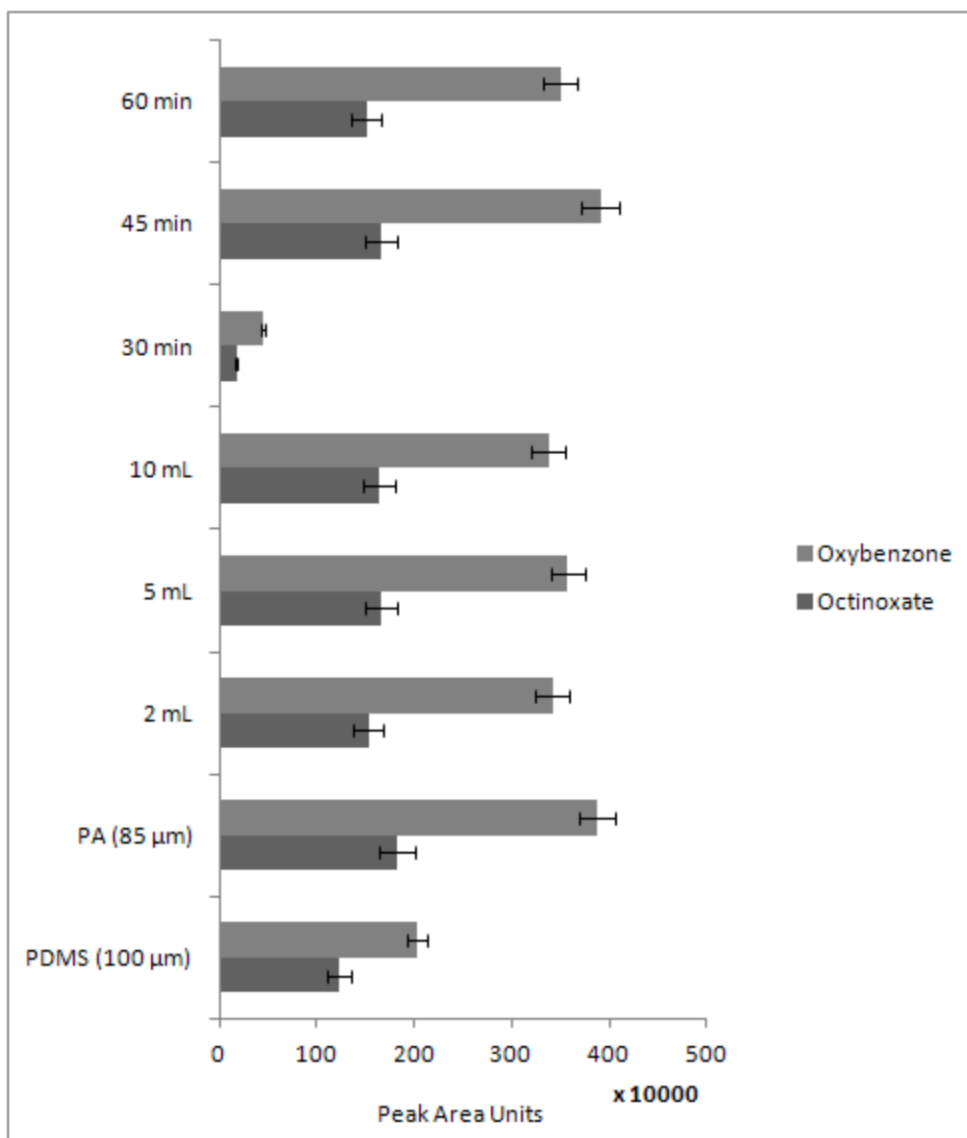


**Figure G2. Comparison of the GC-MS Total Ion Chromatogram (TIC) response and reproducibility (n = 3) for oxybenzone and octinoxate using different SPME fibers, sample volume, extraction time. Extraction conditions are given in the Experimental section.**

### ***G.3.2.2. Extraction Mode***

SPME sampling is performed in two basic modes: direct extraction and headspace extraction. In the direct extraction (direct immersion, DI) mode, the coated fiber is inserted into the sample and the analytes are transported directly from the bulk of the sample to the extracting phase. In headspace (HS) mode, the analytes are extracted from the gas phase equilibrated with the sample. Due to the exothermic character of the extraction process, the effect of the extraction temperature was considered trivial when direct extraction is performed. For this reason, for the DI mode the extraction procedure was performed only at room temperature, having also in mind the possibility of field application. However, when the HS mode was investigated, three different extraction temperatures were selected (room temperature, 40°C and 60°C). An increase in the extraction temperature causes an increase in the extraction rate, speeding up mass transference kinetics from the sample to the fiber. However, a simultaneous decrease in the distribution constant is usually observed, producing a reduction of the compounds' affinity to the fiber coating. Due to these two antagonistic effects, an optimum in the obtained profiles was observed. The overall results are presented in Figure G3, proving that the direct immersion mode performed at room temperature was providing greater extraction efficiencies for both compounds, and was therefore selected for this study.

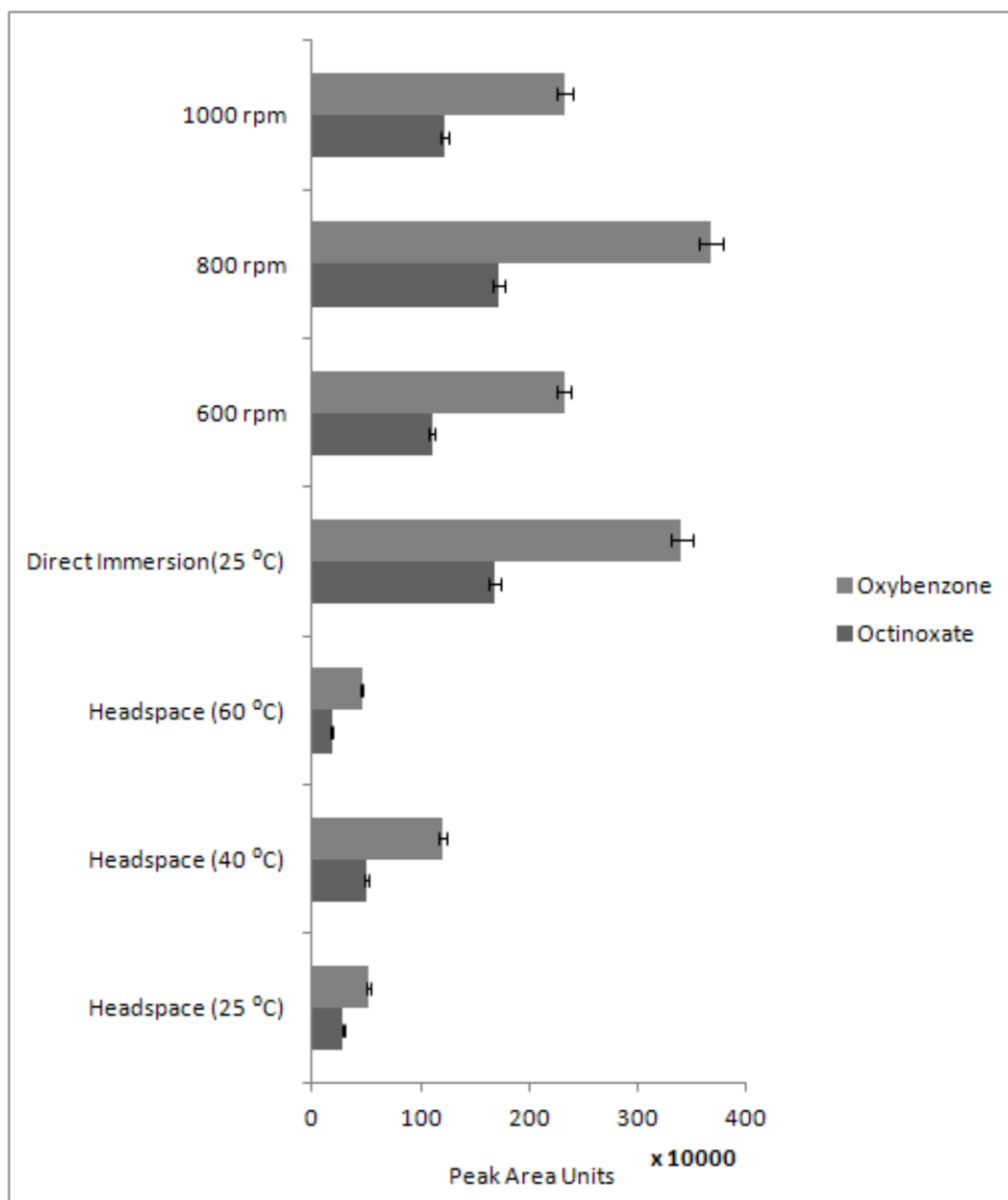


**Figure G3. Comparison of the GC-MS TIC response and reproducibility (n = 3) for oxybenzone and octinoxate using the 85  $\mu$ m PA fiber and performing headspace extraction at the temperatures of 25°C, 40°C and 60°C, and extraction by direct immersion at room temperature and at different stirring rates. Other extraction conditions are reported in the Experimental section.**

### ***G.3.2.3. Sample Volume***

The amount of analyte extracted from a particular sample depends on a variety of factors, such as sample volume ( $V_s$ ), headspace volume ( $V_h$ - only important when extracting from the headspace), fiber coating volume ( $V_c$ ), fiber coating/sample partition constant ( $K_{cs}$ ) and others. In many cases, the fiber coating/sample matrix distribution constant ( $K_{cs}$ ) is relatively small with respect to the phase ratio of



sample matrix to coating volume:  $V_c \ll V_s$ . In this case, the capacity of the sample matrix is significantly larger than the capacity of the fiber coating and the general equation (2)

$$n = \frac{K_{cs} V_c V_s C_0}{V_s + K_{cs} V_c} \quad (2)$$

becomes:

$$n = K_{cs} V_c C_0 \quad (3)$$

which means that it is not necessary to sample a well-defined volume of sample because the amount of analyte extracted by the fiber coating is independent of the sample volume ( $V_s$ ):

$$K_{cs} V_c \ll V_s \text{ or } \frac{C_{\infty c} V_c}{C_{\infty s}} \ll V_s \quad (4)$$

Provided the sample volume  $V_s \gg V_c$ , the amount of analyte extracted is independent of the volume of sample if distribution equilibrium is achieved. If the available sample volume is not significantly greater than the product of coating volume and partitioning constant  $V_c K_{cs}$ , considerable care is needed for keeping the sample volume constant. On the other hand, literature results show that there is a decrease of the method precision with increasing sample volumes<sup>438,448</sup>. Therefore, the sample volume of 5 mL is selected, although, as proved in Figure G2, there was no significant influence of the investigated range of sample volumes in the extraction of the analytes.

#### ***G.3.2.4. Extraction Time***

It is known that for SPME the extraction time and mass transfer conditions have to be strictly controlled to assure good precision. At equilibrium, small variations in the extraction time do not affect the amount of analyte extracted by the fiber. On the other hand, in the steep part of the curve, even small variations in the extraction time may result in significant variations in the amount extracted. The relative error becomes larger the shorter the extraction time. In this study, the extraction time is fixed to 45 min as no further increase, neither in response nor in precision, is seen with larger extraction times (Figure G2). However, shorter extraction times can still be used when the mass transfer conditions and the system temperature remain constant for all experiments, like in the case of using an SPME-autosampler. Under these conditions, the time can be very precisely reproduced, leading to a very good precision of analyte determination, even when equilibrium is not attained in the system. However, as already mentioned, under non-equilibrium conditions the temperature should also be very precisely maintained, since it affects

substantially the rate of diffusion through the water, affecting the amount of analyte absorbed in a short period of time<sup>449</sup>. Another approach towards the reduction of the total analysis time concerns the use of multiple SPME devices for the simultaneous pre-concentration of a number of different samples.

### ***G.3.2.5. Sample pH and salt addition***

Adjustment of the pH can improve the sensitivity of the extraction method for weakly basic or acidic analytes as they need to be kept in the undissociated form. In addition, the effect of increased ionic strength of the sample solution is particularly relevant for polar and non-ionic species<sup>450</sup>. The positive effects of both acid and salt addition can be realized when they are used in combination. Due to the neutral nature of octinoxate there was no significant effect expected for this particular compound when changing the pH of the sample solution. However, oxybenzone has a pKa (negative log of the acid dissociation constant) value of 7.6, leading to the necessity of such a combined investigation. For this reason, extractions were carried out both at the original pH value of the spiked samples (ranging between  $6.7 \pm 0.2$  pH units) and at pH 3, without salt addition and at a salt content of 10 g/L, 20 g/L and 30 g/L. Direct immersion was performed using 5 mL samples at the optimized extraction time of 45 min. Figure G4 depicts how both factors affect the extraction yield of the analytes of interest.

The addition of salt to the water sample, while operating in direct immersion, shifts the extraction equilibrium towards the SPME fiber coating. At the same time the increased sample viscosity will also play an effect, slowing down the extraction kinetics, however this contribution will only be of minor extent. A moderate improvement in the extraction efficiencies of more polar species is expected under these conditions, while at the same time extraction efficiencies decrease with the simultaneous decrease in the efficiencies of compounds that are less soluble in water. This effect, with neutral molecules becoming insoluble as the water molecules prefer to solvate the salt ions, is commonly known as “salting out” effect. For analytes which have a considerable portion of their molecules in the ionized form, the salting out effect leads to a decrease of extraction efficiency. By adding salt, the ionic strength of the solution increases, and more of the ionized molecules are formed at the expense of the neutral ones. For these analytes, the partition equilibrium shifts in favor of the salt-water matrix instead of the fiber coating, and the amount extracted is significantly lower than that extracted under the control conditions. Furthermore, the salt added to the solution may change the physical properties of the static aqueous layer on the fiber, reducing the diffusion rate of the analytes to the fiber through this layer. Both tendencies are reflected by the obtained data for the UV filters. In the case where the sample pH is maintained in its original value, the extraction efficiency of the neutral compound, namely the octinoxate, is increasing with the addition of salt, showing a maximum at around 20 g/L. On the other side, if the pH is not set at a value at least two pH

units lower than the pKa value of oxybenzone, so that the undissociated form of the UV filter molecules are predominant, decreased extraction efficiencies are observed when sodium chloride is added to the water sample. This effect is reversed when the pH of the sample is adjusted to 3 pH units, improving the extraction yield with the maximum performance again at around 20 g/L.

An additional observation involves the performance of the extraction for both compounds at a lower pH without any salt added to the solutions. In this case, both compounds show a significant decrease in their extraction yields, which requires the increase of the ionic strength of the sample in order to reach values similar to those obtained at the original sample pH before the addition of salt, and finally lead to an overall higher extraction yield. Still, under the most favorable conditions these optimizations involve a close to 2-fold increase in the peak areas of the compounds. In order to simplify the extraction process and at the same time avoid the possibility of building up solid residues in the liner of the GC, the addition of salt was not considered for further experiments for practical reasons. In this way we eliminate also the washing step of the fiber after extraction of the analytes, which not only is of very high importance and should be very carefully executed to prevent the fiber from becoming fragile and shorten its lifetime, but may also negatively affect the reproducibility of the measurements<sup>451</sup>.

The overall organic solvent content was maintained below 1%. At such low concentrations of MeOH there is no significant increase in the eluotropic strength of the sample solutions and no detectable effect on the extraction efficiency of the organic analytes can be observed. However, for increased content of the organic solvent, significant suppression of the extraction is typically observed, with respect to the signal intensity. Such a negative effect arrives from the decrease in polarity of the aqueous solution and the corresponding distribution constant of the compounds<sup>449</sup>. But since this was not the case according to our sample preparation procedure, the solvent effect was not considered as a relative parameter for the optimization of the SPME method and further it was not investigated.

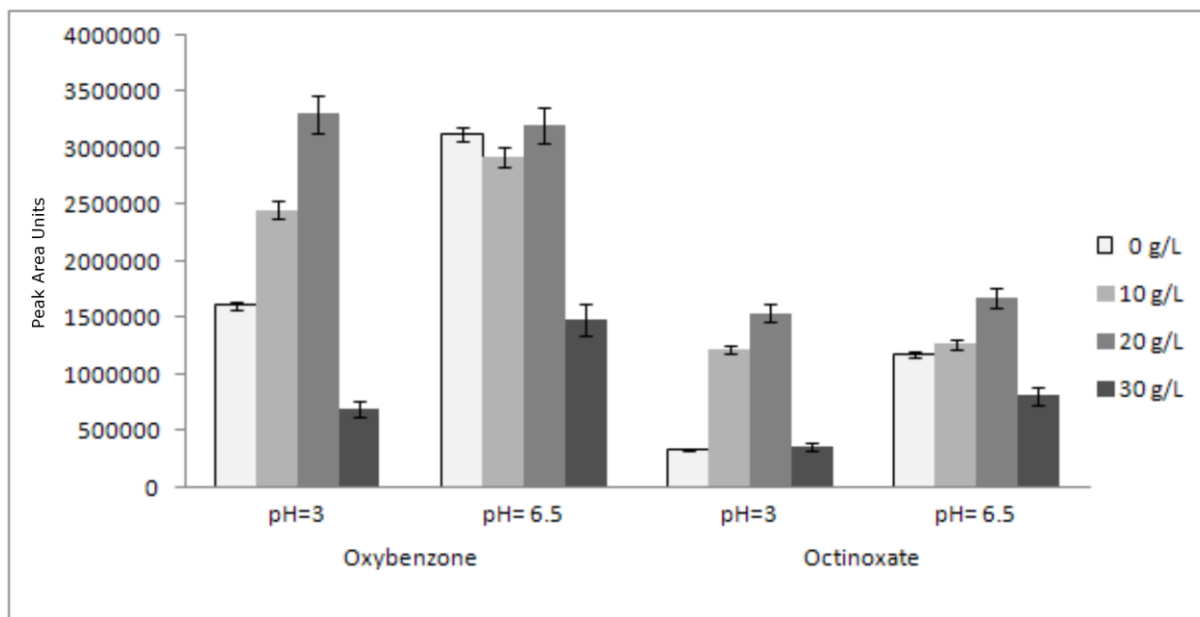


**Figure G4. Influence of pH (original value and pH 3) and salt content (0 g/L, 10 g/L, 20 g/L and 30 g/L) on the chromatographic (TIC) response of oxybenzone and octinoxate and on their reproducibility (n = 3).**

#### ***G.3.2.6. Stirring rate***

In order to enhance the diffusion of the analytes towards the sample and achieve faster equilibration, stirring of the sample is performed before and during the extraction procedure. The positive effect of stirring is demonstrated in Figure G3. Interestingly, independent of the polarity of the analytes (oxybenzone being more polar than octinoxate) the improvement in extraction yield shows a parallel trend for the two compounds with an increase up to 800 rpm stirring rate, and then a decrease when the stirring rate is further increased. While up to a stirring rate of 800 rpm the increasing turbulence of the solution improves the transport and partitioning of the analytes from the aqueous solution into the SPME fiber, a further increase probably disrupts the continuity of the aqueous solution at the solution/fiber interface and thereby causes again a reduction in the extraction efficiency.

#### ***G.2.2.7. Carryover effect***

Both spiked ultra-pure and swimming pool water samples were analyzed by LP-GC-MS using isothermal elution for 2-4 minutes. The lack of any contamination appearing in the initial chromatograms after the second minute allowed the reduction of the total run time. In addition, two-minute runs provided carryover levels lower than 1%, ensuring the quantitative desorption of the analytes from the fiber and therefore

demonstrating that such a reduction in time can reasonably be achieved for the DI-SPME-LP-GC-MS method.

### ***G.3.3. Analytical figures of merit***

Analytical figures of merit, including the limit of detection (LOD), linear range, correlation coefficient ( $R^2$ ) and repeatability were investigated for both, the LP-GC-MS and for the conventional approach in order to compare and evaluate the analytical performance of both methods under optimal conditions. The obtained values for the described figures of merit are presented in Table G2. Linearity of the calibration curve was observed in the range of 5-50  $\mu\text{g/L}$  for the GC-MS and 0.5-25  $\mu\text{g/L}$  for the LP-GC-MS method, showing good correlation coefficients ( $R^2$ ) in both cases. Inter-day and intra-day precision tests ( $n=3$ ) were carried out by extracting a spiked swimming pool water sample of 5  $\mu\text{g/L}$ . In addition, when original (unspiked) swimming pool water samples were analyzed by both methods, neither oxybenzone nor octinoxate were detected in concentrations above the reported LODs for each method.

Lower LODs were obtained with the SPME-LP-GC-MS method when compared to those of other SPME-GC-MS applications reported in the literature<sup>452,453</sup>. Particularly, when Albanis *et al.*<sup>453</sup> performed the analysis of UV filters, including oxybenzone, the LODs that correspond to the reported LOQ values for this compound were in the best case 0.57  $\mu\text{g/L}$  for the DI-SPME-GC-MS and 0.39  $\mu\text{g/L}$  for the DI-SPME-GC-FID method investigated. In comparison to these, our method resulted for the same compound in a LOD as low as 0.29  $\mu\text{g/L}$ , under the SPME conditions described above, being aware that the addition of salt in the SPME step that was excluded for practical reasons would have even further improved the results. In addition, in the case of the GC-FID method proposed by Albanis *et al.*, the total analysis time was more than 20 times higher than that of our fast GC-MS approach, while the analysis speed of their GC-MS method was also more than 10 times lower than that obtained with our LP-GC-MS system. Consequently, both observations prove the clear benefit of our approach in terms of sensitivity and speed. Although an additional SPME-GC-MS study exists<sup>454</sup>, that also involves one of the analytes of interest of the present study, the remarkable sensitivities that are reported by these authors are not demonstrated convincingly and therefore not considered for comparison.

### G.3.4. Recovery studies

Recovery studies to evaluate the percentage of analyte extracted from spiked swimming pool water were conducted by the direct sampling procedure for both conventional and fast GC-MS methods. The relative recovery is determined as the peak area ratio of a real sample and an ultra-pure water sample spiked with analytes at the same concentration level<sup>453</sup>. The recoveries obtained with the GC-MS method ranged between 87 and 95% for octinoxate and oxybenzone respectively, while the corresponding values for the LP-GC-MS method were in the range 80 to 83%. Characteristic chromatograms of the two methods are presented in Figures G5 & G6. Although in the fast method the recoveries of both compounds were slightly lower, their smaller distribution and high reproducibility proves that both methods are equally successful in extracting these sunscreens constituents from water samples.

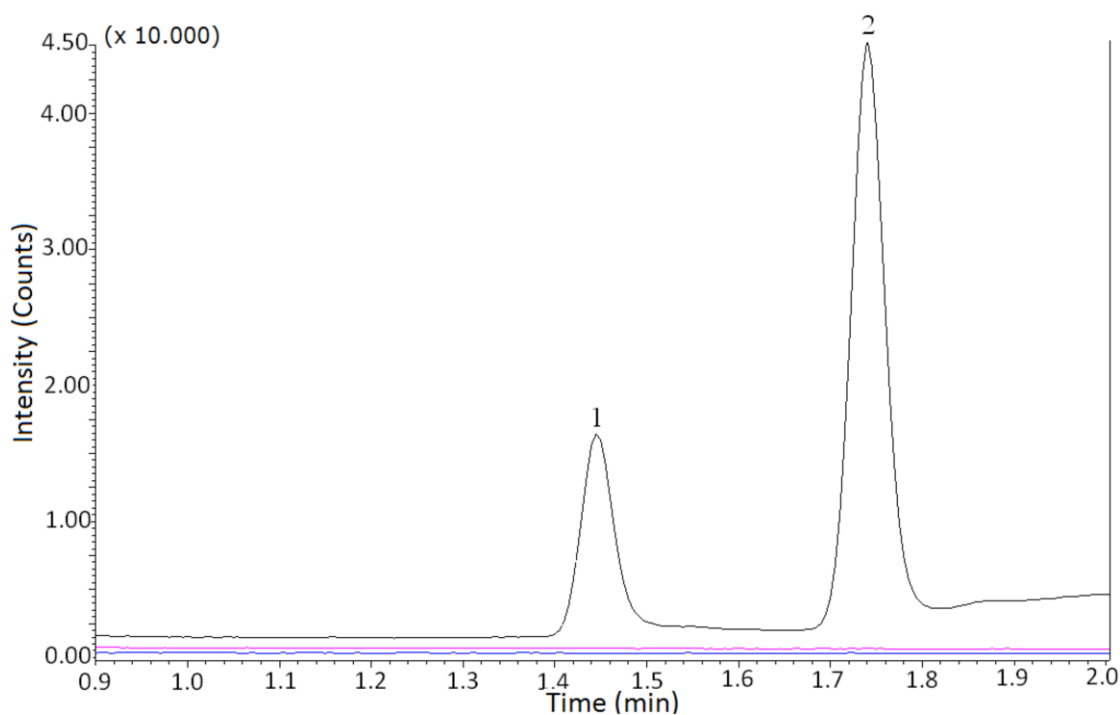


**Figure G5. Overlaid DI-SPME-LP-GC-MS chromatograms. Black line, swimming pool water, spiked with octinoxate (1) and oxybenzone (2) at 5  $\mu\text{g/L}$ . Pink line, unspiked swimming pool water sample. Blue line, column blank.**

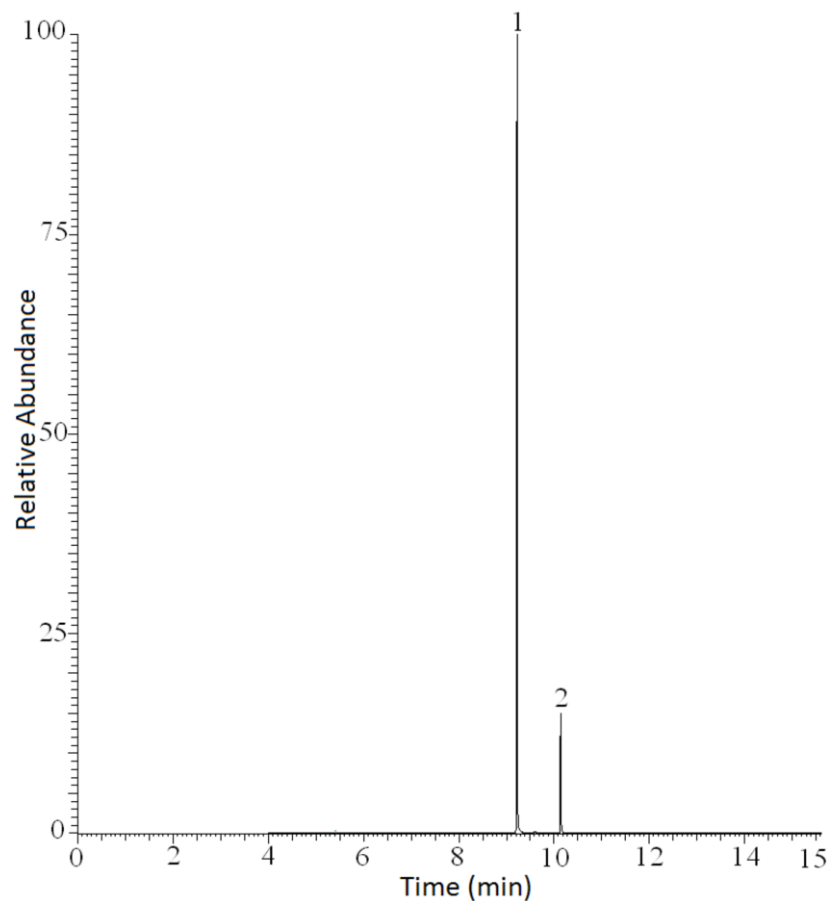


**Figure G6. A typical GC-MS chromatogram of swimming pool water, spiked with octinoxate (1) and oxybenzone (2) after DI-SPME.**

### ***G.3.5. Estimation of the uncertainty budget***

Among the various theory- or experiment-driven approaches for the estimation of uncertainty budgets, there are two commonly used ones, namely: the *bottom-up* approach and the *top-down* approach<sup>446</sup>. We have used in the following the *bottom-up* approach presented in the EURACHEM/CITAC guide<sup>455</sup> according to which the uncertainty associated with the results produced by a given analytical methodology is obtained by taking into consideration the different contributions of uncertainty from the individual steps of the analytical procedure<sup>446</sup>. In this case, we have considered the following four main contributions: (i) the uncertainty associated with the preparation of the standards ( $U_1$ ), (ii) the uncertainty associated with the calibration curve ( $U_2$ ), (iii) the uncertainty associated with the precision of the method ( $U_3$ ), and (iv) the uncertainty to the accuracy of the method ( $U_4$ ). Table G3 gives an overview how these individual contributions are calculated and how they are combined into the combined or global uncertainty<sup>456</sup>. All uncertainties are expressed here as relative uncertainties.

The results of the uncertainty estimation are summarized in Table G3 and in Figure G7. It becomes evident that the uncertainty arising from the calibration curve is the greatest single contribution to the uncertainty budget, and that this contribution becomes dominant at the lower concentrations. This is in agreement with the expectations as, under careful consideration and control of all other method parameters, measurement uncertainty should be relatively small throughout the largest part of the working range of the method, and only assumes greater numeric values when approaching the limit of quantitation and even becomes 100% at the limit of detection.

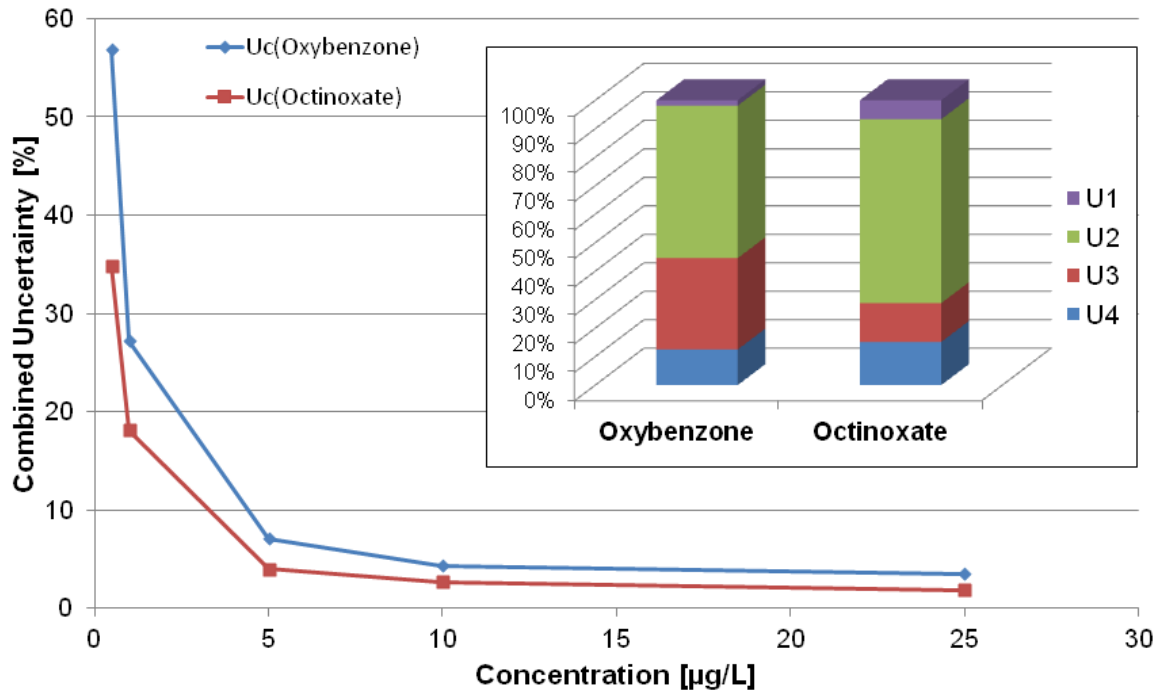


**Figure G7. Plot of the combined uncertainty  $U_c$  of the DI-SPME-LP-GC-MS method for the determination of octinoxate and oxybenzone in water samples as a function of the concentration level. The insert represents the relative contributions of the four sources of method uncertainty ( $U_1-U_4$ , see Table G3) at the concentration level 5  $\mu\text{g/L}$ .**



**Table G3. Identification and description of the four main contributions to the combined uncertainty ( $U$ ) according to the *bottom-up* approach<sup>455</sup>**

Individual contributions to the combined uncertainty			Value (Range) of $U_i$		Interpretation
			Oxybenzone	Octinoxate	
Standard preparation	$U_1 = u_{st}$	$u_{st} = [\sum (\Delta x_i / x_i)^2]^{1/2}$	1.0%	1.1%	$\Delta x_i$ : error associated with the measurement of a given parameter $x_i$ , e.g. reagent weighing or preparation or dilution of a standard solution
Calibration curve	$U_2 = s_{x0} / x_0$	$s_{x0} = (S_{y/x} / b) \{ (1/m) + (1/n) + [(y_i - \bar{y})^2 / b^2 \sum (x_i - \bar{x})^2] \}^{1/2}$	54.3 – 1.3%	34.4 – 0.8%	$s_{x0}$ : standard deviation of the method for a given concentration, calculated from the calibration curve; $x_0$ : concentration calculated from the calibration curve; $b$ : slope of the calibration line; $m$ : number of replicates performed for each $x_i$ value; $n$ : number of standards to build the calibration curve; $y_0$ : experimental value of $y$ calculated by the calibration curve, from the concentration $x_0$ ; $\bar{y}$ : average of $y_i$ values; $x_i$ : concentration of standards ( $x$ ) used in the calibration; $\bar{x}$ : average of $x_i$ values
		$S_{y/x} = [\sum (\hat{y} - y_i)^2 / (n-2)]^{1/2}$			$S_{y/x}$ : residual standard deviation of the method (in signal units), $y_i$ : experimental values, $\hat{y}$ : values calculated by the calibration curve; $n$ : number of standards to build the calibration curve

**Table G3 (continued). Identification and description of the four main contributions to the combined uncertainty ( $U_c$ ) according to the *bottom-up* approach<sup>455</sup>**

Individual contributions to the combined uncertainty			Value (Range) of $U_i$		Interpretation
			Oxybenzone	Octinoxate	
Precision	$U_3 = u_p / x_0$	$u_p = s / \sqrt{n}$	1.8 – 16.8%	0.4 – 5.1%	$s$ : standard deviation of precision assays; $n$ : number of assays
Accuracy	$U_4 = u_e$	$u_e = s(R) / \sqrt{n}$	2.5 % @ 5 µg/L	1.6% @ 5 µg/L	$s(R)$ : relative standard deviation of the average percent recovery, $R$ ; $n$ : number of assays
Combined uncertainty	$U_c = \sqrt{(U_1^2 + U_2^2 + U_3^2 + U_4^2)}$		3.5-56.9%	1.8-34.8%	

#### **G.4. Conclusion**

A very fast and simple analytical method based on the LP-GC-MS technique and its combination with DI-SPME has been developed for the analysis of two representative UV filter substances (octinoxate, oxybenzone) in swimming pool water samples. The proposed fast gas chromatographic approach combines the advantages of both speed and sensitivity over the conventional GC-MS method used for the comparison. In particular, an 8-fold reduction in the total analysis time was succeeded, leading at the same time to a significant improvement in the sensitivity of the method, as a 7-fold decrease in the detection limit of oxybenzone and octinoxate was provided.

The selected micro-extraction method has significant advantages over alternative methods that are traditionally used, since it comprises an environmental friendly, economical and expeditious approach, while offering high extraction efficiency, low LOQs, good repeatability, high selectivity and simplicity in its experimental set-up. All relevant parameters affecting the SPME method were investigated in detail and optimized, leading to the most sensitive and robust sample preparation method possible for manual implementation. Estimation of the method uncertainty based on the *bottom up*-approach demonstrated the method to be run under good quality control as the most important contribution to the combined uncertainty was the uncertainty arising from the statistical calculation of the calibration line.

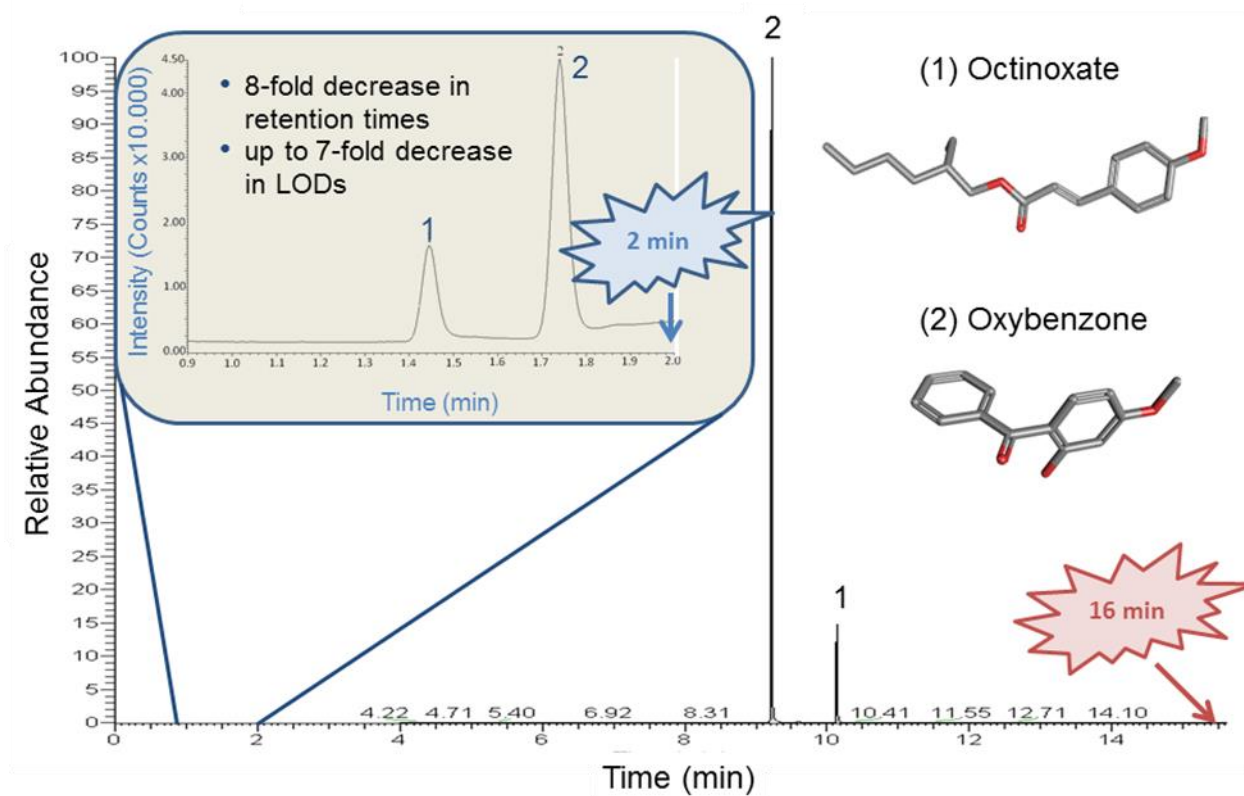


**Figure G8. DI-SPME-LP-GC-MS chromatogram of swimming pool water, spiked with octinoxate (1) and oxybenzone (2) at 5 µg/L (inset) and comparison with separation at normal conditions (large chromatogram).**

The highly favorable performance of the optimized DI-SPME-LP-GC-MS method in the analysis of spiked swimming pool water samples that combines SPME as a fast and sensitive sample preparation method with LP-GC-MS as a fast and efficient determination method proves the superiority of this novel approach applied to the determination of UV filters, suggesting the feasibility of the method for the fast routine analysis of environmental water samples. This application also demonstrates the actual advantages of vacuum outlet when the investigated compounds belong to the optimum range of volatilities for the technique.

## H. Overall conclusions

In the frame of this research work, the formation of volatile degradation products of LIBs' electrolyte solutions was investigated. Conventional and fast GC approaches were used, testing their applicability in the determination of highly volatile compounds. Both *ex situ* and *in situ* experiments were performed, with the formation pathways of the identified degradation compounds being discussed. Critical evaluation of the results was performed, based on the summarized current knowledge on proposed reaction mechanisms occurring inside the cells during normal and abused conditions of use. The potential toxicity of the identified species was also discussed, on the basis of literature data and the results extracted from the Toxtree software. Different GC detectors, namely the MS and the BID, were also applied in the determination of produced gases from LIBs, comparing additionally their performance. For the fast GC approaches, combination of FTIR with a GC-MS system provided fast screening of the evolved gases from in-house assembled and commercially available cells. The Vacuum Outlet technique was finally investigated in terms of relevant optimization parameters and optimum range of volatilities for the targeted analytes. Based on these data, the applicability of the technique was demonstrated, with the development of a fully automated SPME-LP-GC-MS method for the identification and quantification of selected compounds of intermediate volatility and with a high risk of toxicity.

Starting with the *ex situ* measurements, not only the headspace, but also the liquid phase of the thermally aged electrolyte solutions was analysed by GC-MS, revealing a large number of degradation compounds. These compounds belong to various groups, with permanent gases, alcohols, aldehydes, ethers, esters, ketones and fluorinated species dominating the headspace of the thermally abused samples. Additionally, carbonates, glycols and various oxygenated species were also identified, when prolonged storage of samples with increasing complexity was performed at elevated temperatures. The spectrum of these products proved to be even wider when the liquid phase of the samples was analysed, identifying several glycols, alcohols, ethers, carbonates, higher esters and ketones, polymeric products, as well as cyclic, oxygenated and aromatic compounds. Among the identified species with high toxicological relevance are the cyclic solvents (e.g. EC and PC), additives (e.g. biphenyl), frequently detected decomposition products (e.g. 1,4-dioxane and 1,3-dioxolane), and several fluorinated compounds, like the classified neurotoxin diisopropylfluorophosphate, underlining the safety concerns associated with the use of LIBs.

Starting with single component samples and moving towards the entire electrolyte solution, as well as for a cycled electrolyte sample from commercially available cells, the thermal degradation products were identified. The most important observations made for the particular set of experiments comprise (1) the identification of newly documented species formed under thermal aging, (2) the formation of decomposition products exclusively from thermally induced reactions, while the proposed formation paths

in the literature involved the presence of Li ions and (3) the high risk of toxicity assigned to several of the identified compounds. Hence, the need for further investigations is essential for the chemical elucidation of the electrolyte solution and the reaction mechanisms taking place inside the cells under conditions of thermal abuse. Up-scaling of the experiments is necessary for an unambiguous identification of the detected species. However, enhanced safety conditions are required. Considering that not only some of the electrolyte components (e.g. cyclic electrolytes and additives), but also several decomposition products belong to the Cramer Class III, with a potential neurotoxin also being identified, the safety precautions should be at all times respected. Whenever possible, standards of the identified compounds should be used, ensuring the correct assignment of the detected peaks.

Focusing on the more volatile degradation products and on their sensitive detection, the newly released BID detector was employed for electrolyte solutions that were subjected to thermal abuse conditions for shorter time intervals (3 h instead of two weeks). For these experiments, most of the previously investigated sample compositions were again analysed by GC-BID, for the detection of the decomposition products, while GC-MS analysis was also performed, for the purpose of identification. For both measurements, the same PLOT column was used, targeting the gaseous species produced by thermal degradation. The results from these experiments demonstrated the advantage of the BID for the determination of permanent gases. Moreover, further highly volatile compounds were detected exclusively by the BID, indicating a higher sensitivity for a wider range of volatile species. However, only the MS could be used for the identification of the detected species, showing additionally enhanced sensitivity for less volatile compounds. Since the MS was only used in scan mode, it should be considered that a general improvement in sensitivity can be obtained when single ion monitoring is selected and targeted analysis is performed. Therefore, application of the BID is considered favourable (compared to FID) only when quantitative analysis of selected highly volatile (oxygenated) compounds is intended.

*In situ* analyses were also performed, using in house-assembled and commercially available LIBs, focusing on the electrochemically induced reactions and the corresponding electrolyte decomposition products. Overcharging experiments with commercial cells under different charging rates revealed a significant number of degradation products, identified by GC-MS. Different cathode materials and lithium salts were also selected for the in house-assembled cells, for which various electrochemical conditions as well as cyclic voltammetry experiments were performed. By comparing the number, nature and concentration profiles of the reaction products, conclusions on the performance of the different cell chemistries were made. In addition, by comparing the theoretical characteristics of certain materials with their actual performance, the necessity of fast, selective and sensitive techniques was demonstrated.

Targeting the on-line determination of gaseous emissions, a FTIR-GC-MS system, developed at AIT, was employed. The high degree of correlation between the FTIR and the GC-MS data observed for experiments with both in house-assembled and commercially available cells, proved that *in situ* FTIR-GC-

MS measurements are a very promising approach for application with LIBs. In particular, the concentration changes recorded only by FTIR, due to its faster scanning capability, denote its contribution to not only sensitive but also fast detection methods, while the selectivity of the MS may facilitate the elucidation of the occurring reaction mechanisms. However, advances in the data processing and spectral library search algorithm for the FTIR detection are necessary, enabling the development of trustworthy evaluation models with multivariate data analysis.

The alternative approach towards increased time resolution involved the implementation of the Vacuum Outlet technique. A comprehensive investigation of all relevant optimization parameters was performed, focusing on the fast GC identification of highly volatile species. A group of standard compounds was selected and analyzed under vacuum outlet conditions, while the parameters evaluated involved not only the restriction, but also the analytical column. When the restriction dimensions were optimized, different lengths and inner diameters were tested. The corresponding optimization performed for the analytical column was focused on the length of the column and the film thickness. The HETP was calculated in all cases, defining the relevant range of inlet pressures tested (so that a minimum HETP value was included) and showing which value was optimum for each compound at every temperature. However, the measurements were always performed near the optimum. This came as a result of limitations at the low-flow-end of the curve by the pressure drop between inlet and vacuum, which does not allow the use of even smaller flow rates. Similarly, at the high end side of the flows, the physical limits of the instruments were approached, concerning both pumping capacity of the MS and pressure applied to the inlet. If these limitations would not exist, it would be interesting to cover a larger range of parameter values in order to see more pronounced trends and differences. However, from the experiments performed a number of significant observations were still made, including (1) the advantage of using wider and longer restrictions, resulting in higher numbers of theoretical plates, (2) the preference towards lower temperatures for the isothermal elution of most highly volatile compounds investigated, with the 30°C being the optimum temperature for the majority of the standards and column systems tested, (3) the fact that, for highly volatile compounds, longer analytical columns than the conventionally used in VO applications may be required, (4) that unconventionally high film thicknesses are also required for such applications, enhancing the retention and improving the resolution for such targeted group of compounds, while compromising the advantages of the VO technique, (5) the bad correlation in the values produced by the existing software for two-column setups, underlining the significance of experimentally performed method optimizations, (6) the efficient modelling performed by the aforementioned software for atmospheric outlet applications, demonstrated in good correlation between the results produced from the software and the experimentally produced values for a GC-FID system using the column configuration of the VO application; and (7) the reduction of the analysis time by a factor of 2.5 and of the number of theoretical plates by a factor of 3 for equivalent vacuum outlet (GC-MS) compared to atmospheric outlet

(GC-FID) measurements of highly volatile compounds, which, despite the enhanced selectivity provided by the MS, demonstrated that the full advantage of the VO cannot be expected for this range of volatilities.

Utilizing these findings, the application of VO for a better suited group of compounds was targeted, in order to demonstrate what can be achieved when the technique is used under optimum conditions. For this purpose, two compounds of intermediate volatility were selected, owing to their extended use in real-life applications despite the high toxicity hazard assigned to them. These were the octinoxate and oxybenzone, widely used as UV filters in cosmetic samples. Fast and sensitive analysis of the selected compounds in swimming pool waters was successfully performed by combining the LP-GC-MS with the SPME. The fully optimized and automated method developed provided an 8-fold reduction in the total analysis time and a 7-fold increase in sensitivity, when compared to a conventional GC-MS method developed for the same analytes. Thus, the significant improvements that can be realized by the VO were demonstrated, when the technique is used under optimum conditions in terms of volatility range of analytes and corresponding dimensions for the column configuration.

Consequently, the VO may not seem as a very promising technique for application in LIB, when the gaseous emissions of the electrolyte solution are targeted, however, for less volatile compounds significant gains in time-resolution and sensitivity can be expected. Such an application could compromise the need for up-scaling the experiments, accompanied with increased toxicological hazards, for less volatile degradation products. Respectively, the application of GC-BID for the sensitive determination of permanent gases and the FTIR-GC-MS for on-line monitoring of the overall gas species, do represent useful additions to the group of analytical techniques employed in this field of investigations and facilitate the development of safer and more efficient LIBs.

## References

---

- <sup>1</sup> T.B. Reddy, *Linden's Handbook of Batteries*, 4th Edition, McGraw Hill, NY, 2011.
- <sup>2</sup> J.M. Tarascon, M. Armand, Issues and challenges facing rechargeable lithium batteries, insight review articles, *Nature* 414 (2011) 359-367.
- <sup>3</sup> T. Nagaura, K. Tozawa, Lithium ion rechargeable battery, *Prog. Batt. Solar Cells* 9 (1990) 209-212.
- <sup>4</sup> J. Tollefson, Charging up the future, *Nature* 456 (2008) 436-440.
- <sup>5</sup> SHIMADZU Corporation, International Marketing Division, Rechargeable Lithium – Ion Battery Evaluation, C10G-E021.
- <sup>6</sup> H. Nakajima, S. Yamaki, T. Nishine, M. Furuta, Analysis of degradation products in electrolyte for rechargeable lithium-ion battery through high mass accuracy MSn, ASMS 2012 WP26-541.
- <sup>7</sup> Lithium-Ion Batteries Hazard and Use Assessment, July 2011 Fire Protection Research Foundation.
- <sup>8</sup> X. Lan, L. Suli, A. Xinping, Y. Hanxi, Safety enhancing methods for Li-ion batteries, *Prog. Chem.* 23 (2011) 328-335.
- <sup>9</sup> P.G. Balakrishnan, R. Ramesh, T. Prem Kumar, Safety mechanisms in lithium-ion batteries, *J. Power Sources* 155 (2006) 401-414.
- <sup>10</sup> D. Lisbona, T. Snee, A review of hazards associated with primary lithium and lithium-ion batteries, *Process Saf. and Environ. Protection* 89 (2011) 434-442.
- <sup>11</sup> L.J. Fu, H. Liu, C. Li, Y.P. Wu, E. Rahm, R. Holze, H.Q. Wu, Surface modifications of electrode materials for lithium ion batteries, *Solid State Sciences* 8 (2006) 113-128.
- <sup>12</sup> E.J. Cairns, P. Albertus, Batteries for electric and hybrid-electric vehicles. *Annu. Rev. Chem. Biomol. Eng.* 1 (2010) 299–320.
- <sup>13</sup> L. Lu, X. Han, J. Li, J. Hua, M. Ouyang, A review on key issues for lithium-ion battery management in electric vehicles, *J. Power Sources* 226 (2013) 272-288.
- <sup>14</sup> D.H. Doughty, Materials issues in lithium ion battery technology, *SAMPE J.* 32 (1996) 75-81.
- <sup>15</sup> M. Wakihara, Recent developments in lithium ion batteries, *Mater. Sci. Eng.* R33 (2001) 109-134.
- <sup>16</sup> A. Ritchie, W. Howard, Recent developments and likely advances in lithium-ion batteries, *J. Power Sources* 162 (2006) 809-812.
- <sup>17</sup> M.G. Kim, J. Cho, Reversible and high-capacity nanostructured electrode materials for Li-ion batteries, *Adv. Funct. Mater.* 19 (2009) 1497-1514.
- <sup>18</sup> J. Chen, F. Cheng, Combination of lightweight elements and nanostructured materials for batteries, *Acc. Chem. Res.* 42 (2009) 713-723.



- 
- <sup>19</sup> L. Hong, W. Zhaoxiang, C. Liqun, H. Xuejie: Research on advanced materials for Li-ion batteries, *Adv. Mater.* 21 (2009) 4593-4607.
- <sup>20</sup> C.M. Hayner, X. Zhao, H.H. Kung, Materials for rechargeable Lithium-ion batteries, *Annu. Rev. Chem. Biomol. Eng.* 3 (2012) 445-471.
- <sup>21</sup> A. Kraysberg, Y. Ein-Eli, Higher, stronger, better... A review of 5 volt cathode materials for advanced lithium-ion batteries, *Adv. Energy Mater.* 2 (2012) 922-939.
- <sup>22</sup> N-S. Choi, Z. Chen, S.A. Freunberger, X. Ji, Y-K. Sun, K. Amine, G. Yushin, L.F. Nazar, J. Cho, P.G. Bruce, Challenges facing lithium batteries and electrical double-layer capacitors, *Angew. Chem. Int. Ed.* 51 (2012) 9994-10024.
- <sup>23</sup> J. Chen, Recent progress in advanced materials for lithium ion batteries, *Materials* 6 (2013) 156-182.
- <sup>24</sup> T.L. Kulova, New electrode materials for Lithium-ion batteries (Review), *Russ. J. Electrochem.* 49 (2013) 1-25.
- <sup>25</sup> M. Hu, X. Pang, Z. Zhou, Recent progress in high-voltage lithium ion batteries, *J. Power Sources* 237 (2013) 229-242.
- <sup>26</sup> D.S. Jung, Y.N. Ko, Y.C. Kang, S.B. Park, Recent progress in electrode materials produced by spray pyrolysis for next-generation lithium ion batteries, *Advanced Powder Technology*, 25 (2014) 18-31.
- <sup>27</sup> M. Doeff, *Batteries for Sustainability*, Springer, New York (2013) 471-503.
- <sup>28</sup> G. Gachot, S. Grugeon, M. Armand, S. Pilard, P. Guenot, J.M. Tarascon, S. Laruelle, Deciphering the multi-step degradation mechanisms of carbonate-based electrolyte in Li batteries, *J. Power Sources* 178 (2008) 409–421.
- <sup>29</sup> M.S. Whittingham, Lithium batteries and cathode materials, *Chem. Rev.* 104 (2004) 4271-4301.
- <sup>30</sup> F.F.C. Bazito, R.M. Torresi, Cathodes for lithium ion batteries: The benefit of using nanostructured materials, *J. Braz. Chem. Soc.* 17 (2006) 627-642.
- <sup>31</sup> T.F. Yi, Y.R. Zhu, X.D. Zhu, J. Shu, C.B. Yue, A.N. Zhou, A review of recent developments in the surface modification of  $\text{LiMn}_2\text{O}_4$  as cathode material of power lithium-ion battery, *Ionics* 15 (2009) 779-784.
- <sup>32</sup> D. Jugovic, D. Uskokovic, A review of recent developments in the synthesis procedures of lithium iron phosphate powders, *J. Power Sources* 190 (2009) 538-544.
- <sup>33</sup> J.W. Fergus, Recent developments in cathode materials for lithium ion batteries, *J. Power Sources* 195 (2010) 939–954.
- <sup>34</sup> B.L. Ellis, K.T. Lee, L.F. Nazar, Positive electrode materials for Li-ion and Li-batteries, *Chem. Mater.* 22 (2010) 691-714.

- 
- <sup>35</sup> G.Q. Liu, L. Wen, Y.M. Liu, Spinel  $\text{LiNi}_{0.5}\text{Mn}_{1.5}\text{O}_4$  and its derivatives as cathodes for high-voltage Li-ion batteries, *J. Solid State Electrochem.* 14 (2010) 2191-2202.
- <sup>36</sup> W. Zhaoxiang, C. Liqun, H. Xuejie, Structural design and modification of cathode materials for lithium ion batteries, *Prog. Chem.* 23 (2011) 284-301.
- <sup>37</sup> K. Zaghib, A. Mauger, C.M. Julien, Overview of olivines in lithium batteries for green transportation and energy storage, *J. Solid State Electrochem.* 16 (2012) 835-845.
- <sup>38</sup> J. Xu, S. Dou, H. Liu, L. Dai, Cathode materials for next generation lithium ion batteries, *Nano Energy* 2 (2013) 439-442.
- <sup>39</sup> J. Chen, A review of nanostructured lithium ion battery materials via low temperature synthesis *Recent Pat. Nanotechnol.* 7 (2013) 2-12.
- <sup>40</sup> C. Gong, Z. Hue, S. Wen, Y. Ye, X. Xie, Advanced carbon materials/olivine  $\text{LiFePO}_4$  composites for lithium ion batteries, *J. Power Sources* 318 (2016) 93-112.
- <sup>41</sup> K. Li, L. Cao, Z. Huang, L. Chen, Z. Chen, Novel cathode materials  $\text{Li}_x\text{Na}_{2-x}\text{V}_2\text{O}_6$  ( $x = 2, 1.4, 1, 0$ ) for high-performance lithium-ion batteries, *J. Power Sources* 344 (2017) 25-31.
- <sup>42</sup> M. Lu, H. Cheng, Y. Yang, A comparison of solid electrolyte interphase (SEI) on the artificial graphite anode of the aged and cycled commercial lithium ion cells, *Electrochim. Acta* 53 (2008) 3539-3546.
- <sup>43</sup> S. Flandrois, B. Simon, Carbon materials for lithium-ion rechargeable batteries, *Carbon* 37 (1999) 165-180.
- <sup>44</sup> Y. Zhang, X. Hu, Y. Xu, M. Ding, Recent progress of  $\text{Li}_4\text{Ti}_5\text{O}_{12}$  with different morphologies as anode material, *Acta Chimica Sinica* 71 (2013) 1341-1353.
- <sup>45</sup> X. Zuo, J. Zhu, P. Müller-Buschbaum, Y.-J. Cheng, Silicon-based lithium ion battery anodes: A chronicle perspective review, *Nano Energy* 31 (2017) 113-143.
- <sup>46</sup> H. Tian, F. Xin, X. Wang, W. He, W. Han, High capacity group-IV elements (Si, Ge, Sn) based anodes for lithium-ion batteries, *J. Materiomics* 1 (2015) 153-169.
- <sup>47</sup> A. Lewandowski, A. Świdarska-Mocek, Ionic liquids as electrolytes for Li-ion batteries – An overview of electrochemical studies, *J. Power Sources* 194 (2009) 601-609.
- <sup>48</sup> A. Balducci, Ionic Liquids in Lithium-Ion Batteries, *Topics in Current Chemistry Z* (2017) 375-394.
- <sup>49</sup> E. Peled, The Electrochemical behavior of alkali and alkaline earth metals in nonaqueous battery systems—the Solid Electrolyte Interphase model, *J. Electrochem. Soc.* 126 (1979) 2047-2051.
- <sup>50</sup> M.B. Pinson, M.Z. Bazant, Theory of SEI formation in rechargeable batteries: Capacity fade, accelerated aging and lifetime prediction, *J. Electrochem. Soc.* 160 (2013) 243-250.
- <sup>51</sup> C.K. Chan, R. Ruffo, S.S. Hong, Y. Cui, Surface chemistry and morphology of the solid electrolyte interphase on silicon nanowire lithium-ion battery anodes, *J. Power Sources* 189 (2009) 1132-40.

- 
- <sup>52</sup> M. Lu, H. Cheng, Y. Yang, A comparison of solid electrolyte interphase (SEI) on the artificial graphite anode of the aged and cycled commercial lithium ion cells, *Electrochim. Acta* 53 (2008) 3539–3546.
- <sup>53</sup> P.B. Balbuena, Y. Wang, *Lithium-Ion Batteries: Solid-Electrolyte Interphase*, Imp. Coll. Press, London, 2004.
- <sup>54</sup> P. Verma, P. Maire, P. Novak, A review of the features and analyses of the solid electrolyte interphase in Li-ion batteries, *Electrochim. Acta* 55 (2010) 6332-6341.
- <sup>55</sup> E. Peled, D. Golodnitsky, G. Ardel, Advanced Model for Solid Electrolyte Interphase Electrodes in Liquid and Polymer Electrolytes, *J. Electrochem. Soc.* 144 (1997) 208-210.
- <sup>56</sup> D. Aurbach, Review of selected electrode–solution interactions which determine the performance of Li and Li ion batteries, *J. Power Sources* 89 (2000) 206-218.
- <sup>57</sup> E. Peled, D. Golodnitsky, A. Ulus, V. Yufit, Effect of carbon substrate on SEI composition and morphology, *Electrochimica Acta* 50 (2004) 391-395.
- <sup>58</sup> K. Edström, M. Herstedt, D.P. Abraham, A new look at the solid electrolyte interphase on graphite anodes in Li-ion batteries, *J. Power Sources* 153 (2006) 380-384.
- <sup>59</sup> L. Zhao, I. Watanabe, T. Doi, S. Okada, J.-i. Yamaki, TG-MS analysis of solid electrolyte interphase (SEI) on graphite negative-electrode in lithium-ion batteries, *J. Power Sources* 161 (2006) 1275-1280.
- <sup>60</sup> S. Santhanagopalan, Z. Zhang, *Batteries for Sustainability*, Springer, New York (2013) 135-194.
- <sup>61</sup> M. Ue, *Lithium Ion Batteries: Science and Technologies*, Springer, New York (2009) 75-116.
- <sup>62</sup> L. Xiao, X. Ai, Y. Cao, H. Yang, Electrochemical behavior of biphenyl as polymerizable additive for overcharge protection of lithium ion batteries, *Electrochim. Acta* 49 (2004) 4189-4196.
- <sup>63</sup> J. Vetter, P. Novak, M.R. Wagner, C. Veit, K.C. Möller, J.O. Besenhard, M. Winter, M. Wohlfahrt-Mehrens, C. Vogler, A. Hammouche, Ageing mechanisms in lithium-ion batteries, *J. Power Sources* 147 (2005) 269-281.
- <sup>64</sup> K. Xu, Nonaqueous Liquid Electrolytes for Lithium-Based Rechargeable Batteries, *Chem. Reviews* 104 (2004) 4303-4417.
- <sup>65</sup> H. Yoshida, T. Fukunaga, T. Hazama, M. Mizutaki, M. Yamachi, Degradation mechanism of alkyl carbonate solvents used in lithium-ion cells during initial charging, *J. Power Sources* 68 (1997) 311–315.
- <sup>66</sup> T. Sasaki, T. Abe, Y. Iriyama, M. Inaba, Z. Ogumi, Formation mechanism of alkyl dicarbonates in Li-ion cells, *J. Power Sources* 150 (2005) 208–215.
- <sup>67</sup> T. Kawamura, A. Kimura, M. Egashira, S. Okada, J.-I. Yamaki, Thermal stability of alkyl carbonate mixed-solvent electrolytes for lithium ion cells, *J. Power Sources* 104 (2002) 260–264.

- 
- <sup>68</sup> G. Gachot, S. Grugeon, G.G. Eshetu, D. Mathiron, P. Ribière, M. Armand, S. Laruelle, Thermal behaviour of the lithiated-graphite/electrolyte interface through GC/MS analysis, *Electrochim. Acta* 83 (2012) 402–409.
- <sup>69</sup> G. Gachot, P. Ribiere, D. Mathiron, S. Grugeon, M. Armand, J.B. Leriche, S. Pilard, S. Laruelle, Gas Chromatography/Mass Spectrometry As a Suitable Tool for the Li-Ion Battery Electrolyte Degradation Mechanisms Study, *Anal. Chem.* 83 (2011) 478–485.
- <sup>70</sup> B. Ravdel, K.M. Abraham, R. Gitzendanner, J. DiCarlo, B. Lucht, C. Campion, Thermal stability of lithium-ion battery electrolytes, *J. Power Sources* 119-121 (2003) 805–810.
- <sup>71</sup> Y. Matsuda, T. Fukushima, H. Hashimoto, R. Arakawa, Solvation of Lithium Ions in Mixed Organic Electrolyte Solutions by Electrospray Ionization Mass Spectroscopy, *J. Electrochem. Soc.* 149 (2002) A1045-A1048.
- <sup>72</sup> M. Grütze, W. Weber, M. Winter and S. Nowak, Structure determination of organic aging products in lithium-ion battery electrolytes with gas chromatography chemical ionization mass spectrometry (GC-CI-MS), *RSC Adv.* 6 (2016) 57253-57260.
- <sup>73</sup> J.Y. Eoma, I.H. Jung, J.H. Lee, Effects of vinylene carbonate on high temperature storage of high voltage Li-ion batteries, *J. Power Sources* 196 (2011) 9810–9814.
- <sup>74</sup> K. Kumai, H. Miyashiro, Y. Kobayashi, K. Takei, R. Ishikawa, Gas generation mechanism due to electrolyte decomposition in commercial lithium-ion cell, *J. Power Sources* 81–82 (1999) 715–719.
- <sup>75</sup> R. Mogi, M. Inaba, Y. Iriyama, T. Abe, Z. Ogumi, The role of Li-ion battery electrolyte reactivity in performance decline and self-discharge, *J. Power Sources* 119–121 (2003) 597–603.
- <sup>76</sup> D. Aurbach, Y. Jofer, M. Ben-Zion, P. Aped, The behaviour of lithium electrodes in propylene and ethylene carbonate: The major factors that influence Li cycling efficiency, *J. Electroanal. Chem.* 339 (1992) 451-471.
- <sup>77</sup> D. Aurbach, A. Zaban, Y. Ein-Eli, I. Weissman, O. Chusid, B. Markovsky, M. Levi, E. Levi, A. Schechter, E. Granot, Recent studies on the correlation between surface chemistry, morphology, three-dimensional structures and performance of Li and Li-C intercalation anodes in several important electrolyte systems, *J. Power Sources* 68 (1997) 91-98.
- <sup>78</sup> D. Aurbach, E. Zinigrad, Y. Cohen, H. Teller, A short review of failure mechanisms of lithium metal and lithiated graphite anodes in liquid electrolyte solutions, *Solid State Ionics* 148 (2002) 405–416.
- <sup>79</sup> K. Tasaki, A. Goldberg, J.-J. Lian, M. Walker, A. Timmons, S. J. Harris, Solubility of Lithium Salts Formed on the Lithium-Ion Battery Negative Electrode Surface in Organic Solvents, *J. Electrochem. Soc.* 156 (2009) A1019-A1027.
- <sup>80</sup> A.M. Andersson, M. Herstedt, A.G. Bishop, K. Edström, The influence of lithium salt on the interfacial reactions controlling the thermal stability of graphite anodes, *Electrochim. Acta* 47 (2002) 1885-1898.

- 
- <sup>81</sup> D. Aurbach, Review of selected electrode–solution interactions which determine the performance of Li and Li ion batteries, *J. Power Sources* 89 (2000) 206–218.
- <sup>82</sup> R. Dedryvère, L. Gireaud, S. Grugeon, S. Laruelle, J.M. Tarascon, D. Gonbeau, Characterization of Lithium Alkyl Carbonates by X-ray Photoelectron Spectroscopy: Experimental and Theoretical Study, *J. Physic. Chem. B* 109 (2005) 15868-15875.
- <sup>83</sup> T. Eriksson, *LiMn<sub>2</sub>O<sub>4</sub> as a Li-Ion Battery Cathode From Bulk to Electrolyte Interface*, Acta Universitatis Upsaliensis Uppsala, 2001
- <sup>84</sup> N.S. Choi, Z. Chen, S.A. Freunberger, X. Ji, Y.K. Sun, K. Amine, G. Yushin, L.F. Nazar, J. Cho, P.G. Bruce, Challenges Facing Lithium Batteries and Electrical Double-Layer Capacitors, *Angewandte Chemie* 51 (2012) 9994-10024.
- <sup>85</sup> M. Moshkovich, M. Cojocaru, H.E. Gottlieb, D. Aurbach, The study of the anodic stability of alkyl carbonate solutions by in situ FTIR spectroscopy, EQCM, NMR and MS, *J. Electroanal. Chem.* 497 (2001) 84–96.
- <sup>86</sup> D.P. Abraham, E.P. Roth, R. Kostecki, K. McCarthy, S. MacLaren, D.H. Doughty, Diagnostic examination of thermally abused high-power lithium-ion cells, *J. Power Sources* 161 (2006) 648–657.
- <sup>87</sup> D. Aurbach, B. Markovsky, A. Rodkin, M. Cojocaru, E. Levi, H.J. Kim, An analysis of rechargeable lithium-ion batteries after prolonged cycling, *Electrochim. Acta* 00 (2002) 1 -13.
- <sup>88</sup> G.V. Zhuang, H. Yang, P.N. Ross Jr., K. Xu, T.R. Jow, Lithium Methyl Carbonate as a Reaction Product of Metallic Lithium and Dimethyl Carbonate, Lawrence Berkeley National Laboratory 10-16-2005.
- <sup>89</sup> K. Xu, Electrolytes and Interphasial Chemistry in Li Ion Devices, *Energies* 3 (2010) 135-154.
- <sup>90</sup> R. Spotnitza, J. Franklin, Abuse behavior of high-power, lithium-ion cells, *J. Power Sources* 113 (2003) 81–100.
- <sup>91</sup> Q. Wanga, P. Ping, X. Zhao, G. Chu, J. Sun, C. Chen, Thermal runaway caused fire and explosion of lithium ion battery, *J. Power Sources* 208 (2012) 210–224.
- <sup>92</sup> V. Kraft, M. Grützke, W. Weber, J. Menzel, S. Wiemers-Meyer, M. Winter, S. Nowak, Two-dimensional ion chromatography for the separation of ionic organophosphates generated in thermally decomposed lithiumhexafluorophosphate-based lithium ion battery electrolytes, *J. Chrom. A*, 1409 (2015) 201–209.
- <sup>93</sup> M. Holzapfel, A. Wuersig, W. Scheifele, J. Vetter, P. Novak, Oxygen, hydrogen, ethylene and CO<sub>2</sub> development in lithium-ion batteries, *J. Power Sources* 174 (2007) 1156-1160.
- <sup>94</sup> M. Broussely, G. Pistoia, 2007, Industrial applications of batteries. From cars to aerospace and energy storage Chapter 3: Characterization of batteries by electrochemical and non-electrochemical techniques, Elsevier B.V. (2007) 119-201.

- 
- <sup>95</sup> N. Williard, B. Sood, M. Ostermann, M. Pecht, Disassembly methodology for conducting failure analysis on lithium-ion batteries, *J. Mater. Sci. Mater. Electron.* 22 (2011) 1616-1630.
- <sup>96</sup> E. Rosenberg, C. Kanakaki, A. Amon, I. Gocheva, A. Trifonova, Understanding the degradation processes of the electrolyte of lithium ion batteries by chromatographic analysis, *Bulg. Chem. Commun.* 49 (2017) 242-253.
- <sup>97</sup> M. Krajewski, M. Michalska, B. Hamankiewicz, D. Ziolkowska, K.P. Korona, J.B. Jasinski, M. Kaminska, L. Lipinska, A. Czerwinski,  $\text{Li}_4\text{Ti}_5\text{O}_{12}$  modified with Ag nanoparticles as an advanced anode material in lithium-ion batteries, *J. Power Sources* 245 (2014) 764-771.
- <sup>98</sup> G. Lieser, C. Dräger, L. de Biasi, S. Indris, H. Geßwein, S. Glatthaar, M.J. Hoffmann, H. Ehrenberg, J.R. Binder, Direct synthesis of trirutile-type  $\text{LiMgFeF}_6$  and its electrochemical characterization as positive electrode in lithium-ion batteries, *J. Power Sources* 274 (2015) 1200-1207.
- <sup>99</sup> B. Wu, V. Yufit, Y. Merla, R.F. Martinez-Botas, N.P. Brandon, G.J. Offer, Differential thermal voltammetry for tracking of degradation in lithium-ion batteries, *J. Power Sources* 273 (2015) 495-501.
- <sup>100</sup> J.N. Lohmann, P. Weßkamp, P. Haußmann, J. Melbert, T. Musch, Electrochemical impedance spectroscopy for lithium-ion cells: Test equipment and procedures for aging and fast characterization in time and frequency domain, *J. Power Sources* 273 (2015) 613-623.
- <sup>101</sup> M. Inaba, Y. Kawatate, A. Funabiki, S.K. Jeong, T. Abe, Z. Ogumi, STM study on graphite/electrolyte interface in lithium-ion batteries: solid electrolyte interface formation in trifluoropropylene carbonate solution, *Electrochim. Acta* 45 (1999) 99-105.
- <sup>102</sup> R. Hausbrand, G. Cherkashinin, H. Ehrenberg, M. Gröting, K. Albe, C. Hess, W. Jaegermann, Fundamental degradation mechanisms of layered oxide Li-ion battery cathode materials: Methodology, insights and novel approaches, *Mater. Sci. Eng. B* 192 (2015) 3-25.
- <sup>103</sup> J. Park, S.S. Park, Y.S. Won, In situ XRD study of the structural changes of graphite anodes mixed with  $\text{SiO}_x$  during lithium insertion and extraction in lithium ion batteries, *Electrochim. Acta* 107 (2013) 467-472.
- <sup>104</sup> Z. Liang, Z. Lin, Y. Zhao, Y. Dong, Q. Kuang, X. Lin, X. Liu, D. Yan, New understanding of  $\text{Li}_3\text{VO}_4/\text{C}$  as potential anode for Li-ion batteries: Preparation, structure characterization and lithium insertion Mechanism, *J. Power Sources* 274 (2015) 345-354.
- <sup>105</sup> X. Gao, Y. Sha, Q. Lin, R. Cai, M.O. Tade, Z. Shao, Combustion-derived nanocrystalline  $\text{LiMn}_2\text{O}_4$  as a promising cathode material for lithium-ion batteries, *J. Power Sources* 275 (2015) 38-44.
- <sup>106</sup> V. Zinth, C. von Lüders, M. Hofmann, J. Hattendorff, I. Buchberger, S. Erhard, J. Rebelo-Kornmeier, A. Jossen, R. Gilles, Lithium plating in lithium-ion batteries at sub-ambient temperatures investigated by in situ neutron diffraction, *J. Power Sources* 271 (2014) 152-159.

- 
- <sup>107</sup> Y. Zhao, X. Li, B. Yan, D. Li, S. Lawes, X. Sun, Significant impact of 2D graphene nanosheets on large volume change tin-based anodes in lithium-ion batteries: A review, *J. Power Sources* 274 (2015) 869-884.
- <sup>108</sup> Q. Su, J. Zhang, Y. Wu, G. Du, Revealing the electrochemical conversion mechanism of porous  $\text{Co}_3\text{O}_4$  nanoplates in lithium ion battery by *in situ* transmission electron microscopy, *Nano Energy* 9 (2014) 264-272.
- <sup>109</sup> C. Chen, Q. Ru, S. Hu, B. An, X. Song, X. Hou,  $\text{Co}_2\text{SnO}_4$  nanocrystals anchored on graphene sheets as high-performance electrodes for lithium-ion batteries, *Electrochim. Acta* 151 (2015) 203-213.
- <sup>110</sup> S.J. Kim, H.C. Park, M.C. Kim, D.M. Kim, Y.W. Lee, K.W. Park, Sputtered amorphous thin film nanocomposites as an anode for lithium-ion batteries, *J. Power Sources* 273 (2015) 707-715.
- <sup>111</sup> R. Huang, Y. Ikuhara, STEM characterization for lithium-ion battery cathode materials, *Curr. Opin. Solid State and Mater. Sci.* 16 (2012) 31-38.
- <sup>112</sup> J. Zhu, J. Feng, L. Lu, K. Zeng, In situ study of topography, phase and volume changes of titanium dioxide anode in all-solid-state thin film lithium-ion battery by biased scanning probe microscopy, *J. Power Sources* 197 (2012) 224-230.
- <sup>113</sup> S. Ramdon, B. Bhushan, S.C. Nagpure, In situ electrochemical studies of lithium-ion battery cathodes using atomic force microscopy, *J. Power Sources* 249 (2014) 373-384.
- <sup>114</sup> M. Shao, In situ microscopic studies on the structural and chemical behaviors of lithium-ion battery materials, *J. Power Sources* 270 (2014) 475-486.
- <sup>115</sup> R. Dedryvère, S. Laruelle, S. Grugeon, L. Gireaud, J.T. Tarascon, D. Gonbeau, , XPS Identification of the Organic and Inorganic Components of the Electrode/Electrolyte Interface Formed on a Metallic Cathode, *J. Electrochem. Soc.* 152 (2005) A689.
- <sup>116</sup> S. Oswald, K. Nikolowski, H. Ehrenberg, Quasi in situ XPS investigations on intercalation mechanisms in Li-ion battery materials, *Anal. Bioanal. Chem.* 393 (2009) 1871-1877.
- <sup>117</sup> W. Lu, K. Xie, Z. Chen, S. Xiong, Y. Pan, C. Zheng, A new co-solvent for wide temperature lithium ion battery electrolytes: 2,2,2-Trifluoroethyl n-caproate, *J. Power Sources* 274 (2015) 676-684.
- <sup>118</sup> T. Zhang, Y. He, F. Wang, H. Li, C. Duan, C. Wu, Surface analysis of cobalt-enriched crushed products of spent lithium-ion batteries by X-ray photoelectron spectroscopy, *Sep. Purif. Technol.* 138 (2014) 21-27.
- <sup>119</sup> R. Dedryvere, L. Gireaud, S. Grugeon, S. Laruelle, J.-M. Tarascon, D. Gonbeau, Characterization of Lithium Alkyl Carbonates by X-ray Photoelectron Spectroscopy: Experimental and Theoretical Study, *J. Phys. Chem. B* 109 (2005) 15868-15875.

- 
- <sup>120</sup> S. Hy, Felix, Y.H. Chen, J.Y. Liu, J. Rick, B.J. Hwang, In situ surface enhanced Raman spectroscopic studies of solid electrolyte interphase formation in lithium ion battery electrodes, *J. Power Sources* 256 (2014) 324-328.
- <sup>121</sup> D.P. Abraham, E.P. Roth, R. Kostecki, K. McCarthy, S. MacLaren, D.H. Doughty, Diagnostic examination of thermally abused high-power lithium-ion cells, *J. Power Sources* 161 (2006) 648-657.
- <sup>122</sup> P. Niehoff, S. Passerini, M. Winter, Interface investigations on commercial lithium ion battery graphite anode material by sputter depth X-ray photoelectron spectroscopy, *Langmuir* 29 (2013) 5806-5816.
- <sup>123</sup> J.T. Li, J. Swiatowska, V. Maurice, A. Seyeux, L. Huang, S.G. Sun, P. Marcus, XPS and ToF-SIMS Study of Electrode Processes on Sn-Ni Alloy Anodes for Li-Ion Batteries, *J. Phys. Chem. C* 115 (2011) 7012-7018.
- <sup>124</sup> I.V. Veryovkin, C.E. Tripa, A.V. Zinovev, S.V. Baryshev, Y. Li, D.P. Abraham, TOF SIMS characterization of SEI layer on battery electrodes, *Nucl. Instrum. Methods Phys. Res. B* 332 (2014) 368-372.
- <sup>125</sup> E. Peled, D. Bar Tow, A. Merson, A. Gladkikh, L. Burstein, D. Golodnitsky, Composition, depth profiles and lateral distribution of materials in the SEI built on HOPG-TOF SIMS and XPS studies, *J. Power Sources* 97-98 (2001) 52-57.
- <sup>126</sup> R. Dedryvere, L. Gireaud, S. Grugeon, S. Laruelle, J.M. Tarascon, D. Gonbeau, Characterization of Lithium Alkyl Carbonates by X-ray Photoelectron Spectroscopy: Experimental and Theoretical Study, *J. Phys. Chem. B* 109, (2005) 15868-15875.
- <sup>127</sup> Z. Liang, Z. Lin, Y. Zhao, Y. Dong, Q. Kuang, X. Lin, X. Liu, D. Yan, New understanding of  $\text{Li}_3\text{VO}_4/\text{C}$  as potential anode for Li-ion batteries: Preparation, structure characterization and lithium insertion Mechanism, *J. Power Sources* 274 (2015) 345-354.
- <sup>128</sup> E.J. Lee, H.J. Noh, C.S. Yoon, Y.K. Sun, Effect of outer layer thickness on full concentration gradient layered cathode material for lithium-ion batteries, *J. Power Sources* 273 (2015) 663-669.
- <sup>129</sup> J.S. Gnanaraj, E. Zinigrad, L. Asraf, H.E. Gottlieb, M. Sprecher, D. Aurbach, M. Schmidt, The use of accelerating rate calorimetry (ARC) for the study of the thermal reactions of Li-ion battery electrolyte solutions. *J. Power Sources* 119-121 (2003) 794-798.
- <sup>130</sup> M. Broussely, G. Pistoia, Industrial applications of batteries. From cars to aerospace and energy storage Chapter 3: Characterization of batteries by electrochemical and non-electrochemical techniques, Elsevier B.V. (2007) 119-201.
- <sup>131</sup> P. Röder, N. Baba, H.D. Wiemhöfer, A detailed thermal study of a  $\text{Li}[\text{Ni}_{0.33}\text{Co}_{0.33}\text{Mn}_{0.33}]\text{O}_2/\text{LiMn}_2\text{O}_4$ -based lithium ion cell by accelerating rate and differential scanning calorimetry, *J. Power Sources* 248 (2014) 978-987.



- 
- <sup>132</sup> G. Nagasubramanian, C.J. Orendorff, Hydrofluoroether electrolytes for lithium-ion batteries: Reduced gas decomposition and nonflammable, *J. Power Sources* 196 (2011) 8604– 8609.
- <sup>133</sup> X. Feng, J. Sun, M. Ouyang, F. Wang, X. He, L. Lu, H. Peng, Characterization of penetration induced thermal runaway propagation process within a large format lithium ion battery module, *J. Power Sources* 275 (2015) 261-273.
- <sup>134</sup> X. Feng, M. Fang, X. He, M. Ouyang, L. Lu, H. Wang, M. Zhang, Thermal runaway features of large format prismatic lithium ion battery using extended volume accelerating rate calorimetry, *J. Power Sources* 255 (2014) 294-301.
- <sup>135</sup> K. Prasanna, C.S. Kim, C.W. Lee, Effect of SiO<sub>2</sub> coating on polyethylene separator with different stretching ratios for application in lithium ion batteries, *Mater. Chem. Phys.* 146 (2014) 545-550.
- <sup>136</sup> P. Mairez, A. Evans, H. Kaiser, W. Scheifele, P. Novák, Colorimetric Determination of Lithium Content in Electrodes of Lithium-Ion Batteries, *J. Electrochem. Soc.* 155 (2008) A862-A865.
- <sup>137</sup> P. Maire, H. Kaiser, W. Scheifele, P. Novák, Colorimetric determination of lithium-ion mobility in graphite composite electrodes, *J. Electroanal. Chem.* 644 (2010) 127–131.
- <sup>138</sup> E. Endo, M. Ata, K. Sekai, K. Tanaka, Spin Trapping Study of Gradual Decomposition of Electrolyte Solutions for Lithium Secondary Batteries, *J. Electrochem. Soc.*, 146 (1999) 49-53.
- <sup>139</sup> Y. Ren, J. Li, J. Yu, Enhanced electrochemical performance of TiO<sub>2</sub> by Ti<sup>3+</sup> doping using a facile solvothermal method as anode materials for lithium-ion batteries, *Electrochim. Acta* 138 (2014) 41–47.
- <sup>140</sup> T. Waldmann, M. Wilka, M. Kasper, M. Fleischhammer, M. Wohlfahrt-Mehrens, Temperature dependent ageing mechanisms in Lithium-ion batteries e A Post-Mortem study, *J. Power Sources* 262 (2014) 129-135.
- <sup>141</sup> Y.H. Jouybari, S. Asgari, Synthesis and electrochemical properties of LiNi<sub>0.8</sub>Co<sub>0.2</sub>O<sub>2</sub> nanopowders for lithium ion battery applications, *J. Power Sources* 196 (2011) 337-342.
- <sup>142</sup> M. Grütze, V. Kraft, B. Hoffmann, S. Klamor, J. Diekmann, A. Kwade, M. Winter, S. Nowak, Aging investigations of a lithium-ion battery electrolyte from a field-tested hybrid electric vehicle, *J. Power Sources* 273 (2015) 83-88.
- <sup>143</sup> L. Li, S. Song, X. Zhang, R. Chen, J. Lu, F. Wu, K. Amine, Ultrasonic-assisted co-precipitation to synthesize lithium-rich cathode Li<sub>1.3</sub>Ni<sub>0.21</sub>Mn<sub>0.64</sub>O<sub>2</sub> materials for lithium-ion batteries, *J. Power Sources* 272 (2014) 922-928.
- <sup>144</sup> R. Wu, G. Xia, S. Shen, F. Zhu, F. Jiang, J. Zhang, In-situ growth of LiFePO<sub>4</sub> nanocrystals on interconnected carbon nanotubes/mesoporous carbon nanosheets for high-performance lithium ion batteries, *Electrochim. Acta* 153 (2015) 334–342.

- 
- <sup>145</sup> C.C. Chang, Sb-coated mesophase graphite powder as anode material for lithium-ion batteries, *J. Power Sources* 175 (2008) 874-880.
- <sup>146</sup> E. Han, Q. Jing, L. Zhu, G. Zhang, S. Ma, The effects of sodium additive on  $\text{Li}_{1.17}\text{Ni}_{0.10}\text{Co}_{0.10}\text{Mn}_{0.63}\text{O}_2$  for lithium ion batteries, *J. Alloys Compd* 618 (2015) 629-634.
- <sup>147</sup> C. Wang, X. Ma, Z. Li, Y. Liang, J. Sun, Y. Zhou, Simple, rapid and accurate determination of lattice composition and evaluation of electrochemical properties of  $\text{Li}_x\text{Ni}_{2-x}\text{O}_2$  electrode material for lithium ion battery by a novel method, *Electrochem. Commun.* 8 (2006) 289-292.
- <sup>148</sup> B. Li, Y. Yu, J. Zhao, Facile synthesis of spherical  $x\text{Li}_2\text{MnO}_3 \cdot (1-x)\text{Li}(\text{Mn}_{0.33}\text{Co}_{0.33}\text{Ni}_{0.33})\text{O}_2$  as cathode materials for lithium-ion batteries with improved electrochemical performance, *J. Power Sources* 275 (2015) 64-72.
- <sup>149</sup> B. Wang, Z. Wang, Y. Cui, Y. Yang, Z. Wang, B. Chen, G. Qian,  $\text{Cr}_2\text{O}_3@ \text{TiO}_2$  yolk/shell octahedrons derived from a metal-organic framework for high-performance lithium-ion batteries, *Microporous Mesoporous Mater.* 203 (2015) 86-90.
- <sup>150</sup> D.A. Totir, B.D. Cahan, D.A. Scherson, Electrochemical characterization of lithiated transition metal oxide cathode particles in the absence of carbon, binders and other additives, *Electrochim. Acta* 45 (1999) 161-166.
- <sup>151</sup> T.F. Yia, C.L. Hao, C.B. Yue, R.S. Zhu, J. Shu, A literature review and test: Structure and physicochemical properties of spinel  $\text{LiMn}_2\text{O}_4$  synthesized by different temperatures for lithium ion battery, *Synthetic Metals* 159 (2009) 1255-1260.
- <sup>152</sup> D. Yoshikawa, Y. Kadoma, J.M. Kim, K. Ui, N. Kumagai, N. Kitamura, Y. Idemoto, Spray-drying synthesized lithium-excess  $\text{Li}_{4+x}\text{Ti}_{5-x}\text{O}_{12-\delta}$  and its electrochemical property as negative electrode material for Li-ion batteries, *Electrochim. Acta* 55 (2010) 1872-1879.
- <sup>153</sup> H. Rong, M. Xu, B. Xie, X. Liao, W. Huang, L. Xing, W. Li, Tris (trimethylsilyl) borate (TMSB) as a cathode surface film forming additive for 5 V  $\text{Li}/\text{LiNi}_{0.5}\text{Mn}_{1.5}\text{O}_4$  Li-ion cells, *Electrochim. Acta* 147 (2014) 31-39.
- <sup>154</sup> H. Rong, M. Xu, B. Xie, W. Huang, X. Liao, L. Xing, W. Li, Performance improvement of graphite/ $\text{LiNi}_{0.4}\text{Co}_{0.2}\text{Mn}_{0.4}\text{O}_2$  battery at high voltage with added Tris (trimethylsilyl) phosphate, *J. Power Sources* 274 (2015) 1155-1161.
- <sup>155</sup> H. Liu, Y. Yang, J. Zhang, Reaction mechanism and kinetics of lithium ion battery cathode material  $\text{LiNiO}_2$  with  $\text{CO}_2$ , *J. Power Sources* 173 (2007) 556-561.
- <sup>156</sup> M.K. Harrup, H.W. Rollins, D.K. Jamison, E.J. Dufek, K.L. Gering, T.A. Luther, Unsaturated phosphazenes as co-solvents for lithium-ion battery electrolytes, *J. Power Sources*, In Press, Corrected Proof, Available online 24 July 2014.

- 
- <sup>157</sup> Q. Zhang, J. Mei, X. Wang, F. Tang, W. Fan, W. Lu, High performance spinel  $\text{LiNi}_{0.5}\text{Mn}_{1.5}\text{O}_4$  cathode material by lithium polyacrylate coating for lithium ion battery, *Electrochim. Acta* 143 (2014) 265-271.
- <sup>158</sup> M. Memm, M. Koentje, P. Axmann, M. Wohlfahrt-Mehrens, New high-voltage step at 4.8 V in cobalt free manganese based lithium phospho olivines for lithium-ion batteries, *J. Power Sources* 276 (2015) 382-387.
- <sup>159</sup> L.J. Xi, H.E. Wang, Z.G. Lu, S.L. Yang, R.G. Ma, J.Q. Deng, C.Y. Chung, Facile synthesis of porous  $\text{LiMn}_2\text{O}_4$  spheres as positive electrode for high-power lithium ion batteries, *J. Power Sources* 198 (2012) 251-257.
- <sup>160</sup> D. Luo, G. Li, C. Fu, J. Zheng, J. Fan, Q. Li, L. Li,  $\text{LiMO}_2$  (M=Mn, Co, Ni) hexagonal sheets with (101) facets for ultrafast charging/discharging lithium ion batteries, *J. Power Sources* 276 (2015) 238-246.
- <sup>161</sup> L. Terborg, S. Weber, F. Blaske, S. Passerini, M. Winter, U. Karst, S. Nowak, Investigation of thermal aging and hydrolysis mechanisms in commercial lithium ion battery electrolyte, *J. Power Sources* 242 (2013) 832-837.
- <sup>162</sup> P. Verma, P. Maire, P. Novák, A review of the features and analyses of the solid electrolyte interphase in Li-ion Batteries, *Electrochim. Acta* 55 (2010) 6332-6341.
- <sup>163</sup> A. Kominato, E. Yasukawa, N. Sato, T. Ijuuin, H. Asahina, S. Mori, Analysis of surface films on lithium in various organic electrolytes, *J. Power Sources* 68 (1997) 471-475.
- <sup>164</sup> L. Li, G. Jing, R. Chen, F. Wu, S. Chen, X. Zhang, Environmental friendly leaching reagent for cobalt and lithium recovery from spent lithium-ion batteries, *Waste Management* 30 (2010) 2615-2621.
- <sup>165</sup> E. Gratz, Q. Sa, D. Apelian, Y. Wang, A closed loop process for recycling spent lithium ion batteries, *J. Power Sources* 262 (2014) 255-262.
- <sup>166</sup> Z. Niu, Y. Zou, B. Xin, S. Chen, C. Liu, Y. Li, Process controls for improving bioleaching performance of both Li and Co from spent lithium ion batteries at high pulp density and its thermodynamics and kinetics exploration, *Chemosphere* 109 (2014) 92-98.
- <sup>167</sup> M. Zhao, H.D. Dewald, R.J. Staniewicz, Quantitation of the dissolution of battery-grade copper foils in lithium-ion battery electrolytes by flame atomic absorption spectroscopy, *Electrochim. Acta* 49 (2004) 683-689.
- <sup>168</sup> M. Xu, L. Zhou, L. Hao, L. Xing, W. Li, B.L. Lucht, Investigation and application of lithium difluoro(oxalate)borate ( $\text{LiDFOB}$ ) as additive to improve the thermal stability of electrolyte for lithium-ion batteries, *J. Power Sources* 196 (2011) 6794-6801.
- <sup>169</sup> N. Nanbu, K. Takimoto, M. Takehara, M. Ue, Y. Sasaki, Electrochemical properties of fluoropropylene carbonate and its application to lithium-ion batteries, *Electrochem. Commun.* 10 (2008) 783-786.

- 
- <sup>170</sup> G.C. Chung, Reconsideration of SEI: reversible lithium intercalation into graphite electrodes in *trans*-2,3-butylene carbonate, *J. Power Sources* 104 (2002) 7-12.
- <sup>171</sup> S. Wiemers-Meyer, M. Winter, S. Nowak, Mechanistic Insights into Lithium Ion Battery Electrolyte Degradation – A Quantitative NMR Study, *Phys. Chem. Chem. Phys.* 18 (2016) 26595 – 26601.
- <sup>172</sup> S. Wiemers-Meyer, M. Winter, S. Nowak, Battery Cell for In Situ NMR Measurements of Liquid Electrolytes, *Physic. Chem. Chem. Phys.* 19 (2017) 4962-4966.
- <sup>173</sup> S.E. Sloop, J.B. Kerr, K. Kinoshita, The role of Li-ion battery electrolyte reactivity in performance decline and self-discharge, *J. Power Sources* 119-121 (2003) 330-337.
- <sup>174</sup> C. Schultz, S. Vedder, B. Streipert, M. Winter, S. Nowak, Quantitative Investigation of the Decomposition of Organic Lithium Ion Battery Electrolytes with LC-MS/MS, *RSC Advances* 7 (2017) 27853-27862.
- <sup>175</sup> V. Kraft, W. Weber, B. Streipert, R. Wagner, C. Schultz, M. Winter, S. Nowak, Qualitative and quantitative investigation of organophosphates in an electrochemically and thermally treated hexafluorophosphate-based lithium ion battery electrolyte by a developed liquid chromatography-tandem quadrupole mass spectrometry method, *RSC Advances* 6 (2016) 8-17.
- <sup>176</sup> C. Schultz, S. Vedder, B. Streipert, M. Winter, S. Nowak, Quantitative Investigation of the Decomposition of Organic Lithium Ion Battery Electrolytes with LC-MS/MS, *RSC Advances* 7 (2017) 27853-27862.
- <sup>177</sup> C. Schultz, V. Kraft, M. Pyschik, S. Weber, F. Schappacher, M. Winter, S. Nowak, Separation and quantification of organic electrolyte components in lithium-ion batteries via a developed HPLC method, *J. Electrochem. Soc.* 162 (2015) A629-A634.
- <sup>178</sup> H. Nakajima, S. Yamaki, T. Nishine, M. Furuta, Analysis of degradation products in electrolyte for rechargeable lithium-ion battery through high mass accuracy MSn, *ASMS* (2012) WP26-541.
- <sup>179</sup> A.N. Tran, T.N. Van Do, L.P. My Le, T.N. Le, Synthesis of new fluorinated imidazolium ionic liquids and their prospective function as the electrolytes for lithium-ion batteries, *J. Fluorine Chem.* 164 (2014) 38-43.
- <sup>180</sup> C.L. Campion, W. Li, B.L. Lucht, Thermal Decomposition of LiPF<sub>6</sub>-Based Electrolytes for Lithium-Ion Batteries, *J. Electrochem. Soc.* 152 (2005) A2327-A2334.
- <sup>181</sup> R. Meziane, J.P. Bonnet, M. Courty, K. Djellab, M. Armand, Single-ion polymer electrolytes based on a delocalized polyanion for lithium batteries, *Electrochim. Acta* 57 (2011) 14-19.
- <sup>182</sup> R. Rohan, Y. Sun, W. Cai, Y. Zhang, K. Pareek, G. Xu, H. Cheng, Functionalized polystyrene based single ion conducting gel polymer electrolyte for lithium batteries, *Solid State Ionics* 268 (2014) 294-299.

- 
- <sup>183</sup> H. Wang, T. Wang, S. Yang, L. Fan, Preparation of thermal stable porous polyimide membranes by phase inversion process for lithium-ion battery, *Polymer* 54 (2013) 6339-6348.
- <sup>184</sup> Q. Lu, J. Fang, J. Yang, G. Yan, S. Liu, J. Wang, A novel solid composite polymer electrolyte based on poly(ethylene oxide) segmented polysulfone copolymers for rechargeable lithium batteries, *J. Membr. Sci.* 425–426 (2013) 105-112.
- <sup>185</sup> W. Guo, J. Su, Y.H. Li, L.J. Wan, Y.G. Guo, Nitroxide radical polymer/graphene nanocomposite as an improved cathode material for rechargeable lithium batteries, *Electrochim. Acta* 72 (2012) 81-86.
- <sup>186</sup> B. Sun, J. Mindemark, K. Edström, D. Brandell, Polycarbonate-based solid polymer electrolytes for Li-ion batteries, *Solid State Ionics* 262 (2014) 738–742.
- <sup>187</sup> B. Vortmann, C. Lürenbaum, M. Winter, S. Nowak, Determination of Lithium and Transition Metals in Li<sub>1</sub>Ni<sub>1/3</sub>Co<sub>1/3</sub>Mn<sub>1/3</sub>O<sub>2</sub> (NCM) Cathode Material for Lithium-Ion Batteries by Capillary Electrophoresis, *Electrophoresis* 38 (2017) 540–546.
- <sup>188</sup> M. Pyschik, M. Klein-Hitpaß, S. Girod, M. Winter, S. Nowak, Capillary Electrophoresis with Contactless Conductivity Detection for the Quantification of Fluoride in Lithium Ion Battery Electrolytes and in Ionic Liquids - A Comparison to the Results Gained with a Fluoride Ion-Selective Electrode, *Electrophoresis* 38 (2017) 533–539.
- <sup>189</sup> V. Kraft, M. Grützke, W. Weber, M. Winter, S. Nowak, Ion chromatography electrospray ionization mass spectrometry method development and investigation of lithiumhexafluorophosphate-based organic electrolytes and their thermal decomposition products, *J. Chromatogr. A*, 1354 (2014) 92–100.
- <sup>190</sup> V. Kraft, M. Grützke, W. Weber, J. Menzel, S. Wiemers-Meyer, M. Winter, S. Nowak, Two-Dimensional Ion Chromatography for the Separation of Ionic Organophosphates Generated in Thermally Decomposed Lithium Hexafluorophosphate-Based Lithium Ion Battery Electrolytes, *J. Chromatogr. A* 1409 (2015) 201-209.
- <sup>191</sup> Y. Matsuda, T. Fukushima, H. Hashimoto, R. Arakawa, Solvation of Lithium Ions in Mixed Organic Electrolyte Solutions by Electrospray Ionization Mass Spectroscopy, *J. Electrochem. Soc.* 149 (2002) A1045-A1048.
- <sup>192</sup> M. Moshkovich, M. Cojocaru, H.E. Gottlieb, D. Aurbach, The study of the anodic stability of alkyl carbonate solutions by in situ FTIR spectroscopy, EQCM, NMR and MS, *J. Electroanal. Chem.* 497 (2001) 84-96.
- <sup>193</sup> B. Vortmann, S. Nowak, C. Engelhard, Rapid Characterization of Lithium Ion Battery Electrolytes and Thermal Aging Products by Low-Temperature Plasma Ambient Ionization High-Resolution Mass Spectrometry, *Anal. Chem.* 85 (2013) 3433–3438.
- <sup>194</sup> H. Baltruschat, Differential electrochemical mass spectrometry, *J. Am. Soc. Mass Spectrom.* 15 (2004) 1693-1706.

- 
- <sup>195</sup> M. Holzapfel, A. Wuersig, W. Scheifele, J. Vetter, P. Novak, Oxygen, hydrogen, ethylene and CO<sub>2</sub> development in lithium-ion batteries, *J. Power Sources* 174 (2007) 1156-1160.
- <sup>196</sup> M. Lanz, P. Novak, DEMS study of gas evolution at thick graphite electrodes for lithium-ion batteries: the effect of  $\gamma$ -butyrolactone, *J. Power Sources* 102 (2001) 277-282.
- <sup>197</sup> P. Novak, F. Joho, R. Imhof, J.C. Panitz, O. Haas, In situ investigation of the interaction between graphite and electrolyte solutions, *J. Power Sources* 81-82 (1999) 212-216.
- <sup>198</sup> R. Imhof, P. Novak, In situ investigation of the electrochemical reduction of carbonate electrolyte solutions at graphite electrodes, *J. Electrochem. Soc.* 145 (1998) 1081-1087.
- <sup>199</sup> R. Imhof, P. Novak, Oxidative electrolyte solvent degradation in lithium-ion batteries. An in situ differential electrochemical mass spectrometry investigation, *J. Electrochem. Soc.* 146 (1999) 1702-1706.
- <sup>200</sup> F. La Mantia, F. Rosciano, N. Tran, P. Novak, Direct evidence of oxygen evolution from Li<sub>x+1</sub>(Ni<sub>1/3</sub>M<sub>1/3</sub>Co<sub>1/3</sub>)<sub>1-x</sub>O<sub>2</sub> at high potentials, *J. Appl. Electrochem.* 38 (2008) 893-896.
- <sup>201</sup> F. La Mantia, F. Rosciano, N. Tran, P. Novak, Quantitation of oxygen loss from Li<sub>x+1</sub>(Ni<sub>1/3</sub>M<sub>1/3</sub>Co<sub>1/3</sub>)<sub>1-x</sub>O<sub>2</sub> at high potentials by differential electrochemical mass spectrometry, *J. Electrochem. Soc.* 156 (2009) A823-A827.
- <sup>202</sup> A. R. Armstrong, M. Holzapfel, P. Novak, C. S. Johnson, S.H. Kang, M.M. Thackeray, P.G. Bruce, Demonstrating oxygen loss and associated structural reorganization in the lithium battery cathode Li[Ni<sub>0.2</sub>Li<sub>0.2</sub>Mn<sub>0.6</sub>]O<sub>2</sub>, *J. Am. Chem. Soc.* 128 (2006) 8694-8698.
- <sup>203</sup> J. Ufheil, M. C. Baertsch, A. Würsig, P. Novak, Maleic anhydride as an additive to  $\gamma$ -butyrolactone solutions for Li-ion batteries, *Electrochim. Acta* 50 (2005) 1733-1738.
- <sup>204</sup> A. Wuersig, W. Scheifele, P. Novak, CO<sub>2</sub> gas evolution on cathode materials for lithium-ion batteries, *J. Electrochem. Soc.* 154 (2007) A449-A454.
- <sup>205</sup> P. Lanz, H. Sommer, M. Schulz-Dobrick, P. Novak, Oxygen release from high-energy xLi<sub>2</sub>MnO<sub>3</sub>(1-x)LiMO<sub>2</sub> (M = Mn, Ni, Co): Electrochemical, differential electrochemical mass spectrometric, in situ pressure, and in situ temperature characterization, *Electrochim. Acta* 93 (2013) 114-119.
- <sup>206</sup> H. Buqa, A. Wuersig, J. Vetter, M.E. Spahr, F. Krumeich, P. Novak, SEI film formation on highly crystalline graphitic materials in lithium-ion batteries, *J. Power Sources* 153 (2006) 385-390.
- <sup>207</sup> M. Winter, R. Imhof, F. Joho, P. Novak, FTIR and DEMS investigations on the electroreduction of chloroethylene carbonate-based electrolyte solutions for lithium-ion cells, *J. Power Sources* 81-82 (1999) 818-823.
- <sup>208</sup> J. Vetter, M. Holzapfel, A. Wuersig, W. Scheifele, J. Ufheil, P. Novak, In situ study on CO<sub>2</sub> evolution at lithium-ion battery cathodes, *J. Power Sources* 159 (2006) 277-281.

- 
- <sup>209</sup> Y. Fu, S. Lu, K. Li, C. Liu, X. Cheng, H. Zhang, An experimental study on burning behaviors of 18650 lithium ion batteries using a cone calorimeter, *J. Power Sources* 273 (2015) 216-222.
- <sup>210</sup> R.C. Alkire, D.M. Kolb, J. Lipkowski, P.N. Ross (Eds.), *Diffraction and Spectroscopic Methods in Electrochemistry*, Wiley-VCH Verlag, Weinheim (2006) 315-376.
- <sup>211</sup> L. Gireaud, S. Grugeon, S. Laruelle, S. Pilard, J.M. Tarascon, Identification of Li Battery Electrolyte Degradation Products Through Direct Synthesis and Characterization of Alkyl Carbonate Salts, *J. Electrochem. Soc.* 152 (2005) A850-A857.
- <sup>212</sup> S.W. Song, S.W. Baek, S.W. Song, S.W. Baek, Surface layer formation on Sn anode: ATR FTIR spectroscopic characterization, *Electrochim. Acta* 54 (2009) 1312-1318.
- <sup>213</sup> Y. Ikezawa, T. Ariga, In situ FTIR spectra at the Cu electrode/propylene carbonate solution interface, *Electrochim. Acta* 52 (2007) 2710-2715.
- <sup>214</sup> P. Verma, P. Maire, P. Novák, A review of the features and analyses of the solid electrolyte interphase in Li-ion Batteries, *Electrochim. Acta* 55 (2010) 6332-6341.
- <sup>215</sup> S.W. Song, S.W. Baek, Surface layer formation on Sn anode: ATR FTIR spectroscopic characterization, *Electrochim. Acta* 54 (2009) 1312-1318.
- <sup>216</sup> J.T. Li, V. Maurice, J. Swiatowska-Mrowiecka, A. Seyeux, S. Zanna, L. Klein, S.G. Sun, P. Marcus, XPS, time-of-flight-SIMS and polarization modulation IRRAS study of Cr<sub>2</sub>O<sub>3</sub> thin film materials as anode for lithium ion battery, *Electrochim. Acta* 54 (2009) 3700-3707.
- <sup>217</sup> C. Naudin, J.L. Bruneel, M. Chami, B. Desbat, J. Grondin, J.C. Lassègues, L. Servant Characterization of the lithium surface by infrared and Raman spectroscopies, *J. Power Sources* 124 (2003) 518-525.
- <sup>218</sup> A.M. Haregewoin, E.G. Leggesse, J.C. Jiang, F.M. Wang, B.J. Hwang, S.D. Lin, Comparative Study on the Solid Electrolyte Interface Formation by the Reduction of Alkyl Carbonates in Lithium ion, *Electrochim. Acta* 136 (2014) 274-285.
- <sup>219</sup> C. Korepp, W. Kern, E.A. Lanzer, P.R. Raimann, J.O. Besenhard, M. Yang, K.C. Möller, D.T. Shieh, M. Winter, Ethyl isocyanate-An electrolyte additive from the large family of isocyanates for PC-based electrolytes in lithium-ion batteries, *J. Power Sources* 174 (2007) 628-631.
- <sup>220</sup> K. Morigaki, In situ analysis of the interfacial reactions between MCMB electrode and organic electrolyte solutions, *J. Power Sources* 103 (2002) 253-264.
- <sup>221</sup> C.M. Burba, R. Frech, In situ transmission FTIR spectroelectrochemistry: A new technique for studying lithium batteries, *Electrochim. Acta* 52 (2006) 780-785.
- <sup>222</sup> J.T. Li, S.R. Chen, F.S. Ke, G.Z. Wei, L. Huang, S.G. Sun, In situ microscope FTIR spectroscopic studies of interfacial reactions of Sn-Co alloy film anode of lithium ion battery, *J. Electroanal. Chem.* 649 (2010) 171-176.

- 
- <sup>223</sup> G. Lieser, C. Dräger, L. de Biasi, S. Indris, H. Geßwein, S. Glatthaar, M.J. Hoffmann, H. Ehrenberg, J.R. Binder, Direct synthesis of trirutile-type  $\text{LiMgFeF}_6$  and its electrochemical characterization as positive electrode in lithium-ion batteries, *J. Power Sources* 274 (2015) 1200-1207.
- <sup>224</sup> G. Gebresilassie Eshetu, S. Grugeon, G. Gachot, D. Mathiron, M. Armand, S. Laruelle, LiFSI vs. LiPF<sub>6</sub> electrolytes in contact with lithiated graphite: Comparing thermal stabilities and identification of specific SEI-reinforcing additives, *Electrochim. Acta* 102 (2013) 133-141.
- <sup>225</sup> G. Gachot, S. Grugeon, I. Jimenez-Gordon, G. Gebresilassie Eshetu, S. Boyanov, A. Lecocq, G. Marlair, S. Pilarde, S. Laruelle, Gas Chromatography/Fourier Transform Infrared/Mass Spectrometry Coupling: a Tool for Li-Ion Battery Safety Field Investigation, *Analytical Methods* 6 (2014) 6120-6124.
- <sup>226</sup> H. Yoshida, T. Fukunaga, T. Hazama, M. Terasaki, M. Mizutani, M. Yamachi, Degradation mechanism of alkyl carbonate solvents used in lithium-ion cells during initial charging, *J. Power Sources* 68 (1997) 311-315.
- <sup>227</sup> H. Hahn, R. Wagner, F. Schappacher, M. Winter, S. Nowak, In operand X-shaped cell online electrochemical mass spectrometry (OEMS): New online analysis enables insight into lab scale lithium ion batteries during operation, *J. Electroanal. Chem.* 772 (2016) 52-57.
- <sup>228</sup> S.H. Lee, J.M. Jung, J.H. Ok, C.H. Park, Thermal studies of charged cathode material ( $\text{Li}_x\text{CoO}_2$ ) with temperature-programmed decomposition–mass spectrometry, *J. Power Sources* 195 (2010) 5049-5051.
- <sup>229</sup> S.E. Sloop, J.K. Pugh, S. Wang, J.B. Kerr, K. Kinoshita, Chemical Reactivity of  $\text{PF}_5$  and  $\text{LiPF}_6$  in Ethylene Carbonate/Dimethyl Carbonate Solutions, *Electrochem. Solid-State* 4 (2001) A42-A44.
- <sup>230</sup> L. Yang, C. Smith, C. Patrissi, C.R. Schumacher, B.L. Lucht, Surface reactions and performance of non-aqueous electrolytes with lithium metal anodes, *J. Power Sources* 185 (2008) 1359-1366.
- <sup>231</sup> S. Izquierdo-Gonzales, W. Li, B.L. Lucht, Hexamethylphosphoramide as a flame retarding additive for lithium-ion battery electrolytes, *J. Power Sources* 135 (2004) 291-296.
- <sup>232</sup> G.C. Chung, H.J. Kim, S.H. Jun, M.H. Kim, New cyclic carbonate solvent for lithium ion batteries: trans-2,3-butylene carbonate, *Electrochem. Commun.* 1 (1999) 493-496.
- <sup>233</sup> K. Takei, Y. Kobayashi, H. Miyashiro, K. Kumai, N. Terada, T. Iwahori, T. Tanaka, Series-connected multi-cell operation of lithium-ion cells by floating method, *J. Power Sources* 68 (1997) 427-431.
- <sup>234</sup> M. Arakawa, J. Yamaki, Anodic oxidation of propylene carbonate and ethylene carbonate on graphite electrodes, *J. Power Sources* 54 (1995) 250-254.
- <sup>235</sup> L. Terborg, S. Weber, S. Passerini, M. Winter, U. Karst, S. Nowak, Development of gas chromatographic methods for the analyses of organic carbonate-based electrolytes, *J. Power Sources* 245 (2014) 836-840.



- 
- <sup>236</sup> X. Mönnighoff, P. Murmann, W. Weber, M. Winter, S. Nowak, Post-Mortem Investigations of Fluorinated Flame Retardants for Lithium Ion Battery Electrolytes by Gas Chromatography with Chemical Ionization, *Electrochim. Acta* 246 (2017) 1042–1051.
- <sup>237</sup> S. Nowak, M. Winter, Review—Chemical Analysis for a Better Understanding of Aging and Degradation Mechanisms of Non-Aqueous Electrolytes for Lithium Ion Batteries: Method Development, Application and Lessons Learned, *J. Electrochem. Soc.*, 162 (2015) A2500-A2508.
- <sup>238</sup> M. Grützke, V. Kraft, W. Weber, C. Wendt, A. Friesen, S. Klamor, M. Winter, S. Nowak, Supercritical carbon dioxide extraction of lithium-ion battery electrolytes, *J. Supercrit. Fluids* 94 (2014) 216-222.
- <sup>239</sup> W. Weber, V. Kraft, M. Grützke, R. Wagner, M. Winter, S. Nowak, Identification of alkylated phosphates by gas chromatography–massspectrometric investigations with different ionization principles of athermally aged commercial lithium ion battery electrolyte, *J. Chromatogr. A*, 1394 (2015) 128–136.
- <sup>240</sup> M. Grützke, W. Weber, M. Winter, S. Nowak, Structure determination of organic aging products in lithium-ion battery electrolytes with gas chromatography chemical ionization mass spectrometry (GC-CI-MS), *RSC Adv.* 6 (2016) 57253-57260.
- <sup>241</sup> B. Laik, A. Chausse, R. Messina, M.G. Barthes-Labrousse, J.Y. Nedelec, C. Le Paven-Thivet, F. Grillon, Analysis of the surface layer on a petroleum coke electrode in tetraglyme solutions of lithium salts, *Electrochim. Acta* 46 (2000) 691-700.
- <sup>242</sup> B. Laik, F. Gessier, F. Mercier, P. Trocellier, A. Chausse, R. Messina, Influence of lithium salts on the behaviour of a petroleum coke in organic carbonate solutions, *Electrochim. Acta* 44 (1999) 1667-1676.
- <sup>243</sup> M. Jean, A. Chausse, R. Messina, Analysis of the passivating layer and the electrolyte in the system: petroleum coke/solution of  $\text{LiCF}_3\text{SO}_3$  in mixed organic carbonates, *Electrochim. Acta* 43 (1998) 1795-1802.
- <sup>244</sup> J.S. Shina, C.H. Hana, U.H. Jung, S.I. Leeb, H.J. Kim, K. Kim, Effect of  $\text{Li}_2\text{CO}_3$  additive on gas generation in lithium-ion batteries, *J. Power Sources* 109 (2002) 47-52.
- <sup>245</sup> K. Kumai, H. Miyashiro, Y. Kobayashi, K. Takei, R. Ishikawa, Gas generation mechanism due to electrolyte decomposition in commercial lithium-ion cell, *J. Power Sources* 81-82 (1999) 715-719.
- <sup>246</sup> M. Hibino, H. Zhou, I. Honma, Electrode properties of manganese oxide synthesized by sonochemical method in non-aqueous system, *J. Power Sources* 146 (2005) 304-309.
- <sup>247</sup> S.E. Sloop, J.B. Kerr, K. Kinoshita, The role of Li-ion battery electrolyte reactivity in performance decline and self-discharge, *J. Power Sources* 119-121 (2003) 330-337.
- <sup>248</sup> M. Liu, Y.B. He, W. Lu, C. Zhang, H. Du, B. Li, Q.H. Yang, F. Kang, High catalytic activity of anatase titanium dioxide for decomposition of electrolyte solution in lithium ion battery, *J. Power Sources* 268 (2014) 882-886.

- 
- <sup>249</sup> D.J. Lee, D. Im, Y.G. Ryu, S. Lee, J. Yoon, J. Lee, W. Choi, I. Jung, S. Lee, S.G. Doo, Phosphorus derivatives as electrolyte additives for lithium-ion battery: The removal of O<sub>2</sub> generated from lithium-rich layered oxide cathode, *J. Power Sources* 243 (2013) 831-835.
- <sup>250</sup> C. Huang, K. Huang, S. Liu, Y. Zeng, L. Chen, Storage behavior of LiNi<sub>1/3</sub>Co<sub>1/3</sub>Mn<sub>1/3</sub>O<sub>2</sub>/artificial graphite Li-ion cells, *Electrochim. Acta* 54 (2009) 4783-4788.
- <sup>251</sup> H. Lee, S. Kim, J. Jeon, J.J. Cho, Proton and hydrogen formation by cyclohexyl benzene during overcharge of Li-ion batteries, *J. Power Sources* 173 (2007) 972-978.
- <sup>252</sup> Z. Wang, L. Chen, Solvent storage-induced structural degradation of LiCoO<sub>2</sub> for lithium ion batteries, *J. Power Sources* 146 (2005) 254-258.
- <sup>253</sup> W. Kong, H. Li, X. Huang, L. Chen, Gas evolution behaviors for several cathode materials in lithium-ion batteries, *J. Power Sources* 142 (2005) 285-291.
- <sup>254</sup> K. Osawa, K. Oshida, T. Nakazawa, T. Nishizawa, T. Ikeda, M. Narita, N. Saito, T. Ito, M. Endo, S. Bonnamy, Characteristics of heat treated polyparaphenylene for lithium-ion secondary batteries, *J. Phys. Chem. Solids* 65 (2004) 253-256.
- <sup>255</sup> H. Ota, A. Kominato, W.J. Chun, E. Yasukawa, S. Kasuya, Effect of cyclic phosphate additive in non-flammable electrolyte, *J. Power Sources* 119-121 (2003) 393-398.
- <sup>256</sup> C.R. Yang, Y.Y. Wang, C.C. Wan, Composition analysis of the passive film on the carbon electrode of a lithium-ion battery with an EC-based electrolyte, *J. Power Sources* 72 (1998) 66-70.
- <sup>257</sup> B. Stiaszny, J.C. Ziegler, E.E. Krauß, J.P. Schmidt, E. Ivers-Tiffée, Electrochemical characterization and post-mortem analysis of aged LiMn<sub>2</sub>O<sub>4</sub>-Li(Ni<sub>0.5</sub>Mn<sub>0.3</sub>Co<sub>0.2</sub>)O<sub>2</sub>/graphite lithium ion batteries. Part I: Cycle aging, *J. Power Sources* 251 (2014) 439-450.
- <sup>258</sup> W. Li, B.L. Lucht, Inhibition of solid electrolyte interface formation on cathode particles for lithium-ion batteries, *J. Power Sources* 168 (2007) 258-264.
- <sup>259</sup> F.F.C. Bazito, Y. Kawano, R.M. Torresi, Synthesis and characterization of two ionic liquids with emphasis on their chemical stability towards metallic lithium, *Electrochim. Acta* 52 (2007) 6427-6437.
- <sup>260</sup> L.M. Moshuchak, M. Bulinski, W.M. Lamanna, R.L. Wang, J.R. Dahn, Direct comparison of 2,5-di-tert-butyl-1,4-dimethoxybenzene and 4-tert-butyl-1,2-dimethoxybenzene as redox shuttles in LiFePO<sub>4</sub>-based Li-ion cells, *Electrochem. Commun.* 9 (2007) 1497-1501.
- <sup>261</sup> A. Xiao, W. Li, B.L. Lucht, Thermal reactions of mesocarbon microbead (MCMB) particles in LiPF<sub>6</sub>-based electrolyte, *J. Power Sources* 162 (2006) 1282-1288.
- <sup>262</sup> Y. Sasaki, T. Nakajima, H. Groult, Chapter 13: Physical and electrochemical properties and application to lithium batteries of fluorinated organic solvents, *Fluorinated Materials for Energy Conversion*, Elsevier Ltd (2005) 285-304.

- 
- <sup>263</sup> T. Sasaki, T. Abe, Y. Iriyama, M. Inaba, Z. Ogumi, Formation mechanism of alkyl dicarbonates in Li-ion cells, *J. Power Sources* 150 (2005) 208-215.
- <sup>264</sup> U. Heider, R. Oesten, M. Jungnitz, Challenge in manufacturing electrolyte solutions for lithium and lithium ion batteries quality control and minimizing contamination level, *J. Power Sources* 81–82 (1999) 119-122.
- <sup>265</sup> B.A. Johnson, R.E. White, Characterization of commercially available lithium-ion batteries, *J. Power Sources* 70 (1998) 48-54.
- <sup>266</sup> P. Murmann, R.W. Schmitz, S. Nowak, N. Ignatiev, Electrochemical performance and thermal stability studies of two lithium sulfonyl methide salts in lithium-ion battery electrolytes, *J. Electrochem. Soc.* 162 (2015) A1738-A1744.
- <sup>267</sup> G. Gachot, S. Grugeon, I. Jimenez-Gordon, G. Gebresilassie Eshetu, S. Boyanov, A. Lecocq, G. Marlair, S. Pilard, S. Laruelle, Gas chromatography/Fourier transform infrared/mass spectrometry coupling: a tool for Li-ion battery safety field investigation, *Anal. Methods* 6 (2014) 6120-6124.
- <sup>268</sup> P. Handel, G. Fauler, K. Kapper, M. Schmuck, C. Stangl, R. Fischer, F. Uhlig, S. Koller, Thermal aging of electrolytes used in lithium-ion batteries-An investigation of the impact of protic impurities and different housing materials, *J. Power Sources* 267 (2014) 255-259.
- <sup>269</sup> K.W. Leitner, H. Wolf, A. Garsuch, F. Chesneau, M. Schulz-Dobrick, Electroactive separator for high voltage graphite/LiNi<sub>0.5</sub>Mn<sub>1.5</sub>O<sub>4</sub> lithium ion batteries, *J. Power Sources* 244 (2013) 548-551.
- <sup>270</sup> I. Belharouak, G.M. Koenig Jr., K. Amine, Electrochemistry and safety of Li<sub>4</sub>Ti<sub>5</sub>O<sub>12</sub> and graphite anodes paired with LiMn<sub>2</sub>O<sub>4</sub> for hybrid electric vehicle Li-ion battery applications, *J. Power Sources* 196 (2011) 10344-10350.
- <sup>271</sup> SHIMADZU Corporation, International Marketing Division, Analysis of Electrolyte Solution in Lithium Ion Rechargeable Battery (LIRB) and Evolved Gas from LIRB, Application News, Gas Chromatography Mass Spectrometry No.M264, LAAN-A-MS-E030.
- <sup>272</sup> H. Yoshida, T. Fukunaga, T. Hazama, M. Terasaki, M. Mizutani, M. Yamachi, Degradation mechanism of alkyl carbonate solvents used in lithium-ion cells during initial charging, *J. Power Sources* 68 (1997) 311-315.
- <sup>273</sup> S. Mori, H. Asahina, H. Suzuki, A. Yonei, K. Yokoto, Chemical properties of various organic electrolytes for lithium rechargeable batteries 1. Characterization of passivating layer formed on graphite in alkyl carbonate solutions, *J. Power Sources* 68 (1997) 59-64.
- <sup>274</sup> G. Gachot, P. Ribiere, D. Mathiron, S. Grugeon, M. Armand, J.B. Leriche, S. Pilard, S. Laruelle, Gas Chromatography/Mass Spectrometry As a Suitable Tool for the Li-Ion Battery Electrolyte Degradation Mechanisms Study, *Anal. Chem.* 83 (2011) 478–485.

- 
- <sup>275</sup> G. Gachot, S. Grugeon, G. G. Eshetu, D. Mathiron, P. Ribiere, M. Armand, S. Laruelle, Thermal behaviour of the lithiated-graphite/electrolyte interface through GC/MS analysis, *Electrochim. Acta* 83 (2012) 402–409.
- <sup>276</sup> B. Ravdel, K.M. Abraham, R. Gitzendanner, J. DiCarlo, B. Lucht, C. Campion, Thermal stability of lithium-ion battery electrolytes, *J. Power Sources* 119-121 (2003) 805-810.
- <sup>277</sup> M. Caillon-Caravanier, J. Jones, M. Anouti, F. Montigny, P. Willmann, J.P. David, S. Soonckindt, D. Lemordant, Gamma ray degradation of electrolytes containing alkylcarbonate solvents and a lithium salt, *J. Power Sources* 195 (2010) 614-620.
- <sup>278</sup> J. Kerr, S. Sloop, Analysis of Gen 2 electrolytes and samples extracted from Gen 2 cell components, C10-C14 (<http://www.ipd.anl.gov/anlpubs/2005/07/53944.pdf>, last visit:16/08/2015).
- <sup>279</sup> B.A. Johnson, R. E. White, Characterization of commercially available lithium-ion batteries, *J. Power Sources* 70 (1998) 48-54.
- <sup>280</sup> D. Aurbach, B. Markovsky, A. Rodkin, M. Cojocar, E. Levi, H.J. Kim, An analysis of rechargeable lithium-ion batteries after prolonged cycling, *Electrochim. Acta* 00 (2002) 1-13.
- <sup>281</sup> L. Gireaud, S. Grugeon, S. Pilard, P. Guenot, J.M. Tarascon, S. Laruelle, Mass spectrometry investigations on electrolyte degradation products for the development of nanocomposite electrodes in lithium ion batteries, *Anal. Chem.* 78 (2006) 3688-3698.
- <sup>282</sup> M. Grütze, V. Kraft, W. Weber, C. Wendt, A. Friesen, Supercritical Carbon Dioxide Extraction of Lithium-Ion Battery Electrolytes, *J. Supercrit. Fluids* 94 (2014) 216-222.
- <sup>283</sup> S. E. Sloop, Patent No.: US 7.198.865 B2, 2007.
- <sup>284</sup> M. Grütze, X. Mönnighoff, F. Horsthemke, V. Kraft, M. Winter, S. Nowak, Extraction of lithium-ion battery electrolytes with liquid and supercritical carbon dioxide and additional solvents, *RSC Advances* 5 (2015) 43209-43217.
- <sup>285</sup> S. Nowak, M. Winter, The Role of Sub- and Supercritical CO<sub>2</sub> as “Processing Solvent” for the Recycling and Sample Preparation of Lithium Ion Battery Electrolytes, *Molecules Special Issue Green Chem.* 22 (2017): 403.
- <sup>286</sup> X. Mönnighoff, A. Friesen, B. Konersmann, F. Horsthemke, M. Grütze, M. Winter, S. Nowak, Supercritical Carbon Dioxide Extraction of Electrolyte from Spent Lithium Ion Batteries and its Characterization by Gas Chromatography with Chemical Ionization, *J. Power Sources* 352 (2017) 56–63.
- <sup>287</sup> C.S. Cheng, W.R. Liu, F.M. Wang, A novel ionic host solid electrolyte interface formation on reduced graphene oxide of lithium ion battery, *Electrochim. Acta* 106 (2013) 425-431.
- <sup>288</sup> L. Xing, W. Li, M. Xu, T. Li, L. Zhou, The reductive mechanism of ethylene sulfite as solid electrolyte interphase film-forming additive for lithium ion battery, *J. Power Sources* 196 (2011) 7044-7047.

- 
- <sup>289</sup> H. Ota, T. Sato, H. Suzuki, T. Usami, TPD-GC/MS analysis of the solid electrolyte interface (SEI) on a graphite anode in the propylene carbonate/ethylene sulfite electrolyte system for lithium batteries, *J. Power Sources* 97–98 (2001) 107-113.
- <sup>290</sup> N.C. Gallego, C.I. Contescu, H.M. Meyer III, J.Y. Howe, R.A. Meisner, E.A. Payzant, M.J. Lance, S.Y. Yoon, M. Denlinger, D.L. Wood III, Advanced surface and microstructural characterization of natural graphite anodes for lithium ion batteries, *CARBON* 72 (2014) 393-401.
- <sup>291</sup> A. Kominato, E. Yasukawa, N. Sato, T. Ijuuin, H. Asahina, S. Mori, Analysis of surface films on lithium in various organic electrolytes, *J. Power Sources* 68 (1997) 471-475.
- <sup>292</sup> J.Y. Eom, I.H. Jung, J.H. Lee, Effects of vinylene carbonate on high temperature storage of high voltage Li-ion batteries, *J. Power Sources* 196 (2011) 9810- 9814.
- <sup>293</sup> A.W. Golubkov, D. Fuchs, J. Wagner, H. Wiltsche, C. Stangl, G. Fauler, G. Voitic, A. Thaler, V. Hacker, Thermal-runaway experiments on consumer Li-ion batteries with metal-oxide and olivin-type cathodes , *RSC Adv.* 4 (2014) 3633-3642.
- <sup>294</sup> Y. Ein-Eli, Dimethyl carbonate (DMC) electrolytes – the effect of solvent purity on Li-ion intercalation into graphite anodes, *Electrochem. Commun.* 4 (2002) 644-648.
- <sup>295</sup> Pyrolysis/gas chromatography/mass spectroscopy analysis of the surface film formed on graphite negative electrode, *J. Power Sources* 97-98 (2001) 156-158.
- <sup>296</sup> R. Mogi, M. Inaba, Y. Iriyama, T. Abe, Z. Ogumi, Study on the decomposition mechanism of alkyl carbonate on lithium metal by pyrolysis-gas chromatography/mass spectroscopy, *J. Power Sources* 119–121 (2003) 597–603.
- <sup>297</sup> H. Yoshizawa, T. Ohzuku, An application of lithium cobalt nickel manganese oxide to high-power and high-energy density lithium-ion batteries, *J. Power Sources* 174 (2007) 813-817.
- <sup>298</sup> K. Shinada, S. Horiike, S. Uchiyama, R. Takechi, T. Nishimoto, Development of New Ionization Detector for Gas Chromatography by Applying Dielectric Barrier Discharge, *Shimadzu Review*, 2012
- <sup>299</sup> High Sensitivity Gas Chromatograph System: Tracera, Shimadzu, C184-E032
- <sup>300</sup> S. Kanazawa, M. Kogoma, T. Moriwaki, and S. Okazaki, Stable glow plasma at atmospheric pressure, *J. Phys. D: Appl. Phys.* 21 (1988) 838-840.
- <sup>301</sup> T. Andrews, P.G. Tait, On the Volumetric Relations of Ozone, and the Action of the Electrical Discharge on Oxygen and Other Gases, *Philosophical Transactions of the Royal Society of London*, 150 (1860) 113-131.
- <sup>302</sup> U. Kogelschatz, Dielectric-Barrier Discharges: Their History, Discharge Physics, and Industrial Applications, *Plasma Chem. Plasma Process.* 23 (2003) 1–46.

- 
- <sup>303</sup> W. Siemens, Über die elektronische Induction und die Verzögerung des Stroms in Flaschendrähnen, Poggendorff's Ann. *Phys. Chem.* 102 (1857) 66–122.
- <sup>304</sup> A. Michels, S. Tombrink, W. Vautz, M. Miclea, J. Franzke, Spectroscopic characterization of a microplasma used as ionization source for ion mobility spectrometry. *Spectrochim. Acta Part B Atomic Spectroscopy* 62 (2007) 1208–1215.
- <sup>305</sup> J. Hu, W. Li, C. Zheng, X. Hou, Dielectric Barrier Discharge in Analytical Spectrometry, *Appl. Spectrosc.* 46 (2011) 368–387.
- <sup>306</sup> H.R. Snyder, G.K. Anderson, Effect of air and oxygen content on the dielectric barrier discharge decomposition of chlorobenzene, *IEEE Transactions on Plasma Science*, 26 (1998) 1695–1699.
- <sup>307</sup> R. Gras, J. Luong, M. Monagle, B. Winniford, Gas Chromatographic Applications with the Dielectric Barrier Discharge Detector, *J. Chromatogr. Sci.* 44 (2006) 101-107.
- <sup>308</sup> F. Andrawes, R. Ramsey, The helium ionization detector, *J. Chromatogr. Sci.* 24 (1986) 513-518.
- <sup>309</sup> Ionization Energies of Atoms and Ions, <https://dept.astro.lsa.umich.edu/~cowley/ionen.htm> (last visit: 15.07.2016, 11:05 am)
- <sup>310</sup> Tracera (GC-BID) Solution, Shimadzu, LAAN- B- GC004
- <sup>311</sup> C.A. Weatherly, R.M. Woods, D.W. Armstrong, Rapid Analysis of Ethanol and Water in Commercial Products Using Ionic Liquid Capillary Gas Chromatography with Thermal Conductivity Detection and/or Barrier Discharge Ionization Detection (lower ionization temp., higher sensitivity), *J. Agric. Food Chem.* 62 (2014) 1832–1838.
- <sup>312</sup> L.A. Frink, C.A. Weatherly, D.W. Armstrong, Water determination in active pharmaceutical ingredients using ionic liquid headspace gas chromatography and two different detection protocols, *J. Pharm. Biomed. Anal.* 94 (2014) 111-117.
- <sup>313</sup> L.A. Frink, D.W. Armstrong, The utilisation of two detectors for the determination of water in honey using headspace gas chromatography, *Food Chem.* 205 (2016) 23–27.
- <sup>314</sup> M. Antoniadou, Master Thesis: A comparative study of the Barrier Charge Ionization Detector and the Flame Ionization Detector in the analysis of organic compounds by Gas Chromatography, Thessaloniki, Greece, 2016
- <sup>315</sup> F. Pena-Pereira, Ł. Marcinkowski, A. Kloskowski, J. Namnieśnik, Silica-Based Ionogels: Nanoconfined Ionic Liquid-Rich Fibers for Headspace Solid-Phase Microextraction Coupled with Gas Chromatography–Barrier Discharge Ionization Detection, *Anal. Chem.* 86 (2014) 11640–11648

- 
- <sup>316</sup> G.M. Cramer, R.A. Ford, R.L. Hall, Estimation of Toxic Hazard – A Decision Tree Approach, *Fd Cosmet. Toxicol.* 16 (1987) 255 – 276.
- <sup>317</sup> I.C. Munro, R.A. Ford, E. Kennepohl, G.J. Sprenger, Correlation of Structural Class with No-Observed-Effect Levels: A Proposal for Establishing a Threshold of Concern, *Food and Chemical Toxicology* 34 (1996) 829 - 867.
- <sup>318</sup> <https://apps.ideaconsult.net/data/ui/toxtree>
- <sup>319</sup> H. Kalkhof, M. Herzler, R. Stahlmann, U. Gundert-Remy, Threshold of toxicological concern values for non-genotoxic effects in industrial chemicals: re-evaluation of the Cramer classification, *Arch Toxicol* 86 (2012) 17–25.
- <sup>320</sup> S. Lapenna, A. Worth, Analysis of the Cramer classification scheme for oral systemic toxicity - implications for its implementation in Toxtree, *JRC Sci. Tech. Rep.* (2011) EUR 24898 EN.
- <sup>321</sup> M. Arakawa, J.-I. Yamaki, Anodic oxidation of propylene carbonate and ethylene carbonate on graphite electrodes, *J. Power Sources* 54 (1995) 250-254.
- <sup>322</sup> L. Xiao, X. Ai, Y. Cao, H. Yang, Electrochemical behavior of biphenyl as polymerizable additive for overcharge protection of lithium ion batteries, *Electrochim. Acta* 49 (2004) 4189-4196.
- <sup>323</sup> D.K. Lim, B. Hoskins, I.K. Ho, Effects of diisopropylfluorophosphate on brain acetylcholinesterase, butyrylcholinesterase and neurotoxic esterase in rats, *Biomed. Environ. Sci.* 3 (1989) 295-304.
- <sup>324</sup> S. Nowak, M. Winter, Chemical Analysis for a Better Understanding of Aging and Degradation Mechanisms of Non-Aqueous Electrolytes for Lithium Ion Batteries: Method Development, Application and Lessons Learned, *J. Electrochem. Soc.* 162 (2015) A2500-A2508.
- <sup>325</sup> [http://el-cell.com/wp-content/uploads/manuals/ECC\\_DEMS\\_manual.pdf](http://el-cell.com/wp-content/uploads/manuals/ECC_DEMS_manual.pdf) (last visit: 16/02/2016, 13:23)
- <sup>326</sup> X. Rui, Q. Yan, M. Skyllas-Kazacos, T.M. Lim,  $\text{Li}_3\text{V}_2(\text{PO}_4)_3$  cathode materials for lithium-ion batteries: A review, *Journal of Power Sources*, 258 (2014) 19–38. (DOI: 10.1016/j.jpowsour.2014.01.126)
- <sup>327</sup> A. Amon, Mater Thesis: Gas evolution from Lithium ion batteries studied in-situ by coupled GC/MS-FTIR, 2014.
- <sup>328</sup> K. Hu, Nonaqueous Liquid Electrolytes for Lithium-Based Rechargeable Batteries, *Chem. Rev.* 104 (2004) 4303-4417.
- <sup>329</sup> P.A. Leclercq, C.A. Cramers, Review: High-Speed GC/MS, *Mass Spectrom. Rev.* 17 (1998) 37–49.
- <sup>330</sup> C.A. Cramers, P.A. Leclercq, Consideration on Speed of Separation, Detection and Identification Limits in Capillary GC and GC/MS, *Crit. Rev. Anal. Chem.* 20 (1988) 117–147.
- <sup>331</sup> P. Donato, P.Q. Tranchida, P. Dugo, G. Dugo, L. Mondello, Rapid analysis of food products by means of high speed gas chromatography, *J. Sep. Sci.* 30 (2007) 508–526.

- 
- <sup>332</sup> E. Matisova, M. Dömötörova, Review: Fast gas chromatography and its use in trace analysis, *J. Chromatogr. A* 1000 (2003) 199–221.
- <sup>333</sup> M.S. Klee, L.M. Blumberg, Theoretical and Practical Aspects of Fast Gas Chromatography and Method Translation, *J. Chromatogr. Sci.* 40 (2002) 234–247.
- <sup>334</sup> P. Korytar, H.-G. Janssen, E. Matisova, Practical fast gas chromatography: methods, instrumentation and applications, *Trends Anal. Chem.* 21 (2002) 558–572.
- <sup>335</sup> K. Mastovska, S.J. Lehotay, J. Hajslova, Optimization and evaluation of low-pressure gas chromatography–mass spectrometry for the fast analysis of multiple pesticide residues in a food commodity, *J. Chromatogr. A*, 926 (2001) 291–308.
- <sup>336</sup> S. Dagan, A. Amirav, Fast, Very Fast and Ultra-Fast Gas Chromatography–Mass Spectrometry of Thermally Labile Steroids, Carbamates and Drugs in Supersonic Molecular Beams, *J. Am. Soc. Mass Spectrom.* 7 (1996) 737–752.
- <sup>337</sup> M.J. Gonzalez-Rodriguez, A. Garrido-Frenich, F.J. Arrebola, J.L. Martinez Vidal, Evaluation of low-pressure gas chromatography linked to ion-trap tandem mass spectrometry for fast trace analysis of multiclass pesticide residues, *Rapid Commun. Mass Spectrom.* 16 (2002) 1216–1224.
- <sup>338</sup> M.L. Trehy, R.A. Yost, J.G. Dorsey, Short Open Tubular Columns in Gas Chromatography/Mass Spectrometry, *Anal. Chem.* 58 (1986) 14–19.
- <sup>339</sup> J.C. Giddings, Theory of Minimum Time Operation in Gas Chromatography, *Anal. Chem.* 34 (1962) 314–319.
- <sup>340</sup> C.A. Cramers, G.J. Scherpenzeel, P.A. Leclercq, Increased speed of analysis in directly coupled Gas Chromatography–Mass Spectrometry systems. Capillary columns at sub-atmospheric outlet pressures, *J. Chromatogr.* 203 (1981) 207–216.
- <sup>341</sup> P.A. Leclercq, G.J. Scherpenzeel, E.A. Vermeer, C.A. Cramers, Increased speed of analysis in directly coupled Gas Chromatography–Mass Spectrometry systems. II. Advantages of vacuum outlet operation of thick-film capillary columns, *J. Chromatogr.* 241 (1982) 61–71.
- <sup>342</sup> C.A. Cramers, P.A. Leclercq, Consideration on Speed of Separation, Detection and Identification Limits in Capillary GC and GC/MS, *Crit. Rev. Anal. Chem.* 20 (1988) 117–147.
- <sup>343</sup> L.M. Blumberg, Theory of Fast Capillary Gas Chromatography Part 1: Column Efficiency, *J. High Resolut. Chromatogr.* 20 (1997) 597–604.
- <sup>344</sup> L.M. Blumberg, Theory of Fast Capillary Gas Chromatography Part 2: Speed of Analysis, *J. High Resolut. Chromatogr.* 20 (1997) 678–687.
- <sup>345</sup> L.M. Blumberg, Theory of Fast Capillary Gas Chromatography Part 3: Column Performance vs. Gas Flow Rate, *J. High Resolut. Chromatogr.* 22 (1997) 403–413.



- 
- <sup>346</sup> L.M. Blumberg, Theory of Fast Capillary Gas Chromatography Part 4: Column Performance vs. Liquid Film Thickness, *J. High Resolut. Chromatogr.* 22 (1999) 501–508.
- <sup>347</sup> P. J. Marriott, R. A. Shellie, High-Speed Techniques, Gas Chromatography, Elsevier Ltd. (2005) 58–65.
- <sup>348</sup> C.A. Cramers, P.A. Leclercq, Strategies for speed optimisation in gas chromatography: an overview, *J. Chromatogr. A*, 842 (1999) 3–13.
- <sup>349</sup> C.A. Cramers, H.-G. Janssen, M. M. van Deursen, P.A. Leclercq, High-speed gas chromatography: an overview of various concepts, *J. Chromatogr. A* 856 (1999) 315–329.
- <sup>350</sup> K. Mastovska, S. J. Lehotay, Practical approaches to fast gas chromatography–mass spectrometry, *J. Chromatogr. A* 1000 (2003) 153–180.
- <sup>351</sup> S.R. Palamand, D.O. Thurow, Low pressure gas chromatography, *J. Chromatogr.* 40 (1969) 152–155.
- <sup>352</sup> L. Puig, R.D. Sacks, Low-pressure gas–chromatography with split injection and photoionization detection, *J. Chromatogr. Sci.* 29 (1991) 158–164.
- <sup>353</sup> J.J. Whiting, C.J. Lu, E.T. Zellers, R.D. Sacks, A portable, high-speed, vacuum outlet GC vapor analyzer employing air as carrier gas and surface acoustic wave detection, *Anal. Chem.* 73 (2001) 4668–4675.
- <sup>354</sup> J. de Zeeuw, J. Peene, H.-G. Jansen, X. Lou, A Simple Way to Speed up Separations by GC-MS Using Short 0.53 mm Columns and Vacuum Outlet Conditions, *J. High Resolut. Chromatogr.* 23 (2000) 677–684.
- <sup>355</sup> K. Ravindra, A.C. Dirtu, A. Covaci, Low-pressure gas chromatography: Recent trends and developments, *Trends Anal. Chem.* 27 (2008) 291–303.
- <sup>356</sup> M. van Deursen, H.-G. Janssen, J. Beens, P. Lipman, R. Reinierkens, G. Rutten, C. Cramers, Fast Gas Chromatography Using Vacuum Outlet Conditions, *J. Microcolumn Sep.* 12 (2000) 613–622.
- <sup>357</sup> S.D.H. Poynter, R.A. Shellie, High-speed, low-pressure gas chromatography–mass spectrometry for essential oil analysis, *J. Chromatogr. A* 1200 (2008) 28–33.
- <sup>358</sup> S.J. Lehotay, U. Koesukwiwat, H. van der Kamp, H.G.J. Mol, N. Leepipatpiboon, Qualitative Aspects in the Analysis of Pesticide Residues in Fruits and Vegetables Using Fast, Low-Pressure Gas Chromatography-Time-of-Flight Mass Spectrometry, *J. Agric. Food Chem.* 59 (2011) 7544–7556.
- <sup>359</sup> J. de Zeeuw, S. Reese, J. Cochran, S. Grossman, T. Kane, C. English, Simplifying the setup for vacuum-outlet GC: Using a restriction inside the injection port, *J. Sep. Sci.* 32 (2009) 1849–1857.

- 
- <sup>360</sup> U. Koesukwiwata, S. J. Lehotay, N. Leepipatpiboon, Fast, low-pressure gas chromatography triple quadrupole tandem mass spectrometry for analysis of 150 pesticide residues in fruits and vegetables, *J. Chromatogr. A* 1218 (2011) 7039–7050.
- <sup>361</sup> P.E. Joos, A.F.L. Godoi, R. De Jong, J. de Zeeuw, R. Van Grieken, Trace analysis of benzene, toluene, ethylbenzene and xylene isomers in environmental samples by low-pressure gas chromatography–ion trap mass spectrometry, *J. Chromatogr. A* 985 (2003) 191–196.
- <sup>362</sup> M.E. Hail, R.A. Yost, Theoretical and Practical Aspects of Short Open Tubular Columns at Sub-ambient Pressures in Gas Chromatography/Mass Spectrometry, *Anal. Chem.* 61 (1989) 2402–2410.
- <sup>363</sup> J.V. Hinshaw, Hydrogen carrier gas and vacuum compensation, *LCGC N. Am.* 29 (2011) 36.
- <sup>364</sup> S. Walorczyk, B. Gnusowski, Fast and sensitive determination of pesticide residues in vegetables using low-pressure gas chromatography with a triple quadrupole mass spectrometer, *J. Chromatogr. A* 1128 (2006) 236–243.
- <sup>365</sup> A. Amirav, N. Tzanani, S.B. Wainhaus, S. Dagan, Megabore versus microbore as the optimal column for fast gas chromatography/mass spectrometry, *Eur. J. Mass Spectrom.* 4 (1998) 7–13.
- <sup>366</sup> M. Kirchner, E. Matisova, R. Otrekal, A. Hercegova, J. de Zeeuw, Search on ruggedness of fast gas chromatography–mass spectrometry in pesticide residues analysis, *J. Chromatogr. A* 1084 (2005) 63–70.
- <sup>367</sup> P.A. Leclercq, C.A. Cramers, Minimum Analysis Time in Capillary Gas Chromatography Vacuum-versus Atmospheric-Outlet Column Operation, *J. High Resolut. Chromatogr. & Chromatogr. Commun.* (1987) 269–272.
- <sup>368</sup> U. Koesukwiwat, S.J. Lehotay, S. Miao, N. Leepipatpiboon, High throughput analysis of 150 pesticides in fruits and vegetables using QuEChERS and low-pressure gas chromatography–time-of-flight mass Spectrometry, *J. Chromatogr. A* 1217 (2010) 6692–6703.
- <sup>369</sup> J. de Zeeuw, J.A. Peene, R.C.M de Nijs, US Patent No. 6,301,952, October 16 2001.
- <sup>370</sup> Y. Sapozhnikova, S. J. Lehotay: Review of recent developments and applications in low-pressure (vacuum outlet) gas chromatography, *Analytica Chimica Acta* 899 (2015) 13–22.
- <sup>371</sup> A. Garrido-Frenich, F.J. Arrebola, M.J. Gonzalez-Rodriguez, J.L. Martinez Vidal, N. Mora Diez, Rapid pesticide analysis, in post-harvest plants used as animal feed, by low-pressure gas chromatography–tandem mass spectrometry, *Anal. Bioanal. Chem.* 377 (2003) 1038–1046.
- <sup>372</sup> F.J. Arrebola, J.L. Martinez Vidal, M. J. Gonzalez-Rodriguez, A. Garrido-Frenich, N. Sanchez Morito, Reduction of analysis time in gas chromatography. Application of low-pressure gas chromatography–tandem mass spectrometry to the determination of pesticide residues in vegetables, *J. Chromatogr. A* 1005 (2003) 131–141.
- <sup>373</sup> K. Mastovska, J. Hajslova, S.J. Lehotay, Ruggedness and other performance characteristics of low-pressure gas chromatography–mass spectrometry for the fast analysis of

---

multiple pesticide residues in food crops, *J. Chromatogr. A* 1054 (2004) 335–349.

<sup>374</sup> M.J. Gonzalez-Rodriguez, F.J. Arrebola Liebanas, A. Garrido Frenich, J.L. Martinez Vidal, F.J. Sanchez Lopez, Determination of pesticides and some metabolites in different kinds of milk by solid-phase microextraction and low-pressure gas chromatography-tandem mass spectrometry, *Anal. Bioanal. Chem.* 382 (2005) 164–172.

<sup>375</sup> A. Garrido Frenich, M.J. Gonzalez Rodriguez, J.L. Martinez Vidal, F.J. Arrebola, M.E. Hernandez Torres, A study of the disappearance of pesticides during composting using a gas chromatography-tandem mass spectrometry technique, *Pest Manag. Sci.* 61 (2005) 458–466.

<sup>376</sup> J.L. Fernandez Moreno, F.J. Arrebola Liebanas, A. Garrido Frenich, J.L. Martinez Vidal, Evaluation of different sample treatments for determining pesticide residues in fat vegetable matrices like avocado by low-pressure gas chromatography–tandem mass spectrometry, *J. Chromatogr. A* 1111 (2006) 97–105.

<sup>377</sup> S.C. Cunha, J.O. Fernandes, A. Alves, M.B.P.P. Oliveira, Fast low-pressure gas chromatography–mass spectrometry method for the determination of multiple pesticides in grapes, musts and wines, *J. Chromatogr. A* 1216 (2009) 119–126.

<sup>378</sup> S. Walorczyk, Fast Identification of trace-level pesticide residues in agricultural crops applying low-pressure, *J. Plant Prot. Res.* 44 (2004) 117–124.

<sup>379</sup> A. Hercegova, M. Dömötörova, E. Matisova, M. Kirchner, R. Otrekal, V. Stefuca, Fast gas chromatography with solid phase extraction clean-up for ultratrace analysis of pesticide residues in baby food, *J. Chromatogr. A* 1084 (2005) 46–53.

<sup>380</sup> J.L. Martinez Vidal, M.J. Gonzalez-Rodriguez, F.J. Arrebola, A. Garrido Frenich, F.J. Sanchez Lopez, Selective Extraction and Determination of Multiclass Pesticide Residues in Post-Harvest French Beans by Low-Pressure Gas Chromatography/Tandem Mass Spectrometry, *J. AOAC Int.* 86 (2003) 856–867.

<sup>381</sup> A. Hercegova, M. Dömötörova, D. Kruzlicova, E. Matisova, Comparison of sample preparation methods combined with fast gas chromatography – mass spectrometry for ultratrace analysis of pesticide residues in baby food, *J. Sep. Sci.* 29 (2006) 1102–1109.

<sup>382</sup> M. Anastassiades, S.J. Lehotay, D. Stajnbaher, F.J. Schenck, Fast and easy multiresidue method employing acetonitrile extraction/partitioning and “dispersive solid-phase extraction” for the determination of pesticide residues in produce, *J. AOAC Int.* 86 (2003) 412–431.

<sup>383</sup> T. Cajka, J. Hajslova, O. Lacina, K. Mastovska, S.J. Lehotay, Rapid analysis of multiple pesticide residues in fruit-based baby food using programmed temperature vaporiser injection-low-pressure gas chromatography-high-resolution time-of-flight mass spectrometry, *J. Chromatogr. A* 1186 (2008) 281–294.

<sup>384</sup> H. Kwon, S.J. Lehotay, L. Geis-Asteggiane, Variability of matrix effects in liquid and gas chromatography-mass spectrometry analysis of pesticide residues after QuEChERS sample preparation of different food crops, *J. Chromatogr. A* 1270 (2012) 235–245.

- 
- <sup>385</sup> S.J. Lehotay, K.A. Son, H. Kwon, U. Koesukwiwat, W.S. Fu, K. Mastovska, E. Hoh, N. Leepipatpiboon, Comparison of QuEChERS sample preparation methods for the analysis of pesticide residues in fruits and vegetables, *J. Chromatogr. A* 1217 (2010) 2548–2560.
- <sup>386</sup> K. Mastovska, S.J. Lehotay, M. Anastassiades, Combination of analyte protectants to overcome matrix effects in routine GC analysis of pesticide residues in food matrixes, *Anal. Chem.* 77 (2005) 8129–8137.
- <sup>387</sup> Y. Sapozhnikova, S.J. Lehotay, Multi-class, multi-residue analysis of pesticides, polychlorinated biphenyls, polycyclic aromatic hydrocarbons, polybrominated diphenyl ethers and novel flame retardants in fish using fast, lowpressure gas chromatography-tandem mass spectrometry, *Anal. Chim. Acta* 758 (2013) 80–92.
- <sup>388</sup> M.A. Gonzalez-Curbelo, S.J. Lehotay, J. Hernandez-Borges, M.A. Rodriguez-Delgado, Use of ammonium formate in QuEChERS for high-throughput analysis of pesticides in food by fast, low-pressure gas chromatography and liquid chromatography tandem mass spectrometry, *J. Chromatogr. A* 1358 (2014) 75–84.
- <sup>389</sup> L. Geis-Asteggiate, S.J. Lehotay, H. Heinzen, Effects of temperature and purity of magnesium sulfate during extraction of pesticide residues using the QuEChERS method, *J. AOAC Int.* 95 (2012) 1311–1318.
- <sup>390</sup> Y. Sapozhnikova, Evaluation of low-pressure gas chromatography-tandem mass spectrometry method for the analysis of >140 pesticides in fish, *J. Agric. Food. Chem.* 62 (2014) 3684–3689.
- <sup>391</sup> V.C. Fernandes, S.J. Lehotay, L. Geis-Asteggiate, H. Kwon, H.G.J. Mol, H. van der Kamp, N. Mateus, V.F. Domingues, C. Delerue-Matos, Analysis of pesticide residues in strawberries and soils by GC-MS/MS, LC-MS/MS and two dimensional GC-time-of-flight MS comparing organic and integrated pest management farming, *Food Addit. Contam.* 31 (2014) 262–270.
- <sup>392</sup> L.J. Han, Y. Sapozhnikova, S.J. Lehotay, Streamlined sample cleanup using combined dispersive solid-phase extraction and in-vial filtration for analysis of pesticides and environmental pollutants in shrimp, *Anal. Chim. Acta* 827 (2014) 40–46.
- <sup>393</sup> Y. Sapozhnikova, S.J. Lehotay, Evaluation of different parameters in the extraction of incurred pesticides and environmental contaminants in fish, *J. Agric. Food. Chem.* 63 (2015) 5163–5168.
- <sup>394</sup> Y. Sapozhnikova, T. Simons, S.J. Lehotay, Evaluation of a fast and simple sample preparation method for polybrominated diphenyl ether (PBDE) flame retardants and dichlorodiphenyltrichloroethane (DDT) pesticides in fish for analysis by ELISA compared with GC-MS/MS, *J. Agric. Food. Chem.* 63 (2015) 4429–4434.
- <sup>395</sup> L. Han, Y. Sapozhnikova, S.J. Lehotay, Method validation for 243 pesticides and environmental contaminants in meats and poultry by tandem mass spectrometry coupled to low-pressure gas chromatography and ultrahigh-performance liquid chromatography, *Food Control* 66 (2016) 270–282.
- <sup>396</sup> A.F.L. Godoi, K. Ravindra, R.H.M. Godoi, S.J. Andrade, M. Santiago-Silva, L. Van Vaeck, R. Van Grieken, Fast chromatographic determination of polycyclic aromatic hydrocarbons in aerosol samples from sugar cane burning, *J. Chromatogr. A* 1027 (2004) 49–53.

- 
- <sup>397</sup> K. Ravindra, A.F.L. Godoi, L. Bencs, R. Van Grieken, Low-pressure gas chromatography–ion trap mass spectrometry for the fast determination of polycyclic aromatic hydrocarbons in air samples, *J. Chromatogr. A* 1114 (2006) 278–281.
- <sup>398</sup> A.F.L. Godoi, W. Vilegas, R.H.M. Godoi, L. Van Vaeck, R. Van Grieken, Application of low-pressure gas chromatography–ion-trap mass spectrometry to the analysis of the essential oil of *Turnera diffusa* (Ward.) Urb., *J. Chromatogr. A* 1027 (2004) 127–130.
- <sup>399</sup> A. Mena Granero, F.J. Egea González, A. Garrido Frenich, J.M. Guerra Sanz, J.L. Martínez Vidal, Single step determination of fragrances in Cucurbita flowers by coupling headspace solid-phase microextraction low-pressure gas chromatography–tandem mass spectrometry, *J. Chromatogr. A* 1045 (2004) 173–179.
- <sup>400</sup> J.L. Martínez Vidal, A. Belmonte Vega, F.J. Arrebola, M.J. Gonzalez-Rodriguez, M.C. Morales Sanchez, A. Garrido Frenich, Trace determination of organotin compounds in water, sediment and mussel samples by low-pressure gas chromatography coupled to tandem mass spectrometry, *Rapid Commun. Mass Spectrom.* 17 (2003) 2099–2106.
- <sup>401</sup> E. Jover, Z. Moldovan, J. M. Bayona, Complete characterisation of lanolin steryl esters by sub-ambient pressure gas chromatography–mass spectrometry in the electron impact and chemical ionisation modes, *J. Chromatogr. A* 970 (2002) 249–258.
- <sup>402</sup> K. Hájková, J. Pulkrabová, J. Schůrek, J. Hajšlová, J. Poustka, M. Nápravníková, V. Kocourek, Novel approaches to the analysis of steroid estrogens in river sediments, *Anal. Bioanal. Chem.* 378 (2007) 1351–1363.
- <sup>403</sup> Y. Sapozhnikova, W.C. Byrdwell, A. Lobato, B. Romig, Effects of UV-B radiation levels on concentrations of phytosterols, ergothioneine, and polyphenolic compounds in mushroom powders used as dietary supplements, *J. Agric. Food. Chem.* 62 (2014) 3034–3042.
- <sup>404</sup> S. J. Lehotay, J. Hajslova, Application of gas chromatography in food analysis, *Trends Anal. Chem.* 21 (2002) 688–697.
- <sup>405</sup> A.C. Dirtu, K. Ravindra, L. Roosens, R. van Grieken, H. Neels, R. Blust, A. Covaci, Fast analysis of decabrominated diphenyl ether using low-pressure gas chromatography-electron-capture negative ionization mass spectrometry, *J. Chromatogr. A* 1186 (2008) 295–301.
- <sup>406</sup> J.W. Cochran, Fast Gas Chromatography–Time-of-Flight Mass Spectrometry of Polychlorinated Biphenyls and Other Environmental Contaminants, *J. Chromatogr. Sci.* 40 (2002) 254–268.
- <sup>407</sup> H. Brust, S. Willemse, T.Y. Zeng, A. van Asten, M. Koeberg, A. van der Heijden, A. Bolck, P. Schoenmakers, Impurity profiling of trinitrotoluene using vacuumoutlet gas chromatography-mass spectrometry, *J. Chromatogr. A* 1374 (2014) 224–230.
- <sup>408</sup> E. Rosenberg, C. Kanakaki, The Vacuum Outlet GC-MS Technique: A Versatile Technique for Fast GC Separations, *Chrom + Food Forum* 5 (2015) 37–39.

- 
- <sup>409</sup> Ö. Yilmazcan, C. Kanakaki, B. Izgi, E. Rosenberg, Fast Gas Chromatographic-Mass Spectrometric Determination of Octinoxate and Oxybenzone UV Filters in Swimming Pool Waters after Solid Phase Microextraction, *J. Sep. Sci.* (2015) DOI: 10.1002/jssc.201401250.
- <sup>410</sup> P.Q. Tranchida, F.A. Franchina, P. Dugo, Luigi Mondello, Flow-modulation low-pressure comprehensive two-dimensional gas chromatography, *J. Chromatogr. A* 1372 (2014) 236–244.
- <sup>411</sup> <http://www.sigmaaldrich.com/analytical-chromatography/analytical-products.html?TablePage=110861433>
- <sup>412</sup> J. Beens, H.-G. Janssen, M. Adahchour, U.A.T. Brinkman, Flow regime at ambient outlet pressure and its influence in comprehensive two-dimensional gas chromatography, *J. Chromatogr. A* 1086 (2005) 141–150.
- <sup>413</sup> <http://www.shimadzu.com/an/hplc/support/lib/lectalk/34/34tec.html>
- <sup>414</sup> A. Salvador, A. Chisvert, Sunscreen analysis: a critical survey on UV filters determination, *Anal. Chim. Acta* 537 (2005) 1–14.
- <sup>415</sup> R.H. Waring, R.M. Harris, Endocrine disrupters-A threat to woman's health?, *Maturitas* 68 (2011) 111–115.
- <sup>416</sup> T. Poiger, H.R. Buser, M.E. Balmer, P.A. Bergquist, M.D. Müller, Occurrence of UV filter compounds from sunscreens in surface waters: regional mass balance in two Swiss lakes, *Chemosphere* 55 (2004) 951–963.
- <sup>417</sup> M. Schlumpf, B. Cotton, M. Conscience, V. Haller, B. Steinmann, W. Lichtensteiger, In vitro and in vivo estrogenicity of UV screens., *Environ. Health Perspect.* 109 (2001) 239–244.
- <sup>418</sup> Y.-S. Liu, G.-G. Ying, A. Shareef, R. S. Kookana, Simultaneous determination of benzotriazoles and ultraviolet filters in ground water, effluent and biosolid samples using gas chromatography–tandem mass spectrometry, *J. Chromatogr. A* 1218 (2011) 5328–5335.
- <sup>419</sup> P. Cuderman, E. Heath, Determination of UV filters and antimicrobial agents in environmental water samples, *Anal. Bioanal. Chem.* 387 (2007) 1343–1350.
- <sup>420</sup> I. P. Román, A. Chisvert, A. Canals, *Dispersive solid-phase extraction based on oleic acid-coated magnetic nanoparticles followed by gas chromatography–mass spectrometry for UV-filter determination in water samples*, *J. Chromatogr. A*, 1218 (2011) 2467–2475.
- <sup>421</sup> D.L. Giokas, V.A. Sakkas, T.A. Albanis, Determination of residues of UV filters in natural waters by solid-phase extraction coupled to liquid chromatography–photodiode array detection and gas chromatography–mass spectrometry, *J. Chromatogr. A* 1026 (2004) 289–293.

- 
- <sup>422</sup> M. S. Díaz-Cruz, P. Gago-Ferrero, M. Llorca, D. Barceló, Analysis of UV filters in tap water and other clean waters in Spain, *Anal. Bioanal. Chem.*, 402 (2012) 2325–2333.
- <sup>423</sup> W. Li, Y. Ma, C. Guo, W. Hu, K. Liu, Y. Wang, T. Zhu, Occurrence and behavior of four of the most used sunscreen UV filters in a wastewater reclamation plant, *Water Research* 41 (2007) 3506–3512.
- <sup>424</sup> J.L. Benedé, A. Chisvert, A. Salvador, D. Sánchez-Quiles, A. Tovar-Sánchez, Determination of UV filters in both soluble and particulate fractions of seawaters by dispersive liquid–liquid microextraction followed by gas chromatography–mass spectrometry, *Anal. Chim. Acta* 812 (2014) 50–58.
- <sup>425</sup> I. Tarazona, A. Chisvert, Z. León, A. Salvador, Determination of hydroxylated benzophenone UV filters in sea water samples by dispersive liquid–liquid microextraction followed by gas chromatography–mass spectrometry, *J. Chromatogr. A*, 1217 (2010) 4771–4778.
- <sup>426</sup> Y. Zhang, H. K. Lee, Determination of ultraviolet filters in water samples by vortex-assisted dispersive liquid–liquid microextraction followed by gas chromatography–mass spectrometry, *J. Chromatogr. A* 1249 (2012) 25–31.
- <sup>427</sup> M. Moeder, S. Schrader, U. Winkler, R. Rodil, At-line microextraction by packed sorbent-gas chromatography–mass spectrometry for the determination of UV filter and polycyclic musk compounds in water samples, *J. Chromatogr. A* 1217 (2010) 2925–2932.
- <sup>428</sup> D.L. Giokas, V.A. Sakkas, T.A. Albanis, D.A. Lampropoulou, Determination of UV-filter residues in bathing waters by liquid chromatography UV-diode array and gas chromatography–mass spectrometry after micelle mediated extraction-solvent back extraction, *J. Chromatogr. A* 1077 (2005) 19–27.
- <sup>429</sup> H.-K. Jeon, Y. Chung, J.-C. Ryu, Simultaneous determination of benzophenone-type UV filters in water and soil by gas chromatography–mass spectrometry, *J. Chromatogr. A* 1131 (2006) 192–202.
- <sup>430</sup> N. Negreira, P. Canosa, I. Rodríguez, M. Ramil, E. Rubí, R. Cela, Study of some UV filters stability in chlorinated water and identification of halogenated by-products by gas chromatography–mass spectrometry, *J. Chromatogr. A* 1178 (2008) 206–214.
- <sup>431</sup> C.P. da Silva, E.S. Emídio, M.R.R. de Marchi, Method validation using weighted linear regression models for quantification of UV filters in water samples, *Talanta* 131 (2015) 221–227.
- <sup>432</sup> C.P. da Silva, E.S. Emídio, M.R.R. de Marchi, UV filters in water samples: experimental design on the SPE optimization followed by GC-MS/MS analysis, *J. Braz. Chem. Soc.* 24 (2013) 1433–1441.
- <sup>433</sup> R. Rodil, M. Moeder, Development of a method for the determination of UV filters in water samples using stir bar sorptive extraction and thermal desorption–gas chromatography–mass spectrometry, *J. Chromatogr. A* 1179 (2008) 81–88.
- <sup>434</sup> M. Kawaguchi, R. Ito, N. Endo, N. Sakui, N. Okanouchi, K. Saito, N. Sato, T. Shiozaki, H. Nakazawa, Stir bar sorptive extraction and thermal desorption-gas chromatography-mass spectrometry for trace analysis of benzophenone and its derivatives in water sample, *Anal. Chim. Acta* 557 (2006) 272–277.

- 
- <sup>435</sup> M. Kawaguchi, H. Ito, R. Honda, N. Endo, N. Okanouchi, K. Saito, Y. Seto, H. Nakazawa, Simultaneous analysis of benzophenone sunscreen compounds in water sample by stir bar sorptive extraction with in situ derivatization and thermal desorption–gas chromatography–mass spectrometry, *J. Chromatogr. A* 1200 (2008) 260–263.
- <sup>436</sup> M. G. Pintado-Herrera, E. González-Mazo, P.A. Lara-Martín, Atmospheric pressure gas chromatography–time-of-flight-mass spectrometry (APGC–ToF-MS) for the determination of regulated and emerging contaminants in aqueous samples after stir bar sorptive extraction (SBSE), *Anal. Chim. Acta* 851 (2014) 1–13.
- <sup>437</sup> M.J. Gómez, M.M. Gómez-Ramos, A. Aguera, M. Mezcua, S. Herrera, A.R. Fernández-Alba, A new gas chromatography/mass spectrometry method for the simultaneous analysis of target and non-target organic contaminants in waters, *J. Chromatogr. A* 1216 (2009) 4071–4082.
- <sup>438</sup> J. Pawliszyn, *Applications of Solid Phase Microextraction*, RSC Press, Cambridge 1999.
- <sup>439</sup> Y. Zhang, H. K. Lee, Simultaneous determination of ultraviolet filters in aqueous samples by plunger-in-needle solid-phase microextraction with graphene-based sol–gel coating as sorbent coupled with gas chromatography–mass spectrometry, *Anal. Chim. Acta* 742 (2012) 67–73.
- <sup>440</sup> P.A. Azar, M.S. Tehrani, S. Mohammadiazar, S.W. Husain, Simultaneous determination of ultraviolet filters in aqueous samples by plunger-in-needle solid-phase microextraction with graphene-based sol–gel coating as sorbent coupled with gas chromatography–mass spectrometry, *J. Sep. Sci.* 35 (2012) 3354–3360.
- <sup>441</sup> B. Bojko, E. Cudjoe, G.A. Gómez-Ríos, K. Gorynski, R. Jiang, N. Reyes-Garcés, , S. Risticovic, E.A.S. Silva, O. Togunde, D. Vuckovic, J. Pawliszyn, Sample preparation with solid phase microextraction and exhaustive extraction approaches: Comparison for challenging cases, *Anal. Chim. Acta* 873 (2015) 14–30.
- <sup>442</sup> A. Mehdinia, M.O. Aziz-Zanjani, Advances for sensitive, rapid and selective extraction in different configurations of solid-phase microextraction, *Trends Anal. Chem.* 51 (2013) 13–22.
- <sup>443</sup> E.A. Souza Silva, S. Risticovic, J. Pawliszyn, Recent trends in SPME concerning sorbent materials, configurations and in vivo applications, *Trends Anal. Chem.* 43 (2013) 24–36.
- <sup>444</sup> C.L. Arthur, J. Pawliszyn, Solid phase microextraction with thermal desorption using fused silica optical fibers, *Anal. Chem.* 62 (1990) 2145–2148.
- <sup>445</sup> Z. Zhang, J. Pawliszyn, Headspace solid-phase microextraction, *Anal. Chem.* 65 (1993) 1843–1852.
- <sup>446</sup> ISO/IEC Guide 98-3:2008: Uncertainty of Measurement – Part 3: Guide to the expression of uncertainty in measurement, Geneva (2008) 120.
- <sup>447</sup> A. Penalver, E. Pocurull, F. Borrull, R.M. Marce, Comparison of different fibers for the solid-phase microextraction of phthalate esters from water, *J. Chromatogr. A* 922 (2001) 377–384.



- 
- <sup>448</sup> Z. Mester, R. Sturgeon, J. Pawliszyn, Solid phase microextraction as a tool for trace element speciation, *Spectrochim. Acta B* 56 (2001) 233–260.
- <sup>449</sup> C.L. Arthur, L.M. Killam, K.D. Buchholz, J. Pawliszyn, Automation and optimization of solid-phase microextraction, *J., Anal. Chem.* 64 (1992) 1960–1966.
- <sup>450</sup> P. Canosa, I. Rodriguez, E. Rubi, M.H. Bollain, R. Cela, Optimisation of a solid-phase microextraction method for the determination of parabens in water samples at the low ng per litre level, *J. Chromatogr. A* 1124 (2006) 3–10.
- <sup>451</sup> M. de F. Alpendurada, Solid-phase microextraction: a promising technique for sample preparation in environmental analysis, *J. Chromatogr. A* 889 (2000) 3–14.
- <sup>452</sup> T. Felix, B. J. Hall, J. S. Brodbelt, Determination of benzophenone-3 and metabolites in water and human urine by solid-phase microextraction and quadrupole ion trap GC–MS, *Anal. Chim. Acta* 371 (1998) 195–203.
- <sup>453</sup> D.A. Lambropoulou, D.L. Giokas, V.A. Sakkas, T.A. Albanis, M.A. Karayannis, Gas chromatographic determination of 2-hydroxy-4-methoxybenzophenone and octyldimethyl-p-aminobenzoic acid sunscreen agents in swimming pool and bathing waters by solid-phase microextraction, *J. Chromatogr. A* 967 (2002) 243–253.
- <sup>454</sup> H. Liu, L. Liu, Y. Xiong, X. Yang, T. Luan, Simultaneous determination of UV filters and polycyclic musks in aqueous samples by solid-phase microextraction and gas chromatography–mass spectrometry, *J. Chromatogr. A* 1217 (2010) 6747–6753.
- <sup>455</sup> S.L.R. Ellison, A. Williams, (eds.) *Eurachem/CITAC Guide: Quantifying Uncertainty in Analytical measurement*, Third Edition, 2012. Available from: [www.eurachem.org](http://www.eurachem.org).
- <sup>456</sup> N. Ratola, L. Santos, P. Herbert, A. Alves, Uncertainty associated to the analysis of organochlorine pesticides in water by solid-phase microextraction/gas chromatography–electron capture detection—Evaluation using two different approaches, *Anal. Chim. Acta* 573 (2006) 202–208.